CRANFIELD UNIVERSITY

PEDRO MIGUEL SEQUEIRA ALMEIDA

PROCESS CONTROL AND DEVELOPMENT IN WIRE AND ARC ADDITIVE MANUFACTURING

SCHOOL OF APPLIED SCIENCES

PhD Thesis

Academic Year: 2011 - 2012

Supervisor: Professor Stewart Williams

April 2012

CRANFIELD UNIVERSITY

SCHOOL OF APPLIED SCIENCES

PhD Thesis

Academic Year 2011 - 2012

PEDRO MIGUEL SEQUEIRA ALMEIDA

PROCESS CONTROL AND DEVELOPMENT IN WIRE AND ARC ADDITIVE MANUFACTURING

Supervisor: Professor Stewart Williams

April 2012

Abstract

This thesis describes advancements in the modelling, optimisation, process control and mechanical performance of novel high deposition rate gas metal arc welding processes for large scale additive manufacturing applications. One of the main objectives of this study was to develop fundamental understanding of the mechanisms involved during processing with particular focus on single layer welds made of carbon steel using both pulsed-current gas metal arc welding and cold metal transfer processes. The effects of interactions between critical welding process variables and weld bead and plate fusion characteristics are studied for single and multi-layers. It was shown that several bead and plate fusion characteristics are strongly affected by the contact tip to work distance, *TRIM*, wire feed speed, wire feed speed to travel speed ratio, and wire diameter in pulsed-current gas metal arc welding. The arc-length control, dynamic correction and the contact tip to work distance are shown to strongly influence the weld bead geometry in the cold metal transfer process. This fundamental knowledge was essential to ensure the successful development of predictive interaction models capable of determining the weld bead geometry from the welding process parameters. The models were developed using the least-squares analysis and multiple linear regression method.

The gas tungsten constricted arc welding process was utilised for the first time for out-of-chamber fabrication of a large scale and high-quality Ti-6Al-4V component. The main focus was, however, in the use of the cold metal transfer process for improving out-of-chamber deposition of Ti-6Al-4V at much higher deposition rates. The effect of the cold metal transfer process on the grain refinement features in the fusion zone of single layer welds under different torch gas shielding conditions was investigated. It was shown that significant grain refinement occurs with increasing helium content. The morphological features and static mechanical performance of the resulting multi-layered Ti-6Al-4V walls were also examined and compared with those in gas tungsten constricted arc welding. The results show that a considerable improvement in static tensile properties is obtained in both testing directions with cold metal transfer over gas tungsten constricted arc welding. It was suggested that this improvement in the mechanical behaviour could be due to the formation of more fine-grained structures,

which are therefore more isotropic. The average ultimate tensile strength and yield strength of the as-deposited Ti-6Al-4V material processed via cold metal transfer meet the minima specification values recommended for most Ti-6Al-4V products.

Neutron diffraction technique was used to establish the effect of repeated thermo-mechanical cycling on the generation, evolution and distribution of residual stresses during wire and arc additive manufacturing. The results show a significant redistribution of longitudinal residual stresses along both the substrate and multi-bead with repeated deposition. However, a nearly complete relaxation occurs along the built, once the base plate constraint is removed.

Keywords:
Additive manufacturing, arc welding, wire and arc additive manufacturing, cold metal transfer, pulsed-current gas metal arc welding, Ti-6Al-4V, weld bead geometry, regression analysis, residual stresses, neutron diffraction.

to my dearly beloved Eli

for her infinite support, source of strength, and unconditional love

Acknowledgments

I gratefully acknowledge the funding sources and those who made this doctoral thesis possible. This work was conducted as part of the EPSRC/IMRC sponsored project called Ready to Use Additive Manufacturing (RUAM) with significant funding from industry, in particular Airbus UK.

I would like to express my sincere gratitude to my supervisor Professor Stewart Williams for the support and guidance showed throughout this research work, and for the opportunity to join the welding research group at Cranfield University. I would also like to extend my gratitude to all lecturers, co-workers and friends involved, in one way or another, in the Ready to Use Additive Manufacturing (RUAM) research program.

I am most grateful to Professor Luisa Coutinho for her vote of confidence, friendly help and advice, which have led to an enjoyable, educational, and stimulating experience overseas.

My very special thanks go out to the technical staff of the welding engineering and laser processing centre, Fleming Nielsen and Brian Brooks, for their support, patience and valuable assistance throughout this research work.

And to my colleagues and dearest friends who fought hard alongside on their PhD's during the last years, in particular Nuno Pépe, Hua Wang, Suder Wojciech, Eurico Assunção, Tamas Nagy and Matthew Rush. In particular, I am truly indebted and thankful to both Tamas Nagy and Matthew Rush for their help and support in so many different ways.

I would like to thank my parents Amélia and José for the love and support they have provided me throughout my entire life. Words cannot express my heartfelt gratitude, appreciation, and thanks to the Smith's family, Shelli, Willow, Ginge, Socks, Kitty, and Flo for their love and kindness, and for making me feel so at home.

Finally, my deepest gratitude and appreciation goes to my beloved life partner Eli for her unending patience, sacrifice, understanding, and support, which has given me the motivation and strength to realising this achievement.

Table of contents

List of figures

List of tables

Acronyms

A_1	Penetration area
A_2	Reinforcement area
AC	Alternating current
AE	Arc energy
AIP	Average instantaneous power
ALC	Arc-length control
AM	Additive manufacturing
AMF	Additive manufacturing file format
ANOVA	Analysis of variance
ANSI	American national standards institute
AP	Arcing period
AR	Aspect ratio
BTF	Buy-to-fly
BR	Burn-off rate
CA	Contact angle
CAD	Computer aided design
CALM	Centre for additive layer manufacturing
CAM	Computer aided manufacturing
CC	Constant current
CCD	Charged coupled device
CFRP	Carbon fibre reinforced polymer
CIMRC	Cranfield innovative manufacturing research centre
CLSM	Confocal laser scanning microscopy
CMT	Cold metal transfer
CNC	Computer numerical control
CO_2	Carbon dioxide
CTE	Coefficient of thermal expansion
CTWD	Contact tip to work distance
CV	Constant voltage
CW	Continuous-wave
D	Dilution

DC	Direct current
DCEP	Direct current electrode positive
DC_{orr}	Dynamic correction
DDM	Direct digital manufacturing
Delta-z	Relative bead height increment
d.f.	Degree-of-freedom
DLF	Direct laser fabrication
DMD	Direct metal deposition
DMLS	Direct metal laser sintering
DoE	Design of experiment
DR	Deposition rate
DSLS	Direct selective laser sintering
DX	Design expert
E	Young's modulus
EADS	European aeronautic defence and space /company
EBW	Electron beam welding
EBM	Electron beam melting
EMA	Electromagnetic action
ε_{max}	Percentage elongation at fracture
EMS	Electromagnetic stirring
EPSRC	Engineering and physical sciences research council
f	Frequency
FCAW	Fluxed cored arc welding
FEA	Finite element analysis
FEM	Finite element modelling
FGM	Functionally graded materials
FL	Fusion line
FZ	Fusion zone
GMAW	Gas metal arc welding
GMAW-P	Pulsed gas metal arc welding
GTAW	Gas tungsten arc welding
GTCAW	Gas tungsten constricted arc welding
H	Bead height

HAZ	Heat affected zone
HI	Heat input
HIP	Hot isostatic pressing
H_n	Relative bead height increment of the n^{th} layer or Delta-*z*
HSL	Heat source length
I	Welding current
I_{AVG}	Average current
I_{AP}	Arcing period current
I_b	Base current
I_{inst}	Instantaneous current
I_p	Pulse current
I_{SCP}	Short circuiting period current
IMRC	Innovative manufacturing research centre
I_b	Background current
I_p	Pulse current
L_0	Original gauge length
L-direction	Longitudinal direction to the rolling
LAM	Laser additive manufacturing
LADMD	Laser assisted direct metal deposition
LALM	Laser additive layer manufacturing
LDC	Load duty cycle
LENS	Laser engineering net shape
LLM	Laser layered manufacturing
LMDS	Laser metal deposition shaping
LT-direction	Longitudinal transverse direction to the rolling
L_u	Final gauge length after fracture
MAM	Metal additive manufacturing
MDE	Metal deposition efficiency
MLR	Multiple linear regression
MS	Mean square
NHAZ	Near heat affected zone
NSS	Neutron strain scanner
OCV	Open-circuit-voltage

ODPP	One droplet per pulse
P	Penetration depth
PAW	Plasma arc welding
PM	Parent metal
PRESS	Prediction error sum of squares
PS	Plane stress
RAMAC	Rapid manufacture of high integrity aerospace components
RAPOLAC	Rapid production of large aerospace components
RESW	Resistance electro slag welding
RM	Rapid manufacturing
RP	Rapid prototyping
RP&T	Rapid prototyping & tooling
RR	Remelting ratio
RS	Residual stress
RSM	Response surface methodology
RT	Rapid tooling
RUAM	Ready to use additive manufacturing
SAW	Submerged arc welding
SCP	Short circuiting period
SDM	Shape deposition manufacturing
SEA	Systematic experimental approach
SFF	Solid freeform fabrication
SIGMA	Shielded inert gas metal arc
SLS/M	Selective laser sintering/melting
SM	Shape melting
SMAW	Shield metal arc welding
SMD	Shaped metal deposition
SMT	Shape melting technology
S/N	Signal-to-noise ratio
SS	Sum of squares
StdErr	Standard error
SW	Shape welding
SW_{av}	Surface waviness

T_b	Duration of background current
TE	Tissue engineering
THP	Thermohydrogen processing
TOF	Time-of-flight
T_p	Duration of pulse current
TRL	Technology readiness level
TS	Travel speed
T_{sub}	Substrate/interpass temperature
UTS	Ultimate tensile strength
VI	Volt-ampere characteristic
VIF	Variance inflation factor
V_{inst}	Instantaneous voltage
VP-GTAW	Variable polarity gas tungsten arc welding
W	Bead width
WAAM	Wire and arc additive manufacturing
WELPC	Welding engineering and laser processing centre
WERC	Welding engineering research centre
WD	Wire diameter
WFS	Wire feed speed
W_{eff}	Effective wall width
W_n	Maximum bead width of the n^{th} layer
WM	Weld metal
YS	Yield strength
2D	Two-dimensional
3D	Tree-dimensional
3D Welding	Three-dimensional welding

Publications

The following documents have been reproduced partially from this dissertation:

Sequeira Almeida, P. M. and Williams, S. (2010a), Innovative process model of Ti–6Al–4V additive layer manufacturing using cold metal transfer (CMT), in: *Proccedings of the 21st Annual International Solid Freeform Fabrication Symposium*, August 9-11, The University of Texas at Austin, Austin, Texas, USA, p. 25-36.

Ding, J., Colegrove, P., Mehnen, J., Ganguly, S., Sequeira Almeida, P. M., Wang, F., and Williams, S. (2011), Thermo-mechanical analysis of wire and arc additive layer manufacturing process on large multi-layer parts*, Computational Materials Science*, **50**(12), p. 3315-3322.

Sequeira Almeida, P.M., Williams, S., Wang, F., Kazanas, P., Ding, J., and Martina, F. (2011) Wire plus Arc ALM: Developments for large scale aircraft metal components, in: *22nd Advanced Aerospace Materials and Processes Conference and Exposition (AeroMat 2011)*, May 23-25, Long Beach Convention Center, Long Beach, California, USA.

Kazanas, P., Deherkar, P., Sequeira Almeida, P. M., Lockett, H., and Williams, S. (2012), Fabrication of geometrical features using wire and arc additive manufacture, *Proceedings of the Institution of Mechanical Engineers, Part B: Journal of Engineering Manufacture*, **226** (6), p. 1042-1051 (first published on February 22, 2012).

1 Introduction

1.1 Project introduction

This dissertation was part of a major four year £2m IMRC/EPSRC research project denominated by Ready to Use Additive Manufacturing (RUAM). This project was established by Cranfield Innovative Manufacturing Research Centre (IMRC) as a result of a recent surge in interest in metallic additive manufacturing (AM) technology (see section 1.2). The project was partially funded by the Engineering and Physical Sciences Research Council (EPSRC) and by significant industrial input from Airbus UK, Bombardier Aerospace UK, EADS Astrium, BAE Systems, Alstom, Lockheed Martin, Messier Dowty, Doncasters, amongst others.

The aim of the RUAM project was to supply leading edge manufacturing industry with technological capability in order to increase the ability to fabricate net shape functional metallic components with high aggregate value for a wide range of applications, *e.g.* aero engine and airframe components. The goal of the project is to integrate wire and arc additive manufacturing (WAAM) technology, subtractive technology, *e.g.* multi-axis precision grinding or milling, process modelling, and design rules and guidelines on the same machine.

The project was initially divided in two phases. In the earlier phase, fundamental research and optimisation methods have concentrated on WAAM and subtractive technologies, as well as three-dimensional (3D) shape and deformation measurement, whereas in the second phase integration took place.

The scientific knowledge and technology know-how generated through the RUAM research project aimed at contributing to the development of different WAAM systems as follows:

- A relatively high cost and large working envelope system with increased functionality for producing titanium and other high-value components.

- A relatively low cost and small working envelope system suitable for the production of general engineering components, *e.g.* steel.
- An integrated WAAM system with subtractive technology, *e.g.* grinding or milling.

This dissertation focuses on the control and development of WAAM deposition technology for integrating in the automated systems (a) and (b) referred to above.

1.2 Background

Additive manufacturing (AM) technologies have over 80 years of history. AM is becoming an increasingly important technology in the manufacturing field for direct fabrication of structural metal components. The basic and common principle of these AM technologies involves the direct production of 3D objects from computer aided design (CAD) data by adding material in layers.

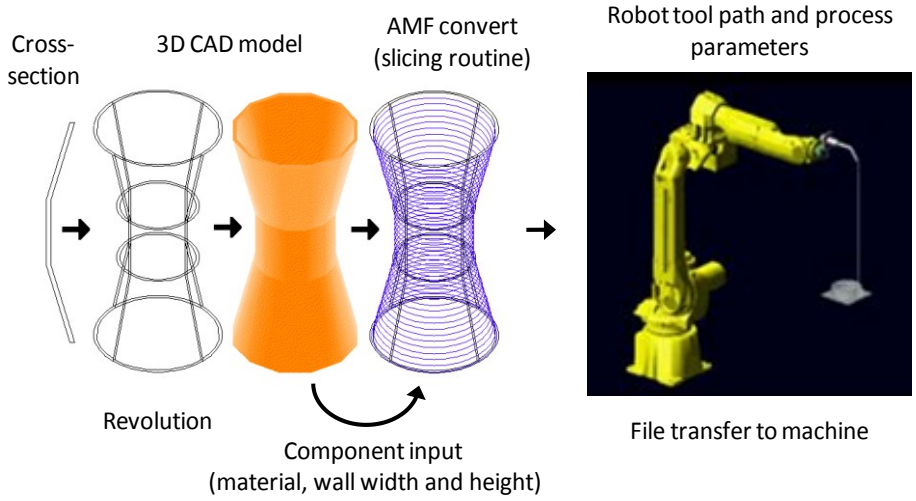

Figure 1.1. The generic additive manufacturing file format conversion and robot tool path generation processes (adapted from Ribeiro (1998)).

Typically, the 3D CAD representation is converted into a XML-based format, *i.e.* additive manufacturing file format (AMF)[1], allowing the external closed surfaces of the model to be described and subsequently sliced by a computer into a number of discrete planar layers. Tool paths are then calculated from the slicing routine and process

[1] According to ASTM F2915 - 11: Specification for additive manufacturing file format (AMF).

parameters derived, which are uploaded to the AM equipment *e.g.* robot, in order to build the pre-defined geometry in a layer upon layer sequence from the bottom-up (see Figure 1.1).

Although, the research and industrial activity worldwide in the metal additive manufacturing (MAM) field have been carefully documented throughout the years, AM technologies have been described using a variety of terms such as solid freeform fabrication (SFF), direct metal deposition (DMD), electron beam melting (EBM), 3D welding, shaped metal deposition (SMD), laser additive layer manufacturing (LALM), laser engineered net shaping (LENS®), amongst others. In general, many of these AM terms are defined according to: the heat source utilised for melting/sintering the raw material, *e.g.* focused laser or electron beam, or arc; feedstock material, *i.e.* wire and/or powder form; feedstock delivery, *i.e.* powder on bed or coaxial; or system configuration, *i.e.* purely additive or additive/subtractive processes.

1.3 Challenges in modern manufacturing industry

Nowadays, modern manufacturing industries, such as automotive and aerospace, are continuously seeking applications and systems that enable direct production of large and relatively complex full density metal parts, with low production volumes, high structural integrity, accurate dimensions, and that can be directly used in operational systems.

In recent years, there has been a growing interest in the use of rapid manufacturing (RM) for direct fabrication of near net shape, fully dense end-use metallic components with fully functional capability. The key advantages of these manufacturing processes are minimum waste, tool-less production, reduced “time to market”, and cost-effective low batch manufacturing. The economic benefits and environmental impact of the manufacturing technology used becomes even more significant in the fabrication of components with high aggregate value, *e.g.* titanium, nickel, and aluminium alloys and stainless steels, when compared with traditional machining methods.

Titanium and its alloys are used extensively in aerospace industries because of their high specific strength and thermal and electrochemical compatibility with advanced

composite materials. Demand for aerospace titanium mill products is expected to increase at 14 % per annum until 2015 (Bihlman, 2010). However, components made from titanium and titanium alloys are very expensive when compared with other metals. The extraction and production of titanium sponge are highly energy intensive processes, and titanium alloys are classified as "difficult-to-machine" materials.

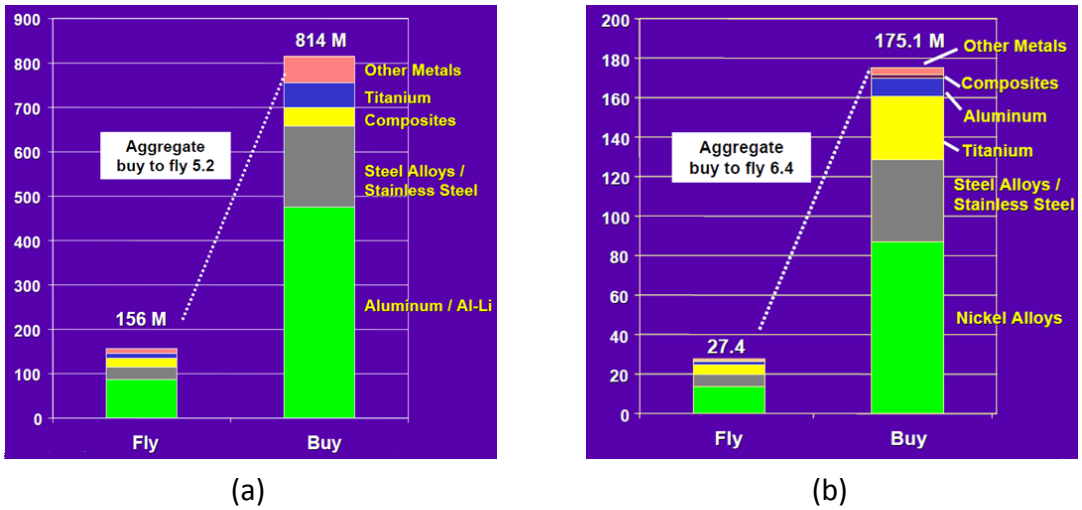

Figure 1.2. Total fly and buy weight in million pounds for (a) airframes and (b) aero engines production. Buy weight figures exclude the impact of recycling (source: *Aerostrategy 2008*).

Moreover, titanium aircraft components used in airframes and aero engines are typically machined out from a solid block or a forged blank. The former manufacturing technique, *i.e.* machining, consumes more material and produces more waste than forging methods. Nevertheless, forging combined with machining is more inflexible to new design requirements due to the high costs associate with changes to the die. Additionally, the forging process is expensive and there is a long lead time from design to production.

The buy-to-fly ratio (BTF) reflects the material efficiency of a manufactured component and is often referred to within the aerospace community to establish the amount of material needed to purchase in order to manufacture the final "flying" part. Traditional machining methods typically produce components with average BTF ratios of 5:1, but sometimes greater than 20:1 (Arcella and Froes, 2000), due to large amount of waste and difficult-to-recycle material (see Figure 1.2). Therefore, the development of new low-cost and more efficient manufacturing methods is critical for improving BTF ratios and to meet future sustainable manufacturing requirements. AM technologies are being

considered for many high-tech industries due to their great potential for rapid production of high quality parts with minimal waste.

Wood (2009) suggests that widespread adoption of AM technologies could reduce titanium ore extraction to a 25th of the current amount when compared with current fabrication processes, such as forging, machining or casting. Moreover, Wood (2009) also highlights that this decline in the extraction of titanium ore would lead to drastic falls in carbon dioxide (CO_2) emissions - extracting 1 kg of titanium from titanium ore produces 9 t of CO_2. Potential environmental and economic benefits of metal AM technologies over conventional machining, forming and joining processes have been well documented elsewhere (Froes *et al.*, 1980; Groneck and Harmon, 2003).

Figure 1.3. Topology optimised A380 stainless steel bracket fabricated with conventional method (back) and using direct metal laser sintering technology (front). (Image courtesy of EADS Innovation Works, centre for additive layer manufacturing).

There is a wide range of commercial and fully automated powder based MAM systems, which rely mostly on laser and electron beam welding (EBW) technology as localised heating sources. In these systems the heat source consolidates by sintering/melting metallic powders in order to produce or remanufacture extremely complex structures, while increasing the potential for structural optimisation and weight saving (see Figure 1.3).

However, metal powder based AM systems have several critical constraints, namely:

1. Low deposition rate and processing speeds leading to high specific cost
2. Low alloy efficiency
3. High capital cost of systems
4. Cost, quality and availability of consumables
5. Small build volumes
6. Poor material properties with often a need for post processing

These constraints make them an unsuitable and costly option for large component manufacture. In order to overcome these limitations, recent developments in the field of arc welding have led to a renewed interest in high deposition rate MAM systems by using arc welding deposition processes. Wire and arc additive manufacturing (WAAM) techniques have now expanded the MAM market from small scale and high-resolution parts to large scale manufacture. The real breakthrough for these WAAM techniques would be new fabrication methods to produce customised metal components with deposition capacities ranging from several kilograms to a few tonnes at a much lower build and investment cost.

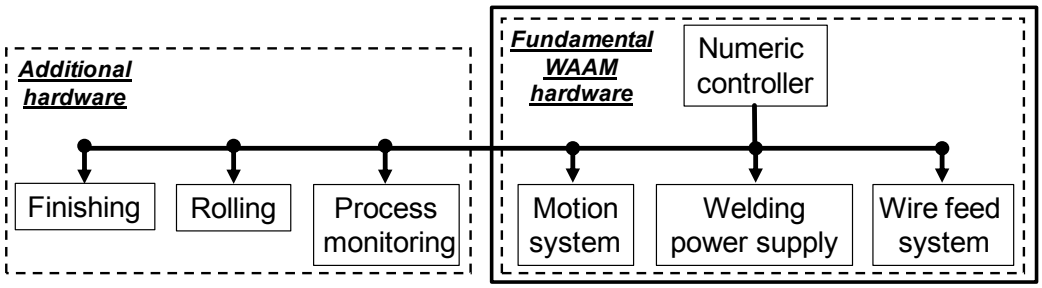

Figure 1.4. Schematic showing the basic and additional hardware of a wire and arc additive manufacturing system.

Figure 1.4 schematically shows the fundamental and additional hardware elements that comprise the automated WAAM system. A number of different arc welding processes, such as gas metal arc welding (GMAW), gas tungsten arc welding (GTAW), plasma arc welding (PAW), or submerged arc welding (SAW), can be employed as heating sources. The retrofitting of a basic WAAM system with a standard three or five axis computer numerical control (CNC) milling or machining centre is also possible.

1.4 The research challenges

Since the late 1960s, considerable efforts have been put into researching WAAM using high deposition rate arc welding systems, such as SAW and GMAW. A substantial level of automation and computer monitoring control was utilised, for example, in shape melting (SM) and shape welding (SW) technologies (Kußmaul *et al.*, 1983; Doyle, 1991).

Online process controls were assured by a number of automated techniques and auxiliary equipment in order to guarantee the highest quality requirements of the shape welded components produced. The automated production station was integrated with motion and process control system via a robotic controller. Cleaning devices were incorporated in the system to remove oxides and surface contaminants from the welded metal, while water vapour cooling nozzles and heating devices were employed to control temperature. This research and development was, however, driven mainly by the heavy industries' interest (*e.g.* power generation, nuclear, chemical and petrochemical) in manufacturing large components, originally derived for relatively simple rotational geometries with thick-walled sections mainly of low alloy ferritic and martensitic steels. Although on the brink of being commercially adopted, these solutions have not spread widely.

It was believed that a high level of knowledge and technical expertise in arc welding, residual stress engineering, and distortion were still required for industrial implementation of WAAM. SW technology was still posing significant technical risks, in particular in fabricating large components in more complicated shapes and high-strength materials. In addition, the market demand and prices for heavy components from nuclear industry had fallen since the mid-1980s, which eventually lead to a significant capital investment in new technological development. Possibly, these can be considered the main reasons to be put forward to explain why commercial systems for WAAM technology are still not available nowadays on any scale. The scientific understanding of numerous process variables in real time involved in WAAM technology is critical in order to control microstructures, residual stress, and the final geometry of the part to achieve higher dimensional tolerances. A complete automated

WAAM system would include the support control software shown in Figure 1.5. The intellectual property of the WAAM system, which is embedded in the support control software, resides in the process, materials and design knowledge bases. At the beginning of the RUAM project none of these were available. In particular, the process algorithms needed to control the deposition process were not known.

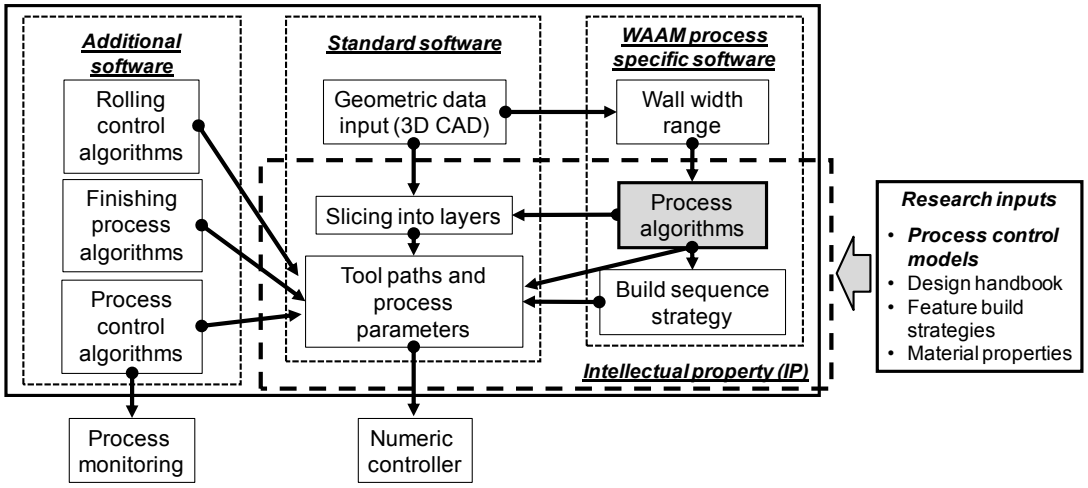

Figure 1.5. Schematic showing the control software supporting a fully automated WAAM system. Process algorithms for controlling weld bead shape is shaded grey in figure.

Several studies have been carried out in the past on the relationship between process parameters and bead geometry in arc welding for single and multi-pass deposition due to an increasing demand for welding automation and quality in the last half century (Shinoda and Doherty, 1978; McGlone, 1982; Benyounis and Olabi, 2008). However, there are still insufficient data available for inclusion in commercial WAAM systems. This is especially so for the newer welding process variants available for both GMAW and GTAW. ***The development of accurate process control models capable of determining the weld bead geometry and plate fusion characteristics of the deposited beads from the welding process parameters is one of the crucial software components for WAAM technological and commercial development which would lead to widespread industrial application***.

In the 1990s, shaped metal deposition (SMD) was originally developed at the Welding Engineering Research Centre (WERC) in Cranfield University. Numerous arc welding approaches were employed in the fabrication of high temperature materials for aero engine components and lightweight structures (Ribeiro, 1995; Ribeiro *et al.*, 1997;

Serrano, 1999). One of the key developments of this process was to combine deposition with a robotic system. Consequently the focus for research was on development of slicing routines and implementation into a robotic manipulator. Mostly this was done using GMAW and GTAW, and applied to relatively simple single walled parts with a focus on titanium and aluminium. Due to a non-disclosure agreement the technology was not developed further at Cranfield but has been used in production for several years by Rolls-Royce. Meanwhile, new and innovative commercial arc welding technologies that produce spatter free welds at relatively low net heat input became available, such as cold metal transfer (CMT) and gas tungsten constricted arc welding (GTCAW). In addition, these leading edge arc welding technologies would offer the potential for microstructure optimisation due to better control over melt pool solidification.

GMAW has significant economic and technical advantages over GTAW practices for WAAM technology, particularly for large scale manufacture. The productivity levels can be increased dramatically with the use of GMAW because of its higher deposition rate capability of several kilograms per hour, when compared to that of GTAW. Another major advantage of GMAW is the design flexibility offered by the coaxial wire feeding, which allows additive patterning of more intricate objects independently of torch orientation, and therefore the translational omni-directionality, and also facilitates positional welding. However, the wandering of the cathode spot onto the sides is a major problem in conventional GMAW of titanium and titanium alloys, which causes arc instability, severe spattering conditions and imprecise weld bead placement. ***A key question is whether the new variants of GMAW are suitable for WAAM applications, especially in titanium***.

One of the most critical issues in WAAM is the build-up of residual stress-induced warping and deformations, which can lead to unacceptable losses in dimensional tolerance and premature failure (Klingbeil *et al.*, 2002; Mughal *et al.*, 2005; Alimardani *et al.*, 2007). The problem has often limited the use of the welding-based technology in the manufacturing of some potential, and more critical, applications in the aerospace industry. ***Therefore, there is a crucial need to better understand how residual stresses generate and develop during WAAM in order to define potential strategies for mitigating their effects on distortion and mechanical properties.***

1.5 Aims and objectives

The aim of this research was to improve the control, understanding and influence of key GMAW process variables in WAAM technology by:

- Investigating the use of process algorithms to control weld bead geometry.
- Determining the suitability of GMAW processes for WAAM of titanium.
- Providing better understanding of residual stress generation, development and tolerance loss in WAAM.

The specific following objectives were set:

1. Investigate the benefit of CMT technology compared to other GMAW variants, such as pulsed-current gas metal arc welding (GMAW-P) for WAAM.
2. Study the relationship between arc welding parameters and weld bead geometry in single and multi-layer deposits.
3. Develop process control algorithms based on this study.
4. Evaluate the process behaviour and stability in GMAW of titanium.
5. Investigate the suitability of CMT welding process for titanium deposition when compared with GMAW-P and DCEP-GMAW.
6. Develop a process control algorithm for titanium deposition.
7. Study the build-up of residual stresses of WAAM structures.

1.6 Thesis outline

The overall structure of this dissertation takes the form of nine main chapters, including this introductory chapter. Chapter 2 gives a description of the state of development of rapid manufacturing technologies where particular attention is given to high deposition rate metal additive manufacturing technologies. Fundamentals of the state of the art CMT welding process and typical issues associated with conventional GMAW titanium deposition are described. The neutron diffraction principles and governing equations are also reviewed, and a particular emphasis is given to the ENGIN-X strain scanner at ISIS.

A detailed description of the experimental procedures utilised along different steps of this research study is presented in chapter 3. The base materials, welding consumables, metallographic preparation and data acquisition methods are provided. The chapter concludes with detailed procedures employed for the development of the process control models.

The main scientific outcomes of this work are reported in chapters 4 to 8, where part of the results presented in chapters 4, 7, and 8 were submitted for publication. Chapter 4 presents the findings of the process control model development of single and multi-layer welds in mild steel. These results include detailed and fundamental characterisation of the CMT and GMAW-P processes. Chapter 5 discusses the results presented in chapter 4, focusing on the effects of the process parameters on both the weld bead shape and metal transfer characteristics, while chapter 6 draws the main conclusions of the study. Chapter 7 describes the application of novel arc welding solutions, such as CMT and GTCAW, in the fabrication of large structural Ti-6Al-4V components using WAAM technology. In the same chapter, static tensile properties of the as-deposited Ti-6Al-4V component fabricated with CMT are determined. The second part of the chapter focuses on the influence of shielding gas composition on grain size distribution and morphology of single and multi-layer welds.

In chapter 8, the generation of residual stresses and their development during WAAM of rectilinear components made of mild steel is investigated. Neutron diffraction technique was applied to establish the influence of repeated WAAM thermo-mechanical cycling on the generation, evolution and distribution of the residual stress field.

Chapter 9 summarises the overall conclusions of the research work and identifies some potential areas for further research.

2 Literature review

2.1 Advanced manufacturing industries: Challenges and opportunities

Nowadays, advanced manufacturing industries such as aerospace, automotive and medical, face great challenges due to escalating customer and societal demands, driving the imperative for superior product quality requirements and sustainable products and processes. In order to stay competitive and thrive in the global market advance manufacturers are required to remain innovative, produce high quality products in the most dynamic way, at reasonably low cost and in a sustainable manner. In high technology industries the product profit cycles are shrinking, and global competition requires manufactures to reduce their delivering schedules while fulfilling customer needs (Raja *et al.*, 2006). Aerospace manufacturers are required to produce functional and customised high-integrity metallic engineering components in low volumes. Besides the stringent technical specification requirements in the aerospace industry for higher quality, accuracy and resolution, there is still a need to reduce the purchase price, which can only be attained by reducing the product development cycle and/or production time in the factory.

Numerous studies have attempted to identify the general requirements of next generation manufacturing companies in the competitive, and ever-changing, manufacturing environment by recognising that to survive these enterprises must be able to react to changes rapidly and cost effectively (Koren *et al.*, 1999; Mehrabi *et al.*, 2000; Bi *et al.*, 2008). These requirements can be summarised as follows:

1. **Short lead-time**[2]**.** New and fast product introduction to the market is an advantage over potential competitors, which typically implies higher profit margins, larger share of the market and higher reputation.
2. **More product variants.** Products need to become more versatile in order to allow for additional functions and features, as well as extensive customisation.

[2] Lead-time means the time to design and build or reconfigure the manufacturing system, and to ramp-up to full-volume, high quality production (Koren *et al.*, 1999).

3. **Low and fluctuation volumes.** Required product volumes are falling because (1) market niches are now shared by global competitors; (2) the life cycles of products are becoming shorter and products are more reliable; (3) of product customisation that fragments the market in smaller portions.
4. **Low product price.** Reasonable purchase price is a primary feature to most costumers, since globalised markets offer more windows to purchase low-price products with similar quality and service. The price margin of a product can reach its limit very soon after market introduction making its price heavily time-dependent.

The fact that production volumes and product life cycles have both tumbled over the past decades has been well documented in more recent years. For instance, previous studies have reported that the average life cycle for electronic products declined from 9 to 4 years (56 % reduction) between 1965 and 1990, whilst the product life cycle for car components fell by nearly 28 % between 1981 and 1991 (Ettlie and Stoll, 1990; Syan and Menon, 1994).

In particular, the United Kingdom aerospace sector faces increased competition from nations such as United States, Spain, Germany, Singapore, and Russia. Emerging markets such as China, India, and Brazil are also looking to increase their share of the global market. With 17 % global market share, the UK aerospace sector is the largest in Europe and second largest in the world after the US (IMechE, 2011). The UK aerospace sector has long-established a world-class reputation for high quality manufacturing in areas such as aero engines, wings, landing gear and flight control systems. For instance, the expertise and production capacity of the UK aerospace sector means 25 % of the value of a Boeing Dreamliner and 50 % of an Airbus A380[3] are produced in the UK (IMechE, 2011).

Meanwhile, advanced manufacturing industries have also focused on instruments to further strengthen the UK competitive advantage in environmental issues and sustainable manufacturing. In order to achieve progress towards sustainable

[3] When fitted with Rolls-Royce aero engines.

manufacturing the sector is required to invest in advanced process technologies to improve environmental performance and to comply with stricter environmental regulation.

During the last two and a half decades, researchers have shown an increased interest in additive technologies for producing cost-effective near net shape structures in a layer by layer fashion. Additive manufacturing (AM) technology enables high technology manufacturers to reduce production and material costs, reduce development cycle and lead-time, and improve performance (Taminger *et al.*, 2006). Likewise the rapid manufacture of high integrity aerospace components (RAMAC) project (Raja *et al.*, 2006) has recently demonstrated the economic and environmental benefits to be gained by adopting AM technology. The European Commission also identified AM as one of the future key technologies for sustainable manufacturing (Geyer *et al.*, 2003).

More recent developments suggest that AM technology is gaining momentum through mainstream media coverage as shown by the 25-year old Wohlers Associates, Inc. consulting firm (2012). For instance, AM technology has received significant attention in recent issues of *The Economist* which have started to include a dedicated section named "Digital fabrication" in its topics index in January 2012. One of the most important articles was the cover story, "Print me a Stradivarius" (The Economist, Feb2011a) that briefly surveys hints of the future on how AM technologies will impact the future global economy, along with major implications on the adoption of the technology for manufacturing, jobs, and intellectual property. In the same issue there was another article entitled "The printed world" (The Economist, Feb 2011b) exploring the use of AM technology by *EADS Innovation Works (Filton, Bristol, UK)* for the fabrication of functional aerospace-grade titanium components, or rapid manufacturing (RM), rather than only prototypes. The article also discusses the lower cost and risk associated with the manufacture of high integrity metal components and how this technology is expected to change the world.

In a recent webinar entitled "Emerging Technology Hype Cycle 2010: What's hot and what's not" (Fenn, 2010), Gartner's *Hype Cycle* research report has put strong emphasis on the potential of AM as transformational technology in the trigger phase of the *Hype Cycle* (Fenn and Raskino, 2008), and has been foreseen to hit the mainstream adoption

in the next 5 to 10 years. The latest Strategic Foresight Initiative report sponsored by The Atlantic Council of the US (Campbell *et al.*, 2011) has given great importance and strength to emerging AM technologies, due to their potential disruptive effect, and implications on a global scale.

2.2 From rapid prototyping to rapid manufacturing

Commercial RP systems have been widely used in the last two and a half decades by high end manufacturers as a design visualisation tool, mainly in the aerospace, medical and automotive industries. These RP systems have become more competitive with traditional manufacturing technologies in recent years, by offering clear advantages over current production alternatives, such as injection moulding, casting, and machining. This is due to the short product development cycles, increased components complexity and low and fluctuating product volumes of modern RP systems. RP technologies also provide a certain customisation level with variable production volumes and design freedom, which reduces the number of constraints encountered in traditional manufacturing methods (Hague *et al.*, 2003b; Mehnen *et al.*, 2010).

RP techniques use the underlying concept of layered manufacturing, whereby 3D geometries are created directly from computer aided design (CAD) to produce solid models with layer-by-layer building via the processing of solid sheet, liquid or powder material stocks (Kruth, 1991; Hopkinson and Dickens, 2003; Leong *et al.*, 2003). RP systems typically take 3D shape data of a component, slice this into layers to generate tool paths and more commonly, use laser heating sources to consolidate, sinter or melt the raw material. These models are only to be dimensionally representative of the design so that the concept can be changed and adjusted for best fit for purpose. The additive nature of the process allows the physical part to be rapidly produced in a layer upon layer fashion while the raw material is added. RP technologies are essentially used by designers in the stages of product development and manufacturing cycle for assessing the form, fit and functionality of a design before significant investment in tooling is made (Pham and Gault, 1998). Originally introduced for design optimisation purposes, RP technologies have now been widely adopted to aerospace and automotive industries for building patterns to be used in investment and vacuum casting. Recently, a number

of studies have also demonstrated that RP technologies are emerging in the biomedical industry as powerful methods of producing high quality medical models (Winder and Bibb, 2005), and becoming increasingly more popular for fabricating tissue engineering (TE) scaffolds owing to their advantages over conventional, manual-based techniques (Yang *et al.*, 2002; Leong *et al.*, 2003; Yeong *et al.*, 2004; Khademhosseini *et al.*, 2006).

The RP field has expanded in recent years through the development of commercial systems for RP of structures with very limited structural performance such as resins, water soluble-wax, plastics, ceramics or paper. The rapid physical conversion of a complex component into a solid replica allows the so-called "art to part" in a matter of hours or days, whereas most conventional manufacturing routes would take weeks or months (Raja *et al.*, 2006). Selective laser sintering/melting (SLS/M) is one of the most important and commonly used RP technique that involves the addition of fine powders as a raw material, and a heating laser source to form material layers (*e.g.* nylon, nylon composites, sand wax, and more recently metals). The basic principles of SLS/M machine operation are shown in Figure 2.1.

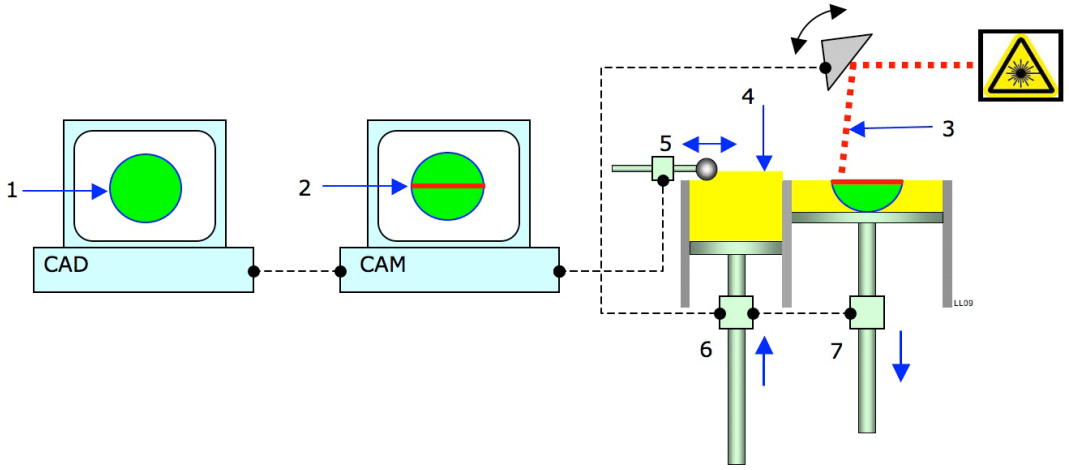

Figure 2.1. Selective laser sintering/melting process showing (1) CAD model, (2) CAM tool path, (3) laser, (4) powder feed, (5) powder feed/levelling roller, (6) powder delivery piston, and (7) fabrication piston (courtesy Wikipedia).

In this technique the laser focused beam (3) is scanned over the surface of the powder bed selectively sintering or melting a patterned layer of the CAD model. When the layer is complete, the powder bed build chamber lowers by a single layer thickness (typically 100μm) by means of a piston (7). A new layer of loose powder (4) provided by the feed chamber is deposited over the bed with a roller (5) and the process is repeated. When

the 3D object is complete the piston (7) is raised, the component removed from the bed, and excess powder is removed.

A considerable amount of worthwhile literature has been published on RP technologies over the last couple of decades. These studies present state-of-the-art overviews of the current RP technologies aiming to provide accurate and authoritative resources about RP operating principles, strengths and weaknesses (Kruth, 1991; Yan and Gu, 1996; Kruth *et al.*, 1998; Pham and Gault, 1998).

The use of RP has been widespread and companies have been more recently established to provide a bureau service to the engineering and research community. Several approaches for producing physical models from various polymeric materials were explored and developed.

A number of major players in the prototyping field came to the conclusion that the real breakthrough in RP technology would only occur with the application of RP technologies for the direct production of end-use products rather than simple prototypes. The impact on the future trend and development of this manufacturing technology was remarkable by opening new windows of opportunity for engineering design and manufacturing of new products and materials, at significantly lower cost. This new manufacturing paradigm based upon traditional RP has led to the concept of rapid manufacturing (RM), or direct digital manufacturing (DDM)[4]. There have been numerous studies published on the potential advantages to be gained with the use of RM technologies for direct components' production (Hopkinson and Dickens, 2001; Hague *et al.*, 2003a; Hopkinson and Dickens, 2003; Levy *et al.*, 2003; Pham and Dimov, 2003).

In particular, the terms RM and DDM of metals represent the use of three dimensional computer aided design (3D CAD)-based automated AM technologies for the fabrication and production of functional metallic long-term models, or end-use products that are used directly as finished products or components (Levy *et al.*, 2003; Hopkinson *et al.*, 2006; Santos *et al.*, 2006; Gibson *et al.*, 2010).

[4] RM is the common definition in the UK and Europe, whilst DDM is preferred in North America.

2.3 Metal additive manufacture

In more recent years, interest has grown for RM applications and systems that provide the capability of producing fully functional parts made of 100 % metal of high structural integrity and within specified dimensional tolerances. The next natural step was to convert traditional RP equipment into robust freeform fabrication systems to produce fully functional parts from powders capable of processing engineering polymers, metals, ceramics and a wide range of composites (Kruth *et al.*, 2007). A considerable amount of literature can be found on the use of RP technologies for the fabrication of structurally sound metal and ceramic parts; for example SLS (Bourell *et al.*, 1992; Agarwala *et al.*, 1995), and stereolithography method (Griffith and Halloran, 1996).

This manufacturing concept evolved from the now mature rapid prototyping & tooling (RP&T) technologies and is currently named as additive manufacturing (AM). AM technologies combine high flexibility and low cost manufacture with the advantages of what is known as the "3F's" provided by RP, *i.e.* **F**orm, **F**it and **F**unction, to produce or repair fully dense components.

A wide range of fully automated metal additive manufacturing (MAM) solutions are currently being commercialised, most commonly in the powder bed configuration. The technology readiness level (TRL)[5] for mass industrial adoption of MAM systems is at a mature technological stage (6 or higher) and it is becoming an increasingly significant manufacturing technology as the part complexity to size ratio increases. In 2006 Kobryn *et al.* (2006) from the US Air Force Research Laboratory (AFRL/ML) reported a TRL of 7 for the AeroMet's LAM^{SM} (laser additive manufacturing) system to producing non-safety-of-flight-critical components, and a TRL of 9 for repairing parts. The maturity of the manufacturing technology was confirmed and further demonstrated when qualified for the production of two airframe components (Boyer and Briggs, 2005).

MAM can be broadly classified in two main categories according to the physical state (or form) of the raw materials utilised in processing: powders (using blown powder and

[5] TRL is a scale from 1 to 10 that indicates how mature a product or technology is prior to incorporating that technology into a system or subsystem.

powder laser bed) and wire based techniques (Kruth, 1991). One such method of direct fabrication is to scan a tightly focused laser beam across the surface of a metallic powder bed, which selectively heats and fuses layers of consecutive cross sections of the CAD model, until a 3D object is built (see Figure 2.1). The other fabrication method involves the supply of blown metal powder, or solid wire, into a thin melt pool that is typically formed due to laser or electron beam heating where the material melts and quickly solidifies into metal layers.

The most common used heating sources in powder based MAM machines are electron beam and laser. Extremely small and highly complex metal parts can be produced, remanufactured or cladded using fine metal powders enabling either weight saving or added functionality to existing or future components (see Figure 2.2).

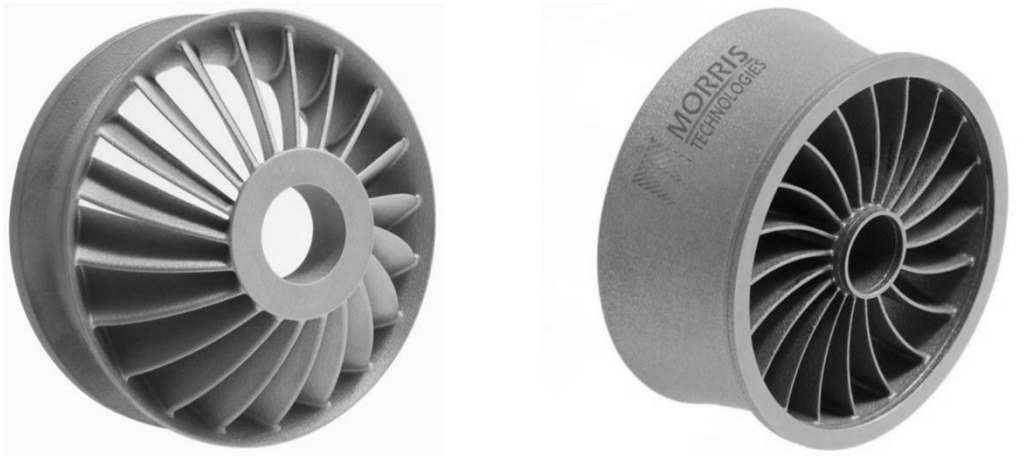

Figure 2.2. Examples of laser-sintered titanium (Ti-6Al-4V) aerospace components fabricated using a 3D EOS laser sintering system (image courtesy of *Morris Technologies, Inc.*).

These structures are made of a wide selection of different materials such as titanium, nickel, cobalt, stainless, tool steel, cermets or refractory materials (Costa and Vilar, 2009). In addition, there is great potential for tailoring and controlling the material composition and properties through the build direction and thickness of the component in order to produce functionally graded materials (FGM), as demonstrated by Kieback *et al.* (2003).

Laser engineering net shape (LENS) (Griffith *et al.*, 1999; Griffith *et al.*, 2000; Vasinonta *et al.*, 2001) or direct laser fabrication (DLF) (Wu *et al.*, 2004), direct metal deposition (DMD) (Mazumder *et al.*, 1997), laser assisted direct metal deposition

(LADMD) (Lewis and Schlienger, 2000), direct selective laser sintering (DSLS) (Agarwala *et al.*, 1995; Das *et al.*, 1999), laser additive manufacturing (LAM) (Kobryn *et al.*, 2000; Kobryn and Semiatin, 2001), laser layered manufacturing (LLM) (Kruth *et al.*, 2007), electron beam melting (EBM) (Cormier *et al.*, 2004; Li *et al.*, 2009), and AeroMet's Lasform (Arcella and Froes, 2000) are some of the most popular beam systems. Santos *et al.* (2006) provides a very comprehensive overview of commercially available laser forming systems and techniques for direct fabrication of metal components. A supplementary list of existing research on MAM techniques using powder materials as feedstock is provided in Table B 1 (see Appendix B).

Commercial laser powder based systems typically feature build rates between few tens to hundreds of grams an hour (Taminger and Hafley, 2003; Bernard and Karunakaran, 2007) and effective build volumes up to about $0.70 \times 0.38 \times 0.58$ m^3 (*e.g.* EOSINT P 730). An important technical and safety requirement of these systems is to use an environmental chamber with controlled atmosphere to prevent contamination in which an inert gas such as argon is filled. These systems also need the powder-bed to be pre-heated in the processing area to minimize thermal distortion and facilitate consolidation of the previous layers. Moreover, processing in these systems is typically carried out inside a high temperature process chamber that can reach up to 800°C (Bertrand *et al.*, 2004). Nevertheless, major practical difficulties need to be overcome in order to reduce the associated building cost of such systems due to the system complexity and slow build rates. These drawbacks are summarised as follows:

1. **Low build rates** and **build volumes** of limited size.
2. **Low capture efficiencies** of the metal powders, typically 10-33 % (Syed *et al.*, 2006; Wang *et al.*, 2007).
3. **Low quality of the metal powder feedstock** as a result of high susceptibility to contamination by oxygen, nitrogen, carbon, hydrogen and other impurities due to the small size of the powder particles and their large specific surface area. Poor quality powder feedstock can detrimentally impact the corrosion and mechanical response of the as-deposited material (Brandl *et al.*, 2009).
4. **Metal powders are required to comply with high specifications**, *e.g.* particle shape control such as surface texture and morphology, size distribution, powder flow, packing density, alloy capability.

5. **Recycling of the metal powders is still difficult** in particular when different powders are sent from different nozzles or oxygen-sensitive materials are used, *e.g.* titanium (Das *et al.*, 1998b; Bernard and Karunakaran, 2007).
6. **Low integrity of the deposited material** resultant from gas porosity and lack of fusion defects (Kobryn *et al.*, 2000; Morgan *et al.*, 2004; Wu *et al.*, 2004; Choi and Chang, 2005).
7. **Post-processing steps such as hot-isostatic pressing (HIP) method is typically necessary** to increase the final density and the mechanical properties in high performance metallic engineering components (Das *et al.*, 1998a; Das *et al.*, 1999).
8. **A subsequent machining step is often needed** to achieve the final form and the required surface quality (Paul and Baskaran, 1996; Syed *et al.*, 2006).
9. **High system investment and running costs** (high power laser up to 30 kW, powder feedstock, argon consumption) (Arcella and Froes, 2000).
10. **Low laser energy efficiency,** since less than 10 % of the plug input energy is converted to beam energy. Beam reflections can go up to 98 % in aluminium and copper (Taminger and Hafley, 2003).
11. **Human intervention is needed for complex shapes** (Bernard and Karunakaran, 2007).
12. **Concerns for the health and safety risks** associated with the use of high power lasers, handling and/or exposure to hazardous reactions of some fine powders, *e.g.* aluminium.

In recent years significant efforts have been put into researching simultaneous powder and wire feeding in order to overcome the foregoing difficulties and disadvantages found when using powder feed alone. For instance, Syed *et al.* (2006) reported an overall increase in deposition efficiency with improvement in surface finish when combining lateral wire and coaxial powder feeding into the same laser generated melt pool. Another important finding was the generation of 20-30 % less porosity in samples produced with simultaneous wire and powder delivery, when compared with samples fabricated with powder feed alone. The important point to note here is that no porosity was found in samples produced with wire feed alone. Recently, Wang *et al.* (2007) successfully demonstrated the feasibility of simultaneous wire (grade Ti-6Al-4V) and powder (TiC) feeding to producing a functionally graded composite material TiC/Ti-

6Al-4V using the DLF technique.

A comparative study of wire and powder feed systems alone was first carried out by Syed *et al.* (2005) using direct laser deposition (DLD) technique. This study examined process characteristics of both feeding methods by cladding tracks side by side and by building walls with four layers height. Significantly higher deposition efficiencies were achieved with wire compared with that obtained with powder feeding, while no discernible microstructural changes were observed within the stainless steel deposits for both methods. The authors showed that compared to powder feed, wire feed has the advantage of forming a more stable melt pool, thus allowing for a better control of the weld pool shape. Wire feeding could also be used more effectively for cladding in position, *e.g.* cladding of the inner wall of a tube (Kim and Peng, 2000). Further, solid metal wires are typically cheaper to manufacture than metal powders.

A considerable amount of literature has been published over recent years focused on metallic wire deposition using laser heating sources for AM applications. The effect of the wire feeding direction, angle and location in the liquid pool formed by a Nd:YAG laser was investigated, for example, to deposit Inconel 600 (Kim and Peng, 2000), 316L stainless steel (Syed and Li, 2005) and Ti-6Al-4V (Mok *et al.*, 2008a). A consensus was reached on the fact that front wire feeding at the leading edge of the melt pool with angles $\leq 45°$ can improve deposition characteristics. Miranda *et al.* (2008) carried out a feasibility study for producing cylindrical Ti-6Al-4V components using a fibre laser with an 8 kW continuous-wave output. The authors considered that the wire position relative to the substrate, *i.e.* angle of attack and the distance between the wire tip and the substrate, as well as the laser beam to wire width ratio were important process parameters affecting the process characteristics. Stable metal transfer conditions, *i.e.* transfer by surface tension, and improved surface finish were successfully achieved with low wire feeding angles. Kim and Peng (2000) have successfully overcome the difficulties associated with the wire melting and drop metal transfer problem by plunging the wire directly into the laser generated melt pool. However, the authors offered no explanation for discarding the rear feeding method.

More recently, several studies investigating microstructure and mechanical properties, *i.e.* hardness and tensile properties, of single wall multi-layer Ti-6Al-4V structures

(Mok *et al.*, 2008b) and Ti-6Al-4V blocks (Brandl *et al.*, 2012), deposited with wire and diode laser have been carried out. The observation of Ti-6Al-4V macrostructures revealed that long columnar prior β-grains were found growing parallel to the build direction across the multiple layers. Layer bands, visible as periodic layers of differential optical contrast, were formed due to reheating of previously deposited material caused by subsequent deposition passes in either case. The band regions formed from the $\alpha + \beta \rightarrow \beta$ solid state phase transformation (β-transus line) were also found in laser deposited powder based Ti-6Al-4V systems (Kobryn and Semiatin, 2001; Kelly and Kamper, 2004). In both studies, hardness tests were conducted in the as-deposited materials with different nominal test force values, showing very good agreement. Static tensile tests carried out on as-deposited single wall multi-layer Ti-6Al-4V structures (Mok *et al.*, 2008b) and Ti-6Al-4V blocks (Brandl *et al.*, 2011b) fulfilled the requirements of as cast material, *i.e.* ASTM F1108. A significant effect of stress relief and β-solution heat treatments on microstructure and mechanical properties was reported.

Although a substantial amount of literature has been published on the influence of processing conditions on laser-deposited Ti-6Al-4V microstructures, porosity, and build heights, these studies have mostly focused on deposition with powder (Brice *et al.*, 1999; Kobryn *et al.*, 2000; Kelly and Kamper, 2004; Wu *et al.*, 2004). Relatively little research has been devoted to laser deposition with wire feeding. Mok *et al.* (2008a) investigated the effect of laser power, traverse speed and wire feed rate on the weight and dimensions of single layer deposits using a systematic approach. It was found that the bead width was mainly determined by laser power, whereas traverse speed was more important in influencing the bead height. The relationship between laser processing parameters and solidification microstructures of Ti-6Al-4V deposits has been reported in (Mok *et al.*, 2008a; Brandl *et al.*, 2011a). It seems clear, however, that laser wire feed methods have serious disadvantages including:

1. **The process is difficult to automate** due to an extremely high sensitivity to orientation and alignment of the wire relative to the laser beam (Vilar, 1999; Pinkerton *et al.*, 2007).

2. **Consistent and reproducible results are difficult to guarantee** due to wire bending and vibration caused by variation of wire tension during feeding. The effect can easily change wire positioning and as a result pool agitation, track perturbations, ripples or serrations are most likely to occur.
3. **The coupling of the laser energy into the material is inefficient and difficult to control** due to variations in wire absorption coefficient and shadowing effect on the surface (Vilar, 1999). Saminen *et al.* (1996) showed that up to 57 % of the incoming laser power may be reflected in the wire-beam[6] with a contribution to the melt drop of about 70 % of the total reflection from the wire.
4. **Dilution levels of about 20 % may become excessively high** as compared to less than 5 % in powder systems (Hensel *et al.*, 1992).
5. **The process is directionally dependent** due to wire feeding from a lateral feed nozzle. The use of a coaxial feeding system becomes advantageous because of its omni-directionality (Lin and Steen, 1998; Pinkerton and Lin, 2004).

Over the past decades a number of researchers have sought to investigate the use of standard arc welding processes, *e.g.* gas metal arc welding (GMAW) and gas tungsten arc welding (GTAW), for the near net shape processing of 3D metal components with high mechanical strength. Wire and arc additive manufacturing (WAAM) has been receiving special attention because of its various advantages in comparison to the traditional fabrication methods such as casting, forging and machining. WAAM technologies have the potential for directly fabricating large volume engineering parts with high structural integrity at high production rate, and thus much lower cost. Table B 2 (see Appendix B) provides a supplementary list of current research on MAM techniques that uses wire material only and wire + powder materials as feedstock.

[6] A structural mild steel wire of 0.8 mm diameter fed at an angle of 45° to the laser beam.

2.4 History and development of wire and arc additive manufacturing

Wire feed weld-based AM techniques have their roots in a 1920 patent filed by Baker (1925) assigned to the *Westinghouse Electric & Manufacturing Company*, who claimed a new method for fabricating 3D metallic objects in a layer-by-layer fashion using arc welding. Receptacles and containers of ornamental shapes (see Figure 2.3) were produced manually by superimposing successive adjacent welded beads utilising a consumable electrode shielded metal arc welding (SMAW) process.

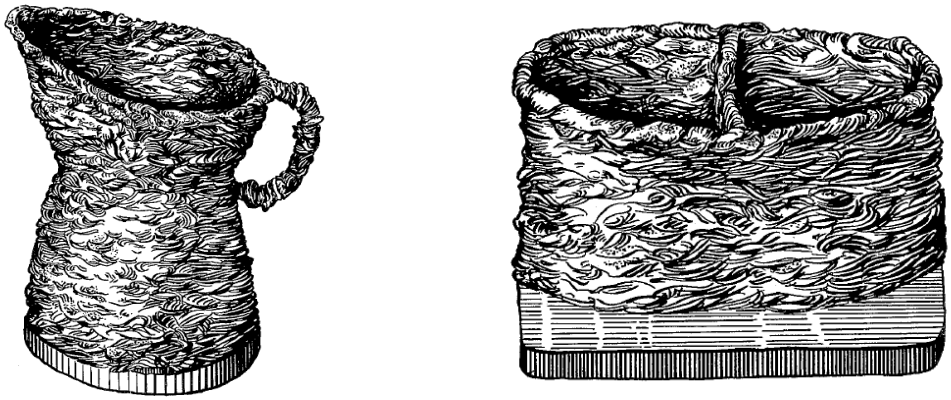

Figure 2.3. Examples of 3D weld-based components created manually in a layer-additive fashion using shielded metal arc welding (Baker, 1925).

The potential benefits of the fabrication technique were clearly foreseen by Baker who pointed out that the method was well suited to mechanization. Technical problems of thermal management related with heat transfer and temperature distributions involved during the thermal processing were at that time described.

In a patent filed in 1920 by Eschholz (1925), a method for forming different types of non-adherent ornaments and structures is reported, and once again using the SMAW process. However, what was perhaps most interesting to note in the work of Eschholz were the contributions made in welding process control and development. This method described the importance of welding process conditions, such as arc current (I), travel speed (TS), or electrode oscillation for controlling the weld bead geometry, such as bead width (W), bead height (H), and penetration depth (P). Moreover, the author had established that the size of the substrate heat sink is a key factor in determining

metallurgical bonding and fusion characteristics. Metallic copper substrates were utilised extensively in applications where very little fusion was required due to the high thermal conductivity and heat capacity of these materials.

The economic benefits associated with wire and arc welding deposition technology enabled its widespread adoption to cladding applications for improving the lifetime of components subjected to abrasive wear. In the 1930 patent of Shockey (1932) a method whereby worn brake drums could be reclaimed more efficiently at much lower cost was described (see Figure 2.4). Single weld beads of resisting abrasive wear material were continuously deposited in a spiral fashion onto a rotating drum until the entire worn surface was cladded.

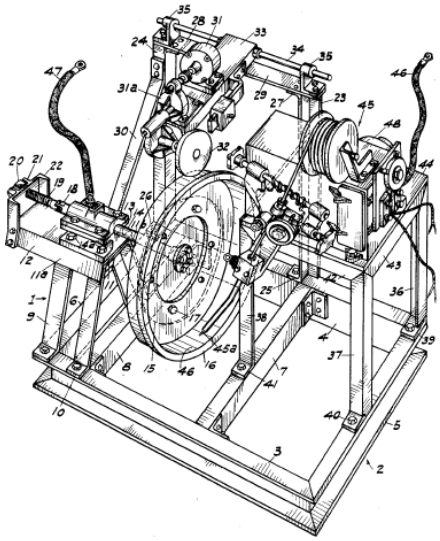

Figure 2.4. Perspective view of the wire and arc welding machine for reconditioning of worn brake drums (Shockey, 1932).

The author concedes that the weld bead dimensions were determined by the welding current and speed of rotation of the drum and adjusted so that one third of the preceding bead overlaps. After this cladding operation was completed, the component was machined to size and placed in service.

Noble (1933), in a patent filed in 1919 and assigned to *General Electric Co.*, disclosed a cost-effective wire feed arc welding mechanism whereby shaft diameters could be enlarged via layer-by-layer approach was firstly described (see Figure 2.5).

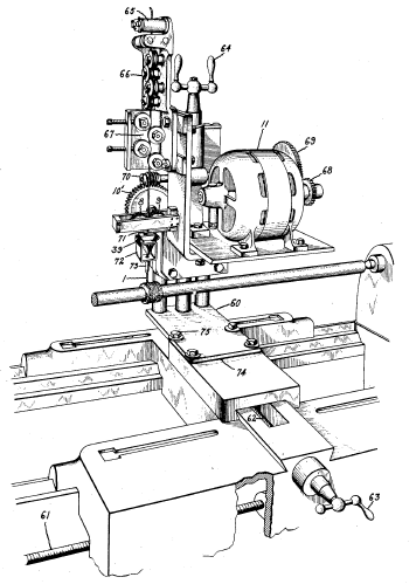

Figure 2.5. Perspective view of a wire and arc welding machine for repair and fabrication of metal shafts (Noble, 1933).

The external diameter of the shaft was increased by continuously depositing layers of welded metal side by side onto the rotating shaft while the welding head was moving parallel to the shaft axis. Additional weld beads could be superimposed by reversing the welding head direction along the longitudinal axis of the shaft, until the desired diameter was reached. Features such as curved or straight flanges could be produced if little or no longitudinal movement was provided to the welding head. In his perceptive work, the author seeks to highlight the crucial need for monitoring and controlling welding process variables, such as arc-length and wire feed rate, in an attempt to automate the process.

Important developments were made by *The Babcock & Wilcox Co.* in a patent application filed in 1943 by Carpenter and Kerr (1947), which have had far-reaching implications in the sector of heavy manufacturing industry. The invention can be considered the precursor of the low cost, fully-automated shape melting technology (SMT) that allowed the rapid fabrication of large-scale near net shaped metal parts. Carpenter and Kerr described a cost-effective cladding method for coating retorts using submerged arc welding (SAW) for depositing alloys with high percentage of chromium (24-27 %) and nickel (19-22 %). These retorts were required to withstanding high temperatures, coupled with severe oxidant and corrosive environments, usually encountered in the process of producing magnesium.

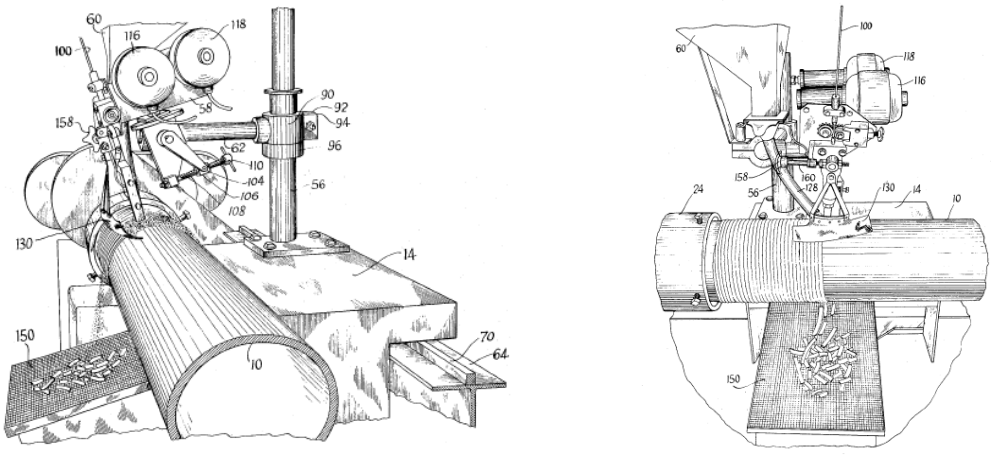

Figure 2.6. Perspective view of a wire and arc welding machine for the manufacture and cladding of retorts (Carpenter and Kerr, 1947).

The low chromium and nickel contents and high amount of oxide inclusions in the cladding resulted in poor quality retorts due to low oxidation/corrosion resistance and high intergranular stress corrosion cracking susceptibility. The cladding method based on wire and arc welding deposition described by the authors revealed how to overcome the shortcomings of previous efforts for producing high-quality retorts.

The most obvious, and perhaps the most important contribution this invention makes from the processing standpoint, is the fact that the automation of the process requires integrated on-line monitoring and process control systems for producing to high quality standards. This method describes a high deposition rate SAW deposition process employed in conjunction with a slag self-cleaning device for laying down weld beads in an elliptical fashion onto a pre-heated rotating retort (see Figure 2.6). The authors have clearly demonstrated that suitable processing conditions were of paramount importance for obtaining better quality cladding results. For instance, low currents (350 to 380 A) and travel speeds (0.5 m min^{-1}) were found to increase and maintain the desired levels of chromium found in the deposited alloy. Surface cracks were eliminated by maintaining the retort member within a temperature range between 205 and 315 ºC. In order to achieve this, water was sprayed or allowed to pass within the retort member. Surface cracks were also reported to be influenced by the weld bead penetration and dilution level, thus welding conditions. Low dilutions were desirable to avoid excessive migration of carbon from the base metal into the cladding alloy, which could result in carbide segregation in the grain boundaries. Attention was drawn to the fact that dilution levels were strongly influenced by the relative angle between the welding head

and the retort member. In addition, the importance of process parameters in controlling the bead geometry for obtaining uniform coatings was highlighted.

A renewed interest in wire and arc welding deposition technology was witnessed in the beginning of the 60s for repairing worn surfaces of large metal pressure rollers, such as roller mills or rolls for compressing vegetable matter or other grains. Rollers were typically prepared from forged or cast solid steel. In the 1962 patent application filed by White (1964) a reconditioning method for repairing pressure rollers by utilising a SAW process was described (see Figure 2.7).

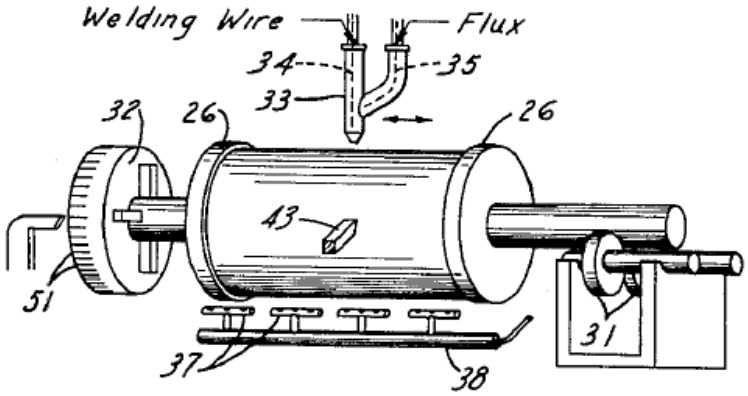

Figure 2.7. Schematic showing the reconditioning method of pressure rollers using wire and arc welding (White, 1964).

The most interesting aspect of this fabrication method was the incorporation of gas burners along the length of the roller. The author argued that pre-heating the roller up to 315 ºC before welding was advantageous for improving wetting and spreading properties of the weld bead. Moreover, a post-weld stress relief heat treatment was for the first time applied for about 2 hours followed by gradual cooling.

Other exciting developments were expedited by *Mitsubishi Heavy Industries Co. Ltd*, in a patent application filed in 1967 by Ujiie (1971), who claimed a low cost method of fabricating thick-walled circular cross section pressure vessels solely by progressively depositing molten weld metal. This manufacturing technique proved to reduce the high cost associated with traditional fabrication of large components from thick plates where large pressers, rollers, annealing furnaces, or welding apparatus would be necessary. In his major study, Ujiie examines for the first time high deposition rate welding processes with a multiple-wire electrode arrangement, such as resistance electro slag welding

(RESW) and shielded inert gas metal arc (SIGMA), for manufacturing large vessels, though, SAW could be also employed (see Figure 2.8(a)).

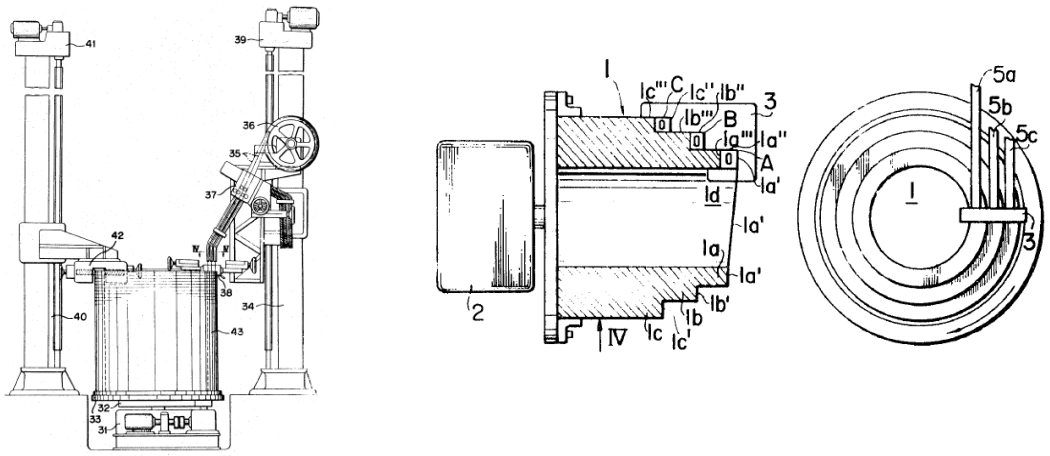

(a) (b)

Figure 2.8. View of (a) the apparatus employed in the manufacture of large thick-walled pressure vessels (Ujiie, 1971), and (b) cross-section of a functionally graded wall (Ujiie, 1972).

The achievement of good mechanical properties of samples extracted from the fabricated wall can be considered the most important accomplishment of this research and development study. The improved mechanical properties resulted from controlled solidification conditions provided by the forced cooling, along with normalization and tempering heat treatment effects caused by progressive deposition.

Ujiie has further developed his project in a patent application filed in 1970 (Ujiie, 1972) where a method of forming functionally graded thick-walled pressure vessels with improved strength is described. The author suggests the use of three wire-electrodes in axially contiguous relation to each other for independently depositing successive convolutions of helical surfaces with different respective radii (see Figure 2.8(b)). One of the most important findings highlighted in this study was that extremely high volumetric build rates, *i.e.* multiple-wire feeding into a single melt pool, were expected to have a significant detrimental effect on material quality. In particular, a large weld pool volume not only contributes to grain coarsening, but also to the formation of blowholes, cracks, and distortion. The second important point emerging from this work from the processing development standpoint relates to the fact that thick-walled components with altered metallurgical compositions through the thickness were possible to be produced. This processing technique enabled the introduction of unique

tailor-made parts with different physical and chemical properties in the bulk and on the surface in order to meet specific application needs.

In 1970, evidence of other interesting activities focused on the "instant fabrication" of pressure vessels, tubing and steel mill rolls by non-traditional routes was reported by *Electrotherm Corp.* a subsidiary of *Arcos Corp., Philadelphia*. A large 2¼ Cr-1Mo cylindrical shell course 3600 mm long, 1090 mm in diameter and 50 mm thick was fabricated in 80 hours using continuous electro slag melting (CESM) (Irving, 1970; Irving, 1971).

Since the late 1960s great investments were made in heavy manufacturing technologies due to a growing demand for units of increasing size from key industrial sectors of more industrialised economies, *e.g.* nuclear, petrochemical, power generation and coal-liquefaction industries. The production of large heavy components such as turbines and pressure vessels was significantly influenced by the steelmaking practice, forging and forming capacity. It is believed that by recognising limitations on domestic steel production capacity, some nations became concerned that their industrial capabilities could be strongly influenced by other nations' practices (Weber and Dingman, 1988). For instance, Japan revealed a special interest in developing forging technology further for producing ingots with weights up to 570 t, which in turn led the country to dominate the market in this field.

To cope with this increasing competitive pressure in the forging sector, demand for more efficient manufacturing technologies was particularly notorious in West Germany where companies, such as *Thyssen*, *Krupp* or *Sulzer*, and the *German Federal Ministry for Research and Development (BMBF)*, invested heavily on alternative solutions. Technologies such as shape welding (SW), shape melting technology (SMT), shape metal deposition (SMD) or 3D welding were developed since then. Various high deposition rate arc welding processes have been employed to shape-weld large metallic components, such as SAW, GMAW or GTAW. However, there have been very few notable recent developments on this topic in more recent years.

The real industrial breakthrough in the application of high metal deposition rate with arc welding technology for producing heavy components occurred at the beginning of the

1970s by the largest German steelmaker at the time, *Thyssen-Hütte AG*. In the 1974 patent of Brandi (1976), who can be considered the precursor of shape welding (SW) technology, a method for fabricating large one-piece shafts and rotors for turbines and electric generators to high quality standards was introduced. These large parts were typically made from steel castings or forged blanks, subjected to extreme service conditions, *i.e.* high stresses, temperatures and pressures. In his perceptive work, a cost-effective freeform fabrication process of heavy parts based on arc welding deposition was proposed for overcoming several major drawbacks associated with conventional manufacturing techniques. The results clearly showed that large shafts of any desired mass were produced with little loss of material and isotropic mechanical properties, *i.e.* independent of the direction of testing, near the outer surface and near the core. The author has heightened the need for implementing automatic online thermal-management mechanisms to producing the desired microstructures and control welding-induced stresses and distortion. Process monitoring systems for controlling the welding arc power, pre- and post-cooling temperatures, holding temperatures of the workpiece, were some of the key factors to ensure suitable operating conditions.

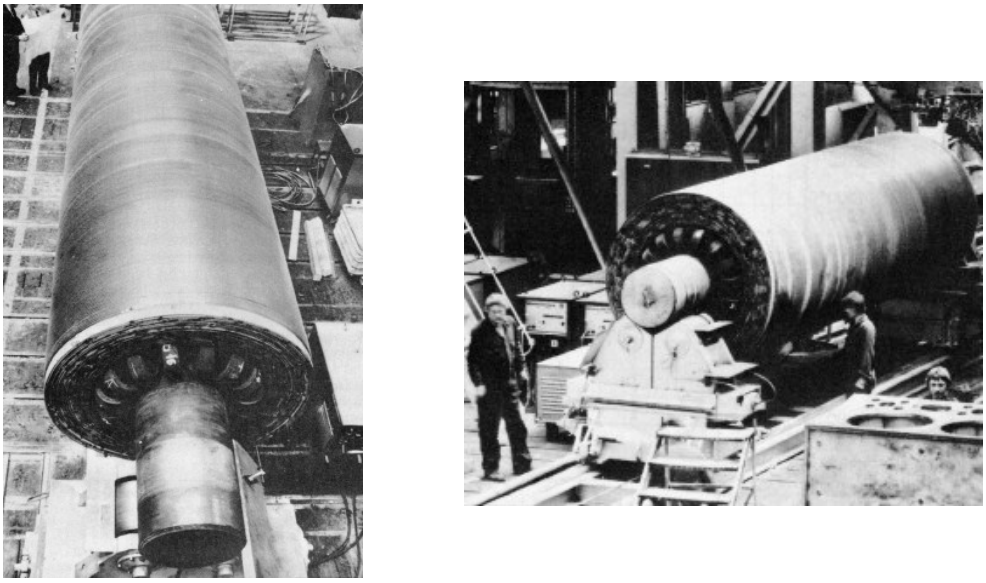

Figure 2.9. Shape welded 79 t cylindrical test shell and production machine (Kußmaul *et al.*, 1983).

The process development of SW technology was conducted in the following years through numerous experimental studies. These studies have mainly concentrated on welding processes, MnMoNi steels for nuclear components, and process engineering

studies, however without public exposure. In the beginning of the 1980s, a number of shape welded products such as rotors and cylindrical courses up to 11 t were reported (Grosse-Wördemann, 1980). Immediately after the technology development was completed, a 10 MnMoNi 5-5 shape welded hollow test cylinder with 79 t was fabricated totally from weld metal by *Blohm+Voss Industries GmbH*; a subsidiary of *ThyssenKrupp Marine Systems*; in the harbour of Hamburg (see Figure 2.9).

This shape welded component was subsequently utilised for a full range of mechanical testing and microstructure analysis carried out by *Thyssen AG* and the *State Materials Testing Institute*, at the University of Stuttgart. In his detailed description of the fabrication process, Kußmaul *et al.* (1983) reported a 6-week production time for the production of the 79 t cylinder. Four tandem SAW heads were used to depositing rods of 4 mm in diameter at a rate of 20 kg h^{-1} per head.

The use of multiple SAW welding heads in a tandem arrangement constituted one of the most important technological developments brought into play during the fabrication process. Compared with the RESW system developed by *Mitsubishi Heavy Industries Co. Ltd* (see Figure 2.8(a)), the introduction of multiple deposition heads enabled the deposition of smaller weld beads with much more refined grain structures, hence with improved and more isotropic mechanical properties.

The mechanical testing study conducted on 10 MnMoNi 5-5 material by Wördemann (1980) clearly showed the excellent ductility properties of non-annealed shape welded material. In the University of Stuttgart, Schoch (1984) carried out an extensive fracture mechanics testing programme in similar steel grades suitable for the manufacture of nuclear primary components. Significant improvements in static tensile, toughness and fracture resistance properties of these shape welded structures, when compared with forged and rolled materials were reported.

According to German design codes for high-pressure vessels (Piehl, 1989), the improvement in mechanical performance allowed a significant weight reduction since the wall-thickness could be reduced by up to 30 %,. Moreover, by using multiple head arrangements SW was still economically attractive because of its potential for high deposition rates and low production times, as demonstrated by Schmidt *et al.* (1990).

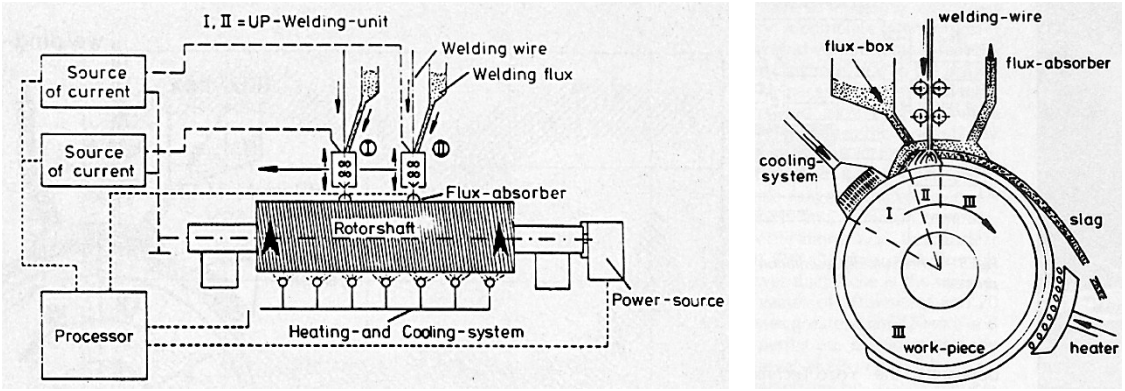

(a) (b)

Figure 2.10. Schematics of a shape welding production machine using the horizontal rolling method showing (a) the process control system, and (b) the tandem submerged arc welding head apparatus (Kußmaul *et al.*, 1983).

Figure 2.10 schematically shows the general process control (Figure 2.10(a)) and automated thermal management systems (Figure 2.10(b)) utilised to shape weld the hollow test cylinder shown in Figure 2.9. A better understanding of the process variables governing the material properties, and the development of the most suitable processing conditions for obtaining the desired mechanical performance, were of crucial importance for the widespread adoption and commercialisation of the technology.

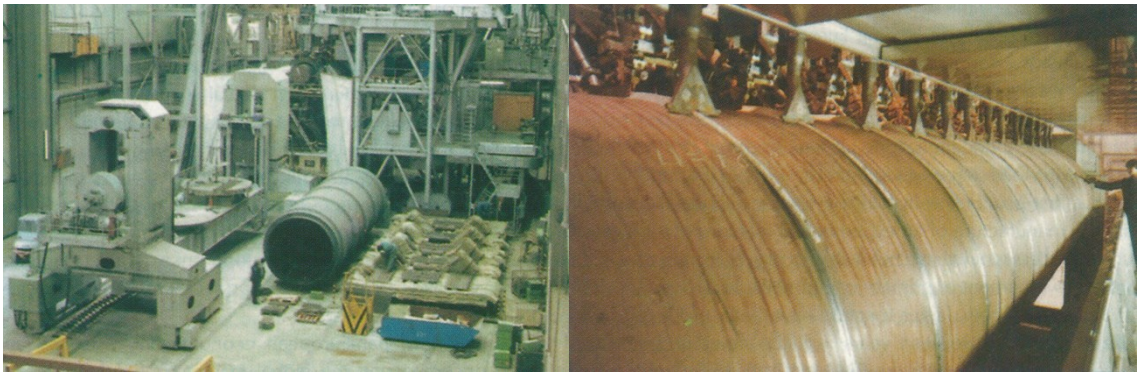

(a) (b)

Figure 2.11. Views of (a) industrial shape welding installation for individual weights up to 500 t, (b) 16 multiple submerged arc welding deposition heads in a tandem arrangement in operation (Piehl, 1989).

In the autumn of 1983, the research and development work carried out by *Thyssen AG* culminated in the construction of a shape welding facility with a maximum production capacity of 500 t (see Figure 2.11(a)) for shape welding cylindrical shell courses up to a length of 11 m and diameters between 2.5 to 5.8 m (Kußmaul *et al.*, 1983).

(a) (b)

Figure 2.12. Views of (a) the first shape welded high pressure vessel delivered to a pilot coal-liquefaction plant, weighing 80 t and standing 12.3 m high, (b) 72 t shell with dome attached seamlessly in 10 MnMoNi 5-5 material, thickness of 300 mm, diameter of 1.8 m, and length of 6 m (Piehl, 1989).

The equipment comprised a computer controlled apparatus equipped with 16 tandem SAW deposition heads and a maximum metal deposition rate capability of 300 kg h^{-1} (see Figure 2.11(b)). Two large rotary tables were later added to the installation with the aim of developing the technical knowledge for producing dome-shaped and large conical end pieces. A number of large demonstration components with weights of several tonnes, *e.g.* shells (Figure 2.13(a)), turbine shafts, conical end pieces, and high pressure vessels, were shape welded in various materials such as 10 MnMoNi 5-5, 20 NiCrMoV 14-5, 10 CrMo 9-10. The fabrication and delivery of an 80 t shape welded high-pressure vessel (10 CrMo 9-10) to a pilot coal-liquefaction plant was considered the most important step towards the commercialisation of this technology (see Figure 2.12(a)).

In order to comply with strict German specifications and the nuclear regulatory guide, there was a need to ensure careful process control and to demonstrate that SW technology was capable of reliable fabrication with consistent mechanical properties. In order to achieve this, introducing modern automation technologies must be viewed as highly desirable. An automatic height sensing control system was utilised for each of the tandem SAW heads to maintain a constant CTWD. The welding current and arc power were continuously monitored throughout processing from each separate head, to ensure consistent quality of deposited weld metal. Local heating and cooling devices were employed to guarantee the effusion of hydrogen and desired interpass temperature. Another important improvement with regard to product quality control of shape welded products occurred with the inspection of thick-sections (up to 340 mm) by means of

non-destructive ultrasonic methods. The good ultrasonic testability achieved resulted from the highly uniform and extremely fine grains of the shape welded material.

Despite the fact that support for nuclear energy in Germany was strong in the 1970s, after the oil price shock of 1973, this policy faltered shortly after the Chernobyl disaster in 1986. Due to strong anti-nuclear movements and political pressure, the last new German nuclear power plant of Neckarwestheim was commissioned in 1989, *v. **G**emeinschafts**k**raftwerk **N**eckar* (or GKN II). The rapid decline in market demand and prices for heavy components in the nuclear industry halted additional technological developments of SW in the nuclear engineering field. Instead, a renewed and fast-growing interest in new applications and materials for SW technology, such as pressure vessels for the chemical and petrochemical industry or heavy turbine shafts, were seen as new main focal points.

(a) (b)

Figure 2.13. Views of (a) shape welded shells with weights of 75 t and 225 t made of 10 CrMo 9-10 with lengths of around 11 m, (b) catastrophic failure of a 225 t shape welded shell made of 10 CrMo 9-10 (Piehl, 1989).

During the transition phase from MnMoNi materials to other steel grades, appreciable difficulties arose from 10 CrMo 9-10 and 20 NiCrMoV 14-5 materials due to the higher susceptibility to stress-corrosion cracking and propagation. Despite the important technological efforts in providing more precise control during processing, a catastrophic failure of a large 10 CrMo 9-10 shape welded pressure vessel weighting 225 t, during grinding of the reinforcing ring flanks (see Figure 2.13(b)), was reported by Piehl (1989). Cracks were also found in a demonstration turbine shaft made of 20 NiCrMoV 14-5 material in the interfacial areas between the disks and body, and between the shape welded metal and the forged base shaft. An important investigation into the underlying

mechanisms for crack formation, established that multi-axial residual stress and poor toughness properties, were the principal causes of failure in the 225 t pressure vessel (Piehl, 1989). In other cases, cracks were observed in CrMo and NiCrMoV steel grades after annealing, in particular on the surface and interior of the component, and in material regions with high toughness. These cracks were formed during stress-relief annealing due to the influence of the strain on the process of precipitation. According to Dilthey *et al.* (2006), the "winding process" (horizontal rolling) method induced a higher susceptibility to cracking than the "potter process" (vertical rotating), due to uncontrollable multi-axial shrinkage stresses. This explains why SW using the "potter process" configuration was later considered better suited for fabricating large components.

The adverse results obtained in materials with high susceptibility to cracking must be considered a major setback for the widespread use and commercialisation of SW technology. The SW of heavy components made of high strength materials was still facing a number of unresolved technical challenges and therefore presenting serious technical risks.

Nevertheless, the significant technological progress made throughout a period of over ten years on shape welded low carbon MnMoNi bainitic steels has never been called into question, given that no evidence of cracking had ever been found (Piehl, 1989). In fact, the research and development work carried out by *Thyssen AG* and the University of Stuttgart on MnMoNi steels laid the foundation for the qualification of both the 8 MnMoNi 5-5 and 10 MnMoNi 5-5 steels as new base materials for the manufacture of nuclear primary components. The 8 MnMoNi 5-5 and 10 MnMoNi 5-5 steel grades were certified by the German Nuclear Safety Standards Commission (KTA) as worldwide first shape welded base material for product forms and components fabricated by shape welding (Million *et al.*, 2005). The German standard *KTA 3201.1 – Section 29, Product forms and components from ferritic steels fabricated by shape welding (KTA 3201.1, 1998)* "applies to rotationally symmetric product forms or components that are fabricated by multiple layer deposition of molten-off electrode material and are subsequently not subjected to a heat treatment of a higher temperature than is permitted for stress-relief heat treatment".

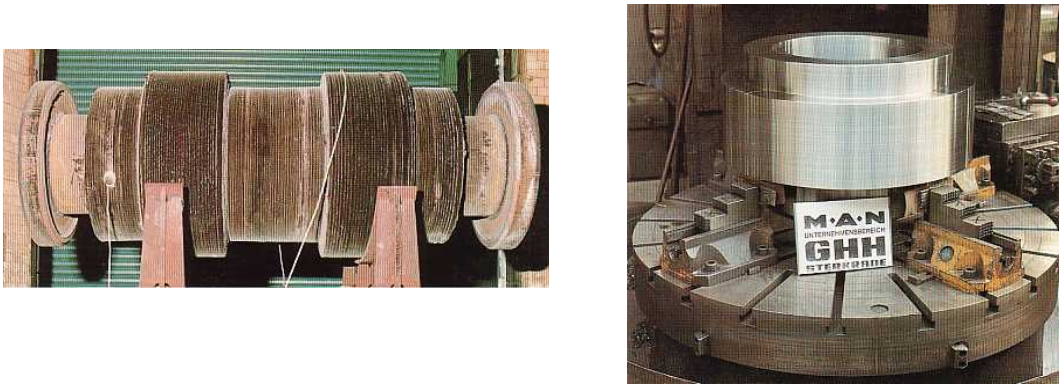

(a) (b)

Figure 2.14. Views of a shape welded (a) semi-finished product after stress-relieving, (b) machined blank taken from the semi-product for the manufacture of 2 nozzles.

Other German corporations have also contributed to the development of SW technology, *e.g. MAN/GHH* or *Mannesmann AG*, by producing other shapes and configurations such as pipe tees or nozzles (see Figure 2.14). In another example, SW technology was employed by the Swiss company *Sulzer Brothers Limited* for forming channels in a shape welded shaft member (Geisseler, 1989).

In his cost-benefit analysis study, Schmidt (1990) points out interestingly that SW can hardly be seen as an alternative to forging in fabricating heavy and simple geometries. In these conditions, the viability of SW technology over forging methods becomes entirely dependent on the metal deposition rate which can be achieved. For this reason, only SAW processes (with wire or strip) using multiple electrodes/heads are considered by the author to be of economic interest for the fabrication of simple geometries.

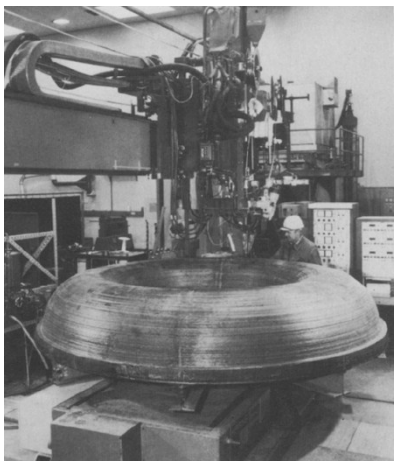

Figure 2.15. Fabrication of a half-toroidal part (10 MnMoNi 5-5) employing a submerged arc welding head with two wires in tandem using the "potter process" – total fabrication time of 5 weeks (Schmidt *et al.*, 1990).

The competitive advantages of SW over forging become more apparent when complexity increases. Therefore, the most important implication is that the metal deposition rate is not the decisive factor in these cases (Schmidt *et al.*, 1990). The use of arc welding deposition methods with lower metal deposition rates, such as GMAW and GMAW-P, could potentially improve the control over the size and volume of the melt pool and thereby obviate the need to orientate the part for allowing downhand deposition technique, as proposed in the patent application filed in 1985 by Million and Zimmerman (1987). Schmidt (1990), demonstrated that larger and relatively more complex shape welded geometries, *i.e.* toroidal geometry (see Figure 2.15), could be produced within specified tolerances of the geometrical dimensions of the part design.

The numerous advantages of using SW technology as a production method were also recognised in the United States in the 1980s. In 1985, The *Babcock & Wilcox Co. (B&W)* invested approximately $10 million in the development of its own shape melting (SM) capability (McAninch and Conrardy, 1991).

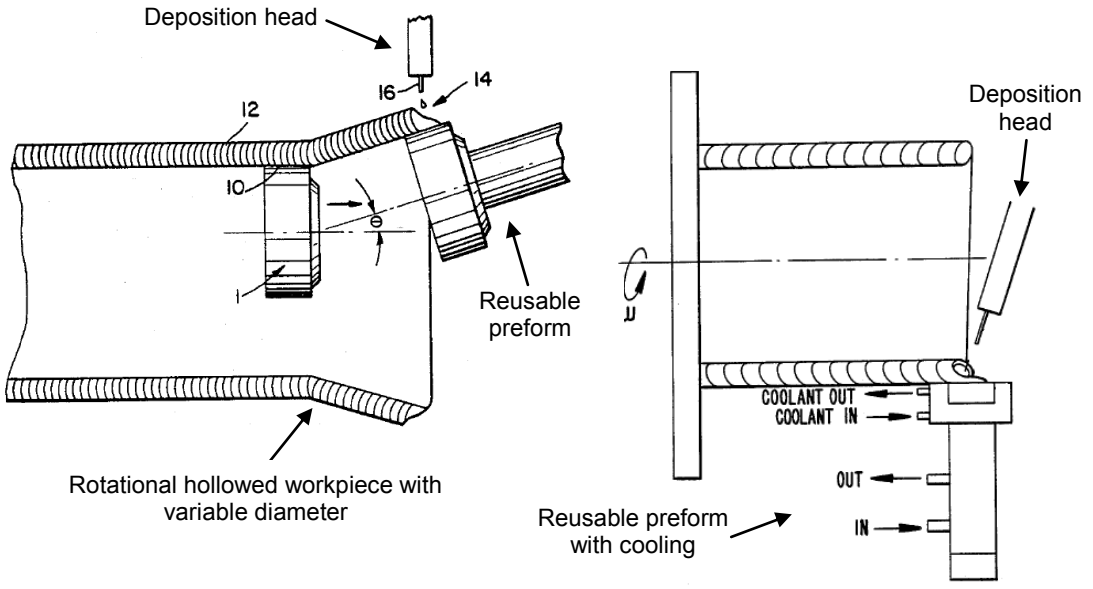

Figure 2.16. Fabrication principle of shape melting technology (Doyle and Ryan, 1989).

Most research efforts have concentrated on the implementation of automation and computer controlled production techniques, as well as on the development of the necessary auxiliary equipment, for fabricating near net shape components. The SM fabrication technology has focused primarily in the use of arc welding processes, *i.e.* GMAW or plasma-GMAW, for producing relatively small components made of

austenitic stainless steels, nickel-based superalloys alloys, *e.g.* Inconel 625, or iron nickel-based alloys. The main difference between both the SM and SW fabrication techniques is that the former used a non-consumable preform for providing the underlying form, weld bead support, and cooling for the weld metal as it solidifies (see Figure 2.16), whereas the latter utilises a consumable mandrel to deposit metal onto, which would be later removed by machining. Therefore, SM technology allowed for more geometric freedom, eliminating the need for a conventional consumable preform, *e.g.* mandrel, and reducing the production costs associated with machining. The SM fabrication method has its roots in a patent application filed in 1988 by Doyle *et al.* (1989), who can be considered the forerunners of this technology.

As identified by McAninch and Conrardy (1991), the application of on-line process control and thermal management technologies in SM technology must be viewed as fundamental pre-requisites for the production to high quality standards.

The GMAW process with synergic capability was preferentially employed for SM processing of structural components with intricate geometry, in particular for manufacturing parts made of Inconel 625 material. This means that more shape capability for out-of-position welding, and more control over microstructural and bead shape features, could be achieved due to the lower heat input and the ability to produce much smaller weld beads by GMAW. Moreover, the introduction of synergic welding was an important step for ensuring the production of good quality parts by allowing for better control over metal transfer and spatter conditions. Based on the work of Doyle (1991) and McAninch and Conrardy (1991), one may consider that the control of the bead shape achieved through process parameters is a major determining factor in producing high quality defect-free parts. Important progress was made in this area by *B&W*, in a patent application filed in 1987 by Ayres *et al.* (1988), of far-reaching significance towards automation of SM technology. The inventors disclosed a method for eliminating microfissure defects in shape melted austenitic material by closely controlling the geometry of the weld bead shape. In their major study, the authors have found that both the weld bead and fusion characteristics have a first order effect on cracking susceptibility, highlighting the fact that formation of distinct deep “finger-like” penetration profiles are highly undesirable. Weld bead penetration profiles without

sharp deep "finger-like" discontinuities were highly desirable for decreasing the susceptibility for microfissuring. As a result, optimum deposition welding conditions were obtained for producing fissure-free deposits of Inconel 625-alloy through optimisation of process parameters such as welding current (I), voltage (V), contact tip to work distance (CTWD), heat input (HI), travel speed (TS), wire feed speed (WFS), and welding head oscillation. This fundamental research study established the foundations for the development of welding process control algorithms capable of making bead geometry predictions of Inconel 625-alloy from process parameters. These functional relationships were subsequently incorporated in the process control of the SM equipment.

In a patent filed in 1984, Million *et al.* (1985) described a method of producing fine-grained shape welded components entirely made of 10 MnMoNi 5-5 ferritic steel by incorporating precise control of critical weld bead and fusion characteristics.

In the 1988 patent of Doyle and Ryan (1989), assigned to *The Babcock & Wilcox Co.*, an automatic feedback cooling device for sensing and controlling the average temperature of the workpiece, cooling rate and interpass temperature was disclosed. There was a consensual recognition in *The Babcock & Wilcox Co.* that if no means of temperature control was provided, the desired metallurgical and geometric properties of the finished parts would be negatively influenced by the excess residual heat generated during processing. The excess residual heat would have a significant impact on microstructures, residual stress and distortion, and weld bead geometry. Various other investigators have developed prior art methods for cooling shape welded parts. One of the most interesting contributions was made by *MAN AG* in a patent application filed in 1983 by Million and Zimmermann (1985), where the use of carbon dioxide in the solid state was suggested for intense cooling of the deposited material.

In the beginning of the 1990s MAM technologies based on arc welding methods received considerable interest in the high-tech manufacturing sector. The disruptive effects of the "new" fabrication approach and its potential in replacing traditional subtractive manufacturing routes were identified as such by *Rolls-Royce*. Preliminary research undertaken at *Rolls-Royce* involved investigating basic performance parameters and different techniques to reduce the costs of aero engine components by

reducing the level of waste of expensive high-performance alloys.

Subsequent research and development of a MAM process named 3D welding was carried out at Nottingham University in the department of manufacturing engineering and operations management, most notably by Dickens *et al.* (1992; 1993). In this approach a welding robot was used in conjunction with a GMAW system to fabricate unsupported three-dimensional carbon steel parts in a layer-by-layer fashion. The potential of the welding fabrication technique was successfully demonstrated for performing vertical and sloping unsupported walls, and for the production of parts featuring heavy sections, *e.g.* wall thicknesses greater than 6 mm (Norman and Dickens, 1995; Spencer and Dickens, 1995).

Dickens *et al.* (1992), highlighted the critical role of the welding parameters and weld bead dimensions in determining the desired wall thickness and the surface quality of the part produced. At the time, numerous single beads on plate experiments were conducted for a range of welding conditions based on the "one variable at the time" experimental method. The primary objective of this investigation was to generate an empirical and functional knowledge base for tightly coupling the relationship between weld bead geometry characteristics and primary welding parameters. The chosen factors for this study were the wire feed speed (WFS), travel speed (TS), wire diameter (WD), voltage, and contact tip to work distance (CTWD), whereas the responses were bead width (W) and bead height (H), current (I) and voltage (V). In this study, the WFS and WD were found to have a positive effect on W and H, whereas TS had a negative influence. Wider and shallower weld beads were obtained with increased voltage. The author suggested that further work was needed to assess the effects of interactions between process variables and geometric features in multiple layered structures. In addition, the need for real time on-line sensing and monitoring for controlling the process was heightened, in line with comparable research.

Norman and Dickens (1995) successfully demonstrated the fabrication of sloping vertical walls in a predictable way using a tilt and rotating table method to re-orient the part being produced. It is important to note, however, that a GMAW-P system was proved most suitable for this set of experiments for minimising heat input in order to reduce the excess residual heat produced during fabrication, while enabling better

control over important process parameters.

The effect of the excess residual heat on the surface quality, microstructure, residual stress, and geometry (*i.e.* hollow box, horizontal, and vertical slab) of mild steel parts produced by 3D welding was examined by Spencer *et al.* (1998). It was found that improvements to the surface finish of 3D welded parts were achieved by introducing temperature control sensing. This improvement in the surface quality was achieved by checking the temperature of the part at the starting point of each pass. If the temperature was above a pre-established maximum (T_{max}), welding would not be performed until the part had cooled bellow T_{max}. The improvement in surface finish was particularly clear in vertical test parts. The implementation of cooling methods to avoid incurring excessive time penalties, which could negatively affect the process efficiency are suggested by the author. Microstructural analysis of 3D welded parts confirmed the occurrence of a martensitic transformation at the top surface, indicating rapid cooling. Large columnar grains were readily observed at the very top layers, analogous to those obtained in the as-casted material. A fine grained ferrite-pearlite microstructure was found in the main body of all structures, characteristic of a recrystallisation mechanism caused by repeated thermal cycling.

In the mid-1990s further progress was made at the Welding Engineering Research Centre (WERC) in Cranfield University with the development of WAAM technology – shaped metal deposition (SMD) - for advanced high-temperature materials for the aircraft engine manufacturer *Rolls-Royce, PLC (Bristol, UK)*. The automatic robotic arc welding SMD work cell comprised a GMAW torch for producing complex three-dimensional parts in various materials. The apparatus used in the development of SMD was very similar to that of 3D welding process developed at Nottingham University (Ribeiro *et al.*, 1994; Ribeiro and Norrish, 1996b; Ribeiro and Norrish, 1996a; Ribeiro *et al.*, 1997). However, it should be noted that the pre-defined geometry of the components in 3D welding was manually programmed, eventually becoming a tedious, time-consuming, and error prone process. An on-line programming technique was utilised in 3D welding for processing more complex geometries using a CAD image of the part to generate robot welding trajectories. Once the spatial positions were generated further post processing written in “C” language was required to include robot command

words. In order to overcome the major drawbacks described above, Ribeiro and Norrish developed an automated off-line programming procedure for generating slicing data, and therefore a robot program from CAD data for enabling direct creation of MAM parts (Ribeiro, 1995). This system successfully produced a user friendly interface between the CAD models, slicing routine, simulation, robot, and the workpiece. The procedure also enabled a certain level of process control through the automatic generation of useful operational reports. The construction of an accurate parameter knowledge base was particularly important in the development of the automated off-line programming procedure. Ribeiro *et al.* (1997) used the method of regression analysis for developing algorithms capable of predicting the weld bead W and H from welding process parameters such as current and TS for Inconel 718. However, the research failed to consider a wider parameter operating window and did not take into account a number of other important factors, *e.g.* CTWD, WFS, WD, weld bead and fusion characteristics.

Numerous MAM experiments were conducted at the WERC using various approaches and materials with the aim of investigating the benefits and limitations of different WAAM techniques. As a result of several research programmes, the WAAM activities at the WERC have concentrated on process development and optimisation. Welding processes such as DCEP-GMAW, GMAW-P, CMT, GTAW, GTCAW, PAW and VP-GTAW (variable polarity GTAW) were employed to produce parts made of exotic materials in which sponsors had great economic interest, such as stainless steel Jethete, Inconel 718, Ti-6Al-4V, bronze (Cu97Si3), and aluminium alloys (Blackman, 1997; Serrano, 1999; Stott, 1999; Emmanuel, 2009; Deherkar, 2010; Lorant, 2010; Martina, 2010; Leinonen, 2011). In parallel with this work, other research studies were carried out in the field of WAAM. The relationship between GTCAW process parameters and weld bead characteristics, as well as microstructural features, was investigated in (Emmanuel, 2009). Deherkar (2010) conducted a series of trials to study the influence of inclined walls on multi-layer characteristics of aluminium alloys, using CMT in positional welding. The study of the effect of microstructure on static tensile properties, fatigue crack growth rate, and fracture toughness properties of Ti-6Al-4V parts produced with GTCAW was reported in (Lorant, 2010). Martina (2010) established a stable process window for depositing Ti-6Al-4V using wire feed PAW. Process control models were developed for determining multi-layer characteristics from process

parameters based on regression analysis. A recent study by Leinonen (2011) involved the use of CMT for fabricating structures made of Cu97Si3 wire onto structural steel, where macrostructural and mechanical test analysis was performed.

SMD manufacturing technology was patented by *Rolls-Royce* – the first patent filed in Europe in 1999 by Stone and Pearce (2000), and in 2001 in the UK by Jones (2002) – who has more recently carried out research and development work for near net shape processing of aero engine components made of nickel-based superalloy 718 (Clark *et al.*, 2008; Clark *et al.*, 2010).

In more recent years, there has been an increasing amount of literature published on process control and development of the SMD process as a result of a major three and a half year €2.7m European research project entitled rapid production of large aerospace components (RAPOLAC). The project aimed at developing the SMD process, based on cold wire feed GTAW, to a stage where it can reliably produce large aerospace parts from a variety of materials for commercial use.

A closed-loop welding controller was developed and validated for the SMD process using GTAW based on key process parameters, such as welding current (I), mass of injected material (WFS), traverse speed (TS), and relative bead height step increment – Delta-*z* (Muscato *et al.*, 2008; Bonaccorso *et al.*, 2011). The underlying idea behind this automatic real-time operating control system was to measure by video feedback the amount of material deposited on each layer in a given instant. The feedback information was collected using a charged coupled device (CCD) image sensor with a resolution of 640×480 and 24-bit colour at 30 fps refresh rate. In order to maintain a nearly constant arc-length, the amount of material deposited must be equal to the step height increment (Delta-*z*). An image processing algorithm was developed and employed for measuring the weld pool dimensions, such as step height, width, length and the arc gap. The embedded control architecture provided connections to other modules such as wire feed speed motor control, video feedback, and temperature measurements. For instance, the arc gap was used to gather indirect information relating to the amount of material deposited. One such control strategy adjusts the WFS to maintain a nearly constant arc-length along the deposition path. Any alterations in the nominal arc-length values are interpreted as a result of an incorrect amount of deposited material, which can thus be

used to determine the adjustment in the required WFS. Escobar-Palafox *et al.* (2011b) considered that stable deposition conditions are reached faster with closed-loop control than in "manually" deposited parts, while surface quality of the parts produced can also be considerably improved.

Empirical process models were developed using a design of experiments (DoE) approach capable of predicting responses such as shrinkage, part geometry, surface finish, and portion of finer Widmanstätten of Ti-6Al-4V builds processed via GTAW (Escobar-Palafox *et al.*, 2011a). The experimental design was based on a fractional factorial design with four factors at two levels. Mathematical models were developed to predict the effect of the component diameter, step size, travel speed and 'energy level' on shrinkage, part geometry, surface finish, and portion of Widmanstätten of Ti-6Al-4V. The 'energy level' was considered as the ratio of the heat source power to the volume of raw material input. Results have shown all factors had a strong effect on the responses studied. The wall thickness and the surface finish of the part were significantly influenced by the energy level, whereas the TS played an important role in determining part thickness and portion of finer Widmanstätten. It was also found that step height had a great effect on surface finish and portion of finer Widmanstätten, while the component size had a major effect on the percentage shrinkage. The empirical validation of these models showed a maximum error of 38.5 % for the surface finish predictions, whereas the predicted shrinkage had an error of less than 11 %. The author failed to fully acknowledge the significance of including centre points, replicates and complementary data points for improving model predictions. This fact can explain the large errors obtained in these experiments.

In addition, thermo-metallurgical and mechanical models were developed and validated for predicting the as-welded microstructure and residual stress levels of SMD Ti-6Al-4V structures (Anca *et al.*, 2011a; Anca *et al.*, 2011b). A large and growing body of literature has investigated the microstructure and mechanical properties of Ti-6Al-4V, Inconel 718, and 300M steel of SMD parts (Baufeld and Van Der Biest, 2009; Baufeld *et al.*, 2009; Baufeld *et al.*, 2010; Baufeld, 2011). However, the main weakness of the work related with the static tensile testing of Ti-6Al-4V material was that micro tensile specimens were used, which were much smaller than the prior β-grains. A recent study

by Baufeld (2012) involved the examination of the effect of deposition parameters on mechanical properties of SMD parts. The technological developments made within the RAPOLAC project have been recently overviewed in more detail by Escobar-Palafox *et al.* (2011b).

Wang *et al.* (2001) from Southern Methodist University proposed a WAAM system based on a VP-GTAW heating source for directly building cylindrical parts made of aluminium alloys, such as Al-5356 and Al-4043. The authors emphasised the need for on-line monitoring and control systems of process parameters such as pre-heating, arc-length, heat input, and bead geometry knowledge base for achieving good quality parts.

One of the paramount concerns of WAAM systems is the quality of the manufactured components. Quality in the MAM field is usually evaluated from two perspectives, the geometric accuracy, and metallurgical properties of the part (Zhang *et al.*, 2003). The geometric accuracy is typically broken down into properties such as dimensional accuracy and surface finish quality of the as-deposited parts. However, the surface quality requirements are rarely met - especially when high quality surface finish is expected - which means further post processing stages are needed, *e.g.* milling or grinding. WAAM systems, providing relatively low resolution with high deposition rates necessitates the combination of both manufacturing and post processing stages in one machine tool – this is called hybrid layered manufacturing (Song *et al.*, 2005; Karunakaran *et al.*, 2009; Xiong *et al.*, 2009). This process produces 100 % dense metallic parts, metallurgically bonded, geometrically accurate, and with a good surface appearance.

Nevertheless, good quality parts can be reliably produced by WAAM if suitable welding and heat transfer conditions are applied in combination with closed-loop process sensing and adaptive control systems (Kovacevic and Zhang, 1997; Jandric *et al.*, 2004). In order to do so, the relationship between the welding process parameters and the weld bead characteristics of the deposited layer need to be fully understood.

2.5 Modelling of the weld bead shape

Over the past decades there has been a surge in interest in the use of mathematical modelling techniques for predicting and controlling the final shape of the weld bead, in order to understand the influence of process variables on its formation. Nevertheless, the inter-relationships between input process parameters and output bead geometry responses in arc welding systems are highly complex, and typically involve the nonlinear interaction of several welding variables. Typically, suitable welding procedures relied on established practices or on a trial-and-error approach for determining appropriate parameter settings. However, the selection of optimal parameter values by a trial-and error approach was often tedious and time-consuming.

Over the past decades, with the increasing demand for automated and/or robotic arc welding systems many efforts have been made to predict and better understand the effect of the welding variables on the bead geometry. Therefore, modelling the relationship between variables is highly desirable to improve the welding process efficacy and the quality of the welds produced.

Historically, great emphasis has been given to developing mathematical models for the SAW process, which focused mainly on bead-on-plate studies for hardfacing applications. McGlone (1982) has advocated the selection of SAW, based upon the fact that input parameters could be made sufficiently distinct from one another to permit a better understanding of the relationship between input and output variables. The development was followed by researching other welding processes in subsequent years, such as GMAW, GTAW and laser techniques. An extensive and in-depth review of work related to mathematical modelling of weld bead geometry prior to 1978 was published by (Shinoda and Doherty, 1978). In their major review, the authors identified two distinct approaches – theoretical and empirical. A wide range of prediction models have been proposed. These models varied from entirely theoretical with various degrees of complexity, *i.e.* based on physical and heat flow theory, to more pragmatic methods based on empirical data. Overall, and although some progress was made in the field until then, most of the efforts based on the theoretical approach resulted in an unrealistic range of predictive solutions due to major difficulties in dealing with a large number of

complex and interacting arc welding variables (Shinoda and Doherty, 1978). Although reasonably accurate models were obtained for predicting the extent of the heat affected one (HAZ), little success was achieved in obtaining useful theoretical models for predicting weld dimensions (Thorn *et al.*, 1982). The poor predictive theoretical outcomes were partially due to the fact that in most of these cases, convective mass-transport such as Marangoni and/or arc forces were not taken into account by the conductive heat transfer solutions (Christensen *et al.*, 1965).

The rapid development of computing technology allied with the use of more reproducible power supplies and welding equipment, has facilitated the use of mathematical techniques in favour of more pragmatic methods, *e.g.* multiple regression analysis. It should be noted that because regression analysis was adopted in this study to obtain relationships between process variables and various weld bead shape features, particular emphasis is placed on empirical modelling in this review.

Regression analysis was applied by Thorn *et al.* (1982) to investigate the interactions between process variables and weld pool geometry for GMAW spray transfer welds in steel. The results of the applied linear fitting method between: (a) current and WFS, (b) arc power and WFS, and (c) energy input and reinforcement area (A_2), showed a reasonable agreement with the experimental results. The comparison of the weld bead dimensions with the theoretical models developed by Wells (1952) and Christensen *et al.* (1965) indicated a good agreement between theoretical and empirical approaches for bead width (W) and A_2, whereas penetration depth (P) and weld pool length were respectively overestimated and underestimated by the conductive heat flow solution obtained.

In the mid-1970s, a large body of literature (Jones, 1976; Doherty and McGlone, 1977; McGlone and Chadwick, 1978; Shinoda and Doherty, 1978) has resulted from a systematic work carried out at *The Welding Institute (TWI)* in an early approach to procedure optimisation of SAW using a statistical modelling approach. The objective was to establish acceptable procedural fields using a widely spaced factorial experiment – called “tolerance box” approach – for producing acceptable welds according to a pre-defined quality criterion, based on welding geometry. However, the “tolerance box” approach suffered from a number of drawbacks. It was difficult to implement in process

control situations when dealing with three or more input variables. The lack of any quantitative information with respect to the accuracy of the models developed was a major limitation. In addition, obtaining an acceptable operational window was expensive and time consuming.

To overcome these limitations, equations based on factorial design of experiments (DoE) technique and multiple linear regression analysis were developed using the previous work carried out at *TWI* for constructing a "tolerance box" and procedure optimisation programs using computational methods (Doherty and McGlone, 1977; McGlone, 1980; Salter and Doherty, 1981).

The same factorial technique method was utilised by McGlone *et al.* (McGlone and Chadwick, 1978; McGlone, 1982) to identify the effects of interactions of main factors in controlling the weld quality of SAW process. The empirical data were utilised to develop mathematical models based on regression analysis to predict the weld bead dimensions such as penetration depth (P), bead width (W), bead height (H), reinforcement area (A_2) and heat affected zone (HAZ), from input variables such as welding current (I), voltage (V), travel speed (TS), bevel angle and wire diameter (WD). Mathematical relationships between welding variables and fillet weld geometry for the fluxed cored arc welding (FCAW) process were developed by Doherty *et al.* (1978). The empirical relationships developed in (Salter and Doherty, 1981) for SAW and GTAW, using design of experiments, could be accurately used for selecting robust welding procedures and predicting the shape of the weld bead deposited, in order to satisfy the visual quality acceptance criteria.

A statistical modelling approach, derived from experimental results, was successfully used by Chandel and Bala (1986), for evaluating the effects of interactions between SAW variables and determining bead geometry. The same technique was subsequently applied by Chandel (1988) to examine the correlation between parameters and bead shape of bead-on-plate welds using GMAW process. The results confirmed that the most influential factor affecting the bead geometry was the welding current, and that empirical mathematical models can be successfully used to accurately predict bead geometry.

The use of statistics for determining the relationships between welding variables and weld bead and plate fusion characteristics has been reported in the literature for many years. Regression analysis has been one of the most used statistical techniques for determining the functional relationships between welding inputs and weld bead geometry outputs. In particular, multiple linear regression (MLR) models, using the least-squares method, have been successfully applied for analysing and developing mathematical expressions of multifactor data. A wealth of information on linear regression analysis basics is provided in the reference textbook source (Montgomery *et al.*, 2006).

Nevertheless, during the last two decades a wide variety of optimisation methods have emerged for developing mathematical models between input parameters and output variables in order to obtain optimum operating conditions. Statistical design and analysis of experiments techniques, *e.g.* design of experiments (DoE), evolutionary algorithms and computational network have been successfully used for modelling, control and optimisation of different welding processes. Since the emphasis of the present study is on regression analysis, it is not intended to pose descriptive learning theory on all optimisation methods applied to weld bead geometry. A comprehensive literature review synthesis of the studies which have reported the use of the above methods in conventional welding was recently undertaken by Benyounis and Olabi (2008). Therefore, this review will briefly summarise the current knowledge on optimisation methods in conventional welding, with emphasis on mathematical and statistical design experiment (DoE) techniques such as factorial design, linear regression, and response surface methodology. An important introductory source of information on design and analysis of experiments is available in (Montgomery, 2009).

Factorial Design

Mathematical models were developed for FCAW by Raveendra and Parmar (1987) using a fractional factorial experiment for predicting weld bead and fusion characteristics such as penetration depth (P), bead width (W), bead height (H), W/P

ratio, and dilution (D). A fractional factorial planning[7] was the most suitable for use with the large number of welding variables utilised in the previous work, *i.e.* arc voltage, current, travel speed (TS), torch angle, and contact tip to work distance (CTWD). The models developed can be used in process control of fully automated systems, in which suitable process conditions could be determined for obtaining the desired bead geometry within the range of factors studied. A fractional factorial planning was also employed by Grupta and Parmar (1989) for predicting bead geometry relationships for SAW of steel plates with thicknesses ranging between 10 and 16 mm. Mathematical models were developed to predict the effect of WFS, open-circuit-voltage (OCV), CTWD, TS, and plate thickness on the weld bead geometry. A five level factorial technique was used by Murugan *et al.* (Murugan *et al.*, 1993; Murugan and Parmar, 1994) to predict the bead geometry of a 316L stainless steel cladding onto structural steel using SAW and GMAW. The effects of OCV, WFS, TS, and CTWD on weld bead and fusion characteristics such as P, A_2, W, and D were studied. In the basic factorial design strategy all factors are varied together and all possible combinations of the levels of the factors are investigated, instead one at the time (Montgomery, 2009).

Linear Regression

Yang *et al.* (Yang *et al.*, 1993a; Yang *et al.*, 1993b) successfully used linear and a curvilinear model techniques for predicting weld bead features such as melting rate, penetration area ($A_{1)}$, reinforcement area (A_2), P, W, and H from SAW variables, such as welding voltage, current, TS, and CTWD using both positive and negative polarity conditions. Statistical experimental design and linear-regression modelling techniques were utilised by Starling *et al.* (1995) to study the influence of the welding parameters on the bead shape in a narrow gap-GTAW process with magnetic arc oscillation. The results showed that arc oscillation has little effect on the lateral fusion of the joint. However, the weld bead shape was favourably influenced when its concavity was increased. Kim *et al.* (2003) used statistically designed experiments together with a factorial technique in the development of mathematical models in order to investigate

[7] A fractional factorial design is a variation of the basic factorial design in which only a subset of runs are used. This strategy of experimentation is preferred when dealing with four to five or more factors.

the main and interaction effects between variables and bead penetration for controlling the automated/robotic GMAW process. In this study, four two-level process variables such as arc voltage, welding current, TS and welding angle were considered for predicting weld bead penetration. The results demonstrated that penetration was affected by all the processing variables, and the developed empirical models can be used to control the process in order to achieve the desired geometry and quality. Lee *et al.* (Lee and Rhee, 2000; Lee and Um, 2000) applied a multiple regression model for developing predicting regression equations to obtain the desired geometry of the back-bead in GMAW, where a gap exists.

The authors investigated the effect of independent process variables such as arc voltage, welding current, TS, and the groove gap on weld bead shape features such as width and depth of the back-bead. It was concluded that the groove gap was the most difficult parameter to predict.

Response surface methodology (RSM)

Gunraj and Murugan (1999) used the response surface methodology (RSM) technique by designing a four-factor five-level central composite rotatable design in the development of mathematical models for selecting optimum process parameters to achieving the desired quality and process optimisation. The authors have utilised input parameters such as OCV, WFS, TS, and CTWD for predicting bead geometry responses such as P, A_2, W, and D in the manufacture of pipes by SAW. The results have shown that all responses decrease with increasing TS. Further, all responses increased with the WFS, but the W remained unchanged. The effect of various FCAW process variables, such as welding current, CTWD, and torch angle, on weld bead parameters for duplex stainless steel cladding, such as W, H, P, and D, of low carbon structural steel plates was investigated by Kannan and Murugan (2006). The investigation was conducted based on four-factor five-level central composite rotatable design and response surface models developed using the multiple regression method. The developed mathematical models have been checked for their adequacy and significance. It was concluded that process parameters have a significant effect on the quality and bead geometry of the cladding. The main and interaction effects between process variables and responses are represented in graphical form and can be directly used to select optimal conditions for

achieving the required quality of cladding. More recently, Benyounis *et al.* (2005a) successfully applied a three level Box-Behnken design and RSM for developing mathematical models which can be used to predict the heat input (HI), P, W, and width of the HAZ of laser butt-welding of medium carbon steel plates of 5 mm in thickness. The continuous-wave (CW) CO_2 laser input parameters considered were the laser power, travel speed, and focused position. RSM was applied to the experimental data using the statistical software design-expert (DX). It was found that the HI plays an important role in the weld bead parameters dimension. The increase in TS has shown to decrease all responses studied indicating a negative effect, whereas the laser power has shown to increase, therefore indicative of positive influence. The models developed were subsequently utilised to optimise the welding process (Benyounis *et al.*, 2005b). Numerical and graphical optimisation techniques were applied to optimise the keyhole parameters using DX software in order to improve the weld quality, increase productivity, and minimize the total operation cost. Multi-objective optimisation was performed by superimposing contour plots of various response surfaces for producing overlay plots. Mathematical models were derived using RSM by Manonmani *et al.* (2007) for predicting the main and interaction effects of laser input parameters, *e.g.* beam power, welding speed, and beam angle, on the weld bead geometry of a 2.5 mm thick sheet of stainless steel 304, *e.g.* P, W, and penetration area (A_1). The experiments were based on a three-factor five-level central composite rotatable design. Regression analysis was applied to develop the models and the analysis of variance method was used to test their adequacy. It was found that this technique can be used effectively in analysing the cause and effect of laser input parameters on bead responses.

Fachinotti and Cardona (2008) focused on computational models to predict weld bead geometry based on empirical data as well as on the modelling of GTAW heat source. Doumanidis and Kwak (2001; 2002) established a dynamic modelling and sensor based closed-loop feedback control using laser scanner and infrared pyrometer. The control system relied on the physical principles of material transfer to control the bead geometry profile.

However, it is important to note that all the studies reviewed so far in the field of mathematical modelling applied to bead shape predictions and optimisation have been

limited mainly to conventional welding methods and cladding applications, rather than metal additive manufacturing (MAM).

Very recently, Martina *et al.* (2012) attempted to adopt a D-Optimal design to develop mathematical models to predict the main geometric features of Ti-6Al-4V multi-layer deposits from transferred plasma welding and wire deposition (PWD). The selected input parameters were WFS, TS, and welding current, while the output parameters were total wall width (TWW), effective wall width (EWW) and layer height. Having established a feasible 3D PWD operating window by setting out a number of constraints, it was then possible to compute a D-Optimal design approach using design-expert (DX) software. ANOVA was the method adopted in this study to carry out statistical significance tests. The significant main effects of interactions between process variables and responses were represented graphically by contour plots.

It is important to point out that systematically designed experiments were regarded by a number of researchers as a valid and useful strategy of experimentation in identifying the influences of process parameters on forming characteristics in MAM. Zhang *et al.* (2007) carried out a comprehensive set of experiments with nickel-based superalloy to systematically investigate the effect of different laser metal deposition shaping (LMDS) processing parameters on single-clad forming characteristics. The main and interaction effects of laser input parameters such as powder-feeding rate, scanning velocity, laser power, spot diameter, and scanning space on the width and height of single-clad layer, and the surface smoothness were examined. Based on this initial systematic study, optimal processing parameters were selected to fabricate nickel-based superalloy components through the LMDS system. Both the bead width and height were the most important output characteristics, which were affected by almost all the processing parameters. Systematically designed experiments were also conducted by Li *et al.* (2003) with stainless steel 316L and nickel-base alloy, in order to investigate the influence of laser powder feed processing parameters on forming characteristics. The experimental results showed that the height of single cladding layer was an important parameter in laser rapid forming being affected by the majority of the processing parameters considered. However, the powder injection point was the most important parameter. The width of single clad was mainly affected by laser power, scanning

velocity and diameter of laser spot. Oxidation and powder adhesion were found to be the most important factors influencing the surface quality.

So far there is no published evidence of any fundamental study or systematic exercise using mathematical modelling techniques for determining the main and interaction effects between GMAW process variables and forming characteristics.

2.6 Properties and weldability of titanium

Since the early 1950s, the use of titanium and its alloys have become more widespread across many sectors of the industry, such as aerospace, petroleum refining, chemical processing, surgical implantation, food processing, and marine applications (Myers *et al.*, 1984). With particular reference to the aerospace industry, titanium alloys have been an attractive choice for special purpose applications in both military and commercial aircraft for several decades, *e.g.* heavy loaded structures such as bulkheads wing box, or landing gear applications (Williams and Starke Jr, 2003). Titanium and its alloys offer an excellent combination of high specific strength, *i.e.* strength-to-weight ratio, which is maintained at high-temperature, fracture toughness and crack growth resistance (good damage tolerance), allied to exceptional corrosion resistance (Ezugwu and Wang, 1997; Williams and Starke Jr, 2003). The most widely used titanium alloy is the high strength α+β alloy Ti-6Al-4V, accounting for more than 50 % of all titanium tonnage produced in the world. The aerospace industry accounts for more than 80 % of this usage (Welsch *et al.*, 1994). Nowadays, wrought Ti-6Al-4V is used extensively in the turbine engine, *i.e.* blades, discs, and wheels, and airframe components.

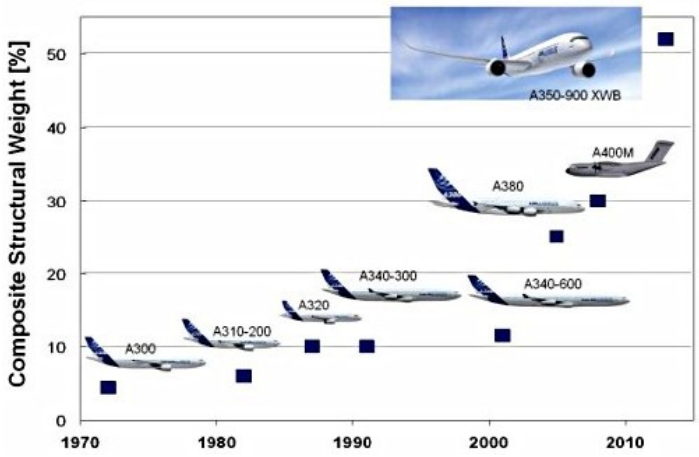

Figure 2.17. Increase in Airbus composite parts as percentage of total aircraft weight from 1970 to 2013 (image courtesy of Airbus).

The increasing use of titanium in the aerospace sector can be largely attributed to the demand for modern aircraft designs with increased carbon fibre reinforced polymer (CFRP) material (see Figure 2.17). Galvanic corrosion has become a major issue with the higher utilisation of composite materials within an aircraft in both primary and secondary structures. Titanium is galvanically compatible with carbon fibres in the composite structure, whereas aluminium, low alloy steels, and carbon generate a significant galvanic potential (Boyer, 1996). Moreover, by sharing the same coefficient of thermal expansion (CTE) as many common composite materials, such as fibre–epoxy composites which are used as components in aircraft structures, titanium is highly desirable as a composite interface material. Thermal stresses are typically induced during cooling of the composite due to the large difference in the CTE between carbon fibres and aluminium, resulting in loads too high for efficient use of aluminium (Boyer, 1996).

However, and despite the increased usage and production of titanium and its alloys, the high cost of the final titanium components appears to be a serious obstacle to its wider adoption. The high cost of titanium components when compared with other metals is due to the following factors:

1. Titanium production is highly energy intensive. The energy required to produce a tonne of titanium sponge[8] from its ore is 16 times that needed to produce a tonne of steel, 3.7 times that needed for ferrochrome, 1.7 times that needed for aluminium, and more than needed for producing one tonne of magnesium (Welsch et al., 1994).
2. Titanium is expensive to refine, process, and fabricate. The processing cost per cubic inch is 5 times more expensive to refine and more than 10 times as expensive as aluminium to form into ingots and to fabricate into finished products (Boyer, 1996).
3. Difficulties encountered during machining due to the high rate of work hardening of titanium alloys. The machining cost is at least 10 times that to machine aluminium (Boyer, 1996).

[8] Titanium sponge is the commercially pure form of titanium metal that is refined from titanium ore. It is called sponge because of its porous, sponge-like appearance.

4. Large buy-to-fly (BTF) ratios which can often be greater than 20:1 (Arcella and Froes, 2000).
5. The incompatibility of titanium and titanium alloys with high production rate welding processes, *e.g.* SAW, FCAW, or electroslag welding (ESW) (Welsch et al., 1994).

Welded titanium components are typically processed to high quality standards by welding processes that are optimally suited to a particular material thickness and joint configuration, such as GTAW, PAW or electron beam welding (EBW) (Welsch *et al.*, 1994; Lütjering and Williams, 2007). Nevertheless, such process suitability is often limited by the size and shape of the component to be welded, *i.e.* EBW vacuum chamber dimensions, and on whether adequate protection by auxiliary inert gas shielding from the ambient air atmosphere can be provided until it has cooled bellow 427 ºC, post weld processing requirements, speed and deposition rate (GTAW and PAW), and therefore the associated cost (see AWS A5.16/A5.16M:2007). In order to reduce the fabrication cost of welded titanium components, GMAW processes can be used to achieve greater productivity than GTAW or PAW processes due to increased deposition rates. However, historical difficulties caused by the generation of severe spattering conditions, which is a potential cause of weld contamination and defect formation, have limited the industrial use of the process to joints with lower weld-quality requirements (Stark *et al.*, 1962; Wolfe *et al.*, 1965; Stark, 1966; Mitchell and Feige, 1967; Salter and Scott, 1967).

2.6.1 Gas metal arc welding of Ti-6Al-4V

Poor welding conditions are typically obtained and reproduced by gaseous titanium arcs in general (Edward Ries, 1983; Eickhoff and Eagar, 1990; Zhang and Li, 2001). In particular, GMAW under direct current electrode positive (DCEP) of titanium and titanium alloys, is typically characterized as unstable, uncontrollable and very prone to severe spattering conditions, reducing therefore the quality of the beads deposited and the overall process efficiency.

The erratic arc behaviour in titanium welding with GMAW is caused by a dynamic cathode spot relocation mechanism often observed on the active cathodic region, *i.e.*

molten pool. The existence of such stable, but highly mobile cathodic emission spots (see Figure 2.19) are most detrimental in arc welding, since the control over both the arc column and its direction are easily lost. The effect has been attributed primarily to the physical properties of titanium, and therefore to the operating cathode emission mechanism.

This phenomenon is far from new. Guile (1971) has shown that cold cathodes, or low-boiling-point metals, such as aluminium, silver or iron, are unable to continuously supply electrons to feed the current flow lines within the arc. As a result, these materials cannot operate continuously, at a sufficiently high temperature, without melting. These metals are commonly referred to operate under the **mechanism of field emission** (Guile, 1971). In contrast, the most important mechanism of electron emission for hot cathodes, or high-boiling-point metals, such as tungsten, tantalum, rhenium, molybdenum or zirconium, is the **thermionic emission mechanism**. Note, however, that transitions between thermionic and non-thermionic modes of cathode emission may occur.

Titanium and titanium alloys fall within the refractory and hot cathodes group. Their high melting temperature, low work function, and intermediate boiling temperature and emissivity, are key in promoting a very stable thermionic emission sites.

In earlier studies, it was shown that erratic and unstable arc welding conditions, commonly induced by DCEP-GMAW titanium arcs, are strongly related to the metal transfer mode, thus with a cut-off threshold welding current (Salter and Scott, 1967; Eickhoff and Eagar, 1990). Welding conditions were reported to improve when extremely high current levels were used, *i.e.* 300 A in excess for 1.6mm wires. High current regimes caused the Lorentz[9] pinch force to be predominant, in spray mode, over the gravity dominant globular metal transfer. Additionally, a strong plasma jet is observed issuing from the active cathode spot, when low to intermediate current levels are applied in particular. This plasma jet typically relocates on the top of the already

[9] Lorentz force results from the interaction of the arc current with its self-induced electromagnetic field. This force exercises a pinch effect on the molten globule, aiding in neck formation and drop detachment.

incorporated droplet, or on the molten pool top surface. Hence, the main cause of repulsion of the filler metal droplets in low current DCEP-GMAW of titanium is due to strong Lorentz pinch forces, as opposed to the plasma jet momentum acting on the drop (Eickhoff and Eagar, 1990).

Another major concern in GMAW of titanium and its alloys, whether utilising DCEP-GMAW or GMAW-P, is the arc wandering phenomenon. This detrimental effect causes a significant lack of control over the arc column in the direction perpendicular to the weld seam, resulting in poor quality deposition characteristics. This phenomenon appears to be induced by an electron emission mechanism, *i.e.* metal work function. In thermionic emission the relationship between current density, J (A cm^{-2}) and both temperature, T (K) and work function of the metal, ϕ (eV) is determined by Richardson-Dushman equation as follows:

$$J(T) = AT^2 \exp(-\phi / kT) \tag{2.1}$$

where k is Boltzmann's constant (J K^{-1}) and A is a theoretical constant of 120 A cm^{-2} deg^{-2}. In general, it is easier to "boil" and remove electrons from oxidized adjacent areas with relatively low work function values (*e.g.* TiO_2), then from a "cleaned" and purer cathodic site, *i.e.* molten pool, providing the oxide has been previously dissociated by the high temperature of the cathode. Essers and Van Gompel (1984) have documented this effect for aluminium and steel cathodes.

Various approaches have been examined to overcome these problems. Recently, Zhang and Li (2001) proposed a modified active control technology to improve the robustness of one-droplet-per-pulse (ODPP) metal transfer condition of titanium alloys in GMAW-P. In addition, Shinn *et al.* (2005) have successfully reported a hybrid approach in order to contain the cathode spot and suppress severe spatter formation. The authors have utilised a low power CW Nd:YAG laser with a minimum power of 200 W and a spot diameter of 0.6 mm, in combination with a GMAW-P power source for deposition of Ti-6Al-4V.

A recent study carried out by *TWI* demonstrated that improvements in GMAW of titanium can be achieved with a novel wire produced by *Daido Steel Co. Ltd* called **G-Coat**, for making the process more applicable to high productivity manufacture of

quality titanium structures (Kostrivas *et al.*, 2008). *Daido Steel Co. Ltd* has produced a titanium wire that is claimed to create greater arc stability with reduced porosity and spatter. This wire has been produced using a novel wire production process, which modifies both the surface and grain size of the wire.

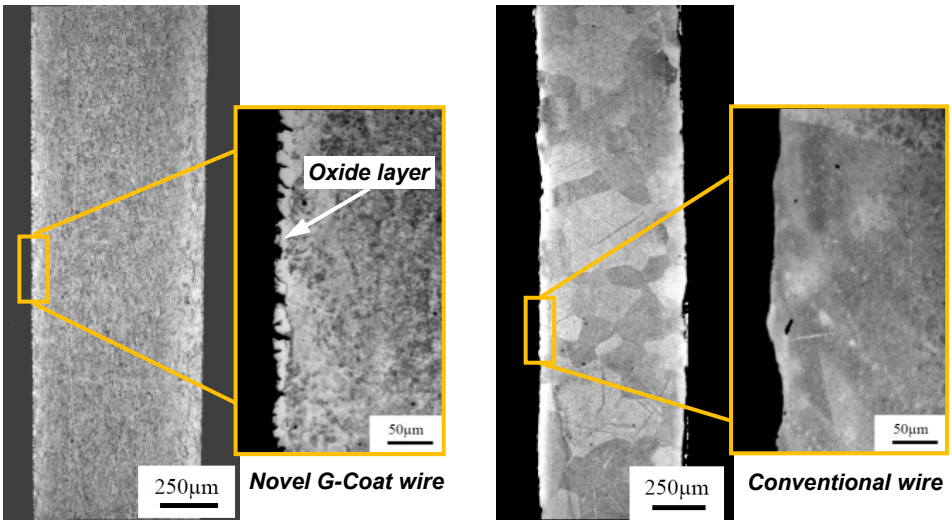

Figure 2.18. Optical micrographs showing the differences in macrostructrures and in surface profiles of the two welding wires. Note the difference in grain size and surface roughness (courtesy of the University of Birmingham).

Daido Steel Co. Ltd claims that the wire surface has a significantly lower, and more uniform, surface roughness than conventional titanium wires (see Figure 2.18). This is achieved by oxidising the surface layers of the wire prior to the final stages of drawing. The manufacturer claims that allied with an increase in strength due to the grain size refinement (see Figure 2.18), the new **G-Coat** wire provides better wire feeding characteristics and greater resistance to buckling. As a result, it gives better arc stability and eliminates variations in weld appearance, spatter formation and weld metal porosity (Makoto, 2004).

2.6.2 Cold metal transfer

The widespread application of exotic and metallurgically sensitive materials on high performance systems, with stringent quality requirements has called for innovative arc welding technologies. The landmark position in the welding and joining field has been established by cold metal transfer (CMT), where first developments started in the late nineties by *Fronius International GmbH*, Wels, Austria headquarters.

CMT is a gas metal arc welding (GMAW) variant based on a controlled dip transfer mode mechanism. The innovative concept delivers nearly spatter free welds with excellent overall quality, at lower thermal heat input. Although primarily developed for aluminium applications, in particular thin sheets, practical benefits have spread to other applications and materials. The process overcomes common difficulties encountered in conventional short circuiting GMAW, such as unstable process behaviour and severe spatter formation (Hermans and Ouden, 1999). The reciprocating motion of the wire is the key pioneering distinction when compared with conventional GMAW. For the first time the mechanical movement of the wire is directly integrated into the electrical process control. The reciprocating cycle is synchronized with a high speed digital control that senses the arc-length, short circuiting phase and thermal input transferred to the weld (Pickin and Young, 2006).

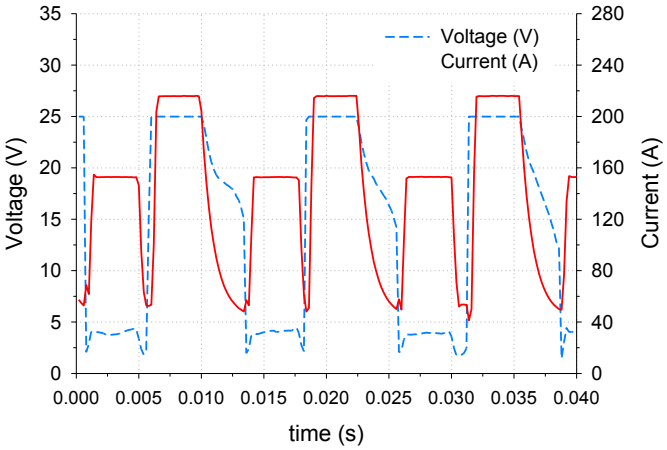

(a)

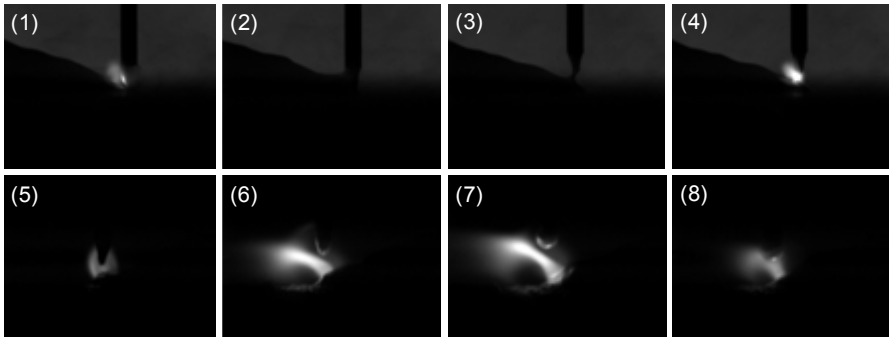

(b)

Figure 2.19. Welding sequence of Ti6Al4V using cold metal transfer showing, (a) electrical transients combined with (b) high speed video imaging. The welding conditions were WFS=8.5 m min^{-1}, WD=1.2 mm, and a shielding gas mixture containing Ar-He (75 %).

Figure 2.19 shows a typical CMT welding cycle sequence of Ti6Al4V, where the captured electrical transients are paired with high speed video imaging at the same instant in time (Sequeira Almeida and Williams, 2010b). When the wire moves forward and dips into the molten pool the digital process control senses the voltage drop, and that the short circuiting period (SCP) has occurred (see point 1 in Figure 2.19). The current is then reduced to a significantly lower level (nominal base current, I_b) in order to suppress the action of the electromagnetic pinch effect on the conductive bridging liquid. While the wire is dipping into the molten pool, an additional pulse of current is provided (see point 2 in Figure 2.19). The current flowing through the conductor wire is then converted into additional heat by *Joule heating* effect calculated according to equation (2.2):

$$Q = I^2 \times R \times t \tag{2.2}$$

where Q is the heat generated (J), I is the current flowing through the conductor (A), R is the electrical resistance of the conductor (Ω), and t is the time of the measurement (s). The extra energy supplied, *i.e.* Q, is intended to melt the additional solid wire, helping also the metal transfer by surface tension (see point 3 in Figure 2.19).

A feedback signal then returns to the process controller in order to reverse the front wire-drive feeding direction. The wire retraction force assists the liquid bridge fracture after another drop in current (Feng *et al.*, 2009), whilst in the meanwhile droplet detachment occurs by surface tension at the nominal I_b (see point 4 in Figure 2.19). Lorenzin and Rutili (2009) documented that the reciprocating movement of the front wire-drive unit is based on optimised arc characteristics, rather than predefined times or speeds.

In the arcing period (AP), arc ignition (see point 5 in Figure 2.19) is initiated by a considerably high current pulse ($I_{AP}>I_{SCP}$) that re-establishes the arc to the nominal arc-length, and melts a considerable amount of wire (see point 6 in Figure 2.19). Arc ignition is also assisted by the reversing movement of the wire. Current is also dropped to a substantially lower magnitude in order to avoid droplet detachment during the arcing period. Hence, the molten globule remains attached to the end of the wire tip as the current descends rapidly. This is caused by: (1) a negative electromagnetic Lorentz

force (Greene, 1960; Amson, 1965) imposed by the low current level applied, and (2) by solid/liquid interfacial forces, as opposed to gravitational.

The start and the duration of the short circuit period are dependent on the welding conditions, *e.g.* changes in the contact tip to work distance (CTWD). The latter effect supports the reason why the WFS and reciprocating frequency vary with time, up to 70 Hz in average. In CMT the arc voltage, or arc-length, is controlled by the speed and time the wire takes to retract from a near zero voltage position, *i.e.* short circuit. In contrast various arc-length control strategies might be used in GMAW-P, however and most commonly, voltage measurements are taken and compared to a reference using a feedback control system (Essers and Van Gompel, 1984). In practice the arc-length in CMT is detected and mechanically re-adjusted at every single short circuit, and as a result approximately 70 times per second (Lorenzin and Rutili, 2009).

2.6.3 Grain refinement of titanium

Prior studies have noted that the presence of coarse prior-β grains in the fusion zone (FZ) and HAZ of titanium fusion welds cause detrimental effects on the mechanical properties (Baeslack III and Hallum, 1990; Karimzadeh *et al.*, 2005). It is well established that the size of prior-β grains in the FZ and HAZ depends primarily on the weld energy input, with higher energy promoting larger grain sizes. In addition, the size and morphology of prior-β grains depends on the nature of the heat flow that occurs during weld solidification (Welsch *et al.*, 1994). Therefore, a reduction in the energy input is considered beneficial since it is usually accompanied by a reduction in grain size. However, high cooling rates associated with low heat input welding processes, such as laser or EBW, promote the formation of acicular, at least partially intragranular α' martensitic microstructures with high aspect ratio in the weld zone of α+β alloys, resulting in poor ductility and impact toughness properties (Welsch *et al.*, 1994; Sundaresan *et al.*, 1999; Barreda *et al.*, 2001; Zhou and Chew, 2003; Rao *et al.*, 2008). High energy input welding processes, such as GTAW and GMAW, typically produce prior-β grain coarsening in the HAZ and competitive growth in the fusion zone with extremely low tensile ductility properties (Baeslack III and Banas, 1981; Nagarajan *et al.*, 1992; Kishore Babu *et al.*, 2007; Balasubramanian *et al.*, 2008). Therefore, it would

be desirable to find alternative methods for obtaining grain refinement in titanium fusion welds, in order to improve ductility and impact properties.

In the past, a considerable amount of research has examined the potential for obtaining grain refinement in welded FZs of conventional aluminium and titanium alloys, *e.g.* by using an argon stream pointing onto the melt pool surface, electromagnetic stirring (EMS), inoculation techniques, vibratory techniques, thermohydrogen processing (THP), and pulsed-current welding techniques (Garland, 1974; Vivès, 1996a; Vivès, 1996b; Senkov and Froes, 1999; Sundaresan *et al.*, 1999; Mizutani *et al.*, 2004; Tamirisakandala *et al.*, 2005). In particular, the potential of direct current (DC) and alternating current (AC) pulsed in GTAW to refining the FZ grain structure of α + β titanium alloys, *e.g.* Ti-6Al-4V alloy, has been previously demonstrated (Sundaresan *et al.*, 1999; Kishore Babu *et al.*, 2007; Balasubramanian *et al.*, 2008). The effect of grain refinement was attributed primarily to the periodic interruption of the solidification process in the melt pool, the fluid flow, and the thermal gradients, as a result of fluctuations in temperature and arc force induced by the periodic current excursions of the waveform. These current pulses result in a continual change in the weld pool size and shape, causing a continuous change in the direction of the maximum thermal gradient with time at the solid/liquid interface. These fluctuations in the growth rate at the solid/liquid interface can yield an effective mechanism for supplying newer and more favourably orientated grains over small distances, with respect to the instantaneous direction of the maximum thermal gradient (Sundaresan *et al.*, 1999). At the same time, the fluid motion[10] and vibration of the weld pool - includes the buoyancy force, the Lorentz force, the shear stress induced by the surface tension gradient at the weld pool surface, and the shear stress acting on the pool surface by the arc plasma (Kou, 2003) - further enhance the convective forces already existing in the liquid pool. Sundaresan *et al.* (1999) highlighted that AC was much more effective than DC in refining the FZ of Ti-6Al-4V welds, justifying this result on the fact that a greater agitation in the weld pool was caused by pulsed AC.

[10] In GTAW the effect of the arc pressure on fluid flow is small at currents below 200 A.

In contrast to earlier findings in conventional welding, however, no evidence of grain refinement was observed by Wang *et al.* (2011) in WAAM walls of Ti-6Al-4V produced using both low and/or high frequency modulated current modes in the GTCAW Interpulse system. The authors have justified the observed inability of GTCAW for grain refinement by a dendrite-tip fragmentation mechanism in light of a research work carried out by Abralov *et al.* (1978), where the effect of electromagnetic action (EMA) on the primary solidification mode of cp-titanium was investigated. The results of Abralov and co-works showed that EMA in the welding of cp-titanium increases the stability of planar and cellular modes of solidification, whereas the interruption of the magnetic field was found to promote cellular or cellular-dendritic fronts.

The principal mechanism by which grain refinement occurs during EMS[11] has frequently been attributed in the literature to a mechanism based on a dendrite-tip fragmentation mechanism in aluminium alloys (Matsuda *et al.*, 1979), austenitic stainless steels (Matsuda *et al.*, 1983), nickel alloys (Lim *et al.*, 2010), and copper-based alloys (Campanella *et al.*, 2004). Many authors have argued that such mechanism of grain refinement would be difficult to occur in titanium and titanium alloys due to the relatively narrow region of constitutional supercooling at the S/L interface, often called *mushy zone*, in relation to the alloys referred to above (Baeslack III and Hallum, 1990; Sundaresan *et al.*, 1999). According to the constitutional supercooling theory proposed in (Rutter and Chalmers, 1953; Tiller *et al.*, 1953), the higher temperature gradients and lower solidification growth rate conditions associated with narrow *mushy zones* makes it easier for a planar S/L interface to be stable, rather than cellular or cellular-dendritic fronts. Therefore, for a planar S/L interface to be stable at the steady state, the following criterion must be met (Kou, 2003):

$$\frac{G}{R} \geq \frac{\Delta T}{D_L} \tag{2.3}$$

[11] EMS is typically introduced by applying an external alternating magnetic field perpendicular to the surface of the specimen.

where G is the thermal gradient (ºC cm^{-1}), R is the growth rate or solidification rate[12] (cm s^{-1}), *i.e.* ratio of cooling rate to thermal gradient, ΔT is the solidification range (ºC), and D_L is the diffusion coefficient (cm^2 s^{-1}). According to equation (2.3), for an alloy to be able to grow with a planar solidification mode, the ratio G/R must be no less than $\Delta T / D_L$. A relatively wider solidification range might be expected to form in more highly alloyed titanium alloys such as Ti-6Al-4V, offering therefore new favourable conditions for dendritic solidification, and increased potential for dendrite-tip fragmentation. Bermingham and co-workers (2007) supported the idea that it remains unclear whether the S/L interface of prior-β grains in either cp-titanium, Ti-6Al or Ti-6Al-4V grows via a dendritic or cellular mechanism.

The potential for GTCAW grain refinement of WAAM walls made of Ti-6Al-4V was demonstrated in Wang *et al.* (2011), by increasing the cold wire feed rate into the leading edge of the melt pool, for a constant weld energy input. Bearing in mind that the cooling rate ($\frac{\partial T}{\partial t}$) has a maximum at the top surface in autogenous weld pools, and decreases with depth within the melt pool (Bontha *et al.*, 2006), this result appears to corroborate the interpretation that an increase in cold wire feed rate causes a decrease in the thermal gradient (G). However, and most importantly, a large increase in the cooling rate is expected to occur at the bottom of the weld pool. This suggests a substantial decrease in the G/R ratio capable of triggering the breakdown of a planar S/L interface during solidification by constitutional supercooling. These favourable solidification conditions have most probably caused the solidification mode to change from planar to columnar dendritic, or even to equiaxed dendritic as the degree of constitutional supercooling continued to increase. Additionally, other factors such as, the increase in the molten pool turbulence, mechanical stirring, and dendrite-tip fragmentation mechanism might have played a major role in the observed grain refinement.

[12] $R = \frac{1}{G}\frac{\partial T}{\partial t}$

2.7 Neutron diffraction

Neutrons are sub-atomic particles with almost exactly the same size and mass as protons (a neutron has about $1/10^{th}$ of one percent more mass), however, with no electric charge. Over the years, neutron diffraction has become an increasingly important technique for determining residual strain distributions in bulk crystalline and engineering materials, in both research and industry fields (Withers and Bhadeshia, 2001; Pearce *et al.*, 2008).

Nonetheless, several other methods are still available to determine residual stress and these are commonly broken down into destructive, and non-destructive techniques. Examples of the former are hole drilling (Schajer, 1988) or the contour method (Withers and Bhadeshia, 2001), whilst x-ray diffraction (Peel *et al.*, 2003), ultrasonic or magnetic methods (Pulnikov *et al.*, 2004) fulfil the latter. Both x-ray and neutron techniques are closely related in the sense that the same basic physical phenomenon applies – diffraction, based on the Huygens–Fresnel principle (Crew *et al.*, 1900). However, neutron's penetrating capability is typically of many centimetres into the interior of components or adjacent to surfaces non-destructively (Withers and Bhadeshia, 2001). This is due to the fact that neutrons interact with the atoms nuclei and x-rays with electrons. In general, neutron beam sources are typically about a thousand times more penetrating than x-rays, in the normal diffraction wavelength range of $0.7 < \lambda < 4$ Å (Prask and Choi, 1984).

For large and complex geometries the typically higher diffraction angles of the neutron sources, when compared with those from synchrotron x-ray, makes it easier to measure stresses at angles near parallel to the incident beam or normal to the surface of the specimen. As a result of the short path lengths, a cuboid sample gauge volume may be employed making it easier to measure strains in all three principal directions without the need to assume a simplifying plane stress condition (Withers, 2007).

2.7.1 Diffraction principles and governing equations

With the neutron diffraction technique coherent elastic scattering, or diffraction, occurs for very specific and well-defined scattering angles as the white neutron beam passes throughout a polycrystalline component.

Elastic strain components are obtained by measuring the changes in the lattice plane spacing (d_{hkl}) of crystalline materials and using the fundamental Bragg's law (Bragg and James, 1948; Cullity and Stock, 2001), that is shown as follows:

$$n\lambda = 2d_{hkl}\sin\theta_{hkl} \tag{2.4}$$

where n is the integer that represents the order of the diffraction peak, λ is the incident neutron wavelength, d_{hkl} is lattice spacing of a family of crystallographic planes indicated herein with the Miller indices *(hkl)*, and $2\theta_{hkl}$ is the diffraction angle. When stresses are acting on a sample, changes in the lattice spacing d_{hkl} will occur and can be then detected and used as an atomic strain gauge, by comparing the actual d_{hkl} with a nominally "strain-free" lattice spacing $d^{o}{}_{hkl}$ of the same material. The elastic strain ε_{hkl} for plane-specific analogues *(hkl)*, as referred by Withers and Bhadeshia (2001), can then be computed using equation (2.5).

$$\varepsilon_{hkl} = \frac{d_{hkl} - d^{0}{}_{hkl}}{d^{0}{}_{hkl}} = -\cot\theta\,\Delta\theta \tag{2.5}$$

Where $d^{o}{}_{hkl}$ denotes the unstrained lattice spacing, and d_{hkl} is the strained lattice spacing condition for a family of crystallographic planes. In general, to describe a stress state in the material accurately strain measurements in 6 directions are required (Webster and Ezeilo, 2001). If three orthogonal directions are known, and assuming the shear stresses between the measurements directions to be small, three measurements will suffice, *i.e.* the measurement directions equal the principal directions. As a result, three principal elastic stress components $(\sigma_{xx}, \sigma_{yy}, \sigma_{zz})$, directed along the principal strain tensor components can be then computed from three measured strain components $(\varepsilon_{xx}, \varepsilon_{yy}, \varepsilon_{zz})$ using Hooke's law (see ISO/TTA3, 2001), as shown in the following equations:

$$\begin{aligned}\sigma_{xx} &= \frac{E_{hkl}}{(1+\upsilon_{hkl})(1-2\upsilon_{hkl})}\left[(1-\upsilon_{hkl})\varepsilon_{xx}+\upsilon_{hkl}\left(\varepsilon_{yy}+\varepsilon_{zz}\right)\right]\\ \sigma_{yy} &= \frac{E_{hkl}}{(1+\upsilon_{hkl})(1-2\upsilon_{hkl})}\left[(1-\upsilon_{hkl})\varepsilon_{yy}+\upsilon_{hkl}\left(\varepsilon_{xx}+\varepsilon_{zz}\right)\right]\\ \sigma_{zz} &= \frac{E_{hkl}}{(1+\upsilon_{hkl})(1-2\upsilon_{hkl})}\left[(1-\upsilon_{hkl})\varepsilon_{zz}+\upsilon_{hkl}\left(\varepsilon_{xx}+\varepsilon_{yy}\right)\right]\end{aligned} \tag{2.6}$$

where, $\sigma_{xx},\sigma_{yy},\sigma_{zz}$ and $\varepsilon_{xx},\varepsilon_{yy},\varepsilon_{zz}$ are the principal stress and strain components in the *x, y* and *z* directions, respectively. E_{hkl} and υ_{hkl} are the plane-specific analogues of the Young's modulus and Poisson's ratio. In the present investigation and for calculation purposes, constant values for E_{hkl} and υ_{hkl} of 206 GPa and 0.29 were assumed, respectively. Nonetheless, an in-plane stress condition can be assumed if one dimension is much smaller than the other two. In this case, one considers that strain component is in this direction is negligible, *i.e.* direction of the smaller dimension, and assume that is only caused by Poison's contractions. The triaxial state of stress equations (2.6) converts to a biaxial or in-plane stress, as follows:

$$\begin{aligned}\sigma_{xx} &= \frac{E_{hkl}}{(1-\upsilon_{hkl}^{2})}\left(\varepsilon_{xx}+\upsilon_{hkl}\varepsilon_{yy}\right)\\ \sigma_{yy} &= \frac{E_{hkl}}{(1-\upsilon_{hkl}^{2})}\left(\varepsilon_{yy}+\upsilon_{hkl}\varepsilon_{xx}\right)\end{aligned} \tag{2.7}$$

The errors of the stress components $\sigma_{xx},\sigma_{yy},\sigma_{zz}$ in the *x, y* and *z* directions are shown in equations (2.8).

$$\begin{aligned}\Delta\sigma_{xx} &= \frac{E_{hkl}}{(1+\upsilon_{hkl})}\sqrt{\left(\frac{\upsilon_{hkl}}{(1-2\upsilon_{hkl})}\left(\Delta\varepsilon_{xx}\right)^{2}+\left(\frac{\upsilon_{hkl}}{(1-2\upsilon_{hkl})}\right)^{2}\left(\Delta\varepsilon_{xx}{}^{2}+\Delta\varepsilon_{yy}{}^{2}+\Delta\varepsilon_{zz}{}^{2}\right)\right)}\\ \Delta\sigma_{yy} &= \frac{E_{hkl}}{(1+\upsilon_{hkl})}\sqrt{\left(\frac{\upsilon_{hkl}}{(1-2\upsilon_{hkl})}\left(\Delta\varepsilon_{yy}\right)^{2}+\left(\frac{\upsilon_{hkl}}{(1-2\upsilon_{hkl})}\right)^{2}\left(\Delta\varepsilon_{xx}{}^{2}+\Delta\varepsilon_{yy}{}^{2}+\Delta\varepsilon_{zz}{}^{2}\right)\right)}\\ \Delta\sigma_{zz} &= \frac{E_{hkl}}{(1+\upsilon_{hkl})}\sqrt{\left(\frac{\upsilon_{hkl}}{(1-2\upsilon_{hkl})}\left(\Delta\varepsilon_{zz}\right)^{2}+\left(\frac{\upsilon_{hkl}}{(1-2\upsilon_{hkl})}\right)^{2}\left(\Delta\varepsilon_{xx}{}^{2}+\Delta\varepsilon_{yy}{}^{2}+\Delta\varepsilon_{zz}{}^{2}\right)\right)}\end{aligned} \tag{2.8}$$

In this work instead of a nuclear reactor source capable of generating a continuous monochromatic beam; where Bragg's law would be applied directly; neutron strain scanner (NSS) measurements were performed using a spallation pulsed beam source technique that operates on the time-of-flight (TOF) principle, as detailed in section 2.7.2.

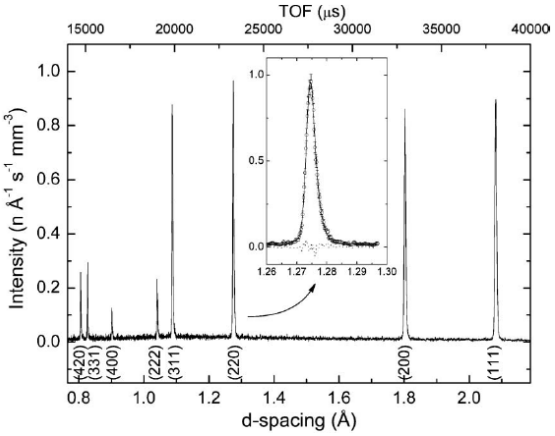

Figure 2.20. Multiple peak diffraction spectrum of a stainless steel specimen obtained from the time-of-flight ENGIN-X instrument at ISIS (adapted from Santisteban *et al.* (2006)).

From the underlying Bragg's law in equation (2.4), a characteristic diffraction multi peak profile is obtained (see Figure 2.20). The lattice plane spacing d_{hkl} is plotted as function of a broad range of neutron beam energies, or wavelengths λ, at a constant angle of approximately 2θ. The strain value is obtained by shifting peak positions after a least-squares refinement and fit to the (220) edge (see inset in Figure 2.20). Thus, the characteristic wavelength (λ) of each individual non-relativistic (thermal) neutron in TOF instruments, are as follows:

$$\lambda = \frac{h}{m_n v} = \frac{h t_{hkl}}{m_n L_n} = \frac{h t_{hkl}}{m_n \left(L_1 + L_2 \right)} \tag{2.9}$$

where h is Plank's constant, t and m_n are the neutron's time-of-flight and mass, L_1 and L_2 are the primary and secondary flight paths respectively (see Figure 2.21).

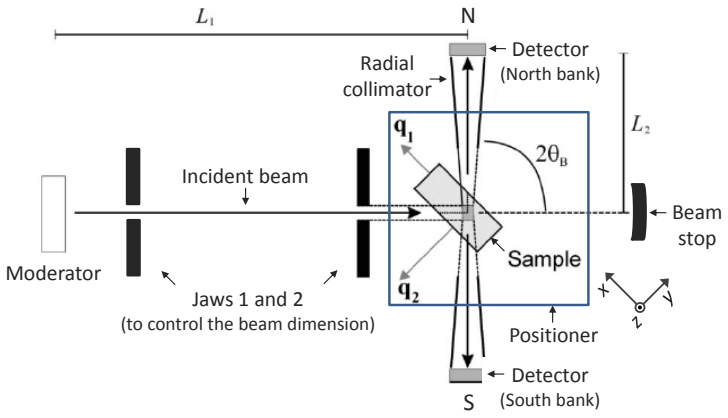

Figure 2.21. Schematic layout of the ENGIN-X time-of-flight neutron strain scanner (adapted from Santisteban *et al.* (2006)).

Finally, and as given by Santisteban *et al.* (2006), the lattice plane spacing d_{hkl} of a given family of crystallographic lattice planes is then computed as follows:

$$d_{hkl} = \frac{h}{2\sin\theta\, m_n (L_1 + L_2)} t_{hkl} \tag{2.10}$$

Withers and Bhadeshia (2001) highlighted that TOF instruments are well suited for situations where fast scanning speeds and/or the whole diffraction profile is required. This is of particular importance for analysis to be carried out on multiphase materials and/or where intergranular (or type II) stresses are to be expected. In fact, adequate accuracy on the measurements are typical characteristics of large gauge volumes settings (Price *et al.*, 2008). This is based on the fact of simultaneous contribution of several *(hkl)* families of crystallographic lattice planes to the intensity profile spectrum. Simultaneous contribution from various crystallographic planes also minimizes the existence of biased diffraction data allowing for good representation of the macroscopic elastic strain. The effect is typically attributed to elasto-plastic anisotropy (Daymond *et al.*, 1997), large grain size distribution and the presence of texture. One should note that strain values are typically determined by averaging over many diffraction *(hkl)* planes; using whole-pattern-structure-refinement such as Pawley-type[13] refinement procedure (Pawley, 1981) accounting therefore for possible texture effects; and finally obtained from changes in the lattice parameter *a* defining the unit cell dimensions (see *DD CEN ISO/TS 21432:2005 – Incorporating corrigendum January 2008*). The average strain ε is calculated for cubic materials according to equation (2.11).

$$\varepsilon = \frac{a - a_0}{a_0} = \frac{\Delta a}{a_0} \tag{2.11}$$

Where, a and a_0 are the unit cell lattice parameters for the strained and unstrained conditions, respectively (Hauk, 1997). In this work the *multiple measurement* method (Withers *et al.*, 2007) was utilised, under both triaxial state of stress and plane stress assumption cases, in order to obtain an estimate of the global unstrained a_0 unit cell

[13] As opposed to Rietveld refinement that tries to correct texture effect of the specimen (McCusker *et al.*, 1999).

parameter. Note that for the plane stress condition it is assumed that one component of the stress tensor is zero, which in the present case is considered to be the transverse direction TD_y. In other words, the transverse strain will be due solely to Poisson effects arising from the stress state induced by the other two in-plane directions. Finally, the relationship between the lattice plane spacing d_{hkl}, of a given family of crystallographic lattice planes, and the unit cell lattice parameter can also be given as (Hauk, 1997):

$$d_{hkl} = \frac{a}{\sqrt{\left(h^2 + k^2 + l^2\right)}} \tag{2.12}$$

2.7.2 The ENGIN-X strain scanner at ISIS

The ENGIN-X strain scanner, an optimised version of the ENGIN (Johnson *et al.*, 1997) instrument, is a pulsed source TOF neutron diffractometer specifically designed to perform accurate measurements of the lattice parameter *a* in polycrystalline materials at specific locations in a component. Neutrons are "*spalled*" or stripped off as high energy protons, accelerated to about 800 MeV in a 52 m diameter synchrotron, impact heavy atomic nucleus, such as a tantalum or tungsten metal target with atomic numbers 73 or 74, respectively. On impact a time-pulsed beam containing 2.5×10^{13} protons and a time extent of 0.4 μs per pulse, at a repetition frequency ranging between 5 to 50 Hz are produced, as quantified by Hutchings *et al.* (2005). Additionally, a neutron flux on the order of 25 neutrons per proton is typically generated on impact. As a result, a beam with a broad spectrum of high energies (3 to 4 MeV on average) is produced and in order to be used for diffraction purposes, moderation to thermal energies is then required (Hutchings, 2005).

To slow down the neutrons, and most importantly without a significant increase on the peak pulse width in time, moderators fabricated from hydrogenous materials such as water at 316 K, methane at 100 K and hydrogen at 20 K are utilised (Eccleston and Wilson, 2004) to preserve a constant cooling load. Important to note is for each pulse of neutrons generated by TOF instruments at the moderated target a large range of neutron energies (E) are produced.

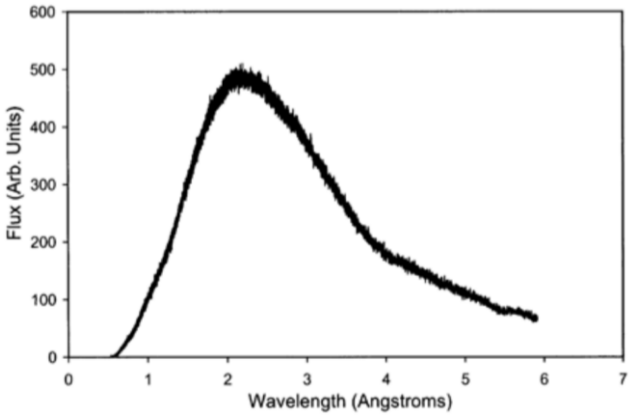

Figure 2.22. Pattern of an incident neutron flux spectrum measured on the ENGIN-X pulsed neutron source at ISIS (adapted from Hutchings (2005)).

Thus an incident beam flux spectrum is brought forth containing neutrons at differing velocities and thus wavelengths (λ), as observed in Figure 2.22. According to Withers and Bhadeshia (2001) the final diffraction profile measured by the detectors at any instant of time at constant Bragg's angle, relating the neutrons' E and their λ, can be directly deducted from the total time-of-flight (L_1 and L_2 in Figure 2.21) elapsed from the metal target to the detector, according to equation (2.9). An extensive description of the ENGIN-X neutron diffractometer instrument principle, as well as key improvements in performance, when compared with its predecessor ENGIN, is reported by Santisteban and Daymond *et al.* (2006).

2.7.3 Residual stress-induced deformations in metal additive manufacturing

The non-uniform plastic deformation due to non-uniform thermal loading involved in welding-based AM processes leads to an inevitable build-up of complex welding-induced residual stresses and deformation during fabrication. Thermal expansion and contraction occurs as a result of severe thermal excursions and sharp thermal gradients (Tsui and Clyne, 1997). The generation and development of residual stresses is considered an issue of major concern in welding-based AM processes. In particular, tensile welding-induced residual stresses can reduce the mechanical performance and life span of produced parts (see section 2.4) as they reduce the effective fatigue and tensile properties of the structure (Buschow, 2001). However, tolerance loss is still the primary concern in most processes (Amon *et al.*, 1998; Beuth and Klingbeil, 2001;

Mughal *et al.*, 2006). There is general agreement that there is a critical need for fundamental knowledge about how welding-induced residual stresses generate and develop in AM, particularly in WAAM. This knowledge would help in research efforts aimed at mitigating the stresses in either fabrication and/or subsequent heat treatment stages and also aiding in planning post-processing machining (Rangaswamy *et al.*, 2005). The research to date tended to focus on numerical thermo-mechanical modelling of laser cladding (Suárez *et al.*, 2010), laser hardening (Bailey *et al.*, 2009), laser-based SFF (Wang *et al.*, 2008; Alimardani *et al.*, 2009; Kamara *et al.*, 2011), and process mapping (Beuth and Klingbeil, 2001) for predicting the temperature history and residual stress field during laser processing, rather than arc welding processing.

The residual stress distribution and the effect of deposition patterns in laser-based SFF have been the subject of detailed studies. Nickel *et al.* (2001) examined the effect of deposition patterns on residual stresses and deflections in laser deposited metal parts. Finite element analysis showed that deposition patterns have a significant effect on the residual stress-induced deflection. The highest principal stresses were found in the longitudinal direction, whilst a raster pattern with scan lines orientated perpendicular to the longitudinal axis produced the lowest deflections. Lower and more uniform deflections were also produced using a spiral pattern scanned from the outside to the inside in plate substrates. Labudovic and Kovacevic (2003) developed a three-dimensional model for heat flow and residual stresses for laser-based SFF using both analytical and numerical methods. Residual stresses were measured using an x-ray diffraction technique, and the results were correlated with those obtained by FEM. The simulation and experimental results were in good agreement.

Far too little attention has been paid to the use of neutron diffraction technique to characterise the residual stresses introduced by laser and arc welding processing. Rangaswamy *et al.* (2005) mapped the residual stress distributions in LENS® samples of 316 stainless steel and Inconel 718 samples by neutron diffraction and contour method of samples with rectangular and square cross-sections. Contrary to their expectations, the neutron diffraction results have showed the presence of uniaxial stresses over most of the volume. The stresses are perpendicular to the substrate (corresponding to the normal, ND_z direction in this work), where compression stresses

are localised at the centre of the samples and tension at the edges. The authors have also found little sensitivity to the rastering direction.

The residual stress distributions in laser direct metal deposits of Wapalloy onto an Inconel 718 substrate were evaluated using neutron diffraction and the contour method by Moat *et al.* (2011). The study examined thick walled structures produced using a range of pulse parameters to identify the influence of pulse length and duty cycle on the residual stress fields. A very good agreement was found between neutron diffraction and the contour method. It was found that near the top of the wall a parabolic distribution of tensile stresses was observed in the longitudinal direction, with a maximum of around 420 MPa at the mid-length. This value decreased to almost zero at the bottom of the wall. The normal stresses showed a large compressive residual stress at the interface with the base plate of about 410 MPa, becoming close to zero near the vertical free surface.

Several studies have been published about the thermal process and temperature distributions in arc welding-based AM, but there is still insufficient residual stress data from experimental measurements. Mughal and co-workers (Mughal *et al.*, 2005; Mughal *et al.*, 2006; Mughal *et al.*, 2007) proposed FEM analysis to estimate the effects of process parameters, heat sink characteristics, rate of deposition, and deposition patterns on the development of residual stresses and deformation in WAAM using GMAW. It was found that residual stresses and deformation can be controlled and potentially reduced by adopting suitable deposition sequences. The sequence starting from the outer paths and ending at the centre produced minimum warpage. The deflection of the substrate is reduced by around 12 % when no interpass cooling is used. However, continuous deposition causes excessive residual heat and large remelting of the underlying layers, typically leading to tolerance loss, larger residual stresses and poor surface finish.

Klingbeil *et al.* (2002) performed a similar series of experiments utilising shape deposition manufacturing (SDM) and GMAW methods. The author suggested that both deposition methods and deposition patterns have a substantial effect in residual stress-induced warping. Paths and deposition methods that take greatest advantage of pre-heating effects were found to result in the least warping.

Zhao *et al.* (2011) investigated the thermal behaviour of WAAM of mild steel walls utilising direct current GMAW as heat source, using experimental data and numerical simulation methods. The thermal stress evolution, residual strain and stress, and the effect of deposition direction were also investigated (Zhao *et al.*, 2012). The residual stress distributions were measured using the hole drilling strain-gage method, and were found to be in good agreement with the FEM.

2.8 Technical approach to the project

The work flow detailed in Figure 2.23 was defined according to the key research aims and objectives presented in section 1.5 (see page 10).

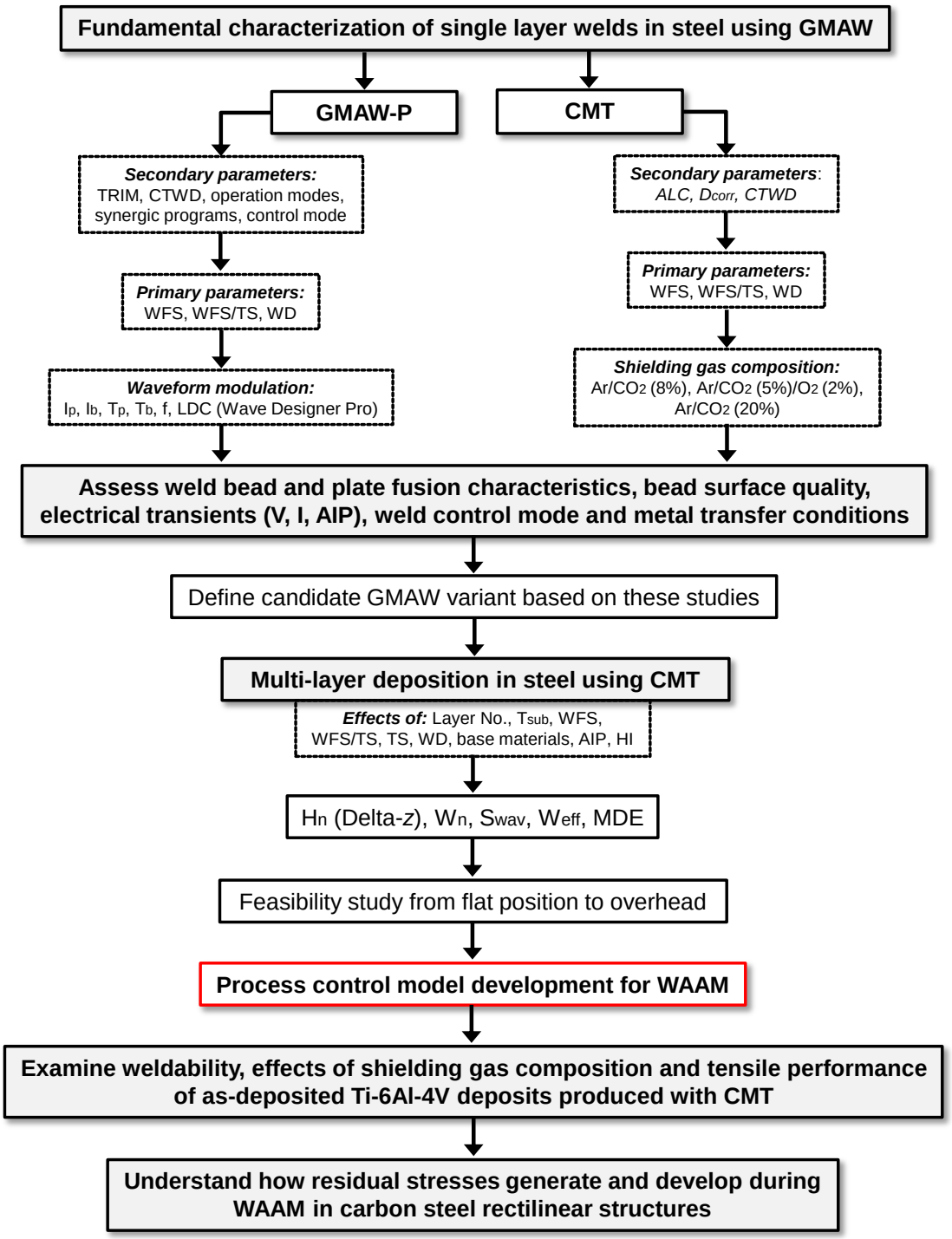

Figure 2.23. PhD work flow. The process algorithms development task is highlighted in red.

3 Experimental procedure

This chapter specifies the base materials, dimensions, welding consumables, and procedures utilised during the research study. Moreover, the chapter includes the substrate preparation method used to ensure stable and reproducible deposition conditions. Additionally, data acquisition methods and metallographic preparation steps are also included.

Details about the operational welding conditions and the welding set-up used in different stages of the research, including welding power supplies, such as GMAW-P and CMT, and welding rigs, are given. Note that many technicalities in the experimental procedure are analogous as the work progresses.

In section 3.8, the procedures utilised in the fundamental characterisation stage of single layer welds, employing both GMAW-P and CMT, is provided. More detailed experimentation is then described during single and multi-layer deposition studies, in section 3.9 and section 3.10. Section 3.11 reports the experimental methods used in the feasibility study carried out in the overhead position. The chapter concludes with the procedure utilised for the development of the process model which is included in section 3.12.

3.1 Materials and welding consumables

The experiments were conducted on as rolled S355J2+N grade structural steel substrates (or C-Mn steel), delivered according to specifications BS EN 10025:2004 and ASTM A1011/1011M. Mild steel solid wire consumable electrodes G3Si1 were utilised throughout the investigation in various diameters, such as 0.8, 1.0 and 1.2 mm (conform to EN 440.94 and AWS: A5.18ER70S-6). Maximum nominal compositions in wt. % for substrates and wire electrodes are summarised in

Table 3.1. The base material was selected to comply with the minimum mechanical and chemical requirements of the filler wire (*i.e.* G3Si1), minimum yield and ultimate strength, in particular. Other reasons for its use were due to its low cost and widespread application in almost every facet of structural fabrication.

Table 3.1. Nominal compositions[1] (in wt.%) of the mild steel substrates and solid wire electrodes.

	C	Si	Mn	P	S	N	Cu	Ni	Mo	Al	Ti+Zr	Fe
Plates[2]	0.20	0.55	1.60	0.025	0.025	0.012	0.55	0.05	-	-	-	balance
Wire	0.06-0.14	0.70 – 1.00	1.30 – 1.60	0.025	0.025			0.15	0.15	0.02	-	balance

[1] Single compositions indicate the maximum allowed element content; [2] maximum carbon equivalent (CEV) in % is 0.45.

Typical applications include bridge components, offshore structures, power plants, load-handling equipment, or wind tower components. The shielding gas mixtures were argon blends. These mixtures were selected according to the welding program requirements and/or plan of experiments for each welding power source.

3.1.1 Process modelling of single layer welds in steel

The dimensions of the base plates utilised in this study are shown in Figure 3.1. Two oxidising shielding gas mixtures from group M21 (according to BS EN 439) with different CO_2 contents were used in this particular study (balance argon). Overall, a shielding gas mixture containing 8% CO_2 was chosen in the GMAW-P based system, whereas a composition of 20% CO_2 was selected for the CMT. An additional tri-mixture containing 5% CO_2 / 2% O_2 was also utilised to access the effect of different shielding gas compositions on the CMT electric transient (section 4.1.3.2). A shielding gas flow rate of 15 l min^{-1} was maintained throughout this particular study for all welding trials.

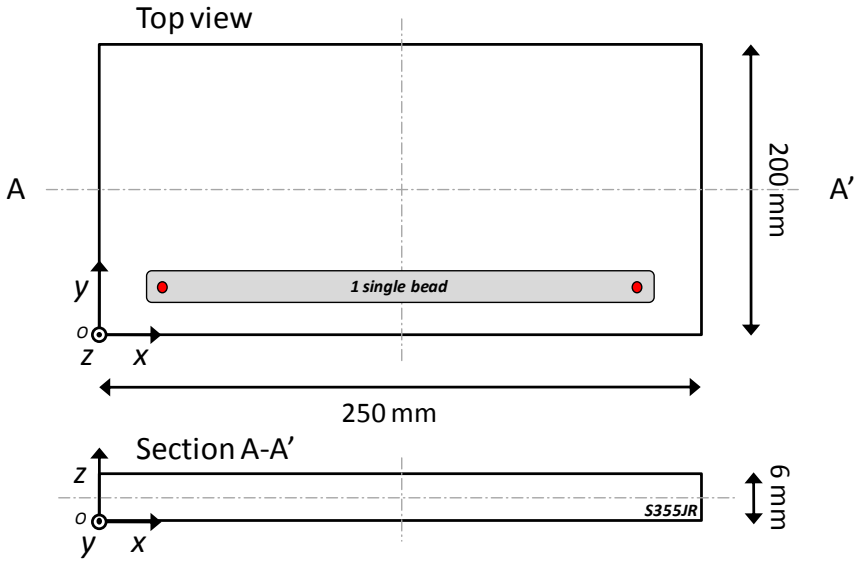

Figure 3.1. Schematic of the substrate dimensions (top and cross section A-A' views).

3.2 Substrate preparation

Repeatable and steady state welding conditions were assured by removing the top surface iron oxide from the as-received base plates before welding. The substrates were mechanically cleaned using wire brush (stainless steel wire), degreased with ethanol, and dried for at least 1 hour before welding (see Figures 3.2(a) and (b)). The positions of the thermocouples were also marked when applicable (see Figure 3.2(c)).

Figure 3.2. Sequence of base plate preparation; (a) as-received, (b) brushed and degreased, (c) marking of the thermocouple positioning.

3.3 Electrical data transient acquisition

The electric transient data (voltage and current), as well as the wire feeding rate, were recorded by a Yokogawa DL750 ScopeCorder (see Figure 3.3(a)) instrument utilising 5 kHz acquisition rate. The bandwidth filter feature was set to auto[14] mode and applied to all channels throughout the full experimental procedure, eliminating possible high-frequency noise induced by the input signal. After phase-correction (see Yokogawa manual) an isolated Yokogawa probe (ref. 700929) was then used to monitor the voltage output with an attenuation ratio of 10:1 (see Figure 3.3(c)). The current output was monitored by a battery-powered *Hall-Effect* sensor Fluke i1010 AC/DC clamp (1:1 attenuation ratio) and positioned perpendicular to the conductor, after being zero adjusted (see Figure 3.3(d)). Finally, a mechanical tachometer was attached to the wire spool in order to obtain the actual wire feeding speed readings in mV. As a result the dependence of the WFS actual on the WFS setting for the CMT welding system was established by first-order calibration curves shown in Figure A 1 (see Appendix A).

[14] Uses *anti-aliasing* and *low-pass filters* to limit the bandwidth (or cut-off frequency) of an input signal.

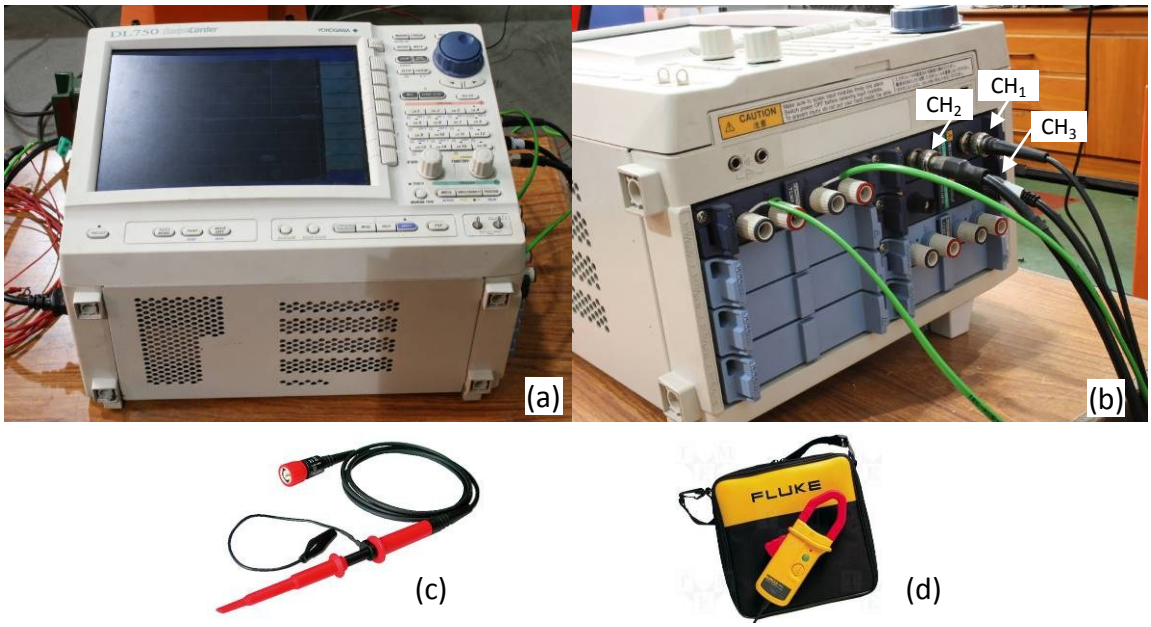

Figure 3.3. Yokogawa DL750 ScopeCorder data acquisition instrument (a) general view, (b) detail of the BNC output channels/connections (CH_1=V, CH_2=WFS, and CH_3=I), (c) Yokogawa probe, (d) current probe (model Fluke i1010).

The average welding arc power and arc energy were calculated using equations (3.1) and (3.2), according to the average instantaneous power (AIP) method.

$$AIP\,[W] = \sum_{i=1}^{n} \frac{I_i \cdot V_i}{n} \tag{3.1}$$

$$Arc\ Energy\,[J\ mm^{-1}] = \frac{API\,[W]}{TS\,[mm\ s^{-1}]} \tag{3.2}$$

$$HI\,[J\ mm^{-1}] = \eta \cdot \frac{API\,[W]}{TS\,[mm\ s^{-1}]} \tag{3.3}$$

Where $I_i \cdot V_i$ is the product of the instantaneous current and the instantaneous voltage during every instant in time, at the nominal acquisition rate, *i.e.* 5 kHz. The arc energy (AE) is calculated as the total electric arc power delivered at the very end of the contact tube (AIP) over the traverse speed (TS). The heat input (HI) is a quantitative measure of the efficacy of the welding process and is quantified according to equation (3.3). It measures the effective amount of energy absorbed by both, the weld region and substrate per unit length during the thermal cycle. As a result, an additional welding process efficiency factor (η) is necessary to determine and quantify more accurately the

heat input, which depends largely on the welding process. Welding process efficiency factors of η=0.9 for CMT and η=0.8 for GMAW-P were utilised throughout this work. These efficiency values were determined by liquid nitrogen calorimetric method in more recent studies (Hsu and Soltis, 2003; Pépe, 2010). It should be noted that when traverse speed values are given in m min^{-1}, equations (3.2) and (3.3) need to be multiplied by 0.06 for converting AE and HI to J mm^{-1} units. The experimental error associated with the acquisition procedure was estimated to be less than 0.25%.

3.4 Cooling and clamping arrangement

The specific positions where the substrates were to be fixed to the aluminium backing plate were initially marked. Substrates were then clamped at 4 points (6 points in residual stress and titanium investigations) onto a water cooled aluminium backing plate (see Figure 3.4). This preparation guaranteed the exact positioning of the base plates, minimising at the same time the welding-induced distortion of the substrate during welding.

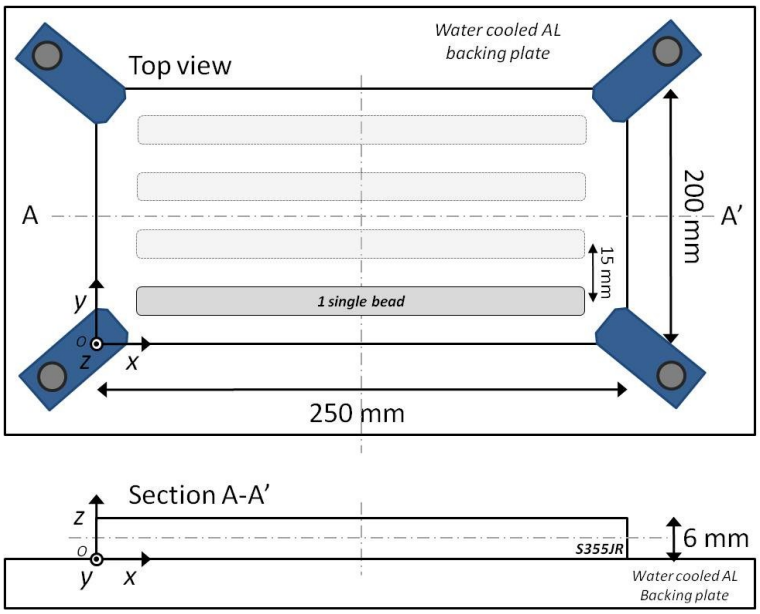

Figure 3.4. Schematic of the substrate in a four point clamping arrangement (shown in dark blue) positioned on water cooled aluminium backing plate.

The water cooled base plate was intended to provide a larger *heat sink* to improve the heat flow during the manufacturing cycle and therefore reduce the waiting time between subsequent deposited layers. The interpass temperature in single and multi-layer

experiments was set to room temperature, approximately 25 °C. The substrate temperature was monitored by an infrared pyrometer (model *Raytek Raynger S.T.*). Note that the cooling backing plate was employed exclusively in steel and titanium multi-layer studies (see section 3.10 and chapter 6).

3.5 Thermal imaging

Thermal infrared (TIR) measurements were performed with a FLIR A320 thermal video camera at up to 30 Hz over a 7.5-13 μm spectral range, with a field of view of 25° by 18.8°, and a minimum focus distance of 0.4 m. After recording the data was analysed using *ThermaCAM Researcher*™ software.

3.6 Metallographic preparation

Metallographic specimens were both prepared and examined in the metallographic laboratory at Cranfield University. During sectioning acute thermal damage *e.g.* overheating and severe surface damage of the specimens may occur due to faulty cutting conditions causing microstructural phase changes and as a result misleading metallographic characterization. This was prevented by selecting at the correct cutting speed, load, liquid coolant, and abrasive silicon carbide cut-off wheel. Specimens were then cut into adequate dimensions and mounted in cold-setting resin (epoxy). Specimens of large dimensions were prepared in the un-mounted condition. Metallographic samples were then prepared conforming to specification ASTM E3-01:2007, and macroetched according to ASTM E340-00:2006, followed by macro and microscopic inspection. In short, specimens were manually plane ground with rotating discs utilising abrasive silicon carbide (SiC) paper. On an initial stage wet SiC abrasive grinding paper was employed with typical grit sizes ranging from 120 to 2400 (ANSI[15] grit). Specimens were progressively rotated 90 degrees until all scratches left from the previous grinding direction were removed. Wear rates were maximised by replacing the worn abrasive paper with newer ones. In the first polishing stage, polishing discs were covered with soft cloth and impregnated with abrasive diamond 6 μm paste and an oily

[15] ANSI – American National Standards Institute.

lubricant to produce a polished surface. The final polishing was performed with a diamond suspension and cooling lubricant. The samples were then rinsed with tap water and dried with ethanol (C_2H_5OH) and a strong stream of air. Finally, all specimens were chemically etched with Nital, a solution of 2 % nitric acid (HNO_3) in alcohol (ethanol or methanol), in order to achieve a good contrast and avoid staining. The macrostructures were revealed, examined and macro-photographed using a Nikon Optiphot-66 optical microscope. Images were captured by a Qimaging Go-3-CLR-10 high-resolution digital colour CMOS camera and AcQuis image acquisition software for microscopy (version 4.01.10) from *Syncroscopy*. The boundaries of the weld metal (WM), heat affected zone (HAZ), fusion line (FL), and parent metal (PM) were eventually exposed and photographed.

3.7 Measurement of the weld bead characteristics

Single and multi-layer weld bead specimens were prepared according to steps described in section 3.6. Weld bead and plate fusion characteristics were measured using *AxioVision* image analysis software utilising built-in measurement functions. The experimental error associated with the measurements was estimated to be less than 2.5% after accounting for sample preparation (*e.g.* effect of non-perpendicularity of the sample surface), microscopy, and measurement errors.

3.7.1 Single layer cross section

The relevant parameters of single bead profiles such as bead width (W), bead height (H), remelting ratio (RR), penetration depth (P), dilution (D), contact angle (CA), reinforcement (A_2) and penetration (A_1) areas, and the aspect ratio (AR), were taken from single bead macro etched cross sections, as indicated in Figure 3.5. Note that the results presented for the CA is the average value of two measurements taken from both sides of the weld bead.

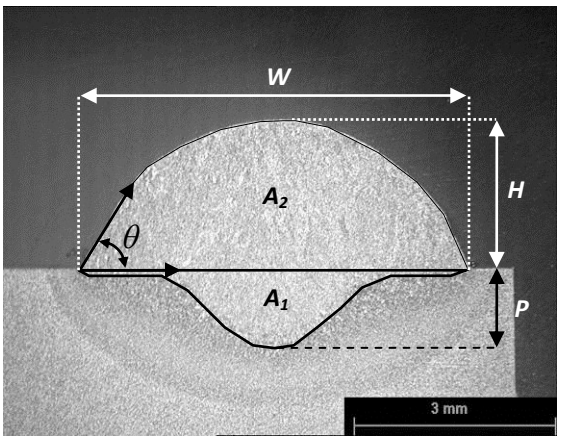

W: Bead width, (mm)
H: Bead height, (mm)
RR: Remelting ratio = A_1/A_2, (%)
P: Penetration depth, (mm)
D: Dilution = A_1/ A_1+A_2, (%)
DR: Deposition rate, (kg h^{-1})
CA: Contact angle θ, (º)
A_1: Penetration area, (mm^2)
A_2: Reinforcement area, (mm^2)
AR: Aspect ratio = H W^{-1}

Figure 3.5. Cold metal transfer macrograph of a single bead transverse cross section defining the measured outputs.

3.7.2 Multi-layer cross section

The initial assessment of multi-layer transverse cross sections was made on 4 layers high mild steel walls (see section 3.10.1). Successive measurements of relative bead height increment H_n (Delta-*z*) and bead W_n dimensions were carried out as a function of the layer number, as shown schematically in Figure 3.6.

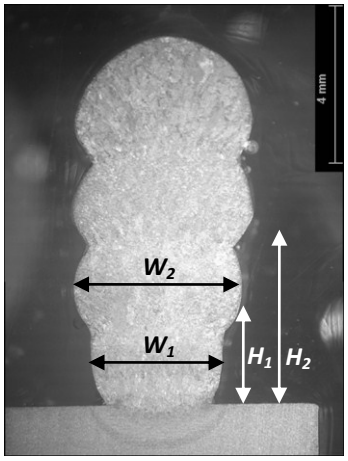

W_n: Maximum bead width of the n^{th} layer, (mm)
H_n (Delta-*z*): Relative bead height increment of the n^{th} layer, (mm)

Figure 3.6. Cold metal transfer macrograph of a multi bead transverse cross section defining the measured W_n and H_n (Delta-*z*) outputs.

For the case of multi bead cross sections with 10 layers high the effective wall width (W_{eff}), metal deposition efficiency (MDE), and surface waviness (SW_{av}) were the principal outputs measured. Both the W_{eff} and MDE were determined from multi bead macro etched cross sections, as shown schematically in Figure 3.7.

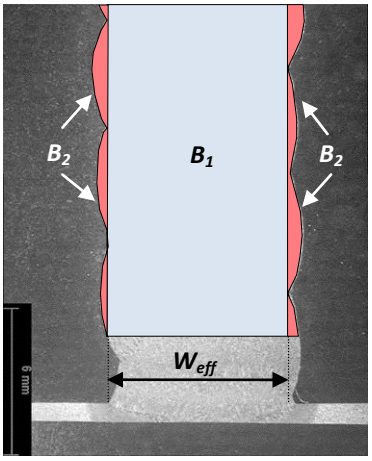

W_{eff}: Effective wall width, (mm)

MDE: Metal deposition efficiency = B_1/ B_1+B_2, (%)

SW_{av} : Surface waviness, (µm)

Figure 3.7. Cold metal transfer macrograph of a multi bead transverse cross section defining the measured W_{eff}, *MDE*, and SW_{av} outputs.

The W_{eff} parameter is a measure of the final maximum constant wall thickness achieved after eventual post-processing milling or machining steps to net shape dimensions (see Figure 3.7). The MDE parameter measures the material utilisation factor associated with the AM technique in percentage. MDE is therefore expressed as a ratio between macro section areas, *i.e.* the effective macro section area (B_1) and the area to be machined, in order to bring down the part to net shape (B_2). It should be noted that both W_{eff} and MDE parameters were determined by measuring single 2D cross sections for every produced specimen (see Figure 3.7). 2D cross sections were selected and cut from an arbitrary location at the mid-length position disregarding therefore positions close to the edges.

The SW_{av} gave an average indication of the surface quality of the as-deposited multi-layer component. The SW_{av} was determined by a *peak to valley* factor and measured by averaging a number of systematic slices. These slices were performed on every single 3D reconstruction of the scanned surface, as described in section 3.7.2.1.

3.7.2.1 Surface waviness

The surface quality of each multi-bead sample was assessed using a high-resolution confocal laser scanning microscope (CLSM), as shown in Figure 3.8. This microscope was utilised to acquire high definition 2D, and subsequently 3D images from a previously established area of interest. Precise and representative surface profiles were then obtained by scanning the largest allowable areas from each individual sample. The

final surface profile consisted of several sub-images that were in the first place captured individually and tiled together afterwards. The data was scanned and collected solely from one of the two facets of each sample because the acquisition process was time consuming, assuming therefore that the data would be representative of both facets.

Figure 3.8. Confocal laser scanning microscope (model *Olympus OLS3000IR*) utilised to map 3D surface profiles of additive manufactured samples (image courtesy of Olympus UK).

A 2D image is created by a laser beam that is focused on the sample with the objective lens by scanning the specimen in the *xy* plane, as shown schematically in Figure 3.9. Light that emerges from the specimen interacts with a dichroic mirror that reflects all infrared radiation, therefore allowing visible light to pass through. Light, that is out of the microscope's focal plane is then excluded by a pinhole that is optically conjugated with the focal point of the lens and therefore with the *confocal plane*. As a result, a high contrast 2D image is captured by the detector. The image is formed by brighter areas (at the focal plane) and thoroughly darkened areas (not at the focal plane). 3D reconstructions of all scanned surfaces are then created automatically by assembling 2D images captured from a sequence of optical sections, imaged along the optical axis at short and regular intervals. A number of other aspects and considerations related to confocal microscopy are covered in more detail elsewhere (Semwogerere and Weeks, 2005). From Figures 3.10 (a) and (b) it is seen that the maximum scanned area was about 25 mm^2 by utilising a 10 times objective in this example whereas the *pitch* or the step increment along the optical axis was set to 2 µm.

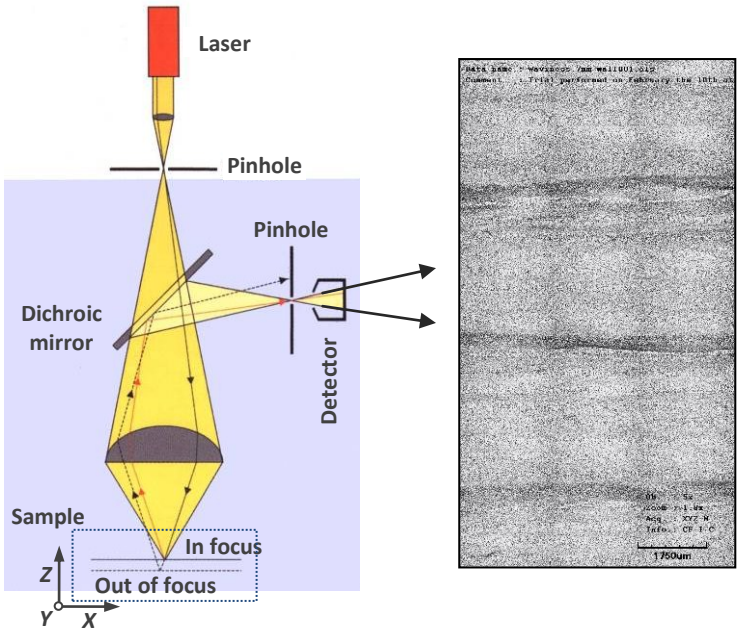

Figure 3.9. Basic principle of a confocal laser scanning microscope. The inset shows a high contrast 2D image as captured by the detector at a particular confocal plane (25 images tiled).

This is to say that different scanning settings were utilised throughout the scanning procedure. These settings were mainly dependant on the observed surface quality (or *SWav*) of the individual specimens to be scanned. The analysis was essentially visual and the scanning strategy defined after that.

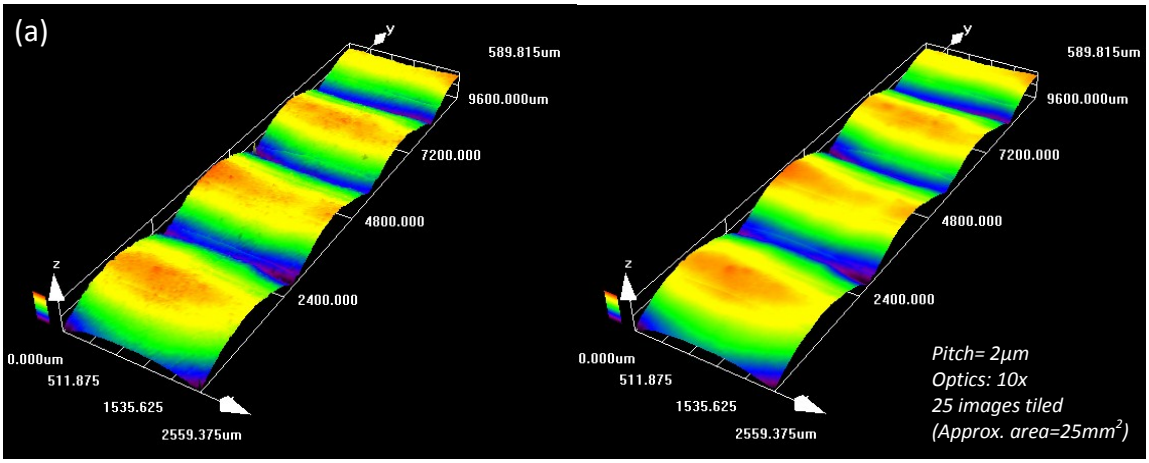

Figure 3.10. 3D reconstruction of a representative additive manufactured scanned area of interest in aluminium showing images in (a) raw condition and (b) after removal of the *spike noise*.

The adopted scanning strategy was based on a trade-off criterion between the scanning speed, scanned area and image resolution. On the one hand, larger scanning areas were favoured in cases where larger *SWav* distributions were to be expected by employing

lower magnifications and faster scanning speeds. On the other hand, better resolved images were chosen for cases where the apparent waviness distributions were small, using in these cases higher magnifications and lower scanning speeds. Following individual 3D reconstructions, functions to filter and remove the spike noise were applied to the raw image (see Figures 3.10(a) and (b)).

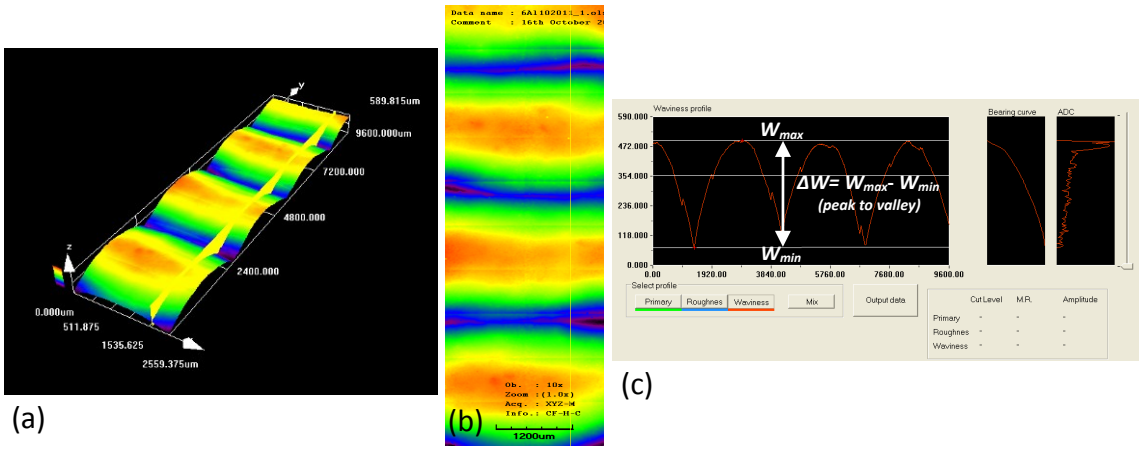

Figure 3.11. Systematic slicing procedure (a) 3D view (b) 2D view and (c) contour curve at the position specified by the yellow section schematically showing how the peak to valley factor was computed.

The *SWav* was then assessed and carried out by systematically slicing individual profiles (see Figure 3.11). Data was converted and exported to an excel spreadsheet in the format of 1025 points from the scanned surface contour. For each sliced profile, the *peak to valley (ΔW)* factor was then computed using the difference between the maxima (W_{max}) and minima (W_{min}) waviness. Equally spaced sections (15 in total) were systematically taken afterwards. The *SWav* was finally obtained by averaging the *ΔW* over 15 sections to obtain representative data for each scanned profile.

3.8 Fundamental characterisation of single layer welds in steel

3.8.1 Pulsed-current gas metal arc welding

All initial experiments were conducted on a five axis rig (*xyz* orthogonal axis, plus *w* rotating table assisted by an *h* manual tilting axis) instructed by a *Trio Motion Coordinator (series 2)* controller (see Figure 3.12). The travel speed (TS) was calibrated and a good correlation coefficient was found between the set and the actual TS, as seen in Figure A 2 (see Appendix A).

In this study the materials and welding consumables described in section 3.1 were utilised to produce single layer deposits using wire diameters of 0.8, 1.0 and 1.2 mm.

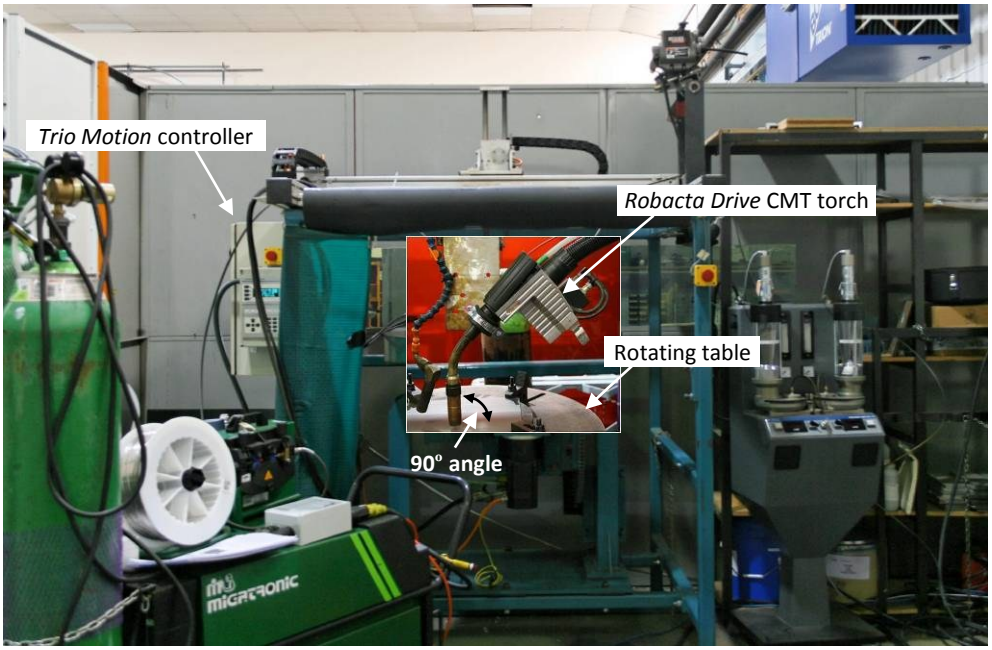

Figure 3.12. Experimental set-up for the single layer deposition study at the WERC welding laboratory. The 5-axis *Trio Motion* rig is coupled with the *Robacta Drive* CMT welding torch (inset).

Substrates were prepared before deposition as detailed in section 3.2, and clamped in a 4 point arrangement onto the rotating table of the 5 axis rig. A Lincoln Power Wave® 455/STT was employed throughout this investigation (Figure 3.13(a)). The torch angle was maintained at 90º relative to the *xy* plane of the substrate Figure 3.12 were deposited next to each other parallel to the welding direction, and the distance between the deposit centrelines was kept at 15 mm (see Figure 3.4). An interpass temperature of approximately 25 ºC was maintained (as described in section 3.4). Note that the *Arc Control*[16] setting was adjusted manually in order to achieve sound weld conditions (see Figure 3.13(b)).

Preliminary weld tests have shown that an OFF and +10 *Arc Control* conditions were the most appropriate settings for the operational conditions utilised throughout this investigation. The nominal waveform characteristic was achieved in GMAW-P by

[16] Fully adjustable on the front control panel of the power source within a range between -10 and +10.

setting the *Arc Control* to the OFF condition, while +10 caused an adjustment to the current waveform to increase the pulsing frequency, while decreasing the background current. In practice the *Arc Control* module provides control signals to the power circuit in order to adjust the arc width, by changing one or more welding output parameters.

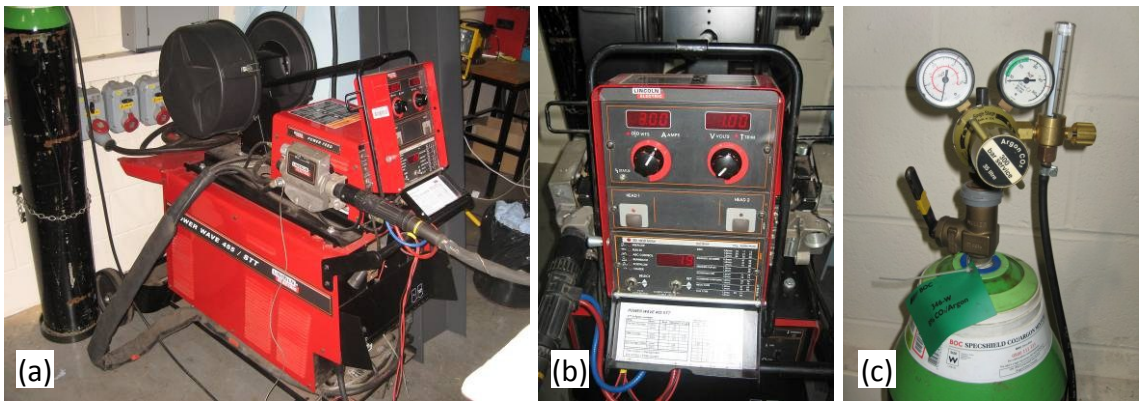

Figure 3.13. Welding set used for the preliminary single layer deposition studies (a) welding power source Lincoln Power Wave® 455/STT, (b) welder front panel, (c) shielding gas mixture Ar/CO_2 (8%).

According to Lincoln (see the manual of Power Wave ^{TM} 455 STT, June 2004), more constricted and stiffer arcs are produced with higher *Arc Control* settings due to higher current pulsing frequencies. These conditions are claimed to best suit high speed and low heat input welding applications. In pulse synergic welding operating modes (*i.e.* GMAW-P only), the *TRIM* setting controls the arc-length. *TRIM* setting is adjustable from 0.5 to 1.5. A set value of 1.0 is typically a good starting point for most welding conditions.

3.8.1.1 Effect of *TRIM* and contact tip to work distance on the weld bead and plate fusion characteristics

A systematic study of the effect of process variables on the weld bead characteristics, such as *TRIM* and contact tip to work distance (CTWD), was first carried out utilising the operation mode *Pulse Soft*. This operation mode was defined by selecting the program 19 (P19) in Lincoln's library of welding programs. P19 was selected for the reason that it was a valid pre-programmed synergic GMAW-P characteristic to be used with both 1.2 mm steel wire diameter and an argon blend (see Appendix J). Optimum pulse output characteristics were as a result established during the investigation by providing the best possible metal transfer conditions for 1.2 mm wire. Sound weld

deposition conditions produced good quality single layer welds, where spatter (metallic projections) was virtually absent. The pre-set operating conditions used in this study are summarised in Table 3.2.

Table 3.2. Nominal pre-set operating conditions utilised on the GMAW-P welding system.

Welding Process	Power source designation	Shielding gas	Flow rate (l min^{-1})	Operation mode	Synergic program	*TRIM*	CTWD (mm)	Effic (η)
GMAW-P	Lincoln Power Wave 455/STT	Ar/CO_2 (8%)	15	*Pulse Soft*	P19	1.0	13	0.8

Shielding gas, torch shielding gas mixture; *Flow rate,* torch shielding gas flow rate; *Operation mode*, selected welding mode on the power source database; *Synergic Program*, selected program on the power source database; *TRIM*, nominal arc-length setting; *CTWD*, nominal contact tip to work distance; E_{ff}, efficiency factor (η) of the welding process/variant.

The welding conditions utilised throughout the individual *TRIM* and CTWD studies are contained in Table 3.3.

Table 3.3. Summary of the welding conditions applied for the *TRIM* and CTWD studies.

Study	WFS (m min^{-1})	TS (m min^{-1})	Arc Control	Wire diameter (mm)	*TRIM*	CTWD (mm)
CTWD	3.0	0.2	+10	1.2	1.0	7 – 20 [2]
TRIM	3.0	0.2	+10	1.2	0.7 – 1.35 [1]	13

[1] *TRIM* settings were 0.7, 0.8, 0.9, 1.0, 1.15, 1.25 and 1.35; [2] *CTWD* discrete increments of one mm.

The experimental design and the weld bead profile measurements, of both *TRIM* and CTWD studies, are detailed in Tables I 1 and I 2, respectively (see Appendix I).

3.8.1.2 Effect of *TRIM* and contact tip to work distance on the weld bead surface quality

The impact of the *TRIM* and CTWD on the top surface quality of single layer deposits is investigated in this section. The analysis of various aspects of the quality of the weld beads top surface is undertaken by utilising the welds produced in the previous section (section 3.8.1.1). The quality of the deposited weld beads was mainly determined visually. The major points taken into account to assess the overall quality of the weld beads were: (1) the smoothness of the weld top surface or roughness; (2) the welding deposition stability; and (3) the weld bead straightness. However, one should note that these assessment criteria are dependent upon the other. For clarification purposes one might expect that sound weld conditions result from good metal transfer characteristics and thus stable deposition conditions. Poor welding conditions are more likely to detrimentally impact deposition characteristics – such as surface roughness, amount and

volume of metallic projections (spatter), occurrence of defects, or the weld bead straightness – and therefore the overall quality of the deposit.

The experiments were carried out using the welding conditions described in section 3.8.1.1. The pre-set welding conditions applied are summarised in Table 3.2 while essential operational welding conditions are listed in Table 3.3.

3.8.1.3 Effect of wire feed speed and wire feed speed to travel speed ratio on the weld bead and plate fusion characteristics

A systematic experimental approach (SEA*)* was undertaken in this investigation to understand the effects of primary welding parameters on the weld bead characteristics. The effect of welding process parameters (such as WFS, WFS/TS and WD) on single layer weld bead outputs (see section 3.7.1) were determined by maintaining a constant deposited cross section area approach (*i.e.* WFS/TS=const.). Such effects were initially established for a wire diameter of 1.2 mm, and 1.0 mm thereafter.

Table 3.4. Nominal pre-set operating conditions utilised on the GMAW-P welding system.

Welding Process	Power source	Shielding gas	Flow rate (l min^{-1})	Operation mode	Synergic program	CTWD (mm)	WD (mm)	Effic (η)
GMAW-P	Lincoln Power Wave ® 455/STT	Ar/CO_2 (8%)	15	*Pulse Soft*	P19	13	1.2	0.8
				Pulse Soft	P14		1.0	

The experiments were conducted by selecting in the first approach the *Pulse Soft* pre-programmed synergic welding characteristics from Lincoln´s library of programs. From the available list of programs (detailed in Appendix J), programmes P19 and P14 were found to be the best alternative selection to be used with an argon blend for 1.2 and 1.0 mm steel wires, respectively. The pre-set operating conditions utilised throughout this study are summarised in Table 3.4.

Table 3.5. Welding conditions utilised in GMAW-P for studying the effect of primary welding parameters on the weld bead characteristics.

Study	Operation mode	Synergic program	WFS_{set} [1] (m min^{-1})	WFS/TS	Arc Control	WD (mm)	*TRIM*	CTWD (mm)
WFS, WFS/TS WD on bead characteristics	*Pulse Soft*	P19	1.5-15.0	10-15-20	+10	1.2	1.0	13
		P14				1.0		

[1] Adjustments for the WFS_{set} were 1.5, 2.0, and discrete increments of 1 m min^{-1} thereafter.

In addition, the welding conditions used in this investigation can also be found in Table 3.5. It should be noted that the selection of the *TRIM* and CTWD settings were primarily based on previously optimised deposition conditions (according to sections 3.8.1.1 and 3.8.1.2). A comprehensive list of the experimental design and welding conditions applied in this investigation are provided in Appendix I, in Tables I 3 to I 5 (program 19), and I 6 (program 14). Measurements of individual weld bead characteristics are also included into these tables.

3.8.1.4 Effect of contact tip to work distance on electrical transients and weld bead profiles

At this stage of the research a modest knowledge about the influence of different welding operation modes and synergic programs on the electrical transient, and thus on the weld bead characteristics was available for 0.8 mm diameter steel wire. From the full list of available welding programs listed in Appendix J, it is seen that several programs could be employed in conjunction with the consumables` binary, 0.8 mm diameter wire and argon blend. Four possible welding operation modes and programs can be identified in Appendix J, namely *Pulse Crisp* – P12, *Pulse Soft* – P14, *Pulse Rapid Arc* – P13 and *Pulse Argon Mix* – P95.

Table 3.6. Nominal pre-set operating conditions utilised on the GMAW-P welding system for different operation welding modes.

Welding Process	Power source	Shielding gas	Flow rate (l min^{-1})	Operation mode	Synergic program	WD (mm)	Effic (η)
GMAW-P	Lincoln Power Wave ® 455/STT	Ar/CO2 (8%)	15	*Pulse Rapid Arc*	P13	0.8	0.8
				Pulse Crisp	P12		
				Pulse Soft	P14		
				Pulse Argon mix	P95		

A systematic investigation was carried out to investigate the effect of the CTWD on the welding electrical transient and weld bead characteristics, on each of the above applicable welding operation modes and programs. Current waveform outputs, *i.e.* I_p, I_b, T_p, T_b, I_p/I_b, T_p/T_b, f and LDC (see Figure 3.14), electrical transients, *i.e.* V_{inst}, I_{inst}, AIP, as well as weld bead characteristics were measured as a function of the CTWD. The experiments were carried out at fixed WFS and TS settings. The pre-set operating conditions utilised throughout this study are summarised in Table 3.6.

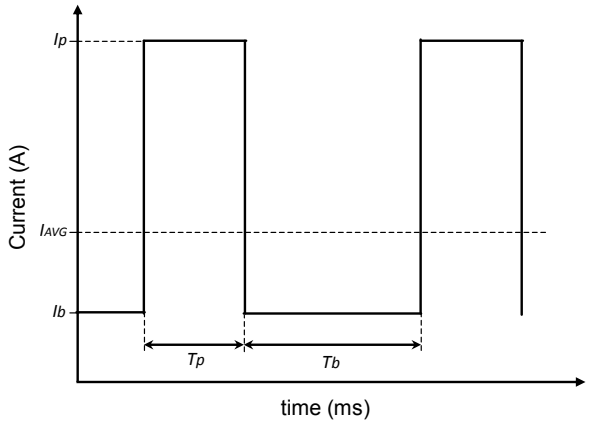

I_p: Pulse current, (A)

I_b: Background current, (A)

T_p: Duration of pulse current, (ms)

T_b: Duration of background current, (ms)

I_{AVG}: Average current=$(I_p\ T_p + I_bT_b)(T_p+T_b)^{-1}$, (A)

f: Frequency=$(T_p+T_b)^{-1}$, (Hz)

LDC: Load duty cycle=$T_p\ (T_p+T_b)^{-1}\times 100$, (%)

Figure 3.14. Schematic diagram of a square pulsed-current waveform as function of time. The basic pulse parameters are also represented.

In addition, the welding conditions utilised in this study are described in Table 3.7. It should be noted, however, that in order to obtain sound weld conditions the *TRIM* setting was fine-tuned accordingly prior to deposition.

Table 3.7. Welding conditions used in GMAW-P for each individual operating mode.

Study	Operation mode	Synergic program	WFS_{set} (m min^{-1})	WFS/TS	Arc Control	WD (mm)	*TRIM*	CTWD[1] (mm)
CTWD on electrical transient and bead characteristics	*Pulse Rapid Arc*	P13	6.0	15	OFF	0.8	0.90	10 - 20
	Pulse Crisp	P12					1.05	
	Pulse Soft	P14					1.00	10 - 22
	Pulse Argon mix	P95					1.20	

[1] Adjustments for the *CTWD* were made in discrete increments of 1 mm.

A complete listing of the experimental design and measurements of the bead profiles, are contained in Appendix I from Table I 7 to I 14, for all studied welding modes.

3.8.1.5 Effect of wire feed speed on the electrical transients

In order to obtain an insight of the effect of the WFS on the waveform of the welding current pulse parameters, a number of experiments were performed using the *Pulse Crisp* welding operation mode. This program was selected for the reason that it was one valid synergic curve to be used with 0.8 mm steel wire diameter and an argon blend. The measured electrical transient outputs obtained were already mentioned in section 3.8.1.4. The pre-set operating conditions utilised in this study were the same as described in Table 3.6 (see section 3.8.1.4). Experiments were carried out at a constant TS, WD, *Arc Control* and *TRIM* settings. The welding conditions employed in this

investigation are provided in Table 3.8. Note, however, that the applied CTWD setting of 19 mm was determined based upon Lincoln's recommendation for achieving optimum dynamic characteristics (see manual of Power Wave ^{TM} 455 STT, June 2004). The full list of the experimental design for this study, detailing precise measurements of individual waveform characteristics, is shown in Table I 15 (see Appendix I).

Table 3.8. Welding conditions utilised in the WFS investigation for GMAW-P and P12.

Study	Operation mode	Synergic program	WFS_{set} (m min^{-1})	TS (m min^{-1})	Arc Control	WD (mm)	*TRIM*	CTWD (mm)
WFS on electrical transient	*Pulse Crisp*	P12	2.0 – 10.0	0.4	OFF	0.8	1.00	19

[1] Adjustments for the WFS_{set} were made in discrete increments of 2 m min^{-1}.

3.8.2 Current waveform modulation in pulsed gas metal arc welding

Although distinct GMAW-P welding operation modes were employed to perform the preliminary studies described in section 3.8, it is worth pointing out that individual operating modes were determined by different waveform characteristics, in other words pre-programmed synergic curves. Thus, a different approach was set to be investigated aiming therefore to exploit the use of a new welding power source in *non-adaptive control* mode. Initially, a preliminary study was carried out to evaluate the influence of small changes in CTWD on both the surface quality and electrical transients of single layer deposits. Then, various weld bead characteristics were produced and measured in *non-adaptive control* mode. These geometrical outputs made using *non-adaptive control* mode were then compared to the ones produced with P13 – in the *adaptive control* mode – for similar welding conditions. The effect of primary welding parameters of the current waveform, such as I_p, I_b, T_p, T_b, f and LDC, on the weld surface quality and arc stability of single layer deposits were also investigated.

Experiments were conducted on a five axis rig (see Figure 3.12) using the same materials, welding consumables (mild steel wire diameter of 0.8 mm), preparation method, and clamping procedure as described in section 3.8.1. The relative angle between the torch and the substrate, the offset position between layers, as well as the interpass temperature were all maintained the same as referred in section 3.8.1.

Figure 3.15. Welding set utilised for the waveform modulation studies (a) Lincoln Power Wave® F355i welding power source, (b) wire feeder (model Power Feed 10 Robotic), and (c) shielding gas mixture Ar-CO_2 (8%).

A modular and multi-process welding Lincoln Power Wave® F355i unit was used in this study in constant current *non-adaptive control* mode (see Figure 3.15(a)). This unit was integrated fully with the Waveform Control Technology ^{TM} for waveform output development purposes. Lincoln "Wave Designer Pro" software was utilised for development and optimisation of pulse welding conditions (Vernyi, 2007), allowing various pulse parameters to be changed on the fly while the system was running. Another interesting feature of the software control system is to ensure that all input pulse parameters remain constant independently of the effect of external factors, *e.g.* changes in the electrode extension.

Table 3.9. Nominal pre-set operating conditions utilised for GMAW-P in *non-adaptive mode*.

Welding Process	Power source designation	Shielding gas	Flow rate (l min^{-1})	Operation mode	Synergic program	WD (mm)	*TRIM*	Arc Control	Effic (η)
GMAW-P	Lincoln Power Wave® F355i	Ar/CO_2 (8%)	15	*non-adaptive*	none	0.8	1.0	OFF	0.8

The power source has no external controls, for the reason that it was especially developed for automated and robotic solutions. The control signals were sent from and to the power source via an Ethernet connection to a computer. The welding set also comprised a robotic wire feeder and a shielding gas mixture of Ar/CO_2 (8%), as depicted in Figures 3.15(b) and (c), respectively. The pre-set operating conditions used in this study are given in Table 3.9. The baseline current waveform was first developed based on a trial and error approach and then uploaded to the welding unit using the *Wave Designer Pro* ^{TM} user interface. Table 3.10 contains the welding conditions used throughout this investigation in *non-adaptive control* mode.

Table 3.10. Welding conditions used for GMAW-P in *non-adaptive mode*.

Operation mode	WFS [1] (m min^{-1})	I_p (A)	Ramp Up/ Overshoot (%)	T_p (ms)	I_b (A)	Tail-out (ms)	T_b (ms)	I_{AVG} (A)	*f* (Hz)	LDC (%)
non-adaptive	6	280	500 / 25	1.2	50	2.8	6	88.3	100	16.7

[1] Set-up to 236 in min^{-1} in the Wave Designer Pro ™ software.

3.8.2.1 Effect of contact tip to work distance on bead surface quality, electrical transients and welding control mode

The effect of small variations of the CTWD on the surface quality, as well as on the electrical transient in *non-adaptive control* mode was investigated, using the set-up described above. The CTWD was increased in 2 mm steps between 13 and 19 mm within the range of CTWD's studied. The WFS was 6 m min^{-1} and TS was held constant at 0.4 m min^{-1}. The surface quality of single layer deposits was determined according to section 3.8.1.2. Simultaneously, electrical transient data were captured, *i.e.* V_{inst} and I_{inst}, and graphically displayed as function of time. The measured profiles were analysed predominantly from the metal transfer mechanism standpoint, and related to the surface quality of the weld beads referred above. Finally, the effect of the CTWD on the electrical transients and bead profiles was investigated in different power source control modes – *adaptive* (P13) and *non-adaptive control* mode. This study was to compare electrical transients and weld bead characteristics at fixed CTWD conditions (13 mm and 19 mm). The pre-set operating and welding conditions applied throughout are summarised in Tables 3.9 and 3.10. The full experimental design detailing measurements of welding conditions, as well as individual bead profiles can be found in Table 4.1 (see chapter 4).

3.8.2.2 The effect of waveform on bead profiles, surface quality, process behaviour and stability

In this investigation, the effect of various welding current parameters and waveforms on metal transfer conditions, weld bead shape, surface quality and appearance of single layer deposits was estimated. The impact of primary welding current parameters (such as I_p, I_b, T_p, T_b), as well as complementary ones (such as *f* and LDC), were evaluated in *non-adaptive control* mode at constant I_{AVG}. Applied nominal welding parameters are contained in Table 3.9, which are the same as in the previous section. Again, the WFS

was fixed at 6 m min^{-1} and TS was held constant at 0.4 m min^{-1}. Note that the baseline current waveform was fine-tuned to a new CTWD condition (14 mm), after a preliminary optimisation study had been carried out. The new baseline welding conditions are listed in Table 3.11. The investigation was broken down into five components (S_1, S_2, ..., S_5), each of them corresponding to a different parametric study.

Table 3.11. Welding conditions used for waveform modulation in *non-adaptive mode*.

Operation mode	WFS_{set} [1] (m min^{-1})	I_p (A)	Ramp Up/ Overshoot (A t^{-1} / %)	T_p (ms)	I_b (A)	Tail-out (ms)	T_b (ms)	I_{AVG} (A)	*f* (Hz)	LDC (%)
non-adaptive	6	280	500 / 20	1.3	38	2.8	5	88.3	110	20

Operation mode, selected welding mode on the power source database; WFS_{set}, wire feed speed setting; I_p , pulse current; *Ramp up*/overshoot, current ramp up rate / percentage increase in current above the nominal I_p; T_p , duration of pulse current; I_b , background current; *Tail-out*, adjusts the rate that the current is changed from I_p to I_b; T_b , duration of background current; I_{AVG}, average current; *f,* frequency; *LDC*, load duty cycle.

Note: Some of these values may be limited to one decimal place by the Wave Designer Pro ™ interface software; [1] Set to 236 in min^{-1} in the Wave Designer Pro ™.

To simplify calculations and estimate the effect of individual parameters on the electric transient and weld bead characteristics, variables had to be adjusted whilst others were held constant. In study number one (S_1) the effects of narrower and progressively taller current peaks (or I_p *vs.* T_p) were investigated (see Figure 3.16(a)). Here, I_p and T_p were the control parameters and I_b and T_b were then adjusted to comply with a constant I_{AVG} and *f* condition. In S_2 the effects of progressively narrower current peak's (or T_p *vs.* I_b) at constant I_p was estimated (see Figure 3.16(b)). In this case, T_p and I_b were the control parameters whereas T_b was regulated accordingly, once more to satisfy a constant I_{AVG} and *f* condition.

S_3 considered the effects of taller current peak's (or I_p *vs.* I_b) at constant T_p and T_b (see Figure 3.16(c)). The control parameter was I_p while I_b was fine-tuned in accordance with a fixed I_{AVG}, *f* and LDC condition.

S_4 investigated the effects of different *f* at constant I_p and T_p at variable LDC (see Figure 3.16(d)). *f* was the control parameter and I_b and T_b attuned accordingly to ensure fixed I_{AVG} circumstances. The last study, S_5, looked into the effects of *f* at constant I_p and I_b at fixed LDC (see Figure 3.16(e)). Once more the *f* was the control parameter and T_p and T_b adjusted appropriately in order to keep I_{AVG} and LDC constant. The complete set of experiments containing all customised current inputs is shown in Tables I 16 to I 20 (see

Appendix I). The analysis of the effect of changes in the waveform structure on the metal transfer mode, and as a result on the overall welding process stability, was carried out by means of current waveform snapshots and supported then by scatter plots (I_{inst} *vs.* V_{inst}). Transient data utilised in scatter plots were recorded according to the method described in section 3.3 for a time period of 10 seconds at 5 kHz, and displayed accordingly.

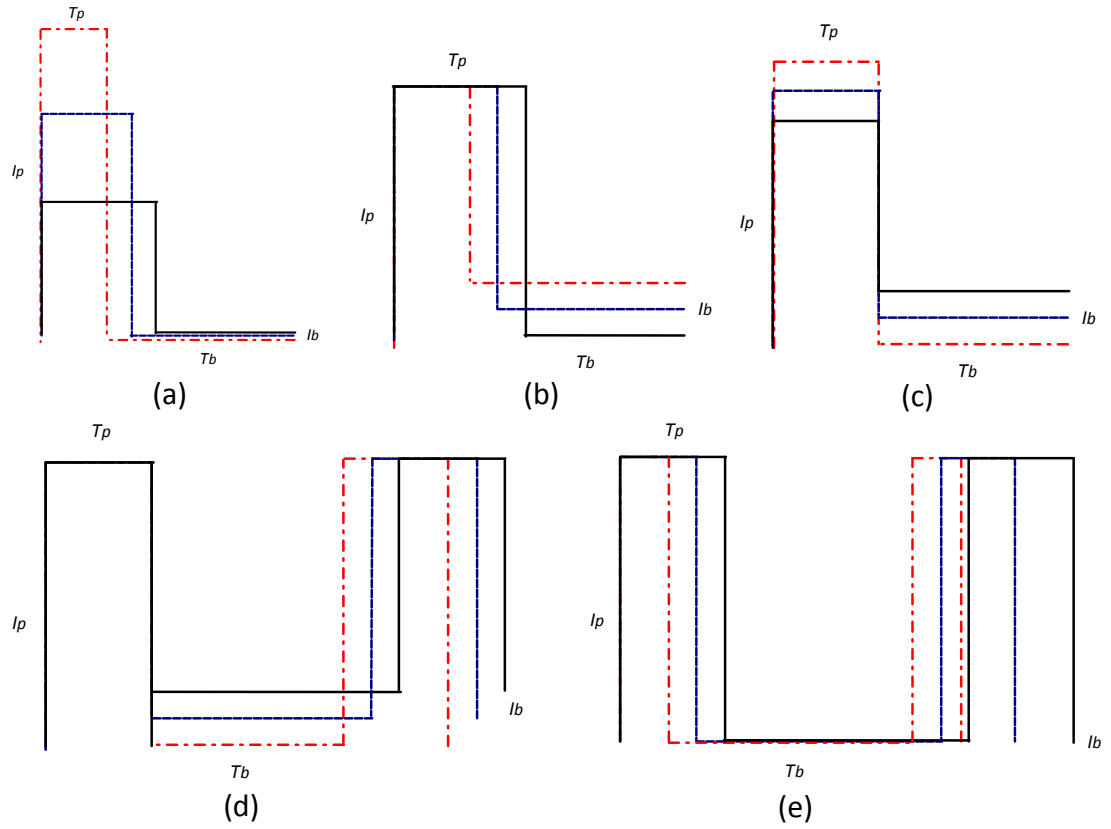

Figure 3.16. Schematics of the followed experimental design strategy for the waveform modulation study (a) S_1, (b) S_2, (c) S_3, (d) S_4, and (e) S_5.

3.8.3 Cold metal transfer

Experiments were conducted on a five axis rig (see Figure 3.12), while the materials and welding consumables described in section 3.1 were utilised to deposit mild steel single bead-on-plate beads in various wire diameters such as 0.8, 1.0 and 1.2 mm. The substrates were prepared prior to deposition as described in section 3.2, and clamped in a 4 point arrangement to a rotating table in the rig mentioned above. A modified GMAW variant based on a controlled dip transfer mode mechanism named Fronius cold

metal transfer (CMT)[17] was utilised in this study (see Figures 3.17(a) and (b)). Again, the relative angle between the *xy* plane of the substrate top surface and the torch, the offset position between layers, as well as the interpass temperature were all maintained identical as referred in section 3.8. The employed shielding gas mixture was Ar/CO_2 (20%) unless stated otherwise (see Figure 3.17(c)), whilst the CTWD was held constant at 13 mm. Welding conditions were applied by setting the arc-length correction (ALC) and dynamic correction (DC_{orr}) to a nominal "zero" setting.

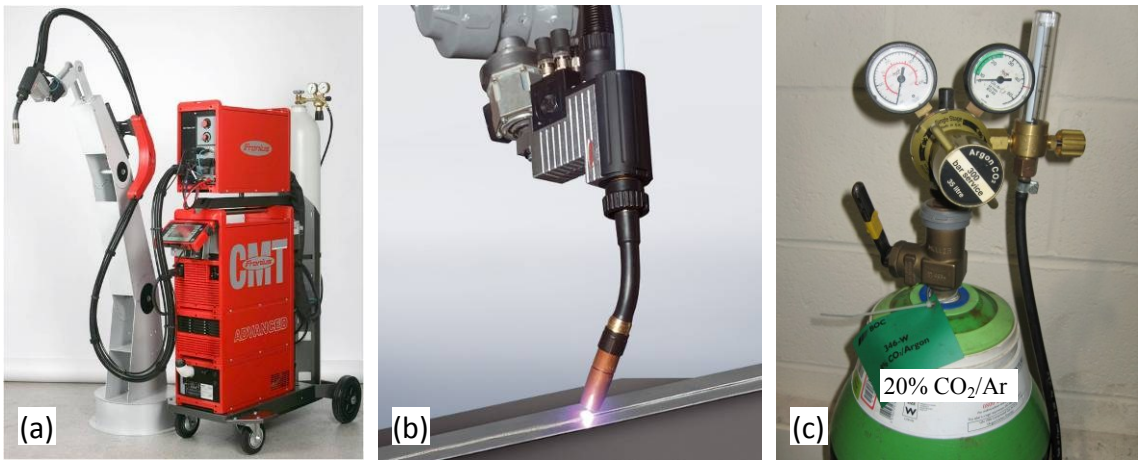

Figure 3.17. Cold metal transfer welding set used for the preliminary single layer deposition studies (a) welding power source, (b) *Robacta Drive* welding torch, (c) shielding gas mixture Ar/CO_2 (20%); photographs courtesy of Fronius International GmBh.

The welding conditions and synergic welding characteristics were selected through the CMT control panel and determined according to the process (pure CMT), material type (G3Si1), wire diameter, and shielding gas mixture to be utilised. It is worth emphasising that the welding characteristics of all pre-programmed synergic curves selected in this study were optimised for a shielding gas mixture containing Ar/CO_2 (18%) from group M21, more commonly used in Europe.

[17] Cold metal transfer power source details: Art No. 4,075,139,R and Serial No. 18142794.

3.8.3.1 Effect of arc-length control, dynamic correction and contact tip to work distance on electric transients and bead profiles

A comprehensive investigation was initially undertaken to find out the impact of important process parameters such as ALC, DC_{orr} and CTWD on the electric transient, and then on single layer weld bead profiles. It is important to point out that a mild steel consumable electrode wire with 1.2 mm in diameter was used invariably in this study. Constant WFS and TS welding conditions were utilised along this investigation. The pre-set operating conditions applied in this study are summarised in Table 3.12.

Table 3.12. Nominal pre-set operating conditions utilised in the CMT welding system.

Welding Process	Power source designation	Shielding gas	Flow rate (l min^{-1})	Operation mode	WD (mm)	CTWD (mm)	Effic (η)
CMT	Fronius CMT	Ar/CO_2 (20%)	15	*Pure CMT*	1.2	13	0.9

The experimental design was developed in the form of three independent set of experiments defined herein as studies ALC, DC_{orr} and CTWD (see Table 3.13). The welding conditions applied in this study are listed in Table 3.13. The full experimental design containing both the electric transient, and individual bead profile data, can be found in Appendix I from Tables I 21 to I 23.

Table 3.13. Welding conditions employed in CMT for studies ALC, DC_{orr} and CTWD.

Study	WFS (m min^{-1})	TS (m min^{-1})	ALC	DC_{orr}	CTWD
ALC	4.0	0.4	-30 to 30 [1]	0	13
DC_{orr}	4.0	0.4	0	-5 to 5 [2]	13 [3]
CTWD	4.0	0.4	0	0	10 to 18

Adjustments were made in discrete increments of 10^1, 2 and 1^2, and 1^3 units.

3.8.3.2 Effect of wire feed speed and shielding gas composition on electrical transients

In this investigation, a number of experiments were carried out to establish the relationship between the WFS and the electrical transients utilising various shielding gas compositions. Shielding gas mixtures with different compositions were used in this study, and these were Ar/CO_2 (8%), Ar/CO_2 (20%), and Ar/CO_2 (5%)/O_2 (2%). The impact of these different shielding gas compositions on the stability of the welding arc was also analysed using scatter plots data captured at every instant in time for a period

of 10 seconds at 5 kHz. Single layer weld tracks were deposited by using a mild steel wire electrode with diameter of 0.8 mm, at constant TS of 0.4 m min^{-1}. It is important to note that for the above material type and wire diameter optimal operational welding conditions were attainable using a nominal gas mixture containing Ar/CO_2 (18%), as required by the synergic curve characteristic in the database of welding programs. Nevertheless, good quality sound weld deposits were produced throughout, independently of the shielding gas composition used.

The pre-set welding conditions used in this investigation are listed in Table 3.14. The experimental design was broken down into three individual studies, namely G_1, G_2 and G_3, corresponding in the same order to a separate shielding gas composition Ar/CO_2 (8%), Ar/CO_2 (20%), and Ar/CO_2 (5%)/O_2 (2%). The WFS was set to 4, 6, 8, 10 and 12 m min^{-1} in each of the above studies. The plan of experiments is detailed in full in Table I 24 (see Appendix I).

Table 3.14. Nominal pre-set welding conditions utilised in the CMT welding system.

Welding Process	Power source	Shielding gas	Flow rate (*l* min^{-1})	Operation mode	TS (m min^{-1})	WD (mm)	CTWD (mm)	Effic (η)
CMT	Fronius CMT	Ar/CO_2 (8%), Ar/CO_2 (20%), Ar/CO_2 (5%)/ O_2 (2%)	15	*Pure CMT*	0.4	0.8	13	0.9

3.8.4 Comparison of pulsed gas metal arc welding and cold metal transfer

The experiments reported herein were carried out on the five axis rig (see Figure 3.12). Materials and welding consumables utilised to perform the experiments are described in section 3.1. Mild steel solid wires with diameters of 0.8 and 1.2 mm were used in this study, while substrates were prepared before deposition as described in section 3.2. Two GMAW systems, Lincoln Power Wave® 455/STT and CMT, were utilised in this investigation. The relative angle between the welding torch and the substrate, as well as the interpass temperature was upheld as in section 3.8.1. Shielding gas mixtures with Ar/CO2 (20%), and Ar/CO2 (8%) were utilised in CMT and Lincoln Power Wave® 455/STT, respectively. CTWD was held constant at 13 mm. Nominal welding deposition conditions were applied. Both the ALC and DC_{orr} parameters were set to zero in CMT, whereas that the *Arc Control* and *TRIM* were set to OFF and 1.00 conditions.

3.8.4.1 Effect of wire feed speed and wire feed speed to travel speed ratio on weld bead characteristics

The aim of this study was to provide an insight into the understanding of the effect of primary welding parameters, such as WFS, TS and WFS/TS, on the weld bead characteristics. The second goal of this investigation was to compare the influence of two different welding processes *i.e.* GMAW-P and CMT, on the above parametric study. The operation modes selected in the Lincoln Power Wave® 455/STT welding source for 0.8 and 1.2 mm diameter steel wires were *Pulse Rapid Arc* and *Pulse Soft*, respectively. These operation modes were selected by choosing P13 and P19 in Lincoln's library of welding programs, respectively. As for the CMT welding system the operation mode *Pure CMT* was selected. The welding conditions applied in this study are detailed in Table 3.15, whilst the adopted plan of experiments is listed in full in Table D 1 (Appendix D).

Table 3.15. Pre-set welding conditions used on both the GMAW-P and CMT welding systems.

Welding Process	Power source designation	Shielding gas	Flow rate (l min^{-1})	Operation mode (program)	CTWD (mm)	WD (mm)	Effic (η)
Pulsed- GMAW	Lincoln Power Wave 455/STT	Ar/CO_2 (8%)	15	*Rapid Arc (P13)* / *Pulse Soft* (P19)	13	0.8 / 1.2	0.8
Fronius (CMT)	Fronius Cold Metal Transfer	Ar/CO_2 (20%)	15	*Pure CMT*	13		0.9

3.8.4.2 Weld bead and plate fusion characteristics comparison of cold metal transfer and pulsed gas metal arc welding

In this section the effect of both welding processes, CMT and GMAW-P, on the weld bead, and fusion characteristics is investigated and compared for constant welding conditions. A mild steel consumable electrode wire with 0.8 mm in diameter was used in this investigation, while a WFS_{actual} of 6 m min^{-1} and TS of 0.4 m min^{-1} were applied invariably. Pre-set welding conditions are summarised in Table 3.15 (see section 3.8.4.1).

3.8.4.3 High speed electrical transients

The objective of this work was to characterise and compare the underlying welding operation modes in both CMT and GMAW-P systems, by examining the captured electric transient data. V_{AVG}, I_{AVG} and AIP were graphically represented as function of

the actual wire feeding rate. A 0.8 mm diameter mild steel solid wire was employed in this study. The pre-set welding conditions used are summarised in Table 3.15 (see section 3.8.4.1). *Pulse Rapid Arc* (P13) was the selected operation mode in Lincoln Power Wave® 455/STT welding source, whereas *Pure CMT* was chosen in Fronius CMT. Note, however, that *TRIM* was adjusted in a range between 0.9 and 1.1 in the Lincoln power source, according to the WFS regime. *TRIM* was adjusted to 0.9, 1.0 and 1.1 within WFS regimes between: 3 to 8, 8 to 12, and 12 to 20 m min^{-1}, respectively. Electrical transients were captured according to section 3.3.

3.9 Single layer welds in steel

3.9.1 Apparatus and welding conditions

Two GMAW variants, GMAW-P[18] and Fronius CMT, were employed in this study. Secondary process parameters such as ALC and DC_{orr} (in CMT), and the *Arc Control* (in GMAW-P), were kept fixed to a nominal "zero" setting throughout the investigation. Experiments were carried out on the five axis rig shown in Figure 3.12. Single layer welds were deposited using the materials and welding consumables described in section 3.1.1, using 0.8, 1.0 and 1.2 mm wire diameters. The applied pre-set operating conditions are contained in Table 3.16.

Table 3.16. Pre-set operating conditions used for modelling single layer welds in steel.

Welding Process	Power source designation	Shielding gas	Flow rate (l min^{-1})	Synergic programs	CTWD (mm)	Substrate T (°C)	Effic (η)
GMAW-P	Lincoln Power Wave 455/STT	Ar/CO_2 (8%)	15	*Rapid Arc (P13)*	13	≈ 25	0.8
Fronius (CMT)	Fronius Cold Metal Transfer	Ar/CO_2 (20%)	15	*Pure CMT*	13	≈ 25	0.9

A systematic experimental approach (SEA) was adopted in this study. As a result an operational process window was first established for each wire diameter and welding process. The welding conditions used are summarised in Table 3.17. These limit conditions, in particular WFS, were essentially determined by the maximum welding power source electric output capability. Weld beads were laid on substrates by utilising

[18] Lincoln Power Wave® 455/STT.

a constant WFS/TS ratio. Constant transverse cross section areas were deposited while interactions between primary process parameters and single bead characteristics were measured (see section 3.7.1). The experimental design is contained in full in Tables C 1 and C 2 (see Appendix C), alongside measurements of weld bead characteristics for the CMT welding process.

Table 3.17. Summary of the welding conditions for GMAW-P and CMT experiments.

Fronius (CMT)	Wire diameter (mm)			GMAW-P	Wire diameter (mm)		
	0.8	*1.0*	*1.2*		*0.8*	*1.0*	*1.2*
WFS_{set} (m min^{-1}) [1]	2.0 – 14.0	2.0 – 9.0	2.0 – 6.0	WFS (m min^{-1})	2.0 – 20.0	2.0 – 20.0	2.0 – 20.0
WFS/TS[2]	10 – 20	10 – 20	10 – 20	WFS/TS	10 – 20	10 – 20	10 – 20

Discreet increments of [1]one meter per minute and [2]five units.

3.9.2 Welding experimental plan

The substrates were prepared before deposition according to section 3.2, and restrained in a 4 point arrangement to a rotating table in the 5 axis rig. The angle between the *xy* plane of the substrate top surface and the torch was fixed at 90º, as in section 3.8.3.

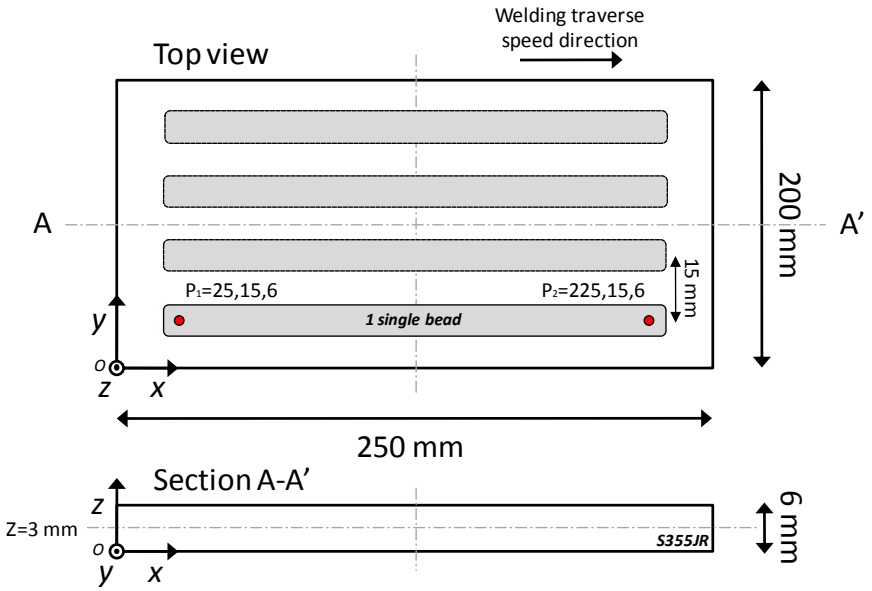

Figure 3.18. Schematic illustration of the base plate dimensions and single layer deposition strategy (top and cross section A-A' views).

Single weld beads were deposited next to each other parallel to the welding direction (moving in the +*y* direction), while the distance between the deposited centrelines was kept at 15 mm (see Figure 3.18). The minimum offset distance of 15 mm was to minimise the impact of thermal and/or mechanical effects in-between weld beads.

Welds were approximately 200 mm long, while an interpass temperature of 25 °C was maintained. Temperature was monitored by an infrared pyrometer (model *Raytek Raynger S.T.*). Experiments were carried out in PA position, or 1G according to PD CEN/TR14633:2003, and the welding conditions detailed in section 3.9.1 were applied. Stable and reproducible welding conditions were assured by a constant CTWD setting at 13 mm, irrespective of the welding system. Electric transients were captured according to the method described in section 3.3.

3.10 Multi-layer deposition in steel

Following the previous study, based on the effect of process parameters on weld bead characteristics in single layer deposition (see section 3.9), a new plan of experiments was formulated to investigate multi-layer deposition features. CMT was employed throughout the studies described in the next sub sections for the manufacturing of multi-layer specimens, as opposed to GMAW-P. The reason why CMT was selected to perform the trials was due to its better plate fusion characteristics (*i.e.* lower RR, P, D, and A_1), insensitivity to variations in the CTWD, and the ability for depositing weld metal free of spatter. ALC and DC_{orr} were again held constant at a nominal "zero" setting.

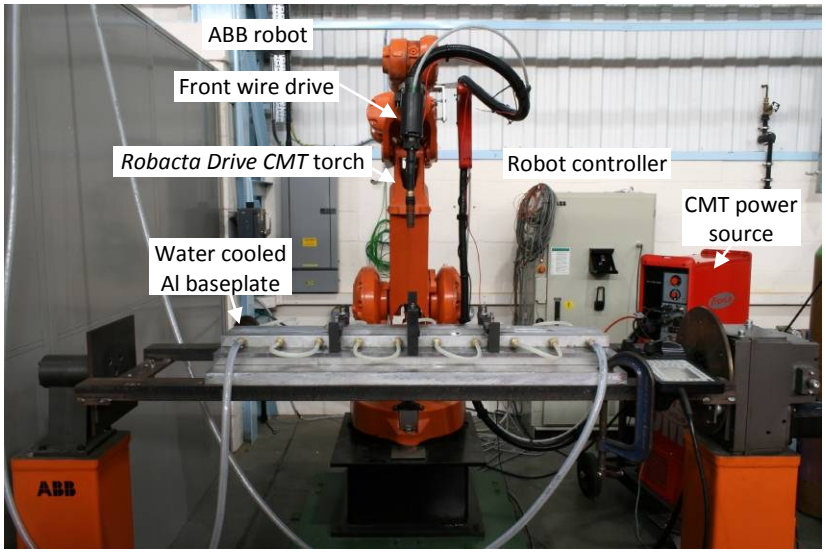

Figure 3.19. Experimental set-up used in the multi-layer deposition study.

A water cooled *Robacta Drive CMT* welding torch was attached to a six-axis ABB industrial manipulator (model *IRB 2400*) to accurately reproduce the torch welding traverse speed and deposition sequence, over a repeated number of cycles (see Figure

3.19). The materials and welding consumables described in section 3.1 were applied. Mild steel wire spools were utilised along the studies with diameters of 0.8, 1.0 and 1.2 mm (unless stated otherwise).

This investigation comprised the manufacturing of individual multi-layer walls (the number of layers is described in the corresponding section) by utilising an identical approach to single layer, *e.g.* constant ratios of deposition rate to weld travel speed (see section 3.9). Substrates were prepared before deposition as described in section 3.2, and clamped thereafter in a water cooled backing plate, according to section 3.4. The welding torch was kept perpendicular to the *xy* plane of the substrate, while interpass temperature was kept fixed at room temperature and monitored in accordance to section 3.4 (unless stated otherwise).

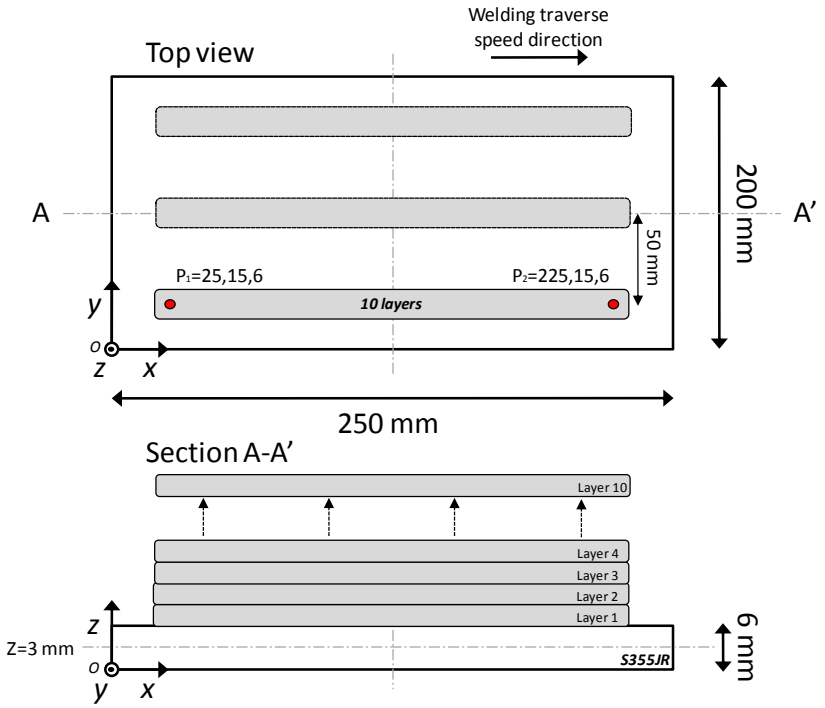

Figure 3.20. Schematic illustration of the base plate dimensions and multi-layer deposition strategy (top and cross section A-A' views).

Experiments were carried out in PA position, or 1G according to PD CEN/TR14633:2003. Stable and reproducible welding conditions were guaranteed by a constant CTWD setting at 13 mm, and electric transients were captured according to the section 3.3. Continuous weld beads of approximately 200 mm long were progressively laid down in an additive fashion one layer at a time in one direction only (+*x*). Measurements of SW_{av} were made in accordance to section 3.7.2.1, while W_{eff} was

measured as described in 3.7.2. A maximum of three straight walls per substrate were built next to each other parallel to the welding direction. This was achieved by offsetting the welding torch position 50 mm in the +*y* direction (see Figure 3.20).

3.10.1 Effect of layer number and interpass temperature on bead characteristics and surface quality

Experiments were carried out in order to determine the effect of successive deposition, *i.e.* layer number, on weld bead characteristics such as bead width and height in multi-layer walls. The influence of interpass temperature (T_{sub}) on the relative bead height increment H_n (Delta-*z*) and on other multi-layer responses such as W_{eff}, SW_{av} and MDE, were examined (see section 3.7.2 for definitions). Transverse cross section and T_{sub} measurements were made according to sections 3.7.2 and 3.5, respectively. A consumable electrode wire with 0.8 mm in diameter was used invariably in this investigation to produce specimens 4 layers high. A shielding gas mixture containing Ar/CO_2 (5%)/O_2 (2%) was chosen. The plan of experiments comprised the manufacturing of specimens at different substrate temperatures (40, 200, and 350 °C), WFS_{set} (4, 6, 8 and 10 m min^{-1}), and WFS/TS (10, 15 and 20), as detailed in Appendix E (see Table E 1). In conjunction with the study described above, a second one off test was carried out to produce a 10 layers high wall. In this case, the applied welding conditions were: WFS_{set}=4 m min^{-1}; WFS/TS=10, 15 and 20; while the temperature of the substrate was maintained at 40 °C.

Table 3.18. Nominal pre-set operating conditions utilised in the CMT welding system.

Welding Process	Power source designation	Shielding gas	Flow rate (*l* min^{-1})	Operation mode	WD (mm)	CTWD (mm)	Effic (η)
CMT	Fronius CMT	Ar/CO_2 (5%)/O_2(2%)	15	*Pure CMT*	0.8	13	0.9

The effect of T_{sub}, AIP and HI on the sidewall surface features of the manufactured specimens (4 layers high) has also been investigated in this section. A number of samples were selected, and one of the sidewalls photographed in order to compare the quality of the produced surfaces visually. AIP and HI were measured in each individual layer according to section 3.3, and averaged thereafter. The applied nominal pre-set operating conditions are summarised in Table 3.18. The experimental design detailing

welding conditions and absolute measurements of bead height increments is contained in Table E 1 (see Appendix E).

3.10.2 Effect of travel speed on surface waviness and effective wall width

The investigation aimed at clarifying the interactions between primary process parameters, such as WFS and TS, and relevant multi-layer deposition characteristics (refer to section 3.7.2). A mild steel wire electrode with 0.8 mm in diameter was utilised through this experimental plan for the manufacturing of 10 layers high walls. The shielding gas mixture used was Ar/CO_2 (20%). It is important to note that interpass temperature was held constant in this study at room temperature of approximately 25° C for all produced specimens. The nominal pre-set operating conditions are summarised in Table 3.19. The experimental design is detailed in Table E 2 in Appendix E.

Table 3.19. Nominal pre-set operating conditions utilised in the CMT welding system.

Welding Process	Power source designation	Shielding gas	Flow rate (l min^{-1})	Operation mode	WD (mm)	CTWD (mm)	Effic (η)
CMT	Fronius CMT	Ar/CO_2 (20%)	15	*Pure CMT*	0.8	13	0.9

3.10.3 Effect of wire diameter and material on surface waviness and effective wall width

In this section the effect of TS on SW_{av} is investigated by utilising different steel wire diameters and base materials. Multi-layer walls with 10 layers high were produced in this study. Wires with diameters of 0.8, 1.0 and 1.2 mm were utilised initially at constant WFS_{set} of 5 m min^{-1} (0.8 mm), and 6 m min^{-1} (1.0 and 1.2 mm). The shielding gas mixture used was Ar/CO_2 (20%). Stainless steel and aluminium walls were produced using 1.0 mm wire diameter, grade G199LSI and AlSi5, with shielding gas compositions of Ar/CO_2 (2.5%) and Ar (100%), respectively. A constant 6 m min^{-1} WFS_{set} was utilised with both stainless and aluminium base materials. Pre-set welding conditions, other than those referred above, are contained in Table 3.19.

3.10.4 Deposition efficiency in carbon steel

In order to determine metal deposition efficiency (MDE) of carbon steel multi-layer walls as a function of the effective wall width (W_{eff}), a series of experiments were undertaken using a wire electrode with 0.8 mm in diameter. The plan of experiments performed in section 3.10.2 was therefore used for the calculations, according to the method described in section 3.7.2. Nominal welding conditions applied throughout this investigation can be found in Table E 2 (Appendix E).

3.11 Overhead deposition

In this section, a feasibility study focused on multi-layer deposition in the overhead position (PD or 4F in accordance to PD CEN/TR14633:2003) was carried out. The quality of the deposited weld beads were evaluated and assessed visually according to the degree of bead uniformity *i.e.* geometry and appearance, along the weld axis.

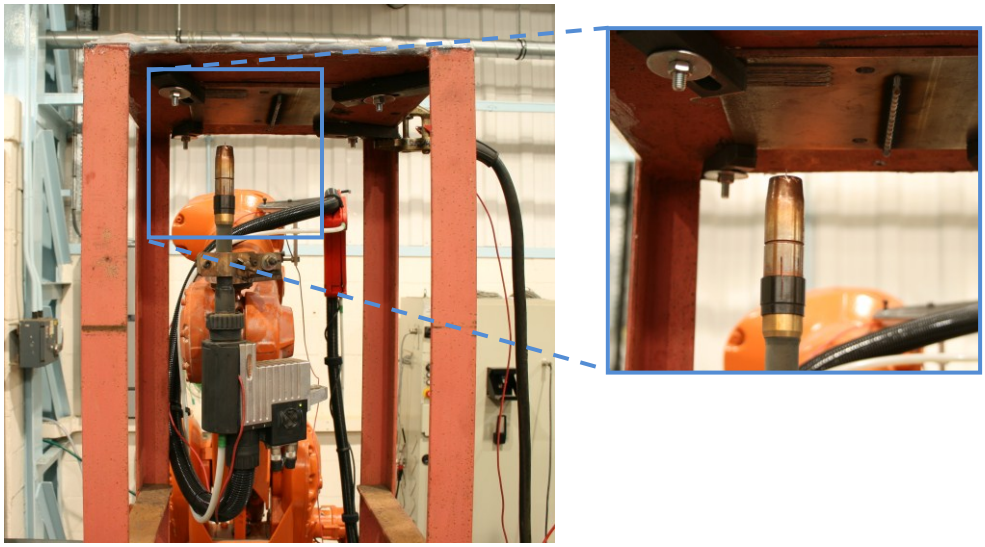

Figure 3.21. Experimental set-up for the overhead multi-layer deposition trials.

The experimental set-up comprised a six-axis ABB robot that was utilised alongside with a Fronius CMT welding power source, Figure 3.21. Secondary process parameters, such as ALC and DC_{orr} were held constant at a nominal "zero" setting. Materials and welding consumables used during the study are described in 3.1. A mild steel solid wire electrode with 0.8 mm in diameter, and a shielding gas with a composition of Ar/CO_2 (20%) were utilised invariably in this investigation. Interpass temperature was kept

constant at room temperature of approximately 25 °C in between deposited layers. Nominal pre-set operating conditions are summarised in Table 3.20.

Table 3.20. Nominal pre-set operating conditions utilised in the CMT welding system.

Welding Process	Power source designation	Shielding gas	Flow rate (l min^{-1})	Operation mode	WD (mm)	CTWD (mm)	Effic (η)
CMT	Fronius CMT	Ar/CO_2 (20%)	15	*Pure CMT*	0.8	13	0.9

The plan of experiments (15 trials in total) followed an identical approach to single and multi-layer studies, *i.e.* constant ratios of deposition rate to weld travel speed, and is summarised in Table 3.21.

Table 3.21. Summary of the welding conditions used for the overhead multi-layer deposition.

WFS (m min^{-1})	WFS/TS				
	10 (a)	15 (b)	20 (c)	25 (d)	30 (e)
5.0	0.50	0.33	0.25	0.20	0.17
7.5	0.75	0.50	0.38	0.30	0.25
10.0	1.00	0.67	0.50	0.40	0.33

Note: experiments coded in brackets.

3.12 Process modelling

The primary objective of this investigation was to develop a statistical WAAM process control model capable of determining the functional relationships between the weld bead geometry characteristics and primary welding parameters. To achieve this, an empirical approach was undertaken. The process model was built for single, then expanded to multi-layer deposition of mild steel wire utilising CMT. The analysis was carried out by applying the least-squares method and multiple linear regression (MLR) technique, using Design Expert®7.15 (DX) software.

3.12.1 Experimental design

The development of the process model was based on the comprehensive single and multi-layer deposition investigation that was previously discussed in section 3.9 and 3.10, respectively. Materials and welding consumables are described in section 3.1. Data was gathered from controlled experiments utilising a three factor design for single layer, and a two factor design for multi-layer deposition. The systematic experimental

designs utilised in both single and multi-layer cases, are contained in full in Appendices C (Tables C 1 and C 2), and E (Table E 2), correspondingly. In total, 84 experiments were performed in the single layer study, and 46 experiments in the multi-layer case. Note that experiments were performed in random order to avoid the influence of uncontrollable nuisance variables, and therefore minimising the occurrence of systematic errors. Stable welding conditions were achieved throughout the investigation for producing deposits of uniform weld quality.

3.12.2 Definition of the input factors and responses

The first step of the model development consisted of the selection of controllable and dependent variables. The most influential independent factors selected in the single layer model included WD, WFS and WFS/TS. However, for the multi-layer model the WFS and WFS/TS were considered only, as WD was held constant to a diameter of 0.8 mm. The selected weld bead characteristics, or outputs, in single layer welds were: bead width, W; bead height, H; remelting ratio, RR; heat input, HI, deposition rate, DR, contact angle, CA; penetration area, A_1; reinforcement area, A_2; penetration, P; dilution, D; and heat source length, HSL; (refer to section 3.7.1 for definitions). As for the multi-layer model, the following responses were included: effective wall width, W_{eff}; metal deposition efficiency, MDE; and surface waviness, SW_{av} (refer to section 3.7.2 for definitions). Measurements of weld bead characteristics were done according to the method described in 3.7.

3.12.3 Integration with statistical software

The welding conditions and experimental results indicated in section 3.9 (single layer) and 3.10 (multi-layer) were utilised for developing the process model equations. Experimental data contained in Tables C 1 and C 2 (see Appendix C), and E 2 (see Appendix E), was then imported into the DX software package. It is worth mentioning that data points shown in strikethrough formatting in these tables were considered *outliners*[19] according to the analysis performed in sections 3.12.5 and 3.12.6, and

[19] "*Outliners*" or "*bad values*" are observations that are numerically distant from the rest of the data.

therefore not included in the MLR study. By default, the degree of association between factors and responses was determined by the least-squares method and MLR analysis technique. The main effects of interactions between independent and dependent variables were then estimated and translated into mathematical expressions. The analysis was made via the ***historical data*** design feature under the ***response surface*** label. Important to note is the input data were based on a planned and comprehensive systematic experimental approach (SEA) data collection strategy rather than on a traditional and initially established reduced approach method, *i.e.* design of experiment (DoE). As a result, the SEA approach may have brought simpler and more accurate least-squares regression models since the analysis of both full factor range with non collinear, or correlated factor terms, ensures consistent data (Whitcomb and Anderson).

3.12.4 Modelling procedure

As mentioned above, a least-squares method and MLR analysis technique were used ordinary to formulate accurate control algorithms to predict optimum welding and control parameters in order to satisfy geometrical output requirements. The response may well be modelled by a linear function, and therefore approximated by a first-order model:

$$\hat{\boldsymbol{y}}_i = \boldsymbol{\beta}_0 + \boldsymbol{\beta}_1\boldsymbol{x}_1 + \boldsymbol{\beta}_2\boldsymbol{x}_2 + \ldots + \boldsymbol{\beta}_k\boldsymbol{x}_k + \in \tag{3.4}$$

where, $\in$ is the noise or random error component observed in the response variable $\hat{\boldsymbol{y}}_i$, $\boldsymbol{x}_k$ is the regressor variable, and β_n is the partial regressor coefficient. However, second-order models give better approximations of true relationships in cases where there is a curvature in the system. These models are described as:

$$\hat{\boldsymbol{y}}_i = \boldsymbol{\beta}_0 + \sum_{\boldsymbol{i}=1}^{\boldsymbol{k}} \boldsymbol{\beta}_i\boldsymbol{x}_i + \sum_{i<j}\sum \boldsymbol{\beta}_{ij}\boldsymbol{x}_i\ \boldsymbol{x}_j + \sum_{\boldsymbol{i}=1}^{\boldsymbol{k}} \boldsymbol{\beta}_{ii}\boldsymbol{x}_i^2 + \in \tag{3.5}$$

where, in this work dependent second order polynomial response variables; $\hat{y}_1(x)=W$, $\hat{y}_2(x)=H$, $\hat{y}_3(x)=RR$, $\hat{y}_4(x)=HI$, $\hat{y}_5(x)=DR$, $\hat{y}_6(x)=CA$, $\hat{y}_7(x)=A_1$, $\hat{y}_8(x)=A_2$, $\hat{y}_9(x)=P$,

which can badly influence the least-squares fit.

$\hat{y}_{10}(x)=D$, $\hat{y}_{11}(x)=HSL$, $\hat{y}_{12}(x)= SW_{av}$, $\hat{y}_{13}(x)= W_{eff}$, and $\hat{y}_{14}(x)=MDE$; were numerically described as a function of their three predictors, or regressor variables; $x_1= WD$[20], $x_2=WFS/TS$ and $x_3=WFS_{cal}$; and their partial regression coefficients (β_0, β_1, ... , β_n). Depending on the final application, other statistical techniques such as response surface methodology (RSM) may be utilised to manipulate these predictive models to optimise or control one or several responses of interest. Accurate model estimates are therefore essential in cases where further optimisation steps are required.

3.12.5 Analysis of variance

ANOVA was the method adopted in this study to carry out statistical significance tests for each of the main effects and interaction terms associated with the response variables presented in section 3.12.4. The significance of the partial regression coefficients was determined by applying Student's t-test and Fisher´s *F*-test[21] using the same statistical package. The test of hypothesis performed in the software background for significance of regression[22] was initiated with the called *null hypothesis, H_0,* and the *alternative hypothesis, H_1* (Montgomery, 2009). This test determined whether a linear relationship exists between the response variable, y_i and any of the regressor variables $x_1, x_2, ..., x_k$. The rejection of H_0 immediately implies that at least one of the regressors is significant to the model. This means that the total sum of squared deviations ($SS_{\text{corrected total}}$), or total variance, is then introduced and partitioned into a sum of squares difference caused by the treatment means and the overall average (SS_{model}), and the unexplained remainder sum of squares difference between the individual observations and the treatment mean, and the summed across all treatments (SS_{residual}).

$$SS_{\text{corrected total}} = SS_{\text{model}} + SS_{\text{residual}} \tag{3.6}$$

Adding important model terms, or candidates to a regression model, is crucial to reduce the residual mean square, $MS_{residual}$. It should be noted that the degree-of-freedom (*d.f.*),

[20] This regressor variable was not included for the development of the multi-layer process model.

[21] *F* value= MS_{model}/ $MS_{residual}$

[22] H_0: $\beta_1 = \beta_2 = \cdots = \beta_k = 0$; H_1: $\beta_j \neq 0$ *for at least one j*

has an additive property[23] and generally accounts for the number of independent pieces of information obtained from the experimental data set. The model mean square (MS_{model})[24] output is thus utilised to compute the signal-to-noise ratio *i.e.* S/N, or the Fisher´s *F*-test ratio value. The F-value is defined as the ratio of the variance of each effect in the model to the residual or noise variance. S/N ratios are purportedly defined so that a maximum value minimised the variability transmitted from the background scatter (noise). Larger F-values are preferable, indicating that more variance is explained by the model rather than by the residual variance (error). Large F-values also support the fact that the slope of at least one $\beta_j \neq 0$.

Another option is to convert the F statistic into the p-value, or conditional probability of observing a value of the computed statistic, testing once again the *null hypothesis,* H_0 (Weisberg, 2005). The p-value is the smallest level of significance (α) that would lead to rejection of H_0, or the smallest α at which the data are significant to calculate the confidence level (Montgomery, 2009). In the present analysis non-significant effects were removed using a fixed significance level of p-value<0.1, or confidence interval of 90%. The p-value<0.1 is indicative that the individual term has a high level of significance on the response, and also a credible evidence against the *null hypothesis*. This p-value threshold allowed borderline effects to be included permitting further improvement of the computed model.

An additional statistical analysis test for significance of regression, and also useful on model adequacy checking (see section 3.12.6), is also provided by the coefficient of determination term, R^2 in the ANOVA screens. This coefficient reflects the strength of the relationship between x_i and the y_i in the data measuring therefore the proportion of the total variability explained by the ANOVA model. The adjusted R^2 term (R^2_{Adj}) is prefered by model builders once it is normalised to the number of parameters in the model. In fact its value can actually decrease if non-significant terms are added to the model, guarding against over fitting the model.

[23] $df_{corrected\ total} = df_{model} + df_{residual}$

[24] $MS_{model} = SS_{model}/df_{model}$

Near-linear dependencies among regression variables, or multicollinearity, is a statistical phenomena that can negatively impact the precision at which partial regression coefficients are estimated in reaction to small changes in the model or data. The variance inflation factor, *VIF*[25], revealed in the ANOVA tables is an important tool for multicollinearity diagnostics. The *VIF* shows how much the variance of the coefficient estimate is being inflated by multicollinearity. If the regressor is orthogonal to all the other regressors in the model, the *VIF* is expected to be 1.0, whereas that *VIF* is greater than 1 when not orthogonal.

The prediction error sum of squares, *PRESS*[26] statistic is an effective diagnostic tool to identify potential outliners. Simultaneously, *PRESS* also determines how well the regression model will perform in predicting new data (Montgomery *et al.*, 2006), showing therefore to be a powerful indicator of the model quality. Overall, models with small *PRESS* values are highly desired. All the models presented in this study were iteratively optimised and guarded against the presence of possible outliners by utilising the *PRESS* statistic as a reference indicator.

The adequate precision statistic, *Adeq Precision* determines the "strength" of the obtained model, or the signal to noise ratio, by comparing the range of predicted values at the design points to the average prediction error. Generally, a high *Adeq Precision* ratio is desirable (greater than 4) indicating that the observed variation is large in relation to the underlying uncertainty of the fitted model.

Important to note that optimised models were first developed by applying a power law transformation when necessary (according to 3.12.6), followed by a selection procedure where non-significant interaction terms with p-values above a critical threshold of p>0.1 were dropped from the model. This iterative routine was carried out manually until no statistical problems were revealed and sufficiently accurate models were obtained.

[25] $VIFj = \frac{1}{1-R_j^2}$

[26] $PRESS = \sum_{i=1}^{n}(\frac{e_i}{1-h_{ii}})^2$, where the $e_i = y_i - y_{ii}$ is the i^{th} ordinary residual and h_{ii} is the i^{th} leverage.

3.12.6 Model adequacy checking

The adequacy of the individual models and the quality of the fit was determined by means of process model diagnostics – *model adequacy checking*. A rigorous model fitting examination added to stringent least-squares regression assumptions have long been recognised to be critical in order to maximise the confidence level on the regression model (Montgomery, 2009). Scaled residuals[27] were originally checked in order to verify that analysis of variance (ANOVA) assumptions were met, and that the observations were adequately described by the model. Three types of residual plots were initially examined in DX using embedded diagnostic tools *i.e.* studentised residual[28] plots, and these were: (1) *normal percentage probability vs. residuals* (e_i), where data points should overlay close to a straight line, or normal pattern, showing no evidence of anomalous contours *e.g.* "S" shape. This should indicate if the assumption of normally distributed errors was met; (2) *residuals* (e_i) *vs. fitted* values ($\hat{y}_i$), where the variance of the errors is plotted as a function of predicted values. Ideally, the reading should be constant and self-contained in a horizontal band and exhibiting no obvious pattern. One should note that marked patterns reveal the presence of large residuals, which possibly mean the existence of potential *outliner* candidates; (3) *residuals* (e_i) *vs. run number*, where the constant variance assumption is checked. Ideally, a pure random scatter should be observed with no detectable trends.

The Box and Cox method (Box and Cox, 1982) was applied thereafter to determine whether a power law transformation was appropriate, as non-normal outputs are likely to be a result of a wrong model fitting option rather than a data problem. An optimum transformation will ensure precise estimates of the model parameters amplifying the sensitivity of statistical tests (Montgomery *et al.*, 2006) by detecting and correcting any

[27] The *n* deviations between the observed sample value y_i and the corresponding sample average or the fitted function value $\hat{y}_i$. It is also a measure of the variability in the response variable not explained by the regression model. The sum of the residuals in any regression model that contains an intercept β_0 always sum to zero $\sum_{i=1}^{n}(y_i - \hat{y}_i) = \sum_{i=1}^{n} e_i = 0\,;\ \ i = 1,2,\ldots,n$; establishing a linear constrain.

[28] Studentised residuals have constant variance Var(r_i)=1, preventing potential variations in the leverage of the data points, rescaling residuals from actual units to units of standard deviation.

model inadequacy, or simply by stabilising the variance. The Box and Cox represents the residuals as function of λ (lambda) or actual power. The best power transformation (λ value) was recommended at all times by DX software, and fine-tuned thereafter in order to make the residuals as close to normally distributed as possible. The minimum of this function indicates the optimum λ value. Power transformations were applied iteratively to all models until the lowest residual sum of squares ($SS_{residual}$) and PRESS outputs were achieved.

Potential outliners were carefully examined and considered for exclusion from the data matrix as they could badly impact the model partial regression coefficients (β_j) and fitted values ($\hat{y}_i$). Other valuable diagnostic statistic tools and methods were also employed to access influent and leverage points. These included the D_i Cook´s[29] distance measure (Cook, 2000), $DFBETAS_{j,i}$ and $DFFITS_i$ (Belsley *et al.*, 1980).

3.12.7 Validation of the models

The accuracy and efficiency of the final developed empirical models were verified in all estimated responses, using both scatter diagrams and confirmation runs. Scatter diagrams were used to provide crucial information on the relationship between the actual response values versus predicted ones. Adequate models should present a minimum spread of points along a reference line drawn at 45° (ideally data points should fall over the 45º line), and keeping therefore the residuals for predicting individual responses to a minimum. Confirmation experiments were conducted to validate model predictions utilising new welding test conditions. These new test conditions were randomly selected from the response surface design range defined a priori in section 3.12.1. Pre-set welding conditions for single and multi-layer deposition were analogous to the ones used to develop the model (see section 3.12.1). Response predictions were obtained using the models developed previously, and the point prediction feature available in the software under the optimisation node.

[29] Measures the influence of the i^{th} observation if it is removed from the data set.

3.12.8 Response optimisation method

Optimisation was implemented in this section using the numerical and graphical techniques available in DX software. The final empirical models for predicting a number of responses of interest (see section 3.12.4), were utilised to determine optimal process conditions according to a specified user defined criteria. In the first case study presented, the goal was to establish near-optimal single layer welding conditions, *i.e.* WFS_{actual}, WFS/TS and WD, under which a target weld bead width of 5 mm would be achieved. Additionally, a quality acceptance criteria ascertained throughout the experimental stage was also included in the exercise for delimiting the optimum operating region after weld bead assessment.

In the second case study, multi-objective optimisation was performed by superimposing the contour plots of various response surfaces for producing overlay plots. Minimum and maximum limits for each response were defined, *e.g.* W, H, DR and CA, and the optimum combination of parameters displayed for a 0.8 mm wire.

4 Results

This chapter presents the results of the experiments detailed in chapter 3. These results are divided into five main sub-sections following in the same order as the experimental procedure (chapter 3). Note, however, that some of the results are referred to appended figures and tables.

The first section (4.1) details the fundamental characterisation work of GMAW-P and CMT single layer deposits in steel. This includes the study of the effect of essential variables, *i.e. TRIM*, CTWD, WFS, TS and WD on the weld bead, fusion, and electric transient characteristics for various GMAW-P operating modes. In addition, a waveform modulation study was undertaken in order to determine the effects of primary welding parameters of the current waveform, *i.e.* I_p, I_b, T_p, T_b, f and LDC, on the arc welding stability and quality of single layer deposits. In a second stage the effect of ALC, DC_{orr}, CTWD and different shielding gas mixtures on the weld bead, fusion, and transient characteristics was investigated for the CMT process.

The results of the experimental programme utilised for the development of multiple linear regression process control models of single layer welds are reported in section 4.2. Section 4.3 focuses on the examination of the effect of WFS, TS, WD, T_{sub}, and material type on SW_{av}, W_{eff} and MDE in multi-layer deposition.

In section 4.4 a feasibility study addressing multi-layer deposition in the overhead position (PD or 4F in accordance to PD CEN/TR14633:2003) was carried out. The quality of the deposited weld beads were evaluated and assessed visually according to the degree of bead uniformity, *i.e.* geometry and appearance, along the weld axis.

The regression modelling results are presented in section 4.5 where graphical techniques, such as *response surfaces* and *overlay plots*, were utilised. The process model validation results for single and multi-layer models are also given in this section.

4.1 Fundamental characterisation of single layer welds in steel

4.1.1 Pulsed-current gas metal arc welding

The set-up and experimental method employed for carrying out this set of experiments are described in full in section 3.8.1 of the experimental procedure (chapter 3).

4.1.1.1 Effect of *TRIM* and contact tip to work distance on the weld bead and plate fusion characteristics

The experiments reported in this section were carried out according to the welding conditions described in section 3.8.1.1. The experimental designs used in these initial trials, defined herein as studies *TRIM* and contact tip to work distance (CTWD), can be found in Tables I 1 and I 2, respectively (see Appendix I). The effect of CTWD on the bead width (W), bead height (H), dilution (D), and penetration depth (P) is plotted in Figure 4.1.

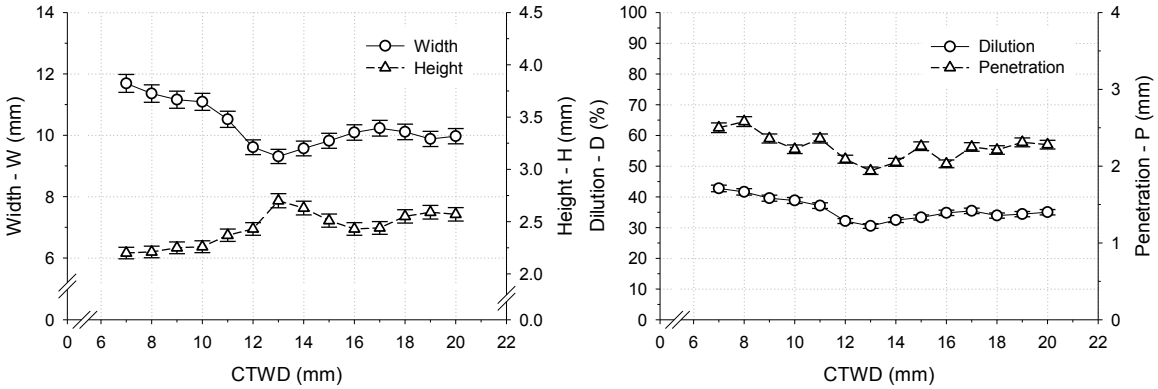

Figure 4.1. Effect of CTWD on (a) bead width (W) and bead height (H), and on (b) dilution (D) and penetration depth (P).

Figure 4.1(a) shows that the W has a maximum for a CTWD of 7 mm, dropping to a minimum at 13 mm. Thereafter, there is a slow increase in the W with the CTWD. The variation observed in the H is commensurate with that of W. Figure 4.1(b) indicates that D drops from a maximum of about 43 % for a CTWD of 7 mm to a minimum of 30 % at 13 mm CTWD. D increases slowly thereafter, becoming nearly constant for CTWD values over 16 mm. P is affected moderately by CTWD, reaching a maximum at 8 mm CTWD. Thereafter, P drops slowly to a minimum at 13 mm CTWD, increasing slowly

thereafter. The effect of CTWD on contact angle (CA) and remelting ratio (RR) is depicted in Figure 4.2.

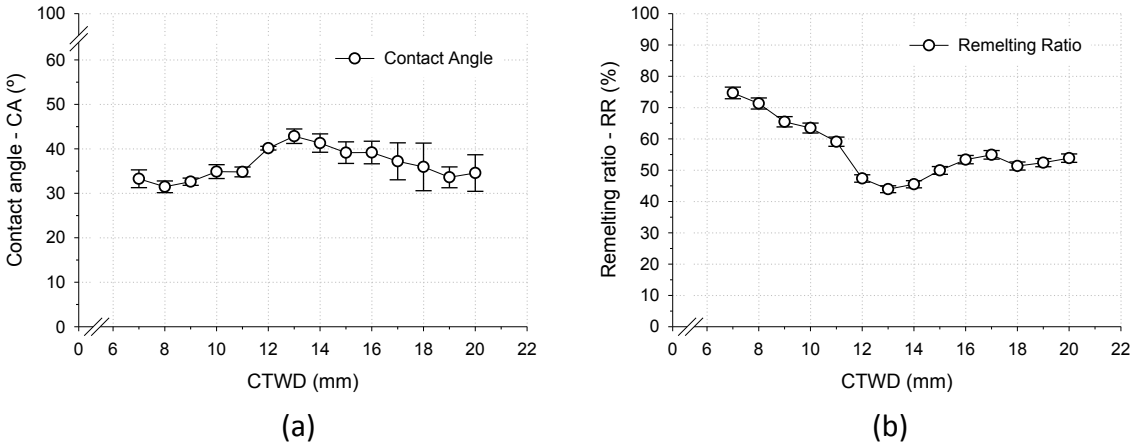

Figure 4.2. Effect of CTWD on (a) contact angle (CA) for a 95% confidence interval, and (b) remelting ratio (RR).

Figure 4.2(a) shows that CA increases slowly with CTWD up to a maximum of about 42 % is reached at 13 mm CTWD, declining gradually thereafter. The RR drops sharply from a maximum at 7 mm CTWD to a minimum at 13 mm, showing a weak dependence on CTWD thereafter. Figure 4.3 illustrates the effect of CTWD on penetration area (A_1) and reinforcement area (A_2).

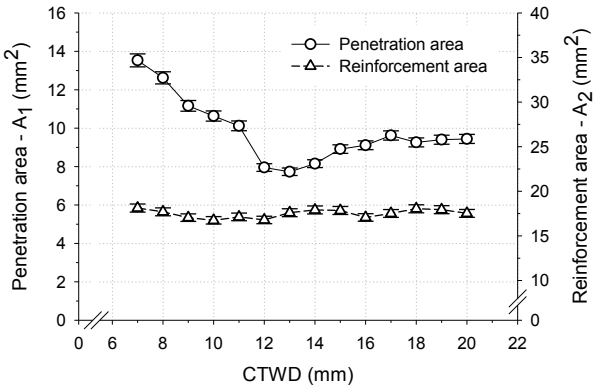

Figure 4.3. Effect of CTWD on penetration area (A_1) and reinforcement area (A_2).

The A_1 has a maximum for 7 mm CTWD, dropping very rapidly with increased CTWD to a minimum at 13 mm (see Figure 4.3). Thereafter, there is a gradual increase of A_1 with the CTWD. As shown in Figure 4.3, the CTWD has very little influence on A_2. The effect of *TRIM* on the bead width (W), bead height (H), dilution (D), and penetration (P) is plotted in Figure 4.4.

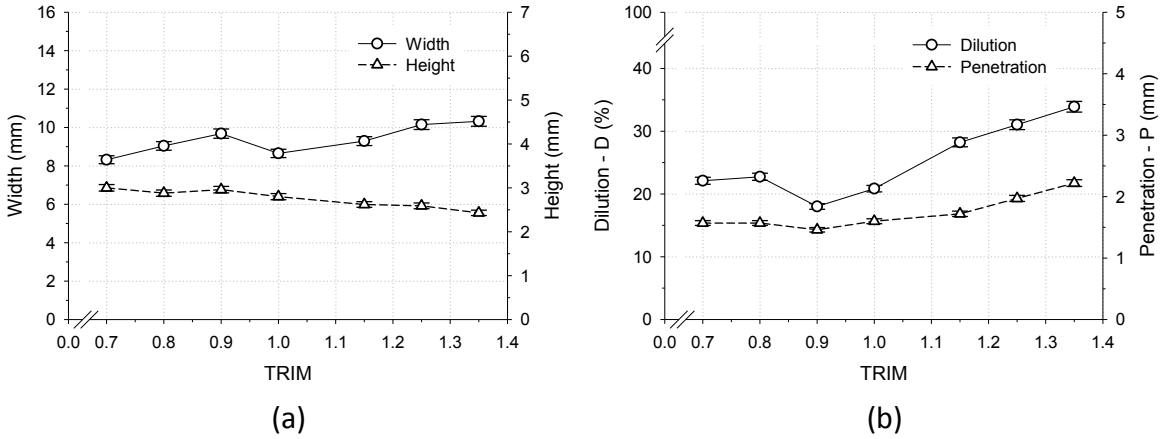

Figure 4.4. Effect of *TRIM* on (a) bead width (W) and bead height (H), and on (b) dilution (D) and penetration depth (P).

Figure 4.4(a) shows a gradual increase in W with a commensurate decrease of H. D and P decrease slowly with *TRIM* to a minimum at 0.9, as indicated in Figure 4.4(b). Thereafter, there is a gradual increase in D and P with *TRIM*, however, with a more significant effect in D. The influence of *TRIM* on contact angle (CA) and remelting ratio (RR) is shown in Figure 4.5.

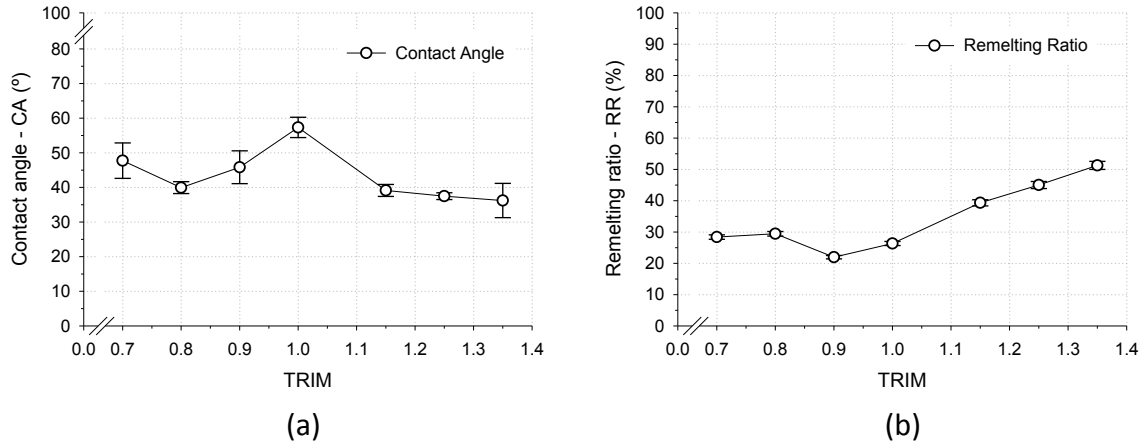

Figure 4.5. Effect of *TRIM* on (a) contact angle (CA) for a 95% confidence interval, and (b) remelting ratio (RR).

It is apparent from Figure 4.5(a) that the CA does not show a trend with values between 35º and 60º. The RR has a minimum at 0.9 *TRIM*, increasing steadily thereafter. The effect of *TRIM* on penetration area (A_1) and reinforcement area (A_2) is depicted in Figure 4.6. *TRIM* has a negligible influence on A_1 up to 0.9 *TRIM*, however, there is a very significant increase thereafter (see Figure 4.6). The A_2 seems moderately positively influenced by *TRIM*.

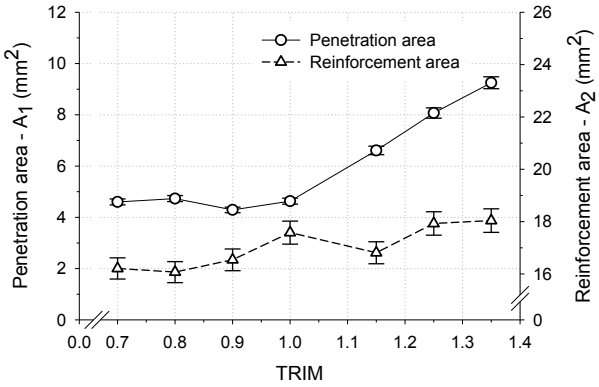

Figure 4.6. Effect of *TRIM* on penetration area (A_1) and reinforcement area (A_2).

4.1.1.2 Effect of *TRIM* and contact tip to work distance on the weld bead surface quality

This section focuses on the analysis of various aspects of the quality of weld beads. The effects of *TRIM* and CTWD on the surface quality of single layer welds are determined according to the criteria defined in section 3.8.1.2. The samples were produced under the same welding conditions as in section 4.1.1.1 (see Tables I 1 and I 2 in Appendix I).

The results obtained from the preliminary analysis of *TRIM* can be compared in Figure 4.7. It is apparent that the *TRIM* has a major effect on the weld bead quality of single layer deposits. *TRIM* values equal or below 0.9 show to induce strong rippling effects which are clearly visible at the weld top surface. Additionally, small *TRIM* values produce excessive spatter near the weld bed toes. However, the results show that the weld quality significantly improves with higher *TRIM* values, where smoother weld bead surfaces were produced with very little spatter.

Figure 4.7. Effect of *TRIM* on the weld bead quality in GMAW-P (using P19).

Figure 4.8 shows the influence of CTWD on the quality of single layer deposits. The results indicate that there is little effect on the quality of the beads with CTWD.

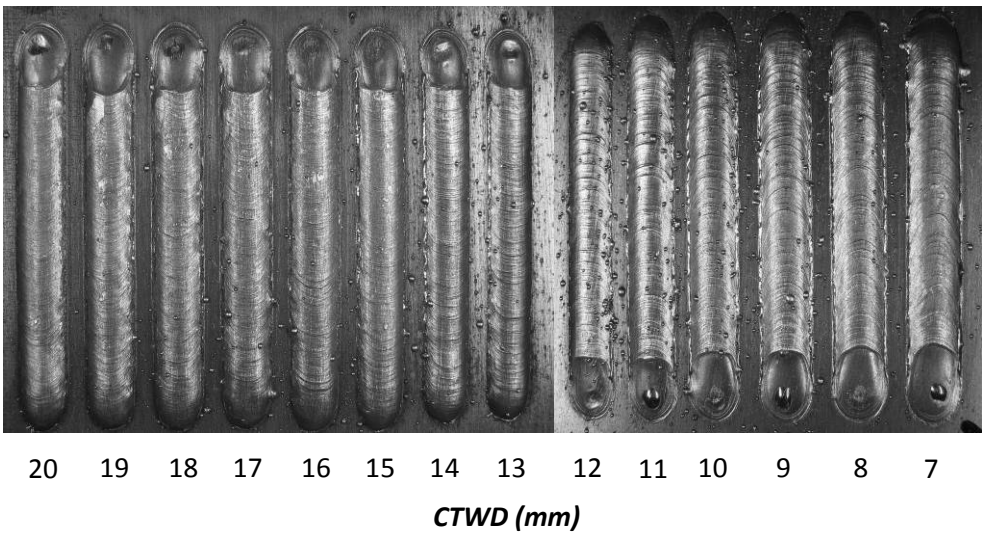

Figure 4.8. Effect of CTWD on the weld bead quality in GMAW-P (using P19).

4.1.1.3 Effect of wire feed speed and wire feed speed to travel speed ratio on the weld bead and plate fusion characteristics for 1.2 mm wire

The experiments detailed in this section were performed in accordance with the welding conditions detailed in section 3.8.1.3. Here, the GMAW-P *Pulse Soft* operation mode (program 19) was selected to deposit single weld beads at constant WFS/TS ratios. The welding conditions and measured bead characteristics are detailed in Tables I 3 to I 5

(see Appendix I). The effect of WFS on bead width (W) and bead height (H) for different WFS/TS ratios is plotted in Figure 4.9.

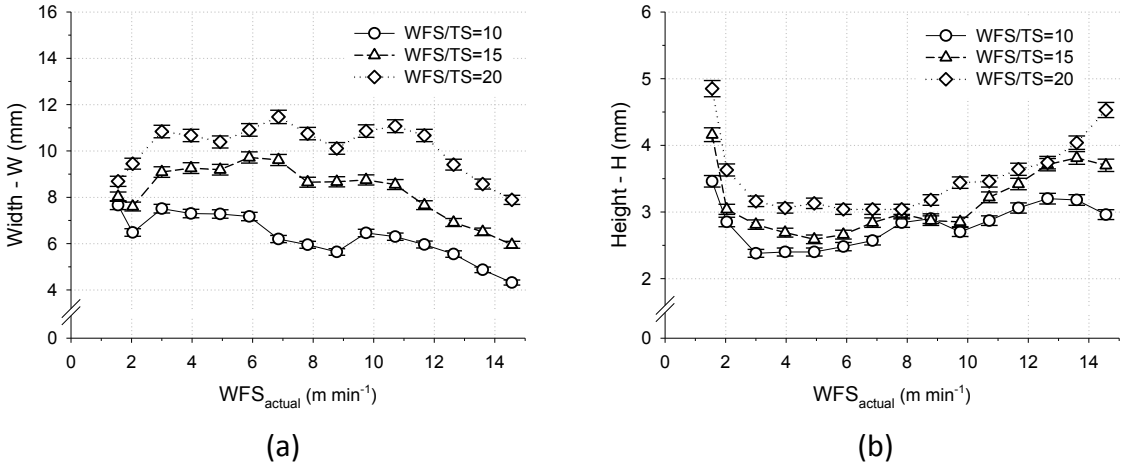

Figure 4.9. Effect of WFS_{actual} on (a) bead width (W) and (b) bead height (H).

Figure 4.9(a) shows that after an initial increase, W gradually decreases with increased WFS. It can also be seen that increasing the WFS/TS, increases the W (Figure 4.9(a)). Bearing in mind that for a given WFS/TS the cross section area should be constant, corresponding changes are seen in H (see Figure 4.9(b)). The influence of WFS on remelting ratio (RR) and penetration depth (P) is presented in Figure 4.10.

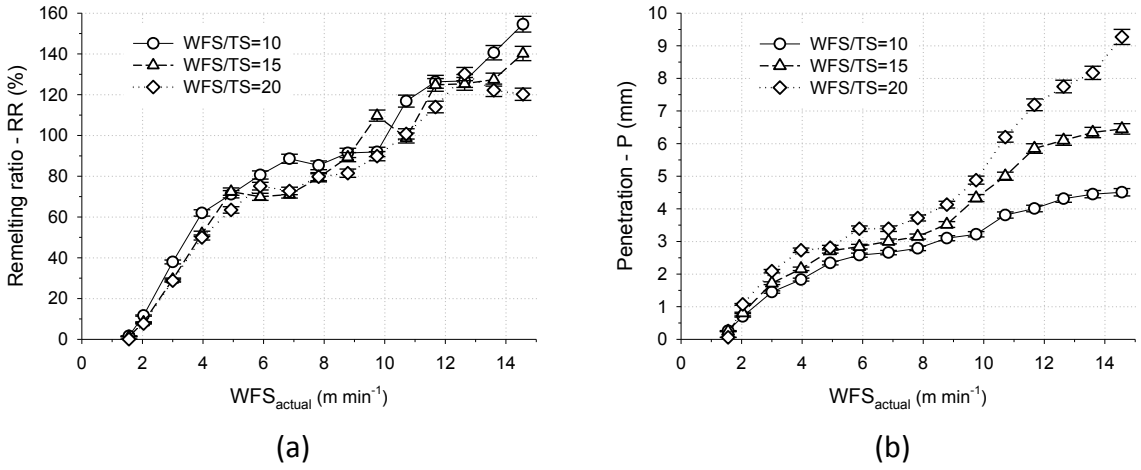

Figure 4.10. Effect of WFS_{actual} on (a) remelting ratio (RR) and (b) penetration depth (P).

Figure 4.10(a) shows that RR increases markedly with WFS, with a very small dependence on WFS/TS. Figure 4.10(b) indicates that P has a similar behaviour up to about 9 m min^{-1} (see Figure 4.10(b)). Thereafter, an increase in the gradient is seen, where a more significant effect of WFS/TS is observed in this region also. The

influence of WFS on dilution (D) and contact angle (CA) is shown in Figure 4.11.

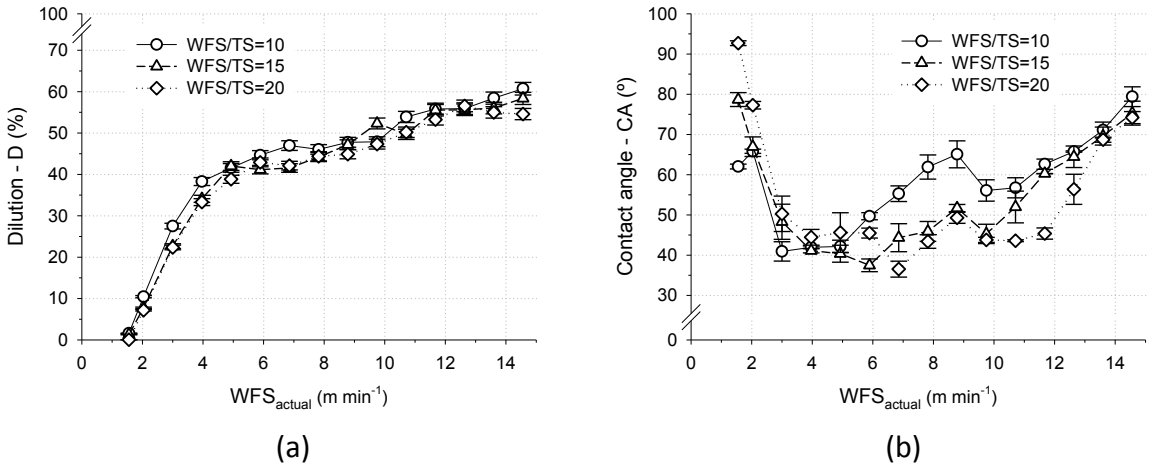

Figure 4.11. Effect of WFS_{actual} on (a) dilution (D), and (b) contact angle (CA).

As shown in Figure 4.11(a), D increases very fast with the WFS up to about 5 m min^{-1}, but the gradient decreases thereafter. Apparently, the dependence of D on the WFS/TS is very little. Figure 4.11(b) shows that the CA drops very rapidly with the WFS at low regimes. Thereafter, there is a gradual increase with the WFS. This increase in the CA appears to occur earlier at higher WFS/TS ratios. Figure 4.12 shows the effect of WFS on penetration area (A_1) and reinforcement area (A_2).

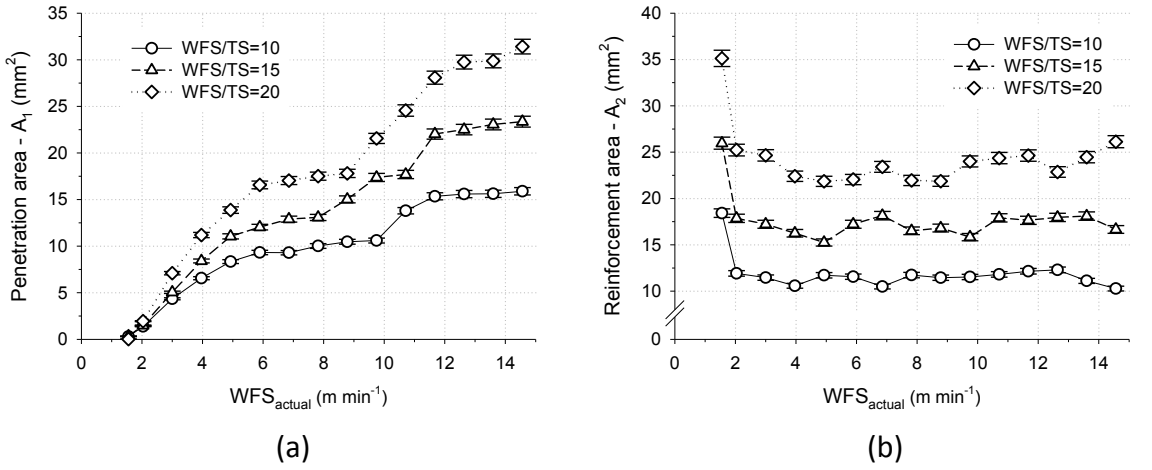

Figure 4.12. Effect of WFS_{actual} on (a) penetration area (A_1) and (b) reinforcement area (A_2).

Figure 4.12(a) shows that A_1 increases gradually with increasing WFS up to 6 m min^{-1}, however, with a larger gradient at higher WFS/TS. Thereafter, a short range *plateau* appears to occur for all WFS/TS. The A_1 then begins to increase again with the WFS, until a new equilibrium is reached. The A_2 is affected very little by WFS (see Figure

4.12(b)). However, there is a significant effect of WFS/TS on A_2 so that higher ratios produce larger A_2.

4.1.1.4 Effect of wire feed speed and wire diameter on the weld bead and plate fusion characteristics for 1.0 and 1.2 mm wire

The experiments reported in this section were carried out in accordance with the welding conditions described in section 3.8.1.3. New experimental data for 1.0 mm steel wires are presented here combined with the 1.2 mm data exhibited in the previous section (see section 4.1.1.3). However, for the sake of simplicity data are presented only for a single WFS/TS ratio of 15 and for both wire diameters. The *Pulse Soft* operation mode was selected for depositing 1.0 mm (program 14) and 1.2 mm (program 19) steel wires (see database of programs in Appendix J). The welding conditions and measured bead profiles are detailed in Table I 4 (1.2 mm) and I 6 (1.0 mm) in Appendix I. The effect of WFS on bead width (W) and bead height (H) for different wire diameters (WD) is shown in Figure 4.13.

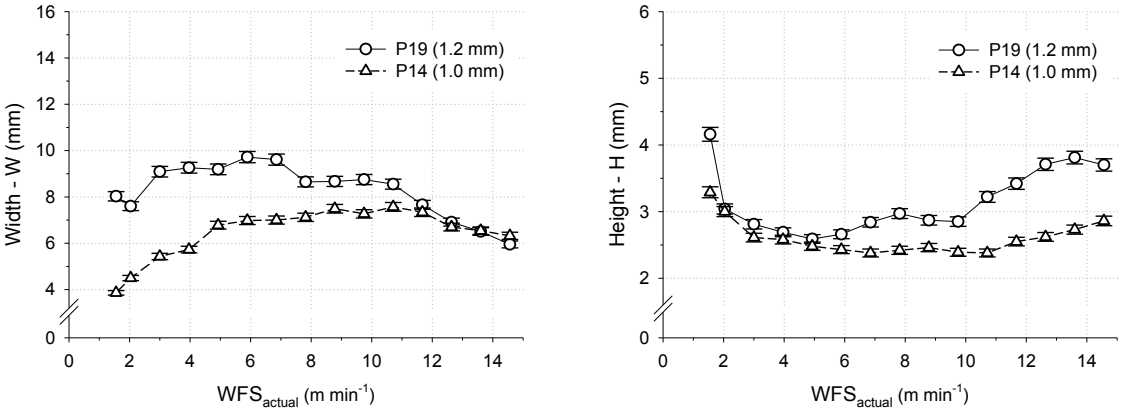

Figure 4.13. Effect of WFS_{actual} and WD on (a) bead width (W) and (b) bead height (H).

Figure 4.13(a) shows that the relationship between the bead W and WFS for 1.2 mm wire is very similar to that of 1.0 mm. Compared to the 1.0 mm wire, wider weld beads can be produced with a 1.2 mm wire up to about 11 m min^{-1}. Thereafter, the bead W is identical. The changes observed in the bead H with the WFS are commensurate with that observed for the bead W (see Figure 4.13(b)). The effect of WFS on remelting ratio (RR) and penetration depth (P) using different WD is shown in Figure 4.14.

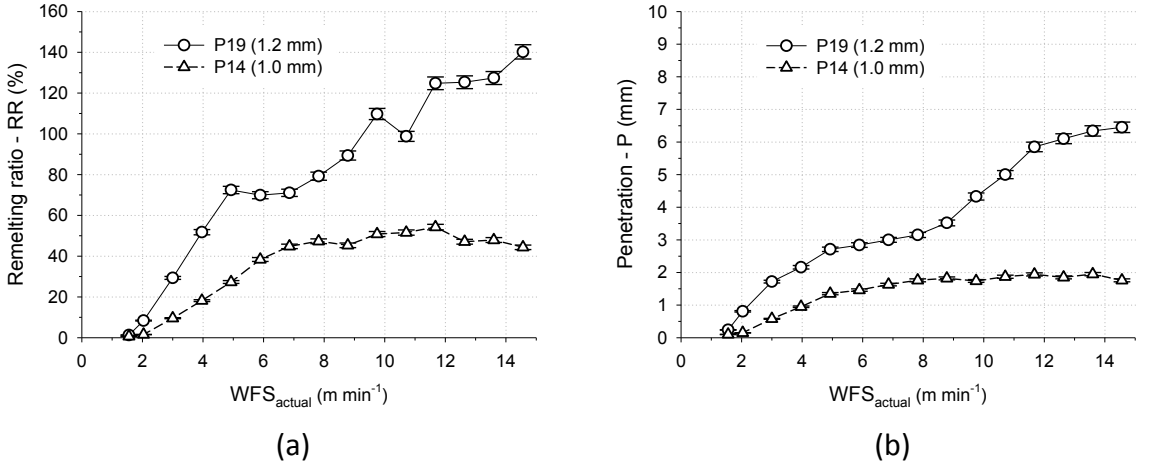

Figure 4.14. Effect of WFS_{actual} and WD on (a) remelting ratio (RR) and (b) penetration depth (P).

From the graphs described above it can be seen that both the RR and P are significantly reduced using 1.0 mm wire. Figure 4.14(a) shows that RR increases gradually with WFS up to about 7 m min^{-1}, becoming stationary thereafter. Then, RR shows to revert its trend at high WFS. P increases slowly with increased WFS up to about 9 m min^{-1}. Thereafter, no change in gradient is observed for 1.0 mm wire. Figure 4.15 shows the effect of WFS on dilution (D) and contact angle (CA) for different wire diameters.

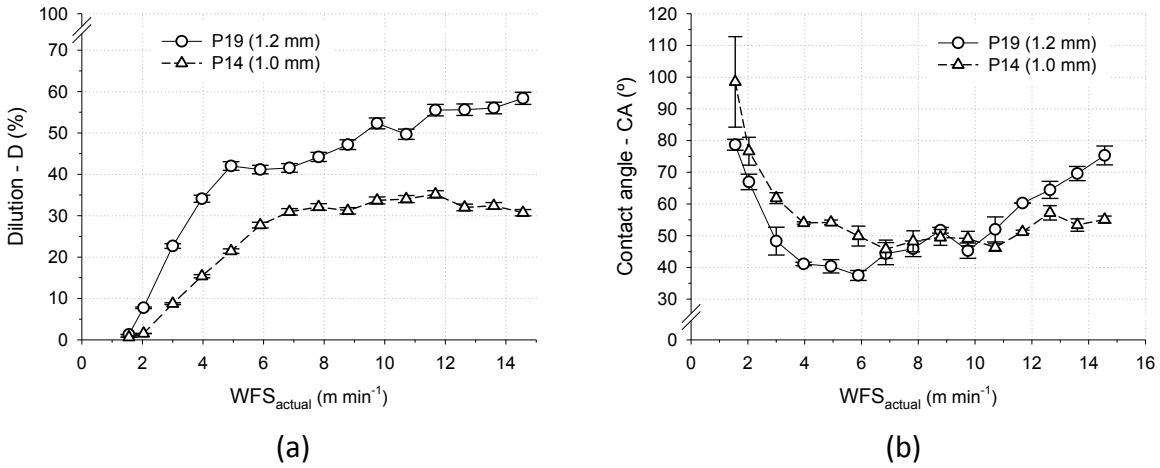

Figure 4.15. Effect of WFS_{actual} and WD on (a) dilution (D), and (b) contact angle (CA) for a 95% confidence interval.

Figure 4.15(a) shows that D is markedly reduced when 1.0 mm wire is utilised in comparison with 1.2 mm. D increases moderately with WFS up to about 8 m min^{-1}, showing to revert its trend at high WFS. Relatively higher CAs are obtained with 1.0 mm wire up to about 8 m min^{-1}. Thereafter, there is a much slower increase in CA for

1.0 mm wire; *cf.* 1.2 mm. The effect of WFS on penetration area (A_1) and reinforcement area (A_2) for different WD is shown in Figure 4.16. Figure 4.16(a) shows that for 1.0 mm wire, A_1 increases very slowly up to 8 m min^{-1}, becoming constant thereafter. Figure 4.16(b) confirms that smaller reinforcement cross-sectional (A_2) are obtained with smaller wire diameters, for constant WFS and WFS/TS.

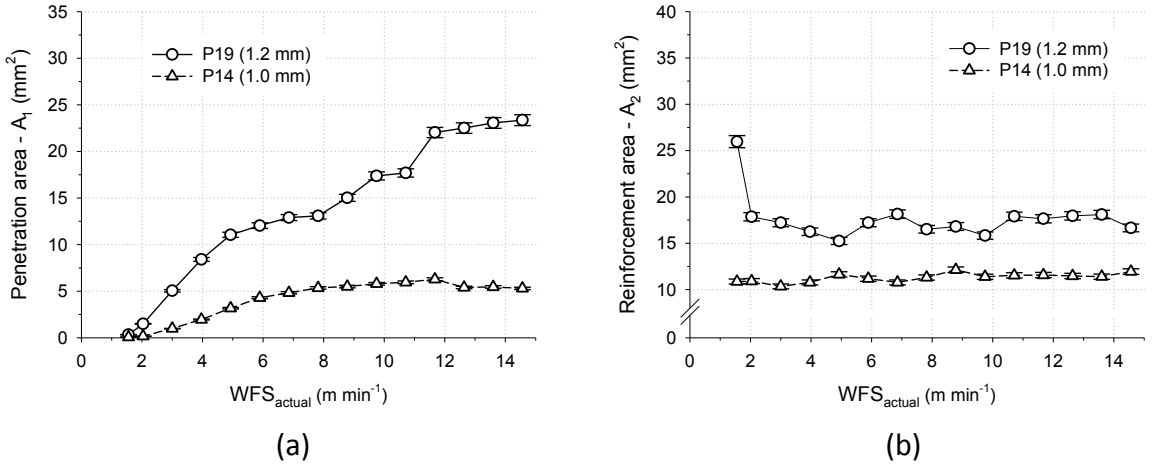

Figure 4.16. Effect of WFS_{actual} and WD on (a) penetration area (A_1), and (b) reinforcement area (A_2).

The effect of WFS on the aspect ratio (AR) for different WD is shown in Figure 4.17. The AR of the weld bead, defined herein as the H/W ratio, is significantly reduced when a 1.0 mm wire is used, in particular at high WFS (see Figure 4.17).

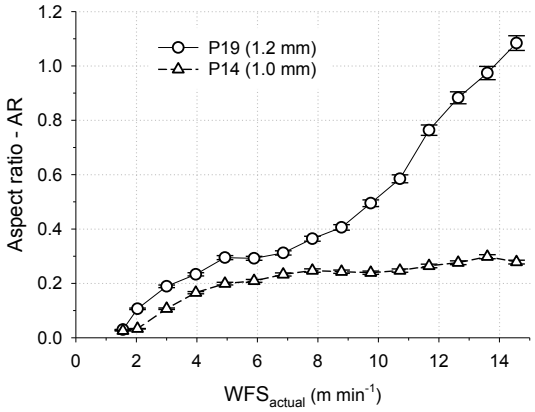

Figure 4.17. Effect of WFS_{actual} and WD on the aspect ratio (AR).

4.1.1.5 Effect of contact tip to work distance on electrical transients and weld bead profiles for different welding programmes

The effects of CTWD on both waveform and bead characteristics are reported in this section for different GMAW-P welding operation modes and 0.8 mm diameter wire. The experiments were carried out according to the welding conditions detailed in section 3.8.1.4. Four different GMAW-P welding operation modes and programs were investigated, *i.e.* P12, P14, P13 and P95. The welding conditions applied in this study are detailed in Table I 7 to I 14 (see Appendix I), alongside measured electrical and bead shape responses. The effect of variations in CTWD on the averaged voltage (V_{AVG}) and current (I_{AVG}) is depicted in Figure 4.18 for different welding operation modes and synergic programs.

Figure 4.18(a) shows that V_{AVG} in P12 and P14 changes with CTWD in a closely similar manner. The V_{AVG} in P12 and P14 remains nearly constant up to 18 mm CTWD, rising very quickly thereafter. A significant positive linear correlation was found between V_{AVG} and CTWD in P13. As for P95, V_{AVG} increases slowly from a minimum at 10 mm CTWD up to 16 mm CTWD, becoming insensitive to CTWD thereafter.

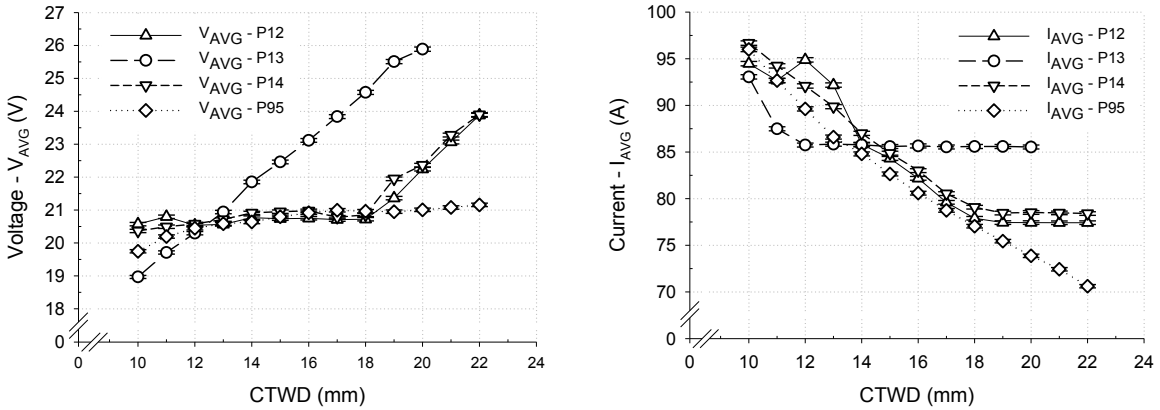

Figure 4.18. Effect of CTWD on (a) average voltage (V_{AVG}) and (b) average current (I_{AVG}) outputs.

From Figure 4.18(b) it is seen that the change of I_{AVG} with CTWD is identical in P12 and P14. I_{AVG} drops very fast from a maximum at 10 mm up to 18 mm CTWD, remaining constant thereafter. In contrast, I_{AVG} in P13 drops very fast from a maximum at 10 mm up to 12 mm CTWD, becoming independent thereafter. Yet, P19 shows that

I_{AVG} decreases linearly with increasing CTWD throughout its full range. The effect of CTWD on the average instantaneous power (AIP) is depicted in Figure 4.19.

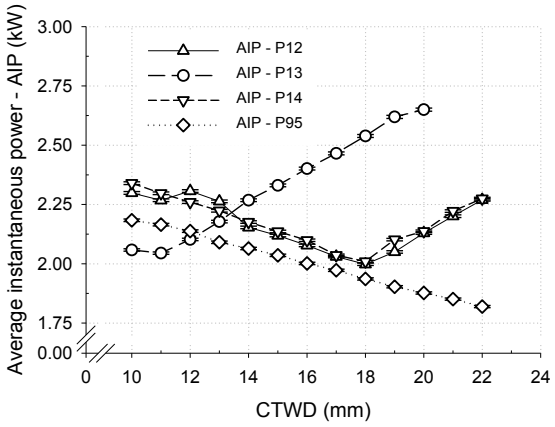

Figure 4.19. Effect of CTWD on the average instantaneous power (AIP).

As shown in Figure 4.19, the AIP in P12 and P14 change with CTWD in a closely similar manner. The AIP decreases from a maximum of around 2.3 kW at 10 mm CTWD to a minimum of 2.0 kW at a CTWD of 18 mm. Thereafter, there is a fast increase in AIP with the CTWD. The AIP in P13 increases very fast with CTWD from a minimum of around 2.0 kW at a CTWD of 11 mm to 2.7 kW for a CTWD of 20 mm. In contrast, P95 shows that AIP decreases linearly with CTWD. Additional effects of CTWD on other welding parameters of the current waveform can be found in the supplemental material provided in Figures L 1 and L 2 (see Appendix L).

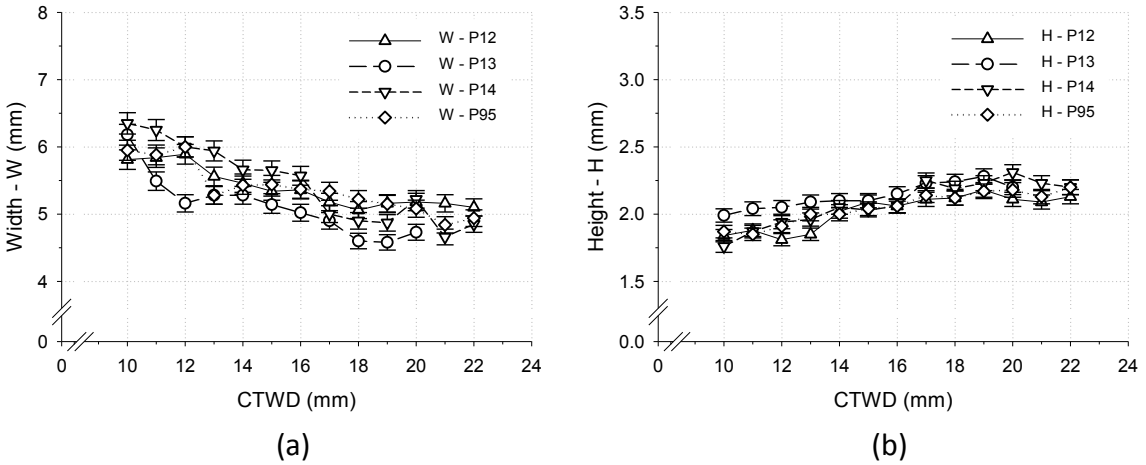

Figure 4.20. Effect of CTWD on (a) bead width (W), and bead height (H).

Figure 4.20 plots the effects of CTWD on the weld bead width (W) and height (H), for distinct welding operation modes and synergic programs. Figure 4.20(a) shows that, in

general, the relationship between W and CTWD is very similar for all welding programs. The W has a maximum at shorter CTWD, dropping slowly up to about 18 mm CTWD. Thereafter, the change of W with CTWD is much less pronounced. The changes in the behaviour in the bead H appear to be roughly commensurate with that observed for the bead W (see Figure 4.20(b)).

The influence of CTWD on remelting ratio (RR) and penetration depth (P) is illustrated in Figure 4.21. From Figure 4.21(a) it is seen that, apart from P95, all programs have a maximum RR value for CTWD of 10 mm, dropping to a minimum at 22 mm CTWD. Note that RR decreases considerably faster with CTWD in P12 and P14, when compared to P13. The RR in P95 shows relatively less sensitivity in RR to CTWD changes in the range between 10 and 16 mm CTWD, decreasing gradually thereafter. Figure 4.21(b) shows that the most significant differences in P occur in the CTWD range between 10 to 15 mm, when comparing all operation modes. Thereafter, P decreases gradually as the CTWD increases up to 22 mm.

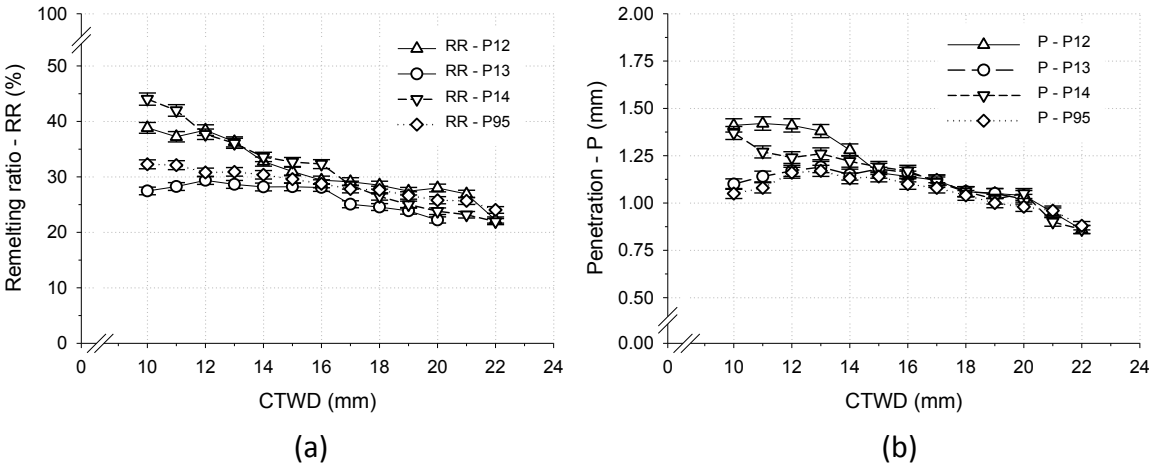

Figure 4.21. Effect of CTWD on (a) remelting ratio (RR), and (b) penetration depth (P).

The effect of CTWD on dilution (D) and contact angle (CA) is depicted in Figure 4.22. D has a maximum for 10 mm CTWD for P12, P14 and P95 (see Figure 4.22(a)). Thereafter, D shows a negative linear relationship with CTWD for these same programs. D shows a slower decrease with CTWD for P95, when compared with P12 and P14.

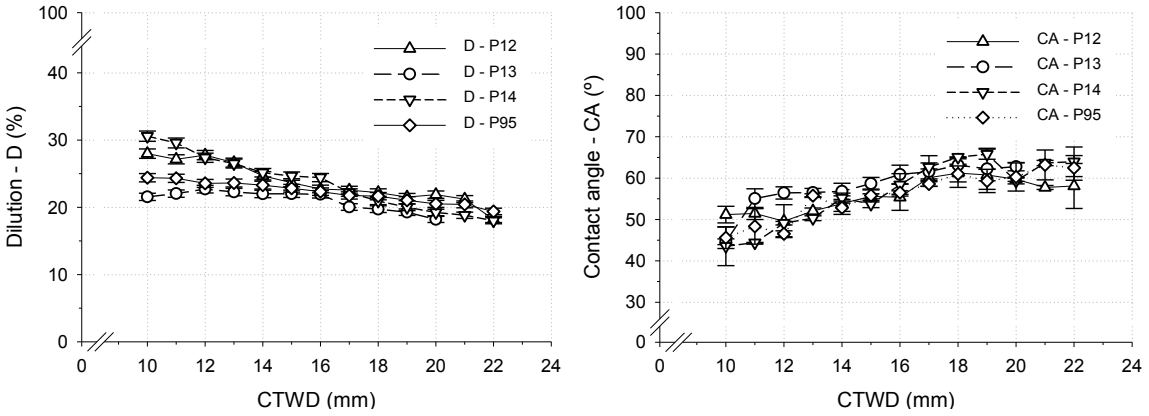

Figure 4.22. Effect of CTWD on (a) dilution (D), and (b) contact angle (CA) for a 95% confidence interval.

It is important to point out that P13 is insensitive to variations in CTWD within the interval between 12 to 16 mm. Although results show some scatter, it is apparent from Figure 4.22(b) that shorter CTWD produces weld beads with lower CA. The CA increases gradually up to about 18 mm CTWD, stabilising thereafter.

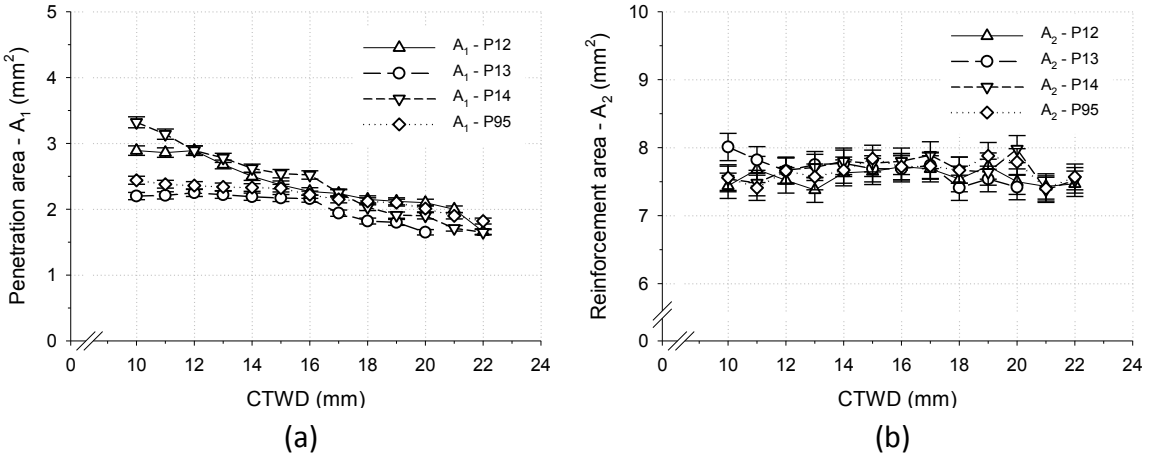

Figure 4.23. Effect of CTWD on (a) penetration area (A_1), and (b) reinforcement area (A_2).

As Figure 4.23(a) data shows, there is a significant effect of CTWD on A_1 in both P12 and P14 throughout the CTWD range investigated. A_1 shows a very week dependence on CTWD up to about 16 mm for P13 and P95, indicating to decrease gradually thereafter. Figure 4.23(b) shows that A_2 is maintained nearly constant at 7.7±0.5 mm^2, independently on the welding program. Additionally, the effect of CTWD on AR can be found in Figure L 3 (see Appendix L).

4.1.1.6 Effect of wire feed speed on electrical transients

This section details on the results of electrical transient measurements, in particular on the influence of WFS on electrical transients for *Pulse Crisp* welding operation mode (P12). The experiments were carried out according to section 3.8.1.5. The welding conditions are detailed in Table I 15 (see Appendix I), alongside measured transients. The effect of WFS on average voltage (V_{AVG}), average current (I_{AVG}), average instantaneous power (AIP) and deposition rate (DR) are shown in Figure 4.24. Overall, V_{AVG}, I_{AVG}, AIP and DR show a positive linear relationship with WFS.

Supplementary results on the effect of the WFS on the pulse parameters of the current waveform, such as I_p, I_b, T_p and T_b (Figure L 4) as well as on I_p/I_b, T_p/T_b, f and LDC (Figure L 5), can be found in Appendix L.

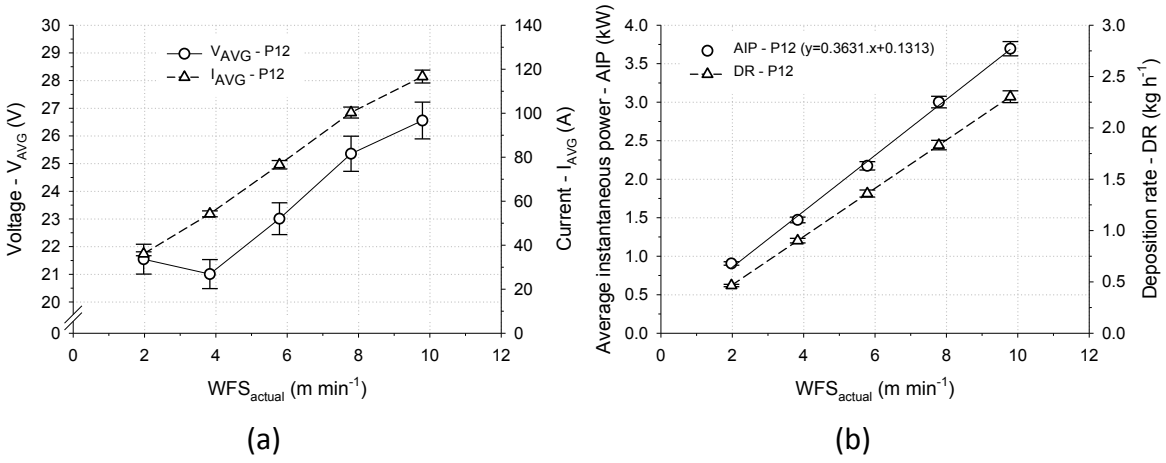

Figure 4.24. Effect of WFS_{actual} on (a) average voltage (V_{AVG}) and current (I_{AVG}), as well as on (b) average instantaneous power (AIP), and deposition rate (DR).

4.1.2 Current waveform modulation in pulse gas metal arc welding

The set-up and experimental method used to carrying out the experiments described below are detailed in section 3.8.2 of the experimental procedure (see chapter 3).

4.1.2.1 Effect of contact tip to work distance on the bead surface quality, electrical transients, and welding control mode

The results described in this subsection were obtained by selecting the *non-adaptive control* mode in the Lincoln Power Wave® F355i unit, and *Pulse Rapid Arc* (P13)

welding mode with *adaptive control* in Lincoln Power Wave® 455/STT. The welding conditions adopted in this study are given in section 3.8.2.1. The experimental design is detailed in Table 4.1, together with electrical transients and weld bead shape response data.

Table 4.1. Welding conditions applied in the study of the effect of the CTWD on the electrical transients and bead profiles (utilising *adaptive* and *non-adaptive control* modes).

Control mode	CTWD (mm)	V_{AVG} (V)	I_{AVG} (A)	AIP (kW)	HI (J mm^{-1})	W (mm)	H (mm)	RR (%)	P (mm)	D (%)	CA (º)	CI (95%)	A_1 (mm^2)	A_2 (mm^2)
Non-adaptive	13	18.87	89.61	1.84	220.95	5.27	2.02	22.30	0.86	18.24	51.66	1.33	1.55	6.95
	15	20.00	85.67	1.91	229.50	5.28	2.01	24.41	0.87	19.62	52.79	1.34	1.75	7.17
	17	21.36	83.57	2.03	243.75	5.45	1.97	30.87	1.11	23.59	53.25	0.37	2.30	7.45
	19	22.96	83.79	2.19	263.30	5.40	2.06	30.31	1.11	23.26	56.02	1.70	2.34	7.72
Adaptive (P13)	13[1]	20.08	84.93	2.04	244.28	5.22	2.10	28.92	1.20	22.43	59.76	0.19	2.23	7.71
	13[2]	20.95	87.29	2.20	264.31	5.43	1.96	32.74	1.27	24.67	53.44	0.73	2.40	7.33
	19	26.00	84.42	2.63	315.25	4.61	2.26	17.78	0.84	15.09	69.11	1.78	1.36	7.65

Control mode, welding parameters may (or may not) be automatically adjusted to an optimum condition in order to select compensate for changes in the CTWD; *CTWD*, contact tip to work distance; V_{AVG}, average voltage; I_{AVG}, average current; *AIP*, average instantaneous power; *W*, bead width; *H*, bead height; *RR*, remelting ratio; *P*, penetration; *D*, dilution; CA_{avg}, average contact angle, *CI*, confidence interval of 95%, A_1, penetration cross section area; A_2, reinforcement cross section area. [1]*TRIM*=0.9 and [2]*TRIM*=1.0.

Figure 4.25 illustrates the effects of CTWD on the weld bead surface quality, weld bead cross sections and DR. The surface quality of the deposits is significantly influenced by the CTWD setting. It is seen that the rippling observed on the top surface of the deposits is reduced notably as the CTWD increases its value. Table 4.1 shows that AIP increases significantly with CTWD when using *non-adaptive control* mode.

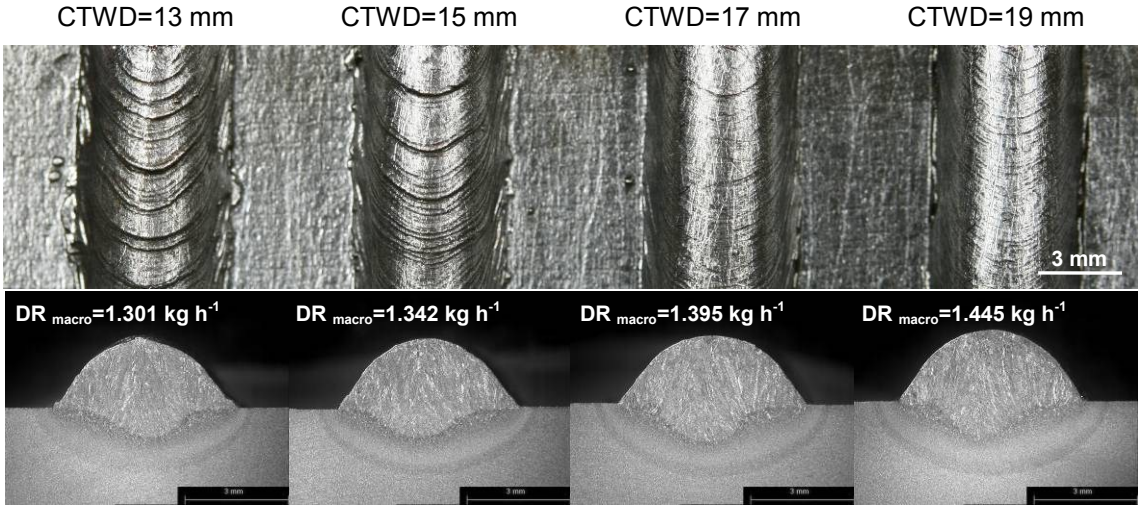

Figure 4.25. Effect of CTWD on the bead surface quality using *non-adaptive control* mode. Transverse macro sections and deposition rates are also shown (insets).

This increase in AIP is caused predominantly by a large positive variation in V_{AVG}. It is also apparent that plate fusion characteristics, such as RR, P, D and A_1 become larger with increased CTWD (see Table 4.1). At the same time, DR_{macro} figures are shown to be positively correlated with the CTWD. Electrical transients, recorded in *non-adaptive control* mode conditions, are depicted in Figure 4.26 and 4.27 for CTWD values of 13 and 19 mm, respectively.

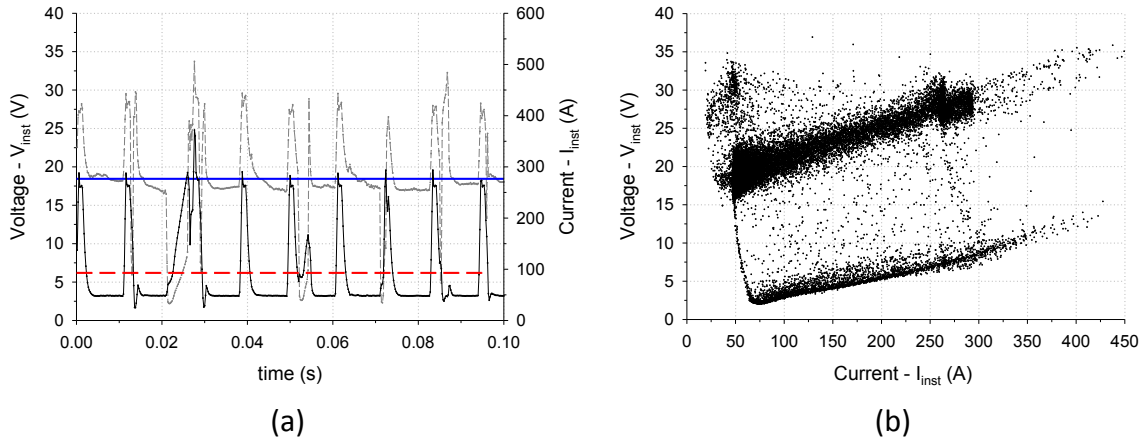

Figure 4.26. Electrical outputs (CTWD=13 mm) in *non-adaptive control* mode showing (a) V_{inst} (dashed silver), and I_{inst} (continuous black) transient profiles, and (b) scatter plots for a period of 10 s. The V_{AVG} (solid blue line) and I_{AVG} (dashed red line) values are also displayed in graph (a).

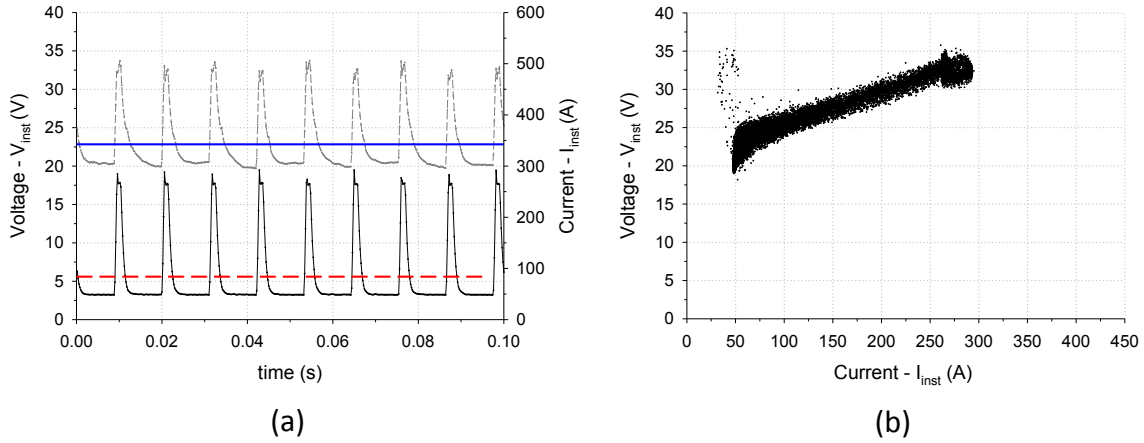

Figure 4.27. Electrical outputs (CTWD=19 mm) in *non-adaptive control* mode showing (a) V_{inst} (dashed silver line), and I_{inst} (continuous black line) transient profiles, and (b) scatter plots.

The electric transients show that a more reproducible and stable electric profile (V and I curves) is achieved when higher CTWD settings are utilised; *cf.* Figures 4.26 and 4.27. Additionally, Figure 4.26 shows that random short circuits (SC) are more likely to occur with shorter CTWD settings, when utilising *non-adaptive control* mode. From Figures 4.26(a) and 4.27(a), it can be seen that the average V_{inst} increases from 18.9 V to about

23.0 V in *non-adaptive control* mode conditions when the CTWD varies from 13 to 19 mm, respectively. Captured electrical transients of P13 are shown in Figure 4.28 where *adaptive control* mode was applied.

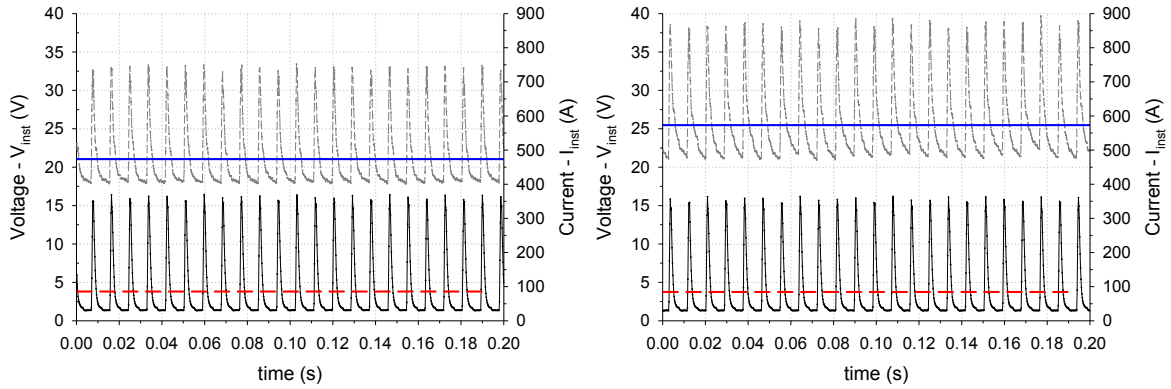

Figure 4.28. Electrical transient profiles (V_{inst} plus I_{inst}) in *adaptive control* mode recorded for P13 for CTWD settings of (a) 13 mm and (b) 19 mm. Also represented are V_{AVG} (solid blue) and I_{AVG} (dashed red) lines.

The recorded transients, for the cases where the CTWD was adjusted respectively to 13 mm and 19 mm, are shown in Figures 4.28(a) and (b). A robust, one droplet per pulse (ODP) transfer mode mechanism was achieved throughout, irrespective of the CTWD setting.

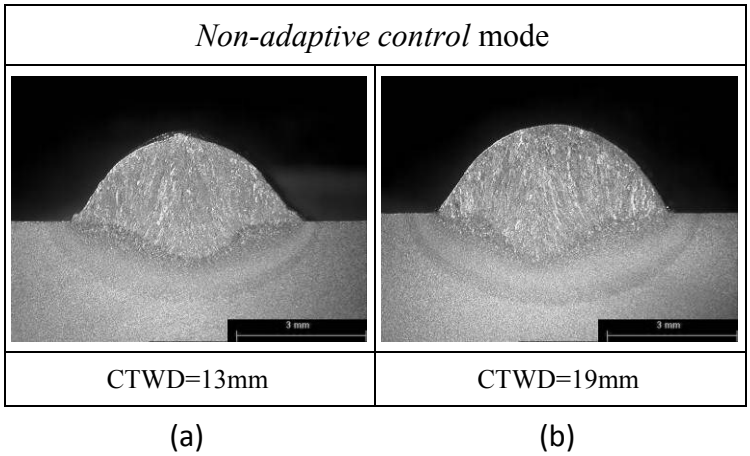

Figure 4.29. Transverse macro sections of single layer deposits produced in *non-adaptive control* mode and utilising a CTWD setting of (a) 13 mm and (b) 19 mm.

The average V_{inst} increases from around 20.9 V to nearly 25.6 V, whilst the average I_{inst} decreases from 87.3 A to 84.5 A, by varying the CTWD from 13 mm to 19 mm. Transverse macro sections produced in *non-adaptive* and *adaptive control* mode conditions are revealed in Figure 4.29 and 4.30, respectively. Welding conditions are

described in Table 4.1 along with measured bead characteristics. It can be seen in Figure 4.29 that A_2 rises with CTWD about 11 % (see Table 4.1). At the same time, A_1 also increases significantly with CTWD within a range between 13mm to 17 mm, becoming nearly constant thereafter.

Adaptive control mode (P13)		
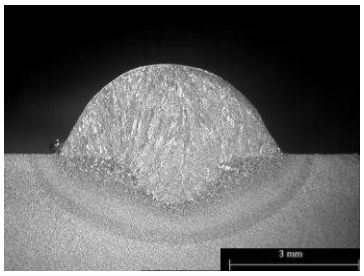	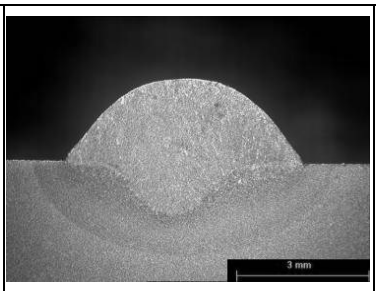	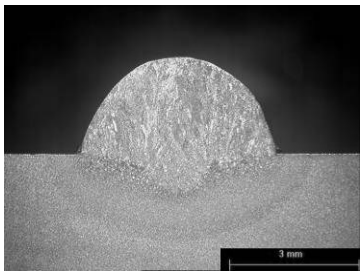
CTWD=13mm	CTWD=13mm	CTWD=19mm
(a)	(b)	(c)

Figure 4.30. Transverse macro sections of single layer deposits produced in *adaptive control* mode and utilising a CTWD setting of (a) 13 mm and *TRIM*=0.9, (b) 13 mm and *TRIM*=1.0, and (c) 19 mm.

A number of weld bead macro sections obtained in *adaptive control* mode (using P13) are shown in Figure 4.30. Figures 4.30(a) and (b) compare deposited transverse macro sections for 0.9 and 1.0 *TRIM* settings, respectively. As can be seen from Table 4.1, AIP increases when higher *TRIM* settings are applied at constant CTWD setting.

4.1.2.2 The effect of waveform on bead profiles, surface quality, process behaviour and stability

In the present section the impact of changes in primary welding parameters of the current waveform on the metal transfer conditions, weld bead characteristics and surface quality of single layer deposits was investigated. The welding conditions adopted in this study are detailed in section 3.8.2.2 of the experimental procedure chapter (chapter 3). A *non-adaptive control* operation mode was utilised throughout these experiments to deposit 0.8 mm diameter steel wire with a shielding gas mixture containing Ar/CO_2 (8%). Additional details about the welding procedure adopted in this investigation are provided in Table I 16 to I 20 (see Appendix I). A schematic diagram of the experimental plan applied to the waveform modulation study is detailed in Figure 3.16 (chapter 3).

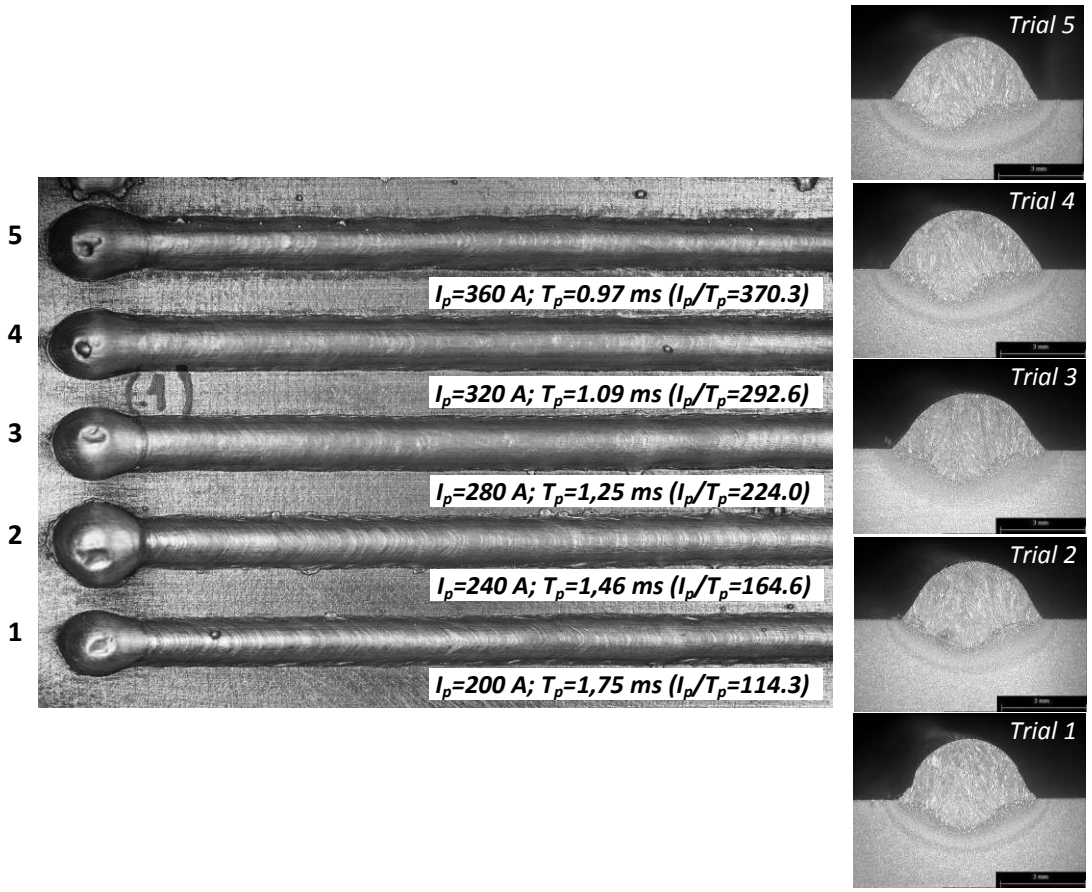

Figure 4.31. Weld bead top surfaces, transverse cross sections, and control parameters applied in study S_1.

The effect of shorter T_p and gradually higher I_p current peaks (study S_1) on the top surface quality and transverse cross sections is illustrated in Figure 4.31, for constant I_{AVG}. The results show that lower I_p/T_p ratios cause an apparent rippling effect that tends to dissolve with gradually larger I_p/T_p ratios. It is also seen in the macrographs that a number of bead characteristics are also altered as changes in I_p/T_p occur. The electrical transients recorded in study S_1 are revealed in Figure 4.32 for trials 1, 3 and 5. Snapshots of the welding cycle waveform for each trial are displayed at the left, and supported by I_{inst} and V_{inst} scatter plots at the right. These data was recorded at every instant in time for a period of 10 seconds at 5 kHz. This sequence shows the effect of the I_p/T_p ratio on the stability of the metal transfer behaviour.

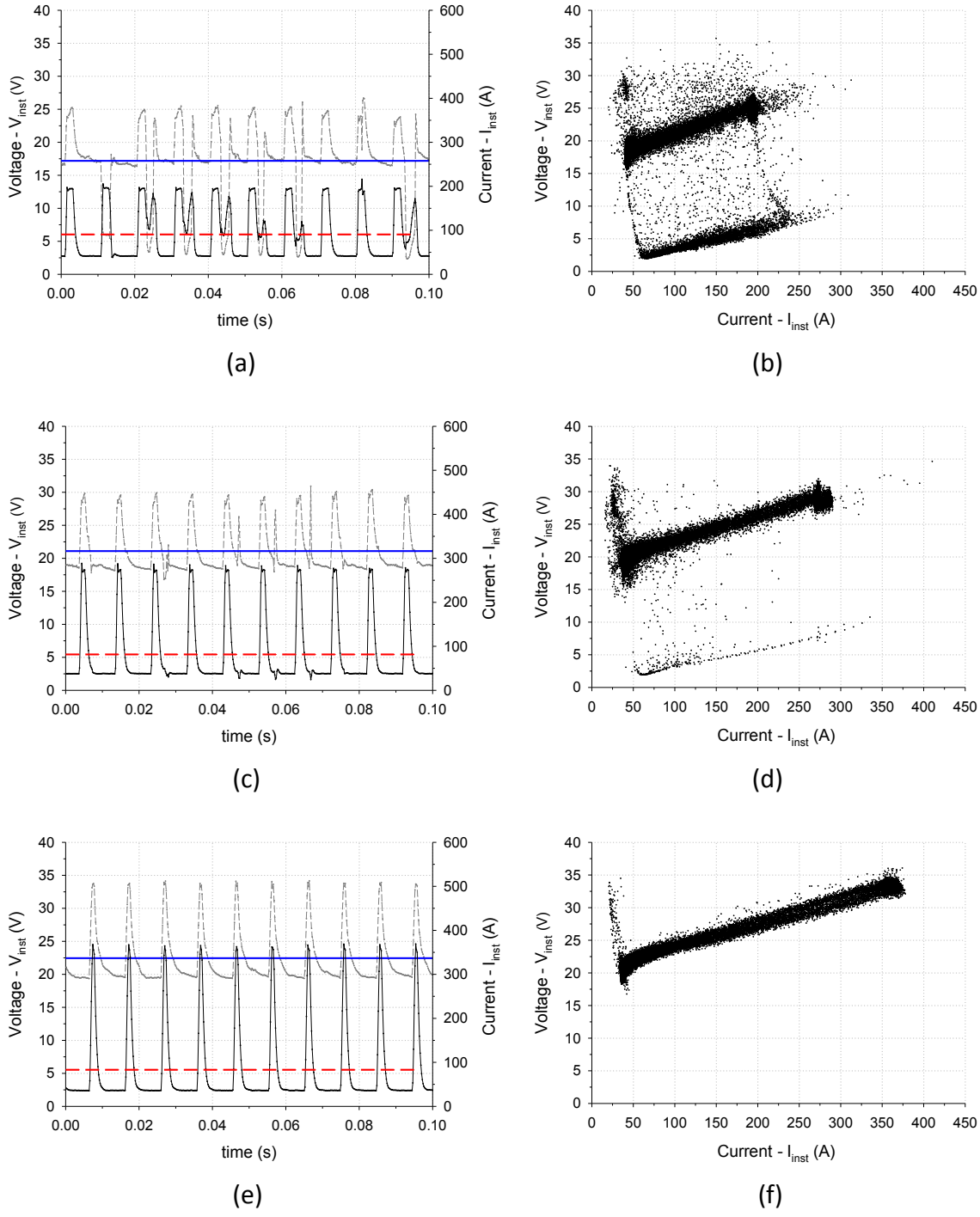

Figure 4.32. Electrical transients in study *S1* showing V_{inst} (dashed grey) and I_{inst} (continuous black) lines on the left, and scatter plots on the right. Trial 1 is represented in (a) and (b), trial 3 in (c) and (d), and trial 5 in graphs (e) and (f). Represented are also the averaged V_{inst} (solid blue) and I_{inst} (dashed red) lines.

Metal transfer by short circuit dominates when small I_p/T_p ratios are applied (see Figures 4.32(a) and (b)). As the I_p/T_p ratio increases the frequency of the short circuits is reduced (see Figures 4.32(c) and (d)). When larger I_p/T_p ratios are applied, the transition

to more stable ODPP metal transfer mechanism is noticeable. The average V_{inst} increases with higher I_p/T_p ratios, whilst the average I_{inst} decreases marginally (see Figures 4.32(e) and (f)).

The effect of the I_p/T_p ratio on the average voltage (V_{AVG}), average current (I_{AVG}), average instant power (AIP) and deposition rate (DR) is displayed in Figure 4.33. The deposition rate was calculated using the rate of mass transfer determined by the actual wire feed speed. Figure 4.33(a) shows that V_{AVG} increases significantly with I_p/T_p from a minimum of about 18 V at 114 I_p/T_p to a maximum of 22 V at 370 I_p/T_p, while I_{AVG} decays slowly with increased I_p/T_p, from a maximum at 114 I_p/T_p to a minimum at I_p/T_p of 293. As shown in Figure 4.33(b), the AIP increases with I_p/T_p from a minimum of 1.75 kW at 114 I_p/T_p to about 2.25 kW at 370 I_p/T_p, whereas DR is independent of the I_p/T_p ratio.

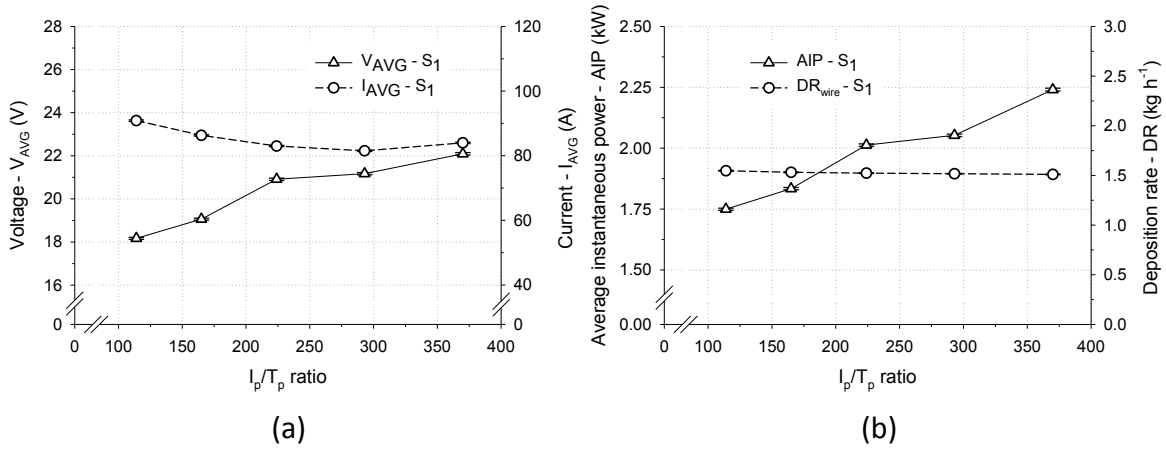

Figure 4.33. Dependence of (a) V_{AVG} and I_{AVG}, and (b) AIP and DR on the I_p/T_p ratio (S_1).

The effect of I_p/T_p on the bead width (W), bead height (H), remelting ratio (RR) and penetration depth (P) is shown in Figure 4.34. W increases with the I_p/T_p ratio from about 4.7 mm at 114 I_p/T_p up to a maximum value of 5.45 mm at I_p/T_p ratio of 224, decreasing slightly thereafter. In contrast, H decays moderately with I $_p/T_p$ up to a minimum of about 2 mm is reached at the I_p/T_p mid-range, increasing slowly thereafter (see Figure 4.34(a)). RR shows a maximum at the I_p/T_p mid-range, decreasing thereafter. Figure 4.34(b) shows that P increases moderately at intermedium I_p/T_p regimes (trials 3 and 4).

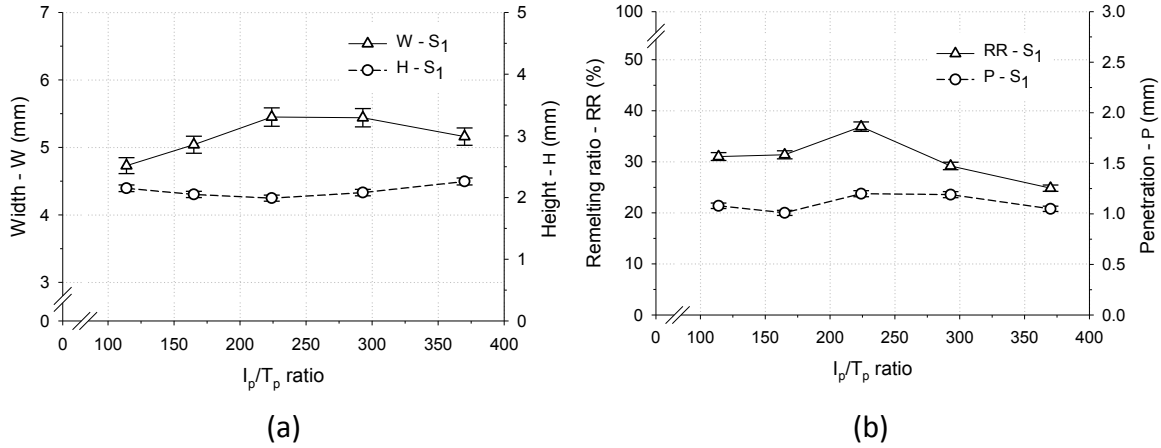

Figure 4.34. Effect of I_p/T_p on (a) bead W and H, and (b) on RR and P depth (S_1).

The effect of I_p/T_p on dilution (D), contact angle (CA), penetration area (A_1) and reinforcement area (A_2) is depicted in Figure 4.35. It can be seen from Figure 4.35(a) that D increases gradually with I_p/T_p up to a maximum of about 27 % for an I_p/T_p of approximately 225, decreasing thereafter. In contrast, the CA decreases slowly with I_p/T_p until a minimum of about 53 % is reached at the same I_p/T_p. A_1 increases with I_p/T_p up to a maximum of 2.7 mm^2 at the I_p/T_p mid-range, whilst A_2 shows to increase slowly with I_p/T_p.

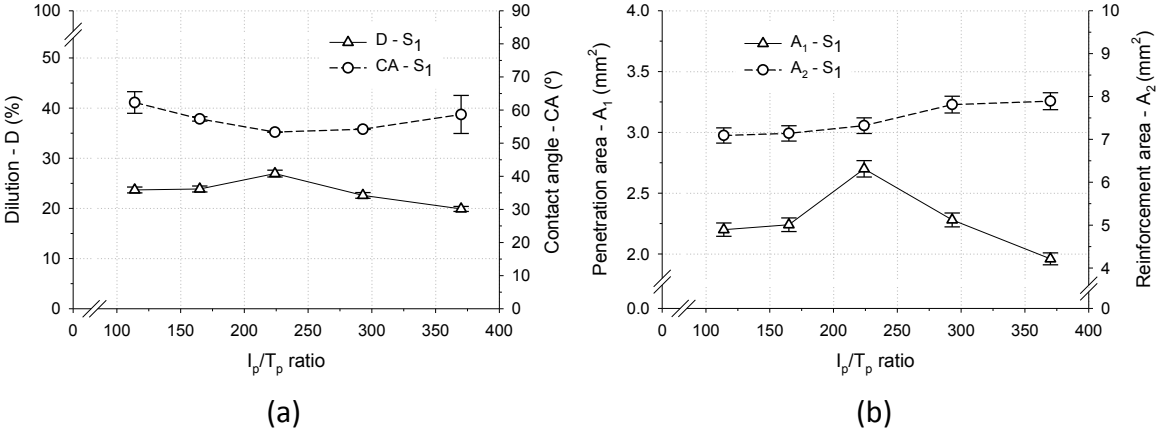

Figure 4.35. Effect of I_p/T_p on (a) D and CA (for a 95% confidence interval), and on (b) A_1 and A_2 (S_1).

The effects of pulse current (I_p) and background current (I_b) on the quality of the bead top surface, and transverse cross section profiles are shown in Figure 4.36 (study S_3). Smaller I_p/I_b ratios produce a noticeable wavelike rippling effect on the bead top surface (see trial 1). This rippling effect is particularly noticeable at smaller I_p/I_b ratios, becoming apparently negligible as the ratio increases (see trials 2 and 3). Macrographs

of transverse cross sections reveal good fusion characteristics with the substrate, while weld bead characteristics also indicate to depend on the I_p/I_b ratio.

Figure 4.37 shows the electrical transient data captured in study *S3* (trials 1, 4 and 5). This series of trials established the effect of small adjustments in the I_p/I_b ratio on the metal transfer characteristics, which can be then related to the surface quality of the deposits.

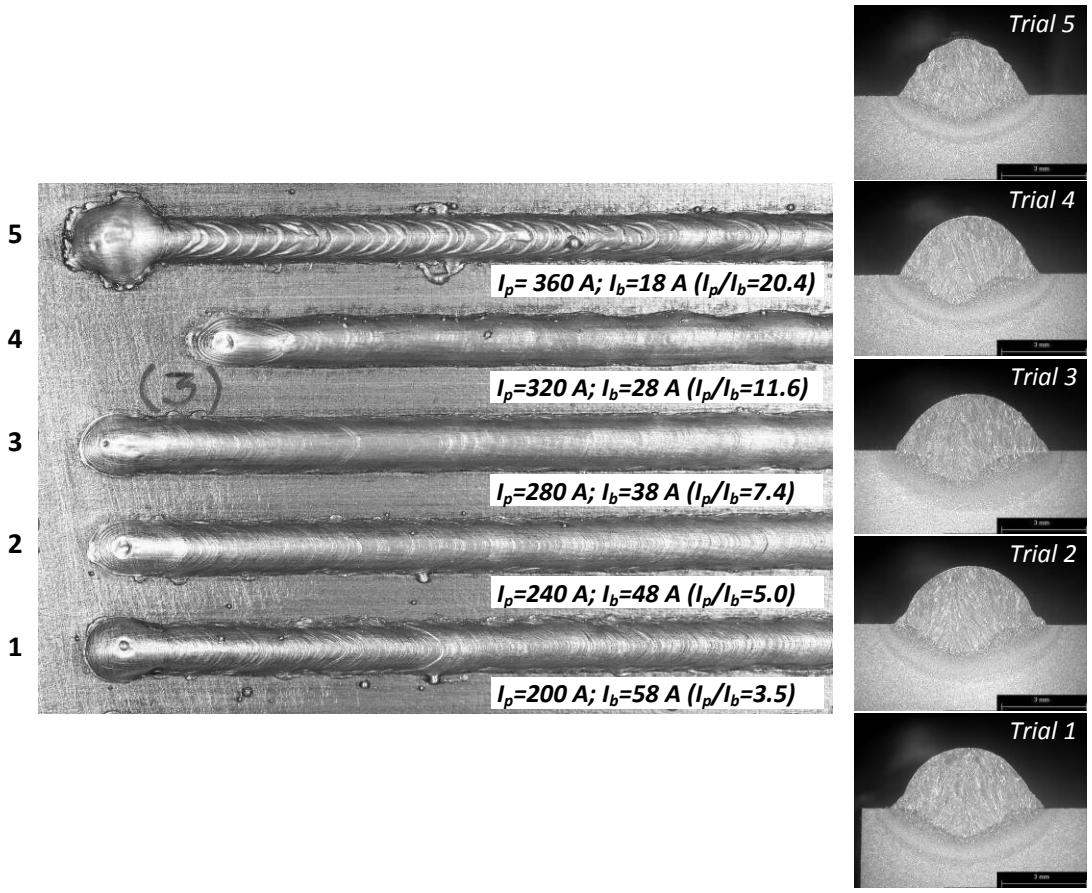

Figure 4.36. Weld bead top surfaces, transverse cross sections, and control parameters applied in study *S3*.

Smaller I_p/I_b ratios have been shown that metal droplets are transferred predominantly by a short circuit mechanism, while larger I_p/I_b assure the transition to a more stable ODPP metal transfer mechanism (see Figures 4.37(a) and (b)). Note, however, that arbitrary droplet detachments are likely to occur particularly when current is in the base current period (see Figure 4.37(c)). Arbitrary droplet detachments are noticeably captured at low currents in the scatter plot shown in Figure 4.37(d).

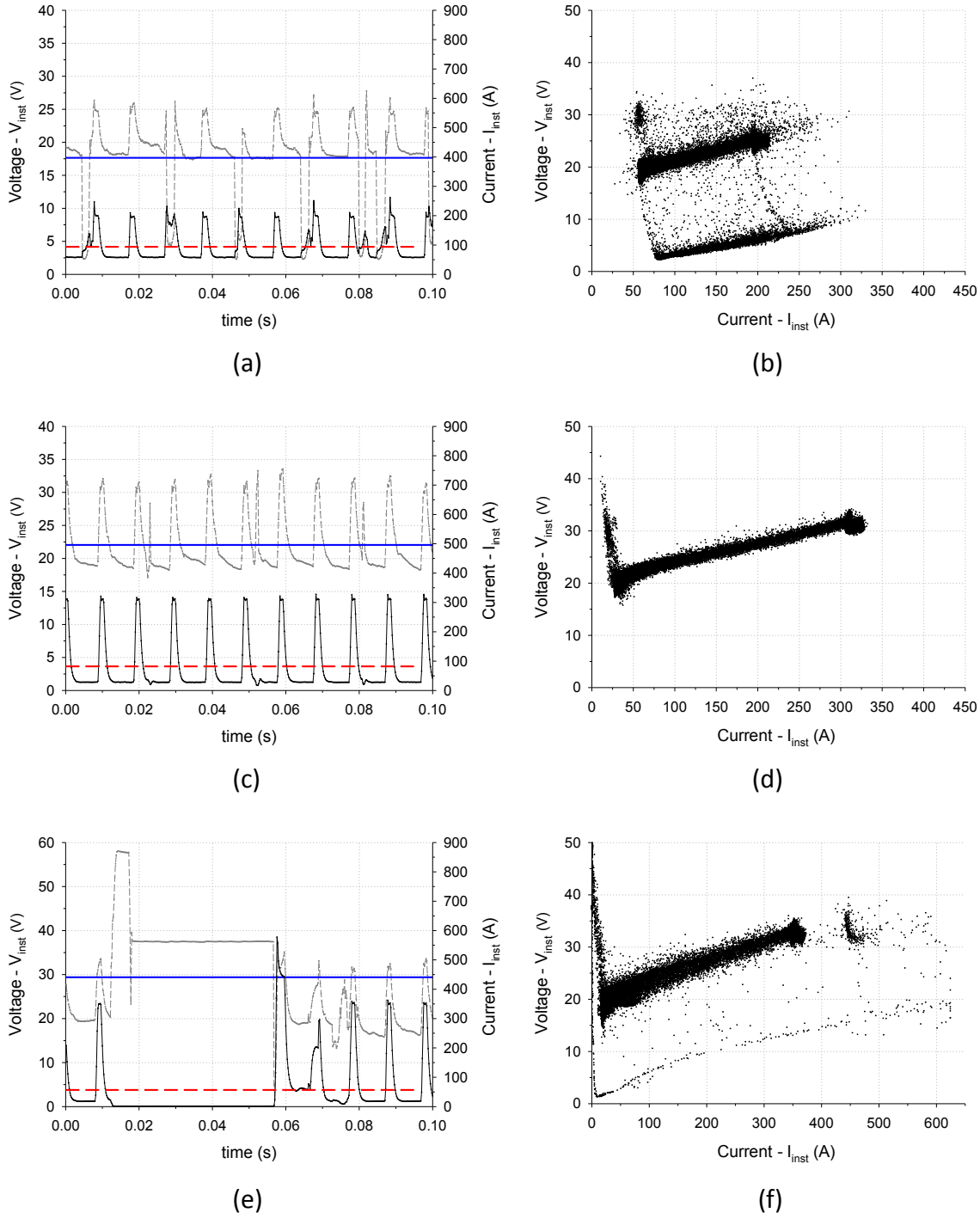

Figure 4.37. Electrical transients in study *S_3* showing V_{inst} (dashed grey) and I_{inst} (continuous black) lines on the left, and scatter plots on the right. Trial 1 is represented in (a) and (b), trial 4 in (c) and (d), and trial 5 in graphs (e) and (f).

These droplet detachment events are characterised by an elongated point cloud tail, positioned in the near zero current region, which expands throughout the higher voltages domain. Moreover, unstable welding conditions dominate when very high I_p/I_b

ratios are applied due to a momentary suppression of the welding arc (see Figure 4.37(e) and (f)). Additionally, both I_{AVG} and V_{AVG} vary significantly with the I_p/I_b ratio. The effect of the I_p/I_b ratio on the average voltage (V_{AVG}), average current (I_{AVG}), average instant power (AIP) and deposition rate (DR) is displayed in Figure 4.38.

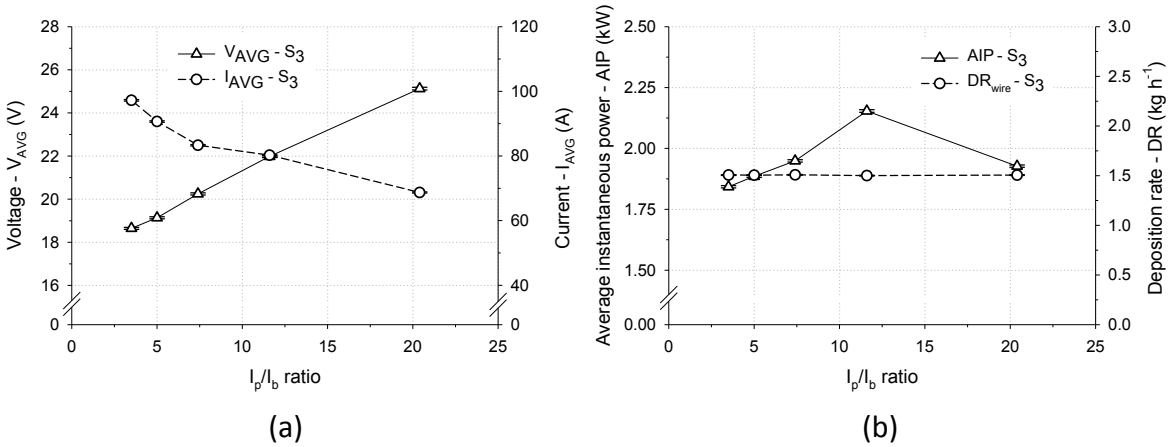

Figure 4.38. Dependence of (a) V_{AVG} and I_{AVG}, along with (b) AIP and DR on the I_p/I_b ratio (S_3).

Figure 4.38(a) shows the rapid increase in V_{AVG} with the I_p/I_b ratio from a minimum of 18.7 V at 3.5 I_p/I_b to 25.3 V at 20.4 I_p/I_b. In addition, I_{AVG} drops notably from a maximum of about 97 A at 3.5 I_p/I_b to 68.7 A at 20.4 I_p/I_b. Figure 4.38(b) shows that AIP, in general, increases with I_p/I_b, whereas DR is constant throughout the I_p/I_b range studied, with a value of 1.505±0.003 kg h^{-1} for a 95 % confidence interval. The effect of I_p/I_b on the bead width (W), bead height (H), remelting ratio (RR), and penetration depth (P) is represented in Figure 4.39.

Figure 4.39(a) shows a slow decrease in W with the I_p/I_b from 7.5 I_p/I_b up to the end of the range studied. The H is practically independent of the I_p/I_b ratio. As shown in Figure 4.39(b), the RR and P increase moderately with I_p/I_b up to its mid-range interval. Thereafter, P drops moderately up to 20.4 I_p/I_b ratio, whereas RR drops to minimum at an I_p/I_b of 11.6. The effect of I_p/I_b ratio on D and CA, as well as on A_1 and A_2 is illustrated in Figure 4.40. Figure 4.40(a) shows a small increase in D for lower I_p/I_b ratios and a drop in its value thereafter. The CA decreases slowly with the I_p/I_b up to a minimum of 53.2° at low I_p/I_b ratios, increasing thereafter. As observed in Figure 4.40(a), A_1 increases slowly up to 7.4 I_p/I_b, dropping considerably thereafter. In addition, A_2 drops fast as the I_p/I_b ratio increases.

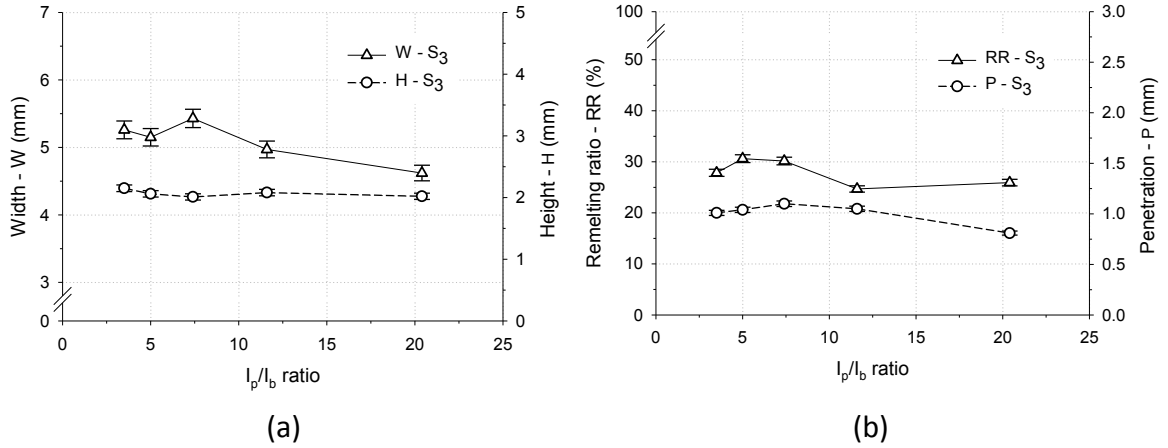

Figure 4.39. Effect of I_p/I_b ratio on the bead (a) W and H, as well as on the (b) RR and P (S_3).

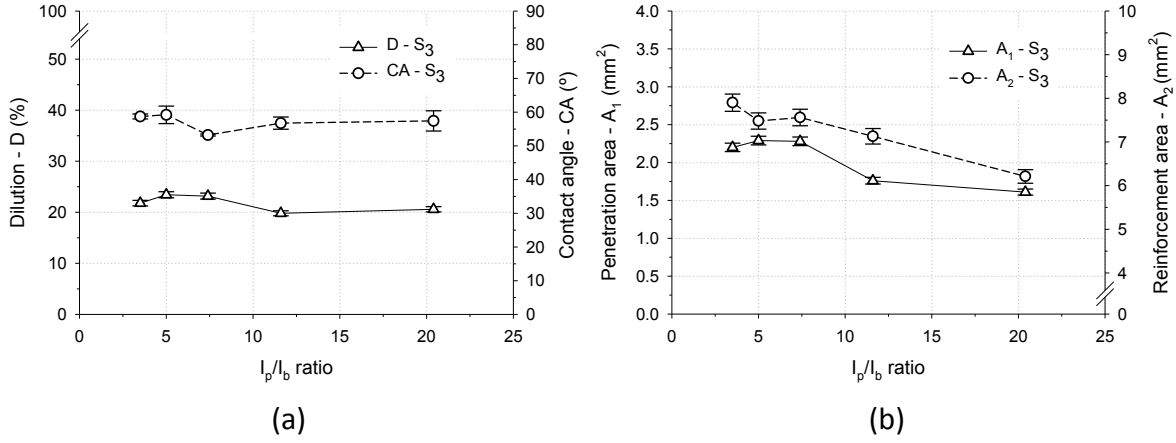

Figure 4.40. Effect of I_p/I_b on (a) D and CA (for a 95% confidence interval), as well as on (b) A_1 and A_2 (S_3).

4.1.3 Cold metal transfer

The set-up, welding equipment, and experimental method applied to carry out the experiments reported in the following subsections are detailed in section 3.8.3 of the experimental procedure chapter (see chapter 3).

4.1.3.1 Effect of arc-length control, dynamic correction and contact tip to work distance on electric transients and weld bead profiles

This section reports the results of a systematic study on the effect of process parameters, such as arc-length control (ALC), dynamic correction (DC_{orr}) and CTWD on electric transients and weld bead characteristics. Experiments were carried out according to the welding conditions described in section 3.8.3.1. CMT was employed to deposit 1.2 mm

steel wire with a shielding gas mixture containing Ar/CO_2 (20%). The experimental designs applied in this study are detailed in Tables I 21 to I 23 along with measured weld bead characteristics (see Appendix I). The effect of ALC on the averaged voltage (V_{AVG}) and current (I_{AVG}) is depicted in Figure 4.41.

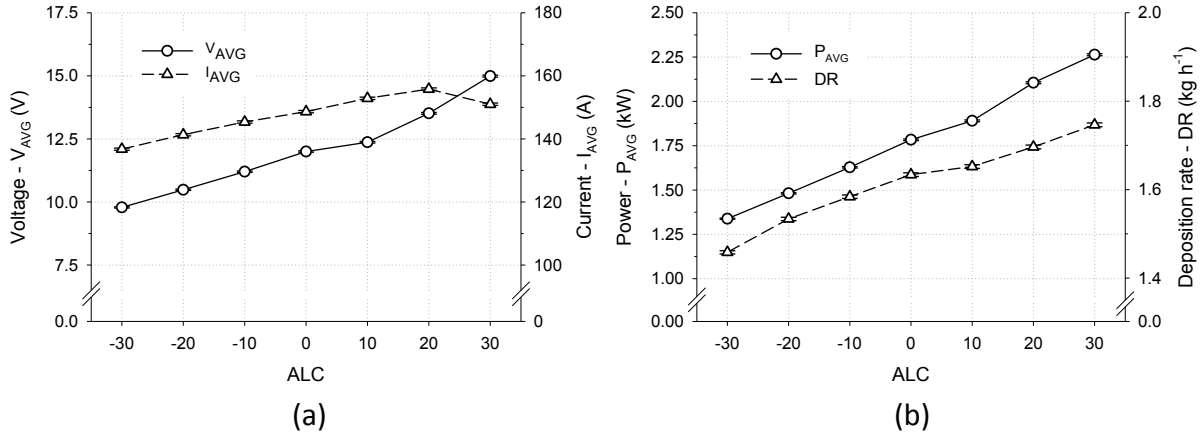

Figure 4.41. Effect of arc-length control (ALC) on (a) average voltage (V_{AVG}) and average current (I_{AVG}), (b) average power (P_{AVG}) and deposition rate (DR).

Figure 4.41(a) shows evidence of a nearly linear relation between the process control parameter ALC and both V_{AVG} and I_{AVG} electric transients. The maximum percentage variations in V_{AVG} and I_{AVG} are 53 % and 14 %, correspondingly. Likewise, both P_{AVG} and DR show a strong positive correlation with ALC. The effect of ALC on the actual wire feed speed (WFS_{actual}), current pulsing frequency (*f*), bead width (W), and bead height (H) is presented in Figure 4.42.

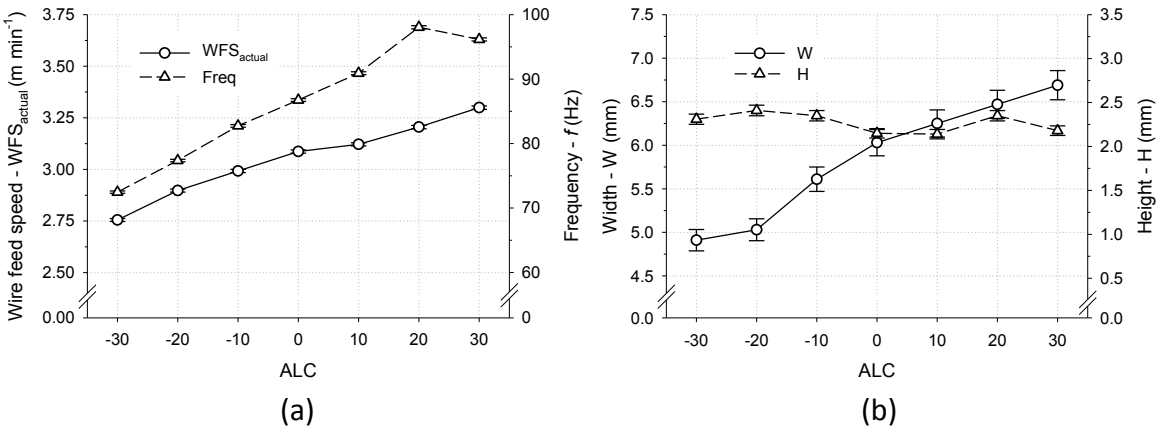

Figure 4.42. Effect of ALC on (a) actual wire feed speed (WFS_{actual}) and frequency (*f*), as well as on (b) bead width (W) and bead height (H).

Figure 4.42(a) shows that ALC has a noticeable positive linear effect on both the WFS_{actual} and on current pulsing frequency. From Figure 4.42(b) it can be seen that ALC correlates positively with W, whilst H is kept nearly unchanged. The effect of ALC on remelting ratio (RR), penetration depth (P), dilution (D), contact angle (CA), penetration area (A_1), and reinforcement area (A_2) is shown in Figure 4.43. Figure 4.43(a) shows that ALC is strongly positively associated with both RR and P. Also, D is positively correlated with ALC, whilst CA appears to decrease slowly with the ALC from nearly 70° for ALC of -30 to around 56° at 30 ALC (see Figure 4.43(b)). As shown in Figure 4.43(c), ALC has a strong positive linear effect on both A_1 and A_2.

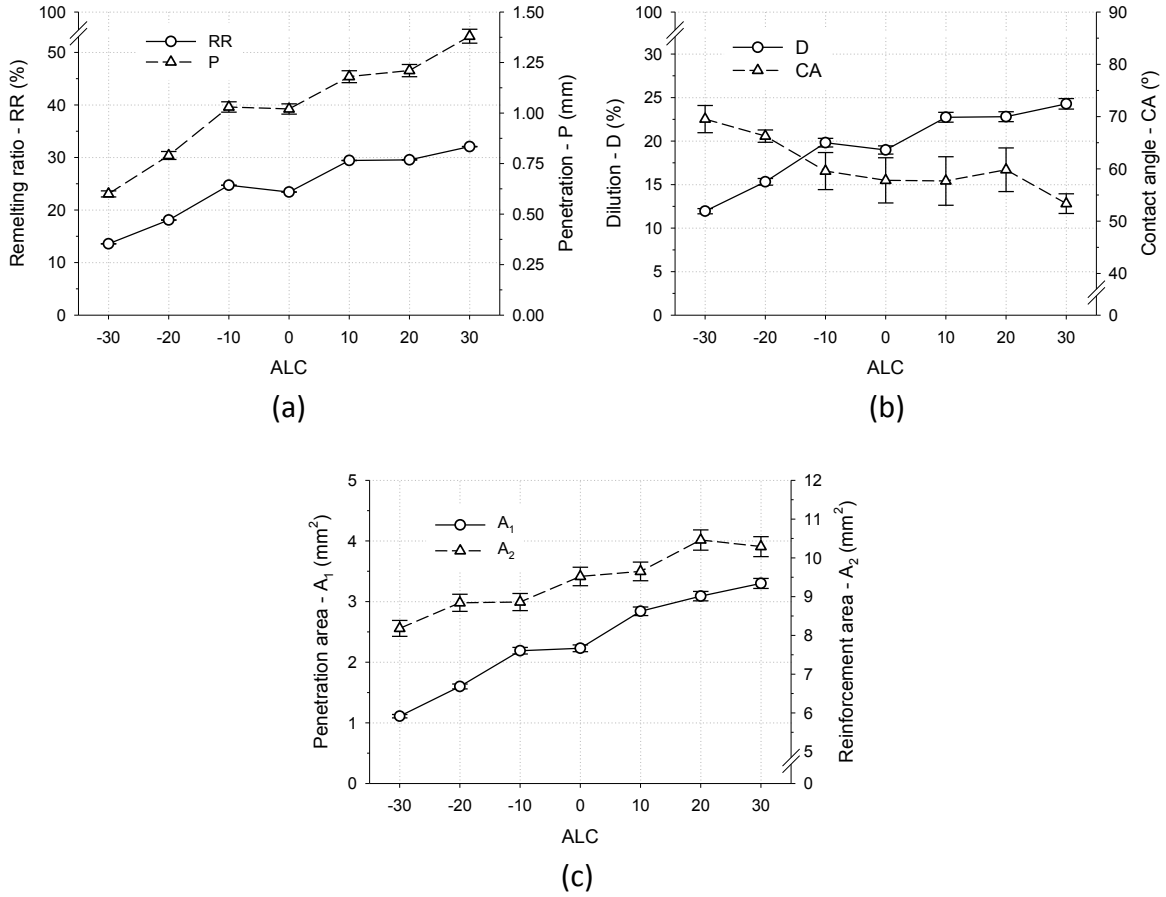

Figure 4.43. Effect of ALC on (a) remelting ratio (RR) and penetration (P), (b) dilution (D) and contact angle (CA) for a 95% confidence interval, as well as on (c) penetration area (A_1) and reinforcement area (A_2).

The effect of DC_{orr} on averaged voltage (V_{AVG}) and current (I_{AVG}), as well as on averaged power (P_{AVG}) and deposition rate (DR) is shown in Figure 4.44. V_{AVG}, I_{AVG}, P_{AVG} and DR are all negatively associated with DC.

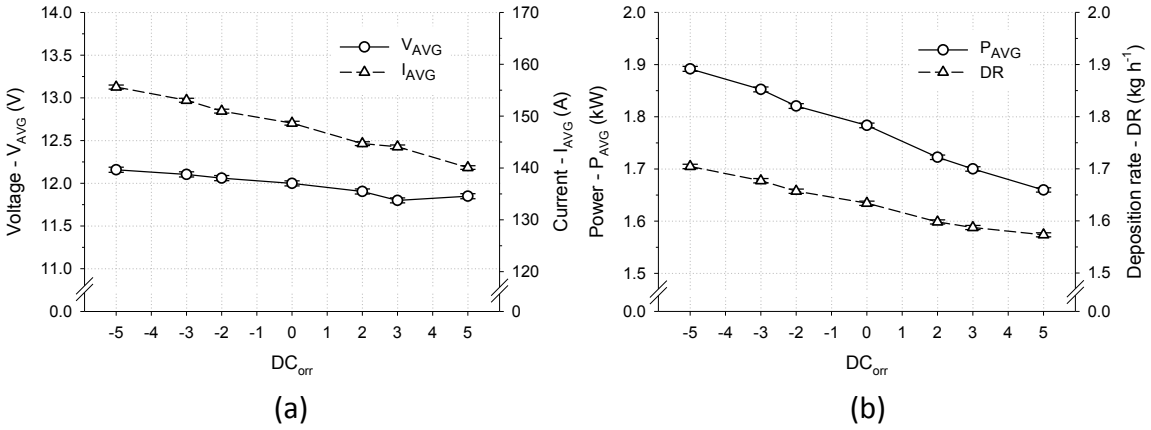

Figure 4.44. Effect of DC_{orr} on (a) V_{AVG} and I_{AVG}, and on (b) P_{AVG} and DR.

The effect of DC_{orr} on actual wire feed speed (WFS_{actual}), current pulsing frequency (*f*), and bead profile characteristics such as bead width (W) and bead height (H), is plotted in Figure 4.45. DC_{orr} has a negative linear effect on WFS_{actual}, whilst no significant effect was observed on *f*. Figure 4.45(b) shows that DC_{orr} has a very weak influence on both W and H. The effect of CTWD on V_{AVG} and I_{AVG}, as well as on P_{AVG} and DR are illustrated in Figure 4.46. Figure 4.46(a) shows that V_{AVG} is positively linear correlated with CTWD, whilst no significant effect is observed on I_{AVG}. CTWD shows to be positively linear associated with both P_{AVG} and DR. The influence of CTWD on the actual wire feed speed (WFS_{actual}), current pulsing frequency (*f*), bead width (W), and bead height (H) is plotted in Figure 4.47.

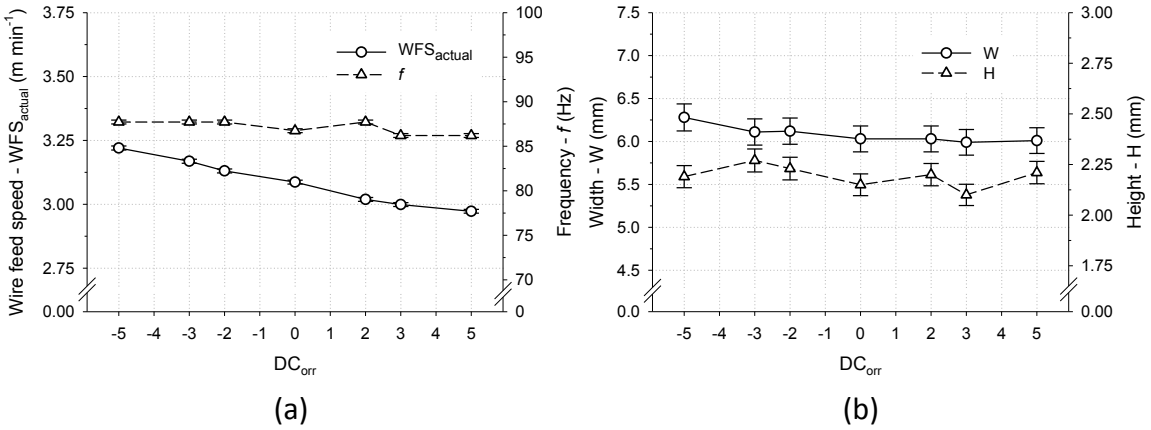

Figure 4.45. Effect of DC_{orr} on (a) WFS_{actual} and *f*, and on (b) W and H.

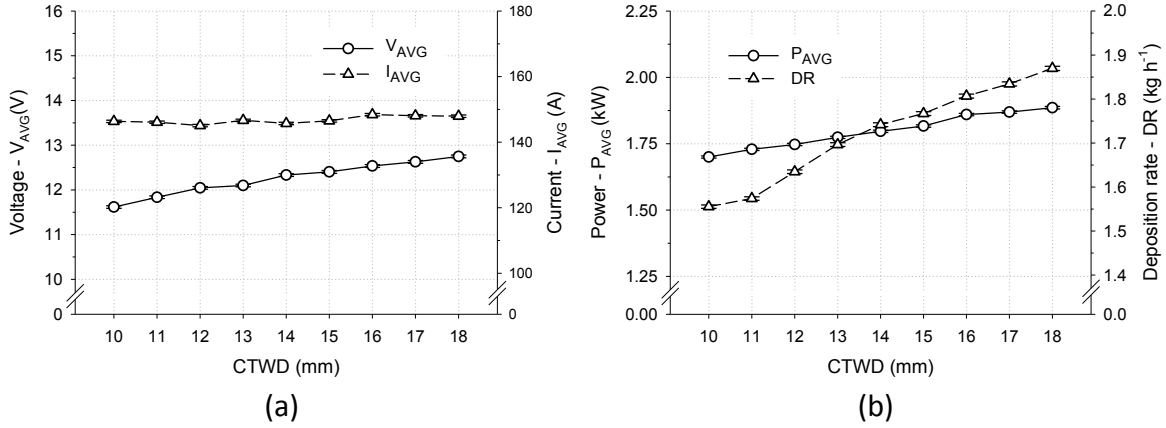

Figure 4.46. Effect of CTWD on (a) V_{AVG} and I_{AVG}, as well as on (b) P_{AVG} and DR.

Figure 4.47(a) shows that WFS_{actual} is strongly associated with CTWD, whilst the effect of CTWD on *f* appears to be negligible. It is apparent from Figure 4.47(b) that both W and H increase from a minimum for CTWD of 10 mm up to about 15 mm. Supplemental results on the effects of both DC_{orr} and CTWD parameters on weld bead characteristics (*i.e.* RR, P, D, CA, A_1, and A_2) are provided in Figures L 21 and L 22 (see Appendix L).

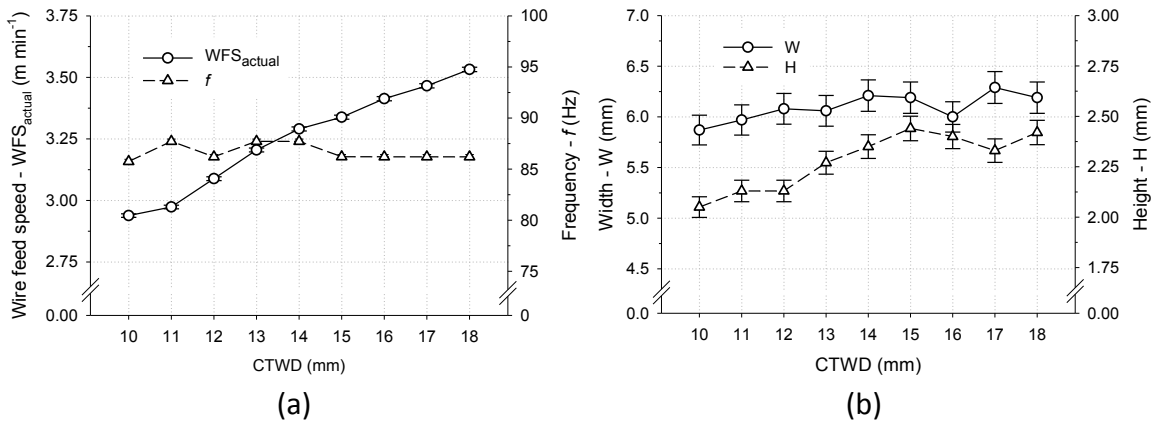

Figure 4.47. Effect of CTWD on (a) WFS_{actual} and *f*, and on (b) W and H.

4.1.3.2 Effect of wire feed speed and shielding gas composition on electrical transients

In this section the impact of different welding shielding gas compositions on CMT electrical transients is reported. The welding conditions applied throughout the investigation are detailed in section 3.8.3.2. The experimental design is listed in Table I 24 (Appendix I), along with electrical transient measurements.

The effect of wire feed speed set (WFS_{set}) on averaged voltage (V_{AVG}), averaged current (I_{AVG}), average instantaneous power (AIP), and deposition rate (DR) for different shielding gas compositions are shown in Figure 4.48. Figure 4.48(a) shows that both V_{AVG} and I_{AVG} have a positive correlation with the WFS. However, Figure 4.48(a) indicates that gas mixtures with higher CO_2 content (*e.g.* Ar/CO_2 (20%)) increase V_{AVG} significantly.

Figure 4.48(a) shows that the effect of different gas mixtures on I_{AVG} is very small. As can be seen from Figure 4.48(b), a significant linear correlation was found between WFS and both AIP and DR. Yet again, mixtures with higher CO_2 content (*e.g.* Ar/CO_2 (20%)) appear to shift the AIP to higher regimes throughout the WFS_{set} range examined. The average percentage increase in AIP relative to Ar/CO_2 (8%) is 10.7±1.9 % and 15.0±3.7 % relative to Ar/CO_2 (5%)/O_2 (2%), when utilising Ar/CO_2 (20%).

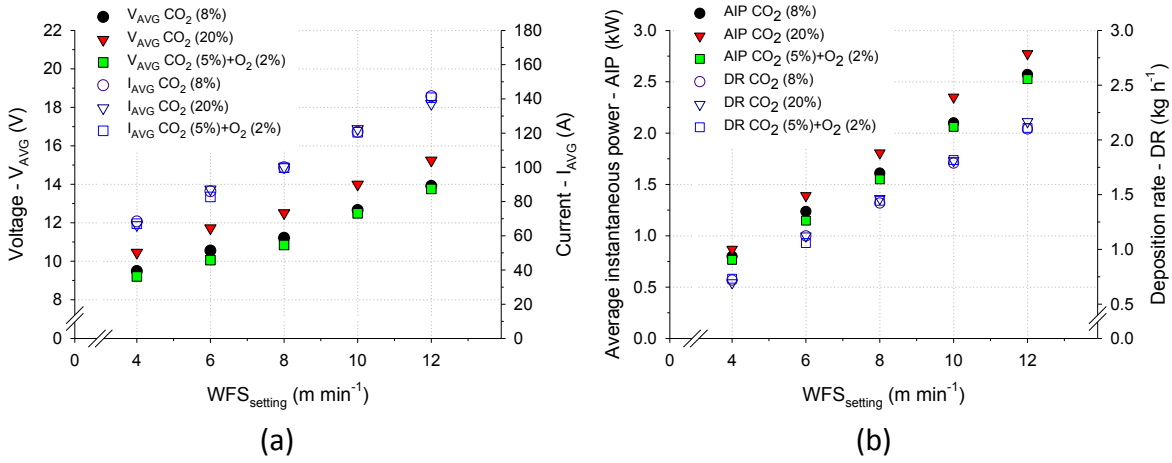

Figure 4.48. Effect of WFS_{set} and shielding gas composition on (a) V_{AVG} and I_{AVG}, as well as on (b) AIP and DR.

Auxiliary data on the impact of different shielding gas compositions on the CMT electrical transients are extensively given in Appendix L. Electrical transients of studies G_1, G_2 and G_3, as well as I_{inst} and V_{inst} oscillograms are shown in Figures L 23 to L 25.

4.1.4 Comparison of gas metal arc welding and cold metal transfer

The experimental set-up, welding power supplies, and experimental method utilised to carry out these experiments are detailed in section 3.8.4 of the experimental procedure chapter (chapter 3).

4.1.4.1 Effect of wire feed speed and wire feed speed to travel speed ratio on weld bead characteristics

The effects of primary process parameters such as WFS, TS and WFS/TS on the weld bead characteristics are presented for both GMAW-P and CMT in this study. A number of experiments were carried out to clarify the basic interactions between process variables and geometric outputs by examining weld bead transverse cross sections.

The experiments were carried out according to the welding conditions described in section 3.8.4.1. The experimental plan is contained in Table D 1 (Appendix D), where applied welding conditions are listed along with measured bead characteristics. Samples were examined as described in section 3.7, whereas the electrical transients were recorded according to section 3.3. Figure 4.49 shows the effect of the WFS_{set} and TS on the weld bead shape evolution for both CMT and GMAW-P systems.

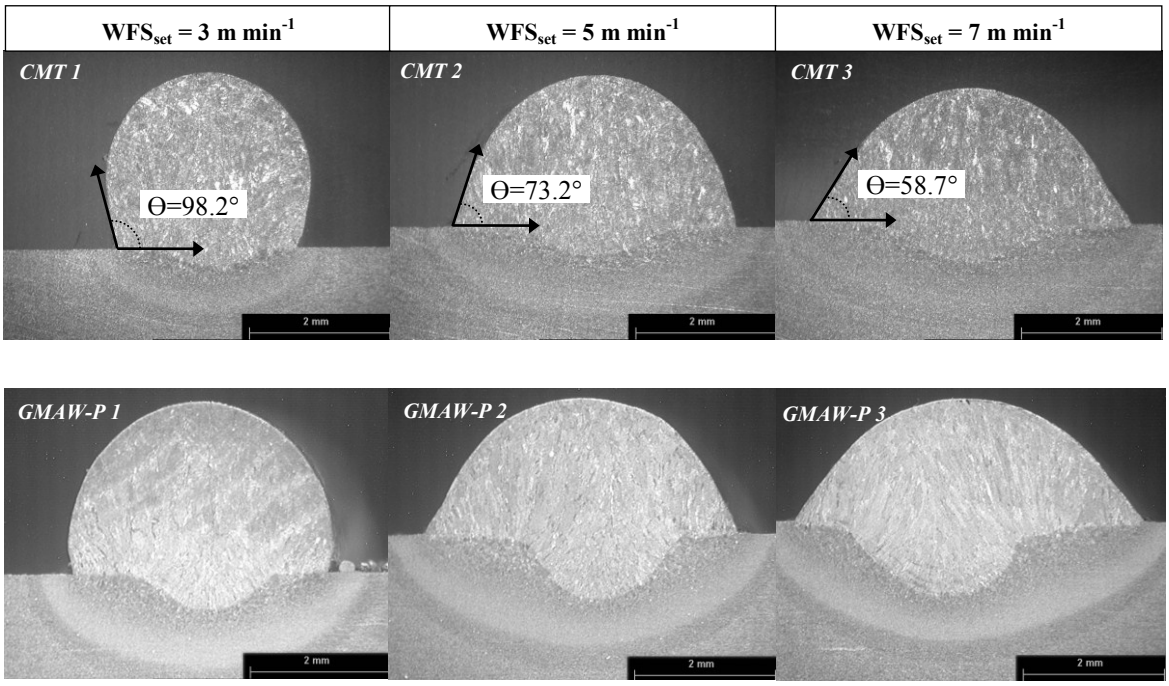

Figure 4.49. Effect of WFS_{set} on the weld bead cross section profiles for the CMT (top) and GMAW-P (bottom) welding processes (WFS/TS=15).

In this set of trials transverse cross section areas (or WFS/TS ratio) were held constant at 15. The sequence shown in Figure 4.49 reveals that the WFS and thus TS have a major influence on the weld bead characteristics for both welding processes. For instance, CA decays sharply with increasing WFS_{set} from 98.2° to 58.7°, as the WFS_{set} increases from 3 to 7 m min^{-1} (see top sequence in Figure 4.49).

The influence of WFS/TS ratio on the weld bead characteristics is illustrated in Figure 4.50 for the CMT welding process. In this series of trials the WFS_{set} was held constant at 2 m min^{-1} while varying the WFS/TS. It is apparent from Figure 4.50 that not only the cross section area increases with increasing WFS/TS, but many other weld bead characteristics change significantly. As an example, CA increases from 96.1° to 132.4° as the WFS/TS ratio increases from 10 to 20, respectively.

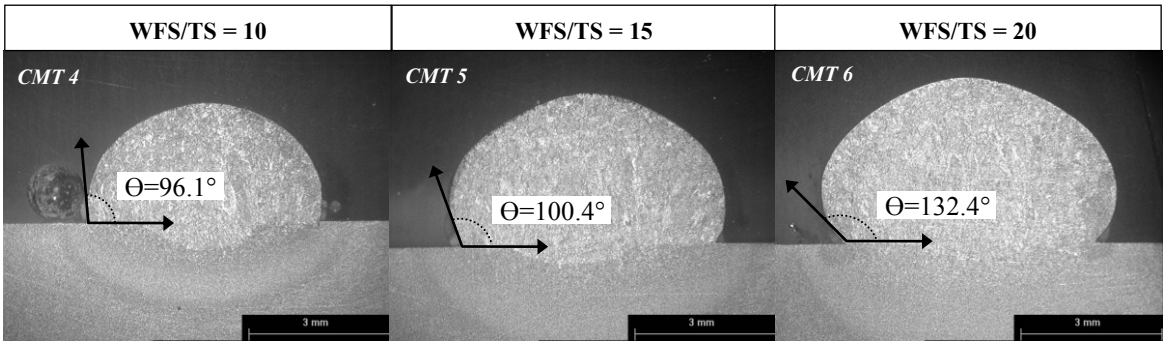

Figure 4.50. Effect of WFS/TS on the transverse cross section area in CMT, WFS_{set}= 2 m min^{-1}.

Figure 4.51 shows the effect of medium to high WFS_{set} regimes on the geometry of the weld bead profiles in GMAW-P. In this group of trials the WFS/TS was held at 15 and a 1.2 mm diameter wire was used. From Figure 4.51 it is seen that WFS and TS have a noticeable effect on a vast number of weld bead characteristics, while cross section areas are kept constant.

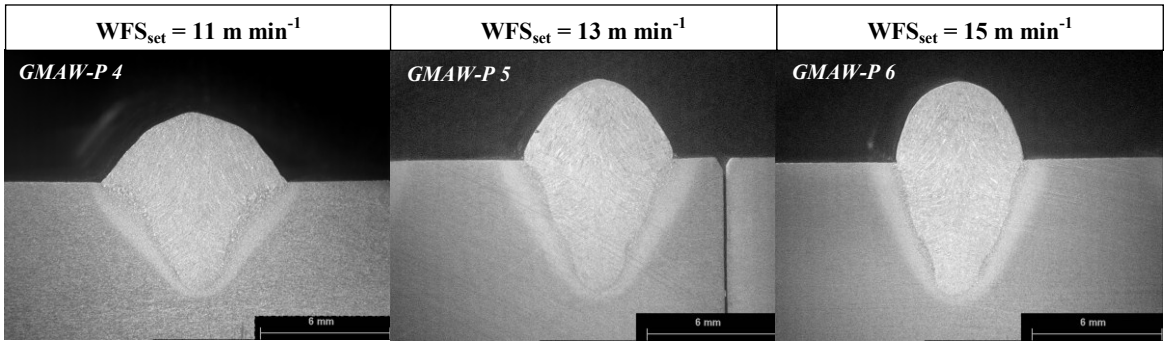

Figure 4.51. Effect of medium to high WFS_{set} regimes on the weld bead cross section profiles in GMAW-P (WFS/TS=15).

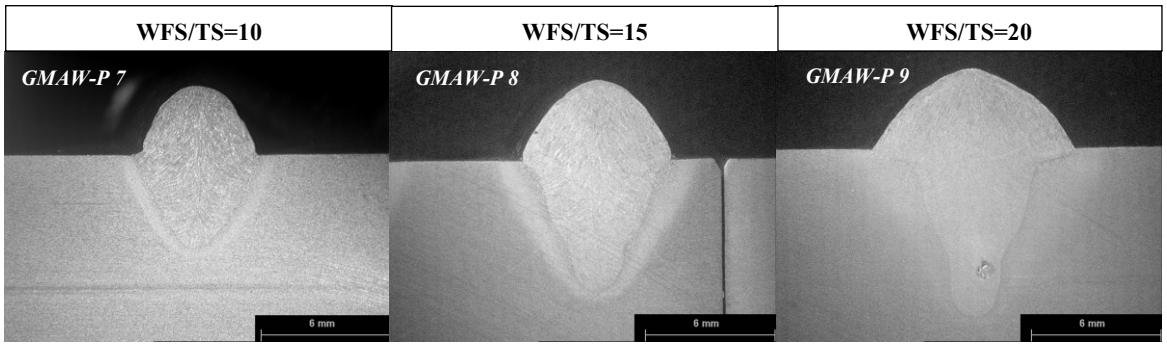

Figure 4.52. Effect of WFS/TS on the cross-sectional area in GMAW-P, WFS_{set}=13 m min^{-1}.

The effect of different WFS/TS on the weld bead characteristics and cross-sectional areas is depicted in Figure 4.52 using GMAW-P. Here, the WFS_{set} was held constant at 13 m min^{-1} and the wire electrode used was 1.2 mm in diameter. It is observed that cross section areas and a number of other weld bead characteristics are notably altered, as changes in the WFS_{set} occur.

4.1.4.2 Weld bead and plate fusion characteristics comparison of cold metal transfer and pulsed gas metal arc welding

The effects of both CMT and GMAW-P processes on the weld bead and fusion characteristics are presented in this subsection, for constant welding conditions. The experiments were performed according to the welding conditions detailed in 3.8.4.2 (see chapter 3).

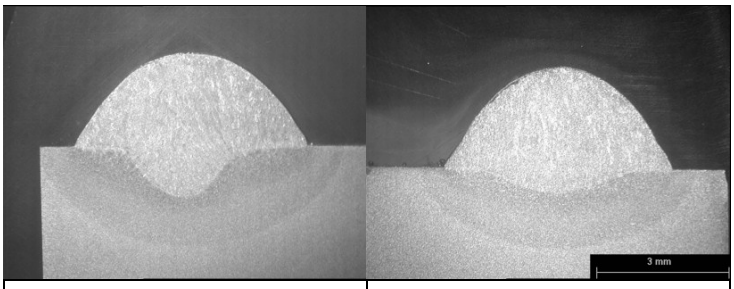

Figure 4.53. Comparison of CMT and GMAW-P macrographs ($WFS_{actual} \approx$ 6 m min^{-1}; TS=0.4 m min^{-1}).

Figure 4.53 exhibits CMT and GMAW-P transverse cross sections and shows the effects of the different welding processes on the bead and fusion characteristics. As shown in Table 4.2, wider and shorter weld beads are obtained with GMAW-P, in comparison with CMT. Another important aspect that emerges from Figure 4.53 is that weld bead fusion characteristics, such as remelting ratio (RR), penetration depth (P),

dilution (D), and penetration area (A_1), are enhanced with the GMAW-P system; *cf.* GMAW-P and CMT in Table 4.2.

Table 4.2. Measured weld bead and fusion characteristics in both CMT and GMAW-P systems.

Welding source	WFS_{set} (m min^{-1})	WFS (mV)	WFS_{actual} (m min^{-1})	W (mm)	H (mm)	RR (%)	P (mm)	D (%)	CA (°)	CI (95%)	A_1 (mm^2)	A_2 (mm^2)	DR_{wire} (kgh^{-1})	DR_{macro} (kgh^{-1})
CMT	8.0	497.94	5.988[1]	5.18	2.31	0.15	0.58	13.22	58.91	2.20	1.24	8.14	1.409	1.524
GMAW-P	6.0	-	5.973[2]	5.29	2.11	0.28	1.16	21.77	56.93	0.69	2.19	7.87	1.405	1.473

Calculations were made using [1]oscilloscope data in mV, and the [2] WFS_{actual} versus $WFS_{setting}$ calibration curve (see Appendix A); TS=0.4 m min^{-1}.

4.1.4.3 High speed electrical transients

This section reports the effect of the WFS_{actual} on the electrical transients, *i.e.* averaged voltage (V_{AVG}), current (I_{AVG}) and average instantaneous power (AIP), for both GMAW-P and CMT welding processes. Experiments were carried out in accordance with the welding conditions detailed in section 3.8.4.3 (see chapter 3).

Figure 4.54(a) shows that the WFS_{actual} has a positive linear correlation with V_{AVG}, irrespective of the welding process. At any constant WFS_{actual}, V_{AVG} is significantly higher in GMAW-P when compared to CMT. Figure 4.54(b) shows that I_{AVG} is positive linear associated with the WFS_{actual} in CMT, whereas the relationship appears nonlinear in GMAW-P.

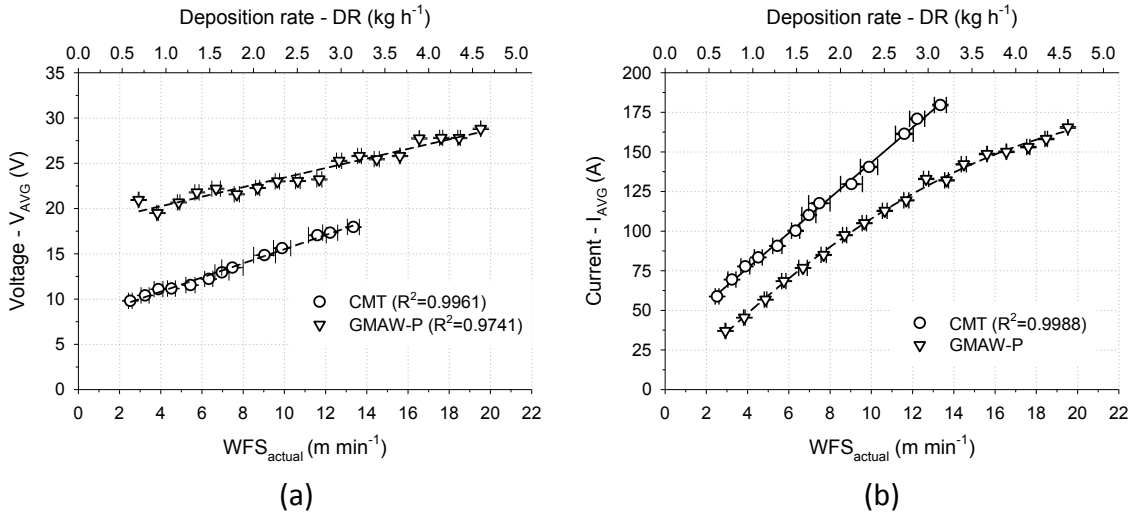

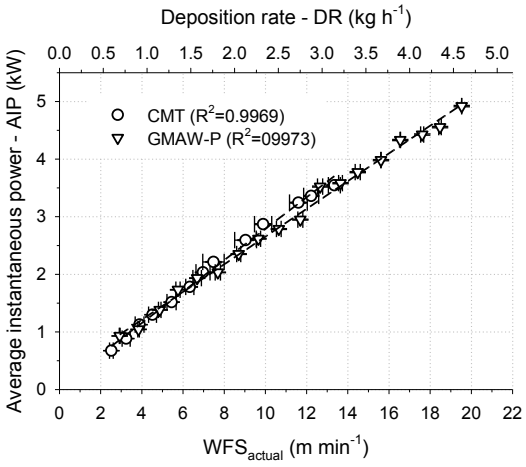

(c)

Figure 4.54. Comparison of CMT and GMAW-P electric transients showing (a) V_{AVG}, (b) I_{AVG}, and (c) AIP outputs (coefficient of determination in brackets).

It is important to highlight that CMT operates at higher I_{AVG} regimes than GMAW-P. Nevertheless, a positive linear relationship between AIP and WFS_{actual} is observed in Figure 4.54(c) for both welding processes.

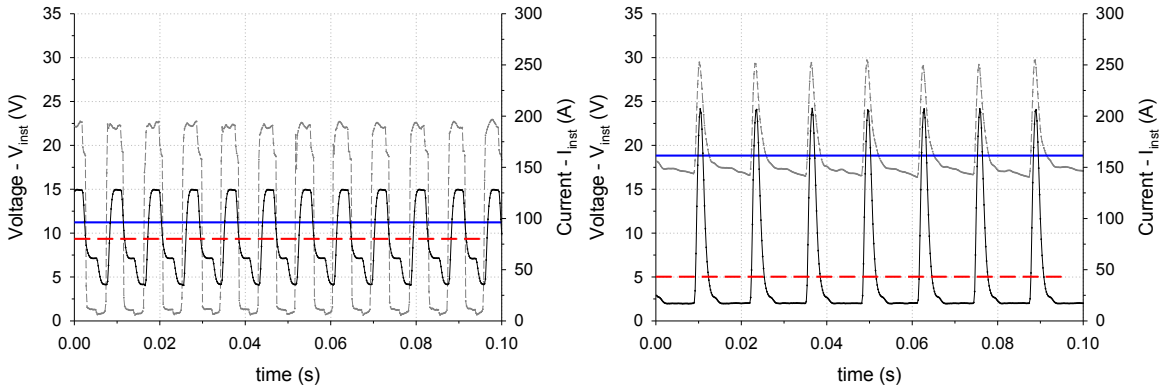

(a) (b)

Figure 4.55. Electrical transients showing V_{inst} (dashed grey) and I_{inst} (continuous black) lines captured in (a) CMT and (b) GMAW-P (P13). Also represented are V_{AVG} (solid blue) and I_{AVG} (dashed red) lines.

The electrical transients obtained from both CMT and GMAW-P systems can be compared in Figure 4.55, for a constant WFS_{actual} of 3.87±0.05 m min^{-1}.

4.2 Single layer welds in steel

The experiments reported in this subsection were carried out according to the set-up, welding conditions, and experimental method detailed in sections 3.9.1 and 3.9.2 (chapter 3). The effects of interactions of primary welding process parameters on weld bead characteristics were investigated in both GMAW-P and CMT. The experimental design and welding conditions are provided in Tables C 1 and C 2 for CMT (see Appendix C), alongside measured responses.

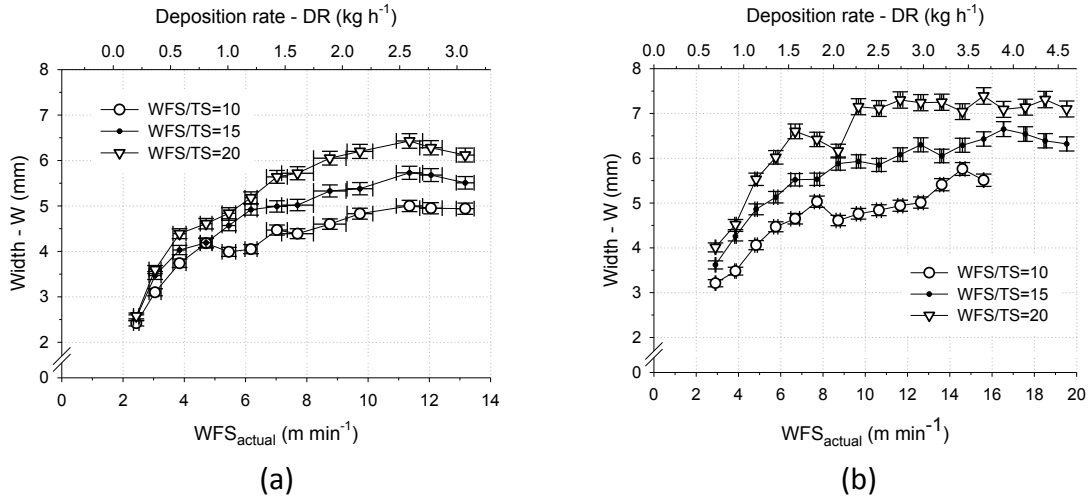

Figure 4.56. Effect of WFS_{actual} on W in (a) CMT and (b) GMAW-P.

Figure 4.56 shows the effect of WFS on W in both welding processes, at constant WFS/TS. The results show that W depends strongly on WFS and WFS/TS ratio for both welding processes.

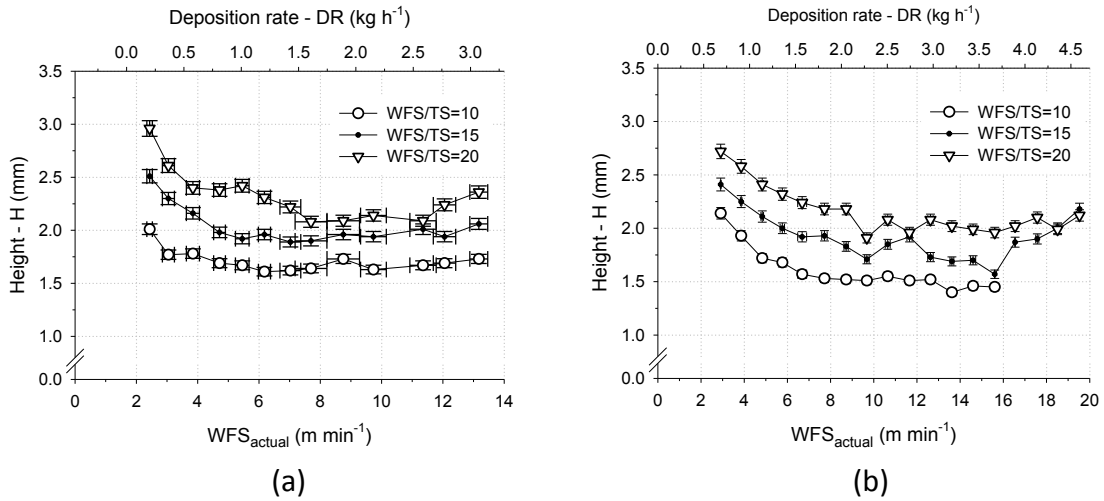

Figure 4.57. Effect of WFS_{actual} on bead height in (a) CMT and (b) GMAW-P.

The influence of WFS on W is more notable at lower and medium WFS regimes, but becomes less significant above 10 m min^{-1} WFS for CMT and about 16 m min^{-1} for GMAW-P. W is inversely correlated to the TS, at fixed WFS. Figure 4.57 shows that the changes observed in H with the WFS are commensurate with that observed in W. The maximum H is in general reached at the lowest feeding rate. Thereafter, H drops slowly with the WFS to a nearly constant value. As shown in Figures 4.56 and 4.57, W and H increase with increasing WFS/TS, at constant WFS.

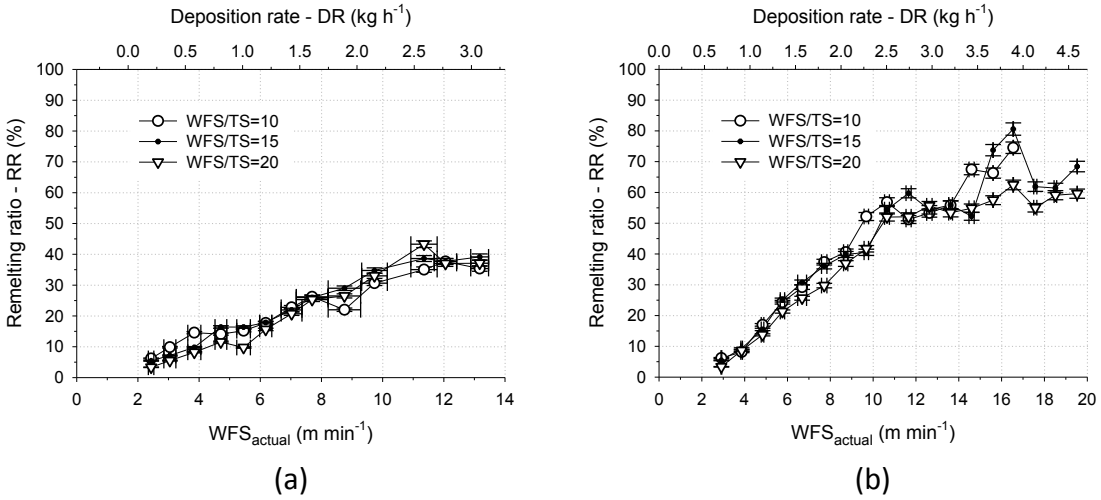

Figure 4.58. Effect of WFS_{actual} on RR in (a) CMT and (b) GMAW-P.

Figure 4.58 shows a positive linear association between WFS and RR up to about 11 m min^{-1} WFS, for both CMT and GMAW-P. However, the correlation appears to be nearly independent of the WFS/TS ratio.

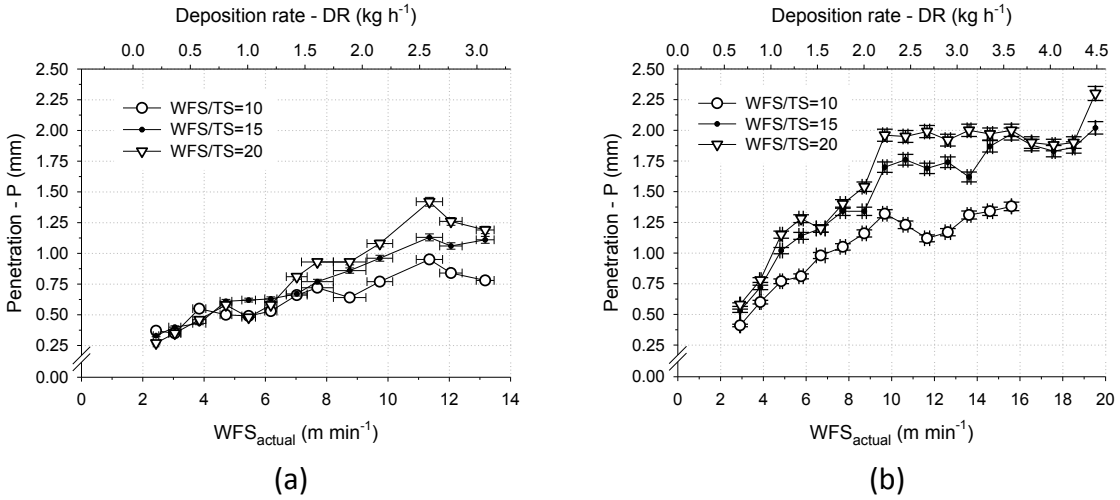

Figure 4.59. Effect of WFS_{actual} on P in (a) CMT and (b) GMAW-P.

Thereafter, the pattern of behaviour becomes less clear for GMAW-P data due to scattering (see Figure 4.58(b)). It should be noted that RR is substantially larger in GMAW-P, compared to CMT. Figure 4.59 shows the effect of WFS on P at constant WFS/TS. P increases gradually with increased WFS and WFS/TS ratio up to about 11 m min^{-1} in both welding processes, however, with a larger gradient for GMAW-P. Thereafter, P appears to drop for CMT. When similar welding conditions are used, larger P is obtained with GMAW-P.

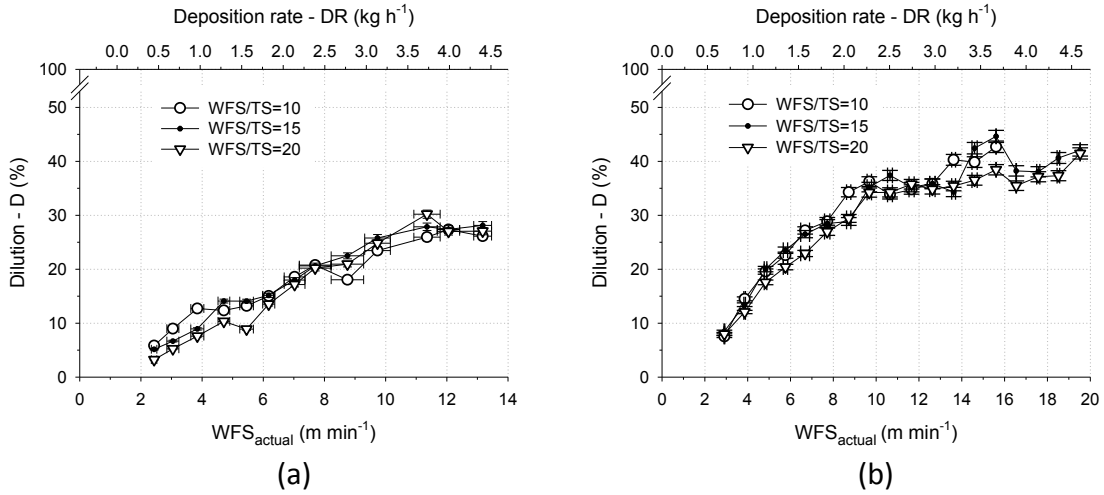

Figure 4.60. Effect of WFS_{actual} on D in (a) CMT and (b) GMAW-P.

As shown in Figure 4.60, D increases with increased WFS up to about 11 m min^{-1} WFS, however, with a larger gradient for GMAW-P. Thereafter, the gradient shows to decrease. D indicates a weak association with the WFS/TS ratio in both processes.

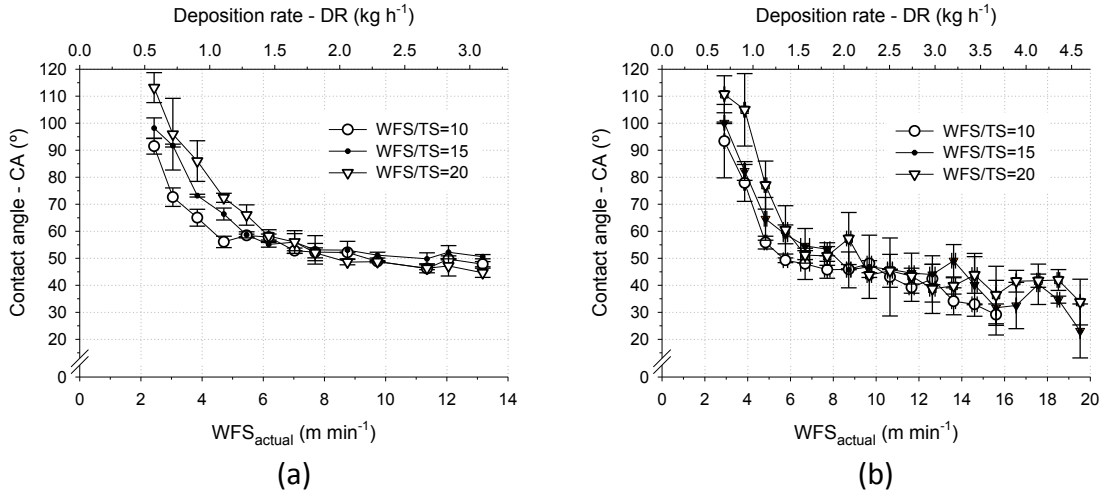

Figure 4.61. Effect of WFS_{actual} on CA in (a) CMT and (b) GMAW-P (for a 95% confidence interval).

The effect of WFS on CA for CMT and GMAW is shown in Figure 4.61. CA drops very rapidly from a maximum with the WFS up to about 8 m min^{-1}, stabilising gradually thereafter. It is apparent from Figure 4.61 that the curve is offset slightly downwards with smaller WFS/TS. Table 4.3 summarises the achievable range of selected outputs, *i.e.* W, H, DR, D and RR, using different wire diameters.

Table 4.3. Output range of CMT and GMAW-P processes for single layer deposits. The intervals represent minimum and maximum achievable dimensions for WFS/TS ratios of 10, 15 and 20.

	Fronius CMT			**GMAW-P**		
	0.8	*1.0*	*1.2*	*0.8*	*1.0*	*1.2*
W (mm)	2.4 – 6.4	3.4 – 8.8	4.9 – 7.9	3.2 – 7.4	3.2 – 8.9	4.2 – 13.2
H (mm)	1.6 – 3.0	2.0 – 3.6	2.2 – 3.5	1.4 – 2.7	1.8 – 3.9	2.0 – 4.9
DR (kg h^{-1})	0.6 – 3.1	0.7 – 3.0	0.9 – 2.9	0.7 – 4.6	0.6 – 5.4	0.8 – 7.7
D (%)	3.24 – 30.20	2.40 – 32.62	2.97 – 32.51	7.53 – 44.63	0.00 – 41.85	0.06 – 60.57
RR (%)	3.35 – 43.27	2.46 – 48.41	3.06 – 48.17	8.14 – 80.59	0.00 – 71.97	0.01 – 1.54

Further interactions of primary welding parameters on bead and plate fusion characteristics, such as DR, A_1 and A_2, can be found in Figures L 26 to L 28 (see Appendix L).

4.3 Multi-layer deposition in steel – preliminary studies

The set-up, welding equipment, and experimental method utilised to carry out the experiments described in this section are detailed in section 3.10 (see chapter 3).

4.3.1 Effect of layer number and interpass temperature on bead characteristics and surface quality

This section reports the influence of layer number on weld bead characteristics, *i.e.* bead width and height in vertical multi-layer overlapped walls. In addition, the effects of interpass temperature (T_{sub}) on the relative bead height increment (Delta-*z*), as well as on other multi-layer responses, such as W_{eff}, SW_{av} and MDE, are examined. The investigation was carried out according to the nominal welding conditions detailed in section 3.10.1. The experimental design is provided in Table E 1, where absolute measurements of bead height increments are also given (see Appendix E). The effect of layer number on Delta-*z* is shown in Figure 4.62(a) for various WFS/TS ratios at constant 6 m min^{-1} WFS_{set} (trials 2, 4 and 8 in Table E 1, Appendix E). The maximum

Delta-*z* is reached when the first layer is deposited. Thereafter, Delta-*z* decreases slowly with the layer number until a more steady state condition is eventually reached.

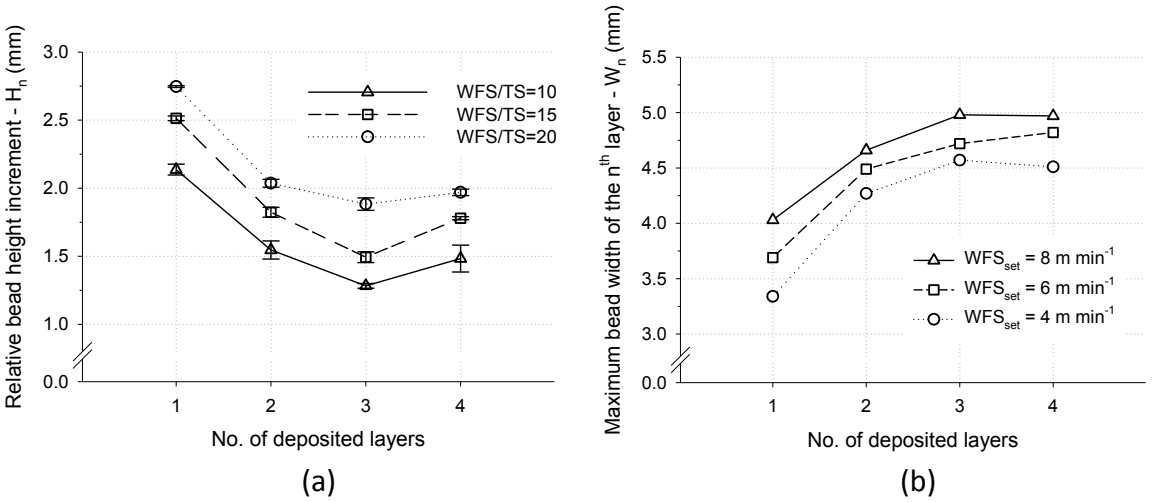

Figure 4.62. Relationship between the number of deposited layers and (a) relative bead height increment (H_n or Delta-*z*), and (b) the maximum bead width of the n^{th} layer (4 layers wall).

Figure 4.62(b) shows that the narrowest W is reached when the first layer is deposited for all WFS_{set} values at constant WFS/TS of 20 (trials 7, 8 and 9 in Table E 1, Appendix E). Thereafter, W increases with the layer number up to the third layer, stabilising afterwards.

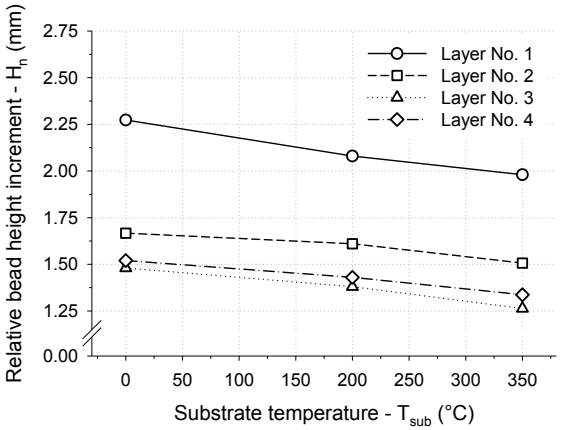

Figure 4.63. Dependence of relative bead height increment (H_n or Delta-z) on T_{sub} for different number of deposited layers (4 layers wall).

Figure 4.63 shows the influence of T_{sub} on H_n (Delta-*z*) for different number of deposited layers. It is seen that the first deposited layer is always the highest, for all T_{sub} considered in this study. It is also interesting to notice that H_n (Delta-*z*) is inversely correlated with the substrate temperature, irrespective on the layer number.

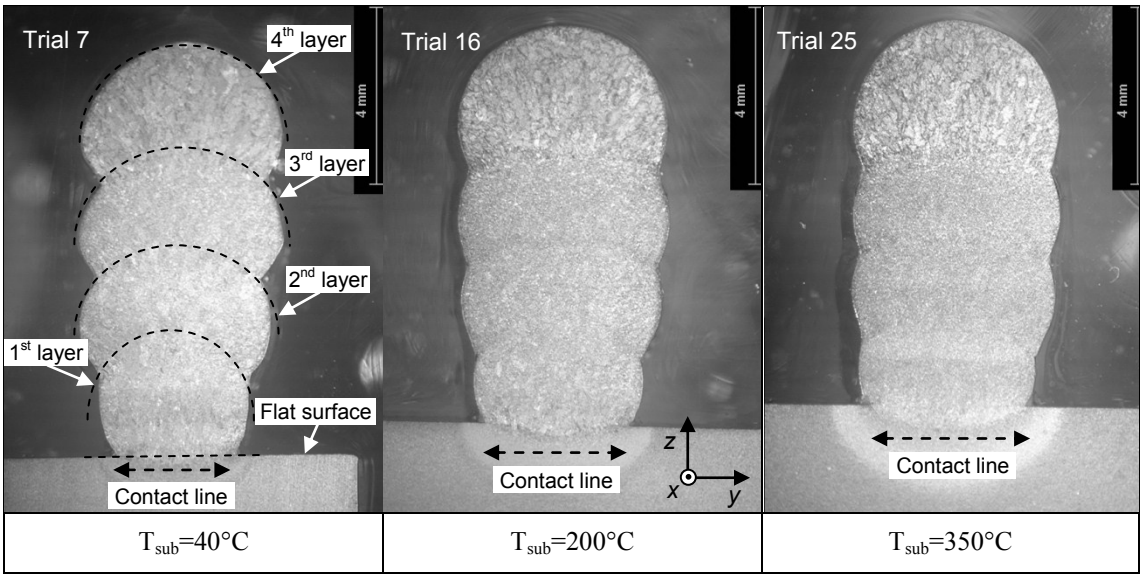

Figure 4.64. Influence of T_{sub} on H_n (Delta-*z*), W_{eff}, SW_{av}, and MDE in a wall of four layers high. Dashed lines represent the top surface profiles of each deposited bead in the cross section of trial 7.

A noticeable effect of T_{sub} on various multi-layer responses (see section 3.7.2 for definitions) is observed from transverse cross sections revealed in Figure 4.64, where constant welding conditions were applied, using 4 m min^{-1} WFS_{set} and 20 WFS/TS (see trials 7, 16 and 25 in Table E 1, Appendix E).

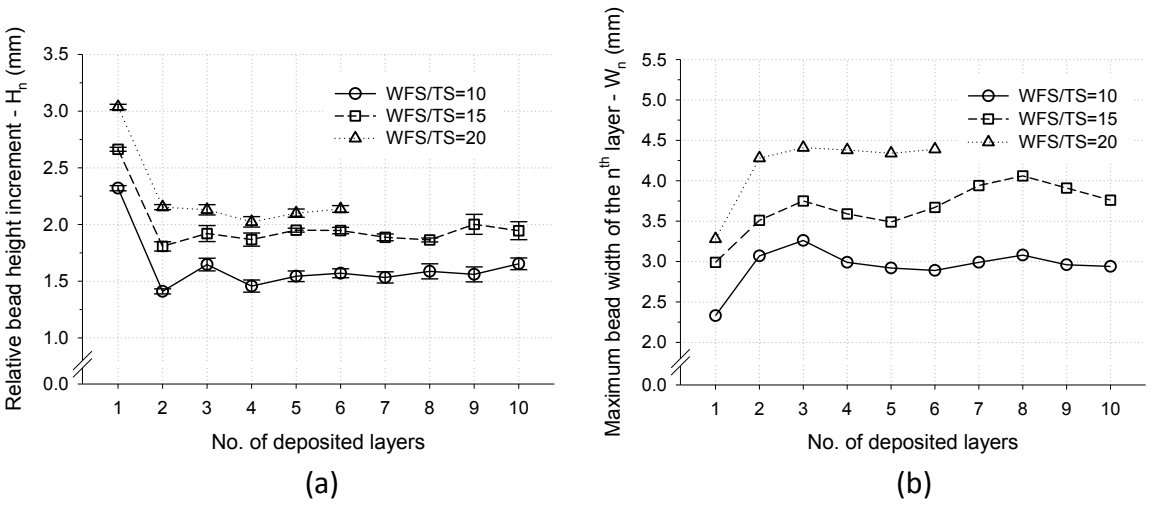

Figure 4.65. Influence of layer number on (a) relative bead height increment (Delta-z), and (b) bead width (10 layers wall).

The effect of the layer number on relative bead height increment H_n (Delta-z) and maximum bead width of the n^{th} layer (W_n) is illustrated in Figure 4.65, for a constant 3.2 m min^{-1} WFS and T_{sub}=40 °C. Yet again, the maximum deviation in H_n (Delta-*z*) and W is observed between the first and second deposited layer, becoming nearly

independent thereafter. This effect can be partially caused by the fact that the first layer is deposited onto a flat surface as well as by the faster rate of cooling achieved. H_n (Delta-*z*) and W also depend strongly on WFS/TS (see Figures 4.65(a) and (b)). The pattern of behaviour observed in Figure 4.65(a) for H_n (Delta-*z*) is accompanied by corresponding changes in W, as shown in Figure 4.65(b).

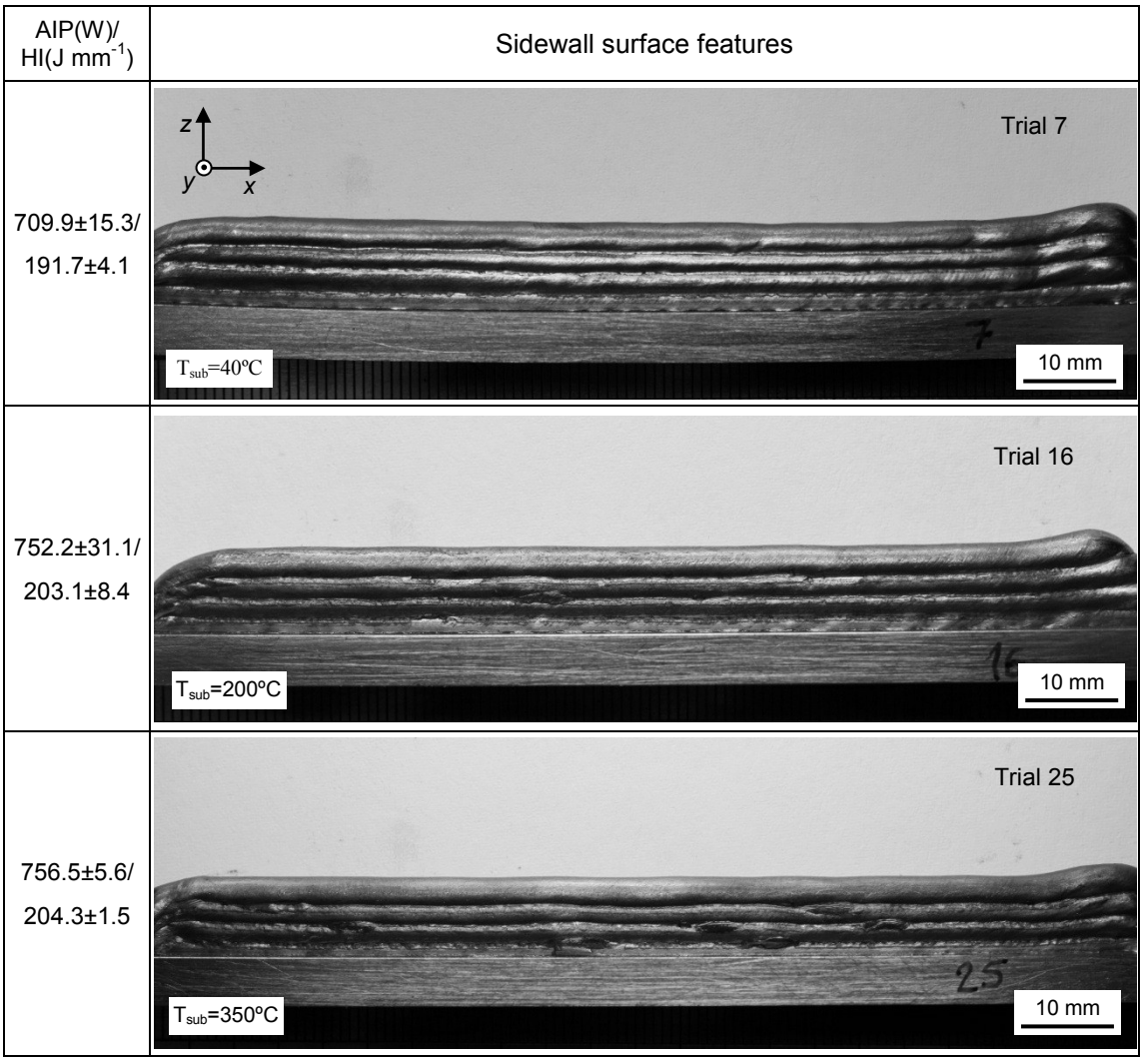

Figure 4.66. Effect of T_{sub} on sidewall surface facets of multi-layer deposits. AIP and HI values are in the 95% confidence interval.

One should note also, that multi-layer deposition at high-energy input, *i.e.* WFS/TS=20, became unstable upon further deposition as a result of changes in thermal processing conditions, such as volume heat sink. Figure 4.66 compares sidewall surface features, *i.e.* surface quality of the walls produced, in specimens with four layers produced at different interpass temperatures (T_{sub}), whilst welding conditions were held nearly constant (see trials 7, 16 and 25 in Table E 1, Appendix E). The results show that T_{sub}

has a noticeable effect on multi-layer characteristics such as surface waviness (SW_{av}) and effective wall width (W_{eff}), irrespective on the WFS/TS (refer to transverse cross sections of Figure 4.64).

Figure 4.67 shows the effect of AIP and TS on the sidewall surface features at constant WFS/TS of 20, T_{sub} of 40 ºC, and HI (see trials 7, 8 and 9 in Table E 1, Appendix E). The sidewall surface profiles show that SW_{av} and W_{eff} multi-layer responses depend significantly on both AIP and TS. The side walls show that the interfaces between adjacent layers become less prominent when larger AIP and TS are applied.

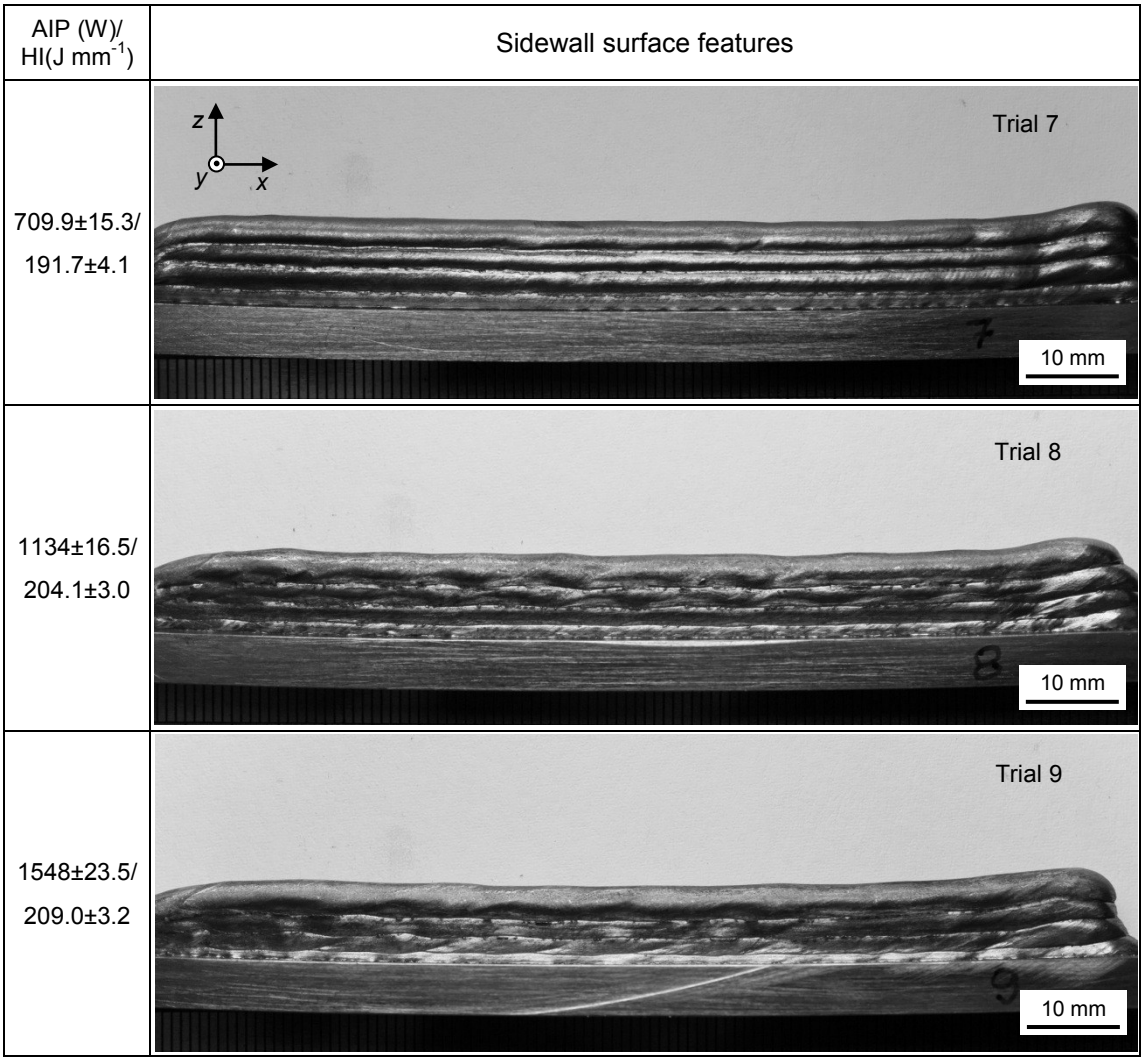

Figure 4.67. Effect of AIP on sidewall surface facets of multi-layer deposits.

The effect of AIP on the sidewall surface features at T_{sub} of 350 ºC, for the same welding conditions as above, is shown in Figure 4.68 (see trials 25, 26 and 27 in Table

E 1, Appendix E). Figure 4.68 shows that T_{sub} has a major impact on the quality of the sidewall facets. It is apparent from the corresponding transverse cross sections that all multi-layer characteristics, such as H_n (Delta-*z*), W_{eff}, SW_{av}, and MDE are significantly influenced by the welding conditions applied in this study (see Figure 4.69).

AIP(W)/ HI(J mm^{-1})	Sidewall surface features
756.5±5.6/ 204.3±1.5	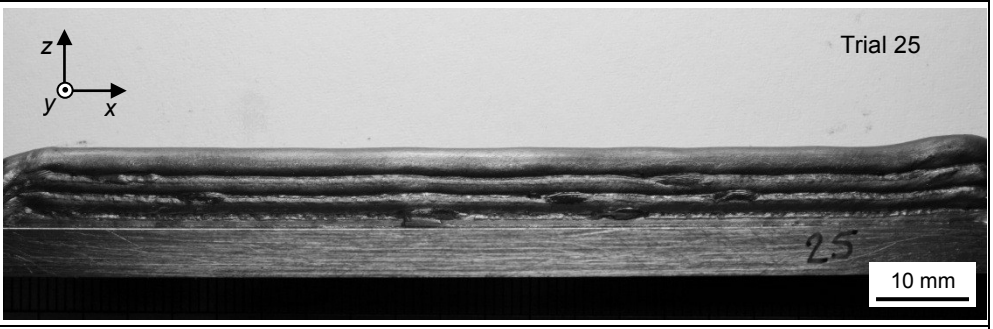
1134±16.5/ 204.1±3.0	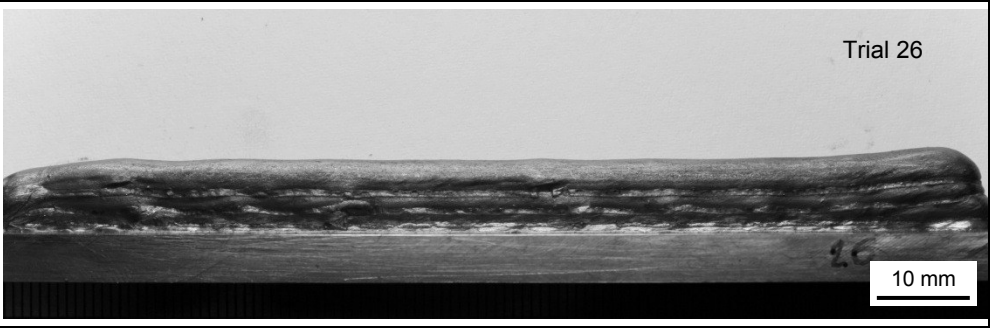
1548±23.5/ 209.0±3.2	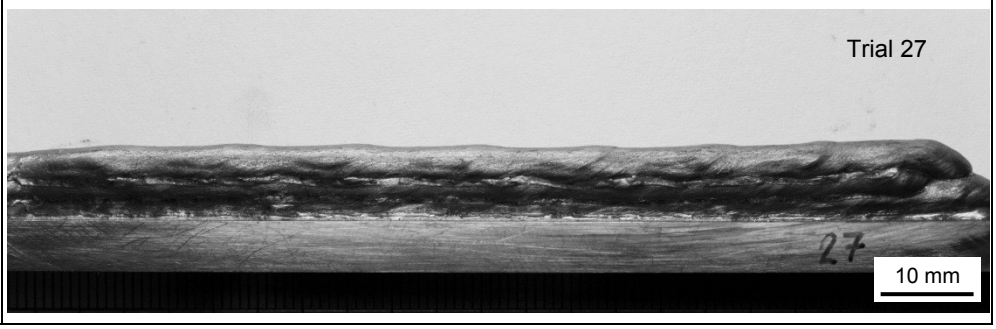

Figure 4.68. Effect of AIP on sidewall surface features of multi-layer deposits at constant T_{sub}=350 °C (see transverse cross section in Figure 4.69).

Figure 4.70 compares the thermal field developed during deposition of the fourth layer using a thermal-infrared imaging system, under the same welding conditions which were described above. This result indicates that conductive heat transfer conditions were significantly altered in multi-layer deposits with increased AIP.

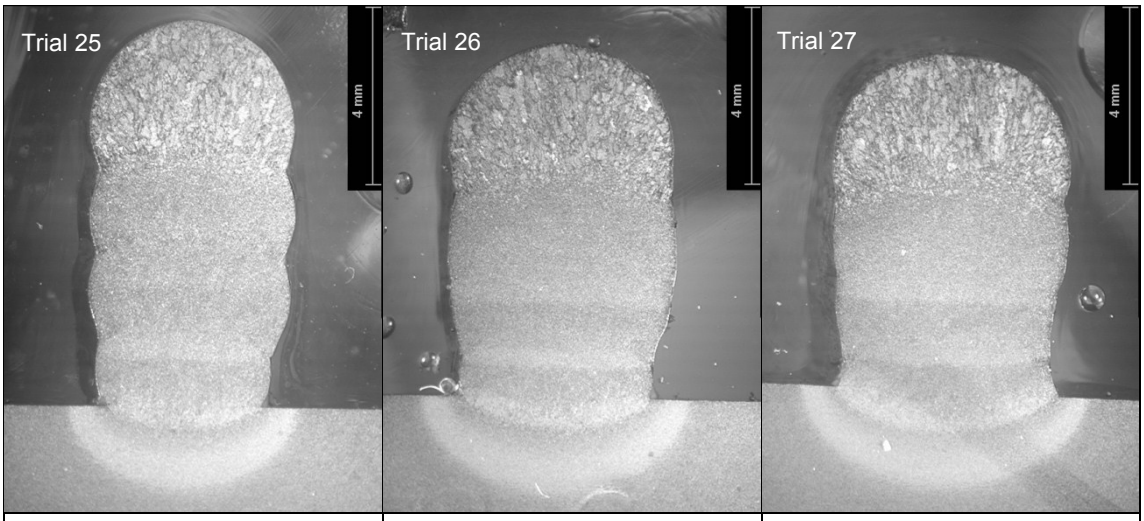

AIP=757±5.6 W	AIP=1134±16.5 W	AIP=1548±23.5 W

Figure 4.69. Effect of AIP on H_n (Delta-*z*), W_{eff}, SW_{av}, and MDE at constant T_{sub}=350 °C (4 layers wall).

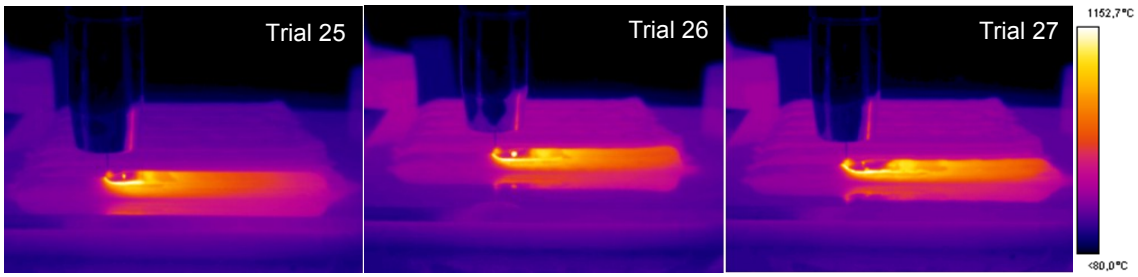

Figure 4.70. Comparison between thermal fields of the forth deposited layer recorded using thermal-infrared imaging.

4.3.2 Effect of travel speed on surface waviness and effective wall width

In this section, the effect of TS and WFS on multi-layer weld bead characteristics such as surface waviness (SW_{av}) and effective wall width (W_{eff}) is presented. Walls with 10 layers high were produced according to the welding conditions detailed in section 3.10.2 (chapter 3). The effect of TS on both SW_{av} and W_{eff} are shown in the cross-sectional macrographs of Figure 4.71 for constant WFS conditions. It is apparent that both the W_{eff} and SW_{av} increase as TS decreases.

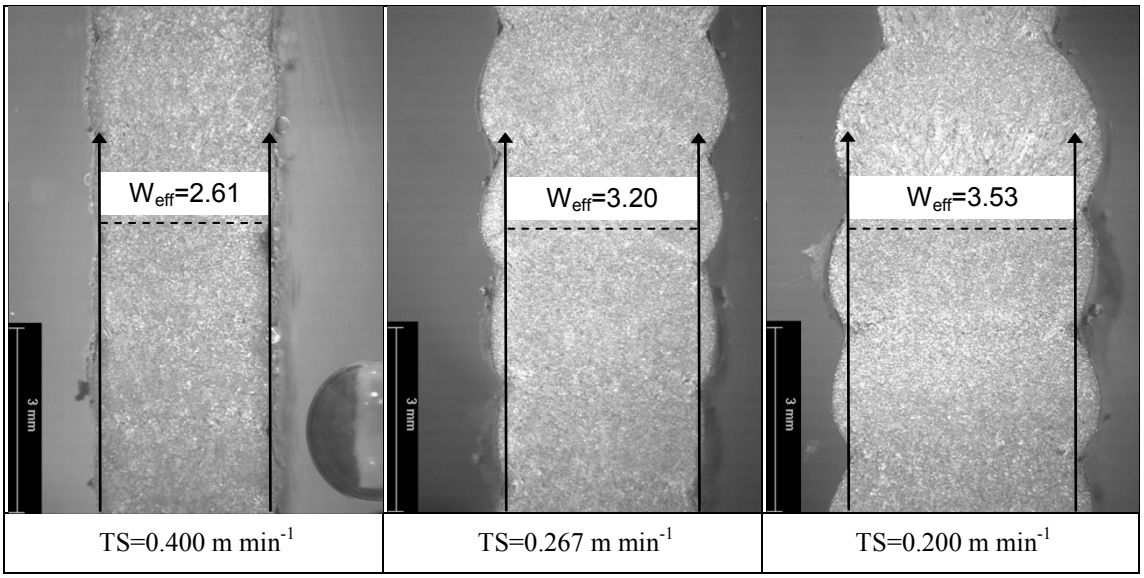

Figure 4.71. Effect of TS on W_{eff} and SW_{av} at 4 m min^{-1} WFS_{set}.

Figure 4.72(a) shows the influence of TS on both SW_{av} and W_{eff}, at constant WFS. SW_{av} drops fast from a maximum at 0.1 m min^{-1} TS to a minimum at 0.5 m min^{-1} for all WFS. Thereafter, TS has a smaller effect on SW_{av}. Also, it can be seen that the SW_{av} versus TS curve pattern is offset to lower SW_{av} values when lower WFS is used.

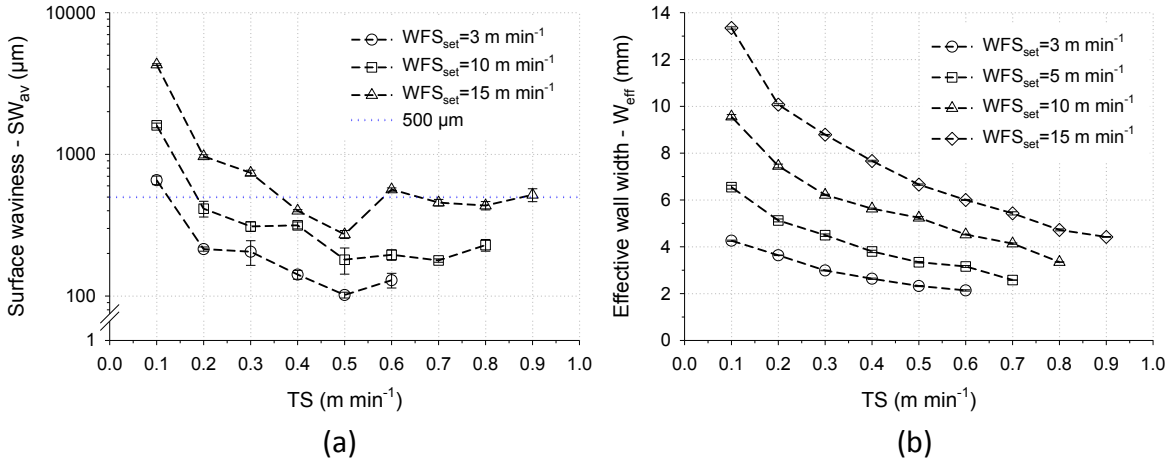

Figure 4.72. Influence of (a) surface waviness (SW_{av}), and (b) effective wall width (W_{eff}) on TS at constant WFS_{set}, for a 95% confidence interval.

Figure 4.72(b) shows that W_{eff} depends significantly on the TS, however, with a larger gradient at higher WFS. W_{eff} increases with increased WFS, for any constant TS. A positive linear association between W_{eff} and WFS can be discerned from Figure 4.72(b) for all range of TS studied. The gradient between W_{eff} and WFS is larger for smaller TS.

4.3.3 Effect of wire diameter and material on surface waviness and effective wall width

This section follows the work presented in section 4.3.2, focusing on the impact of TS on surface waviness (SW_{av}) using different WD (steel), and base materials, *i.e.* stainless steel and aluminium. The welding conditions used are detailed in section 3.10.3 (chapter 3). The relationship between TS and SW_{av} using different wire diameters and base materials is depicted in Figures 4.73(a) and (b), respectively.

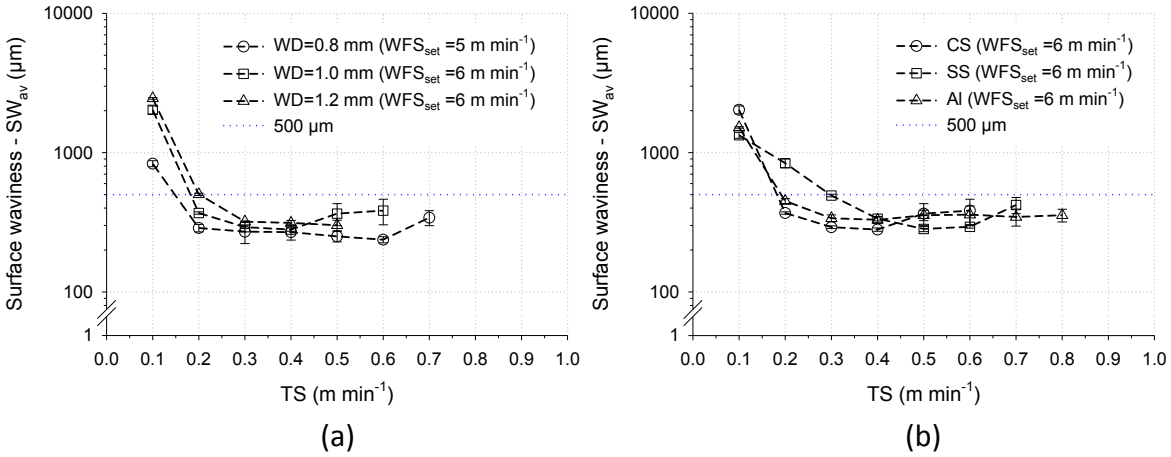

Figure 4.73. Dependence of surface waviness (SW_{av}) on (a) wire diameter (WD), and (b) base materials for a 95% confidence interval.

In general, an analogous association between TS and SW_{av} is observed, for all wire diameters used. However, smaller diameter wires appear to produce less wavy and therefore smoother sidewall surface facets (see Figure 4.73(a)). Overall, the correlation between SW_{av} and TS is very similar for both carbon steel (CS) and aluminium (Al) wires (see Figure 4.73(b)). In contrast, SW_{av} of stainless steel was found to depend more strongly on the TS up to 0.5 m min^{-1} TS, when compared to both CS and Al.

4.3.4 Deposition efficiency in carbon steel

This section reports the results of metal deposition efficiency (MDE) in carbon steel walls for different effective wall widths (W_{eff}). A wire electrode with 0.8 mm in diameter was applied invariably for the manufacture of 10 layers high walls. Welding conditions are described in section 3.10.4 and Table E 2 (Appendix E). Figure 4.74 shows MDE as a function of the W_{eff}, for a range between 3 and 15 m min^{-1} WFS. It can

be seen that W_{eff} ranging from 2 to 9.5 mm can be produced with MDE's over 90 %.

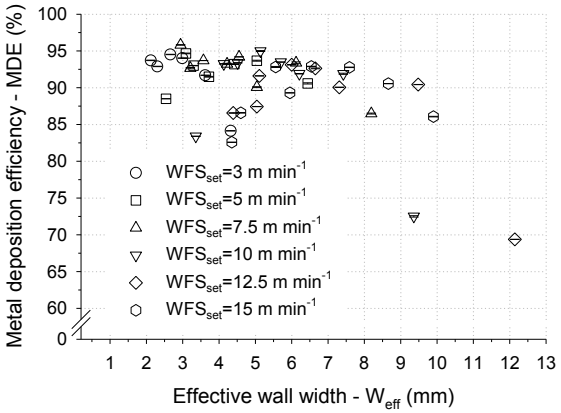

Figure 4.74. Relationship between W_{eff} and MDE in carbon steel walls.

4.4 Overhead deposition

The plan of experiments, set-up, and welding equipment utilised to perform these experiments were according to section 3.11. The results of a feasibility study of multi-layer deposition carried out in overhead welding position are reported in this section. The trials were conducted according to the welding conditions detailed in Table 4.4. The quality of the deposits produced was assessed visually. The experiments were performed at constant WFS and TS of 5 and 0.2 m min^{-1}, respectively (trial 5D).

Table 4.4. Welding conditions utilised in the overhead deposition trials (trial 5D).

Trial No.	WFS_{set} (m min^{-1})	WFS_{actual} (m min^{-1})	WFS/TS	TS (m min^{-1})	I_{inst} (A)	V_{inst} (V)	P_{inst} (W)	HI (J mm^{-1})
5D	5.00	4.26	25	0.2	75.61	11.78	1203.07	324.8

The effect of the welding position on the weld bead profile (top views) in single layer deposition is shown in Figure 4.75. Stable and consistent deposition conditions were achieved, irrespective of the welding position utilised. Note, however, that narrower weld beads were obtained in the overhead, in comparison with the downhand position.

Welding position[1]	Top surface quality
PD/4F	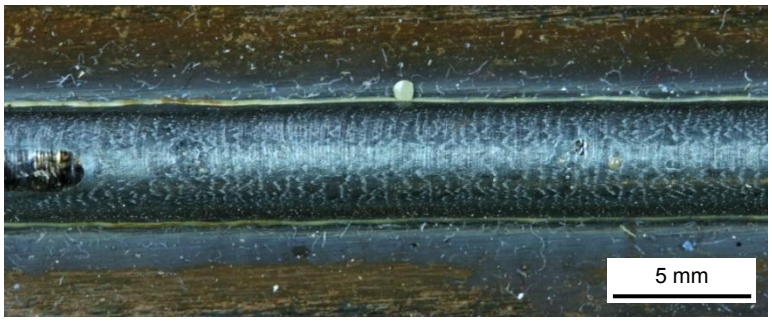
PA/1G	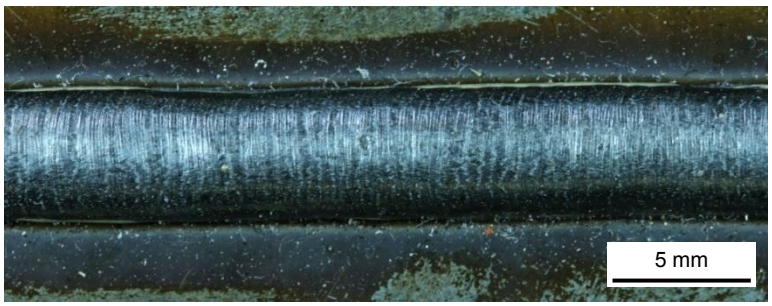

[1] According to ANSI/AWS ASME IX and EN ISO 6947, respectively.

Figure 4.75. Single bead-on-plate deposits carried out in overhead (PD/4F), and downhand (PA/1G) welding positions (trial 5D).

Figure 4.76 depicts the effect of welding position on the weld bead profile (top views) in multi-layer deposition (3 layers high). It should be noted that similar welding conditions, as in Figure 4.75, were applied. It can be seen that very uniform and reproducible multi-layer profiles were obtained in downhand welding position (see PA/1G in Figure 4.76). In contrast, slow weld dripping (or sagging) becomes visible as the third layer was deposited in overhead welding position (see PD/4F in Figure 4.76).

Welding position[1]	Top surface quality
PD/4F	
	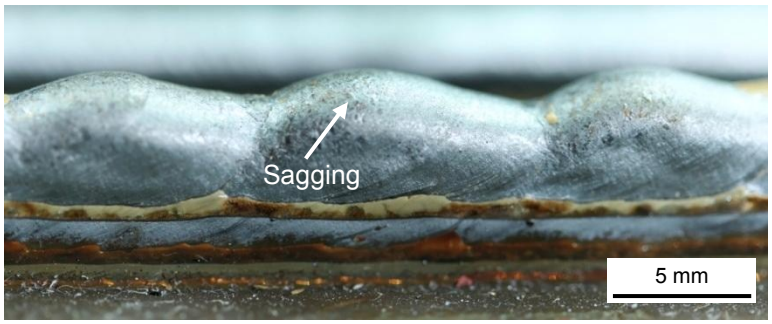
PA/1G	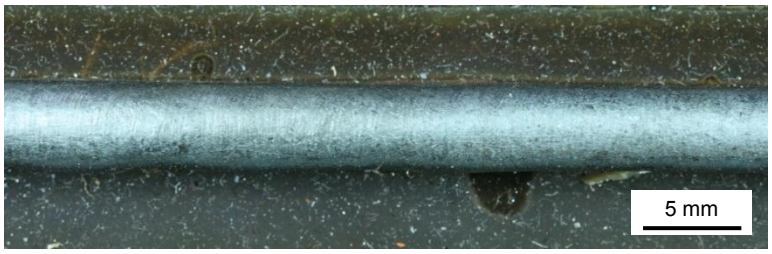
	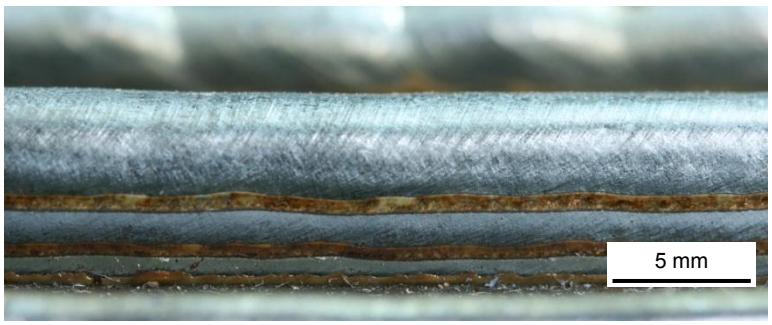

Figure 4.76. Multi-layer deposits carried out in overhead (PD/4F) and downhand (PA/1G) welding positions (trial 5D).

4.5 Process modelling

This section reports the results of the process control model development, performed for the deposition of single and multi-layer mild steel walls utilising CMT. The designed experimental procedure was fully based on an empirical approach, detailed in section 3.12 (see chapter 3). The selection of controllable and dependent variables was made according to section 3.12.2. The integration with the Design Expert®7.15 (DX) software package was then carried out according to section 3.12.3. Modelling results

presented in this section were accomplished in accordance with the experimental design detailed in section 3.12.1. The welding conditions and measured weld bead responses are listed in Tables C 1 and C 2 (Appendix C), as well as in E 2 (Appendix E), for single and multi-layer cases, respectively.

4.5.1 Analysis of variance

The test for significance of the regression models was executed using ANOVA technique as described in section 3.12.5. The ANOVA outputs are shown for single layer in Tables H 1 to H 11, and for multi-layer in Tables H 12 to H 15. In these tables the analysis of variance results and Fisher's hypothesis testing are summarised for all the responses studied. Additionally, the importance in percentage contribution of each individual ANOVA interaction term for the total sum of the squared deviations, alongside the Fisher´s *F*-test analysis are also contained in these tables.

It is seen that the model Prob>F statistic is less than 0.05 in all single and multi-layer responses investigated. The statistically insignificant interaction model terms with probability values greater than 0.1 (p>0.1) were eliminated manually throughout single layer analysis, while less important interaction terms were kept in the multi-layer analysis in order to maintain *hierarchically well-formulated models*.

Other model adequacy measures, such as R^2, adjusted R^2 (R^2_{Adj}), and predicted R^2 (R^2_{Pred}) are additionally provided in the same tables. In general, results indicate that adjusted coefficients of determination over 0.9 were typical for the computed predictions throughout all single layer responses. At the same time relatively lower R^2 statistics were obtained for multi-layer responses, such as SW_{av} and *MDE*. The "strength" of the models (or adequate precision values) also shows to be far greater than 4 in all cases (see section 3.12.5). The calculated Fisher´s *F*-test ratios in all interaction terms for single predictions are also larger than tabulated critical values for a 95% confidence interval (α=0.05).

4.5.2 Development of the final empirical models

The most significant terms were obtained through ANOVA (see section 4.5.1) after applying Student's t-test and Fisher's *F*-test for testing the partial coefficients, and the

lack-of-fit test for verifying the adequacy of the fitting. Non-significant interaction terms were dropped from the model manually. Note that model equations are more often represented in their *coded form* for experimental process optimisation and understanding, since coded coefficients are proportional to the observed effect. By keeping the regression coefficients in the *coded form*, rather than in the *actual form*, any response changes are always relative to the intercept, *i.e.* centre of the design, while units of measure are also normalized. Although both equations give the same predictions, only the *coded* coefficients should be used for explaining the observed effects of interactions. The final mathematical predictive models for single and multi-layer deposition, as determined by DX software in terms of *coded factors*, were as follows:

Bead width:

$$W \text{ (mm)} = (4.32 + 0.80\times WD + 0.67\times WFS/TS + 0.69\times WFS_{actual} + 0.16\times WD\times WFS/TS + 0.28\times WFS/TS\times WFS_{actual} - 0.70\times WFS_{actual}^{2})^{(1/0.75)} \quad (4.1)$$

Bead height:

$$H \text{ (mm)} = (0.24 - 0.086\times WD - 0.10\times WFS/TS - 7.773E^{-4}\times WFS_{actual} + 0.030\times WD\times WFS/TS - 0.058\times WD\times WFS_{actual} + 0.040\times WFS/TS^{2} - 0.071\times WFS_{actual}^{2})^{(-1/1.62)} \quad (4.2)$$

Remelting ratio:

$$RR \text{ (\%)} = (0.50 + 0.15\times WD - 7.640E^{-3}\times WFS/TS + 0.33\times WFS_{actual} - 0.018\times WD\times WFS/TS + 0.098\times WD\times WFS_{actual} + 0.063\times WFS/TS\times WFS_{actual} - 0.017\times WD^{2} - 0.059\times WFS_{actual}^{2})^{(1/0.78)} \quad (4.3)$$

Penetration:

$$P \text{ (mm)} = (1.49 + 0.65\times WD + 0.32\times WFS/TS + 0.72\times WFS_{actual} + 0.15\times WD\times WFS/TS + 0.30\times WD\times WFS_{actual} + 0.26\times WFS/TS\times WFS_{actual} - 0.17\times WFS_{actual}^{2})^{(1/0.81)} \quad (4.4)$$

Dilution:

$$D \text{ (\%)} = (36.73 + 11.32\times WD - 0.74\times WFS/TS + 25.30\times WFS_{actual} - 1.41\times WD\times WFS/TS + 6.96\times WD\times WFS_{actual} + 5.11\times WFS/TS\times WFS_{actual} - 1.80\times WD^{2} - 4.64\times WFS_{actual}^{2})^{(1/1.07)} \quad (4.5)$$

Deposition rate:

$$DR\ (\text{kg h}^{-1}) = (2.89 + 1.16\times WD - 5.090E^{-3}\times WFS/TS + 2.36\times WFS_{actual} - 6.695E^{-3}\times WD\times WFS/TS + 0.91\times WD\times WFS_{actual} - 0.013\times WFS/TS\times WFS_{actual} + 0.073\times WD^2 + 0.034\times WFS_{actual}^2)^{(1/1.04)} \quad (4.6)$$

Contact angle:

$$CA\ (^{o}) = (0.014 + 3.735E^{-5}\times WD + 7.688E^{-4}\times WFS/TS + 3.411E^{-3}\times WFS_{actual} - 8.544E^{-4}\times WD\times WFS_{actual} + 2.731E^{-3}\times WFS/TS\times WFS_{actual} - 4.102E^{-4}\times WD^2 + 1.240E^{-3}\times WFS/TS^2 - 4.516E^{-3}\times WFS_{actual}^2)^{(-1/1.09)} \quad (4.7)$$

Penetration area:

$$A_1\ (\text{mm}^2) = (2.16 + 0.86\times WD + 0.45\times WFS/TS + 1.00\times WFS_{actual} + 0.15\times WD\times WFS/TS + 0.37\times WD\times WFS_{actual} + 0.30\times WFS/TS\times WFS_{actual} - 0.27\times WFS_{actual}^2)^{(1/0.51)} \quad (4.8)$$

Reinforcement area:

$$A_2\ (\text{mm}^2) = (0.18 - 0.058\times WD - 0.069\times WFS/TS + 1.499E^{-4}\times WFS_{actual} + 0.021\times WD\times WFS/TS + 0.016\times WD^2 + 0.033\times WFS/TS^2 + 6.943E^{-3}\times WFS_{actual}^2)^{(-1/0.7)} \quad (4.9)$$

Aspect ratio:

$$AR\ (\text{mm}^2) = (5.32 + 0.31\times WD - 0.33\times WFS/TS + 1.55\times WFS_{actual} - 0.71\times WD\times WFS_{actual} + 0.41\times WFS/TS\times WFS_{actual} - 0.34\times WD^2 - 2.14\times WFS_{actual}^2)^{(-1/1.56)} \quad (4.10)$$

Heat input:

$$HI\ (\text{J mm}^{-1}) = (0.015 - 4.179E^{-3}\times WD - 6.303E^{-3}\times WFS/TS + 1.627E^{-3}\times WFS_{actual} + 2.479E^{-3}\times WD\times WFS/TS + 1.588E^{-3}\times WD\times WFS_{actual} + 1.726E^{-3}\times WD^2 + 3.126E^{-3}\times WFS/TS^2 + 1.507E^{-3}\times WFS_{actual}^2)^{(-1/0.73)} \quad (4.11)$$

Heat source length:

$$HSL\ (\text{mm}) = (5.11 + 1.11\times WD + 0.28\times WFS/TS + 1.76\times WFS_{actual} + 0.43\times WD\times WFS_{actual} + 0.31\times WFS/TS\times WFS_{actual} - 0.64\times WFS_{actual}^2)^{(1/0.56)} \quad (4.12)$$

Surface waviness:

$$SW_{av}\ (\mu\text{m}) = (0.38 - 1.269E^{-3}\times WFS_{actual} + 0.011\times TS + 0.014\times WFS_{actual}\times TS - 4.672E^{-3}\times WFS_{actual}^2 - 0.054\times TS^2 - 0.036\times WFS_{actual}^3 + 0.032\times TS^3)^{(1/-0.18)} \quad (4.13)$$

Effective wall width:

$$W_{eff}\ (\text{mm}) = (0.93 - 0.023\times WFS_{actual} + 0.023\times TS + 7.755E^{-3}\times WFS_{actual}^2 - 6.065E^{-3}\times TS^2)^{(1/0.05)} \quad (4.14)$$

Metal deposition efficiency:

$$MDE\ (\%) = (93.61 + 0.15\times WFS_{actual} - 5.67\times TS - 1.76\times WFS_{actual}\times TS - 0.41\times WFS_{actual}^{2} - 5.80\times TS^{2} + 4.94\times WFS_{actual}^{2}\times TS - 10.18\times WFS_{actual}\times TS^{2} + 8.70\times TS^{3}) \quad (4.15)$$

The final predictive models in terms of *actual factors* are included in Appendix G.

4.5.3 Interaction of process parameters and bead characteristics

The effects of interactions between welding process parameters and weld bead characteristics were evaluated using both 3D and contour graphs (see Figure 4.77). Both response surfaces and contour plots were computed by utilising the final empirical models presented in section 4.5.2. Note, however, that although these models were developed for predicting weld characteristics in various wire diameters, the majority of the predictive responses are presented for a single wire diameter of 0.8 mm.

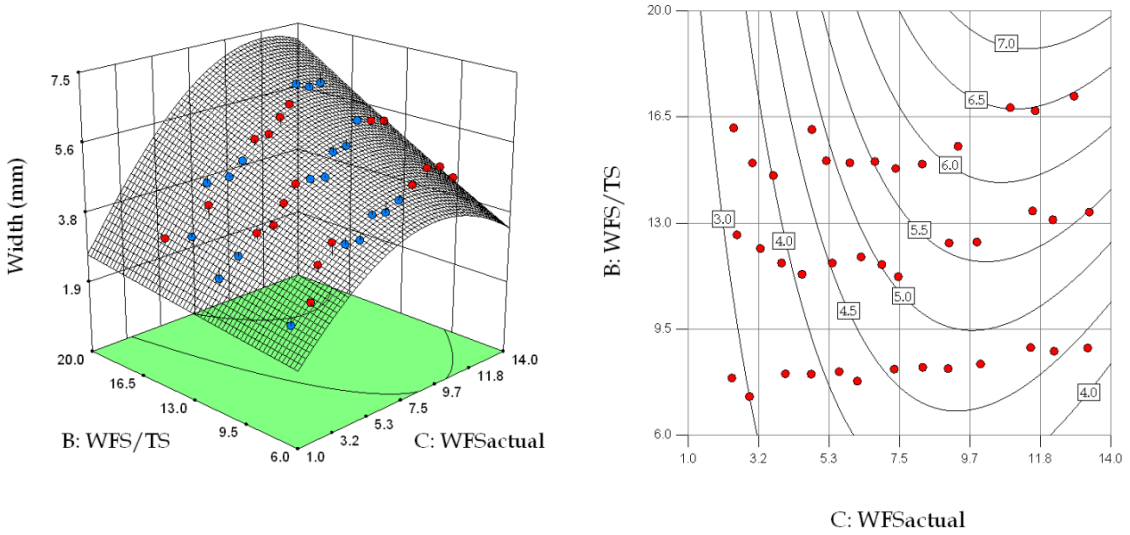

(a)

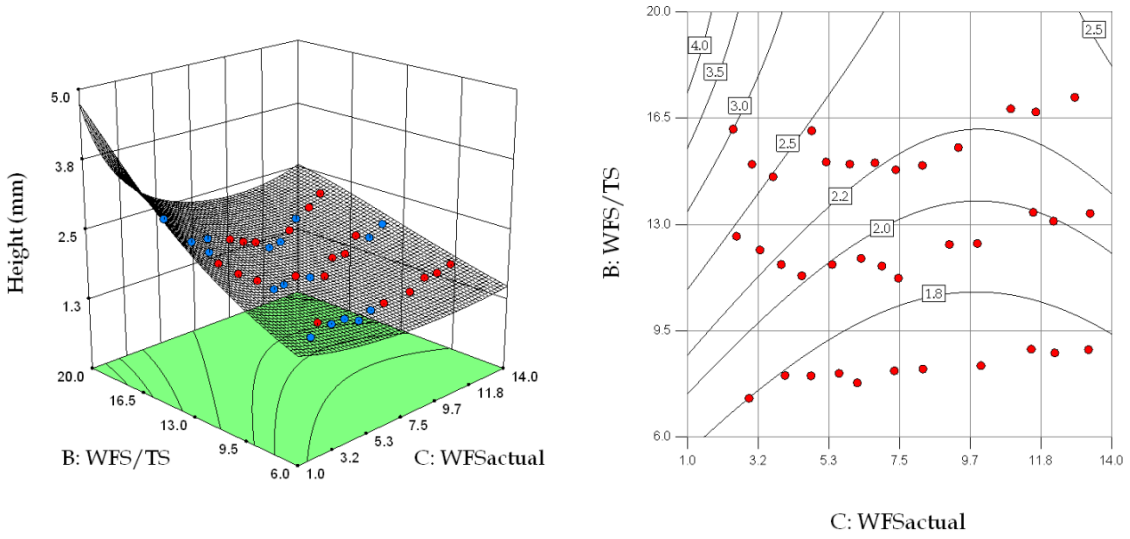
Height (mm)
5.0
3.8
2.5
1.3
20.0
16.5
13.0
9.5
6.0
B: WFS/TS
1.0
3.2
5.3
7.5
9.7
11.8
14.0
C: WFSactual
B: WFS/TS
20.0
16.5
13.0
9.5
6.0
4.0
3.5
3.0
2.5
2.2
2.0
1.8
2.5
1.0
3.2
5.3
7.5
9.7
11.8
14.0
C: WFSactual

(b)

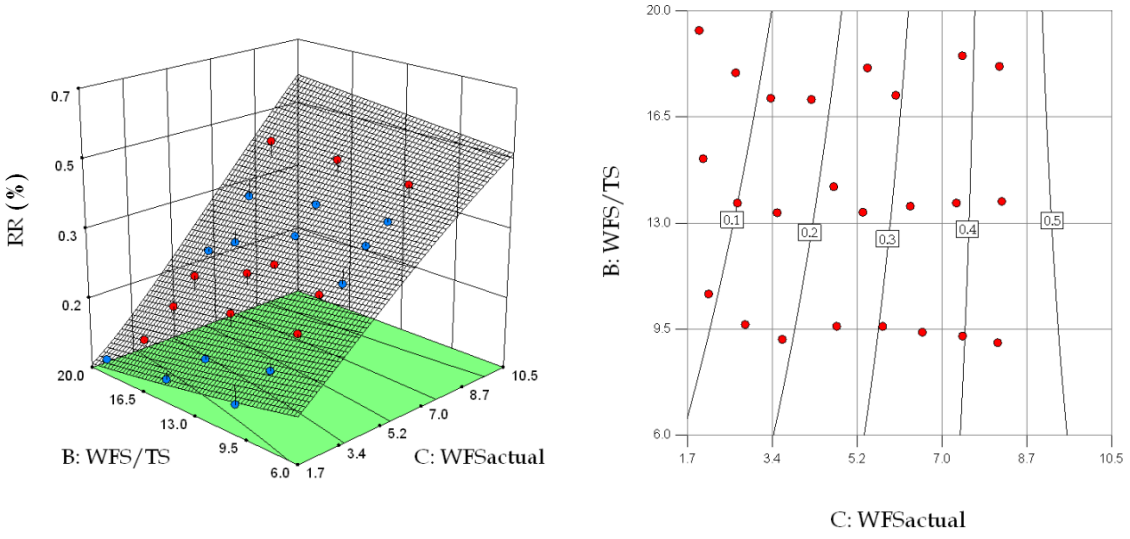
RR (%)
0.7
0.5
0.3
0.2
20.0
16.5
13.0
9.5
6.0
B: WFS/TS
1.7
3.4
5.2
7.0
8.7
10.5
C: WFSactual
B: WFS/TS
20.0
16.5
13.0
9.5
6.0
0.1
0.2
0.3
0.4
0.5
1.7
3.4
5.2
7.0
8.7
10.5
C: WFSactual

(c)

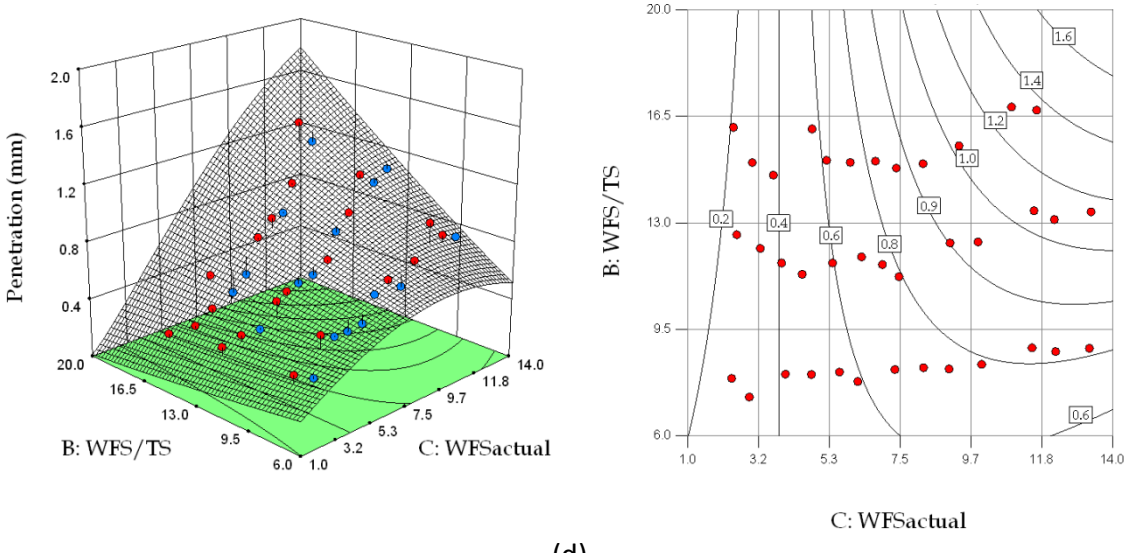
Penetration (mm)
2.0
1.6
1.2
0.8
0.4
20.0
16.5
13.0
9.5
6.0
B: WFS/TS
1.0
3.2
5.3
7.5
9.7
11.8
14.0
C: WFSactual
B: WFS/TS
20.0
16.5
13.0
9.5
6.0
0.2
0.4
0.6
0.8
0.9
1.0
1.2
1.4
1.6
0.6
1.0
3.2
5.3
7.5
9.7
11.8
14.0
C: WFSactual

(d)

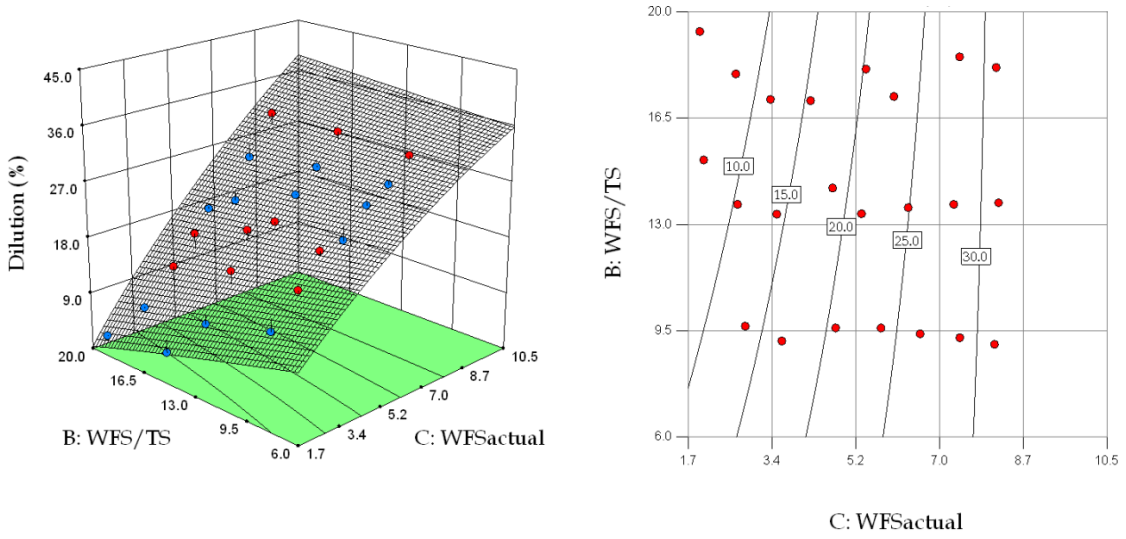
Dilution (%)
45.0
36.0
27.0
18.0
9.0
20.0
16.5
13.0
9.5
6.0
B: WFS/TS
1.7
3.4
5.2
7.0
8.7
10.5
C: WFSactual
B: WFS/TS
20.0
16.5
13.0
9.5
6.0
10.0
15.0
20.0
25.0
30.0
1.7
3.4
5.2
7.0
8.7
10.5
C: WFSactual

(e)

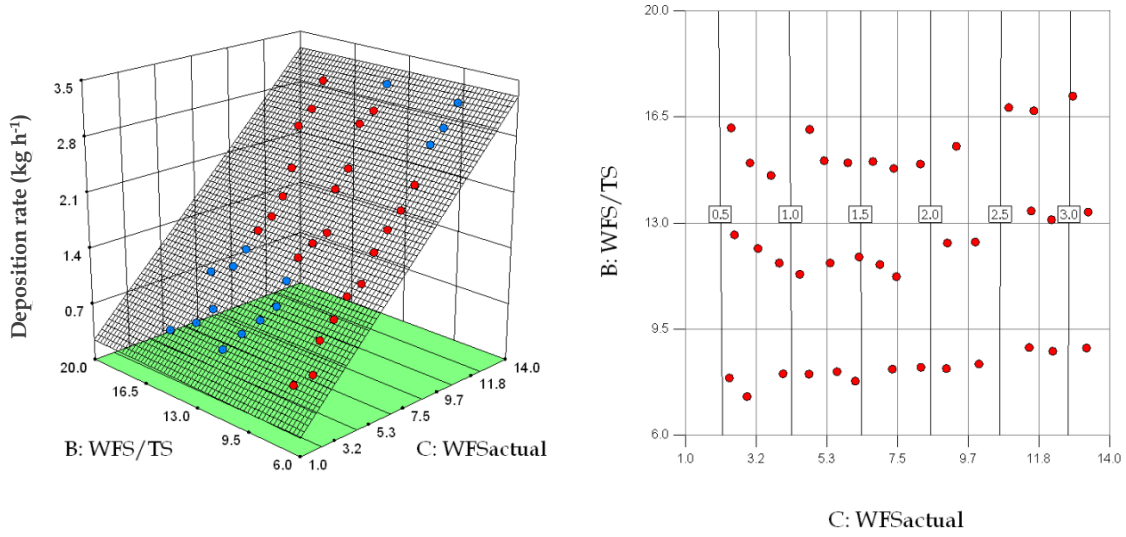
Deposition rate (kg h-1)
3.5
2.8
2.1
1.4
0.7
20.0
16.5
13.0
9.5
6.0
B: WFS/TS
1.0
3.2
5.3
7.5
9.7
11.8
14.0
C: WFSactual
B: WFS/TS
20.0
16.5
13.0
9.5
6.0
0.5
1.0
1.5
2.0
2.5
3.0
1.0
3.2
5.3
7.5
9.7
11.8
14.0
C: WFSactual

(f)

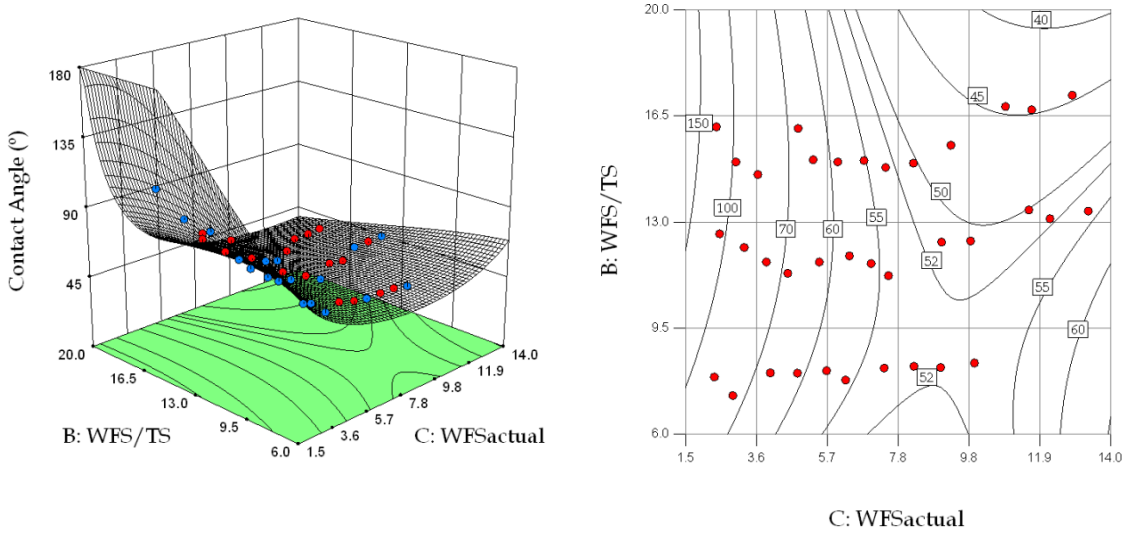
Contact Angle (°)
180
135
90
45
20.0
16.5
13.0
9.5
6.0
B: WFS/TS
1.5
3.6
5.7
7.8
9.8
11.9
14.0
C: WFSactual
B: WFS/TS
20.0
16.5
13.0
9.5
6.0
150
100
70
60
55
52
50
45
40
52
55
60
1.5
3.6
5.7
7.8
9.8
11.9
14.0
C: WFSactual

(g)

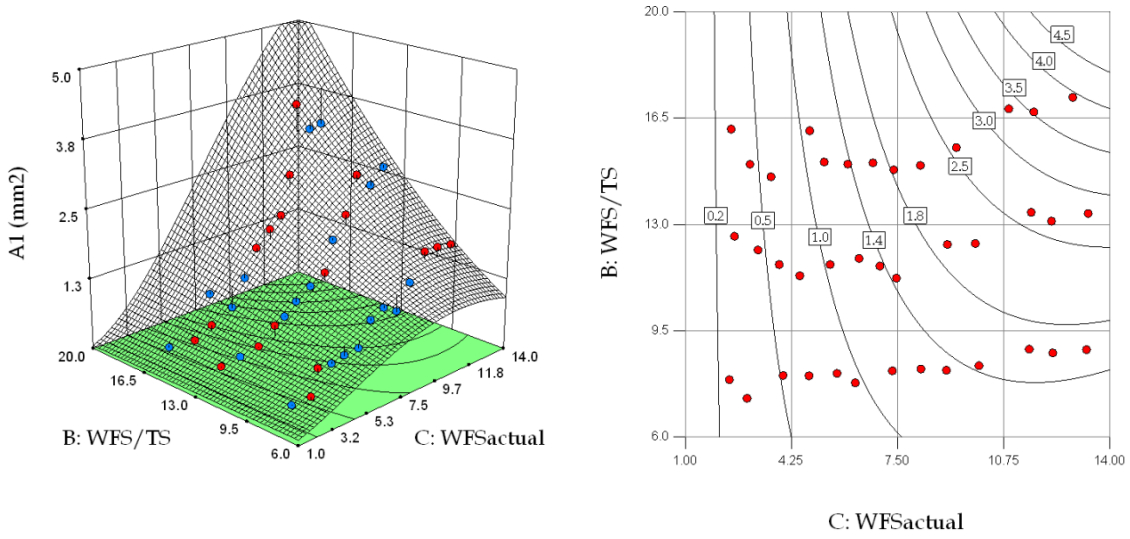
A1 (mm2)
5.0
3.8
2.5
1.3
20.0
16.5
13.0
9.5
6.0
B: WFS/TS
1.0
3.2
5.3
7.5
9.7
11.8
14.0
C: WFSactual
B: WFS/TS
20.0
16.5
13.0
9.5
6.0
1.00
4.25
7.50
10.75
14.00
C: WFSactual
0.2
0.5
1.0
1.4
1.8
2.5
3.0
3.5
4.0
4.5

(h)

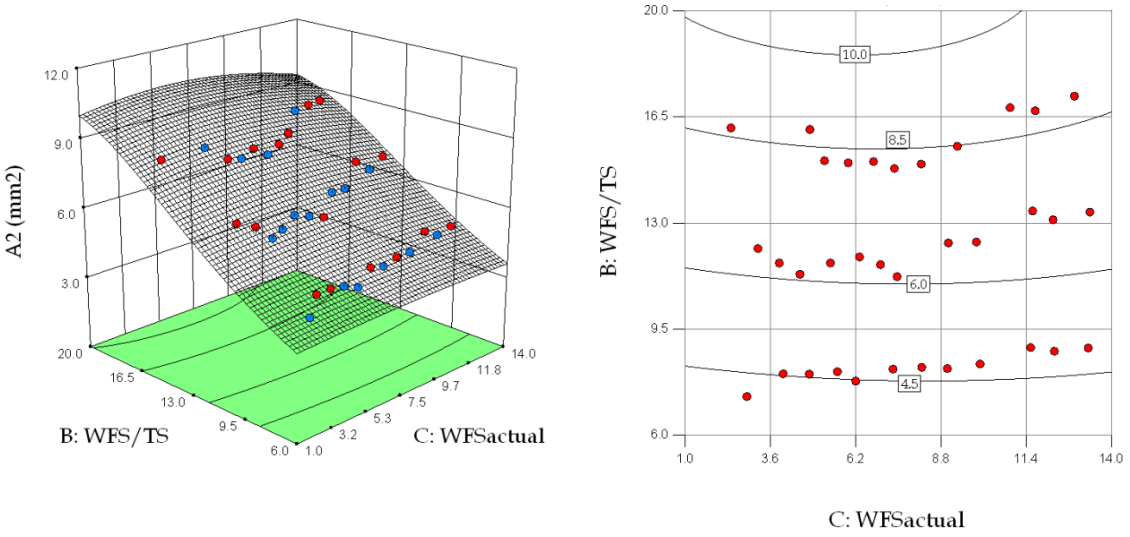
A2 (mm2)
12.0
9.0
6.0
3.0
20.0
16.5
13.0
9.5
6.0
B: WFS/TS
1.0
3.2
5.3
7.5
9.7
11.8
14.0
C: WFSactual
B: WFS/TS
20.0
16.5
13.0
9.5
6.0
1.0
3.6
6.2
8.8
11.4
14.0
C: WFSactual
10.0
8.5
6.0
4.5

(i)

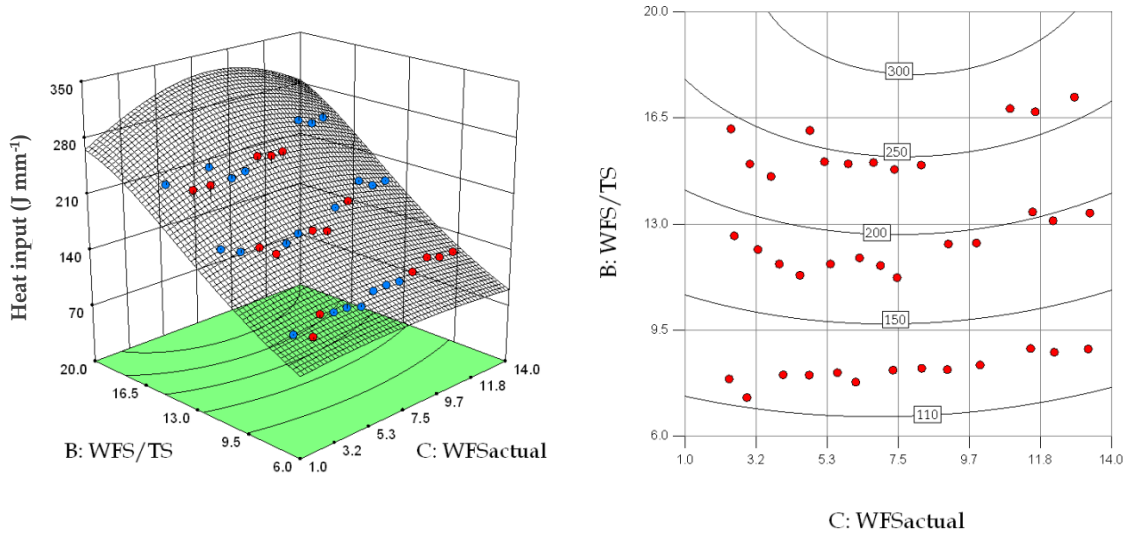
Heat input (J mm-1)
350
280
210
140
70
20.0
16.5
13.0
9.5
6.0
B: WFS/TS
1.0
3.2
5.3
7.5
9.7
11.8
14.0
C: WFSactual
B: WFS/TS
20.0
16.5
13.0
9.5
6.0
1.0
3.2
5.3
7.5
9.7
11.8
14.0
C: WFSactual
300
250
200
150
110

(j)

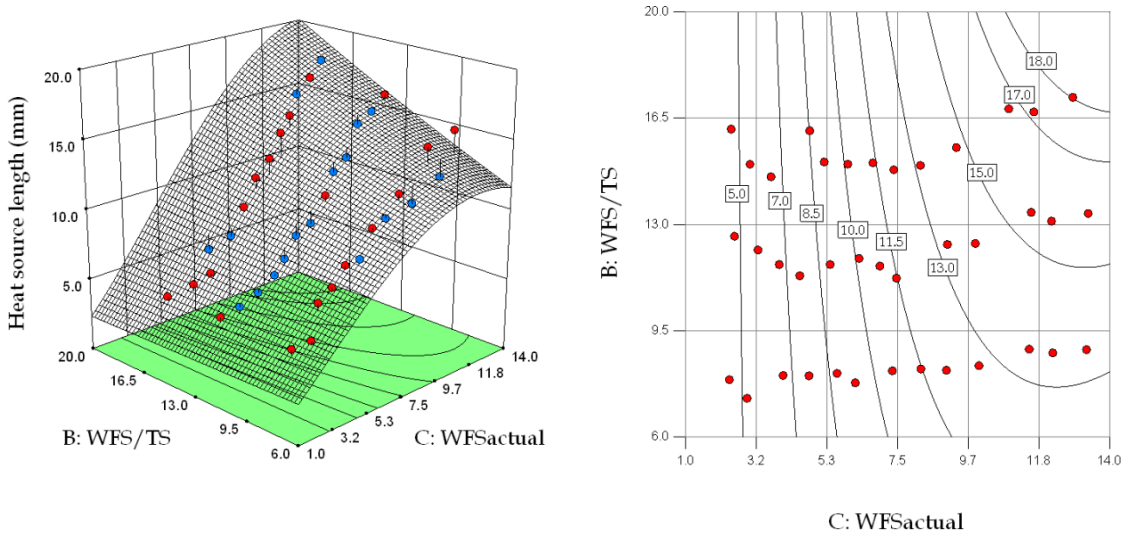
Heat source length (mm)
20.0
15.0
10.0
5.0
20.0
16.5
13.0
9.5
6.0
B: WFS/TS
1.0
3.2
5.3
7.5
9.7
11.8
14.0
C: WFSactual
B: WFS/TS
C: WFSactual
18.0
17.0
15.0
13.0
11.5
10.0
8.5
7.0
5.0

(k)

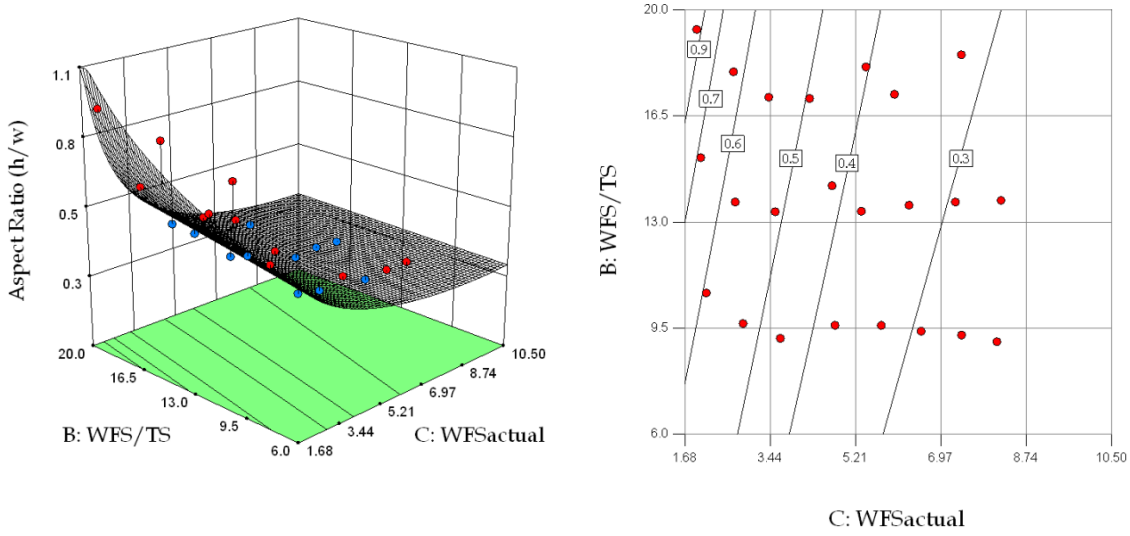
Aspect Ratio (h/w)
1.1
0.8
0.5
0.3
20.0
16.5
13.0
9.5
6.0
B: WFS/TS
1.68
3.44
5.21
6.97
8.74
10.50
C: WFSactual
B: WFS/TS
C: WFSactual
0.9
0.7
0.6
0.5
0.4
0.3

(l)

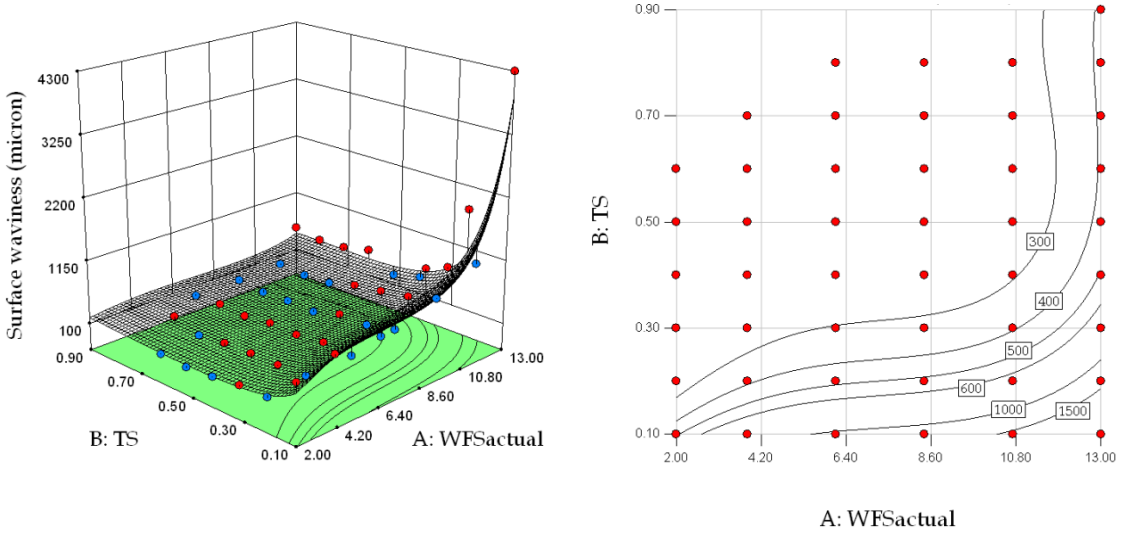
Surface waviness (micron)
4300
3250
2200
1150
100
0.90
0.70
0.50
0.30
0.10
B: TS
2.00
4.20
6.40
8.60
10.80
13.00
A: WFSactual
B: TS
A: WFSactual
300
400
500
600
1000
1500

(m)

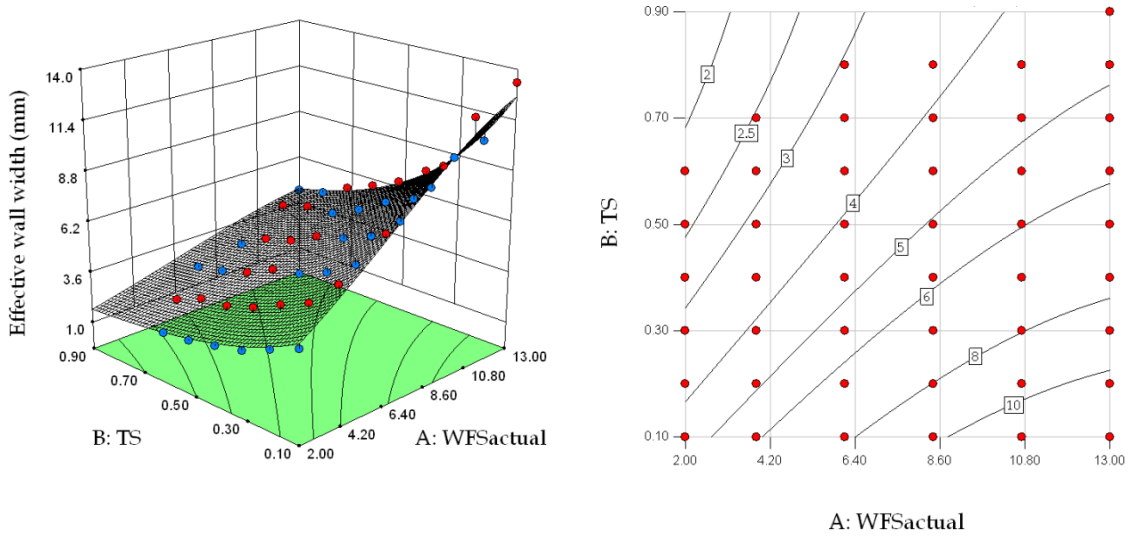

(n)

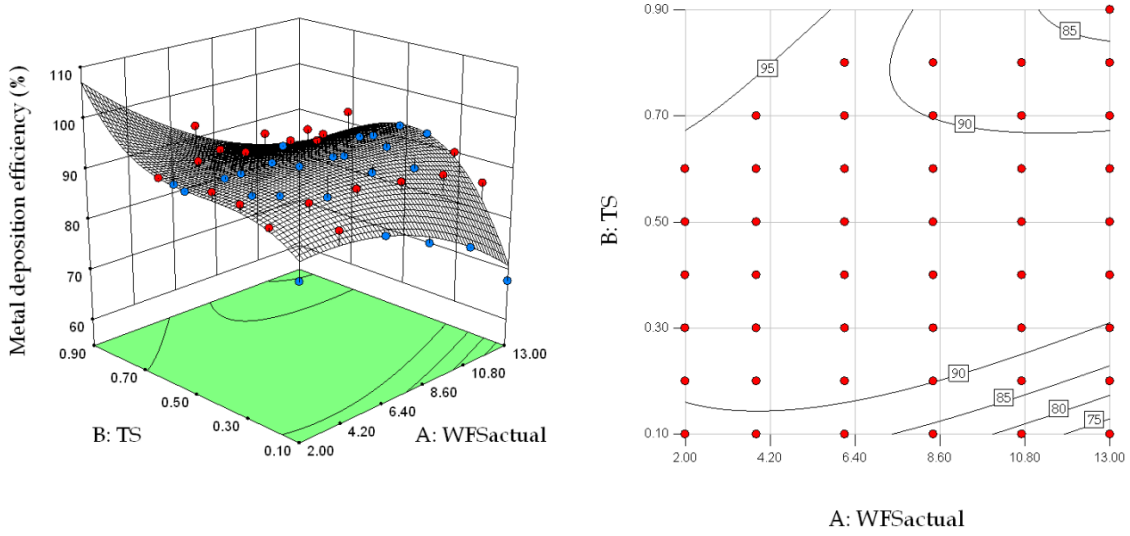

(o)

Figure 4.77. 3D response surfaces (left) and contour (right) graphs showing the interactions of process factors on numerous responses when utilising 0.8 mm (a, b, d, f, g, h, i, j, k, m, n and o), and 1.0 mm wires (c, e, and l). For the 3D response surfaces the experimental dots represent points below (blue) and above (red) the predicted value.

4.5.4 Validation of the models

The adequacy of the models developed herein was verified by applying the procedure described in section 3.12.6. The validation of the models was brought forth by scatter diagrams and a number of confirmation tests, according to section 3.12.7. The correspondence between the predicted and actual values in single layer models for a number of different responses is computed in Figure 4.78. It is observed that despite the large number of data points, these are mostly located at a position adjacent to the 45°. However, a relatively large scatter is observed in some predictors, such as CA and AR.

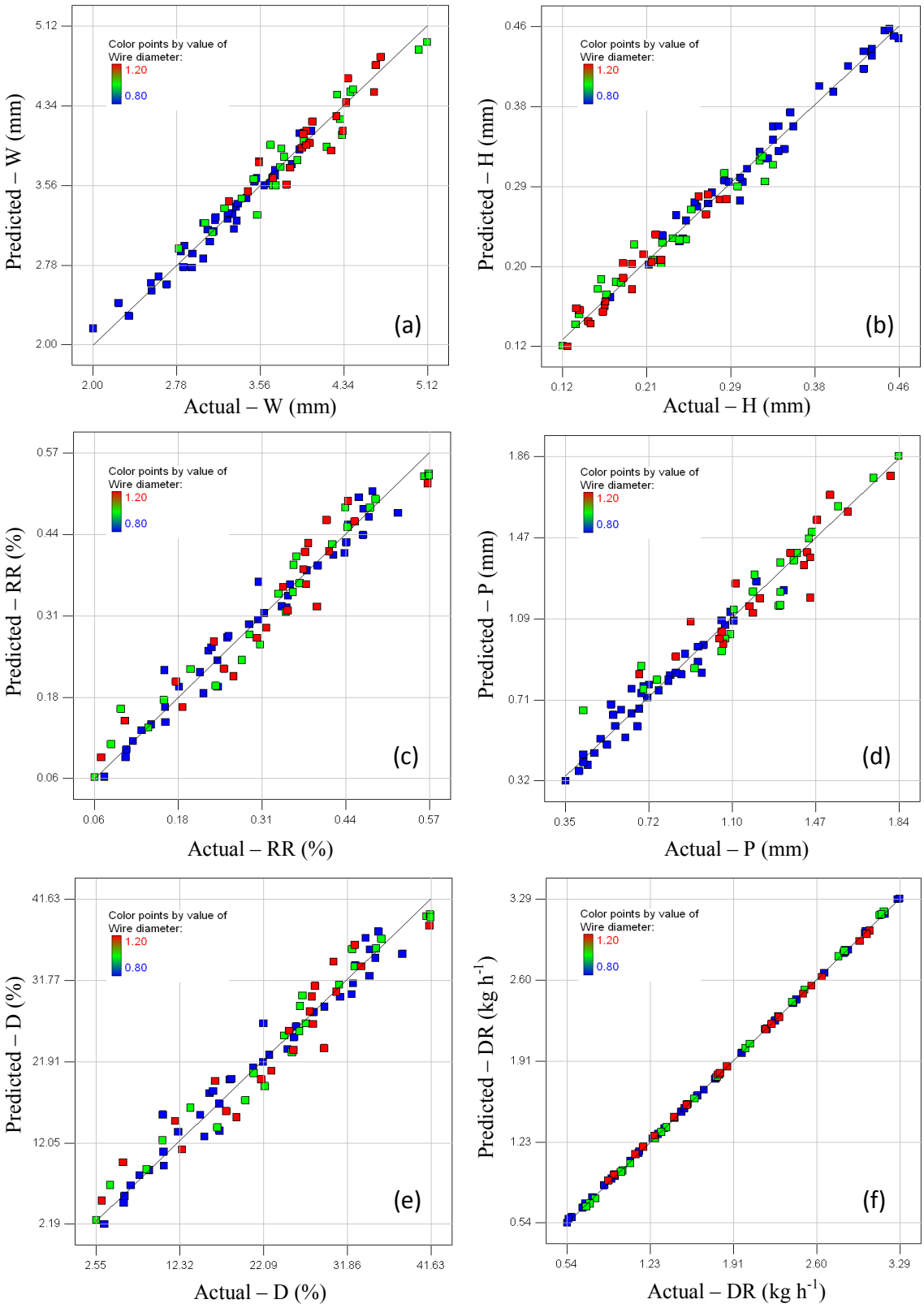
Color points by value of
Wire diameter:
1.20
0.80
Predicted – W (mm)
Actual – W (mm)
5.12
4.34
3.56
2.78
2.00
(a)
Predicted – H (mm)
Actual – H (mm)
0.46
0.38
0.29
0.20
0.12
(b)
Predicted – RR (%)
Actual – RR (%)
0.57
0.44
0.31
0.18
0.06
(c)
Predicted – P (mm)
Actual – P (mm)
1.86
1.47
1.09
0.71
0.32
0.35
0.72
1.10
1.84
(d)
Predicted – D (%)
Actual – D (%)
41.63
31.77
21.91
12.05
2.19
2.55
12.32
22.09
31.86
(e)
Predicted – DR (kg h-1)
Actual – DR (kg h-1)
3.29
2.60
1.91
1.23
0.54
(f)

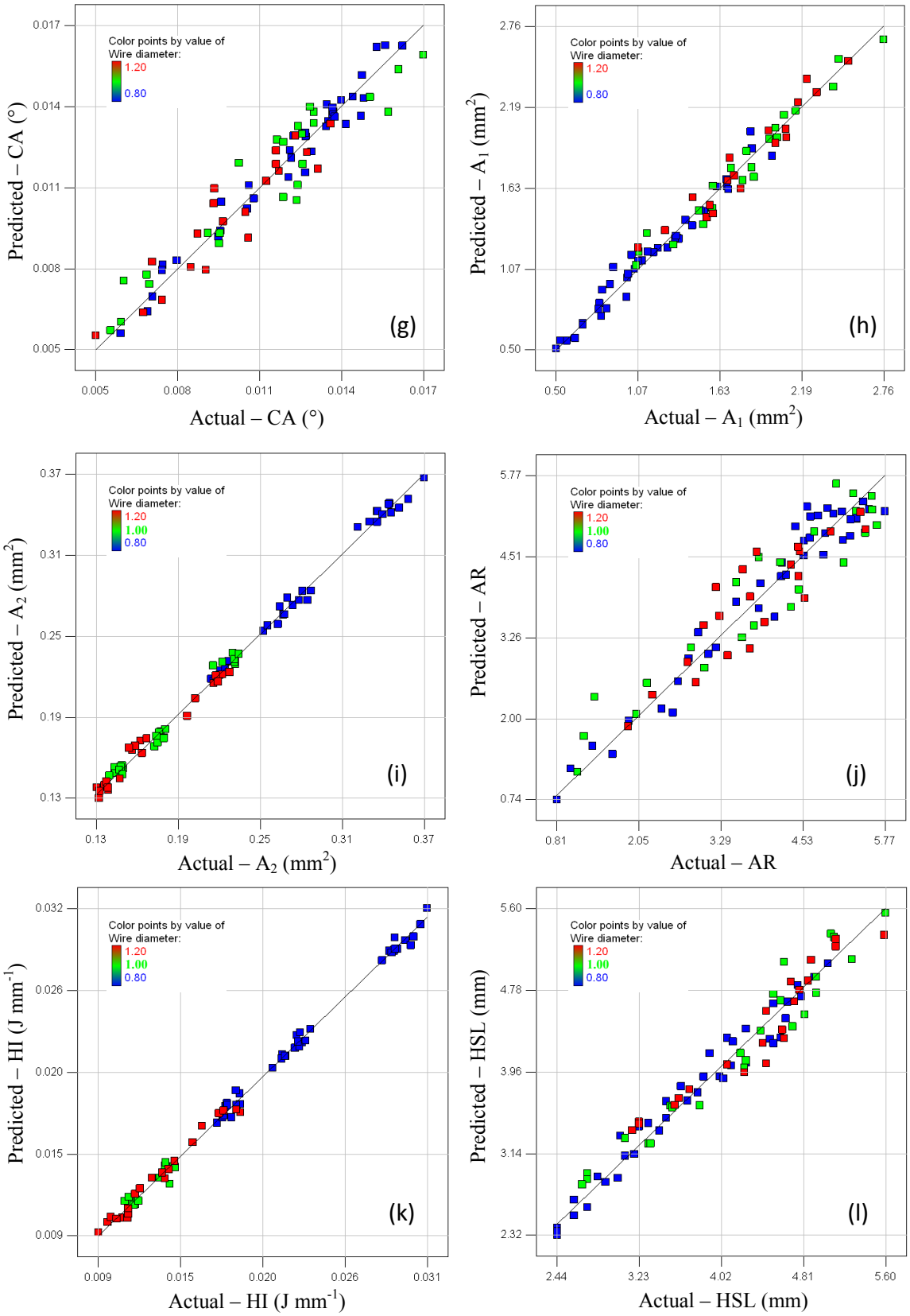

Figure 4.78. Predicted versus actual single layer scatter diagrams computed for each individual response variable, such as: (a) bead W, (b) bead H, (c) RR, (d) P, (e) D, (f) DR, (g) CA, (h) A_1, (i) A_2, (j) AR, (k) HI, and (l) HSL. Data points are distinguished by wire diameter.

Figure 4.79 shows the predicted versus actual response values of the multi-layer models developed (see section 3.7.2 for definitions). Data points are relatively close to the 45° diagonal line. Though, a reasonably large scatter is observed in predictors such as SW_{av} and MDE.

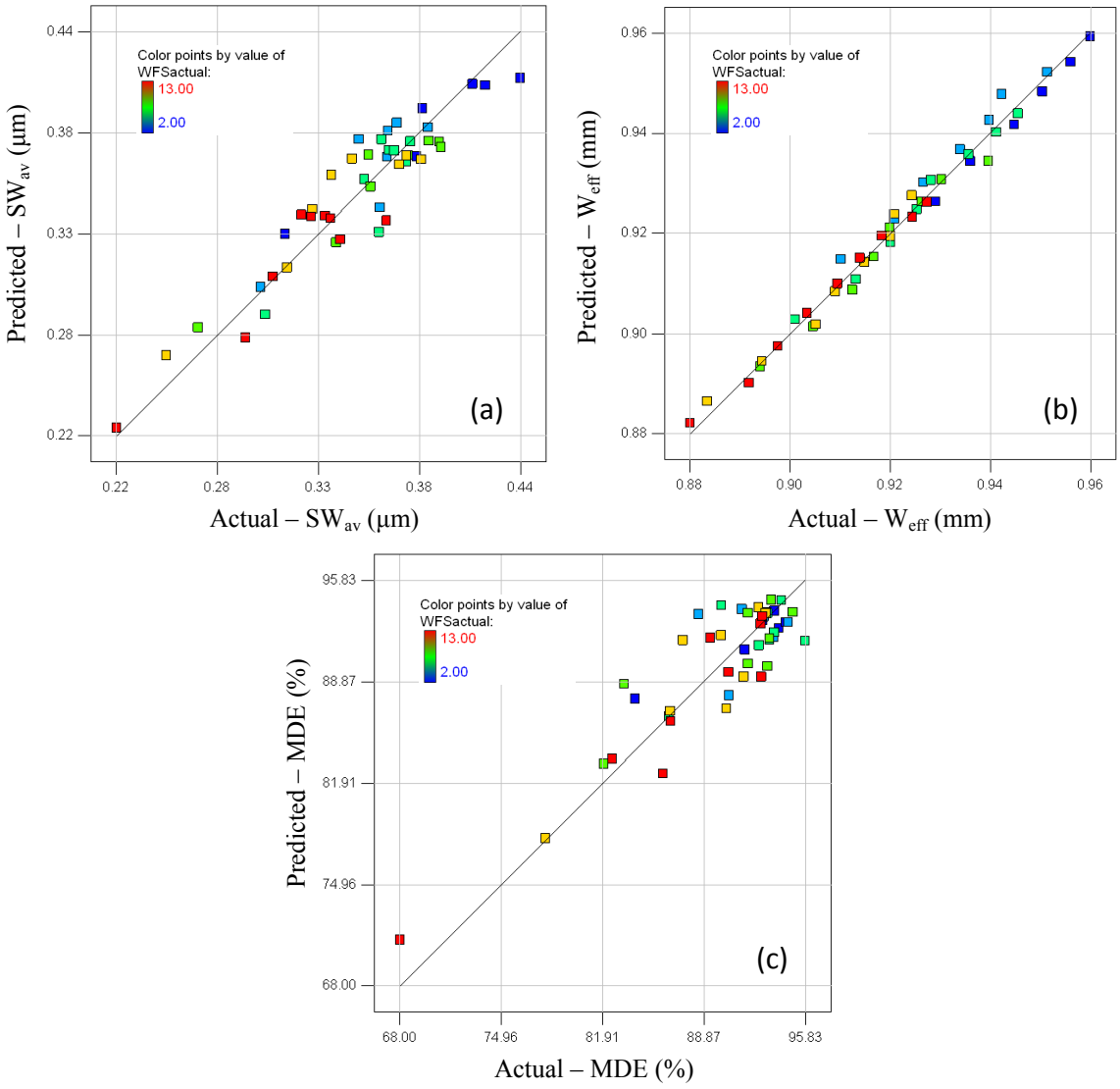

Figure 4.79. Predicted versus actual multi-layer scatter diagrams computed for each response variable, such as: (a) SW_{av}, (b) W_{eff}, and (c) MDE. Data points are distinguished by WFS_{actual}.

In order to verify the validity of the models described in section 4.5.2, confirmation experiments were performed and selected according to the procedure described in section 3.12.7.

Three confirmation tests were carried out to verify the adequacy of single layer models using a new set of welding conditions. Table 4.5 summarises the applied welding conditions, the actual experimental values, the predicted values and the error in percentage.

Table 4.5. Confirmation experiments to validate single layer models.

Confirmation Exp.	W (mm)	H (mm)	RR (%)	HI (J mm^{-1})	DR (kg h^{-1})	CA (°)	A_2 (mm^2)	A_1 (mm^2)	P (mm)	D (%)	AR	HSL (mm)
Exp. 1[a]												
Actual	4.70	2.10	0.17	191.02	1.38	57.14	6.63	1.11	0.59	14.34	0.45	10.01
Predicted	4.77	2.01	0.18	191.04	1.38	59.76	6.66	1.16	0.65	15.05	0.42	9.63
Error (%)	-1.49	4.69	-5.68	-0.01	-0.01	6.88	-0.47	-4.59	-9.37	-4.72	7.40	3.93
Exp. 2[b]												
Actual	5.48	1.98	0.33	202.13	2.24	53.23	7.34	2.44	1.09	24.95	0.36	14.12
Predicted	5.64	1.95	0.34	202.69	2.25	53.46	7.27	2.58	1.14	25.33	0.38	14.59
Error (%)	-2.89	1.44	-1.52	-0.28	-0.45	-0.43	0.99	-5.57	-4.79	-1.49	-5.57	-3.21
Exp. 3[c]												
Actual	6.82	2.90	0.31	380.94	2.37	63.07	14.07	4.30	1.54	23.41	0.43	16.96
Predicted	7.04	2.70	0.32	398.54	2.36	62.43	13.62	4.20	1.57	24.00	0.38	16.85
Error (%)	-3.15	7.46	-4.65	-4.41	0.43	1.01	3.30	2.40	-1.74	-2.48	11.14	0.63

[a]*WD*= 0.8 mm, WFS_{actual}=5.878, *WFS/TS*=12.247; [b]*WD*= 1.0 mm, WFS_{actual}=6.086, *WFS/TS*=8.224; [c]*WD*= 1.2 mm, WFS_{actual}=4.481, *WFS/TS*=10.669; Error (%) = ((Experimental value – Predicted value) / Predicted value) × 100.

Three confirmation experiments were also carried out to verify the adequacy of the multi-layer models developed, using once again the point prediction option in the software. The selected welding conditions, the predicted and actual experimental values, as well as the percentage errors are contained in Table 4.6.

Table 4.6. Confirmation experiments to validate multi-layer models.

Confirmation Exp.	W_{eff} (mm)	W_{eff} PI (95%) low / high	SW_{av} (μm)	SW_{av} PI (95%) low / high	MDE (%)	MDE PI (95%) low / high
Exp. 1[a] (W_{eff}=3mm)						
Actual	3.03±0.16		459.07		87.69	
Predicted	3.04	2.71 / 3.41	224.80	138.12 / 383.44	92.41	86.99 /97.82
Error (%)	-0.41		104.21		-5.11	
Exp. 2[b] (W_{eff}=5mm)						
Actual	4.99±0.12		313.47		95.35	
Predicted	5.33	4.75 / 6.00	234.68	144.22 / 400.18	92.76	87.36 / 98.16
Error (%)	-6.49		33.58		2.79	
Exp. 3[c] (W_{eff}=7mm)						
Actual	6.81±0.04		494.36		93.12	
Predicted	7.20	6.39 / 8.12	353.86	210.66 / 627.05	93.50	88.04 / 98.96
Error (%)	-5.42		39.70		-0.40	

[a]*WD*= 0.8 mm, WFS_{actual}=4.863, *TS*=0.64; [b]*WD*= 0.8 mm, WFS_{actual}=9.901, *TS*=0.55; [c]*WD*= 0.8 mm, WFS_{actual}=11.766, *TS*=0.4; Error (%) = ((Experimental value – Predicted value) / Predicted value) × 100. *PI*, prediction interval indicates what to expect from confirmation runs.

4.5.5 Optimisation

This section presents the results of two optimisation steps (single and multiple-optimisation) that were carried out in accordance with the procedure detailed in 3.12.8. The optimisation block in Design Expert software was employed for the analysis of the final empirical models developed in section 4.5.2. The investigation was broken down into two case studies which are described next.

Case study 1

The objective of this case study was to establish near-optimal operation conditions, *i.e.* best combination of factor levels, such as WFS_{actual}, WFS/TS and WD, for satisfying a desired single layer wall W response within a range of 4.5 to 5 mm. The optimum operating regions, or combination of parameters, are graphically represented in Figure 4.80 for different wire diameters. Note, however, that optimum operating conditions obtained from the software were additionally delimited by a quality acceptance criterion level "A", defined according to Table 4.7.

Table 4.7. Quality acceptance criteria defined for single layer weld beads.

Wire diameter (mm)	Quality level[1] (range of WFS_{actual})		
	A (excellent)	B (acceptable)	C (not acceptable)
0.8	3.0 – 10	11.0 – 13.0	2.0 – 3.0
1.0	2.5 – 7.5	-	7.5 – 8.5
1.2	2.5 – 5.5	-	1.7 – 2.4

[1] Quality of the weld beads was determined visually according to section 3.8.1.2.

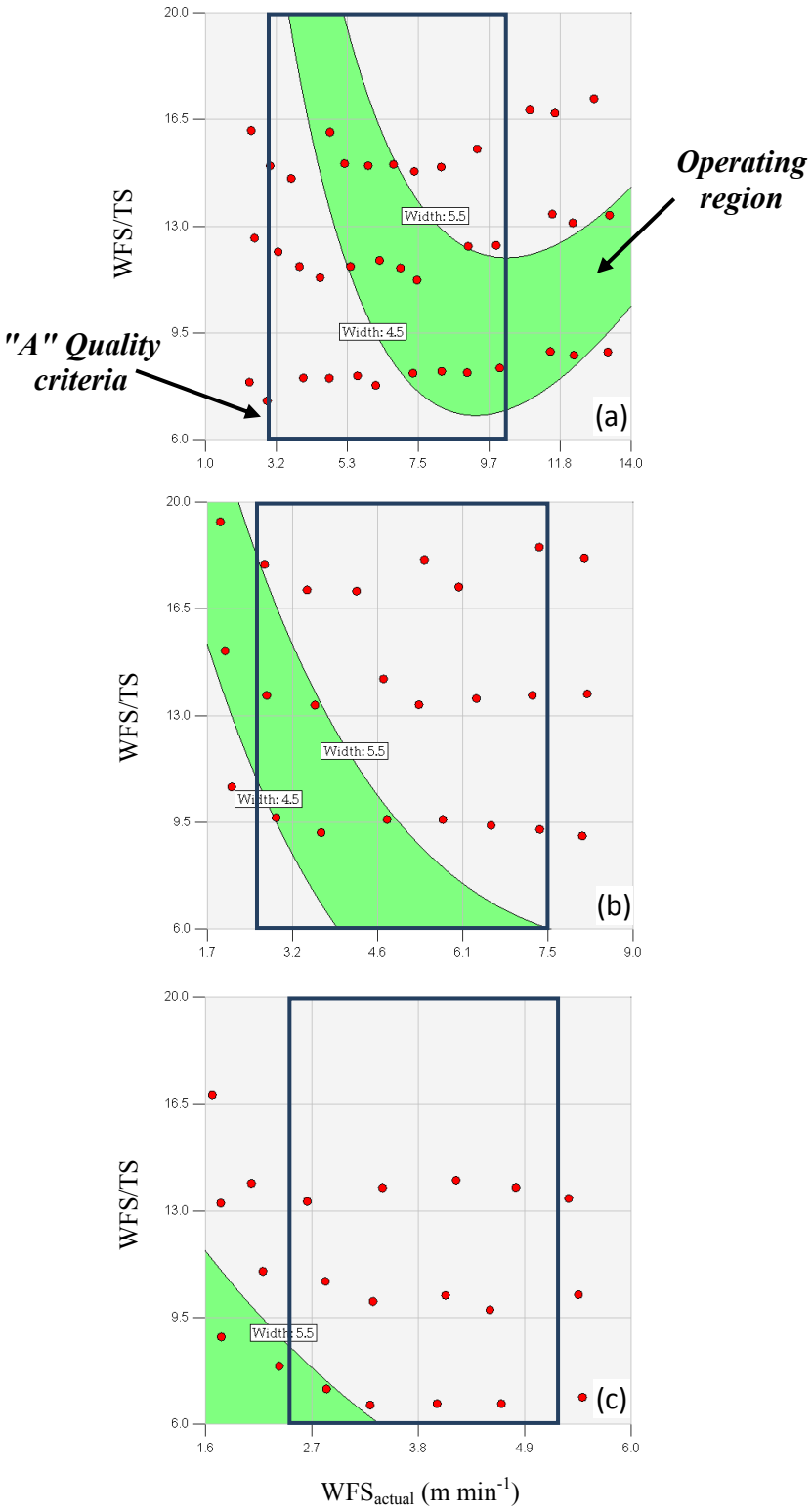

Figure 4.80. Optimum welding operating conditions (green shaded area) determined for a desired bead width response within a range between 4.5 to 5.5 mm utilising wire diameters of (a) 0.8 mm, (b) 1.0 mm, and (c) 1.2 mm. Welds considered to be "A" quality level are contained within the frame (inset).

Case study 2

The objective of the second case study was to establish near-optimal operating conditions for a 0.8 mm wire by setting a number of desired constraints (minimum and maximum limits) for several responses of interest. The operating region was found by overlaying the minimum and maximum contour plots for each response where the requirements simultaneously meet the criteria established beforehand. The output requirements included lower and upper limits for the bead W, H, CA and DR, and these were 4.5-5.5 mm, 1.6-1.9 mm, 45°-90°, and 2.0-3.0 kg h^{-1}, correspondingly (see Figure 4.81). Once again, the final operating region was additionally delimited by the quality level "A" (see Table 4.7).

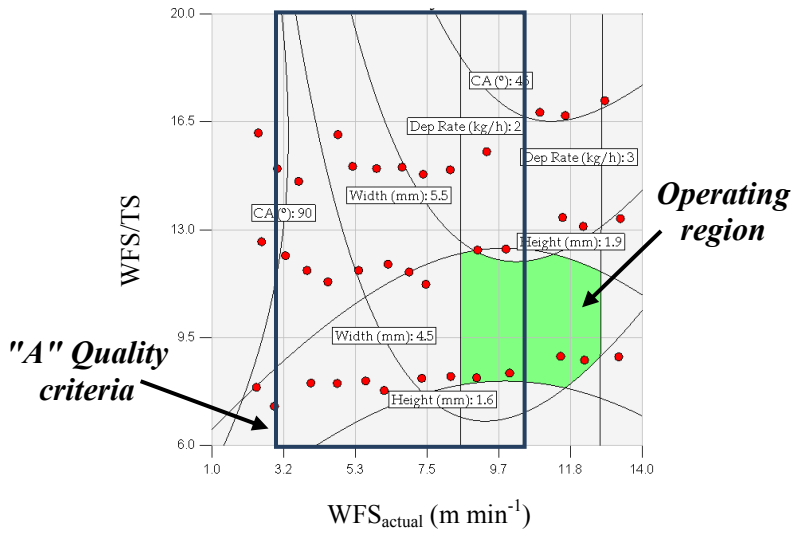

Figure 4.81. Optimum welding operating conditions (green shaded area) determined by overlaying user defined requirements for a number of responses of interest, such as bead W, bead H, CA and DR.

5 Discussion

This chapter discusses the results presented in section 4. Initially, the discussion concentrates upon the effects of fundamental process parameters, such as *TRIM*, CTWD, WFS, WFS/TS and WD on both the weld bead shape and metal transfer characteristics of mild steel single layer welds in GMAW-P. The influence of GMAW-P primary welding parameters of the current waveform by using a *non-adaptive control mode* is then discussed, with respect to geometrical weld bead features, surface quality and metal transfer conditions. The influence of fundamental CMT process parameters, such as arc-length control (ALC), dynamic correction (DC_{orr}) and CTWD are also analysed in the same context as described for GMAW-P. The effects of interactions between process factors and both weld bead and plate fusion characteristics were examined.

The discussion then focuses on the deposition features of multi-layer deposits of mild steel when using CMT. Here, special attention is given to the relationship between travel speed (TS), average instantaneous power (AIP) and heat input (HI), with the side wall surface features of multi-layer deposits. The effect of control variables on multi-layer deposition features is also discussed.

Finally, the discussion centres on the adequacy, validation and optimisation of the proposed single and multi-layer statistical process control models developed using multiple linear regression (MLR) analysis.

5.1 Introduction

When employed in automated WAAM deposition systems, GMAW can offer two distinct economical and technical advantages over current GTAW practices, as follows: (1) high production rates, owing to the use of a continuous-feed consumable wire electrode, which is intrinsically linked to a higher wire melting rate capability, and (2) the design flexibility offered by the coaxial wire feeding delivery, that facilitates additive patterning of more intricate components, along with positional deposition irrespective of torch orientation, *i.e.* translational omni-directionality.

However, the main drawback associated with WAAM systems using high deposition rate GMAW is the tolerance loss observed in the as-welded near net shape parts. The production of components with lower resolution, or in other words with a minimum feature size or detail that is typically high, leads to a significant reduction of the deposition efficiency, since large volumes of material are machined away in order to achieve the required dimensions within the desired tolerances. The quality of the fabricated component is for that reason unfavourably affected as a result of a more limited control over the dimensions of the molten pool size.

The quality of WAAM metal components can be generally characterised on aspects, such as geometric accuracy and achievable range, and metallurgical properties of the as-deposited parts (Zhang *et al.*, 2003). Yet, the geometric accuracy and width range is typically defined by means of both dimensional accuracy and quality of the surface finish of the component. These geometric properties are therefore strongly characterised by the shape and dimensions of the deposited weld beads.

The shape and dimensions of the weld beads are important criteria in determining the range of target widths which can be produced, influencing at the same time the surface finish of the component produced. From the foregoing discussion, it may be concluded that the selection of the proper combination of process parameters is central to improve the quality of metal components produced via WAAM. In this work the W, H, RR, P, D, CA, A_1, A_2, and AR were used to describe the weld bead and plate fusion characteristics in single layer welds, whilst the effective wall width (W_{eff}), surface waviness (SW_{av}) and metal deposition efficiency (MDE) were utilised to describe features in multi-layer walls.

The development of a welding parameter database for controlling the bead geometry, in the form of process control algorithms, represents also a major step in the direction of commercialisation and mass adoption of the WAAM technology, by introducing a substantial level of automation where only minimum technical welding expertise is needed (see section 1.4).

5.2 Single layer welds

5.2.1 Pulsed-current gas metal arc welding

5.2.1.1 Influence of process parameters on weld bead and plate fusion characteristics

The results of this study indicate that contact tip to work distance (CTWD), *TRIM*, wire feed speed (WFS), wire feed speed to travel speed ratio (WFS/TS), and wire diameter (WD) are very influential parameters in determining the weld bead and fusion characteristics. In the current study it has also been found that *TRIM* has a significant effect on the surface quality of single layer welds, whereas CTWD has little effect.

The weld bead and plate fusion characteristics are strongly influenced by CTWD. From the technical view point this is an important result, since inaccurate predictions of the bead geometry during processing can contribute to differential cumulative positioning errors in the nominal distance between the welding torch relative to the part being produced. Poor estimations of the relative bead height increment H_n (or Delta-*z*) in multi-layer deposition can result in torch positions to close or too far away from the previous layer. In addition, poor shielding and welding conditions can occur if the distance between the welding torch and the melt pool becomes too wide (*e.g.* very large CTWD). Under these unfavourable conditions, the welding arc can be brought too close to the edge of the shielding gas envelope due to the increasing pre-bending effect of the wire electrode caused by the adjacent spool. These variations in CTWD are very likely to affect the processing conditions, and thus the final shape and quality of the produced component.

In order to justify the underlying effects of CTWD on the weld bead and fusion characteristics, it is first necessary to introduce herein the well-known empirical relationship between the wire burn-off rate, arc current, and electrode stick-out (Allum, 1983; Smati, 1986; Praveen *et al.*, 2005). The widely accepted mathematical description of the wire burn-off rate (BR) for continuous EPDC-GMAW was developed by Lesnewich (1958) for spray metal transfer mode a given electrode type and diameter, as follows:

$$BR\,(m\,\mathrm{min}^{-1}) = \alpha I_{AVG} + \beta l I_{AVG}^2 \tag{5.1}$$

where, α is a constant which accounts with the localised arc heating at the wire tip, β is a factor describing the distributed resistance heating along the wire length, I_{AVG} is the average current, and l is the electrical stick-out. The first term of the equation describes the contribution of the arc energy due to the voltage drop close to the electrode, whereas the right hand side term describes the contribution to the melting rate due to wire extension heating (*ohmic* resistance). In order to achieve suitable metal transfer characteristics during pulsed direct current (DC) welding, the wire feed speed (WFS) must be balanced with the wire burn-off rate to maintain a constant arc-length. The generic mathematical expression that describes the wire *BR* in pulsed DC welding with square wave pulse shape is described as follows:

$$BR\,(m\,\mathrm{min}^{-1}) = \alpha I_{AVG} + \beta l \left\{ I_{AVG}^2 + \frac{(I_p - I_b)^2 T_p T_b}{(T_p + T_b)} \right\} \tag{5.2}$$

where, I_p is the pulse current, I_b is the background current, T_p is the duration of the pulse current, and T_b is the duration of the background current. When compared with equation (5.1) for EPDC-GMAW, equation (5.2) yields an additional resistance heating term that becomes increasingly important at high current excursions in pulsed welding, especially when utilising high resistivity wires (Allum, 1983; Smati, 1986). Two related points need to be made. Firstly, the *BR* in pulsed welding is higher than in DC welding at constant I_{avg}. Secondly, the *BR* is strongly influenced by the primary welding parameters of the current waveform, such as I_p, I_b, T_p, and T_b.

It should be noted that the relationships disclosed above are well known for decades and that despite the continuing advancements in process control features, such as one-knob or microcomputer process controls, Ohm´s law continues to apply.

The noticeable effect of CTWD on W and H up to 13 mm observed in Figure 4.1 (page 126) can therefore be explained based on the foregoing discussion. At short CTWD values the resistance heating terms of equation (5.2) become less significant, causing the *BR* to decrease. In order to maintain suitable metal transfer characteristics and a constant arc-length, the *BR* is thus increased through an increase in I_{AVG}. As a result, an increase in the average instantaneous power (AIP), heat input (HI) and arc-spread are

also expected, as a result of an increased *BR*. This effect may justify the large variation observed in W and commensurate decrease of H, as well as the improvement of wettability (see Figure 4.2 in page 127). Another important finding was the significant increase in fusion characteristics with decreasing CTWD as a result of a surge in AIP, and therefore the HI. The decrease in CTWD from 13 mm to 7 mm corresponded to a maximum percentage increase in RR, A_1 and D of 70 %, 75 %, and 40 %, respectively; while variations in P and A_2 were found to be less significant. One observation of interest concerns the turning point observed in the majority of the responses studied at 13 mm CTWD. This change probably marked the transition point in the static volt-ampere characteristic from constant voltage (CV) to constant current (CC) mode. Therefore, the much slower increase in W and fusion characteristics is consistent with an associated increase in arc-length at constant current for higher CTWD. Such behaviour was expected since a similar static volt-ampere characteristic (VI) was also observed in P14 for 1.0 mm diameter wire and for the same *Pulse Soft* operation mode, though at 18 mm CTWD (see Figure 4.18 in page 136). Another point that deserves mention is the negligible effect of CTWD on A_2, and therefore deposition rate, which confirms that the build-in process control feature in this power source comprises a constant wire feeder unit.

The *TRIM* setting knob has a direct effect on the welding arc-length in all pulse synergic welding modes (see Power Wave ^{TM} 455/STT operator`s manual). The increase in *TRIM* leads to an increasing arc-length. As a consequence, this effect results in increased arc voltage, which causes an increase in average instantaneous power (AIP), heat input (HI), and arc-spread. This effect is expected since the higher *BR* associated with higher arc power causes the arc-length to increase, owing to a constant electrode feeding rate.

The high welding arc temperatures as a result of increased arc power, results in higher temperatures in both base metal and weld pool. Therefore, the interfacial tension and viscosity of the weld pool are expected to decrease due to an increase in its heat content, while wetting properties in the liquid are improved. This effect is apparent in Figure 4.5(a) (page 128) where the CA decreases slowly with *TRIM* over 1.0. This result is consistent with that of Quintino and Allum (1984), who found CA decreases with increased arc voltage. Overall, the increase in temperature associated with higher arc

voltages appears to explain why single beads become wider and flatter with increased *TRIM*, as seen in Figure 4.4(a) in page 128. Similarly, the increasing power delivered to the weld, and therefore HI, also leads to increasing fusion characteristics, *i.e.* D, P, RR and A_1. The influence of *TRIM* on RR and A_1 is very similar because A_2 does not vary significantly (see Figures 4.5(b) and 4.6 in pages 128 and 129, respectively). *TRIM* was found to affect A_1 more significantly when compared with P for *TRIM* between 0.9 and 1.0, *cf.* Figures 4.4 and 4.6 in pages 128 and 129. The maximum percentage change was 52 % for P and 116 % for A_1. The weaker effect of *TRIM* on P appears to result from the larger arc power, HI, and arc-spread associated with the increased arc-length, as discussed above. As the arc spreads, more heat is distributed away from the centreline of the molten pool in response to the arc action onto the base plate. This thermal effect causes more heat to reach the adjacent areas in the base plate, which can probably explain the formation of a shallower A_1.

Interesting to note at the initial stage of the research, is that factors such as high concentrations of heat, typically allied with large fusion/remelting characteristics, have been in the past documented to have a detrimental impact on the quality of the part in layered manufacturing processes using GMAW-P (Dickens *et al.*, 1992; Dickens *et al.*, 1998; Song *et al.*, 2005; Sreenathbabu *et al.*, 2005). For this reason, and in order to reduce extensive fusion and remelting of previous welding passes, while allowing for better control of the heat generated during the build-up, a suitable CTWD setting could be as an example easily selected from data provided in the initial trials, and that would be 13 mm high.

The negligible effect of CTWD on the weld bead quality of single layer deposits is expected, since these results are directly related with the metal transfer behaviour (see Figure 4.8 in page 130). For achieving optimum metal transfer conditions in GMAW-P with *adaptive control*, two essential requirements need to be verified: (1) stable metal transfer of droplets from the wire to the weld pool, (2) the WFS must be balanced with the *BR* to maintain a constant arc-length (Smati, 1986). Thus, controlled metal transfer characteristics, ideally one droplet per pulse (ODPP), should be preserved in GMAW-P at all times, irrespective of changes in CTWD (Subramaniam *et al.*, 1999; Palani and Murugan, 2006). These optimum transfer conditions are dependent on build-in process

control features which involve continuous monitoring and control of critical pulse parameters.

Another important finding was that *TRIM* is a very influential parameter in determining the surface quality of the beads produced (see Figure 4.7 in page 130). The explanation for this result lies on the metal transfer behaviour. Short-circuit metal transfer conditions are obtained at low *TRIM* values. This transfer mode appears to be a dominating factor in controlling the observed arc instability, which is characterised by poor transfer conditions, typically associated with low AIP and short arc-lengths. The low frequency rippling and excessive spatter observed near the weld bead toes resulted from each individual short circuit along with asymmetrical metal transfer. Therefore, it can be assumed that these are not the optimum metal transfer conditions in the view of spatter generation and final surface quality. Higher *TRIM* values improved the metal transfer conditions to more desirable ODPP mode, resulting in better quality welds.

The discussion is now focused on understanding the underlying effects of primary welding parameters, such as WFS, TS and WD, on the weld bead and fusion characteristics. Note, that the results of the experiments discussed herein were conducted at constant deposited cross-sectional areas, *i.e.* constant ratio of wire feed speed to weld travel speed (WFS/TS), while effects of interactions between control factors and bead/fusion characteristics were determined. The reason why a constant WFS/TS strategy was adopted instead of TS was to ensure that uniform and good quality welds were maintain throughout all the experiments in order to prevent erratic combinations of the welding parameters, *e.g.* excessively high TS and particularly low WFS.

The results of this study indicate that weld bead and fusion characteristics are strongly affected by control variables such as WFS, WFS/TS and WD. Bearing in mind that by holding the WFS/TS ratio constant, the heat input (HI) delivered to the weld is maintained at approximately a constant level, it is interesting to note the strong influence exerted by these control variables on the bead profiles. For reasons of simplicity and by taking Figure 4.9(a) (page 131) as an example, one can see the effect of WFS on W at various WFS/TS ratios, and therefore at relatively constant HI conditions. The larger the WFS/TS, the higher the HI delivered to the weld.

The current study found that W is narrow at low WFS, while both H and CA are notably increased. Thereafter, at intermediate WFS, the bead characteristics do not seem to be greatly affected. However, most importantly, is the pronounced decrease in W with WFS at higher regimes, which is accompanied by a significant increase in H and CA. This interplay between bead characteristics can probably be explained by the combined effects of AIP, TS, and metal transfer characteristics, given that the influence of HI was initially isolated (WFS/TS ≈ constant).

The low spread of the weld bead at low WFS results from the low thermal energy transferred onto the molten pool and base plate. In particular, the heat generated in the arc effectively transferred to the base plate is substantially reduced at very low TS, owing to a shielding effect between the welding arc and the base plate. The effect becomes more noticeable when large deposited volumes are produced, as demonstrated in Figure 4.9(a) in page 131, *i.e.* using high WFS/TS. Under these processing conditions, the welding arc is established predominantly between the tip of the wire electrode and the top of the weld bead, resulting in less heat being transferred to the base plate. In addition, the occurrence of less stable short circuit transfer conditions, which is typically dominated by a mechanism of transfer by surface tension, can also counteract the outward bead spread effect caused by the action of the arc pressure and droplet impingement onto the molten pool, as observed elsewhere in the spray mode of metal transfer for GMAW (Hu and Tsai, 2007).

Another important finding was that significantly narrower and taller weld beads were produced at high WFS, for the entire WFS/TS range. The effect is most noticeable in the weld bead cross-sectional macrographs shown in Figure 4.51 (see page 159). This result can be justified by the combined effects of both WFS and TS. At high current levels, very strong electromagnetic forces are produced as a result of the field generated by the current in the metal wire. According to Essers and Van Gompel (1984) the Lorentz force arising in the drop dominates largely other forces acting on a detaching drop of molten filler metal in GMAW-P, *i.e.* surface tension, drag and gravitational forces. The Lorentz force is expected to obey:

$$F_{inst}(N) = \frac{\mu_0}{4\pi} I_{inst}^2 = 10^{-7} \cdot I_{inst}^2 \tag{5.3}$$

where, F_{inst} is the instantaneous Lorentz force, μ_0 the magnetic permeability, and I_{inst} the instantaneous current. Therefore, strong arc pressure forces are expected to act onto the surface of the weld pool, as a result of high current densities. High current densities also involve large interactions with the base metal, leading to higher P and A_1, as seen in Figures 4.10(b) and 4.12(a) in pages 131 and 132, respectively. The strong convective forces associated with larger interactions and arc pressures, are expected to force the flow of molten metal to the rear of the arc, leading to an increase in H. This effect is possibly associated with a convective mass transport effect induced to the liquid metal which becomes gradually more significant at higher WFS (*i.e.* welding current) and TS (see Figure 4.9(b) in page 131). Note that as WFS increases the TS also increases. The dependence of W and H on the WFS/TS is very significant and nearly independent of WFS, indicating the travel speed potential for controlling W and H. Wider and taller weld beads are produced with higher WFS/TS, at constant WFS. This effect is particularly noticeable in the sequence of cross-sectional macrographs depicted in Figure 4.52 (page 160). This result was expected, and explained by the larger deposited volume per unit length associated with higher WFS/TS.

Another important finding was the crucial role that WD plays in determining the weld bead and fusion characteristics. In this respect, there are several important facts to emphasise in this study. Overall, narrower and shorter weld beads are produced with smaller WD at constant WFS. The minimum and maximum achievable W range is between 4 to 8 mm in 1.0 mm WD, and 6 to 10 mm for 1.2 mm WD, indicating the WD potential for controlling W. Note that W is smaller when utilising smaller wires, up to about 11 m min^{-1} WFS. However, W is similar in both wires at high WFS (over 11 m min^{-1}) whereas H increases noticeably from 6 m min^{-1} WFS onwards (see Figure 4.13 in page 133). A possible explanation might be that less current and mass is delivered through smaller wires at constant WFS. Therefore, lower AIP is produced, resulting in considerably colder and smaller weld pools with worse wetting behaviour. This effect is consistent with the higher CA obtained up to about 7 m min^{-1} WFS (see Figure 4.15(b) in page 134). Another possible explanation for these results may be due to the different current waveform characteristics utilised for depositing each particular WD, since pulse parameters are expected to affect the AIP and HI, and thus bead and fusion characteristics (Pal and Pal, 2011).

As a result of lower currents and reduced mass transport offered by smaller WD (at the same WFS), fusion characteristics, such as RR, P, D, and A_1, were significantly lower for smaller WD. It should be noted that the divergence observed in P and A_1 at WFS over 8 m min^{-1} for 1.2 mm WD is probably due to the onset of a keyhole phenomenon as a result of higher current density. The rapid increase in both P and A_1 is associated with the formation of a distinct "finger" type penetration profile (see Figure 4.52 in page 160). This phenomenon was reported in previous research in GMAW and attributed to the heat transferred into the weld pool via high-frequency spray of molten filler metal droplets (Tsao and Wu, 1988). This effect does not occur for the small WD because the currents involved are assumed to be considerably lower. This study has been unable to demonstrate the tendency for increased penetration with decreasing wire size reported elsewhere (Quintino and Allum, 1984).

It is worth mentioning that higher DR is achieved when using thicker wires at constant WFS. Therefore larger A_2 are expected to be obtained with larger WD at constant WFS and TS (see Figure 4.16(b) in page 135). This result was expected, since higher volume of weld metal is deposited per unit time and length under these processing conditions with larger WD. Constant deposited cross-sectional areas can only be produced with different WD if the mass per unit length is kept constant.

The lack of transient electrical signals can be considered the biggest limitation of this particular study. The access to electrical data would have assisted the previous discussion since interpretation would have become much clearer.

5.2.1.2 Influence of contact tip to work distance on the waveform and bead characteristics

On the basis of the foregoing discussion, the weld bead and fusion characteristics of GMAW-P welds were found to be significantly affected by different welding current waveform characteristics. Advancements in control features in GMAW-P systems have greatly enhanced the control over process parameters by continuously monitoring the welding conditions through feedback control mechanisms. Suitable ODPP metal transfer conditions can be automatically selected by closely controlling and adjusting the pulsed-current waveform parameters for any specified mean current using adaptive

or self-regulating control systems. Appropriate transfer conditions are achieved primarily through manipulation of the main pulse parameters, such as: pulse current (I_p), background current (I_b), duration of pulse current (T_p), duration of background current (T_b), frequency (*f*), and load duty cycle (LDC).

The dynamic response of modern electronically regulated power supplies to CTWD variations depends largely on the static volt-ampere characteristic (VI) and on the adjustment control logic of each particular welding program (see Figure 4.18 in page 136). Typically, the built-in control logic uses proprietary software (pre-programmed algorithms) specific to the power source manufacturer for generating pulsed-current with diverse waveform shapes. Stable and highly desirable ODPP operating conditions can be obtained using varied waveform shapes or combinations of pulsing parameters, which can be selected according to particular user requirements, *e.g.* heat input, melting rate, bead shape. For example, "one-knob control" manipulates all the pulse variables over a wide range of WFS and I_{AVG} using the WFS readings measured by a tachometer, in order to generate the appropriate waveform based on this input. The control logic is typically applied using two different approaches, namely the synergic and self-regulating control. In synergic control the wire feed unit and power source are linked in such way that I_{AVG} may be regarded as being determined by the WFS (Allum, 1983). The pulse current waveform produced by this control logic (Type I) maintains T_p and the excess current I_e (I_e=I_p-I_b) constant, while varying I_p, I_b and T_b. The self-regulating control approach (Type II) can be regarded as a voltage control of I_{AVG}. The system restores the arc-length to a set reference voltage by varying the wire burn-off rate (*BR*). This control logic (Type II) produces a waveform with constant T_p, I_p, and I_b, while varying T_b. The process control in modern microcomputer based systems can be based on arc-length regulation control, achieved through the control of the arc voltage; or wire feed arc voltage control, achieved by controlling the WFS. However, the latter method is difficult to apply due to poor stability and comparatively slower response rate of standard wire feed units (Praveen *et al.*, 2005).

Prior studies have noted the importance of different waveform shapes and dynamic control response on bead and fusion characteristics (Quintino and Allum, 1984; Smati, 1986; Rajasekaran, 1999; Joseph *et al.*, 2005). For this reason, an important goal of this

study was the optimisation of the waveform pulse parameters for improving the control and overall system performance in WAAM. Usually, modern digitally controlled GMAW power supplies offer a vast number of synergic algorithms available from a large database of welding programs, leading to additional difficulties in selecting the optimal conditions for a certain target application.

The objective of this study was to investigate the influence of the CTWD on the output and waveform characteristics of the power source when different welding programs were employed. The study gives an indication of how sensitive welding programs are to variations in CTWD which may naturally occur during manufacturing. Another objective was to evaluate the effect of these changes in CTWD on weld bead and fusion characteristics.

The current study found a very significant effect of CTWD on AIP for all the welding programs applied (see Figure 4.19 in page 137). The variation observed in AIP for each welding program resulted from an interesting, and very unique interplay between V_{AVG} and I_{AVG} (see Figure 4.18 in page 136). This result can be explained on the grounds of different static volt-ampere characteristic (VI) and control logic responses provided by each individual welding program.

The *Pulse Rapid Arc* (P13) program shows a very fast increase of AIP with CTWD as a result of an increase in V_{AVG}, since I_{AVG} is held nearly constant. The AIP showed a maximum percentage difference of about 37 % from 10 to 20 mm CTWD. Note that all primary parameters of the current waveform, such as I_p, I_b, T_p, T_b, I_p/I_b, T_p/T_b, f and LDC are held constant while CTWD is varied (see Figures L 1 and L 2 in page 399). Therefore, one can assume that the increase observed in arc-length due to an increase of wire burn-off rate (*BR*) is caused primarily by the resistance heating terms in equation (5.2), since no coupling effect was observed between the wire feeder and the wire burn-off rate. This explanation is supported by the fact that the measured DR_{wire} values were kept nearly constant and thus independent of changes in CTWD (see Table I 9 in page 373). It is important to point out that stable and controlled ODPP metal transfer conditions were achieved throughout this study (see electrical transients in Figure 4.28 in page 143). From the process control standpoint, these results demonstrate that *Pulse Rapid Arc* (P13) provides excellent arc welding characteristics at constant current (CC).

This mode allows TS to be significantly increased under favourable conditions of low HI (see Figure 4.19 in page 137).

The welding program *Pulse Argon Mix* (P95) showed that CTWD is in a significant inverse relationship with I_{AVG}, whereas there is negligible effect on V_{AVG}. As a result, AIP shows a negative linear association with CTWD throughout the entire range studied, with a maximum percentage decrease of 16.5 % (see Figure 4.19 in page 137). The constant voltage (CV) behaviour with increased CTWD required a constant control of the wire burn-off equilibrium conditions, achieved by dropping I_{AVG} (see Figure 4.18 in page 136). Note that DR_{wire} was kept nearly unchanged (see Table I 13 in page 375). The built-in synergic control feature of *Pulse Argon Mix* (P95) uses a Type I control logic (see Figures L 1 and L 2 in page 399). In view of these results, the use of *Pulse Argon Mix* (P95) in WAAM might be less desirable than *Pulse Rapid Arc* (P13) since the integrity of the parts produced can be seriously compromised. Lack of fusion defects, caused by rapid current swings during welding, are more likely to occur due to natural variations in the CTWD during processing.

The dynamic responses to variations in CTWD were very similar in both *Pulse Crisp* (P12) and *Pulse Soft* (P14) welding modes. It is interesting to note that V_{AVG} is constant up to 18 mm CTWD, having a linear positive relationship thereafter. At the same time, I_{AVG} decreases fast up to 18 mm CTWD but becomes independent thereafter. As a result, the AIP curve shows an inflection point at 18 mm CTWD. These results confirm that the static volt-ampere characteristic (VI) of these welding programs behaves as a constant voltage (CV) controlled source up to 18 mm CTWD, changing to constant current (CC) controlled thereafter. The built-in synergic control feature of *Pulse Crisp* (P12) and *Pulse Soft* (P14) uses a Type II control logic (see Figures L 1 and L 2 in page 399).

Overall, the effect of CTWD on bead and fusion characteristics is significant for all the different waveform characteristics. In general, narrower and taller beads are obtained with increased CTWD. However, it is apparent that H is less sensitive to different pulse conditions than W (*cf.* Figures 4.20(a) and (b) in page 137). When considering all welding programs, the variation in W is within 10 % from the average, whereas H values shown to be far less spread out. The lower AIP delivered by *Pulse Rapid Arc*

(P13) can possibly explain the narrower and taller beads obtained up to about 13 mm CTWD. Note, however, that the effect of large AIP associated with *Pulse Rapid Arc* (P13) at increased CTWD does not show improvement in the wetting behaviour. This effect can be explained by the longer arc-length and wider arc-spread associated with increased V_{AVG}, and thus arc-length. Longer arc-lengths typically produce shallower penetration depths as a result of the lesser concentration of heat in the weld pool and base plate, as reported elsewhere (Nagesh and Datta, 2002). This effect results in considerably colder and smaller weld pools with poorer wetting behaviour, as demonstrated in Figure 4.30 (page 144).

It is encouraging to compare the W and H results obtained in this study with those obtained in section 4.1.1.1, where P19 was used (see Figure 4.1 in page 126). Contrary to expectations, the study carried out with P19 did not confirm the pattern revealed in this section. The notably wider and taller profiles obtained with P19 can be explained by the larger cross-sectional areas produced with thicker WD, when compared with smaller wires.

Another important finding was the significant influence of the welding operating mode up to a CTWD of 16 mm on the fusion characteristics, becoming less sensitive thereafter. In particular, the fusion characteristics of P14, such as RR, P, D and A_1, indicate a maximum percentage increase of 60.3 %, 24.6 %, 41.9 %, and 51.0 %, respectively, when compared with *Pulse Rapid Arc* (P13) at 10 mm CTWD. The higher fusion characteristics of P14 can be justified by the higher AIP, which is approximately 14 % higher than that of *Pulse Rapid Arc* (P13) for the same CTWD. The influence of the current pulse waveform parameters of P14, such as high I_p, I_b, T_p and T_b, may also explain these observations (see Figure L 1 in page 399). When a comparison is made between fusion characteristics of 1.2 mm and 0.8 mm WD, namely RR, P and D, these values increase about 2-fold with large WD, whereas A_1 increases about 5-fold, for a constant CTWD of 10 mm.

5.2.1.3 Current waveform modulation

The investigation was aimed at determining the advantages gained by introducing customised welding current waveforms for the optimisation of the weld bead, fusion,

and metal transfer characteristics. The influence of primary welding current parameters such as I_p, I_b, T_p, T_b, as well as complementary ones such as *f* and LDC, were examined using *non-adaptive control* mode. Preliminary experiments were carried out to examine whether the metal transfer behaviour, and therefore the weld bead quality of single layer deposits, were influenced by CTWD in *non-adaptive control* mode.

The main goal of this study is the understanding of how individual pulse parameters affect the bead, fusion, and transfer characteristics, in order to enable the selection of a suitable and robust combination of pulse parameters for WAAM. From the operational point of view, it would be of particular interest to find an optimum combination of pulse waveform characteristics that could be at some extent reproducible, and applied to any other power source with pulse modulation capability.

The influence of CTWD on the arc welding stability and on the top surface quality of the beads is very significant in *non-adaptive control* mode (see Figure 4.25 in page 141), whereas its effect appears less important when *adaptive control* mode is applied using *Pulse Rapid Arc* (P13).

Metal transfer shows to be dominated by random short circuiting (SC) mechanism when *non-adaptive control* mode is employed at short CTWD. These SC events can be observed in the electrical transient shown in Figure 4.26(a) in page 142, and identified by sharp drops in V_{inst} with a commensurable increase in I_{inst} at the same instant of time. This cause and effect relationship is typical of modern microcomputer process control power supplies with a built-in arc-length regulation control feature, which applies a short pulse of high current, *i.e.* dip pulse, to clear the occurrence of a SC if the arc voltage drops below a predetermined threshold (Praveen *et al.*, 2005). The pattern of these SC excursions is notably captured on the scatter plot shown in Figure 4.26(b) in page 142, where both instantaneous voltages and currents are represented at every instant in time. The point cloud with high point density located in the low voltage *ohmic* region that stretches along the current range, indicates that metal transfer occurs predominantly by short circuit. In contrast, more stable ODPP metal transfer conditions were established with increased CTWD. The transition in metal transfer from SC to more stable and reproducible ODPP transfer conditions is further substantiated by the captured electrical transients. In Figure 4.27(a) in page 142 it can be seen that droplet

detachment occurs at the same frequency as the applied pulsed current, *i.e.* ODPP. The improvement in metal transfer behaviour is supported by Figure 4.27(b) in page 142, where it can be seen that V_{inst} and I_{inst} pairs are now absent of the lower voltage ohmic region. This effect leads to a significant improvement in the metal transfer conditions, and therefore in the quality of the weld beads produced (see Figures 4.25 in page 141).

The rough and rippled weld bead surfaces formed at short CTWD values were caused by the random SC incursions as a result of the electrode dipping into the molten pool. The surface quality of the weld beads improved dramatically with higher CTWD. The transition to ODPP metal transfer regimes produced much finer and smoother rippled surfaces, as a result of the impingement of filler droplets onto the melt pool at higher frequency (see Figure 4.25 in page 141).

Another important result in this investigation is that weld bead characteristics, such as bead W, H and CA, appear to be less sensitive to CTWD when *non-adaptive* conditions are used (see Figure 4.25 in page 141), in comparison with the *adaptive control* provided by *Pulse Rapid Arc* (P13) (see Figure 4.30 in page 144). The weaker dependence of W and H on the CTWD in *non-adaptive control* mode can be attributed to a significantly smaller variation in V_{AVG} than that obtained in *adaptive control* for the same change in CTWD (see Table 4.1 in page 141). The higher concentration of heat at the bead centreline, associated with the short arc-length in *non-adaptive control*, can considerably improve the wetting action. This observation can be further substantiated by the fact that all fusion characteristics associated with this welding mode, such as RR, P, D and A_1, increased with an increase in CTWD. As a consequence, this result suggests that the increased heat transfer rate to the weld bead and base plate in *non-adaptive control*, as a result of a shorter arc-length, is a contributing factor to higher energy density. Another interesting finding in this analysis was that A_2 increased markedly with CTWD in *non-adaptive control*, suggesting therefore a coupling effect between the wire feeder and the wire burn-off rate (see Figure 4.25 in page 141). This consideration could also explain the smaller sensitivity of V_{AVG} to changes in CTWD observed in this type of control (see Table 4.1 in page 141).

The effects of pulse parameters of customised current waveforms on the metal transfer, weld bead, and fusion characteristics were investigated using *non-adaptive control*

mode. The results of this study indicate that weld beads and process characteristics are considerably influenced by gradually narrower and taller current pulses (see Figure 4.31 in page 145). An analysis of the transfer characteristics suggests that SC dominates at low I_p/T_p ratios, whereas highly desirable ODPP conditions are established with progressively higher I_p/T_p. The gradual transition to ODPP with higher I_p/T_p ratios can be attributed to an increase in the AIP due to increasing V_{AVG}, as shown in Figure 4.33 in page 147. The increase in arc-length is expected, since the wire burn-off rate is strongly influenced by the primary welding parameters of the current waveform, as shown in equation (5.2) in page 198. It is interesting to note that SC metal transfer conditions are predominantly determined by low V_{AVG} and high I_{AVG} at low I_p/T_p ratios, as observed in Figure 4.33(a) in page 147.

The influence of I_p/T_p on bead and fusion characteristics appears to be substantial. Overall, wider and shorter weld beads are produced at the mid-range for I_p/T_p of 224 (see Figure 4.34(a) in page 148). Fusion characteristics, such as RR, P and A_1 also appear to increase for the same I_p/T_p ratio, suggesting that a higher melting efficiency is achieved under these processing conditions (see Figures 4.34 and 4.35 in page 148). The drop in the fusion characteristics observed at higher I_p/T_p ratios can be explained by the lower energy density, and therefore lesser concentration of heat in the weld pool and base plate due to the longer arc-length and arc-spread effects. It is interesting to see that A_2 increases slowly with I_p/T_p, suggesting an increase in WFS with I_p/T_p (see Figure 4.35(b) in page 148).

This study has presented evidence that stable welding arc characteristics are greatly dependent on a certain minimum threshold I_b, independently of T_p and I_p (see Figure L 6 in page 401 and 4.36 in page 149, respectively). When this minimum threshold condition is not met, the welding arc momentarily extinguishes as current undergoes I_b, causing V_{inst} to increase very rapidly, up to the open-circuit voltage (OCV). The welding arc is eventually re-established when the wire electrode short circuits the base plate, and I_{inst} increases swiftly. Pronounced rippled surfaces are produced with weak bonding characteristics between the bead and the substrate, under unstable arc characteristics (see Figure L 6 in page 401). The effect of T_p/I_b ratio on bead characteristics was very small.

It is interesting to see that increased I_p/I_b ratio appears to compromise the weld bead straightness (see Figure 4.36 in page 149). This effect can be explained by a considerable lack of directional control over the stream of droplets, as a result of arbitrary droplet detachment while current undergoes I_b, due to the formation of large droplets (see Figures 4.37(c) and (d) in page 150). The large variation in the arc-length with increased I_p/I_b can be considered the main factor influencing the degree of straightness of the weld bead (see Figure 4.38 in page 151).

The current *f* was found to have a small influence on the welding stability, and therefore on the quality of the beads produced (see Figure L 11 in page 404). Although inadvertent droplet detachment appears to occur during I_b period, the surface quality of the weld beads do not seem to be affected. Both W and H appear to be insensitive to *f* variations, however, the weld bead fusion characteristics, such as RR, P, D and A_1 indicate a slow increase with increased *f*.

5.2.2 Cold metal transfer

5.2.2.1 Influence of process parameters on weld bead and plate fusion characteristics

The objective of this research is focused on ascertaining the influence of process control parameters of the CMT welding process, such as arc-length control (ALC), dynamic correction (DC_{orr}), and CTWD on the weld bead and plate fusion characteristics of single layer welds.

This investigation shows that all of the above control parameters play a significant role in determining the electrical output response of the power source, and therefore cannot be neglected for practical bead geometry considerations.

The current study found that ALC has a positive linear effect on P_{AVG}, showing a 70 % difference in P_{AVG} values across the range of ALC (see Figure 4.41(b) in page 153). The increase in P_{AVG} is explained by a marked increase in the welding current *f*, V_{AVG} and I_{AVG}, and consequently in P_{AVG} (see Figure 4.41 in page 153). Another interesting finding was that ALC has a significant positive influence on the WFS. This result suggests a coupling effect between ALC and the wire feeder, which explains the

observed increase in DR in the same proportion as the WFS. Overall, these results show that ALC is a critical parameter in controlling the nominal arc-length, average power, and deposition rate. The results obtained from the electrical transients, as was discussed previously, are consistent with those of weld bead and fusion characteristics. The increase in W with ALC indicated a maximum percentage change of around 36 % (see Figure 4.42(b) in page 153). This effect can be attributed to a significant increase in the arc temperature, HI and arc-spread due to increased P_{AVG}. The higher HI leads to a higher heat content of the weld pool, causing the interfacial tension and viscosity to reduce, while wetting properties are improved. The insensitivity of H to ALC appears to result directly from an increase in WFS. Similarly, the increasing P_{AVG}, HI, and arc-spread leads to increasing fusion characteristics, such as RR, P, D and A_1 (see Figure 4.43 in page 154). Fusion characteristics have shown to be remarkably sensitive to ALC. As an example, A_1 showed a maximum percentage change of about 200 %. Interestingly, the maximum change of about 24 % for A_2 was consistent with the observed WFS variation.

In this study, DC_{orr} was found to affect both the P_{AVG} and WFS, however, to a much lesser extent than ALC, *cf.* Figures 4.44(b) in page 155 and 4.41 in page 153. The reduction in P_{AVG} results from a noticeable drop in I_{AVG} with DC, whilst the variation in the average arc-length (or V_{AVG}) is much smaller (see Figure 4.44 in page 155). As expected, DR decreases with increased DC_{orr} in the same proportion as WFS. This effect shows good agreement with the observed drop in A_2 (see Figure L 21(c) in page 410). The current *f* is nearly constant with DC_{orr}. It was also shown that W decreases very slowly with DC_{orr}, whereas H appears stable and insensitive to such variations. The observed trend in W and H are in good agreement with the slow drop in both P_{AVG} and WFS, as seen in Figure 4.44(b) in page 128. An important finding was the fact that fusion characteristics, such as RR and D, are insensitive to variations in DC_{orr} (see Figure L 21 in page 410). This effect might be related with a decrease in both fusion (A_1) and deposition (A_2) characteristics in similar proportions, since P_{AVG} and WFS also decrease. Although there is some scatter, P and A_1 appear to drop very slowly with increasing DC_{orr}. This result also accords with earlier observations, which showed a slow decrease in P_{AVG}. In general, DC_{orr} has a relatively moderate influence in arc power and deposition rate, due to a large variation in I_{AVG}. However, there is very little

effect of DC on the arc-length, bead and fusion characteristics.

Another major finding was that CTWD has an important effect on P_{AVG} and WFS (see Figure 4.46(b) in page 156). It should be noted, however, that the dynamic electrical response of the CMT power source to variations in CTWD is typical of a CC controlled welding power source (see Figure 4.46(a) in page 156). The maximum percentage change observed in V_{AVG} is about 10 %, while I_{AVG} remains nearly constant throughout the measured CTWD range. The P_{AVG} increases with CTWD with a maximum percentage change of about 11 %. It is interesting to note how the burn-off rate is controlled by a variable wire feeder that assists in maintaining a nearly constant arc-length (see Figure 4.47(a) in page 156). The maximum mean percentage increase in W and H with CTWD was 7 % and 19 %, respectively. The positive variation in W and H with increased CTWD can be explained by the higher deposition rate, P_{AVG}, HI, and, to some extent, due to the arc-spread. The fusion characteristics, such as RR, P, D, and A_1 show a noticeable increase with increased CTWD, particularly at high CTWDs. The maximum percentage increase in A_1 is approximately 33 % for variations in CTWD between 13 mm and 17 mm (see Figure L 22(c) in page 411).

It is encouraging to compare the V_{AVG} results obtained in CMT with those obtained in *Pulse Rapid Arc* (P13), in the same range of CTWD. Although both of these systems operate in a constant current (CC) static output volt-ampere characteristic mode, a considerably larger variation in the arc-length is observed in *Pulse Rapid Arc* (P13) than in CMT. The maximum percentage change in V_{AVG}, is 30 % and 10 % for P13 and CMT, respectively, for a constant interval of CTWD between 10 mm and 18 mm.

5.2.2.2 Influence of wire feed speed and shielding gas composition on electrical transients

The first objective of this study was to determine the relationship between WFS and electrical outputs, such as V_{AVG}, I_{AVG} and AIP. The second objective was to examine the influence exerted by different shielding gas mixtures, *i.e.* Ar/CO_2 (8%), Ar/CO_2 (20%), and Ar/CO_2 (5%)/O_2 (2%), on the above electrical transient profiles. Additionally, the effect of different shielding gas compositions on the stability of the welding arc and metal transfer behaviour was examined with scatter plots.

In the current study, a positive linear correlation between AIP and the WFS was observed, regardless of the gas composition employed (see Figure 4.48(b) in page 157). Moreover, higher AIP values were obtained in argon blends with higher concentrations of carbon dioxide, *i.e.* Ar/CO_2 (20%), when compared with the remaining compositions examined in this study, for all WFS. The AIP increased to some extent with small additions of oxygen, *i.e.* Ar/CO_2 (5%)/O_2 (2%), when compared with Ar/CO_2 (8%). It is interesting to note that the observed increase in the AIP due to increased CO_2 content was mostly determined by a higher sensitivity to V_{AVG}, rather than I_{AVG} (see Figure 4.48(a) in page 157). In average, a percentage increase in V_{AVG} of 10.6±0.7 % was observed when using Ar/CO_2 (20%), in comparison with Ar/CO_2 (8%). This percentage difference observed in V_{AVG} became 13.6±2.0 % when compared to a tri-mixture Ar/CO_2 (5%)/O_2 (2%), for the same operating conditions. This finding corroborates the ideas of Pires *et al.* (2007), who suggested that the arc-length, and thus V_{AVG}, increases with the oxygen potential of the shielding gas mixture in GMAW, for the same current intensity. For shielding gas mixtures with CO_2 contents of 25% or less, the following empirical formula is used for estimating the oxygen potential of a shielding gas (Smith, 1978; Stenbacka and Persson, 1989):

$$Oxygen\ potential\,(\%) = O_2 + \frac{CO_2}{2} \tag{5.4}$$

Shielding gas mixtures with higher CO_2 contents lead to an increase of the oxidation potential, which is further substantiated by a larger oxidising and reactive atmosphere created by the CO_2 dissociation reaction resultant from $CO_2 \rightarrow CO+O$ occurring in the high temperature arc plasma column.

The electrical transients and scatter plots data of CMT showed that neither the welding arc stability nor the reproducibility were significantly affected by different shielding gas mixtures (see Figure L 23 to L 25 from page 412 to page 416). It is interesting to note that inadvertent droplet detachment appears to occur at low and intermediate WFS regimes, for all gas mixtures. These events occur randomly and immediately after the "arc-on" phase is established, which are characterised by sharp V_{inst} incursions to higher voltage regimes (voltage spikes). The I_{inst} is insensitive to these voltage variations. It is encouraging to compare the scatter plots generated by CMT with those of GMAW-P.

As expected, the mapping pattern across the V_{inst} versus I_{inst} region obtained for the CMT welding process is completely different to that of GMAW-P, owing to distinct metal transfer behaviour, *cf.* Figures 4.32 in page 146 and L 23 in page 412).

5.2.3 Effect of cold metal transfer and pulsed-current gas metal arc welding on transients, bead and plate fusion characteristics

One of the main conclusions that can be drawn from the foregoing discussion is that, although utilising the same underlying GMAW principles, *i.e.* where a continuous and consumable wire electrode and a shielding gas are fed through a welding torch, there are significant differences between the CMT and GMAW-P systems. Three of the most important are the built-in process control, the electric output, and the metal transfer mechanism. It is therefore reasonable to expect them to play an important role in determining the weld bead dimensions and fusion characteristics.

For instance, the electrical transient response of CMT is different from that of GMAW-P in a number of respects at constant WFS (*cf.* transients in Figure 4.55 in page 162). For the same acquisition-period, the welding arc developed by CMT combines a considerably lower average voltage (V_{AVG}) and higher current (I_{AVG}), than in GMAW-P. The effect of each of these GMAW processes, and thus metal transfer mechanisms, on V_{AVG} and I_{AVG} becomes noticeable when plotted as a function of the WFS_{actual} (see Figures 4.54(a) and (b) in page 162). Contrary to expectations, the most interesting finding of this study was that no significant differences were found between the AIP in both welding processes, for all the WFS ranges considered in this study (see Figure 4.54(c) in page 162). The conclusion that should be drawn is that the weld heat input delivered by the two processes is identical under the welding conditions described in section 3.8.4.2.

Although, the findings of the current study do not support some of the previous research performed in aluminium and steel (Pickin and Young, 2006; Feng *et al.*, 2009; Lorenzin and Rutili, 2009), they are broadly consistent with those of Colegrove *et al.* (2009). In the latter study an identical width of the tensile residual stress peak in the longitudinal direction was found for both CMT and GMAW-P processes, suggesting that an identical HI was applied. The present study produced results which corroborate the observations

made by Colegrove *et al.*, since the width of the tensile peak should increase with increased HI. Nevertheless, the results of this investigation run counter to the strong linear relationship between HI and A_1 reported by Colegrove *et al.* (2009), as seen in Figure 4.53 in page 160. The results of the present study show that weld fusion characteristics, such as RR, P, D and A_1 are significantly more sensitive to the welding process used, *i.e.* CMT and GMAW-P, than the weld bead shape features, such as bead W, H and CA (see Table 4.2 in page 161). Overall, wider (2 %) and shallower (9 %) weld beads were produced by GMAW-P when compared with CMT, for the welding conditions used in this study. The weld bead fusion characteristics, such as RR, P, D and A_1 have been shown to be greatly affected by GMAW-P process indicating a percentage increase of 87 %, 100 %, 65 %, and 77 %, respectively, when compared with CMT. These results may be associated with the strong link between processing conditions, particularly as a result of distinct metal transfer mechanisms, and weld bead features. The main characteristic that distinguishes the CMT welding process from that of GMAW-P is the mechanism by which transfer occurs.

In CMT the controlled metal transfer occurs during the short circuit phase by a dip metal transfer mechanism, whereby the molten droplet formed on the end of the wire electrode is transferred to the molten pool by surface tension at relatively low current levels (see background information in section 2.6.2 in page 62). In contrast, a controlled spray transfer mode is achieved in GMAW-P at an average current such that globular transfer mode is usually observed. Under suitable processing conditions, a free-flight metal transfer mode occurs across the welding arc in GMAW-P, usually under stable and highly desirable ODPP transfer conditions. Therefore, the crucial role of metal transfer conditions in determining the ultimate bead and fusion characteristics is likely to be significant, as a result of complex heat and fluid transport phenomena.

Compared with CMT welding, the longer arc-lengths associated with GMAW-P processes typically produce wider and shorter weld beads, as demonstrated in Table 4.2 in page 161. This effect is due to the improvement of the wetting and spreading behaviour of the liquid on the solid substrate. The increase in the rate of reduction of the interfacial tension with temperature is usually controlled by the arc power and arc spread (Nagesh and Datta, 2002).

Compared with the CMT welding process, it seems possible that the substantial increase in the fusion characteristics observed in GMAW-P can be justified on the basis of distinct heat and fluid flow conditions introduced by the two processes. Typically, a significantly higher I_p is applied in the current waveforms of GMAW-P control systems, when compared to CMT, whereas I_b is held at a relatively low current level sufficient for maintaining arc stability, *cf.* Figures 4.55(a) and (b) in page 162.

Under these metal transfer conditions, a new balance of forces acting on both the liquid droplet and molten pool is expected to develop. It is well established that the droplet dimensions are strongly influenced by the background conditions of the current waveform, *i.e.* I_b and T_b (Allum, 1983). Nevertheless, it is expected that the molten droplet rapidly forms into its final free-flight nominal dimension during the increase in current (slope-up period). When I_p is reached, the droplet is pinched off towards the weld pool by the action of an inward radial electromagnetic force, gravity, and plasma drag shear force. At the point of detachment, the droplet is accelerated downward by gravity, but more importantly by a normal plasma arc force acting in the direction of the weld pool. The acceleration arising in the detaching drop across the arc plasma is mainly determined by the Lorentz force ($\propto I^2$), according to equation (5.3) in page 202. Assuming that the plasma has a conical shape, and due to a divergent current flow, an axial pressure gradient is generated. This pressure gradient induces a rapid downward flow of the ionized gas that expands approximately 20-fold in volume at the top of the arc due to the arc heating, which may aid by accelerating the droplets in transfer (Greene, 1960; Lim *et al.*, 2009).

Additionally, the detached droplet is superheated from the surface inwards while accelerated and transferred through the centre of the high temperature arc plasma from the electrode to the workpiece. Hence, the base plate liquid film, which is continuously heated by the arc heat flux, is elastically deformed during the impact caused by the mass, momentum, and the thermal energy transferred by the superheated free-flight droplet onto the base metal at a certain frequency (Wang and Tsai, 2001). However, counteracting hydrostatic and surface tension forces in the molten pool are not sufficient to allow the rapid elastic recovery in between individual impingement, and as a result a deep weld penetration will be formed. The large fusion characteristics observed in

GMAW-P welds, but not as evident in CMT welds, are determined by the impinging kinetic force of the droplets and its frequency, thermal energy provided by the superheated droplet and arc flux, and by the effect of the temperature-dependent coefficient of surface tension (Marangoni effect).

5.3 Multi-layer welds

5.3.1 Influence of process parameters on weld bead characteristics

The purpose of this study was to investigate in greater depth the effects of primary welding process parameters, such as WFS, TS, WFS/TS and WD on the evolution of the weld bead characteristics, *i.e.* bead W and H, in vertical multi-layer overlapped deposition. It is yet another objective of this study to provide additional insight on how multi-layer responses, such as W_{eff}, SW_{av} and MDE are affected by new processing conditions, *i.e.* process parameters, temperature of the substrate, or different materials.

In this study it was found that the weld bead characteristics, such as W_n and H_n (Delta-z), are more greatly affected when the first welded layer is deposited in multi-layer deposition (see Figure 4.62 in page 167). The analysis also established that multi-layer output characteristics, namely, W_{eff}, SW_{av} and MDE are especially sensitive to the effects of welding parameters as well as temperature of the previous as-deposited layers. What one should recall here is that by holding the WFS/TS ratio constant, the HI is also maintained at approximately constant level.

The influence of WFS/TS ratio on bead characteristics at constant WFS was expected, as larger constant cross-sectional areas were deposited with decreased TS. This effect can be clearly observed in the sequence of optical macrographs of single layer welds shown in Figures 4.50 (page 159) and 4.52 (page 160) produced with CMT and GMAW-P processes, respectively. The influence of WFS on bead characteristics at constant WFS/TS (*i.e.* heat input) is explained by the fact that wider and shallower weld beads are produced as a result of a commensurate increase in WFS (*i.e.* AIP) and TS. This effect is clearly observed in the sequence of optical macrographs of single layer welds depicted in Figure 4.49 (page 158) obtained with both CMT and GMAW-P processes using a 0.8 mm wire diameter. However, it should be pointed out that the

latter effect was not observed from medium to high WFS regimes for larger diameter wires (1.2 mm), *cf.* Figures 4.49 in page 158 and 4.51 in page 159.

The increase in W with commensurable decrease in H, observed in both CMT and GMAW-P for the smaller diameter wires, can be explained on the grounds of a significant reduction in the interfacial tension and viscosity of the weld pool caused by increased arc power, and therefore due to the improvement in the wetting behaviour. However, these data must be interpreted with caution because these results cannot be extrapolated to larger WDs and high WFSs. A significant increase in the aspect ratio (P/W) of the penetration profile is observed with larger WD at very high WFSs. This effect is explained by a developing keyhole phenomenon due to the significantly higher current densities associated with high WFSs (currents over 320 A), as seen in Figure 4.51 (page 159). As mentioned before, this phenomenon causes the formation of a distinct centreline papilla (*i.e.* finger-type) penetration profile with commensurate changes in W and H.

The results of this study also show that multi-layer weld bead characteristics, such as bead W_n and H_n, are greatly affected in the first and second deposited layer, achieving quasi steady state conditions thereafter (see Figure 4.65 in page 168). There are two possible explanations for this result: the first reason can be attributed to the fact that the first layer is usually deposited onto a flat solid surface of the substrate, whereas the subsequent deposition passes are repetitively deposited onto near curvilinear profiles, *cf.* dashed contour surfaces where the 1st layer, 2nd layer, and so forth are deposited onto in Figure 4.64 at T_{sub}=40 °C in page 168; a second explanation for this effect might be that a faster cooling occurs when depositing the first layer onto the base plate, as a result of a larger volume heat sink, *cf.* shape of the first layer in the sequence presented in Figure 4.64 at different T_{sub}. Thus, another important finding in this study was that T_{sub} affects the interplay between W_n and H_n, as seen in Figure 4.63 in page 167. The H of the first deposited bead is always higher than that for the succeeding ones. This evidence is consistent with the previous argument, which considered that the heat sink volume was a critical factor in determining the weld bead shape. A maximum percentage change of about 13 % was found in the first layer with a T_{sub} change from 40 to 350 °C.

The results of this study showed that all multi-layer characteristics, such as W_{eff}, SW_{av} and MDE, are significantly influenced by T_{sub} when all the other parameters are held constant (see Figure 4.64 in page 168). It is interesting to observe that MDE improves significantly with increased T_{sub}. This results from the achievement of wider effective wall widths as a result of a noticeable improvement in the SW_{av} in the *z* direction. The effect can be associated with the interfacial tension between the contact surfaces, which is expected to decrease with increasing T_{sub}. The increase of T_{sub} acts to reduce the surface tension of the molten pool and thereby improve the wetting and spreading behaviour of the liquid onto a flat solid surface in the first layer, or onto near curvilinear profiles in the second and so forth layers. This is further substantiated by the observation that the length of the contact line between the first deposited bead and the substrate shows to gradually increase with higher T_{sub} (see Figure 4.64 in page 168).

Another very interesting aspect in this study was that the multi-layer sidewall surface facets were found to be uniform and very reproducible along the *x*-direction when constant AIP and HI were applied, irrespective of T_{sub}. The results show a multi-layer deposition pattern with very little deviation from the weld centreline at any *yz*-plane cross section made along the *x*-direction (see Figure 4.66 in page 169).

In this study, the AIP and TS appear to be dominating factors in determining the surface waviness of the sidewall surface facets in the *x*-direction (parallel to deposition), at constant WFS/TS and HI (see Figure 4.67 in page 170). This seems to be a particularly interesting result since it establishes that the SW_{av} is independent of the amount of deposited metal per unit length (WFS/TS) in the *x*-direction, and thus heat input. This finding is in good agreement with that observed for single layers deposited onto flat surfaces (see Figure 4.49 in page 158). The decrease in SW_{av} in the *z*-direction is probably justified by the considerable improvement in the wetting behaviour due to increased AIP, and most probably further enhanced by the curvilinear shape of the previous beads were fresh layers were deposited onto.

In this study, higher T_{sub} were found to increase the surface waviness of the sidewall surface facets in the *x*-direction, particularly at higher AIP, with other deposition conditions being kept identical to the previous study (*cf.* trial 27 in Figure 4.68 on page 171, and trial 9 in Figure 4.67 on page 170). A possible explanation for this might be

due to the heat sink phenomenon, which can hinder the heat transfer rate considerably. In general, the small heat dissipation rates associated with multi-layered structures lead to increased solidification times. As a result, additional difficulties in heat transfer conditions by conduction are expected to arise when lower temperature differences between the weld pool and T_{sub} are established, *i.e.* lower thermal gradient. It is also interesting to observe from the thermal-infrared imaging results shown in Figure 4.70 (page 172), that despite using processing conditions which offer a constant HI, heat dissipation appears to be more difficult when higher AIP is applied, which results in larger weld pools with improved wetting behaviour (see Figure 4.70 in page 172). The deposition of multi-layer welds at higher substrate temperature, with other deposition conditions held constant, can therefore be explained by a loss of control and directionality over the larger weld pool size at high speed, particularly of the contact line in the *x*-direction.

The results of this study indicate that TS has a strong influence on SW_{av} particularly at lower TS values. The higher SW_{av} observed in the *z*-direction can be partially explained by the fact that larger deposited cross sectional areas are obtained when using lower TS values at constant WFS, and thus higher WFS/TS and HI. Bearing in mind that slower TS are associated with larger deposited volumes per unit length, and therefore with higher line energy when the WFS is held constant (see Figure 4.71 in page 173). Another explanation for this might be that the welding arc heat source is predominantly established between the consumable electrode wire and the reinforcement area (A_2), as a result of the larger A_2 produced at lower TSs. This can lead to a thermal cushioning effect that will probably influence and hinder the heat to be transferred to adjacent areas in the base plate, and therefore the wetting behaviour. The observed increase in SW_{av} with increased WFS in the *z*-direction can be explained by the increase in importance of this cushion effect with increased WFS (see Figure 4.72(a) in page 173). The perceived decrease in SW_{av} with increased TS can be explained by the deposition of less volume of material per unit length, at constant WFS.

It comes as no surprise that the range of achievable W_{eff} increases with higher WFS. The higher arc power, HI, and arc spread most probably play an important role in improving the wetting behaviour of the liquid weld pool onto the previous solid layer.

This experiment suggests the use of higher WFSs for obtaining larger W_{eff} (see Figure 4.72(b) in page 173). It is encouraging to compare Figures 4.72(a) and (b), and come to the conclusion that for increasing the metal deposition efficiency (MDE) of multi-layer walls with large W_{eff}, the selection of suitable combination of WFS and TS values becomes necessary. This investigation demonstrated that optimal welding conditions can be determined for producing target geometries made of carbon steel which range from 2 mm to 9.5 mm W_{eff}, with MDE over 90 %. Thus it comes as no surprise to find that combinations of low WFS (*e.g.* 3 m min^{-1} WFS) and TSs over 0.2 m min^{-1} should be applied for producing thin sections with high material utilisation efficiencies (see Figure 4.74 in page 175).

It has been shown that SW_{av} decreases when smaller wire diameters are utilised at constant WFS, as seen in Figure 4.73(a) in page 174. This effect is expected, and can probably be ascribed to the different mass and energy balances associated with different WDs. For instance, higher deposition rates are achieved with larger diameter wires at constant WFS as a result of the higher melting energies, *i.e.* power, applied per unit time for melting the extra volume of solid wire electrode. This leads to the conclusion that for constant WFS and TS settings more material is deposited per unit length with larger WDs, which results in different cross-sectional areas.

The results of this study show a stronger dependence of SW_{av} on TS in multi-layer builds for stainless steel (SS) material, compared to carbon steel (CS) or aluminium (Al), as seen in Figure 4.73(b) in page 174. The more gradual decay in roughness observed for SS appears difficult to explain, though a possible explanation for this might be related with the intrinsic thermophysical properties of the material that formed the melt pool. The relatively higher viscosity of the liquid can probably explain the limited wetting due to the low flow behaviour of the weld pool, leading to a sluggish growth of the weld pool (Mills, 2002).

The narrower and taller weld beads obtained in the overhead welding position and first layer can be explained by an increase in the force due to gravity, which appears to assist the flow of the liquid downward, as opposed to the force acting upward due to surface tension (see Figure 4.75 on page 176). The tendency for weld pool sagging increased with multi-layer deposition, as seen in Figure 4.76 in page 177. Sagging was probably

caused by gradually less efficient heat transfer conditions by conduction through the base plate with progressive deposition, hence causing a significant increase in the downward force due to gravity as a result of an increasingly larger volume of the weld pool.

5.4 Process modelling

The accurate statistical process control models developed in the present study for the CMT process can be used for predicting the weld bead geometry and plate fusion characteristics of single and multi-layer deposits. From the discussion in section 5.2.2, it can be concluded that process control parameters, such as ALC, DC_{orr}, and CTWD are key in determining the weld bead and fusion characteristics. Nevertheless, for simplicity, the process control factors selected in this study for developing the process models were WFS, WFS/TS and WD, while the ALC, DC_{orr} and CTWD were all held constant. The proposed control algorithms were developed for mild steel using the empirical data generated based on systematically designed experiments.

The effects of interactions of factors such as WFS, WFS/TS and WD, on the weld bead and plate fusion characteristics of single and multi-layer deposition responses, namely, bead W and H, RR, P, D, DR, CA, A_1, A_2, AR, HI, HSL, SW_{av}, W_{eff} and MDE, were examined using the response surface methodology (RSM). The functional relationships between parameters and weld bead characteristics were determined by the response surface models that were fitted to experimental data provided by the response surface design (defined in sections 3.9 in page 108 and 3.10 in page 110). The developed models were checked for their adequacy and significance, and used for simultaneous process optimisation of several responses.

5.4.1 Analysis of variance

In general, the results of this study indicate that all adequacy measures show good R^2 statistics with values over 0.9 for all responses, except for the case of the multi-layer response MDE. The adequate precision statistic shows to be far greater than 4 for all responses in this study, indicating good model discrimination.

It seems important to point out that the values of the mean square give a measure of the relative significance of individual model terms in changing any response of interest. The current study found that WD is the most important factor affecting the W model, contributing to the major portion of the total variation (60 %), as observed in Table H 1 in page 363. Although to a smaller extent, the WFS and WFS/TS model terms are the next higher contributors explaining 23 % and 18 % of the total variation, respectively. For the bead height model, the WFS/TS ratio was found the most significant model term contributing 27 % of the total variation (see Table H 2 in page 363). The WD term has a moderate contribution to the model, accounting for 9 % of the variation. The WFS indicates to be the most significant factor associated with the RR model, explaining 24% of the total variation (see Table H 3 in page 363). The effect of WD is also significant, contributing with 10 % for the model. The WFS/TS is the most significant term for the HI model (14 %), whereas WD and WFS/TS indicate a contribution of 3 % and 2 %, respectively (see Table H 4 in page 364). The WFS and WD are the most significant factors associated with the DR model explaining 35 % and 16 % of the total variation, respectively (see Table H 5 in page 364). The second order effect WFS^2, WFS, and the interaction term WFS/TS × WFS were the most important model terms influencing the CA model, contributing in the same order 9 %, 5 %, and 5 % of the total variation (see Table H 6 in page 364). The D and WFS/TS terms were found to be the most significant factors associated with the A_2 model, explaining 25 % and 22 % of the total variation, respectively (see Table H 7 in page 365). The WD, WFS and WFS/TS factors contributed with 30 %, 17 %, and 12 % of the total variation for the A_1 model, respectively (see Table H 8 in page 365). The WD, WFS, and WFS/TS were found the most significant terms influencing the P model, accounting for 32 %, 16 %, and 11 % of the total variability (see Table H 9 in page 365). For the D model, the WFS was the most significant term contributing 24 % of the total variance (see Table H 10 on page 366). The WD term also explains 9 % of the total variability. The AR model indicates that the second order term WFS^2 has a large contribution of 13 % for the total variability (see Table H 11 in page 366). In addition, it was found that both WFS and WD were very important terms for the HSL model, explaining 21 % and 19 % of the total variance, respectively (see Table H 12 in page 366). TS was found the most significant term influencing the SW_{av} model, explaining 10 % of the total variability

(see Table H 13 in page 367). For the W_{eff} model, both WFS and TS are very significant terms to the model, contributing 61 % and 36 % of the total variability (see Table H 14 in page 367). Finally, various interaction and polynomials terms appear to contribute significantly for explaining the total variance of MDE model (see Table H 15 on page 367).

5.4.2 Validation of the models

The correlation between the predicted and actual values for the developed single and multi-layer models is adequate in all cases, though exhibiting relatively larger scatter in the CA, AR and MDE responses (see Figure 4.78 in page 188). The computed scatter graphs show a minimum spread of points along the reference line drawn at 45°, indicating that residuals are kept to a minimum for most of the predictors. Therefore, it can be concluded that robust models were developed, which allow the prediction of responses with good accuracy.

Apart from the AR response case, the maximum percentage errors were far less than 10% for the single layer confirmation runs (see Table 4.5 in page 190). As for the multi-layer cases, the maximum percentage errors associated with the W_{eff} and MDE responses were less than 7% (see Table 4.6 in page 190). However, the SW_{av} revealed to be more difficult to accurately predict, indicating a maximum percentage error of less than 40 % in two of the three runs performed. Therefore, the models proposed in this study can provide robust and accurate predictions of the weld bead and fusion characteristics, suitable for inclusion in the main control software on industrial MAM systems. Two case studies were presented in this study to successfully demonstrate the potential for multi-objective optimisation for determining optimal process conditions for a target geometry criterion (see section 4.5.5 in page 191). The development of accurate and efficient multiple linear regression models are important requirements for process optimisation tasks.

5.4.3 Influence of process parameters on the weld bead and plate fusion characteristics

5.4.3.1 Bead width

In the current study it was found that the gradient of W is larger at low and intermediate WFS values, becoming gradually smaller thereafter (see Figure 4.77(a) in page 186). This trend is similar to that observed for GMAW-P single layer welds with the same WD, *i.e.* 0.8 mm (see Figure 4.56(a) in page 163). It is interesting to note that the gradient of W becomes smaller with increased WD (see Figure 4.13(a) in page 133). The effects of interactions between WFS and W are evident in Figure 4.49 (page 158) at a constant WFS/TS ratio of 15. The effect of WFS on W appears to be less sensitive to the WFS/TS especially at lower WFS values, as shown in the contour plot of Figure 4.77(a) in page 186. The weak effect of WFS/TS on W at low WFS can be seen in Figure 4.50 (page 159).

5.4.3.2 Bead height

The WFS/TS is the most influential parameter in determining the H, particularly at lower WFSs, where the liquid wetting behaviour is less effective. The strong effect of WFS/TS on H at low WFS values is observed in Figure 4.50 (page 159). The WFS has a stronger effect on H at higher WFS/TS, however, this influence becomes less significant with lower ratios. The moderate influence of WFS on H is observed in Figure 4.49 (page 158). The influence of the WFS on H becomes more important when thicker wires are used at higher WFSs in GMAW-P (Figure 4.51 in page 159). This occurs due to the development of a keyhole phenomenon at high speed, which induces intense heat, axial pressure and mass transport to the rear of the weld pool.

5.4.3.3 Penetration

The P indicates to depend significantly on both WFS and WFS/TS ratio (see Figure 4.77(d) in page 186). It can be seen from the corresponding contour plot that WFS has a stronger influence on P at higher WFS/TS, thus at lower TS. P is affected more strongly in GMAW-P process than in CMT, for constant welding conditions (*cf.* Figures 4.60(a) and (b) on page 165). These effects reflect fundamental differences in the mechanisms

of metal transfer between both welding processes, as discussed in section 5.2.3.

5.4.3.4 Remelting ratio and dilution

As expected from the ANOVA analysis, RR and D are mainly determined by the WFS, as shown in Figure 4.77(c) and (e) in page 186. However, RR and D show very little sensitivity to WFS/TS. This result arises from the interplay between A_2 and A_1. Significantly larger fusion characteristics were found for GMAW-P than for CMT (see Figures 4.58 in page 164 and 4.60 in page 165).

5.4.3.5 Penetration area and reinforcement area

In this study, the interaction effects show an increased gradient between A_1 and WFS with the WFS/TS ratio, as seen in Figure 4.77(h) in page 186. A_1 showed little sensitivity to WFS/TS at lower WFS, probably as a result of the arc acting on a cushion of deposited molten metal instead of directly on the base-plate. However, A_1 increases notably with increased WFS/TS ratios, particularly at higher WFSs. The GMAW-P system has a much stronger effect on A_1 than the CMT process, as seen in Figure L 27 in page 416). From Figure 4.77(i) in page 186, it is clearly seen that A_2 depends solely on the WFS/TS ratio. This result should come as no special surprise, since constant deposited cross-sectional areas are determined by constant ratios.

5.4.3.6 Contact angle

This study found that CA depends markedly on the WFS and TS at low regimes, *i.e.* current, arc power and temperature, while the effect of WFS/TS does not appear to be as significant for 0.8 mm wire diameter (see Figure 4.77(g) in page 186). The lower arc temperatures and large thermal cushioning effect induced at low WFS and TS regimes results in significantly lower heat content of both base metal and weld pool. This effect causes the interfacial tension and viscosity[30] of the liquid metal to increase, decreasing

[30] The relationship between temperature and viscosity of liquid metals is typically described by the Arrhenius equation, $\eta(T) = \eta_0 \exp(E \cdot RT^{-1})$ where η_0 is the pre-exponential viscosity, E is the activation energy for viscous flow, R is the gas constant, and T is the temperature in K.

therefore the wetting behaviour, hence raising the CA. The association between CA and WFS in GMAW-P is very similar to that of CMT (see Figures 4.61(a) and (b) in page 165).

The combined effects of interactions between process control factors and various other response variables, such as deposition rate (DR), heat input (HI), heat source length (HSL), and the aspect ratio (AR), were also considered in this investigation for further data analysis (see Figure 4.77(f), (j), (k), and (l) in page 186). Although most of these interactions should be expected, the regression functions developed can be particularly useful for future optimisation steps. For example, these regression models data can be used for integration with thermo-mechanical finite element analysis (FEA) for predicting residual stress and distortion levels in large WAAM structures.

5.4.3.7 Effective wall width

WFS and TS were the most important factors affecting the W_{eff}, according to the ANOVA results (see section 5.4.1). These results show that the gradient between W_{eff} and TS increases significantly with the WFS. This trend is in good agreement with the results in Figure 4.72(b) in page 173. It is also apparent from Figure 4.77(n) in page 186, that W_{eff} is strongly influenced by WFS, particularly at lower TS. The effect of TS on W_{eff} is shown in Figure 4.71 at 4 m min^{-1} WFS.

5.4.3.8 Surface waviness

The SW_{av} was found to depend strongly on TS at higher regimes. There is also a strong positive influence of WFS on SW_{av} at low TSs. The effect of WFS on SW_{av} is more evident at higher WFS, as illustrated in Figure 4.72(a) in page 173.

5.4.3.9 Metal deposition efficiency

MDE is strongly influenced by higher WFS and very low TSs. The low MDE results, associated with low TS and high WFS, are justified by the fact that a large amount of heat and mass is transferred per unit length when these combinations of parameters are applied, *i.e.* high WFS/TS ratios. Despite the high thermal energy transferred onto the top of the weld bead under the latter processing conditions, the heat transfer to the root is considerably small. This effect is caused by a thermal cushioning effect that hinders

the heat transfer to adjacent areas of the base plate, leading to poor wetting characteristics between the liquid and the substrate.

6 Conclusions

The study presented here was designed to determine the effects of interactions of fundamental process variables of GMAW-P and CMT processes on the weld bead and plate fusion characteristics of single bead and multi-layer welds. Another objective of this research was the development of accurate process control algorithms for predicting the relationships between the weld bead characteristics and the welding parameters of single and multi-layer mild steel deposits. The following conclusions can be drawn from the present investigation:

1. Weld bead and plate fusion characteristics are strongly affected by CTWD, *TRIM*, WFS, WFS/TS and WD, in GMAW-P. It was also shown that the weld bead surface quality is mainly determined by the *TRIM* parameter, whereas CTWD has little or no effect.

2. Stable and reproducible arc welding characteristics can be achieved in *adaptive control* mode with various combinations of pulsing parameters at fixed wire feed rate, independently of the static volt-ampere characteristic and control logic. The AIP is strongly influenced by CTWD in all welding programs, however, the weld bead and plate fusion characteristics were found to be particularly affected at smaller CTWDs.

3. The welding arc stability and the weld bead surface quality are more significantly influenced by CTWD in *non-adaptive control* mode. The W, H and CA have been shown to be less sensitive to the CTWD in *non-adaptive control* mode.

4. The primary welding current parameters of the current waveform play an important role in determining metal transfer characteristics in *non-adaptive control* mode, for a fixed average current. The frequency of the short circuits determines the rippling effect of the weld bead top surface. The stability of the welding arc depends on a minimum threshold background current value.

5. The electrical response, weld bead and plate fusion characteristics are extensively affected by process control parameters such as ALC, DC, and CTWD in the CMT

process. Larger AIPs are obtained with shielding gas mixtures with higher CO_2 contents. The effect of different shielding gas compositions on the metal transfer mechanism and overall stability of the welding arc is minimal.

6. The AIP was found to be very similar in both CMT and GMAW-P processes for constant WFS_{actual} conditions. The weld bead plate fusion characteristics are more significantly affected than weld bead profiles in GMAW-P, when compared to CMT.

7. The CMT welding revealed to be appropriate for WAAM applications when compared with other GMAW variants based upon its high welding performance, fast dynamic response and tolerance to CTWD variations, good weld bead quality, and reduced plate fusion characteristics.

8. Multi-layer weld bead characteristics, such as W_n and H_n (Delta-*z*) are more strongly influenced when the first and second layers are deposited. The W and H profiles evolve into a quasi-steady state condition thereafter.

9. The substrate temperature was found to affect notably all multi-layer characteristics, such as W_{eff}, SW_{av} and MDE, while all other welding parameters are held constant. The WFS and TS were also found to be dominating factors determining the above multi-layer characteristics.

10. AIP and TS are important factors affecting the SW_{av} of the sidewall surface facets in the direction parallel to deposition (*i.e. x*-direction), particularly at higher interpass temperatures.

11. The TS and WFS can be used to control the SW_{av} in the z-direction due to enhanced wetting behaviour. It was also shown that relatively lower SW_{av} profiles are produced using smaller WDs compared to larger diameter wires, whereas the effect of different base materials has shown to be less important.

12. Stable welding conditions can be achieved when depositing single bead-on-plate welds in the overhead position with the CMT process, whilst weld pool sagging occurs in vertical multi-layer overlapped walls.

13. Another major finding was that statistical methods can be used for developing accurate process control models for predicting the weld bed geometry and fusion characteristics of single and multi-layer welds.

7 Innovative process model of Ti-6Al-4V additive manufacturing using cold metal transfer

The study reported in this chapter[31] aims to investigate alternative and novel arc welding solutions for producing large structural Ti-6Al-4V parts. Break through arc welding technologies, such as gas tungsten constricted arc welding (GTCAW) and cold metal transfer (CMT), are used to investigate the feasibility of out-of-chamber fabrication of titanium components.

The experimental procedure used in the present study is detailed in section 7.1. In section 7.2.1, a large rectilinear Ti-6Al-4V structural component demonstrated the feasibility of the GTCAW technique made by WAAM. The unstable welding conditions associated with GMAW of titanium were investigated in single layer deposits, when using high productivity welding processes, such as DCEP-GMAW and CMT (section 7.2.2). In section 7.2.3, the effect of different argon-helium shielding gas compositions on the grain structure of single and multi-layer titanium CMT deposits was investigated. A process control model for determining suitable process parameters for target wall width dimensions of Ti-6Al-4V was developed for CMT (section 7.2.5). This model was developed using the same methodology as described in the mild steel study carried out in chapter 4. Section 7.2.4 focuses on the examination of static tensile properties of as-deposited Ti-6Al-4V rectilinear multi-layer specimens fabricated with CMT, orientated both parallel and perpendicular to the welding direction. The main conclusions of this study are drawn in section 7.3.

[31] This chapter is reproduced partly from Sequeira Almeida, P. M. and Williams, S. (2010a).

7.1 Experimental procedure

7.1.1 Materials and welding consumables

The large rectilinear Ti-6Al-4V walls produced by GTCAW (demonstration part) and CMT (for testing mechanical properties) were manufactured onto high strength two phase α + β alloy Ti-6Al-4V base plates, processed according to specification BS 2TA 56:2009 (see Figure 7.1). A number of holes (8 mm in diameter) were drilled through and normal to the base plates' surface permitting the substrate to be fixed onto a water cooled steel backing table. The single and multi-layer titanium experiments performed with GMAW variants were conducted onto Ti-6Al-4V substrates with dimensions 200 mm × 50 mm × 4 mm.

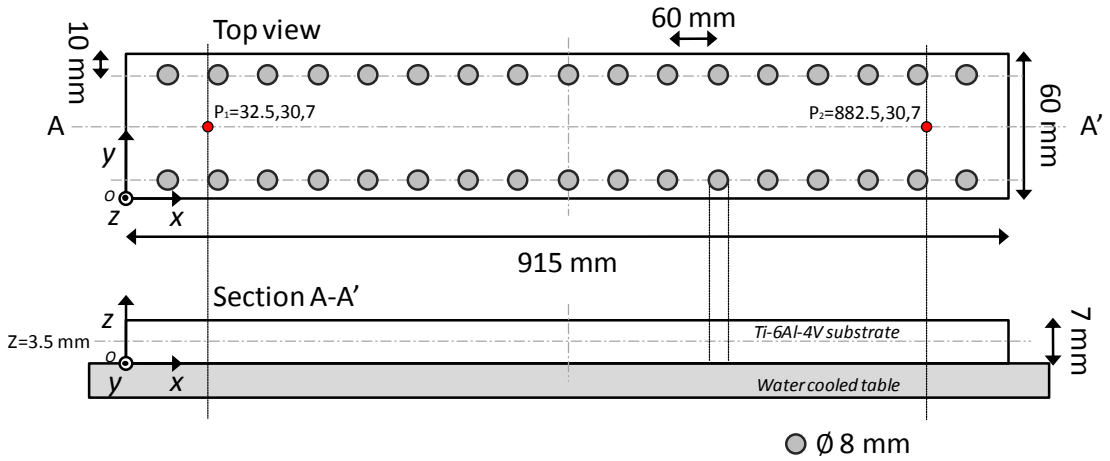

Figure 7.1. Schematic illustration of the substrates used for the fabrication of large rectilinear Ti-6Al-4V walls (top and cross section A-A' views).

The chemical composition of the substrates is provided in Table 7.1. The calculated β-transus[32] temperature for this composition is between 1003.9ºC and 984.4ºC. The microstructure of the as-received base plate; with initial dimensions 2340 mm × 423 mm × 8 mm; is characterised by a fine grained equiaxed α and transformed β phase, which is commonly referred to as in "mill-annealed" condition. The material meets the microstructural requirements of the specification and is free of α case and surface contamination. Substrates were then sectioned into individual plates and sized

[32] Temperature at which α + β → β phase transformation is complete.

accordingly. Normalized Ti-6Al-4V wire spools with diameters of 0.9 mm and 1.2 mm were used conforming to specification AMS4954H. Chemical composition of the filler wires is in Table 7.1.

Table 7.1. Chemical composition of Ti-6Al-4V substrates and wires (wt. %), including alloying elements and impurities content.

	Al	V	Fe	C	O_2	N_2	H_2	Y	Others	Ti
Plates[1]	6.01	3.82	0.19	0.02	0.16	0.010	0.0058	<0.001	0.40	balance
Wire[2]	6.14	3.96	0.18	0.02	0.14	0.011	0.001	-	-	balance

[1] Single compositions indicate the maximum allowed element content, [2] 0.9 and 1.2 mm in diameter.

The shielding gas mixtures were argon blends. These mixtures were selected according to the welding program requirements and/or plan of experiments for each welding power source.

7.1.2 Welding conditions

The cold wire fed GTCAW conditions employed for out-of-chamber fabrication of the large rectilinear demonstration Ti-6Al-4V component are detailed in Table 7.2.

Table 7.2. Welding conditions used during weld deposition of Ti-6Al-4V with both GTCAW, and GTAW-P systems.

Process	WFS (m min^{-1})	TS (m min^{-1})	I_p (A)	InterPulse I (A)	I_b (A)	T_p (s)	T_b (s)	I_{AVG} (A)	HI (J mm^{-1})	Gas/Flow (*l* min^{-1})	DR (kg h^{-1})
GTCAW [1]	1.8	0.210	150	125	70	0.05	0.05	118	242.7	Ar (100%)/20	0.55
GTAW-P [1]	1.6	0.270	250	-	45	0.05	0.14	98.9	158.3	Ar (100%)/20	0.49

I_p, pulse current; *InterPulse I*, InterPulse current; I_b, background current; T_p, duration of pulse current; T_b, duration of background current; *HI*, heat input considering a welding process efficiency of 0.6 for GTAW-P and GTCAW; *CTWD*, contact tip to work distance of 3.5mm; [1] 1.2mm wire.

Electrical transients were recorded in accordance with section 3.3. The AIP, and HI were respectively calculated using equations (3.1) and (3.3). The average current (I_{AVG}) output in the GTCAW system was calculated according to the equation (7.1), where a square current waveform and equal T_p and T_b values were assumed (Leary *et al.*, 2010).

$$I_{AVG}[A] = \frac{(I_p + I_{InterPulse})/2 + (I_b + I_{InterPulse})/2}{2} \tag{7.1}$$

The bead-on-plate welding conditions utilised to investigate whether DCEP-GMAW and CMT were suitable for high deposition rate of titanium are shown in Table 7.3.

Table 7.3. Welding conditions used during weld deposition of Ti-6Al-4V with both CMT, and DCEP-GMAW systems.

Process/ WD	WFS (m min^{-1})	TS (m min^{-1})	I_{AVG} (A)	V_{AVG} (V)	E_{ff} (η)	HI (J mm^{-1})	Gas/Flow rate (l min^{-1})	CTWD (mm)	Substrate T (ºC)	DR (kg h^{-1})
CMT (1.2mm)	8.5	0.567	145.8	14.6	0.9	224.1	Ar/He (50%)/15			2.58
DCEP-GMAW [1]	5	0.300	45.6	16.0	0.8	105.4	Ar (100%)/20	13.0	≈ 25	0.85
DCEP-GMAW [1]	10	0.300	80.1	17.0	0.8	196.1	Ar (100%)/20			1.71

WFS, wire feed speed; *TS*, travel speed; I_{AVG}, average instantaneous current; V_{AVG}, average instantaneous voltage; E_{ff} *(η)*, welding process efficiency; *HI*, heat input considering an efficiency of 0.9 for CMT and 0.8 for DCEP-GMAW; *CTWD*, contact tip to work distance; *Substrate T*, substrate temperature; *DR*, deposition rate of Ti-6Al-4V considering ρ(kg/m^3)=4470; [1] utilising 0.9mm wire.

Table 7.4 details the welding conditions applied in CMT for studying the effect of the shielding gas composition on the grain size of Ti-6Al-4V single layer welds, along with the measured electrical transients.

Table 7.4. CMT welding conditions used to study the effect of the shielding gas composition on Ti-6Al-4V grain size in single layer welds.

Shielding gas [1]	WD (mm).	WFS_{set} (m min^{-1})	TS (m min^{-1})	Flow rate (l min^{-1})	I_{AVG} (A)	V_{AVG} (V)	Arc Power (kW)	HI [2] (J mm^{-1})
Helium (30%)					99.6	16.98	1.69	290.4
Helium (50%)	0.9	12	0.4	20	108.2	17.42	1.88	324.0
Helium (75%)					113.3	18.81	2.13	363.4

[1] balance argon (Ar). [2] assuming a welding process efficiency of η=0.9.

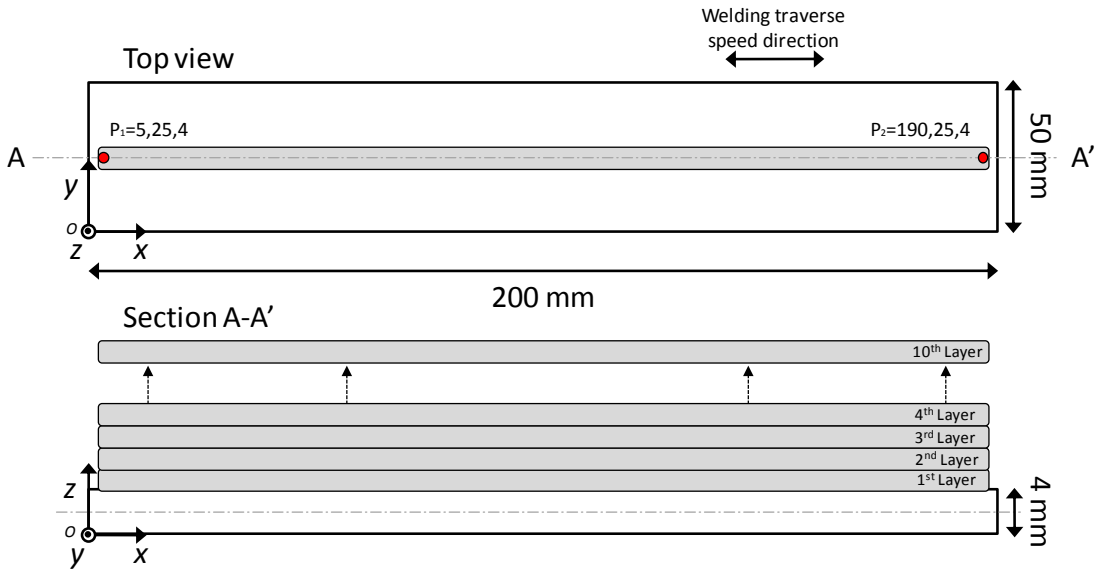

Figure 7.2. Schematic of the experimental WAAM welding procedure used to produce walls 10 layers high. The start (P_1) and stop (P_2) positions were reversed after deposition of each layer.

The welding conditions used for producing two Ti-6Al-4V vertical rectilinear walls 10 layers high using both GTAW-P and CMT are listed in Tables 7.2 and 7.3, respectively. This set of experiments was intended to examine the grain size distribution and

morphology of the deposits made using both welding processes. The walls were produced according to the welding procedure shown in Figure 7.2.

A localised two inlet trailing shield device with argon (99.998 %), and a flow rate of 30 l min^{-1} per inlet (see Figure 7.3), was utilised during processing in order to adequately protect the melt pool and the hot metal zone with an inert atmosphere. The minimum threshold temperature at which detrimental oxides may form at varying thicknesses occurs at 427 ºC, according to AWS G2.4/G2.4M:2007.

(a)

(b)

Figure 7.3. Trailing shield device used during the manufacture of the wall showing both (a) side and (b) bottom views (courtesy of Argweld®Weld Trailing Shields™).

The welding torches, from each individual power source, were coupled with a six-axis ABB industrial robot (model *IRB 2400*) for reproducing accurately the welding traverse speed. Substrates were fixed at 6 points onto a water cooled aluminium backing plate, while temperature was monitored by an IR pyrometer (as detailed in section 3.4). A repeatable and consistent build up strategy was guaranteed throughout the manufacturing stage, by setting the interpass temperature to approximately 25 °C.

The static tensile properties of WAAM rectilinear Ti-6Al-4V walls, deposited using CMT, were preliminarily assessed in the as-deposited condition. An inert shielding gas mixture from group I3 (according to BS EN 439) containing 50 % helium with balance

argon was utilised throughout the experimentation with a gas flow rate of 15 *l* min^{-1}. Additional protection was provided by a trailing shield device filled with pure argon (99.998 %), where a gas flow rate of 15 *l* min^{-1} (per inlet) was utilised in all tensile testing trials. The CMT *Robacta Drive* CMT welding torch was attached to a pre-programmed six-axis Fanuc robot (model *Arc Mate 120i B*), allowing for high levels of accuracy and reproducibility of the welding traverse speed and deposition sequence.

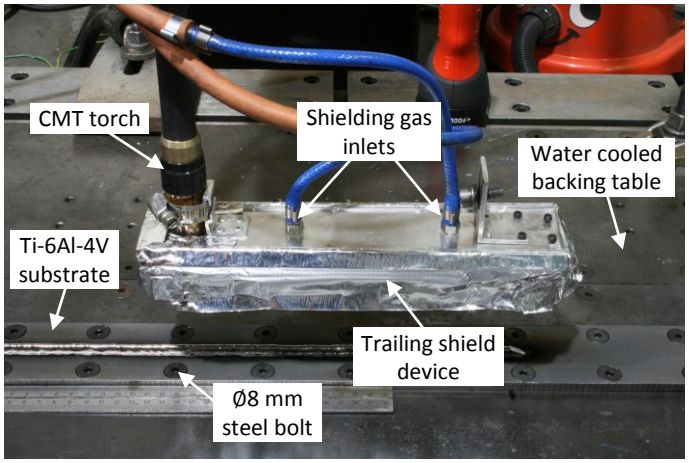

Figure 7.4. Welding jig apparatus showing the fixing and trailing shield arrangements.

Ti-6Al-4V substrates were fixed to a water cooled backing table to ensure precise positioning, reduce welding induced distortion, and control the heat build-up during processing by guaranteeing intimate contact between surfaces. In addition, the cooling fixture allowed for the fabrication process to be carried out without the need to wait between each layer deposited until cooling down to room temperature (≈ 25 ºC), assisting likewise in the reduction of surface oxidation.

Table 7.5. Summary of the CMT welding conditions used for manufacturing the testing walls.

Exp. No.	Testing[1] direction	WFS_{set} (m min^{-1})	I_{AVG} (A)	V_{AVG} (V)	P_{Inst} (kW)	HI (J mm^{-1})	TS (m min^{-1})	WFS/TS	CTWD (mm)	Shielding gas	DR^{2} (kg h^{-1})
PA8 H-TN	H	8.0	123.17	14.23	1.99	336.53	0.32	25	13	Ar/He (50%)	2.43
PA6 H-TN	H	6.0	107.78	13.19	1.52	273.33	0.30	20			1.82
V-TN	V										

[1] *H*, horizontal (parallel to the welding direction); *V*, vertical (perpendicular to the welding direction); [2] the WFS_{set} was used for calculations.

The walls produced for mechanical testing were fabricated in an open atmosphere utilising the fixing arrangement and trailing shield device shown in Figures 7.1 and 7.3, respectively. The apparatus employed for producing the rectilinear Ti-6Al-4V walls

used for mechanical testing is shown in Figure 7.4, whilst welding conditions are summarised in Table 7.5.

7.1.3 Metallographic preparation of Ti-6Al-4V

Titanium specimens were sectioned, mounted in cold-setting resin, and manually plain ground according to the metallographic preparation method detailed in section 3.6. At the initial stage, wet SiC abrasive grinding paper was used with common grit sizes ranging from 120 to 4000 (ANSI[33] grit). Specimens were then manually polished utilising a brand new soft cloth rotating disc impregnated with a mixture of colloidal silica and hydrogen peroxide (H_2O_2) at 30 %. In order to obtain a good polished surface free of scratches, the preparation time varied depending on the specimen area. The latter procedure was repeated as many times as needed. In the end of each polishing step the rotating cloth (impregnated with colloidal silica) was abundantly flushed with pressurized water. After the final polishing step, samples were rinsed under tap water and dried using ethanol (C_2H_5OH) and a strong stream of air. Specimens were then etched in a Kroll´s solution (1 % HF, 2 % HNO_3, and the balance distilled H_2O) for periods ranging from 10 s to 25 s, depending on the cross-sectional area. The revealed macrostructures were then examined and macro-photographed according to the method detailed in section 3.6.

7.1.4 Tensile testing experimental plan

Two WAAM Ti-6Al-4V walls with dimensions of 840 mm × 80 mm × 5 mm (named as PA6 H-TN and PA8 H-TN), and one wall with dimensions of 840 mm × 200 mm × 5 mm (named as V-TN), were fabricated using the materials and welding conditions detailed in sections 7.1.1 and 7.1.2, respectively.

Tensile specimens PA6 H-TN and PA8 H-TN were extracted from two separate walls produced with different welding conditions in PA position, 1G according to PD CEN/TR14633:2003. The purpose of this study was to investigate the influence of different HI on the tensile properties of specimens tested in the direction parallel to the

[33] ANSI – American National Standards Institute.

welding direction (H), *i.e. x*-direction. The dimensions of the walls produced were planned to enable the extraction of three tensile specimens per wall from different locations, as shown in Figure 7.5.

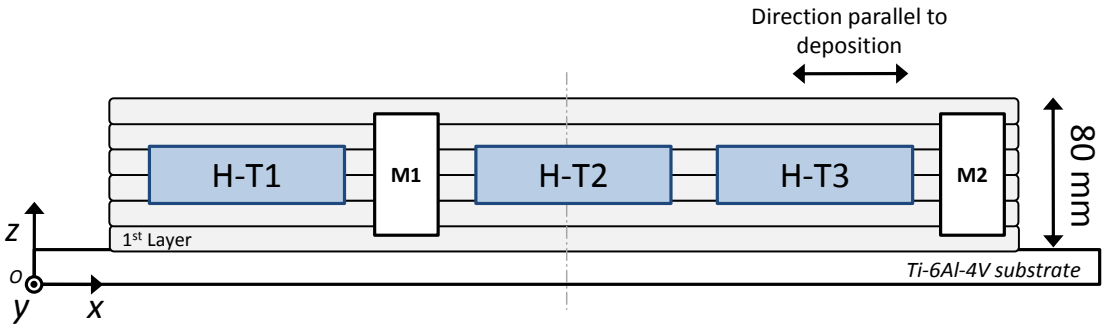

Figure 7.5. Schematic diagram, showing the location and orientation from where horizontal tensile (H-T1, H-T2, and H-T3) and metallographic (M1 and M2) specimens were extracted.

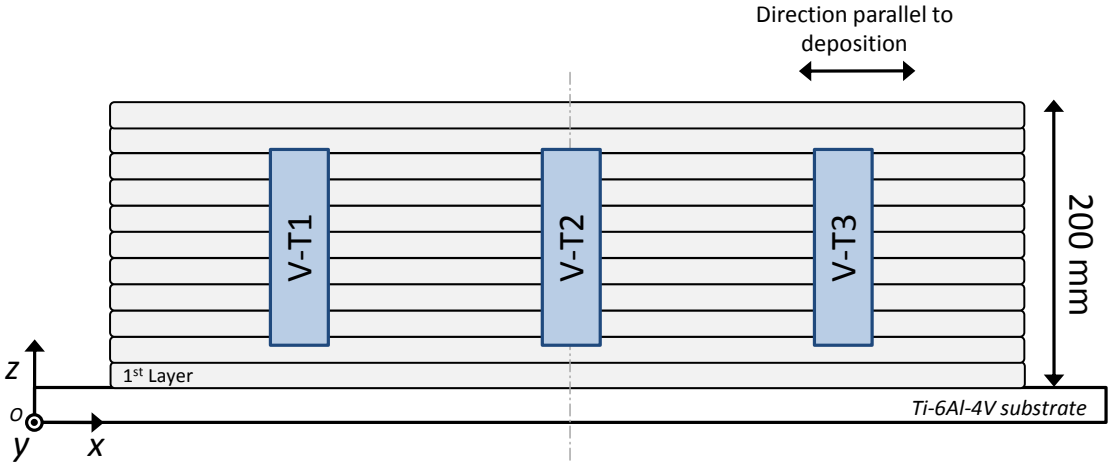

Figure 7.6. Schematic diagram, showing the location and orientation from where vertical tensile specimens were extracted (V-T1, V-T2, and V-T3).

Three other tensile specimens were cut out from the 200 mm high wall with their longitudinal axis perpendicular to the welding direction (V), *i.e. z*-direction, as illustrated in Figure 7.6. Metallographic examination was performed on the remaining samples (named as M1 and M2), which were extracted from different locations in the wall (see Figure 7.5).

For mechanical testing, tensile specimens with a rectangular cross-section were machined from the extracted samples (see Figures 7.5 and 7.6) according to the requirements for dimensional testing of ASTM E8/E8M (see dimensions of the samples in Appendix M). It is important to note that the maximum thickness of the specimens for the tensile testing was 2.3 mm. This was the maximum thickness achieved after machining which could guarantee an even surface of the specimens. The samples for

metallographic examination were prepared in accordance with the procedure described in section 7.1.3.

Six additional control tensile specimens were extracted and machined from a 7 mm thick Ti-6Al-4V plate, delivered according to specification BS TA56:1974 (AMS 4911D). These control samples (named as C) were tensile tested in the ***longitudinal (L-direction)***, *i.e.* CL-T1, CL-T2, and CL-T3, and ***transverse (LT-long transverse)***, *i.e.* CLT-T1, CLT-T2, and CLT-T3, ***direction to the rolling***. Control samples were tested to provide a baseline for comparison with the samples extracted from the WAAM walls referred above.

7.1.5 Tensile testing

An Instron 5500R[34] electromechanical universal testing machine was used to conduct static tensile tests using a 100 kN load cell (see Figure 7.7). Tests were performed at ambient temperature (22 ± 3 °C) with a constant cross-head displacement of 1 mm min^{-1} (according to requirements ASTM E8/E8M-08). Table 7.6 details the width, thickness, and cross-sectional dimensions of the tested specimens alongside the original gauge length, marked for the determination of elongation.

Table 7.6. Dimensions of the tensile test specimens at the centre of the reduced area.

Specimens dimensions	Value (mean)
Width	12.5±0.01 mm
Thickness	2.30±0.01 mm
Cross-sectional area	28.750±0.01 mm^2
Original gauge length[1] (L_0)	50 mm

[1] Marked on the test piece and measured at room temperature before testing.

In addition, strain was measured using a 25 mm gauge length clip-on extensometer model 2620-604, calibrated according to BS EN ISO 9513:2002 (see Figure 7.7). The extensometer was carefully attached to each individual specimen at the mid-length of the reduced area after marking.

[34] Instrument number 5500H1517, last calibrated in March 2011 (according to ASTM E4).

Tensile properties were obtained according to the requirements of ASTM E8/E8M-08. The yield strength (*YS*), Young's modulus (*E*), and ultimate tensile strength (UTS) were determined autographically from the stress-strain diagrams. The *YS* was determined using the 0.2 % offset method, *E* was calculated from linear regression slopes drawn within the proportional elastic limit of the material using a representative range of data points of at least 2000 points, whilst *UTS* was obtained from the maximum engineering stress level reached in the tensile test.

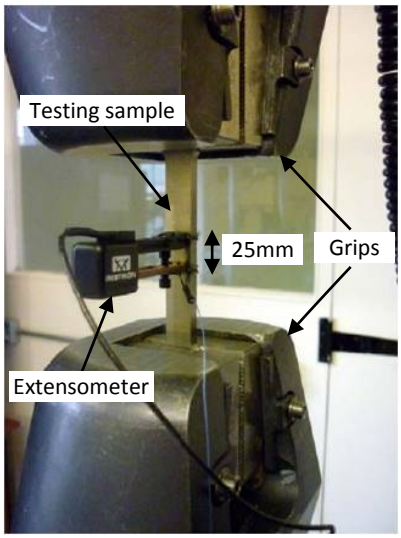

Figure 7.7. Instron 5500R tensile testing set-up showing the wedge gripping ends, extensometer, and testing sample.

The percentage elongation at fracture (ε_{max}) was determined using one of the following two methods: (a) directly from the elongation at fracture data recorded by the extensometer[35]; (b) by fitting together the fractured specimens and then calculating the ε after fracture[36] as follows:

$$\varepsilon = \frac{L_u - L_0}{L_0} \times 100 \tag{7.2}$$

where L_0 is the original gauge length, and L_u the final gauge length after fracture, according to requirements of BS EN ISO 6892-1:2009.

[35] Only valid if the localised extension occurs within the extensometer gauge length, according to BS EN ISO 6892-1:2009 and ASTM E8/E8M-08.

[36] Valid only if the distance between the fracture and the nearest gauge mark is not less than $L_0/3$, according to requirements of BS EN ISO 6892-1:2009.

It is important to note that when using an extensometer the measurement is valid regardless of the position of the fracture if the percentage elongation after fracture is equal or greater than the specified value (BS EN ISO 6892-1:2009).

7.2 Results and discussion

7.2.1 Out-of-chamber fabrication of a large structural Ti-6Al-4V component using gas tungsten constricted arc welding

Cold wire fed gas tungsten constricted arc welding (GTCAW) technology was employed for the first time as a heat source in WAAM applications for out-of-chamber fabrication of a large rectilinear Ti-6Al-4V structural component (see Figure 7.9). GTCAW uses high frequency current converter modules to transform DC current into high frequency current pulses (≈ 20 kHz), in order to produce an electromagnetic constricted arc. The high frequency modulated current can also be superimposed onto a low frequency pulsed gas tungsten arc welding waveform (GTAW-P), allowing a relatively lower net heat input to be delivered to the weld.

The GTCAW technology was originally developed for weld and/or repair of extremely heat sensitive alloys for aircraft industry applications, such as RENE 142 DS, MARM 247, Inconel 718 or CM-SX10 alloys. Nevertheless, the benefits of such an innovative welding solution had yet to be demonstrated far beyond conventional welding and repair procedures, as established in this investigation.

Figure 7.8. Front view of the WAAM large structural Ti-6Al-4V wall manufactured using GTCAW. Note its straightness and high quality surface finish.

This work demonstrated that large and high-quality structural Ti-6Al-4V components can be produced out-of-chamber using GTCAW (see Figures 7.8 and 7.9). The good geometrical accuracy of the manufactured parts, straightness and the outstanding surface finish achieved are three of the main attributes of this WAAM technique.

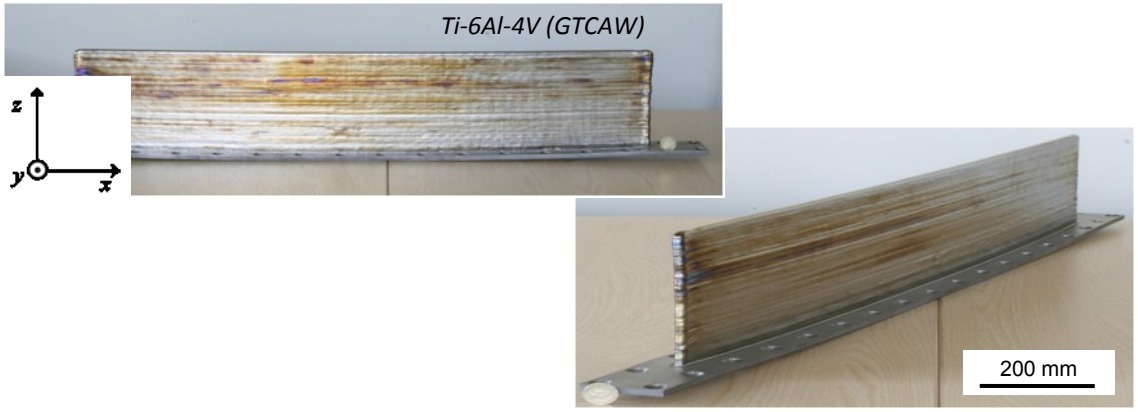

Figure 7.9. WAAM large structural Ti-6Al-4V component manufactured using GTCAW, with dimensions 1000 mm × 200 mm × 4 mm.

The electromagnetic arc constriction phenomenon caused by the high frequency current modulation in GTCAW is claimed to result in a more stable, narrower and stiffer arc plasma (Onuki *et al.*, 2002). The arc constriction effect acting predominantly on the column of the welding arc causes an arc pressure increase, resulting in increasing deposition rate and travel speed, while the desired directional control over the heat source is also improved.

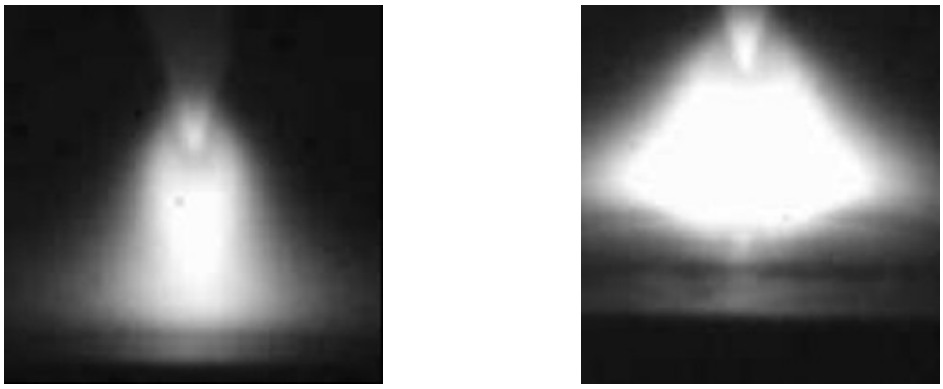

Figure 7.10. GTAW phenomena obtained by (a) high-frequency pulsed-current (constricted arc), and (b) direct current GTAW (non-constricted bell-shaped arc). Both arc welds were produced with a 1.6 mm tungsten electrode (images courtesy of Innosol Precision Welding Division).

Compared with conventional GTAW processes, a narrower arc column is typically obtained with GTCAW (see Figure 7.10). The narrower arc column typically favours higher energy densities, causing less thermal distortion, enabling higher cooling rates, and producing a narrower heat affected zone (HAZ). The independent control of the wire feed speed (WFS) over the net arc power, and vice versa, resulted in a precise control over the molten pool dimensions, and the amount of metal transferred into it. GTCAW technology also allows for more precise control over the final solidification macro and microstructures, by offering additional potential for optimisation of the mechanical properties in $\alpha + \beta$ titanium alloys. Cranfield University is working in partnership with *Bombardier Aerospace (UK) Ltd* as part of a comprehensive ongoing mechanical test research program that aims to investigate tensile, fatigue and crack propagation properties of the component shown in Figure 7.9 in various locations and orientations.

7.2.2 Single bead-on-plate Ti-6Al-4V deposition trials using DCEP-GMAW and CMT

While geometrical accuracy and surface finish are two of the main attributes of the former system for WAAM, the major drawbacks of the GTCAW approach are still the low speed, deposition and productivity rates, and lack of translational omni-directionality associated with the material deposition technique. In order to reduce the cost allied with the fabrication of out-of-chamber Ti-6Al-4V components, a GMAW based process is highly desirable to increase productivity. Typically, WAAM deposition rate capabilities can go up to 1kg h^{-1} for cold wire fed GTAW, while several kilograms per hour can be achieved by utilising a GMAW system. However, cathode spot wandering is a major quality concern in conventional DCEP-GMAW of titanium (see section 2.6.1). The GMAW process also avoids the practical issues involved in building complex shapes which are introduced by the non-coaxial arc and wire feed in GTAW processes.

The use of two consumable electrode GMAW variants in WAAM applications, DCEP-GMAW and CMT, were investigated for high deposition rate of Ti-6Al-4V. The welding performance provided by each independent system was determined. The

assessment criteria included aspects such as arc plasma stability, welding spatter generated, visual quality of the beads deposited, as well as reproducibility of the welds. As anticipated, very poor welding conditions were achieved with the DCEP-GMAW process for depositing Ti-6Al-4V wire. These unstable conditions were found to be independent of the current level applied, as observed in Figure 7.11.

(a) (b)

Figure 7.11. Single bead Ti-6Al-4V deposits in DCEP-GMAW using (a) WFS=5 m min^{-1} and (b) 10m min^{-1}.

At low current regimes, *i.e.* WFSs, the erratic titanium cathode spot behaviour observed throughout the deposition of single layers was associated with very coarse spattering conditions (see Figure 7.11(a)). The cathode spot relocation mechanism, a phenomenon better known as arc wandering, was the main cause of the observed lack of directional control over the arc column, which caused a detrimental effect on the straightness and uniformity of the as-deposited weld bead. In these low current regimes, metal transfer was dominated by a combination of two transfer mechanisms, *i.e.* short circuit and globular. Coarse spattering conditions resulted from both the electromagnetic pinch effect associated with short circuits, and also by the detachment of large molten globules formed at the tip of the wire electrode, asymmetrically transferred by gravity to the vicinity of the weld pool. The results have also shown that arc wandering phenomenon and poor metal transfer conditions were not suppressed when higher currents were applied in DCEP-GMAW (Figure 7.11(b)).

In contrast, the CMT welding process has shown very satisfactory results in preventing the cathode spot relocation mechanism, and coarse spattering conditions when depositing Ti-6Al-4V, as depicted in Figure 7.12. The CMT welding process provided good quality and reproducible welds in a uniform and consistent manner throughout the experimentation. Favourable deposition conditions observed in CMT when compared to DCEP-GMAW can be explained by differences in metal transfer mechanisms between both welding processes.

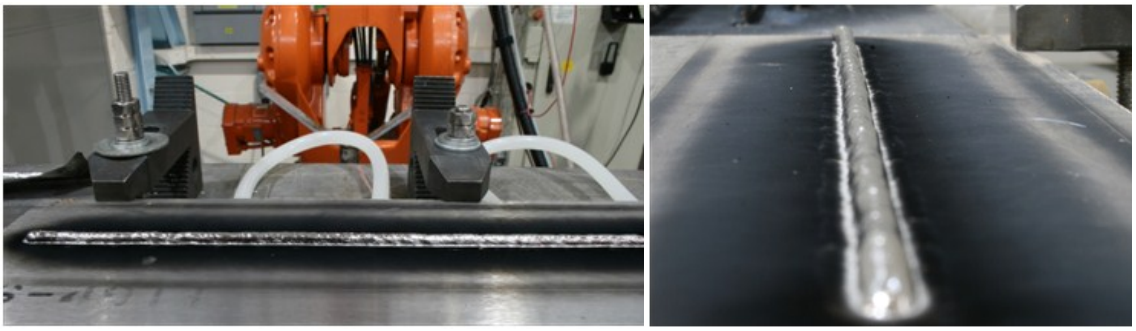

(a) (b)

Figure 7.12. Single bead-on-plate Ti-6Al-4V deposited using CMT showing (a) side and (b) front views.

The controlled dip metal transfer conditions achieved with the CMT process is extremely stable since that no free flight droplet is transferred during the arcing period. As a result, the potential repulsion of filler metal caused by the momentum of external electromagnetic pinch forces, or issuing cathode jets, acting on the incorporated droplets is prevented. Moreover, the metal transfer to the molten pool occurs at low current levels by a surface tension mechanism, where a back-drawing force assists the liquid bridge fracture. The ejection of coarse spatter during the short circuit period is suppressed by cutting-off the flow of current through the liquid conductor, inhibiting repulsion via Lorentz pinch force mechanism.

7.2.3 Effect of the shielding gas composition and welding multipass on Ti-6Al-4V grain size

Optical microstructural analysis was conducted on Ti-6Al-4V single and multi-layer weld samples produced with CMT in light of the encouraging deposition results obtained in section 7.2.2. In the present study, the effect of different shielding gas mixtures on the grain size and morphology of single layer titanium fusion welds in the fusion zone (FZ) and HAZ was investigated. In addition, the influence of repeated thermal cycling on the grain size distribution and morphology of multi-layer deposits was examined and compared for both CMT and GTAW-P processes.

Figure 7.13 shows cross-sectional optical macrographs of Ti-6Al-4V single layer welds, where gas compositions containing 30 %, 50 % and 75 % helium (He) in a balance of argon (Ar) were utilised. The welding conditions employed in this study are listed in

Table 7.4. The HI measured[37] was 290, 324 and 363 J mm^{-1}, corresponding in the same order to contents of 30 %, 50 % and 75 % He. Higher HI was obtained with higher He content. A maximum AIP input of 2.13 kW was measured for a mixture of 75 % He, comparing to 1.88 kW and 1.69 kW for compositions of 50% and 30 % He. These results may be explained by the much higher ionisation potential of H when compared with argon gas only, which are respectively 24.6 eV and 15.8 eV (Menzel, 2003).

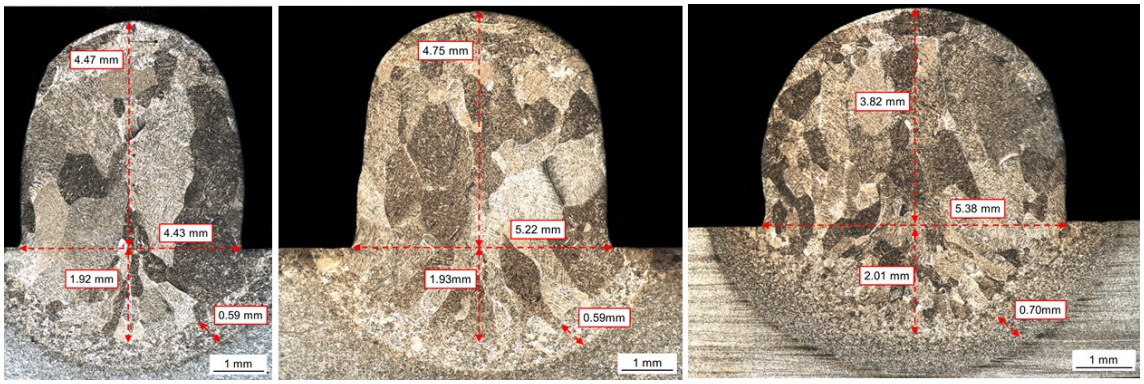

Figure 7.13. Optical macrographs of CMT welds showing the effect of different shielding gases mixtures on the fusion zone, grain size, and morphology of Ti-6Al-4V deposits using (a) 30% He, (b) 50% He and (c) 75% He, in a balance of Ar.

In general, these results also show that the weld bead becomes wider and shorter with higher AIP inputs, thus with larger volume fractions of He. This result was expected, since the increase in the AIP, arc-spread (*cf.* V_{AVG} in Table 7.4), electrical and thermal conductivity, typically influence the temperature distribution of the arc. These processing conditions cause more heat to be distributed away from the weld centreline, and thereby improve considerably the wetting and spreading properties of the weld bead.

Figure 7.13 reveals that Ti-6Al-4V grains nucleate epitaxially upon coarsened β grains in the near heat affected zone (NHAZ), and columnar grains regrow competitively into the molten pool, as observed elsewhere (Baeslack III and Hallum, 1990; Elmer *et al.*, 2004). The newly developed FZ grains grow with the same lattice structure and orientation as the HAZ grains at the S/L interface. During the competitive growth

[37] Using a welding process efficiency of η=0.9.

process, the grains are most favourably orientated parallel to the maximum thermal gradient, as seen noticeably in Figure 7.13(a) and (b). The mode by which solidification occurs in this titanium alloy depends on the region of constitutional supercooling at the S/L interface (see section 2.6.3 in page 65) and therefore on the thermal gradient and the solidification growth rate. It is well established that the grain size, morphology and the crystallographic texture of the solid are controlled by the nucleation rate and growth characteristics of the alloy, and the thermal conditions (or heat flow) present during solidification (Kurz and Fisher, 1998).

In this work, significant grain refinement of the solidification structure in single layer welds was achieved using shielding gas mixtures containing higher percentages of helium, and therefore by applying higher energy input welds (see Table 7.4). Such an occurrence is contrary to expected and apparently difficult to explain, since higher energy inputs are typically associated with outsized prior-β grains. There are several possible mechanisms that may be responsible for this grain refinement effect observed in Figure 7.13, described as follows:

(1) The temperature gradient in the melt pool decreases with higher He content as a result of the higher electrical and thermal conductivity of He in comparison with Ar (Murphy, 1997).

(2) Shielding gas mixtures with higher He content produce a larger specific surface area of contact with the base plate. The increase in the contact area can lead to heat transfer enhancement through the base plate by conduction, causing solidification to occur at a higher cooling rate.

(3) Under solidification conditions of lower temperature gradients (1) and higher cooling rates (2), the planar S/L interface can break down to cellular or cellular-dendritic solidification modes when lowering the ratio G/R.

(4) Dendrite-tip fragmentation may become a potential mechanism of grain refinement. This is probably the result of a wider region of constitutional supercooling at the S/L interface under the favourable solidification conditions referred in (3).

(5) The short circuit transfer mode of CMT process causes vigorous fluid motion and vibration to occur, as a result of mechanical stirring. The mechanically induced turbulence and agitation to the melt pool can further promote dendrite-tip fragmentation.

(6) The dendrite fragments pushed ahead of the S/L interface become preferential sites for heterogeneous nucleation and subsequent crystal growth, since heterogeneous nucleation sites have much lower activation energy barrier than the homogeneous sites.

(7) Newer and more randomly-orientated grains may be supplied due to a continuous change in the direction of the maximum thermal gradient, as a result of fluctuations in temperature and arc force caused by periodic current excursions every seventh of a second.

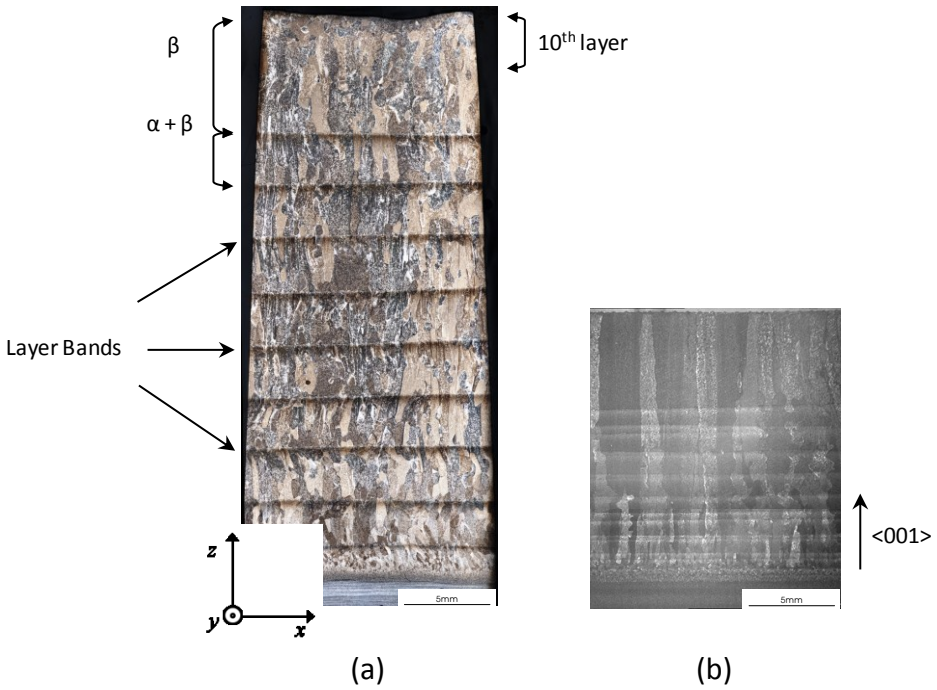

Figure 7.14. Longitudinal Ti-6Al-4V cross sections of WAAM walls deposited using (a) CMT and (b) GTAW-P welding processes.

Following the aforementioned work on single layer welds, two vertical Ti-6Al-4V multi-layer overlapped walls were manufactured using both CMT and GTAW-P processes. In this study the impact of multi-layer deposition and its thermal field on the grain size distribution and morphology was examined. The resulting longitudinal cross sections are shown in Figure 7.14 and the welding conditions are detailed in Tables 7.3

and 7.2. Figure 7.14(b) shows a Ti-6Al-4V multi-layer macrograph processed via GTAW-P exhibiting a typical continuous large columnar prior-β grain structure (1.16±0.21 mm wide, CI=2σ), similarly to the ones observed in (Baufeld and Van Der Biest, 2009; Brandl *et al.*, 2009). These prior-β grains grow epitaxially from the substrate, following a preferential crystallographic direction across multiple deposited layers, *i.e.* <001>.

A relatively fine equiaxed grain structure is identified in the first deposited layer. Here, the heat generated by the welding arc was efficiently extracted by the substrate, and the lower activation energy barrier for heterogeneous nucleation was easily overcome. On subsequent layers, larger and fewer number of prior-β grains acted as nucleation sites, resulting in less crystallographic directions available for grain growth. Consequently, only the most rapid prior-β grains evolving in the direction <001> survived the grain growth process.

Despite the higher HI delivered to the weld, the optical macrograph of CMT cross-section reveals a finer grained macrostructure across the entire specimen area, when compared with GTAW-P (see Figure 7.14). It is encouraging to compare this result with that found by Wang *et al.* (2011) who reported a noticeable effect on grain refinement of WAAM walls made of Ti-6Al-4V when increasing the amount of cold wire feed into the melt pool, for a constant weld energy input rate (see section 7.2.1). In the present example, each successive layer of Ti-6Al-4V was deposited with CMT using 1.4 times the weld input energy of that used with GTAW-P. However, the amount of weld metal deposited per unit time and per layer with CMT was 5.3 times of that used with GTAW-P. These results confirm that significantly less energy was effectively used for depositing the same weight of Ti-6Al-4V material. In the present case, the mechanisms for obtaining grain refinement also accord with the earlier interpretation (see section 7.2.1), which showed that columnar dendritic or equiaxed dendritic solidification conditions have most probably resulted from wider constitutional supercooling conditions. The epitaxial grain growth mechanism shows to occur preferentially in the vertically orientated direction <001>. In addition, one can notice the larger number of available nucleation sites contributing for heterogeneous nucleation per deposited layer, when compared with the GTAW-P (see Figure 7.14(b)).

Typical horizontal layer bands are also observed parallel to the deposition direction in both welding systems as a result of repeated thermal cycling caused by the dual solid α + β phase field region, as it undergoes the transformation. Figure 7.14(a) identifies a number of layer bands along with the thermal history experienced by the 10^{th} layer, *i.e.* α + β → β transformation.

7.2.4 Tensile properties of Ti-6Al-4V

The structural efficiency measures the effectiveness of a structure and is defined as the ratio of load carried to the structure mass. Structural efficiency is one of the most important aspects to take into account during the design stage of any engineering component, by tightly coupling design and materials knowledge bases. The introduction of new materials and/or processing routes into aerospace systems requires a combination of both reliable and consistent static strength responses such as Young's modulus (*E*), yield strength (*YS*), ultimate tensile strength (*UTS*), and elongation properties (ε_{max}). The ultimate and yield static tensile strength results, obtained from both the baseline control samples and from the WAAM wall made of Ti-6Al-4V processed via CMT, are summarised in Figure 7.15.

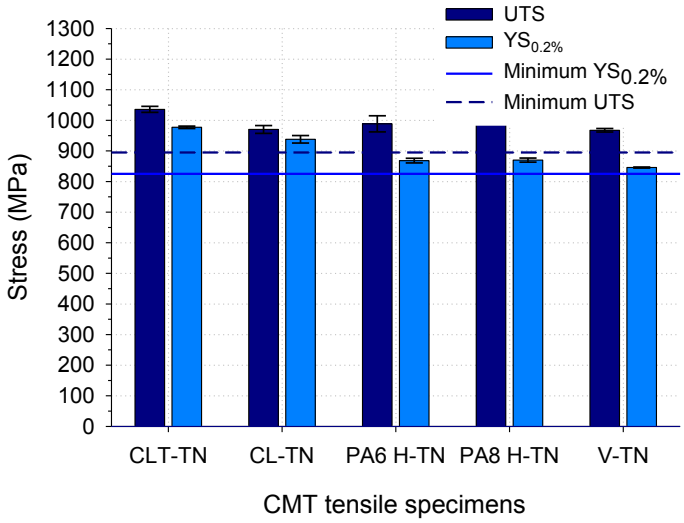

Figure 7.15. CMT static tensile results of specimens extracted from Ti-6Al-4V walls in the as-deposited condition (95% confidence interval). The minimum $YS_{0.2\%}$ and UTS values are specified for rolled plate according to BS 2TA56:2009.

The average UTS and $YS_{0.2\%}$ data for the baseline control samples (named as CLT-TN and CL-TN in Figure 7.15) compare favourably with the data supplied in the material

certificate of conformity provided by the supplier[38]. The values obtained for UTS and YS in the tested control samples were 3.23 % and 2.44 % higher than the certified values. The average ultimate and yield strength of the control samples tested in the *LT*-direction are 1036 and 977 MPa, which are 6.8 % and 4.2 % higher than in the *L*-direction (970 and 938 MPa), respectively. The improvement in the mechanical response in the *LT*-direction was perhaps due to the remaining effects of some induced crystallographic texture by prior thermo-mechanical treatment.

The static tensile strength properties of the as-deposited Ti-6Al-4V material show very little sensitivity to the weld energy input; *cf.* samples PA6 H-TN and PA8 H-TN in Figure 7.15. The average ultimate and yield strength of the as-deposited samples tested in the direction parallel to deposition (*x*-direction in Figure 7.6 and page 242) are about 990 and 870 MPa, which are 2.3 % and 2.8 % higher than in the vertical or *z*-direction in the same figure (968 and 846 MPa), respectively. The average *UTS* of the as-deposited material tested parallel to deposition, *i.e.* PA6 H-TN and PA8 H-TN, was slightly lower than that of control samples in the *LT*-direction. However, the YS of the same as-deposited material was 11 % and 7 % lower than those of control specimens in the LT and L directions, respectively.

Figure 7.15 shows that for identical welding conditions, the average UTS and YS of the as-deposited specimens tested in vertical direction (named as V-TN) are 968 and 846 MPa, which are 2.1 % and 2.6 % lower than as-deposited specimens tested in horizontal direction (named as PA6 H-TN: 989 and 868 MPa), respectively. The UTS and YS of the as-deposited specimens tested in the vertical direction, *i.e.* CL-TN, are 0.3 % and 10 % lower than the control samples tested in the *L*-direction.

The UTS and YS of the as-deposited Ti-6Al-4V material meets the minimum technical specification requirements of the rolled plates (BS 2TA 56:2009), irrespective of the testing direction (see Figure 7.14). Although fulfilling the UTS and YS requirements of several other minima specification requirements (see Table 7.7), the YS of the as-deposited material is still below forging stock (≥970 MPa), sheet (≥900 MPa), bar

[38] ThyssenKrupp Aerospace.

(950±27.0 MPa), and wrought material (860 MPa). In contrast, the average UTS values of the as-deposited material have shown to comply with the majority of the specifications, apart from the requirements for forging stock (1100≤UTS≤1300) and MIL-T-9047 bar (1034±5.6 MPa).

Table 7.7. Technical requirements for Ti-6Al-4V alloy in various forms (according to aerospace series standards), alongside additional experimental data.

Form	Production method	$YS_{0.2\%}$ (MPa)	UTS (MPa)	ε_{max} (%)	Test direction	Specification
Plate (t ≤ 100mm)	Rolled	≥ 825	895≤UTS≤1150	≥ 10[1]	L and LT	BS 2TA 56:2009
Bar and section for machining (t or D ≤ 150mm)	Rolled, forged, drawn or extruded	≥ 830	900≤UTS≤1160	≥ 8	L	BS 3TA 11:2009
Forging stock (t or D ≤ 150mm)	Hot rolled, forged, or extruded	≥ 830	900≤UTS≤1160	≥ 8	L	BS 3TA 12:2009
Forgings (t or D ≤150mm)	Forged from forging stock	≥ 830	900≤UTS≤1160	≥ 8	L	BS 3TA 13:2009
Forging stock and wire (t or D ≤ 20mm)	-	≥ 970	1100≤UTS≤1300	≥ 8	L	BS 3TA 28:2009
Sheet	Rolled	≥ 900	960≤UTS≤1270	≥ 8	LT	BS 3TA 10:2009
Investment casting and HIP	IC and HIP	827	896	-	-	AMS 4985C
Cast material	Casting	758	860	> 8	-	ASTM F1108
Wrought material	-	860	930	> 10	-	ASTM F1472
MIL-T-9047 (bar)[3]	Rolled or forged	950±27.0	1034±5.6	11.67±0.7	L	Military specification
Wall/plate	WAAM (TIG)	759.3±4.7	859±6.8	4.53±2.0	V[4] (build 1)	[3]
	WAAM (TIG)	802.7±6.5	917.8±6.6	14.5±0.8	V (build 2)	[3]
	WAAM (TIG)	786.0±15.5	867.8±18.1	5.5±2.3	H[4] (build 1)	[3]
	WAAM (TIG)	867.7±3.3	970.7±5.8	8.63±2.5	H (build 3)	[3]

[1] For thicknesses between 5<a≤10 mm; [2] Longitudinal (*L*) and longitudinal transverse (*LT*); [3] Bombardier experimental data; [4] *V* and *H*, directions perpendicular (*z*-direction) and parallel (*x*-direction) to the welding direction, respectively; *t* and D, thickness and diameter.

Figure 7.16 compares the average ultimate and tensile strength results obtained for Ti-6Al-4V samples processed via CMT and GTAW-P in the as-deposited condition. The data presented for GTAW-P in both the horizontal and vertical directions to deposition were obtained from the *build 3* and *build 2*, respectively (see Table 7.7). The UTS and YS static tensile properties of Ti-6Al-4V material processed via CMT and GTAW-P tested in the horizontal direction are very similar. However, better results were obtained in the vertical direction for Ti-6Al-4V material processed by CMT. The average UTS

and YS of the as-deposited CMT specimens tested in horizontal are 989 and 868 MPa, which are 1.8% and 0.1% higher than those tested in the same direction processed via GTAW-P (971 and 867 MPa), respectively. The UTS and YS of the as-deposited CMT specimens tested in vertical are 968 and 846 MPa, which are around 5.4% higher than those processed by GTAW-P (918 and 803 MPa).

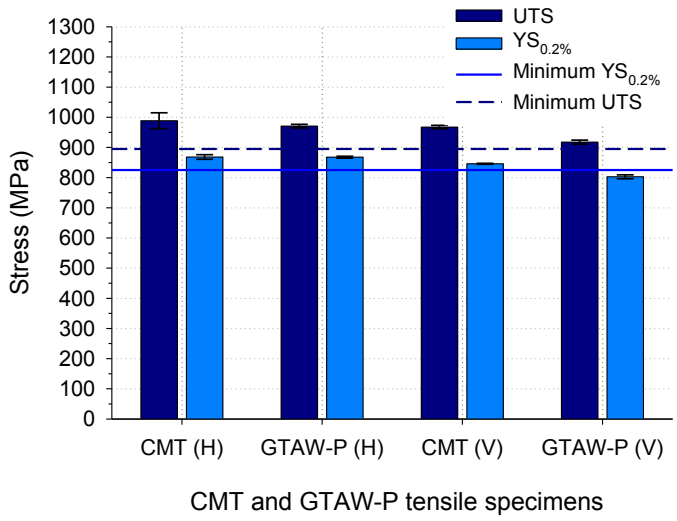

Figure 7.16. CMT and GTAW-P static tensile results of specimens extracted from Ti-6Al-4V walls in the as-deposited condition (95% confidence interval).

The average UTS and YS of the as-deposited Ti-6Al-4V material processed via CMT shows to comply with the minima specification recommended by BS 2TA 56:2009 (rolled plate) in both testing directions, whereas the material processed via GTAW-P fails to meet the minima $YS_{0.2\%}$ requirement in the vertical direction. Overall, the better static tensile results obtained from Ti-6Al-4V material processed via CMT when compared with GTAW-P, can be attributed to the finer and more isotropic macrostructures obtained in the samples processed using CMT (see section 7.2.3).

It is interesting to note that the lower UTS and YS properties of the as-deposited samples produced by GTAW-P are balanced by higher ductility values of around 14 % (see Table 7.7). This result suggests that there is still a wide margin for improving the strength-ductility balance of the as-deposited Ti-6Al-4V material processed via GTAW-P by post-heat treatment. The static tensile results obtained for the average Young's modulus (E), yield strength (YS), ultimate tensile strength (UTS), and percentage elongation at fracture (ε_{max}) are summarised in Table 7.8.

Table 7.8. Tensile test results for WAAM of Ti-6Al-4V using CMT, assigned to a 95% confidence interval.

Specimens	E (GPa)	UTS (MPa)	$YS_{0.2\%}$ (MPa)	ε_{max} (%)[1]
Control (rolled plate)				
CLT-T1	*126.56*	*1043.32*	*973.71*	-
CLT-T2	*129.30*	*1038.07*	*980.74*	-
CLT-T3	*129.83*	*1026.18*	*977.35*	-
Average (95%CI)	*128.56±1.99*	*1035.86±9.94*	*977.27±3.98*	-
CL-T1	*129.10*	*962.28*	*934.42*	18.3
CL-T2	*110.41*	*965.46*	*929.31*	-
CL-T3	*98.65*	*983.30*	*950.22*	16.0
Average (95%CI)	112.72±17.38	970.35±12.82	937.98±12.34	-
Certificate of conformity (rolled plate)				
CCLT-T1	-	*1041.11*	*946.65*	15.75±2.3
CCL-T1	-	*1008.70*	*915.62*	15.45±0.1
Longitudinal axis parallel to the welding direction				
PA6 H-T1	*114.87*	*999.18*	*869.64*	5.9
PA6 H-T2	*114.28*	*1004.62*	*861.00*	-
PA6 H-T3	*114.71*	*961.84*	*874.47*	-
Average (95%CI)	*114.62±0.35*	*988.55±26.35*	*868.37±7.72*	-
PA8 H-T1	*123.53*	*990.98*	*865.28*	-
PA8 H-T2	*118.19*	*988.74*	*868.22*	-
PA8 H-T3	*117.38*	*997.47*	*876.65*	-
Average (95%CI)	*119.70±3.78*	*992.40±5.13*	*870.05±6.68*	-
Longitudinal axis perpendicular to the welding direction				
V-T1	*114.61*	*973.20*	*844.27*	-
V-T2	*113.68*	*962.91*	*846.30*	-
V-T3	*113.77*	*966.50*	*847.11*	-
Average (95%CI)	*114.02±0.58*	*967.54±5.91*	*845.89±1.66*	-

[1] Percentage elongation after fracture.

The static tensile properties were determined autographically from the stress-strain diagrams provided in Figures 7.17 to 7.19. Supplementary stress-strain diagrams are supplied in Appendix N.

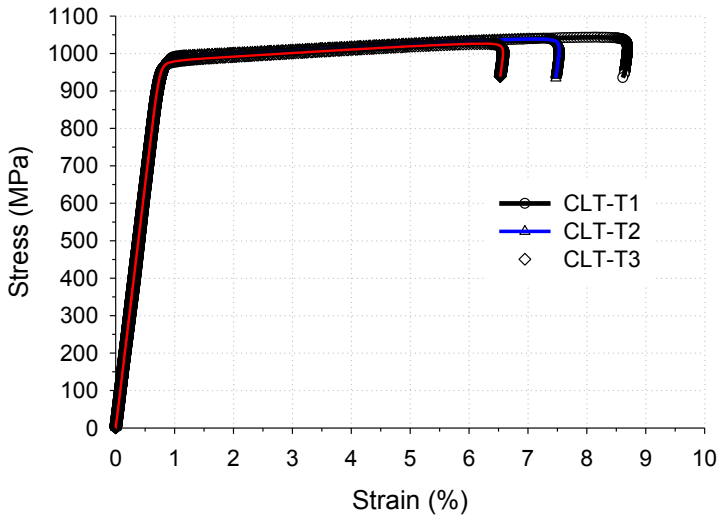

Young Modulus data fitted to equations:

a) *CLT-T1: stress = 126559 × strain + 8.3175 (R^2=0.9998);*
b) *CLT-T2: stress = 129302 × strain - 18.097 (R^2=0.9994);*
c) *CLT-T3: stress = 129828 × strain - 1.531 (R^2=1.0000).*

Figure 7.17. Stress-strain curves and *E* data obtained for specimens CLT-TN.

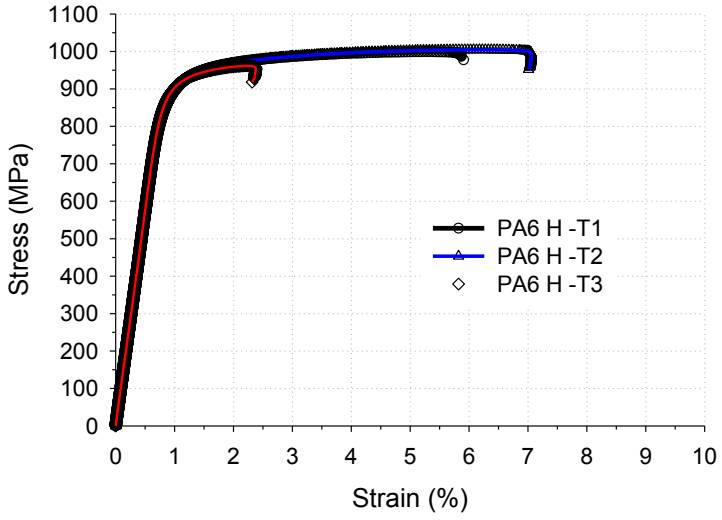

Young Modulus data fitted to equations:

a) *PA6 H-T1: stress = 114865 × strain - 3.6807 (R2=0.9998);*
b) *PA6 H-T2: stress = 114281 × strain - 6.3459 (R2=1.0000);*
c) *PA6 H-T3: stress = 114708 × strain - 0.0210 (R2=0.9999).*

Figure 7.18. Stress-strain curves and *E* data obtained for specimens PA6 H-TN.

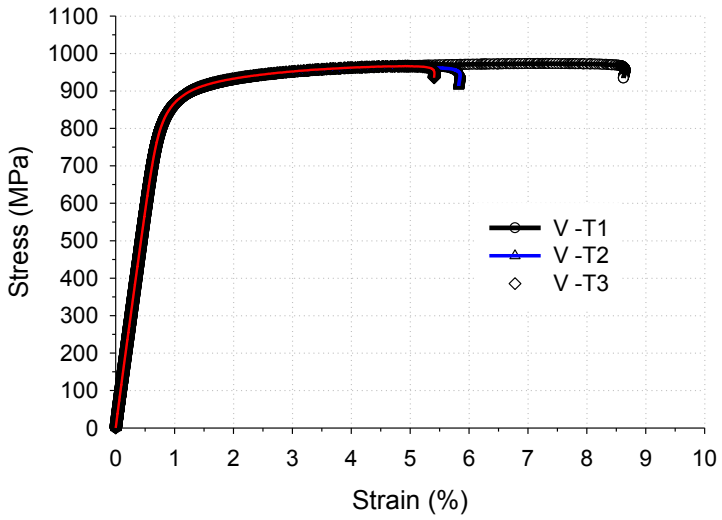

Young Modulus data fitted to equations:

a) *V-T1: stress = 114609 × strain + 13.75 (R2=0.9997);*
b) *V-T2: stress = 113675 × strain - 6.6301 (R2=0.9999);*
c) *V-T3: stress = 113765 × strain + 8.2488 (R2=0.9998).*

Figure 7.19. Stress-strain curves and *E* data obtained for specimens V-TN.

The average Young's modulus (*E*) of the rolled control specimens, *i.e.* CLT-TN and CL-TN, were 128.56±1.99 GPa and 112.72±17.38 GPa, in the *LT* and *L*-directions to rolling, respectively. *E* is approximately 16 GPa higher in the *LT*-direction when compared with the *L*-direction. This trend is in good agreement with the results presented by Larson and Zarkades (1974) on the effect of the specimen orientation on the Young's modulus in textured rolled Ti-6Al-4V sheet (see Figure 7.20).

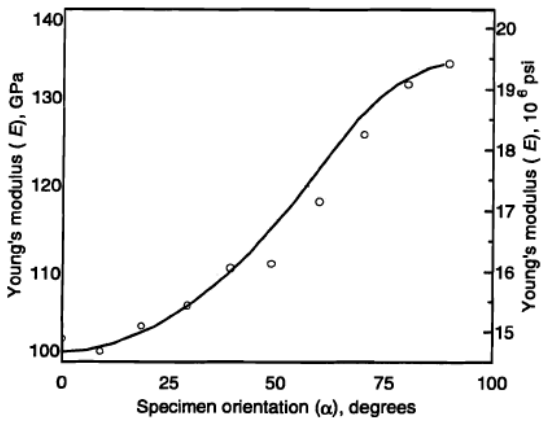

Figure 7.20. Relationship between Young's modulus and specimen orientation in textured rolled Ti-6Al-4V sheet at room temperature. α is the angle between the direction of rolling and the principal axis of the sample.

The dependence of *E* on the testing direction in multi-phase alloy can be attributed to one, or a combination of a number of factors, as follows: (a) the presence of different texture intensities that can cause strong crystallographic anisotropy of the elastic constants of α-Ti (Larson and Zarkades, 1974); (b) the *E* is determined by the specific moduli of the α and β phases and their volume fractions in the matrix, and therefore influenced by the thermo-mechanical treatment (Fan, 1993); (c) the effect of interstitial and substitutional α-stabilising solutes which generally causes *E* to increase, whereas β-stabilising solutes have the opposite effect on *E* (Welsch *et al.*, 1994); (d) the transformation of metastable β into α" martensite phase during thermo-mechanical processing increases the elastic modulus (Lee and Welsch, 1990).

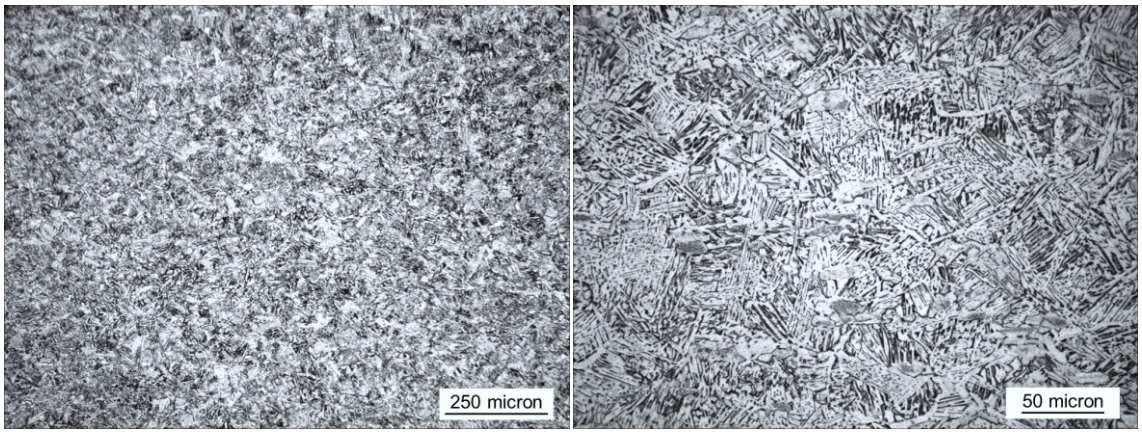

Figure 7.21. Microstructure of the mill annealed Ti-6Al-4V baseline control substrates in the as-received condition at different magnifications. The dark etching is β phase.

The equiaxed microstructure of the as-received control samples is generally achieved by means of a complex thermo-mechanical treatment. In a first stage, the product undergoes extensive mechanical working (normally over 75% reduction) in the α + β field causing the lamellar[39] fine needle-like α phase (or acicular α) to breakup into equiaxed α. A subsequent annealing heat treatment stage in the α + β field at 787.8±3.9 ºC for 6 hours (min.) is followed by moderate air cooling in order to produce a "mill-annealed" microstructure, as shown in Figure 7.21. Although no visible mechanical texture can be noticed immediately, possibly due to a complete recrystallisation process during heat treatment, it seems quite possible that some degree of crystallographic

[39] Produced by slow cooling into the α + β from above β-transus and air cooled.

texture was still present, along with altered volume fractions of α and β phases.

These strengthening mechanisms are regarded as the principal causes for the observed stiffening in the *LT*-direction. Samples tested in the *LT*-direction present the results with lower variability. The average *E* of the as-deposited Ti-6Al-4V samples was 114.62±0.35 GPa (PA6 H-TN) and 119.70±3.78 GPa (PA8 H-TN) in the horizontal, and 114.02±0.58 GPa (V-TN) in the vertical direction. These results show that the Young's modulus is independent of the testing direction in the as-deposited samples. The values of the Young's modulus obtained in this work for the control and as-deposited Ti-6Al-4V samples are in good agreement with the values of 100 to 130 GPa found in the literature (Welsch *et al.*, 1994).

For calculating *E*, the conventional measurement method of slopes in stress-strain curves, via autographically drawing a tangent to the proportional elastic regime as recommended in ASTM E 111-04, can result in inaccurate estimates of the modulus due to contributions to the strain from material creep or deflection of the testing machine (Ashby *et al.*, 2009). These results therefore need to be interpreted with caution.

Baufeld and Van der Biest (2009) found a Young's modulus of 71 GPa in the vertical direction in a SMD Ti-6Al-4V component using the conventional autographic method by measuring *E* in the stress region between 500 and 800 MPa. In the same publication, the authors have used dynamic measurement methods such as longitudinal resonance vibration or impulse excitation technique (IET) for precise determination of *E*. For the same testing conditions as described using the conventional autographic method a Young's modulus of 117 GPa was found in the as-deposited SMD specimens in the vertical direction. This latter result shows good agreement with the result of 114.02±0.58 GPa obtained in this study in the vertical direction (V-TN).

The nominal stress-strain curves for both control and as-deposited Ti-6Al-4V specimens are depicted in Figures 7.17 to 7.19. Supplementary stress-strain diagrams are supplied in Appendix N. The stress-strain curves indicate material strengthening by strain hardening mechanism. A limited capacity of strain hardening was observed in the control specimens (Figures 7.17 and N 1), whereas the effect of strengthening is more significant in the as-deposited specimens irrespective of their orientation (see Figures 7.18 and 7.19 in pages 259 and 260, respectively).

The percentage elongation after fracture was determined according to the procedure and requirements detailed in section 7.1.5. As illustrated in Figure N 3 to N 5 (see Appendix N in pages 422 and 423, correspondingly) the majority of fractures after testing occurred outside the extensometer gauge length during tensile test. As a result, these automated data obtained with the extensometer were considered invalid, according to BS EN ISO 6892-1:2009 and ASTM E8/E8M-08. Moreover, the method (b) defined in section 7.1.5 was also assumed invalid since most of the fractures have occurred outside the marked gauge mark. The elongation values obtained in these tensile tests were extremely low, and thus not representative of the true elongation behaviour of the material.

Overall, and taking into account the above considerations, a very limited number of ductility values were considered valid in this study. The most representative value of percentage elongation after fracture was 18.3 %, which was obtained for the baseline rolled plate in the *L*-direction (see sample CH-T1 in Figure N 3 on page 422). Although slightly higher (approx. 15.5 %), this result is in very good agreement with the as-received material certificate for both testing directions.

7.2.5 Wire and arc additive manufacturing process control model of Ti-6Al-4V using cold metal transfer

The success of "intelligent" and fully automated WAAM systems depends strongly on accurate predictions of optimum welding process parameters in order to achieve a target weld bead geometry, and vice versa. The geometry of the bead is to be specified by a computer aided design (CAD) solid model and should comprise variables such as W_{eff}, MDE, as well as H_n (Delta-*z*) per deposited layer, among others.

A process control model based on an empirical approach is herein described for CMT multi-layer deposition of Ti-6Al-4V using Design Expert®7.15 software. The fundamental principles for developing the model were applied in deposition of mild steel (see section 3.12). A comprehensive systematic experimental approach (SEA) strategy was adopted utilising three factors and several other responses. The controllable variables were WD, WFS and WFS/TS. Wires with diameters of 0.9 and 1.2 mm were used, while WFS_{set} ranged between 2 to 12 m min^{-1} for each individual wire, in a unit

basis. WFS/TS of 15, 20 and 25 were selected in order to assure stable welding conditions and good quality of the deposits throughout the design space.

The steps followed for the integration of the experimental results with the statistical software were made in accordance with section 3.12.3, while the model development procedure was performed as detailed in section 3.12.4. A number of responses were selected and measured, although only the W_{eff} and MDE are reported here. A typical first order 3D response surface for the effective wall width is shown in Figure 7.22. Larger W_{eff} are achieved when a 1.2 mm diameter wire is used in comparison with 0.9 mm, for constant values of WFS_{set} and WFS/TS.

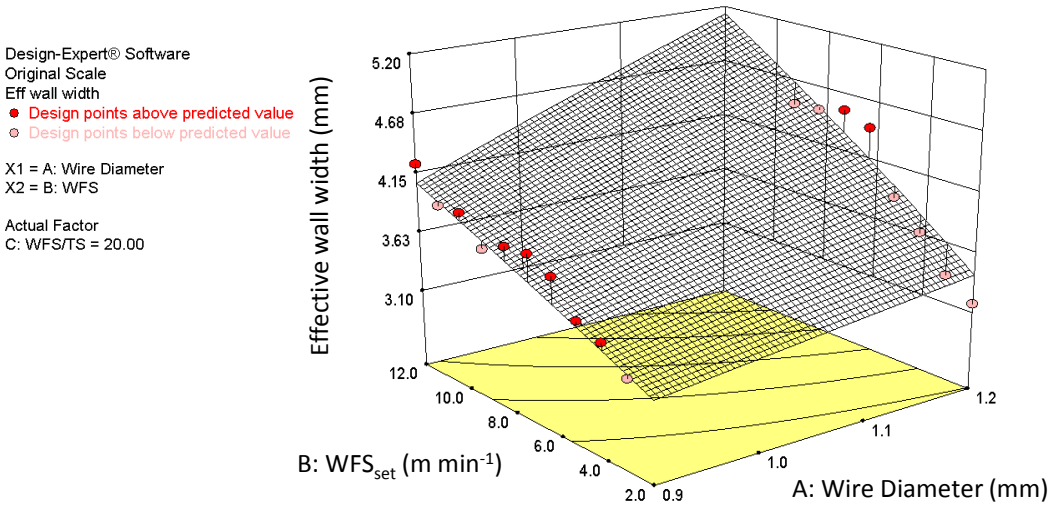

Figure 7.22. Three-dimensional response surface showing the interactions between process factors, *i.e.* WFS_{set} and WD, and the response surface W_{eff} (WFS/TS=20).

To maximise the confidence level on the regression models obtained and hence improve the quality of the fit, the ANOVA method alongside a model adequacy checking procedure were undertaken (according to sections 3.12.5 and 3.12.6, respectively). Scaled residuals were also checked and a pure random scatter was observed with no visible trend or pattern. The sum of squares (SS) output was improved by selecting the best power transformation recommended by the analysis software, *i.e.* λ=1.63. Large correlation values are desired in order to maximise the confidence level of the model predictions. The proportion of the total variability explained by the model, as measured by R^2_{Adj} and R^2_{Pred}, were respectively 0.896 and 0.874 and considered satisfactory.

Moreover, R^2_{Adj} and R^2_{Pred} terms have also shown to be within 0.20 of each other, and as a result in very good agreement. Non-significant interaction effects (p>0.1) were dropped from the model (CI of 90 %), while considerable signal-to-noise ratio in the model was obtained (*F*-value=87.16). Overall, accurate predictions involve reasonable consistency and stable variance during the process model development.

The MDE of Ti-6Al-4V is displayed in the scatter plot shown in Figure 7.23 as a function of W_{eff}, for CMT and a wire diameter of 1.2 mm. An W_{eff} ranging from 3.2 to 5.2 mm is achievable with a MDE over 80 %. It is also apparent that there is a slight dependence of the W_{eff} on the WFS/TS.

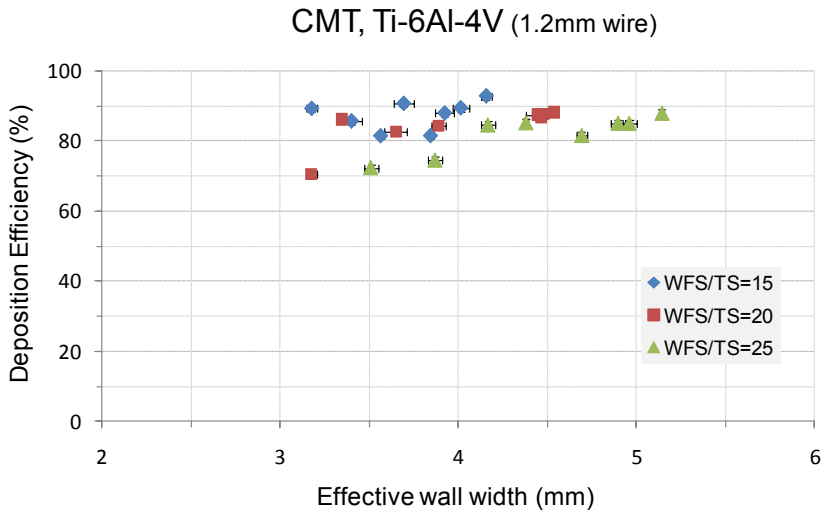

Figure 7.23. Measured MDE of Ti-6-Al-4V as a function of the W_{eff} using CMT (WFS/TS=constant).

7.3 Conclusions

The following conclusions can be drawn from the present study:

1. Gas tungsten constricted arc welding (GTCAW) technology was demonstrated for the first time in WAAM applications for out-of-chamber fabrication of a high quality large structural component made of Ti-6Al-4V.

2. The cold metal transfer (CMT) process was shown to overcome the poor welding conditions associated with DCEP-GMAW of titanium. CMT technology was demonstrated to produce spatter free Ti-6Al-4V deposits with greatly improved weld bead straightness and uniformity.

3. Significant grain refinement of the solidification macrostructure was achieved in single and multi-layer deposits processed via CMT using optimised shielding gas mixtures of Ar-He mixtures, *i.e.* higher helium contents.

4. The finer and more isotropic macrostructures obtained for the as-deposited Ti-6Al-4V material using CMT resulted in the improvement of static tensile properties, when compared with the same as-deposited material processed by GTAW-P.

5. Under identical welding conditions, the average ultimate and yield tensile strength of the as-deposited Ti-6Al-4V material processed via CMT and tested in the vertical direction were 2.1 % and 2.6 % lower than the material tested in the horizontal direction, respectively.

6. The average ultimate and yield tensile strength of the as-deposited Ti-6Al-4V material processed with CMT meet the minima specification values recommended for most Ti-6Al-4V products, particularly in BS 2TA 56:2009 (specification for plate of titanium-aluminium-vanadium alloy) in both horizontal and vertical directions.

7. The average ultimate and yield tensile strength of the as-deposited Ti-6Al-4V material processed via CMT exhibited very little sensitivity to the weld energy input.

8. A process control model was developed for the CMT process of Ti-6Al-4V, which enables the determination of process parameters for specific target wall widths.

9. The effective wall width response was modelled and is in good agreement with the empirical data. The effective wall width ranges from 3.2 to 5.2 mm with deposition efficiencies over 80 %, and deposition rates higher than 3 kg h^{-1} for 1.2mm Ti-6Al-4V wires.

8 Residual stress in single and multi-layer welds

This chapter concentrates on the analysis of the results obtained from several residual stress measurements carried out on large WAAM components. Neutron diffraction technique was applied to characterise the residual stress level introduced by WAAM technology in low carbon steel rectilinear structures. The investigation aimed primarily to establish the effect of repeated thermo-mechanical cycling on the generation, evolution and distribution of the introduced residual stress field. The residual stress measurements were made using the spallation source ENGIN-X at the ISIS facility in the Rutherford Appleton Laboratory in Oxford, UK. In addition, the allied microstructural variations were assessed by optical microscopy and Vickers hardness testing.

The details of the experimental procedure used throughout the investigation are described in the first section of this chapter (section 8.1).

Section 8.2 presents the main research findings and discusses the results of this investigation. Thermal history profiles data obtained from a WAAM instrumented sample are shown in section 8.2.1. The average lattice constant data in both strained and unstrained conditions are given in section 8.2.2. Section 8.2.3 and section 8.2.4 introduces the distribution of the triaxial residual stress state measured along the multi-bead and base plate in a WAAM specimen with five layers high. The effect of successive deposition, and therefore the number of layers, on the generation and re-distribution of residual stress is presented in section 8.2.5, whereas section 8.2.6 focuses on the impact of the base plate removal on the stress field. Section 8.2.7 examines the effect of residual stress distribution on welding-induced distortion. A comparison between the triaxial state of stress and plane-stress assumption is reported in section 8.2.8, whilst the relationship between Vickers hardness and residual stress is examined in section 8.2.9.

Note that the results of residual strain and thermocouple measurements presented herein were used for verifying a thermo-mechanical model for the temperature distribution, distortion and residual stresses generated by FEM (Ding *et al.*, 2011).

8.1 Experimental procedure

8.1.1 Materials and welding consumables

Experiments were carried out on as-rolled S355J2+N low carbon steel substrates supplied according to specifications BS EN 10025:2004/ ASTM A1011/1011M. These structural steels are typically produced through conventional hot rolling process at temperatures of around 1250 ºC and rolling would be completed at temperatures in the order of 1000 ºC. A mild steel solid wire electrode of 0.8 mm diameter grade G3Si1 (conform to EN 440.94/ AWS: A5.18ER70S-6) was used in the present investigation. The maximum nominal compositions in wt. % of substrates and wire electrode are given in Table 3.1 (see section 3.1 in page 82). In this study an oxidising shielding gas mixture from group M21 (according to BS EN 439) containing 20% CO_2, balance argon, was selected while the flow rate was set to 20 l min^{-1}. The x, y and z dimensions of the substrates are schematically shown in Figure 8.1.

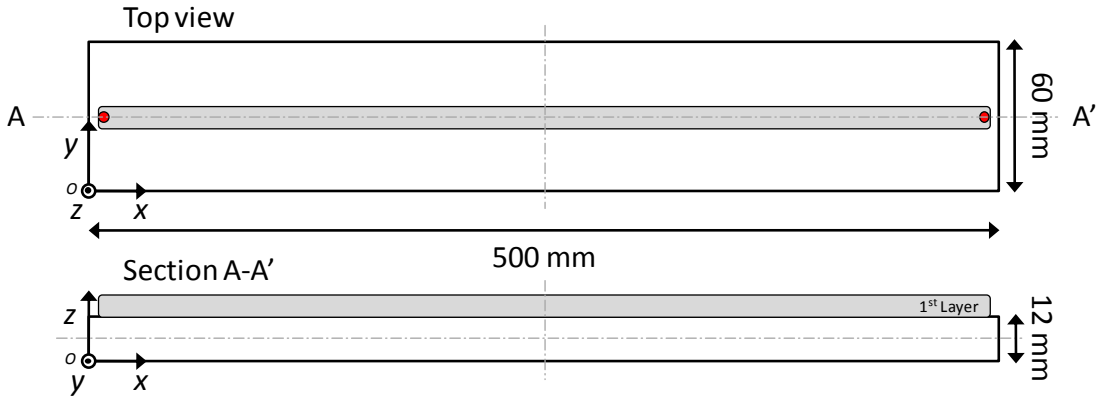

Figure 8.1. Schematic illustration of the substrate dimensions (top and cross section A-A' views).

8.1.2 Apparatus and welding conditions

A cold metal transfer (CMT) welding set was employed to produce the test specimens. Multi-layer walls were manufactured using the materials and welding consumables described in section 8.1.1. Substrates were prepared before deposition according to section 3.2. The experimental welding set-up is shown in Figure 8.2. The dedicated *Robacta Drive* CMT water cooled welding torch was attached to a pre-programmed six-axis ABB industrial welding robot (model *IRB 2400*), in order to accurately reproduce

the welding traverse speed and deposition sequence, over a repeated number of cycles. Some of the welding process parameters utilised in the present experiment, such as WFS, TS and WD, were previously established in a preliminary process model study detailed in section 4.5. The welding conditions were to satisfy three major requirements: (1) a target effective wall width of 5 mm, (2) a maximum surface waviness profile of 200 µm, and (3) a high WFS for maximising the deposition rate. Welding conditions were chosen from the optimised multi-layer process model predictions (detailed in section 4.5.2, in page 178).

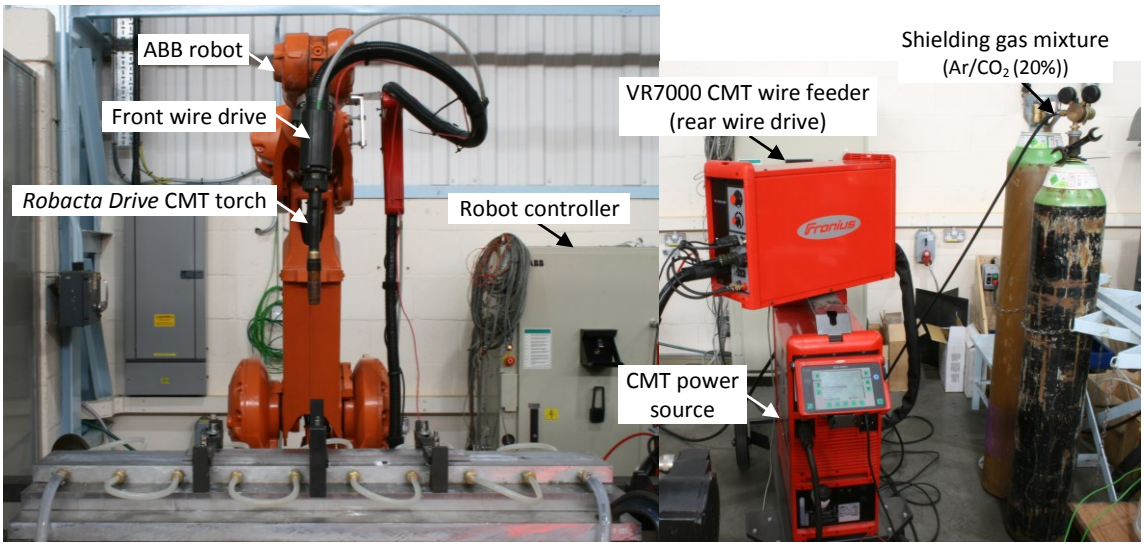

Figure 8.2. Montage of the experimental set-up used to produce the test specimens.

For a constant 0.8 mm wire diameter mild steel electrode and shielding gas mixture of 20% CO_2, and the balance argon, the resultant process model outputs were 10 m min^{-1} WFS and 0.5 m min^{-1} TS. Note that all samples were manufactured under equivalent welding conditions, as summarised in Table 8.1. It should also be borne in mind that secondary process parameters, such as ALC and DC_{orr}, were kept fixed at its nominal zero value.

Table 8.1. Summary of the employed constant CMT welding conditions.

Welding process	WD (mm)	WFS (m min^{-1})	TS (m min^{-1})	E_{ff} (η)	CTWD (mm)	Shielding gas	Flow rate (*l* min^{-1})	Substrate T (ºC)	DR (kg h^{-1})
CMT	0.8	10	0.5	0.9	13	Ar/CO_2 (20%)	20	RT	2.352

The exact position where the base plates were positioned was initially marked on the aluminium backing plate. Substrates were then clamped at 6 points onto a water cooled

aluminium backing plate, as seen in Figure 8.3. This arrangement guaranteed accurate positioning of substrates, while at the same time minimising distortion during welding.

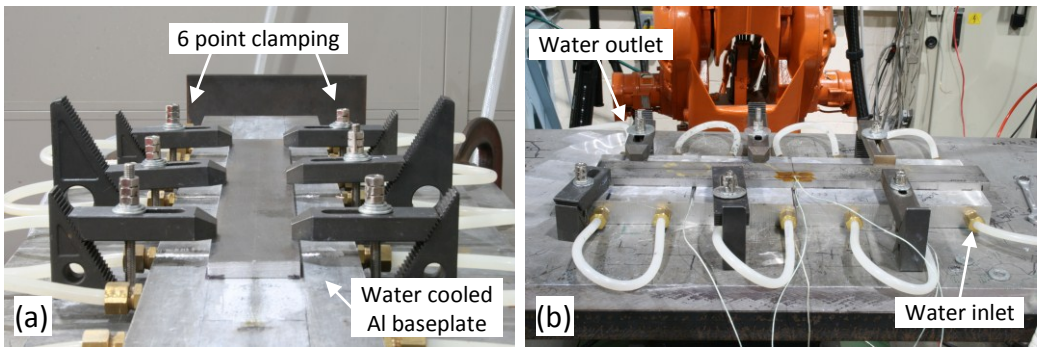

Figure 8.3. Sample positioning method showing (a) the six point clamping arrangement and the water cooled aluminium base plate, (b) the serpentine water cooling piping system.

8.1.3 Welding experimental plan

A similar build up strategy was established throughout the experiment by ensuring an interpass temperature of approximately 25 °C, as described in section 3.4. The substrate temperature was monitored with an infrared pyrometer (model *Raytek Raynger S.T.*). The set-up and welding conditions detailed in section 8.1.2 were employed in the PA position, or 1G (according to PD CEN/TR14633:2003), for manufacturing the specimens, as schematically shown in Figure 8.4. Stable and reproducible welding conditions were ensured by a constant CTWD set for each run at 13 mm. Electric transients were recorded according to the method described in section 3.3.

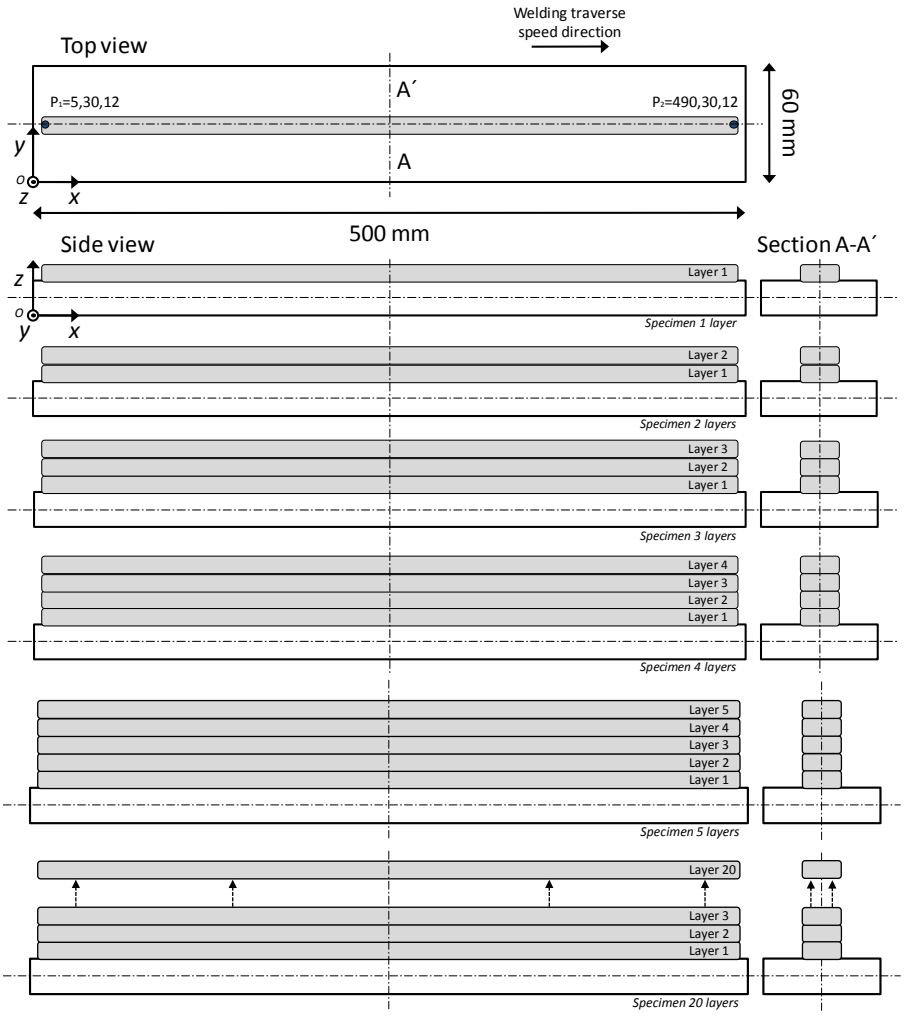

Figure 8.4. Schematic illustration of the experimental welding sequence. Also shown are the substrate top view, welding traverse speed direction, the side views build-up sequence and the A-A' cross sections.

8.1.4 Thermocouple set-up

Temperature was measured during welding at different substrate locations in order to monitor heating and cooling rates. A data logger (model *NI SCXI-1000*) was utilised to read temperatures at an acquisition rate of 100 Hz. The thermal history was recorded using five K-type[40] thermocouples (TC_1, TC_2, TC_3, TC_4 and TC_5) which were spot welded in pre-established positions on the substrate, as shown in Figure 8.5.

[40] Typical operating temperature ranges from -200ºC and 1350ºC.

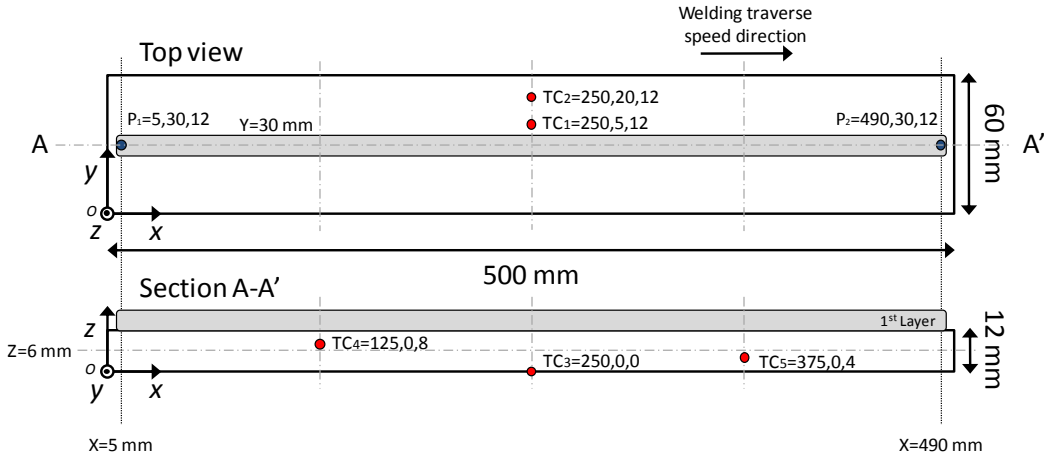

Figure 8.5. Schematic diagram showing the location of the thermocouples (top and cross section A-A' views).

Thermocouples TC_1, TC_2 and TC_3 were directly spot welded to both top and bottom surfaces of the base plate. Two 13 mm diameter holes were drilled in order to allow the thermocouples TC_4 and TC_5 to be firmly fusion welded to the substrate. These were drilled up to four and eight millimetres deep relative to the bottom (see Figure 8.6).

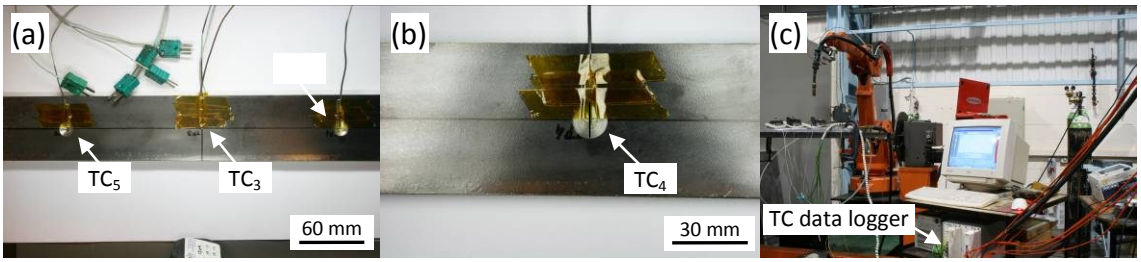

Figure 8.6. Thermocouples arrangement on the substrate bottom side after spot welding (a) TC_3, TC_4 and TC_5, (b) detailed view of TC_4 (13 mm hole drilled), and (c) general view of the data logger.

8.1.5 Neutron strain scanning

In this investigation a systematic analysis of the residual stresses was carried out by a pulsed time-of-flight (TOF) neutron strain scanning instrument (NSS). Welded specimens were produced utilising the apparatus and welding conditions detailed in section 8.1.2 and using the experimental plan described in section 8.1.3. The testing method and subsequent analysis of the raw data was focused on *specimens 1 layer, 2 layers, 3 layers, 5 layers, and 20 layers* (with (P) and without base plate (WP)), and carried out conform to *DD CEN ISO/TS 21432:2005 – Incorporating corrigendum January 2008* (refer to Figure 8.4 for definitions of the labelling).

The lowest achievable wavelength of this TOF instrument is approximately 0.5 Å and its maximum allowable repetition frequency is 50 Hz. However, the repetition frequency was typically set to 25 Hz for practical reasons, as recommended by Santisteban *et al.* (2006). A pulsed white neutron incident beam with a wide range of neutron energies, *i.e.* travel speeds and wavelengths, and therefore with a well-defined neutron energy spectrum, illuminates individual samples placed on a motorized positioner (see plan-view schematic in Figure 2.21 in chapter 2). As a result, and although a large number of grains in the cuboid sample gauge volume (SGV) are illuminated, only a small fraction of these grains are favourably oriented in order to satisfy Bragg's diffraction condition at any time (see equation (2.4) in chapter 2) . The principal strain tensors were then measured with the scattered vector parallel to individual 3D coordinates defined herein as longitudinal, LD_x transverse, TD_y and normal, ND_z directions (see Figure 8.8 for identifying the coordinate system). For clarity reasons it is seen that the scattered vectors q_1 and q_2 resulting (see Figure 2.21) are the principal strain tensor components measured in the LD_x and TD_y directions, respectively. To measure the longitudinal strain tensor direction along the *x*-direction the slit aperture (S_x and S_y) and collimator (S_z) were adjusted to a cuboid SGV geometry of 2×2×2 mm^3 in the ENGIX-X. The transverse and normal strain tensor components along both the *y*- and *z*-directions were measured utilising a 2×20×2 mm^3 SGV. A constant gauge length of 2 mm collimator, S_z was utilised for the diffracted beam for all measurements. Note however that faster measurements were made, for the transverse and normal tensors, by opening the vertical slit (S_y) of the incoming beam and therefore permitting a larger neutron flux rastering without affecting the spatial resolution.

Figure 8.7 provides an overview of the actual set-up at ISIS where the exact orientation of specimens *5 layers* and *20 layers-P and WP* (see Figure 8.7(a) and (b), respectively) for simultaneous neutron strain acquisition is observed (in the LD_x and TD_y directions). Two diffraction detector banks North and South are placed approximately at a constant angle of $2\theta_{Bragg}$ (normally θ_{Bragg} for continuous beam sources) or ±90º to the incident beam, and 180 ºfrom one another. As a result, two perpendicular principal strain tensor directions were measured simultaneously from crystallographic planes that satisfy Bragg's law condition.

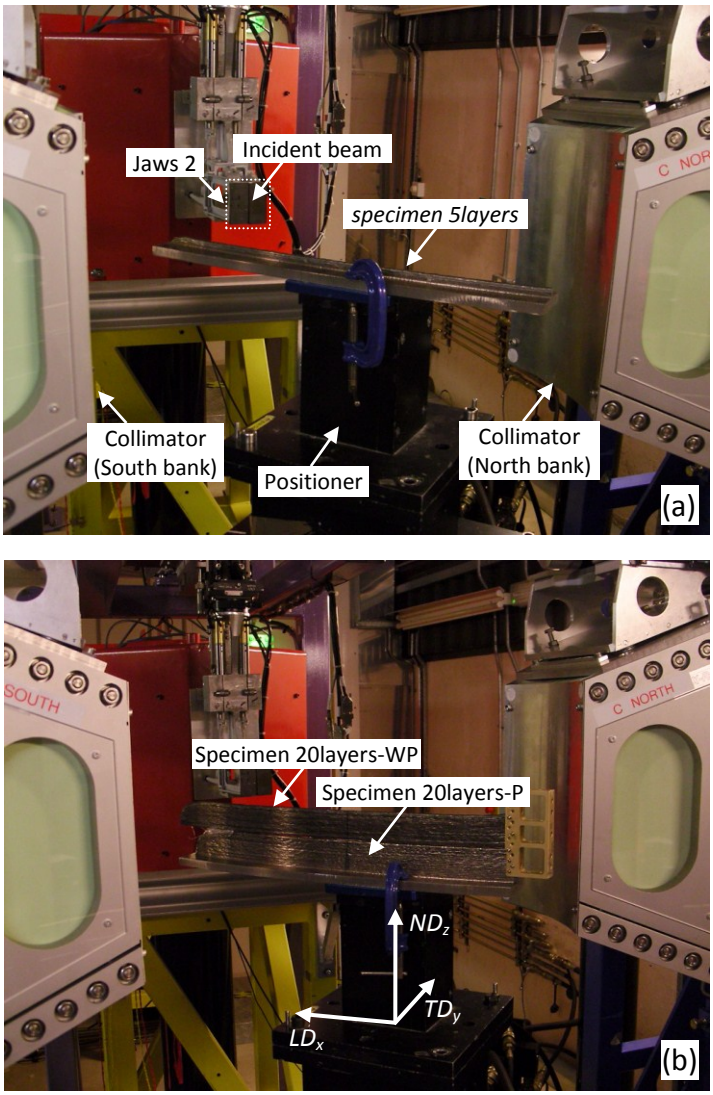

Figure 8.7. General overview of the ENGIN-X neutron strain scanner apparatus showing (a) a number of fundamental elements of the equipment as well as the orientation of specimens 5 layers, and (b) specimens 20 layers-P and WP before neutron strain acquisition.

Strain scanning data was obtained for a TOF spectrum range of 20 to 40 ms typically covering an atomic lattice spacing (d_{hkl} – spacing) range of 1.1 Å to 2.1 Å. Crystallographic planes containing the most intense Bragg edges, *i.e.* (110), (200) and (211) families of lattice planes (Steuwer *et al.*, 2001), were analysed using Bragg's law. The applied TOF spectral range ensured the determination of the average macroscopic strain from the sampling region. By combining a range of neutron energies with different families of crystallographic planes the anisotropic component can be minimised.

The multi-peak neutron diffraction spectra data was used to refine the lattice parameters by refinement and fitting utilising the Pawley-type principle (Pawley, 1981; Steuwer *et al.*, 2001). Processing and analysis of the single crystal diffraction data was carried out using a set of programs from general structure analysis system (GSAS) software (Larson and Dreele, 2004) for a better approach to the macroscopic strain condition by determining the average lattice parameter, a.

Hence, neutron strain data was collected for three principal strain tensor components, ε_{xx}, ε_{yy}, and ε_{zz}, in the longitudinal, transverse and normal directions, respectively. Measurements were carried out over the full set of manufactured samples, as shown in Figure 8.4, with the exception of *specimen 4 layers*. The centroid of the gauge volume was positioned in the base plate along a measurement line at 2 mm below its top surface parallel to the TD_y direction, as well as across a measurement line at the mid-length section of the built specimens parallel to the ND_z direction (see Figure 8.8).

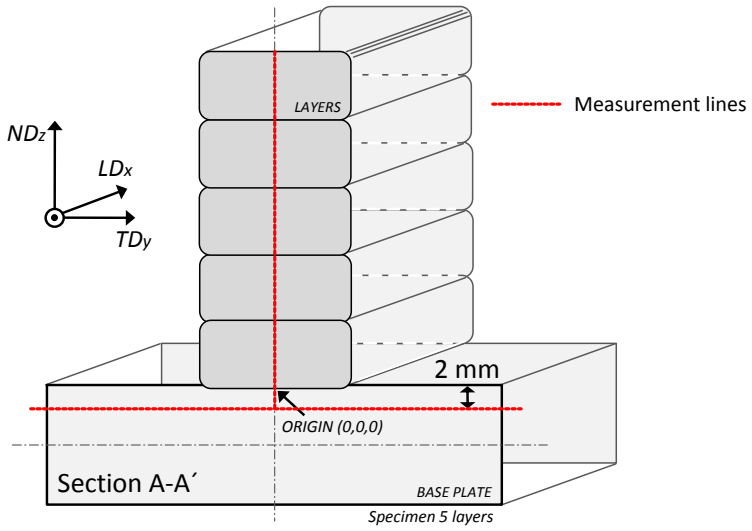

Figure 8.8. Schematic cross section A-A´(see Figure 8.4) showing the neutron strain scanning measurement lines, and principal strain tensor components.

Measurements were systematically made for all specimens. The average lattice spacing, d_0 for the unstressed condition was obtained from the stress-free reference sample. The stress components σ_{xx}, σ_{yy} and σ_{zz}, were determined thereafter and analysed using Hooke's law (see equation (2.6)) and assuming the measured directions were the principal strain directions, LD_x, TD_y and ND_z, as indicated in Figure 8.8.

In order to obtain accurate measurements of the unstressed lattice spacing distance, d_0 for each manufactured specimen, precise reference lattice parameters, a were taken from individual stress-free reference samples. In order to establish discrete stress-free lattice spacing distances and therefore corrected d_0 values, 3 mm wide slices were mechanically cut perpendicular to the longitudinal direction, close to the free end of each particular manufactured specimen. In line with Rogante's work (2000), and assuming that any process induced macro-strain effects would be negligible close to the end surface of the specimens, relative d_0 measurements were made along two principal directions (longitudinal and normal), and their average considered as a valid experimental method to determine d_0.

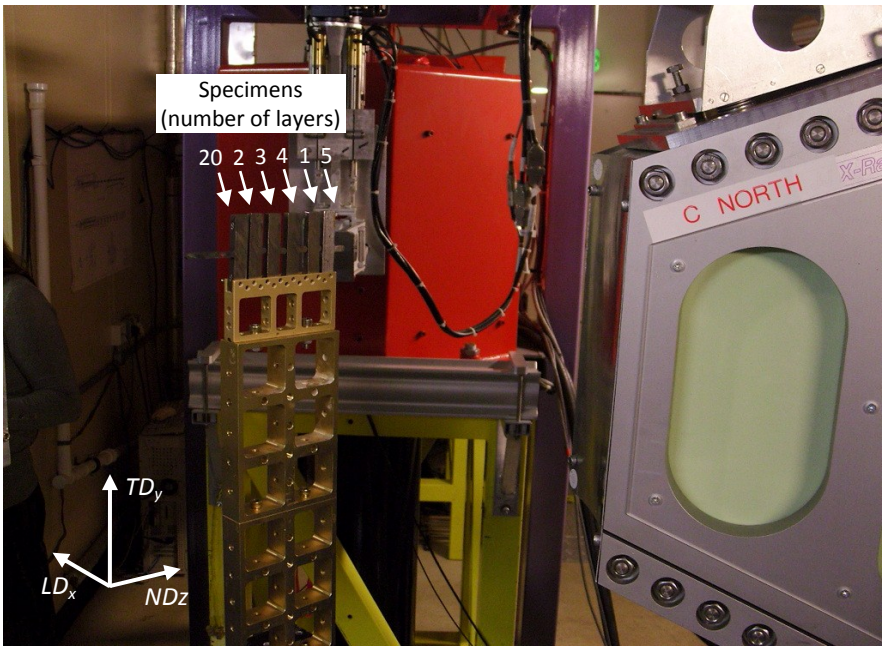

Figure 8.9. Measurement of the stress-free reference samples at the ENGIN-X neutron strain scanner.

Measurements of the stress-free reference samples were performed over the full set of manufactured samples (see Figure 8.9). The centre of the gauge volume was positioned in the base plate along a measurement line at 2 mm below its top surface parallel to the TD_y direction, as well as across a measurement line at the mid-length section of the built specimens parallel to the ND_z direction, as illustrated in Figure 8.10.

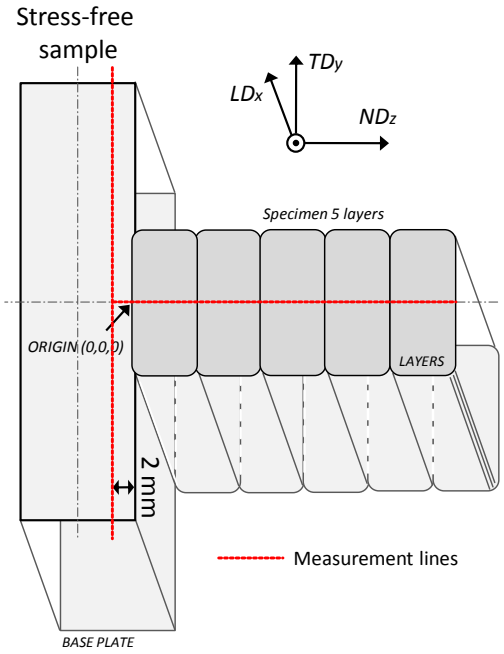

Figure 8.10. Schematic of a stress-free reference sample illustrating the neutron strain scanning measurement lines, and principal strain tensor components.

Neutron strain scanning data was then collected along the longitudinal and normal principal directions and the average lattice parameter, a_0^{avg} determined, again by utilising a Pawley-type full pattern analysis procedure.

8.1.6 Metallographic preparation

Six samples were taken from each of the seven large manufactured specimens (see Figure 8.4). No samples were taken from the second 20 layer build, *i.e. specimen 20 layers (WP)*. Three millimetres thick sections were cut from an area of interest close to where the stress free reference samples were taken. These sections were considered representative of the material under evaluation. The preparation and examination of the samples were carried out according to the procedure described in section 3.6.

8.1.7 Hardness testing

Destructive low-force Vickers hardness (HV) testing was carried out on *specimen 1 layer* and *specimen 5 layers* using a Zwick/Roell hardness testing machine, according to the method specified in BS EN 6507:2005. Samples for hardness tests were extracted perpendicular to the longitudinal direction from approximately the mid-length position

of the specimens produced (section A' – A in Figure 8.4). After extraction, samples were ground to obtain smooth parallel faces to a final fixed thickness of 10 mm, and prepared according to the method described in section 8.1.6, in page 279.

Horizontal and vertical indentation measurement lines for the low-force HV test were performed at the same locations as in NSS study (see Figure 8.8). Hardness measurements were carried out along the horizontal measurement line located 2 mm below and parallel to the base plate top surface, and along a vertical measurement line positioned along the single and multi-bead mid-length section (see Figure K 1 in Appendix K). It should be noted that the origin was positioned at the interception point between both lines.

The low-force HV tests were conducted at room temperature (approx. 20 °C) applying a nominal test force value of 0.5 kgf (or 4.903325 N)[41], a loading time of 10 s, and an approaching speed of the indenter of 0.2 mm s^{-1} (max.). The distance between the centres of adjacent indentations was set to 0.5 mm. The prepared samples were then indented by means of a Vickers-type diamond pyramidal indenter with an angle of 136°. Indentations were finally carried out across the parent metal (PM), heat affected zone (HAZ) and fusion zone (FZ) along both measurement lines.

8.2 Results and discussion

8.2.1 Thermal history

Thermal history profiles were obtained according to the procedure described in section 8.1.4 using an instrumented specimen with four layers.

Figure 8.11(a) shows the heating and cooling cycle profiles measured in thermocouple TC_4 during deposition. A maximum peak temperature of 492 °C in TC_4 was reached during deposition of the first layer as a result of its close proximity to the heat source, *i.e.* 4 mm below the top surface of the substrate (see schematic in Figure 8.5). The maximum temperature per layer deposited decreases then with the distance to the

[41] Where the conversion factor from kgf to N is 9,80665.

welding heat source in the *z*-direction. In addition, the time needed to cool down the 1st, 2nd, 3rd, and 4th deposited layers to 100 °C (shown as t_{100} in Figure 8.11(a)) was 43, 51, 61 and 69 seconds, correspondingly.

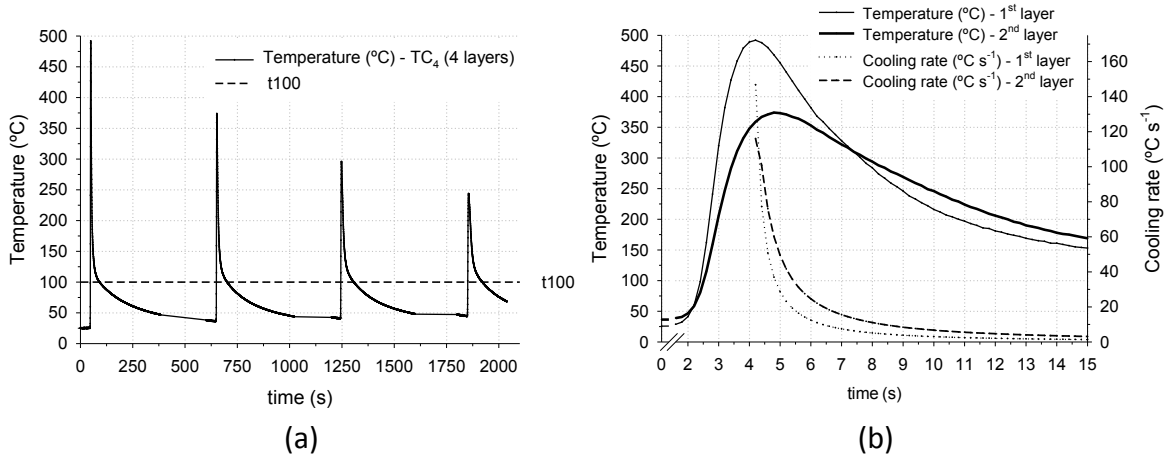

Figure 8.11. Temperature versus time profiles of thermocouple TC_4 during deposition of (a) four layers and (b) one and two layers high. Also represented in (b) are the instantaneous cooling rate curves associated with the deposition of the first and second layers.

Figure 8.11(b) shows the temperature versus time profiles and corresponding cooling rates obtained for a period of 15 seconds, while depositing the 1st and 2nd layers. The maximum peak temperatures reached in the 1st and 2nd layers were 492 °C and 374 °C, whereas maximum instantaneous cooling rates of 147 °C s^{-1} and 116 °C s^{-1} were measured in the same order.

In WAAM most of the heat generated during deposition on the top of the build is transferred primarily through conduction to the component. Nevertheless, the higher thermal gradient observed in TC_4 located in a fixed position in the substrate occurs during deposition of the first layer. At this position, steeper heating and cooling rate conditions were recorded, when compared with the thermal cycle induced by deposition of the second and subsequent layers (see Figure 8.11(b)). The heating rate was controlled by the proximity of the heat source to the thermocouple, whilst cooling appears to be dominated by the heat sink volume provided by the underlying structure. As the number of deposited layers increases (see Figure 8.11(a)), the heat sink volume for heat transfer becomes two dimensional suggesting that the material cools less quickly at the free end, while heat dissipation by convection starts to become also significant.

8.2.2 Average strained $a_{L,T,N}$ and unstrained lattice constant a_0^{avg}

Estimates of the average lattice constant, a_0^{avg} were determined by measurements taken from individual stress-free reference samples, as described in section 8.1.5. The variation of the strained, $a_{L,T,N}$ unstrained, $a_0^{L,N}$ and corrected average reference lattice parameter, a_0^{avg} are shown in Figure 8.12 and Figure 8.13, along the measurement lines for both multi-bead and base plate cases. The strained lattice parameter shows the largest variation in the longitudinal direction a_L, as seen in Figure 8.12. At the same time, the strained lattice parameter in both transverse and normal principal directions, $a_{T,N}$ show a very similar variation along measurement line along the multi-bead. This variation is within an uncertainty interval of ±0.001 Å. It should be pointed out that both the strained, $a_{L,T,N}$ and unstrained, $a_0^{L,N}$ lattice parameters show a steep variation in all directions, at the interface between the multi-bead and base plate. It is believed that the reasons behind such variation can be explained on the grounds of local changes in alloy chemistry, microstructural phase changes, and induced crystallographic texture. Local chemistry variations typically enhance mechanical properties such as strength and hardness, impacting as a result the local strain distribution. These compositional fluctuations involved small variations in the solute content of the alloy by interstitial solid solution mechanism as a result of diffusion and migration of small atoms, *e.g.* carbon, from the base plate in the direction to the "purer" weld reinforcement.

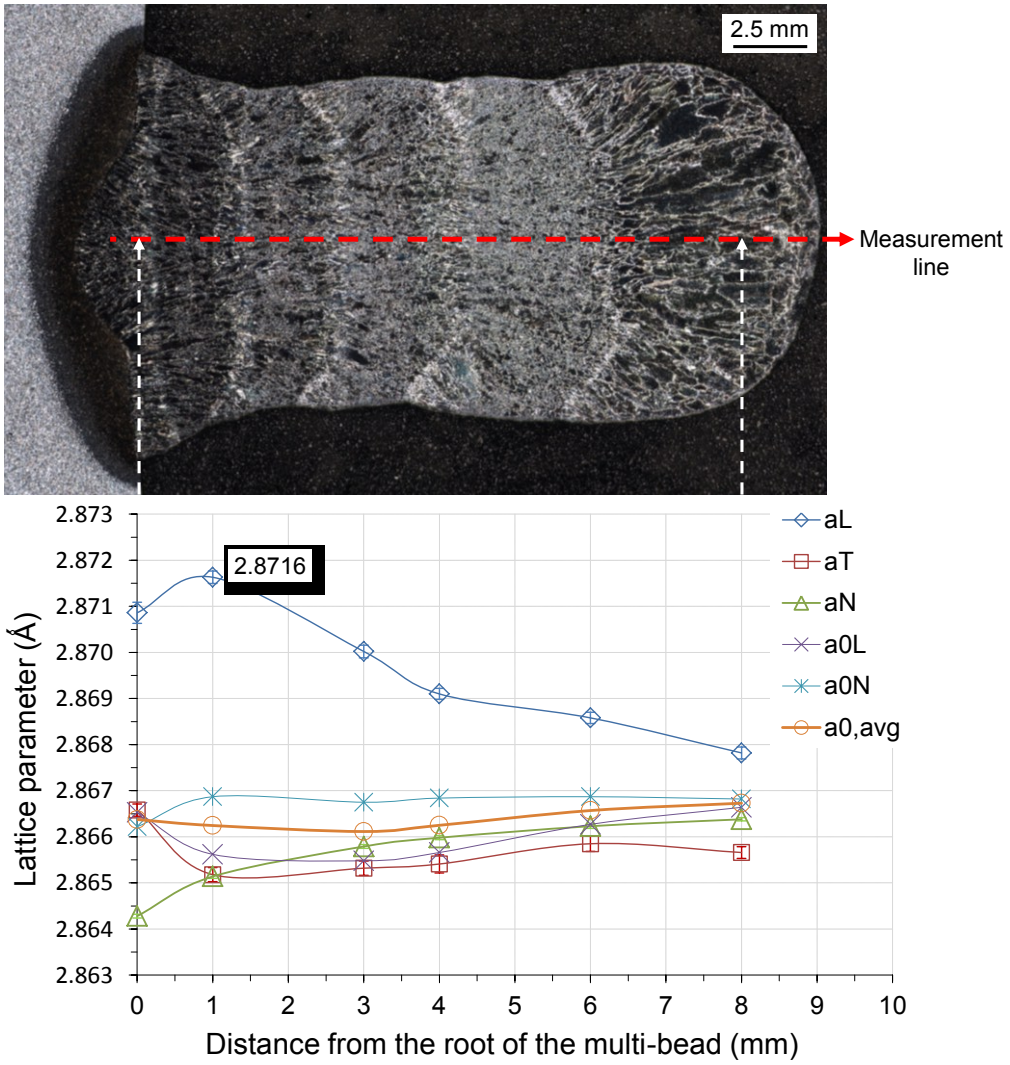

Figure 8.12. Variation of the strained, $a_{L,T,N}$ unstrained, $a_0^{L,N}$ and corrected average reference lattice parameter, a_0^{avg}. Measurements were taken along the measurement centreline of the multi-beads in the ND_z direction.

At the same time metallurgical phase changes may have occurred as the first welded layer as deposited generating as a result interphase strains. The higher thermal gradient experienced upon on cooling may eventually have caused bainitic and/or martensitic transformations to occur, as a result of the larger heat sink volume brought about by the base plate (see section 8.2.1). The medium to fast cooling rates involved during deposition of the first layer may for this reason justify to some extent the observed variation in the strained and unstrained unit cell parameter. In addition, a nearly constant variation of the average reference lattice parameter a_0^{avg}.

Important to note, however, is that a_0^{avg} was obtained by averaging both the unstrained reference lattice parameters in the longitudinal, a_0^L and normal directions, a_0^N and utilised thereafter for correction of the measured strain.

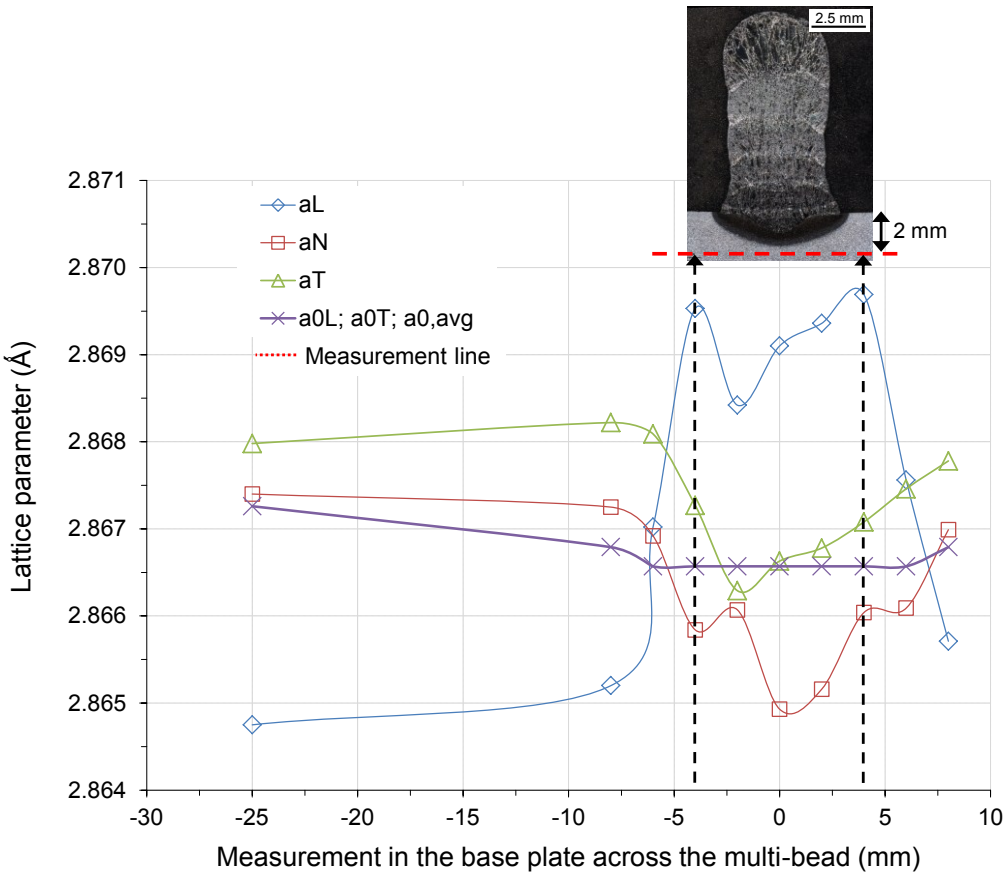

Figure 8.13. Comparison of the variation of the strained $a_{L,T,N}$, unstrained $a_0^{L,N}$, and corrected average reference lattice parameter, a_0^{avg}. Measurements were taken along the line positioned at 2 mm below the base plate surface in the TD_y direction.

In Figure 8.13 a second set of data was collected along the measurement line located at 2 mm below the base plate top surface and parallel to the TD_y direction. The measured strained lattice parameter in the longitudinal direction a_L, shows the largest variation. The peak width of the strained lattice parameter in the longitudinal direction, a_L includes the region located underneath the multi-bead and also the heat affected zone (HAZ). The maximum peaks are identified at a position around $-4 \leq x \leq 4$ mm, followed by a steep decrease in the unit cell dimension further away in the region between $-4 \leq x \leq -7.5$ and $4 \leq x \leq 7.5$ mm.

The strained lattice parameter in both transverse, a_T and normal directions, a_N show a very similar variation, however, a small shift in the direction of slightly larger lattice values was observed in the former case. The average reference lattice parameter, a_0^{avg} also shows a smooth decay in sampling gauge volumes located underneath the multi-bead. This variation falls within an uncertainty interval ±0.0005 Å of the average reference lattice parameter, a_0^{avg}.

It is believed that the unit cell volume change may be developed through local changes in alloy chemistry caused by the large exposure times at relatively higher temperatures encountered in the region, where the thermal flux path by heat conduction through the base layer dominates. The base plate thermal-history was probably lost as a result of thermal heat treatment, namely tempering effects, which are most noticed in adjacent areas such as fusion (FZ), and heat affected zones (HAZ) located underneath the multi-bead.

8.2.3 Distribution of stresses along the multi-bead

The residual stress evolution for the three principal directions were calculated according to equation (2.6), and is plotted in Figure 8.14 for *specimen 5 layers*. The largest tensile stress is observed parallel to the welding direction, σ_L along the centreline of the multi-beads. The σ_L stress component varies from a minimum of 48 MPa measured at the top of the multi-bead wall, to a maximum value of about 424 MPa, close to the base plate. This maximum tensile stress is 19.4 % above the minimum nominal 0.2 % yield point of 355 MPa, as specified in BS EN 10025-2:2004.

The large tensile stress observed close to the interface occurs because of non-uniform compressive plastic flow in the welding heating cycle and tensile plastic flow on the welding cooling cycle (Lohwasser and Chen, 2010). The thermal expansion and contraction of the material in the heating and cooling cycles are predominantly restrained by the surrounding cold material and to a lesser extent by the tooling. The result of this unequal plastic flow is a large tensile stress in the longitudinal direction, σ_L as shown in Figure 8.14.

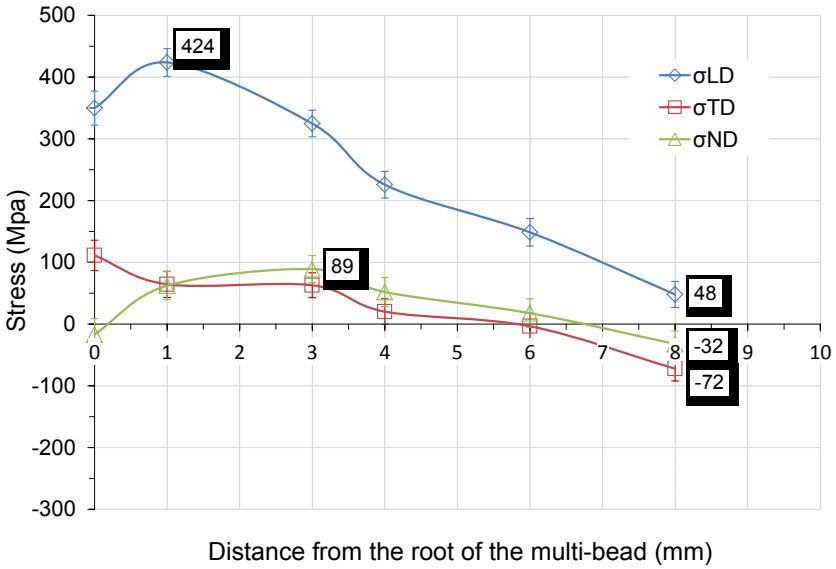

Figure 8.14. Average triaxial residual stress variation along the measurement multi-bead centreline in the ND_z direction, in *specimen 5 layers*.

In contrast, stresses in both transverse and normal directions (σ_T and σ_N in Figure 8.14) follow a very similar distribution and amplitude. A relatively low tensile stress field (below 100 MPa) is observed up to 6 mm high, which then changes into compressive up to the top of the multi-bead. The amount of thermal strain induced in both transverse and normal directions is much lower due to the asymmetric shape of the thermal field that is elongated along the welding direction (Lohwasser and Chen, 2010). The large residual stress in the longitudinal direction, σ_L causes a bending moment to act in the base plate plane in the direction perpendicular to the welding direction.

8.2.4 Distribution of stresses along the base plate

The distribution of residual stresses in three principal directions (σ_L, σ_T and σ_N), measured 2 mm below the base plate top surface, is plotted in Figure 8.15. The profiles show that the largest residual stress measured was parallel to the welding direction, while a very similar multi-peak distribution of stresses was observed in all directions $\sigma_L, \sigma_T, \sigma_N$. It is interesting to note that the width of the tensile stress peak in the longitudinal direction, σ_L extends more than ±7.5 mm from the weld centreline covering the FZ and HAZ regions; *cf.* half-width of the first deposited weld bead of 2.8 mm, in *specimen 5 layers*. A maximum residual tensile value of 293 MPa was recorded

close to the HAZ (this is 17.5 % below the minimum nominal 0.2 % yield strength of 355 MPa as specified in BS EN 10025-2:2004). Interesting to note is the steep drop in the stress distribution in the middle region of the weld at about ±5 mm from the centreline. This drop was a common trend in all measured directions. Further, the stresses distribution also indicates that the distance between the two tensile peaks is approximately 10 mm, irrespective of the direction of the measurement.

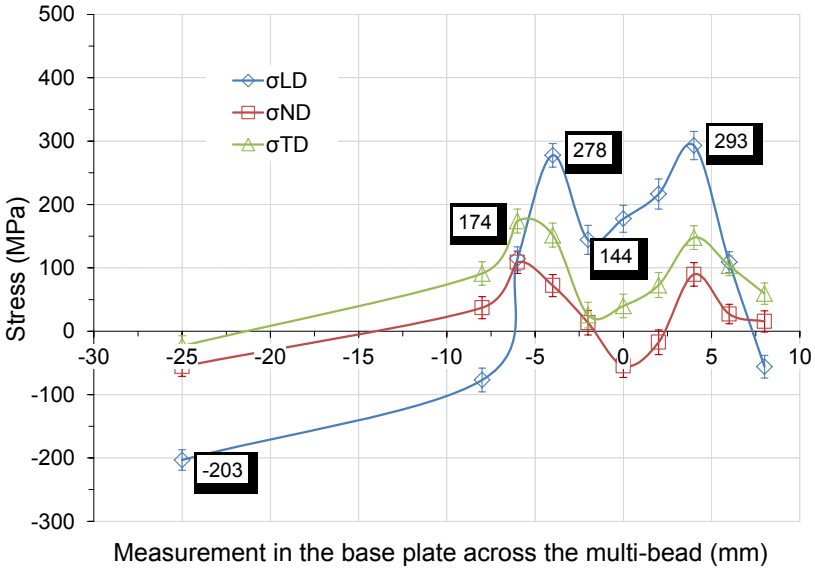

Figure 8.15. Average triaxial residual stress profiles along the measurement line positioned at 2 mm below the base plate top surface in the TD_y direction, in *specimen 5 layers*.

The drop in the stress field at the multi-bead centreline may be attributed to relaxation mechanisms caused by progressive heat treatment, *i.e.* tempering, as a result of progressive deposition. The region located at the bottom of the multi-bead will endure a distribution of temperatures and exposure times. This thermal effect will reflect appreciable changes in the alloy composition (*e.g.* diffusion of carbon) and induce also crystallographic texture. The residual stress dip can be also a result of high temperatures associated with this region due to a strong conduction thermal flux path pointing in the direction of the base plate that would limit the capacity of the material to support the generated load. Note, however, that the double-peaked profile characteristic was only observed in the direction parallel to the weld in *specimen 5 layers* (refer to Figure 8.16).

8.2.5 Distribution of stresses as a function of the layer number

The effect of the number of layers on the longitudinal residual stress distribution, σ_L measured in the base plate and along the multi-bead, is shown in Figure 8.16 and 8.17, respectively. The stress field observed in the base plate across the root of the multi-bead in the direction parallel to the welding is in good agreement with a typical single bead fusion weld, as reported elsewhere (Bailey, 1994).

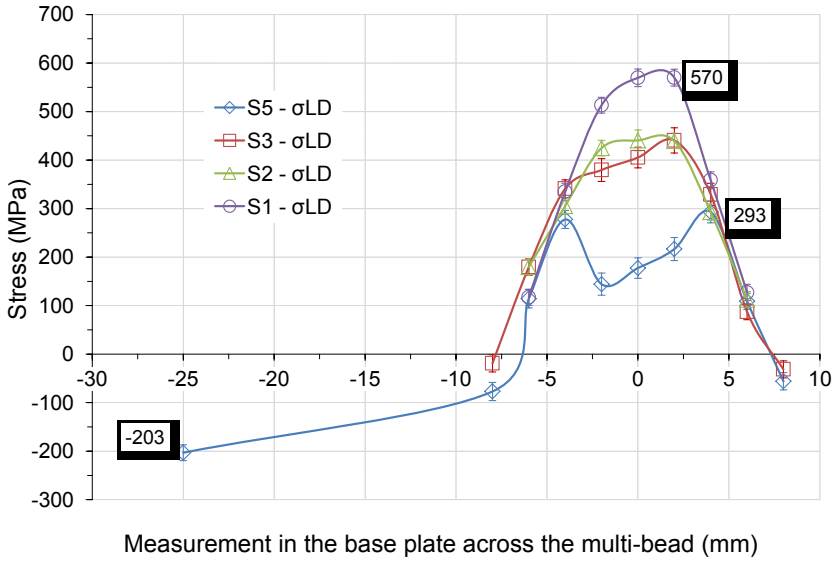

Figure 8.16. Comparison of the average longitudinal residual stresses profiles measured in the base plate across the multi-bead, in *specimens: 1, 2, 3* and *5 layers*.

The largest distribution of stresses in the base plate was measured in *specimen 1 layer* (S_1 in Figure 8.16). A maximum tensile residual stress of 570 MPa was found at +2.5 mm from the centreline, as shown in Figure 8.16. Notice the width of the tensile stress peaks at around ±2.5 mm from the weld centreline, a distance nearly corresponding to the weld bead width at the toe of the weld in *specimen 1 layer*; *cf.* weld bead half-width of ±2.8 mm.

Important to point out, however, is the residual stress development and redistribution caused by the progressive layer upon layer deposition, as succeeding layers are deposited e.g. layer number 1, 2, 3 and so forth. When a comparison is made between *specimen 1 layer* and *specimen 5 layers*, a noticeable drop in the maximum tensile residual stress from 570 MPa to 293 MPa is observed. Additionally, as the maximum tensile stress decreases its tensile stress peak broadens, shifting respectively from ±2.5

to ±4 mm from the bead centreline. The magnitude of peak stresses is higher, and these form closer to the weld centreline when the first weld bead is deposited. This could be a result of the increased thermal gradients encountered close to the base plate during deposition of the first layer (see section 8.2.1). The repeated thermal cycling and slower cooling rates causes therefore the base material to soften further away from the centreline as a result of tempering mechanisms.

Measurements have also shown that a large compressive stress of 203 MPa is present in the parent metal far-field as a result of the tensile residual stress tensile peak observed in the bead centreline, in *specimen 5 layers* (Figure 8.16). This compressive residual stress field, measured solely for *specimen 5 layers*, balances the tensile stress peak identified at the multi-bead centreline.

The residual stress field along the multi-bead centreline redistributes with the number of thermal cycles caused by successive deposition (see Figure 8.17). The residual stresses generated along the multi-bead centreline are balancing the residual stresses introduced into the base plate (see Figure 8.16). The tensile stress reaches a maximum near to the base plate with comparable magnitudes for the majority of the samples. This residual stress distribution and behaviour is apparently caused by the base plate and clamping constraint on the build during multi-bead deposition.

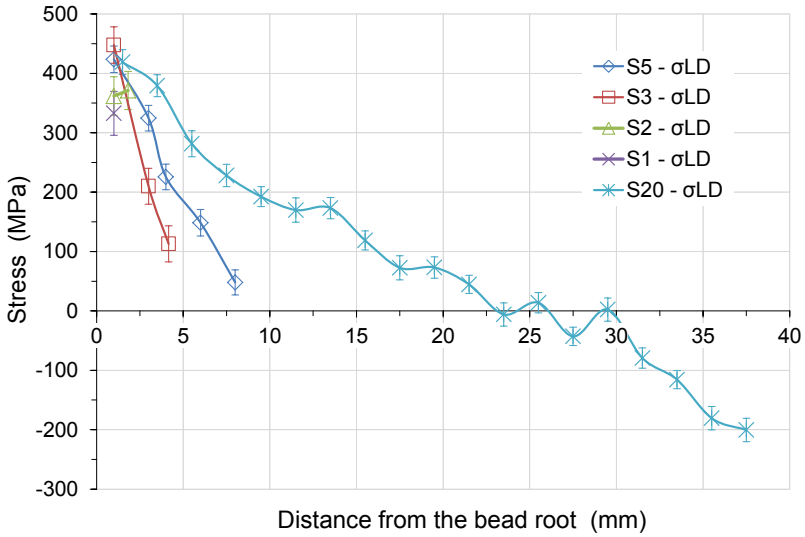

Figure 8.17. Comparison of the average longitudinal residual stress profiles measured along the multi-bead centreline in the ND_z direction, in *specimens 1, 2, 3, 5 and 20 (P) layers*.

In general, a sharp decay from these maxima is observed from the root of the bead, irrespective of the number of layers deposited. This strength relaxation behaviour is associated to plastic deformation that occurs with progressive deposition. As the wall is built up it becomes less restrained and the effect of the base plate on the top layers becomes less. In *specimen 20 layers (P)* it is important to highlight the swift decline from its maximum residual tensile value that reverses in sign for the first time at about 23 mm high. The compressive stress field shows therefore to strengthen with the distance from the root of the bead. A maximum residual compressive value of 200 MPa is reached at the top of the multi-bead (x=37.5mm), in *specimen 20 layers (P)*.

These results show to be in very good agreement with the ones obtained in *specimen 5 layers* (see Figure 8.14) close to the interface in both magnitude and location. While the state of stress in *specimen 5 layers* is exclusively dominated by a positive sign, the stress distribution in *specimen 20 layers (WP)* shows the presence of a steep stress gradient in the longitudinal direction between the lower (tensile) and the higher (compressive) halves of the multi-bead.

Overall, the results clearly show that welding-induced residual stress redistribution occurs predominantly in the longitudinal direction, σ_L along the substrate and multi-bead. It is believed that large stress distributions, as observed in the base plate in *specimen 1 layer*, arises primarily from non-uniform heat expansion and cooling in the material originated by sharp thermal gradients.

Considering yielding has not taken place, one may assume that the enhancement in the static mechanical properties (to about σ_L=570 MPa) was due to thermo-mechanical effects induced by successive deposition. Multiple thermal cycles may have triggered a number of metallurgical effects to occur simultaneously. These metallurgical effects include microstructural transformations, compositional changes, and grain size effects, which are commonly accompanied by variations in the material texture owing to recrystallisation. Metallurgical effects as ascribed above are more likely to occur close to the base plate were faster cooling rates are often observed (see section 8.2.1). High thermal gradients are expected to dominate in the interface, where maximal heat flux conditions can favour metallurgical changes induced by the large heat sink volume.

Moreover, the high level of stresses close to the interface may also be associated with inhomogeneous, or non-uniform, plastic deformation generated by the thermal cycles as proposed by Deng and Murakawa (2006).

8.2.6 The effect of the removal of the base plate on the stress distribution

Figure 8.18 depicts the effect on the stress distribution along the bead centreline on the triaxial stress distribution (σ_L, σ_T and σ_N), after the removal of the base plate in *specimen 20 layers (WP)*. It is seen that a nearly complete relaxation of the elastic residual state of stress occurs after the base plate is removed, particularly in the direction parallel to deposition, σ_L. Residual stress relaxation along the multi-bead centreline occurred because the structure was mechanically unconstrained. This condition allowed the component to deform freely and thus residual stresses relaxation. One should notice that Figure 8.18 compares to Figure 8.17 where the stress distribution is shown for the same specimen without removal of the base plate (*specimen 20 layers (P)*).

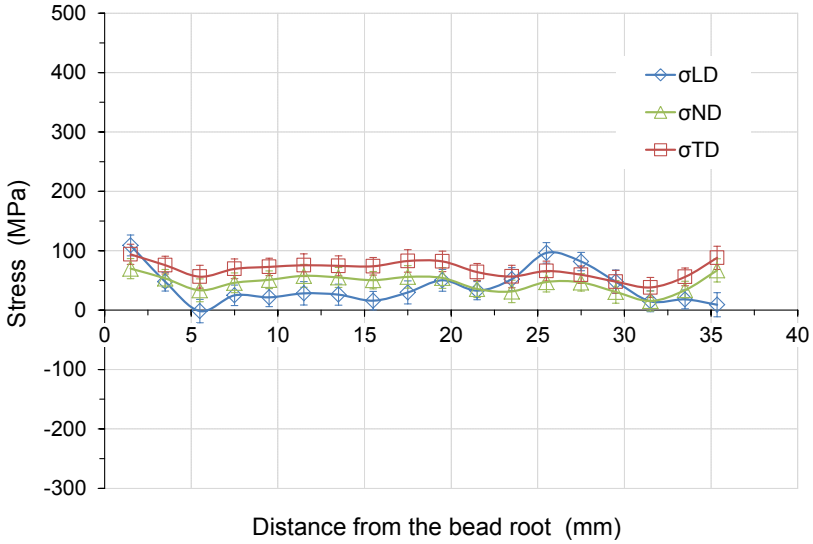

Figure 8.18. Comparison of the average longitudinal, transverse and normal stress profiles along the multi-bead centreline in the *NDz* direction, in specimen 20 layers (WP).

8.2.7 Welding-induced distortion

Figure 8.19 illustrates the effect of welding-induced distortion observed in WAAM as a result of an unbalanced distribution of residual stresses. As reported by Das and Chandra (2003) the total distortion (not quantified in this work) is typically associated to a number of different mechanisms, and these are as follows: (a) non-uniform plastic deformation due to mechanical constraint and/or non-uniform thermal loading, (b) volumetric changes produced by possible solid-state phase transformations, or (c) caused by differential thermal expansion coefficients.

Distortion, as exhibited in Figure 8.19, arises as a result of a bending moment acting in the direction perpendicular to the welding seam (in-plane), since the weld centre of mass is never coincident with the neutral axis of the component's section (Lucas *et al.*, 1999). In the previous sections it was demonstrated that the bending moment, acting on the manufactured rectilinear structure, was essentially generated by a large stress component orientated parallel to the welding direction, σ_L .

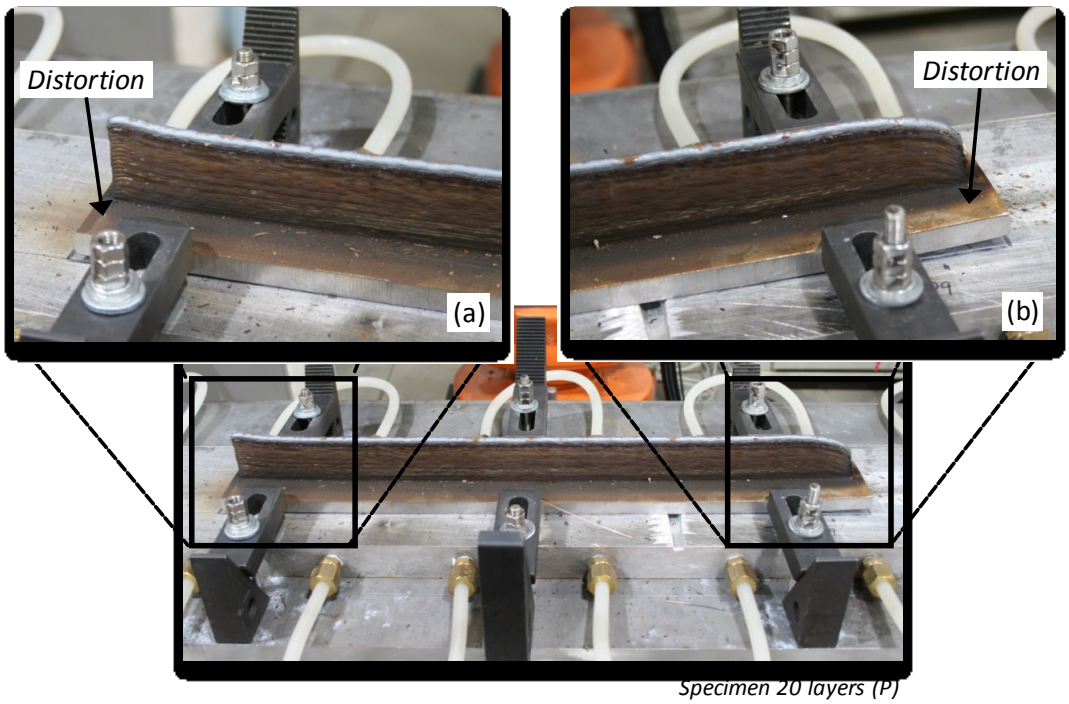

Figure 8.19. *Specimen 20 layers (P)* in the as-welded condition detailing the effect of successive deposition on welding-induced distortion (highlighted in the figure at the bottom left (a) and right (b) ends of the sample).

Section 8.2.5 demonstrated the coexistence of both longitudinal compressive and tensile stress fields along the multi-bead, particularly in the case of *specimen 20 layers*. A compressive residual stress field was found to dominate along the multi-bead from the mid-length section to the top, whilst the tensile stress field was predominantly located close to the base plate. Nevertheless, builds with fewer layers, *e.g. specimen 5 layers*, showed that the longitudinal stress was entirely positive. It is believed that the progressive decline in the tensile stress distribution, along the multi-bead in the direction of the top of the build, attempts to balance the maximum tensile measured close to the base plate interface.

The compressive stress field formed at the top of the wall in taller builds, *e.g. specimen 20 layers*, can be explained by thermal shrinkage effects arising from slower and uniform free thermal contraction, as well as in reaction to the large tensile observed close to the constraint.

In addition, the effect can be also justified in the light of the different heat-transfer conditions determined as follows: (1) by the relative distance between the arc heat source to the base plate (larger heat sink), and (2) by geometrical configuration of the features in the component. Jandric *et al.* (2004) argued that the size of the volume heat sink in WAAM is fundamental in determining the cooling rate and temperature distribution within the component. As an example a 90º corner or a stop edge simulates distinct heat flux conditions, suggesting a fundamental role of the heat sink volume in controlling the heat flux through conduction.

8.2.8 Comparison between triaxial and plane stress conditions

In this section the determination of the internal distribution of stresses was carried out by comparing the triaxial state of stress with a simplified two dimensional or plane stress (PS) assumption. For PS conditions, the out-of-plane stress in the transverse direction (σTD_y) was assumed to be zero. Stresses were considered negligible with respect to the small dimension of the section as they were not able to develop within the material, and therefore considered small when compared to the in-plane stresses.

Figure 8.20 illustrates the σ_L profiles by comparing both the triaxial and PS assumption along the multi-bead centreline, in *specimen 20 layers (P)*. In general, Figure 8.20 shows that the plane stress assumption (where $\sigma TD_y = 0$) is in good agreement with the triaxial state of stress. The plane stress method reproduces very closely the magnitude of the tensile state of stress observed close to the base plate (only 4 % less). The position at which the change in sign occurs from tensile to compressive in the biaxial approach also showed good agreement, when compared with the triaxial state of stress data. Nevertheless, the PS method shows to overestimate the triaxial approach by 26.5 % at the top of the multi-bead.

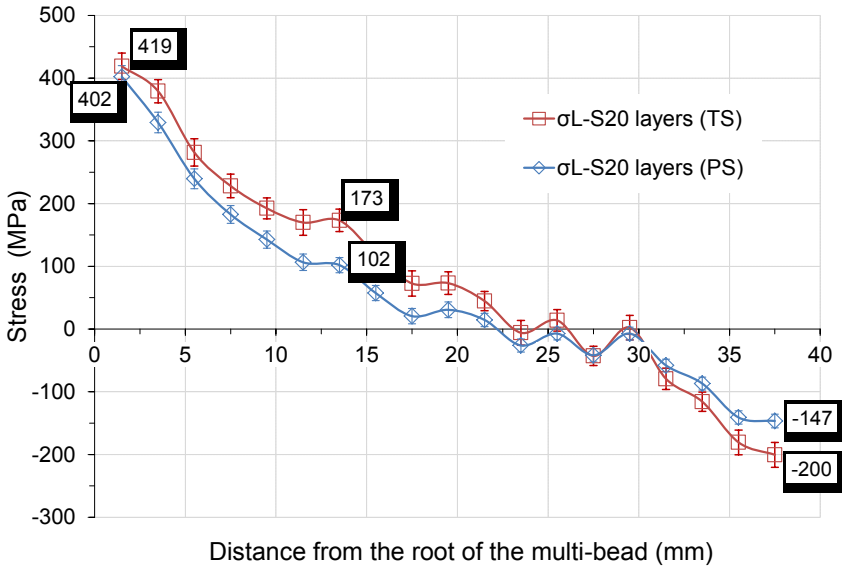

Figure 8.20. Comparison of the average longitudinal σ_L residual stress distribution assuming a plane stress condition (PS), and triaxial state of stress (TS). The profile was taken along the multi-bead centreline in *specimen 20 layers (P)*.

Figure 8.21 compares the average σ_L residual stress distributions assuming both biaxial assumption and the triaxial state of stress along the multi-bead centreline, in *specimen 5 layers*. Figure 8.21 shows that data obtained using PS assumption are in reasonable agreement with triaxial data, indicating to reproduce both the residual stress sign and trend of those obtained with the triaxial methodology. Nevertheless, the in-plane assumption underestimates the magnitude of triaxial data by 15.3 % close to the interface with the base plate, while at the top of the multi-bead shows to overestimate the triaxial conditions in about 60 %.

On the one hand, the larger variability verified in biaxial conditions in *specimen 5 layers* (see Figure 8.21), when compared with PS data obtained in *specimen 20 layers (P)* (see Figure 8.20), can be attributed to the fact that out of plane deformation may have occurred in the former case, as a result of improved heat transfer conditions encountered close to the interface. On the other hand, and in the case of taller builds, cooling occurs at relatively slower rates causing a more uniform and proportional deformation to occur in the $ND_z \times LD_x$ plane, and possibly justifying the smaller variation observed in PS conditions by *specimen 20 layers (P)*.

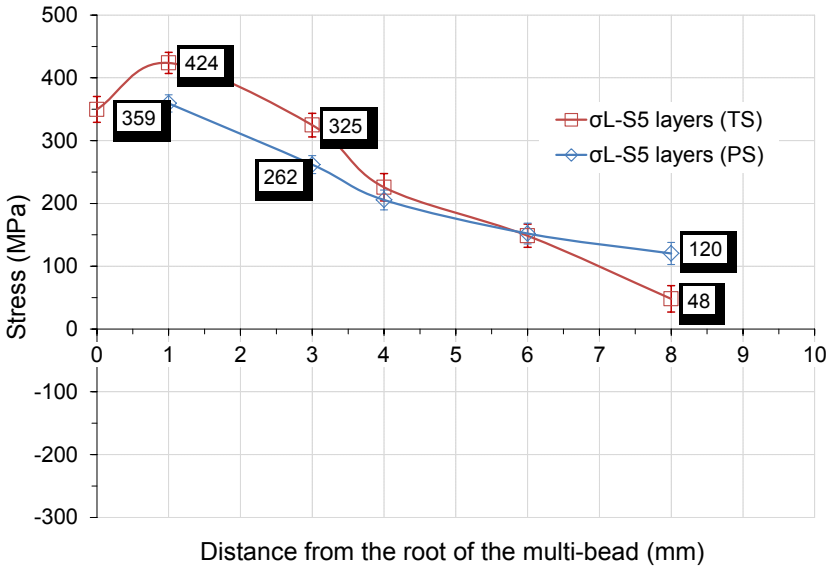

Figure 8.21. Comparison of the average longitudinal σ_L residual stress distribution assuming a plane stress condition (PS), and triaxial state of stress (TS). The profile was taken along the bead centreline in *specimen 5 layers*.

8.2.9 Hardness testing

Vikers hardness (HV) testing was carried out on transverse cross sections of samples *specimen 1 layer* and *specimen 5 layers*, according to the procedure detailed in section 8.1.7 (page 279). Macro-photographs of transverse cross sections in both *specimen 1 layer* and *specimen 5 layers* are additionally provided in Figure K 1 to K 13 (see Appendix K on page 385), revealing the gradient of microstructures obtained in the welds. Hot-rolling processing typically develops a fully recrystallised, coarse austenitic structure which transforms, on cooling to ambient temperature, into a coarse ferrite-pearlite microstructure in low carbon steels, *e.g.* S355J2 (Llewellyn and Hudd, 1998).

The improvement in the impact toughness properties by grain refinement - normally reached with fine dispersion of AlN which pin austenitic grain boundaries - is usually achieve through a *normalising* heat treatment of the rolled product, at about 910 ºC. Figure K 2 on page 386 shows a typical microstructure of that present in most dual-phase steel products (Vander Voort, 1991). The observed microstructure results from the carbon and manganese contents, and low amount of alloying elements in these steels. Although strengthening of ferrite-pearlite steels is primarily dependent on the relative contributions of carbon (mostly by increasing the proportion of pearlite in the structure), and manganese (by solid solution, refinement of the grain size of ferrite[42], and pearlite content[43]), the two most important metallurgical parameters influencing hardenability are both the ferrite grain size and alloy composition (Llewellyn and Hudd, 1998; Bhadeshia and Honeycombe, 2006).

HV indentation profiles measured in the base plate and along the weld bead are plotted in Figure 8.22(a) and (b), in *specimen 1 layer*. Figure 8.22(a) shows that hardness varies in average from about 175HV in the parent metal (PM) to a maximum of 203 HV at the centreline of the weld bead.

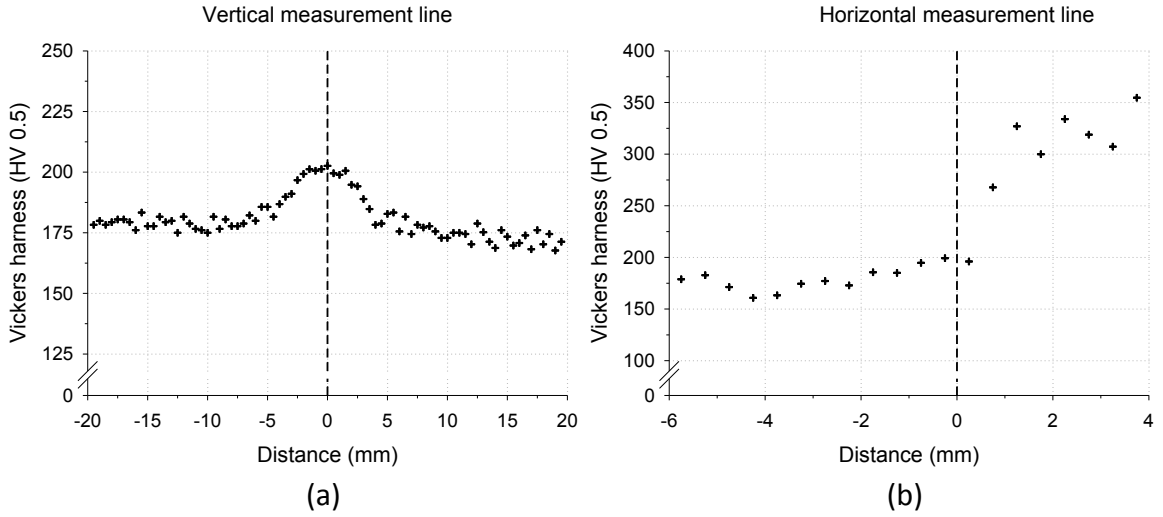

Figure 8.22. Vickers hardness distribution along measurement lines located (a) in the base plate 2 mm below the top surface, and (b) along the bead centreline, in *specimen 1 layer*.

[42] As an austenite stabiliser manganese depresses the temperature of transformation of γ to α.

[43] By causing the eutectoid reaction to occur at lower carbon contents, manganese increases the proportion of pearlite in the microstructure.

Detailed microstructural examination of the specimen revealed that the horizontal indentation measurement line did not reach the visible HAZ, where microstructural changes should be most significant (as seen in Figure K 1 on page 385). According to the thermo-mechanical model for the temperature distribution developed by Ding *et al.* (2011) the predicted peak temperature in the non-visible HAZ area, at the weld bead centreline, is around 795 ºC. In theory, this temperature should suffice to form a partially austenitic microstructure. However, and as seen in Figure K 3 (page 387), tempering effects owing to maximum peak temperatures below Ac_1[44] were most likely to have occurred. Nevertheless, the increase in hardness observed in Figure 8.22(a) underneath the bead centreline is difficult to justify on these grounds since a tempering mechanism is typically associated with softening rather than hardening. Besides, no dramatic differences in the microstructures could be discerned by comparing the non-visible HAZ (Figure K 3 on page 387) with the PM (Figure K 2 on page 386).

Instead, it is suggested that hardening by a mechanism of ferrite strain ageing is the principal cause of such behaviour, probably induced by diffusion of the solute into α-ferrite, *i.e.* carbon or nitrogen. Interstitial concentrations, or *Cottrell atmospheres*, form in the vicinity of dislocations explaining thus the mechanism by which dislocations can be pinned in metals (Cottrell and Bilby, 1949). Strain ageing phenomenon can even occur in the range of temperatures between 20 ºC to 150 ºC as reported by Bhadeshia and Honeycombe (2006).

Hardness shows to vary little along the vertical measurement line, from the PM at the bottom of the base plate up to about -2 mm of the horizontal measurement line (see Figure 8.22(b)). Moving closer into the non-visible HAZ an increase in the measured hardness values is observed from around 175 HV to 200 HV. As a result of the heating and cooling thermal cycle, a partially or fully austenitised microstructure starts to develop at y=0.75 mm which is characterised by a *fine grained zone* (see Figure K 4, page 388).

[44] Ac_1 and Ac_3 temperatures indicate respectively the starting and finishing transformation temperatures from α-ferrite to γ-austenite during heating.

The refinement of the grain size of ferrite, as demonstrated by the Hall-Petch[45] relationship, is in line with the observed increase in the level of hardness. Additionally, one may also argue that an increase in hardness may be also associated with the formation of a number of locally hardened zones caused by carbon-enriched austenite.

At the same time, areas adjacent to the fusion line are transformed completely to austenite. Due to the high peak temperatures involved in the thermal cycle (much higher than Ac_3) austenite grains coarsen exponentially during heating to form a *coarse grained austenite zone* (see Figure K 5, page 389). Typically, a coarse grain structure leads to an increase in hardenability, as it becomes easier to avoid intermediate transformation products, so that untempered martensite or other hard phases can form upon cooling (Bhadeshia and Honeycombe, 2006).

Figure 8.22(b) shows that hardness in the as-deposited microstructure is typically over 300 HV, however, a maximum of 355 HV was measured at the top of the weld bead. The resultant solidification microstructures are inhomogeneous due to non-equilibrium solidification conditions, as a result of chemical segregation mechanisms and composition variations (see Figures K 6 and K 7 on pages 390 and 391, respectively). Although small amounts of α-allotriomorphic can be detected in the form of continuous ferrite layers nucleated at the grain boundaries of austenite upon cooling, the essential features of the as-deposited transformed microstructure appears to be dominated by competitive formation of α-Widmanstätten plates, and α-acicular. The lower aspect ratio of ferrite plates in the FL (see Figure K 5 on page 389), when compared with those in the welded metal, were favoured by the higher carbon content diffused from the base plate, causing the rate of growth of ferrite to decrease.

[45] The Hall-Petch relationship describes the grain size dependence of yield strength and is mathematically described as follows: $\sigma_y = \sigma_0 + \frac{k_y}{\sqrt{d}}$ where σ_y is the yield stress, σ_0 is a material constant related with the starting stress for dislocation movement, K_y is the strengthening coefficient constant and d is the average grain size.

Figure K 7 (on page 391) also shows the presence of low carbon martensite aggregates characterised by long lath- or plate-shaped α'-martensite, grouped together in packets with low angle boundaries between each lath, as observed by Bhadeshia and Honeycombe (2006). The presence of α'-martensite at the top of the weld bead demonstrates that the critical rate of cooling was exceed in that region, justifying therefore the maximum in hardness.

Hardness profiles in the base plate and along the weld bead centreline are shown in Figures 8.23(a) and (b), in *specimen 5 layers*. Along the base plate hardness varies in average from 175 HV in the PM to a maximum of around 200 HV beneath the multi-bead centreline (see Figure 8.23(a)). Thermal induced softening effects are noticeable in the hardness profile at locations adjacent to the centreline, when compared to the single layer case (see Figure 8.22(a)). Peak temperatures in this region are not expected to exceed Ac_1 as in the former single layer case. However, thermal softening caused by tempering mechanism may now be justified owing to repeated thermal cycling and slow cooling.

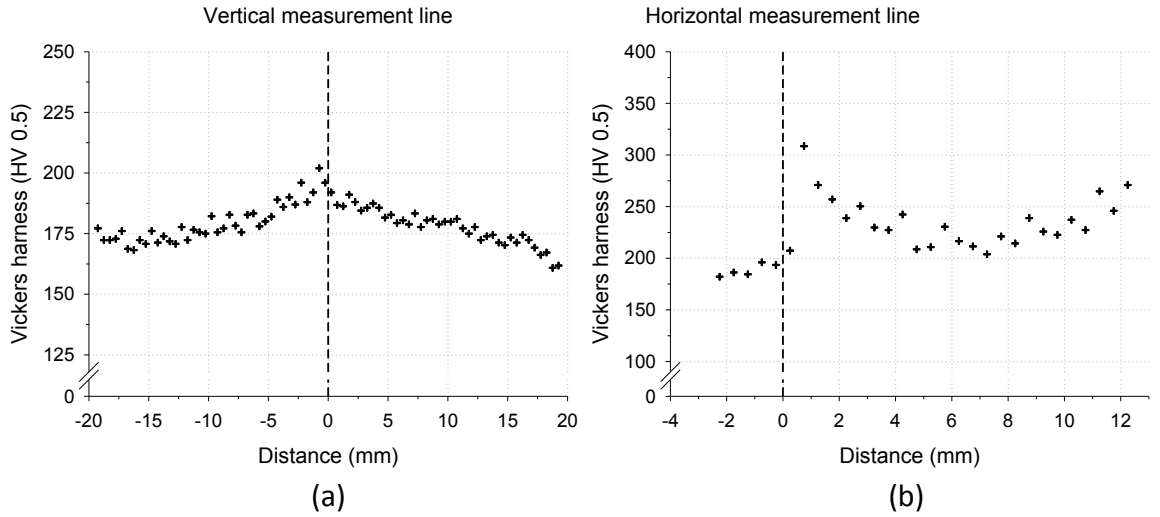

Figure 8.23. Vickers hardness distribution along measurement lines located (a) in the base plate 2 mm below the top surface, and (b) along the bead centreline, in *specimen 5 layers*.

Figure 8.23(b) shows a maximum hardness of 308 HV at y=0.75 mm, where a microstructure characterised by a *fine grained zone* can be observed (see Figure K 11 on page 395). Hardness decreases gently to a minimum at around the mid-height position in the wall. The trend is explained in the light of successive heat treatment of the underlying microstructure to temperatures high enough to cause partial and/or fully

austenitised microstructures. During the manufacturing and processing stages, as-welded microstructures are reheated as a result of repeated thermal cycling, causing the formation of a gradient of microstructures.

The microstructure at the mid-height of the build (see Figure K 12 on page 396) consists of a significantly refined ferrite-pearlite grained structure, when compared with the PM (see Figure K 2 on page 386). Recrystallisation occurred in this region as a result of successive thermal cycling and slow cooling rate (Spencer *et al.*, 1998). However, this ferrite-pearlite microstructure is still significantly coarser than the *fine grained zone* observed in Figure K 11 (page 395).

At the top of the multi-bead, and in agreement with the findings reported in Dickens *et al.* (1992; 1993)and Sreenathbabu *et al.* (2005), hardness increases gradually until a new maximum of about 275 HV is reached. In this zone (upper section) a significantly coarse structure of ferrite-pearlite with a characteristic columnar solidification microstructure of the austenitic grains is observed (see Figure K 8 and K 13 in pages 392 and 397 correspondingly). This effect is clearly confined to the very top layer resulting from the fact that this region has not been subjected to reheating and thermal cycling by further weld layers. These observations corroborate the results of similar experiments carried out on mild steel by Dickens *et al.* (1993). By comparing both single and multi-layer microstructures at the top layer (see Figures K 7 and K 13 in pages 391 and 397), major microstructural differences between these areas can be seen as a result of different cooling conditions (see section 8.2.1). Upon cooling a small amount of residual austenite, enriched in carbon, may have been formed in *specimen 5 layers*. Bhadeshia and Honeycombe (2006) established that under slower cooling conditions (*e.g.* multi-layer builds) the formation of degenerated pearlite (no lamellar) over martensite is facilitated, leading to the formation of *microphases* which are inherently hard.

The results obtained from the residual stress analysis were compared with the hardness measurements for *specimen 1 layer* and *specimen 5 layers* as shown in Figure 8.24 and Figure 8.25, respectively. The analysis carried out along the base plate measuring line gives a strong correlation between hardness and residual stress values (see Figure 8.24(a)). The increase in hardness observed underneath the weld bead centreline is

accompanied by an increased tensile residual stress peak. The width of the maximum tensile residual stress peak is approximately 5 mm from the weld centreline, which coincides with the maximum hardness values. It can be seen in Figure 8.24(a) that the maximum hardness and residual stress values fall within the weld bead width deposited; *cf.* weld bead half-width of ±2.8 mm; before dropping sharply. The drop in hardness with distance from the weld centreline was in good agreement with a drop in the tensile residual stresses. It is important to emphasise that the increase in hardness was not strongly influenced by the significant microstructural modifications or phase transformations that usually occur in weld beads. This increase in hardness suggests the idea of its origin in interstitial concentrations, *i.e.* carbon or nitrogen, supporting the mechanism of strain ageing proposed by Cottrell and Bilby (1949), already referred to in this section.

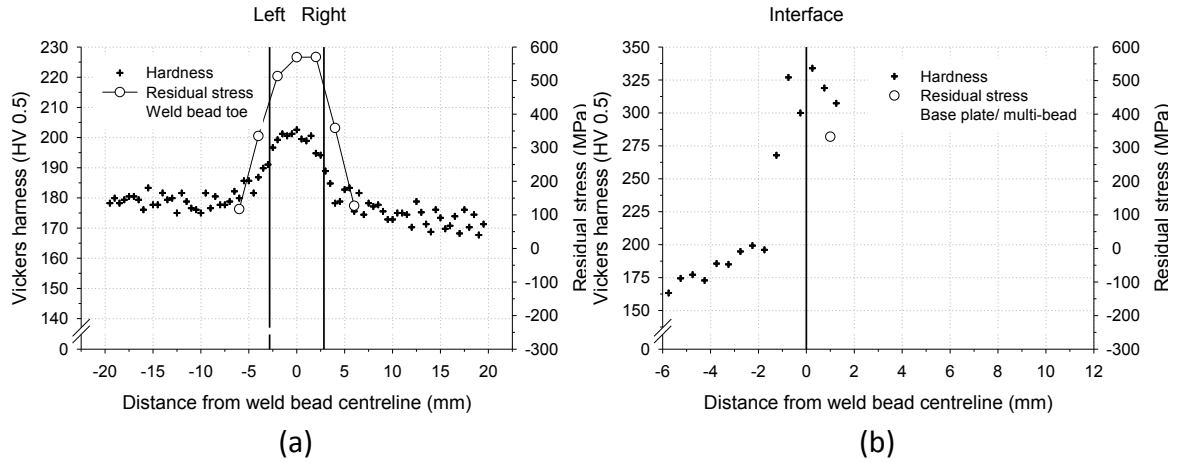

Figure 8.24. Relationship between longitudinal residual stresses, σ_L and low-force Vickers hardness (HV) measured (a) in the base plate and (b) along the multi-bead centreline, in *specimen 1 layer*. Vertical solid lines represent (a) the toe of the weld, and (b) the base plate/weld bead interface.

Figure 8.25 (a) also shows a good correlation between hardness and residual stresses in *specimen 5 layers*. The large variation observed in the hardness values at the multi-bead centreline can be well described by the residual stress profile. The drop in the residual stress values at the multi-bead centreline appears to be congruous with a general decrease in hardness; *cf.* Figure 8.24(a); due to thermally induced softening effects caused by progressive deposition.

It is interesting to note, however, that the residual tensile stress region extends further to about ±4.0 mm from the centreline, before dropping sharply to compressive values at

about ±8.0 mm from the weld line; *cf.* weld bead half-width of ±2.8 mm. This decrease apparently correlates well with the transition observed in the hardness profile. Although exhibiting some scatter, the compressive region at around ±8.0 mm from the weld line apparently corresponds to a region at which the hardness plateaus (see right-hand side of the weld in Figure 8.25 (a)). A strong relationship between hardness and residual stresses along the weld multi-bead measuring line was also found in *specimen 5 layers* (see Figure 8.25(b)). The residual tensile stress decay observed at the interface is consistent with the measured hardness values. In the case of *specimen 1 layer* (Figure 8.24(b)), the high residual tensile stress is in line with the large hardness values measured close to the interface.

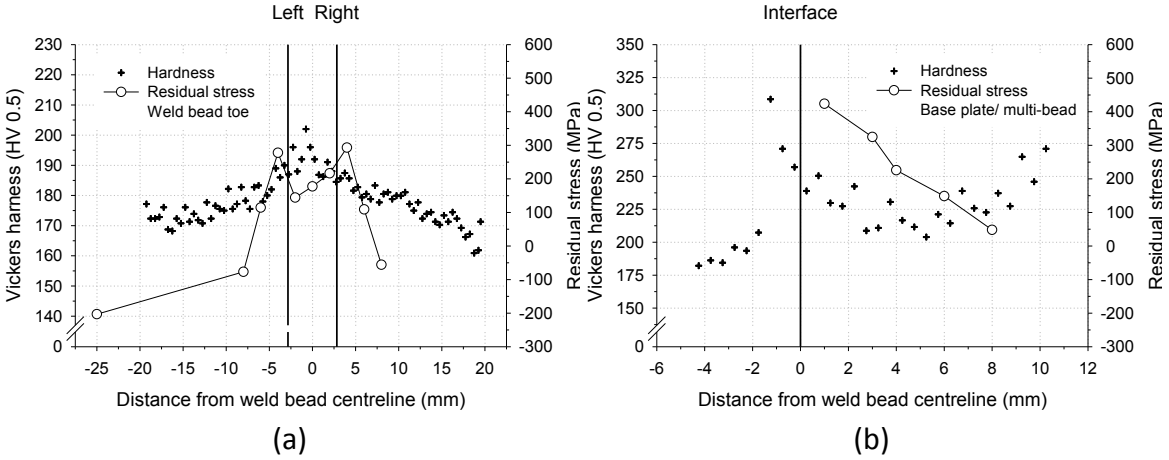

Figure 8.25. Relationship between longitudinal residual stresses, σ_L and low-force Vickers hardness (HV) measured (a) in the base plate and (b) along the multi-bead centreline, in *specimen 5 layers*.

8.3 Conclusions

This study set out to determine the effect of repeated thermo-mechanical cycles introduced by WAAM technology on the residual stress generation and distribution in low carbon steel rectilinear structures by neutron diffraction. The following conclusions can be drawn from the present study:

1. The residual stresses in the first layers are predominantly in the longitudinal direction, σ_L similar to that observed in conventional welding.

2. The residual stresses generated close to the base plate in the first deposited layer are very significant due to the base plate and clamping constraint as a result of non-uniform heat expansion and cooling in the material originated by sharp thermal gradients.

3. The repeated thermo-mechanical cycles associated with processing originates a significant redistribution of longitudinal residual stresses along the substrate and multi-bead.

4. As more layers are added, the residual stresses vary from tensile to compressive along the weld bead.

5. A nearly complete relaxation of the elastic residual stresses distribution occurs along the multi-bead once the base plate is removed.

6. Bowing distortion results from the bending moment acting in the direction perpendicular to the weld as a result of the large longitudinal stress component.

7. The plane stress method has shown good agreement with the triaxial stress state results of taller builds, demonstrating that the biaxial assumption can be applied.

8. Indentation hardness profiles have shown to be consistent with the measured distribution of residual stresses along the base plate and as-deposited weld beads.

9 Overall conclusions

The following conclusions can be drawn from the present study:

1. Empirical process models can be developed using the least-squares analysis and the multiple linear regression method. These algorithms can be translated into mathematical library software for inclusion in the process control of wire and arc additive manufacturing systems.

2. The cold metal transfer process is appropriate for wire and arc additive manufacturing applications based upon its excellent deposition characteristics, process behaviour and arc welding stability. The constant current static volt-ampere characteristic of the power source ensures constant current flow conditions through the workpiece. The digital process control offered by the cold metal transfer process, allied with a variable wire feed speed control feature, allows the arc-length to be maintained nearly constant during processing with respect to variations in contact tip to work distance.

3. Modified gas metal arc welding processes, namely cold metal transfer, can be used to deposit titanium wire. When compared with more traditional gas metal arc welding methods, the cold metal transfer process shows excellent arc welding characteristics resulting in spatter free Ti-6Al-4V deposits with greatly improved weld bead straightness and uniformity. However, arc wandering is still observed due to increased instability, which causes a certain loss of process efficiency compared to GTAW or PAW.

4. Empirical process models can be developed for titanium using cold metal transfer following a similar reasoning as for other materials and processes.

5. The static mechanical performance of material processed via cold metal transfer shows better average ultimate and yield tensile strength of the as-deposited Ti-6Al-4V material than that processed via gas tungsten arc welding. As-deposited Ti-6Al-4V walls processed with cold metal transfer meet the minima specification values recommended for most Ti-6Al-4V products, both in the horizontal and vertical directions.

6. The residual stresses are determined by the level of restrain of the surrounding material and clamping in the region where processing is occurring. The residual stress level should to be taken into account as part of the control software when developing fabrication strategies.

7. The residual stresses in the base plate and multi-bead change significantly during processing as more layers are deposited. However, a nearly complete relaxation occurs along the multi-bead as the base plate is removed.

8. A thermo-mechanical finite element model has been developed and validated against experimental data. Therefore, finite element modelling may be used to optimise the build-up strategies for mitigating residual stresses and their effects on distortion and mechanical properties.

9.1 Suggestions for future work

The study presented here has highlighted the importance of primary and secondary welding parameters for process control of the weld bead shape, residual stresses and microstructure of single and multi-layer welds made of low carbon mild steel material. In addition, this study has addressed the influence of processing conditions and actual solidification macrostructure on the static mechanical behaviour of the as-deposited Ti-6Al-4V material. With the aim of increasing the technology readiness level of wire and arc additive manufacturing technologies, it is recommended that further research be undertaken in the following areas:

1. A full assessment of the static and dynamic mechanical behaviour of the as-deposited Ti-6Al-4V material produced with cold metal transfer is recommended.

2. Development of control algorithms for different arc welding processes, *e.g.* GMAW, GTAW, PAW, SAW, etc., and other difficult to weld materials, *e.g.* nickel based alloys, cobalt based alloys, titanium alloys, aluminium based alloys, high strength steels.

3. Development and testing of process control software based on these algorithms.

4. Process development and optimisation of micro and macrostructures developed during solidification, weld chemistry, rolling, post weld heat treatment, residual stresses and deformation, and surface finish for enhancing mechanical properties and dimensional tolerances.

5. Development of new methods to control residual stresses and distortion, *e.g.* rolling, laser shock peening.

6. Establishment of a reliable material property database for a wide range of processing conditions.

7. Investigation of other wire and arc additive manufacturing hybrid approaches, *e.g.* wire and powder, for producing functionally graded materials.

8. Development and integration of online sensing and monitoring technologies for process control and optimisation, *e.g.* heating, cooling, non-destructive testing, and machine vision.

9. Development and optimisation of a local shielding for controlling the contamination level during Ti-6Al-4V deposition under challenging processing conditions.

10. Further work needs to be done to establish new approaches for improving the transfer conditions and arc stability during gas metal arc welding of titanium, namely:

    a. Investigate laser stabilisation of arc cathode spots in titanium welding using arc processes such as cold metal transfer and pulsed gas metal arc welding (hybrid approach).

    b. Examine the weldability and mechanical performance of the novel G-Coat titanium wire.

    c. Investigate the modified active control method to improve metal transfer conditions of pulsed-current gas metal arc welded titanium alloys.

References

Print me a Stradivarius: How a new manufacturing technology will change the world (2011a), *The Economist*, Section: Leaders and Technology, February 10th.

The printed world: Three-dimensional printing from digital designs will transform manufacturing and allow more people to start making things (FILTON) (2011b), *The Economist*, Section: Briefing and 3D Printing, February 10th.

Wohlers Associates Inc. (2012), available from: http://www.wohlersassociates.com/technical-articles.html (accessed 19th January 2012).

Abralov, M. A., Abdurakhmanov, R. U. and Iuldashev, A. T. (1978), The effect of electromagnetic action on the primary solidification of titanium, *Welding Production*, **25**(5), p. 1-3.

Agarwala, M., Bourell, D., Beaman, J., Marcus, H. *et al.* (1995), Direct selective laser sintering of metals, *Rapid Prototyping Journal*, **1**(1), p. 26-36.

Alimardani, M., Toyserkani, E. and Huissoon, J. P. (2007), A 3D dynamic numerical approach for temperature and thermal stress distributions in multilayer laser solid freeform fabrication process, *Optics and Lasers in Engineering*, **45**(12), p. 1115-1130.

Alimardani, M., Toyserkani, E., Huissoon, J. P. and Paul, C. P. (2009), On the delamination and crack formation in a thin wall fabricated using laser solid freeform fabrication process: An experimental-numerical investigation, *Optics and Lasers in Engineering*, **47**(11), p. 1160-1168.

Allum, C. J. (1983), MIG welding- Time for a reassessment, *Metal Construction*, **15**(6), p. 347-353.

Amon, C. H., Beuth, J. L., Weiss, L. E., Merz, R. *et al.* (1998), Shape deposition manufacturing with microcasting: Processing, thermal and mechanical issues, *Journal of Manufacturing Science and Engineering, Transactions of the ASME*, **120**(3), p. 656-665.

Amson, J. C. (1965), Lorentz force in the molten tip of an arc electrode, *British Journal of Applied Physics*, **16**(8), p. 1169-1179.

Anca, A., Cardona, A., Risso, J. and Fachinotti, V. D. (2011a), Finite element modeling of welding processes, *Applied Mathematical Modelling*, **35**(2), p. 688-707.

Anca, A., Fachinotti, V. D., Escobar-Palafox, G. and Cardona, A. (2011b), Computational modelling of shaped metal deposition, *International Journal for Numerical Methods in Engineering*, **85**(1), p. 84-106.

Arcella, F. G. and Froes, F. H. (2000), Producing titanium aerospace components from powder using laser forming, *Journal of Minerals, Metals and Materials Society*, **52**(5), p. 28-30.

Ashby, M., Shercliff, H. and Cebon, D. (2009), *Materials: engineering, science, processing and design*. 2nd ed., Butterworth-Heinemann, Oxford.

Ayres, P. S., Edmonds, D. P., Hartwig, D. D., Merker, D. E. *et al.*, The Babcock & Wilcox Company (New Orleans, LA) (1988), *Method and apparatus for controlling weld bead shape to eliminate microfissure defects when shape melting austenitic materials*, United States Patent No.4,782,206.

Baeslack III, W. A. and Banas, C. M. (1981), Comparative evaluation of laser and gas tungsten arc weldments in high-temperature titanium alloys*, Welding Journal (Miami, Fla)*, **60**(7), p. 121s-130s.

Baeslack III, W. A. and Hallum, D. L. (1990), Nature of grain refinement in titanium alloy welds by microcooler inoculation*, Welding Journal*, **69**(9), p. 326s-336s.

Bailey, N. (1994), *Weldability of ferritic steels*, Abington, Cambridge.

Bailey, N. S., Tan, W. and Shin, Y. C. (2009), Predictive modeling and experimental results for residual stresses in laser hardening of AISI 4140 steel by a high power diode laser*, Surface and Coatings Technology*, **203**(14), p. 2003-2012.

Baker, R., Westinghouse Electric & Manufacturing Company (1925), *Method of making decorative articles*, United States Patent No.1,533,300.

Balasubramanian, M., Jayabalan, V. and Balasubramanian, V. (2008), Effect of microstructure on impact toughness of pulsed current GTA welded α-β titanium alloy*, Materials Letters*, **62**(6-7), p. 1102-1106.

Barreda, J. L., Santamaría, F., Azpiroz, X., Irisarri, A. M. *et al.* (2001), Electron beam welded high thickness Ti6Al4V plates using filler metal of similar and different composition to the base plate*, Vacuum*, **62**(2-3), p. 143-150.

Baufeld, B. (2012), Effect of deposition parameters on mechanical properties of shaped metal deposition parts*, Proceedings of the Institution of Mechanical Engineers, Part B: Journal of Engineering Manufacture*, **226**(1), p. 126-136.

Baufeld, B. (2011), Mechanical properties of inconel 718 parts manufactured by Shaped Metal Deposition (SMD)*, Journal of Materials Engineering and Performance*, p. 1-6.

Baufeld, B., Biest, O. V. D. and Gault, R. (2010), Additive manufacturing of Ti-6Al-4V components by shaped metal deposition: Microstructure and mechanical properties*, Materials and Design*, **31**(SUPPL. 1), p. S106-S111.

Baufeld, B. and Van Der Biest, O. (2009), Mechanical properties of Ti-6Al-4V specimens produced by shaped metal deposition*, Science and Technology of Advanced Materials*, **10**(1), p. 10.

Baufeld, B., Van Der Biest, O. and Gault, R. (2009), Microstructure of Ti-6Al-4V specimens produced by shaped metal deposition*, International Journal of Materials Research*, **100**(11), p. 1536-1542.

Belsley, D. A., Kuh, E. and Welsch, R. E. (1980), *Regression diagnostics : identifying influential data and sources of collinearity*, Wiley, New York ; Chichester.

Benyounis, K. Y. and Olabi, A. G. (2008), Optimization of different welding processes using statistical and numerical approaches - A reference guide, *Advances in Engineering Software*, **39**(6), p. 483-496.

Benyounis, K. Y., Olabi, A. G. and Hashmi, M. S. J. (2005a), Effect of laser welding parameters on the heat input and weld-bead profile, *Journal of Materials Processing Technology*, **164-165**, p. 978-985.

Benyounis, K. Y., Olabi, A. G. and Hashmi, M. S. J. (2005b), Optimizing the laser-welded butt joints of medium carbon steel using RSM, *Journal of Materials Processing Technology*, **164-165**, p. 986-989.

Bermingham, M. J., McDonald, S. D., Dargusch, M. S. and StJohn, D. H. (2007), Microstucture of cast titanium alloys, *Materials Forum*, **31**, p. 84-89.

Bernard, A. and Karunakaran, K. P. (2007), Rapid manufacturing of metallic objects: A challenge for research and industry, in: *Proceedings of the 3rd International Conference on Advanced Research in Virtual and Rapid Prototyping: Virtual and Rapid Manufacturing Advanced Research Virtual and Rapid Prototyping*, 24-29th September, Leiria, Portugal, p. 7-13.

Bertrand, P., Yadroitsev, I. and Smurov, I. (2004), Prototypage rapide et fabrication directe par laser d'objets multimatériaux multifonctionnels in: *10ème édition des Assises Européennes de Prototypage Rapide*, 14-15th September, Paris, France, p.

Beuth, J. and Klingbeil, N. (2001), The role of process variables in laser-based direct metal solid freeform fabrication, *Journal of the Minerals, Metals and Materials Society*, **53**(9), p. 36-39.

Bhadeshia, H. K. D. H. and Honeycombe, R. W. K. (2006), *Steels: microstructure and properties*. 3rd ed., Elsevier/Butterworth-Heinemann, Amsterdam.

Bi, Z. M., Lang, S. Y. T., Shen, W. and Wang, L. (2008), Reconfigurable manufacturing systems: The state of the art, *International Journal of Production Research*, **46**(4), p. 967-992.

Bihlman, B. (2010), Aerospace titanium demand outlook, in: *Titanium 2010 conference*, AeroStrategy Mangement Consulting, 3-6 October, Orlando, Florida, p. 1-20.

Blackman, S. (1997), Development of pulsed GMAW parameters for titanium SMD components (unpublished report), Shool of Industrial and Manufacturing Science, Welding Engineering Research Centre (WERC), Cranfield University, UK, April 1997.

Bonaccorso, F., Cantelli, L. and Muscato, G. (2011), An arc welding robot control for a shaped metal deposition plant: Modular software interface and sensors, *IEEE Transactions on Industrial Electronics*, **58**(8), p. 3126-3132.

Bontha, S., Klingbeil, N. W., Kobryn, P. A. and Fraser, H. L. (2006), Thermal process maps for predicting solidification microstructure in laser fabrication of thin-wall structures, *Journal of Materials Processing Technology*, **178**(1-3), p. 135-142.

Bourell, D. L., Marcus, H. L., Barlow, J. W. and Beaman, J. J. (1992), Selective laser sintering of metals and ceramics, *International Journal of Powder Metallurgy*, **28**(4), p. 369-381.

Box, G. E. P. and Cox, D. R. (1982), An Analysis of Transformations Revisited, Rebutted, *Journal of the American Statistical Association*, **77**(377), p. 209-210.

Boyer, R. R. (1996), An overview on the use of titanium in the aerospace industry, *Materials Science and Engineering A*, **213**(1-2), p. 103-114.

Boyer, R. R. and Briggs, R. D. (2005), Titanium cost reduction for Boeing aircraft, *Materials Forum*, **29**, p. 47-54.

Bragg, W. L. S. and James, R. W. (1948), *The optical principles of the diffraction of X-rays*, Bell, S.l.

Brandi, H. T. and Luckow, H., Thyssen-Hutte Aktienges (1976), *Method of making large structural one-piece parts of metal, particularly one-piece shafts*, United States Patent No.3,985,995.

Brandl, E., Leyens, C., Donne, C. D. and Holzinger, V. (2009), Deposition of Ti-6Al-4V using Nd:YAG laser & wire: Microstructure and mechanical properties, in: *NATO/RTO/MP AVT-163 Specialists Meeting on Additive Technology For Repair of Military Hardware (NATO unclassified)*, Bonn, p. 1-14.

Brandl, E., Michailov, V., Viehweger, B. and Leyens, C. (2011a), Deposition of Ti-6Al-4V using laser and wire, part I: Microstructural properties of single beads, *Surface and Coatings Technology*, **206**(6), p. 1120-1129.

Brandl, E., Palm, F., Michailov, V., Viehweger, B. *et al.* (2011b), Mechanical properties of additive manufactured titanium (Ti-6Al-4V) blocks deposited by a solid-state laser and wire, *Materials and Design*, **32**(10), p. 4665-4675.

Brandl, E., Schoberth, A. and Leyens, C. (2012), Morphology, microstructure, and hardness of titanium (Ti-6Al-4V) blocks deposited by wire-feed additive layer manufacturing (ALM), *Materials Science and Engineering A*, **532**, p. 295-307.

Brice, C. A., Schwendner, K. I., Mahaffey, D. W., Moore, E. H. *et al.* (1999), Process variable effects on laser deposited Ti-6Al-4V, in: *Proceedings of the 10th Annual International Solid Freeform Fabrication Symposium*, The University of Texas at Austin, Austin, Texas, USA, p. 369-374.

Buschow, K. H. J. (2001), *Encyclopedia of materials: science and technology*, Elsevier, Amsterdam; London.

Campanella, T., Charbon, C. and Rappaz, M. (2004), Grain refinement induced by electromagnetic stirring: A dendrite fragmentation criterion, *Metallurgical and Materials Transactions A: Physical Metallurgy and Materials Science*, **35 A**(10), p. 3201-3210.

Campbell, T., Williams, C., Ivanova, O. and Garrett, B., Could 3D printing change the world? Technologies, potential, and implications of additive manufacturing (2011), available from: http://www.acus.org/publication/could-3d-printing-change-world (accessed 19th January 2012).

Carpenter, O. R. and Kerr, H. J., The Babcock & Wilcox Company (New Orleans, LA) (1947), *Method and apparatus for metal coating metal pipes by electric fusion*, United States Patent No.2,427,350.

Chandel, R. S. (1988), Mathematical modeling of gas metal arc weld features, in: *Proceedings of the Fourth International Conference on Modeling of Casting and Welding Processes* Warrendale, PA: The Metals, Materials, and Minerals Society, April 17-22, Palm Coast, Florida, p. 109-120.

Chandel, R. S. and Bala, S. R. (1986), Effect of welding parameters and groove angle on the soundness of root beads deposited by the SAW process, in: *Advances in Welding Science and Technology - TWR '86: Proceedings of an International Conference on Trends in Welding Research.*, ASM Int, 12-22 May, Gatlinburg, Tennessee, TN, USA, p. 379-385.

Choi, J. and Chang, Y. (2005), Characteristics of laser aided direct metal/material deposition process for tool steel, *International Journal of Machine Tools and Manufacture*, **45**(4-5), p. 597-607.

Christensen, N., Davies, V. d. L. and Gjermundsen, K. (1965), Distribution of temperatures in arc welding, *British Welding Journal*, **12**(2), p. 54-75.

Clark, D., Bache, M. R. and Whittaker, M. T. (2010), Microstructural characterization of a polycrystalline nickel-based superalloy processed via tungsten-intert-gas-shaped metal deposition, *Metallurgical and Materials Transactions B: Process Metallurgy and Materials Processing Science*, **41**(6), p. 1346-1353.

Clark, D., Bache, M. R. and Whittaker, M. T. (2008), Shaped metal deposition of a nickel alloy for aero engine applications, *Journal of Materials Processing Technology*, **203**(1-3), p. 439-448.

Colegrove, P., Ikeagu, C., Thistlethwaite, A., Williams, S. *et al.* (2009), Welding process impact on residual stress and distortion, *Science and Technology of Welding and Joining*, **14**(8), p. 717-725.

Cook, R. D. (2000), Detection of influential observation in linear regression, *Technometrics*, **42**(1), p. 65-68.

Cormier, D., Harrysson, O. and West, H. (2004), Characterization of H13 steel produced via electron beam melting, *Rapid Prototyping Journal*, **10**(1), p. 35-41.

Costa, L. and Vilar, R. (2009), Laser powder deposition, *Rapid Prototyping Journal*, **15**(4), p. 264-279.

Cottrell, A. H. and Bilby, B. A. (1949), Dislocation theory of yielding and strain ageing of iron, *Proceedings of the Physical Society. Section A*, **62**(1), p. 49-62.

Crew, H., Fresnel, A. J., Huygens, C. A. and Young, T. M. D. F. R. S. (1900), *The wave theory of light. Memoirs by Huygens, Young and Fresnel. Edited by Henry Crew*, New York, etc.: American Book Co.

Cullity, B. D. and Stock, S. R. (2001), *Elements of X-ray diffraction*. 3rd ed., Prentice Hall ; London : Prentice-Hall International, Upper Saddle River, New Jersey.

Das, S., Beaman, J. J. and Bourell, M. W. D. L. (1998a), Direct laser freeform fabrication of high performance metal components, *Rapid Prototyping Journal*, **4**(3), p. 112-117.

Das, S. and Chandra, U. (2003), *Handbook of Aluminum: Physical metallurgy and proceses* CRC Press.

Das, S., Wohlert, M., Beaman, J. J. and Bourell, D. L. (1999), Processing of titanium net shapes by SLS/HIP*, Materials and Design*, **20**(2-3), p. 115-121.

Das, S., Wohlert, M., Beaman, J. J. and Bourell, D. L. (1998b), Producing metal parts with selective laser sintering/hot isostatic pressing*, Journal of Minerals, Metals and Materials Society*, **50**(12), p. 17-20.

Daymond, M. R., Bourke, M. A. M., Von Dreele, R. B., Clausen, B. *et al.* (1997), Use of Rietveld refinement for elastic macrostrain determination and for evaluation of plastic strain history from diffraction spectra*, Journal of Applied Physics*, **82**(4), p. 1554-1562.

Deherkar, P. (2010), Study of building horizontal and inclined walls using Additive Layer Manufacture (unpublished MSc thesis), School of Applied Sciences (SAS), Welding Engineering and Laser Processing Centre (WELPC), Cranfield University, Cranfield, UK.

Deng, D. and Murakawa, H. (2006), Numerical simulation of temperature field and residual stress in multi-pass welds in stainless steel pipe and comparison with experimental measurements*, Computational Materials Science*, **37**(3), p. 269-277.

Dickens, P. M., Cobb, R. C., Gibson, I. and Pridham, M. S. (1993), Rapid prototyping using 3D welding*, Journal of Design and Manufacturing*, **3**(1), p. 39-44.

Dickens, P. M., Pridham, M. S., Cobb, R. C., Gibson, I. *et al.* (1992), 3-D Welding, in: *Proceedings of the First European Conference on Rapid Prototyping*, 6-7th July, University of Nottingham, England, p. 81-93.

Dickens, P. M., Spencer, J. D. and Wykes, C. M. (1998), Rapid prototyping of metal parts by three-dimensional welding*, Proceedings of the Institution of Mechanical Engineers, Part B: Journal of Engineering Manufacture*, **212 Part B**(3), p. 175-182.

Dilthey, U., Stein, L., Berger, C., Million, K. *et al.* (2006), Future prospects of shape welding*, Welding and Cutting*, **5**(3), p. 164-172.

Ding, J., Colegrove, P., Mehnen, J., Ganguly, S. *et al.* (2011), Thermo-mechanical analysis of wire and arc additive layer manufacturing process on large multi-layer parts*, Computational Materials Science*, **50**(12), p. 3315-3322.

Doherty, J. and McGlone, J. C. (1977), Relationships between process variables and weld geometry, *The Welding Institute*, Research Report 52/1977/PE, December.

Doherty, J., Shinoda, T. and Weston, J. (1978), The relationships between arc welding parameters and fillet weld geometry for MIG welding with flux cored wires, *The Welding Institute*, Research Report 82/1978/PE, 1978.

Doumanidis, C. and Kwak, Y. M. (2001), Geometry modeling and control by infrared and laser sensing in thermal manufacturing with material deposition*, Journal of Manufacturing Science and Engineering, Transactions of the ASME*, **123**(1), p. 45-52.

Doumanidis, C. and Kwak, Y. M. (2002), Multivariable adaptive control of the bead profile geometry in gas metal arc welding with thermal scanning, *International Journal of Pressure Vessels and Piping*, **79**(4), p. 251-262.

Doyle, T. E. (1991), Shape Melting Technology, in: *The 3rd International Conference on Desktop Manufacturing: Making Rapid Prototyping pay back, The Management Round Table*, 7-8th October, USA.

Doyle, T. E., Edmonds, D. P., Mcaninch, M. D. and Ryan, P. M., The Babcock & Wilcox Company (New Orleans, LA) (1989), *Method and apparatus for building a workpiece by deposit welding*, United States Patent No.4,842,186.

Doyle, T. E. and Ryan, P. M., The Babcock & Wilcox Company (New Orleans, LA) (1989), *Method and apparatus for automatic vapor cooling when shape melting a component*, United States Patent No.4,857,694.

Eccleston, R. and Wilson, C. (2004), Correspondent's reports: A guided tour of ISIS (2004 update), *Neutron News*, **15**(1), p. 15-18.

Edward Ries, D. (1983), Gas metal arc welding of titanium (MSc), Department of Ocean Engineering, Massachusetts Institute of Technology (MIT), Cambridge, Massachusetts.

Eickhoff, S. T. and Eagar, T. W. (1990), Characterization of Spatter in Low-Current GMAW of Titanium Alloy Plate, *Welding Journal (Miami, Fla)*, **69**(10), p. 382s-388s.

Elmer, J. W., Palmer, T. A., Babu, S. S., Zhang, W. *et al.* (2004), Phase transformation dynamics during welding of Ti-6Al-4V, *Journal of Applied Physics*, **95**(12), p. 8327-8339.

Emmanuel, E. (2009), VBC welding system parameter effect on the shape and microstructure of additively manufactured Ti-6Al-4V titanium alloy (unpublished MSc thesis), School of Applied Sciences (SAS), Welding Engineering and Laser Processing Centre (WELPC), Cranfield University, Cranfield, UK.

Eschholz, O. H., Westinghouse Electric & Manufacturing Company (1925), *Ornamental arc welding*, United States Patent No.1,533,239.

Escobar-Palafox, G., Gault, R. and Ridgway, K. (2011a), Preliminary empirical models for predicting shrinkage, part geometry and metallurgical aspects of Ti-6Al-4V shaped metal deposition builds, *IOP Conference Series: Materials Science and Engineering (Trends in Aerospace Manufacturing Conference, TRAM09, 9-10th September 2009)*, **26**(1), p. 1-8.

Escobar-Palafox, G., Gault, R. and Ridgway, K. (2011b), Robotic manufacturing by shaped metal deposition: State of the art, *Industrial Robot*, **38**(6), p. 622-628.

Essers, W. G. and Van Gompel, M. R. M. (1984), Arc control with pulsed GMA welding, *Welding Journal (Miami, Fla)*, **63**(6), p. 26-32.

Ettlie, J. E. and Stoll, H. W. (1990), *Managing the design-manufacturing process*, McGraw-Hill, New York.

Ezugwu, E. O. and Wang, Z. M. (1997), Titanium alloys and their machinability - A review, *Journal of Materials Processing Technology*, **68**(3), p. 262-274.

Fachinotti, V. D. and Cardona, A. (2008), Computational simulation of shaped metal deposition, in: *Asociación Argentina de Macánica Computacional*, 10-13th November, San Luis, Argentina

Fan, Z. (1993), On the young's moduli of Ti6Al4V alloys, *Scripta Metallurgica et Materiala*, **29**(11), p. 1427-1432.

Feng, J., Zhang, H. and He, P. (2009), The CMT short-circuiting metal transfer process and its use in thin aluminium sheets welding, *Materials and Design*, **30**(5), p. 1850-1852.

Fenn, J., Emerging Technology Hype Cycle 2010: What's hot and what's not (2010), available from: http://www.gartner.com/it/content/1395600/1395613/august_4_whats_hot_hype_2010_jfenn.pdf (accessed 19th January 2012).

Fenn, J. and Raskino, M. (2008), *Mastering the hype cycle : how to choose the right innovation at the right time*, Harvard Business School Press, Cambridge, Massachusetts.

Froes, F. H., Eylon, D., Eichelman, G. E. and Burte, H. M. (1980), Developments in titanium powder metallurgy, *Journal of Metals*, **32**(2), p. 47-54.

Garland, J. G. (1974), Weld pool solidification control, *Metal Construction*, **6**(4), p. 121-127.

Geisseler, M. E., CH), Sulzer Brothers Limited (Winterthur, CH) (1989), *Process for producing a weld-built member*, United States Patent No.4,798,930.

Geyer, A., Scapolo, F., Boden, M., Döry, T. *et al.* (2003), *The future of manufacturing in Europe 2015-2020: The challenge for sustainability*, European Commission Joint Research Centre and Institute for Prospective Technological Studies.

Gibson, I., Rosen, D. W. and Stucker, B. (2010), *Additive manufacturing technologies: rapid prototyping to direct digital manufacturing*, Springer, New York; London.

Greene, W. J. (1960), An analysis of transfer in gas-shielded welding arcs, *Transactions of the American Institute of Electrical Engineers (Part 2)*, **79**, p. 194-203.

Griffith, M. L., Ensz, M. T., Puskar, J. D., Robino, C. V. *et al.* (2000), Understanding the microstructure and properties of components fabricated by Laser Engineered Net Shaping (LENS), in: *Materials Research Society Symposium - Proceedings*, Vol.625, San Francisco, CA, p. 9-20.

Griffith, M. L. and Halloran, J. W. (1996), Freeform fabrication of ceramics via stereolithography, *Journal of the American Ceramic Society*, **79**(10), p. 2601-2608.

Griffith, M. L., Schlieriger, M. E., Harwell, L. D., Oliver, M. S. *et al.* (1999), Understanding thermal behavior in the LENS process, *Materials and Design*, **20**(2-3), p. 107-113.

Groneck, D. and Harmon, D. (2003), Design development of unitized titanium structure, *Journal of Engineering for Gas Turbines and Power*, **125**(1), p. 252-256.

Grosse-Wördemann, J. (1980), The shape welding of heavy semi-finished parts, *Materialprüfung*, **22**(4), p. 168-173.

Guile, A. E. (1971), Arc- electrode phenomena, *Proceedings of the Institution of Electrical Engineers*, **118**(9 R), p. 1131-1154.

Gunaraj, V. and Murugan, N. (1999), Application of response surface methodology for predicting weld bead quality in submerged arc welding of pipes, *Journal of Materials Processing Technology*, **88**(1), p. 266-275.

Gupta, V. K. and Parmar, R. S. (1989), Fractional factorial technique to predict dimensions of the weld bead in automatic submerged arc welding, *Journal of the Institution of Engineers (India): Mechanical Engineering Division*, **70**(pt 4), p. 67-75.

Hague, R., Campbell, I. and Dickens, P. (2003a), Implications on design of rapid manufacturing, *Proceedings of the Institution of Mechanical Engineers, Part C: Journal of Mechanical Engineering Science*, **217**(1), p. 25-30.

Hague, R., Mansour, S. and Saleh, N. (2003b), Design opportunities with rapid manufacturing, *Assembly Automation*, **23**(4), p. 346-356.

Hauk, V. (1997), *Structural and residual stress analysis by nondestructive methods: evaluation, application, assessment -NEW*, Elsevier, Amsterdam; Oxford.

Hensel, F., Binroth, C. and Sepold, G. (1992), A comparison of powder- and wire-fed laser beam cladding, in: Mordike, B. L., (editor), *Laser Treatment of Materials*, Dgm Metallurgy Information, p. 39-44.

Hermans, M. J. M. and Ouden, G. D. (1999), Process Behaviour and Stability in Short Circuit Gas Metal Arc Welding, *Welding Journal (Miami, Fla)*, **78**(4), p. 137-141-s.

Hopkinson, N. and Dickens, P. (2003), Analysis of rapid manufacturing - Using layer manufacturing processes for production, *Proceedings of the Institution of Mechanical Engineers, Part C: Journal of Mechanical Engineering Science*, **217**(1), p. 31-40.

Hopkinson, N. and Dickens, P. (2001), Rapid prototyping for direct manufacture, *Rapid Prototyping Journal*, **7**(4), p. 197-202.

Hopkinson, N., Hague, R. J. M. and Dickens, P. M. (2006), *Rapid manufacturing: an industrial revolution for the digital age*, John Wiley, Chichester.

Hsu, C. and Soltis, P. (2003), Heat input comparison of STT vs. short-circuiting and pulsed GMAW vs. CV processes, in: *6th International Conference on Trends in Welding Research*, 15-19 April, Phoenix, AZ p. 369-374.

Hu, J. and Tsai, H. L. (2007), Heat and mass transfer in gas metal arc welding. Part II: The metal, *International Journal of Heat and Mass Transfer*, **50**(5-6), p. 808-820.

Hutchings, M. T. (2005), *Introduction to the characterization of residual stress by neutron diffraction*, CRC, Boca Raton, Fla.

IMechE (2011), Aero 2075: Flying into a bright future? - Part I:The importance of the UK aerospace sector to UK manufacturing, Institution of Mechanical Engineers, London, October.

Irving, R. R. (1970), An all electroslag welded vessel, *Iron Age*, **205**(5), p.

Irving, R. R. (1971), Why not combine melting, fabrication, *Iron Age*, **207**(10), p. 53-55.

Jandric, Z., Labudovic, M. and Kovacevic, R. (2004), Effect of heat sink on microstructure of three-dimensional parts built by welding-based deposition, *International Journal of Machine Tools and Manufacture*, **44**(7-8), p. 785-796.

Johnson, M. W., Edwards, L. and Withers, P. J. (1997), Engin - A new instrument for engineers, *Physica B: Condensed Matter*, **234-236**, p. 1141-1143.

Jones, S. A., Rolls-Royce PLC (2002), *Apparatus and method for forming a body*, Great Britain Patent No.GB2,373,749A.

Jones, S. B. (1976), Process tolerance in submerged arc welding, *The Welding Institute*, Research Report 1/1976/PE, February.

Joseph, A., Farson, D., Harwig, D. and Richardson, R. (2005), Influence of GMAW-P current waveforms on heat input and weld bead shape, *Science and Technology of Welding and Joining*, **10**(3), p. 311-318.

Kamara, A. M., Marimuthu, S. and Li, L. (2011), A numerical investigation into residual stress characteristics in laser deposited multiple layer waspaloy parts, *Journal of Manufacturing Science and Engineering, Transactions of the ASME*, **133**(3), p. 0310131-9.

Kannan, T. and Murugan, N. (2006), Effect of flux cored arc welding process parameters on duplex stainless steel clad quality, *Journal of Materials Processing Technology*, **176**(1-3), p. 230-239.

Karimzadeh, F., Salehi, M., Saatchi, A. and Meratian, M. (2005), Effect of microplasma arc welding process parameters on grain growth and porosity distribution of thin sheet Ti6Al4V alloy weldment, *Materials and Manufacturing Processes*, **20**(2), p. 205-219.

Karunakaran, K. P., Suryakumar, S., Pushpa, V. and Akula, S. (2009), Retrofitment of a CNC machine for hybrid layered manufacturing, *International Journal of Advanced Manufacturing Technology*, **45**(7-8), p. 690-703.

Kelly, S. M. and Kamper, S. L. (2004), Microstructural evolution in laser-deposited multilayer Ti-6Al-4V builds: Part 1. Microstructural characterization, *Metallurgical and Materials Transactions A: Physical Metallurgy and Materials Science*, **35 A**(6), p. 1861-1867.

Khademhosseini, A., Langer, R., Borenstein, J. and Vacanti, J. P. (2006), Microscale technologies for tissue engineering and biology, *Proceedings of the National Academy of Sciences of the United States of America*, **103**(8), p. 2480-2487.

Kieback, B., Neubrand, A. and Riedel, H. (2003), Processing techniques for functionally graded materials, *Materials Science and Engineering A*, **362**(1-2), p. 81-105.

Kim, I. S., Son, J. S., Kim, I. G., Kim, J. Y. *et al.* (2003), A study on relationship between process variables and bead penetration for robotic CO2 arc welding, *Journal of Materials Processing Technology*, **136**(1-3), p. 139-145.

Kim, J. D. and Peng, Y. (2000), Plunging method for Nd:YAG laser cladding with wire feeding, *Optics and Lasers in Engineering*, **33**(4), p. 299-309.

Kishore Babu, N., Ganesh Sundara Raman, S., Mythili, R. and Saroja, S. (2007), Correlation of microstructure with mechanical properties of TIG weldments of Ti-6Al-4V made with and without current pulsing, *Materials Characterization*, **58**(7), p. 581-587.

Klingbeil, N. W., Beuth, J. L., Chin, R. K. and Amon, C. H. (2002), Residual stress-induced warping in direct metal solid freeform fabrication, *International Journal of Mechanical Sciences*, **44**(1), p. 57-77.

Kobryn, P. A., Moore, E. H. and Semiatin, S. L. (2000), The effect of laser power and traverse speed on microstructure, porosity, and build height in laser-deposited Ti-6Al-4V, *Scripta Materialia*, **43**(4), p. 299-305.

Kobryn, P. A., Ontko, N. R., Perkins, L. P. and Tiley, J. S. (2006), Additive manufacturing of aerospace alloys for aircraft structures. Meeting Proceedings RTO-MP-AVT-139, Paper 3, in: *Cost Effective Manufacture via Net-Shape Processing*, Neuilly-sur-Seine, France: NATO Research & Technology Organisation (RTO). p. 3.1-3.14.

Kobryn, P. A. and Semiatin, S. L. (2001), The laser additive manufacture of Ti-6Al-4V, *Journal of the Minerals, Metals and Materials Society*, **53**(9), p. 40-42.

Koren, Y., Heisel, U., Jovane, F., Moriwaki, T. *et al.* (1999), Reconfigurable manufacturing systems, *CIRP Annals - Manufacturing Technology*, **48**(2), p. 527-540.

Kostrivas, A., Plewka, A., G.B., M. and Smith, L. S. (2008), Pulsed MIG welding of titanium with a novel wire, *The Welding Institute*, Research Report 900/2008, June, 2008.

Kou, S. (2003), *Welding metallurgy*. 2nd ed., Wiley, New Jersey.

Kovacevic, R. and Zhang, Y. M. (1997), Real-time image processing for monitoring of free weld pool surface, *Journal of Manufacturing Science and Engineering, Transactions of the ASME*, **119**(2), p. 161-169.

Kruth, J. P. (1991), Material incress manufacturing by rapid prototyping techniques, *CIRP Annals - Manufacturing Technology*, **40**(2), p. 603-614.

Kruth, J. P., Leu, M. C. and Nakagawa, T. (1998), Progress in additive manufacturing and rapid prototyping, *CIRP Annals - Manufacturing Technology*, **47**(2), p. 525-540.

Kruth, J. P., Levy, G., Klocke, F. and Childs, T. H. C. (2007), Consolidation phenomena in laser and powder-bed based layered manufacturing, *CIRP Annals - Manufacturing Technology*, **56**(2), p. 730-759.

Kurz, W. and Fisher, D. J. (1998), *Fundamentals of solidification*. 4th revised ed., Trans Tech, Uetikon-Zuerich.

Kußmaul, K., Schoch, F.-W. and Luckow, H. (1983), High quality large components 'Shape Welded' by a SAW process, *Welding Journal (Miami, Fla)*, **62**(9), p. 17-24.

Labudovic, M., Hu, D. and Kovacevic, R. (2003), A three dimensional model for direct laser metal powder deposition and rapid prototyping, *Journal of Materials Science*, **38**(1), p. 35-49.

Larson, A. C. and Dreele, R. B. V. (2004), General Structure Analysis System (GSAS) Los Alamos National Laboratory Report LAUR 86-748, Los Alamos, September.

Larson, F. and Zarkades, A. (1974), Properties of textured titanium alloys, *MCIC Rep MCIC-74-20*, June.

Leary, R. K., Merson, E., Birmingham, K., Harvey, D. *et al.* (2010), Microstructural and microtextural analysis of InterPulse GTCAW welds in Cp-Ti and Ti-6Al-4V*, Materials Science and Engineering A*, **527**(29-30), p. 7694-7705.

Lee, J. I. and Rhee, S. (2000), Prediction of process parameters for gas metal arc welding by multiple regression analysis*, Proceedings of the Institution of Mechanical Engineers, Part B: Journal of Engineering Manufacture*, **214**(6), p. 443-449.

Lee, J. I. and Um, K. W. (2000), Prediction of welding process parameters by prediction of back-bead geometry*, Journal of Materials Processing Technology*, **108**(1), p. 106-113.

Lee, Y. T. and Welsch, G. (1990), Young's modulus and damping of Ti6Al4V alloy as a function of heat treatment and oxygen concentration*, Materials Science and Engineering A*, **128**(1), p. 77-89.

Leinonen, M. (2011), Additive-Layer-Manufacturing by CMT using Cu97Si3 wire on steel (unpublished MSc thesis), School of Applied Sciences (SAS), Welding Engineering and Laser Processing Centre (WELPC), Cranfield University, Cranfield, UK.

Leong, K. F., Cheah, C. M. and Chua, C. K. (2003), Solid freeform fabrication of three-dimensional scaffolds for engineering replacement tissues and organs*, Biomaterials*, **24**(13), p. 2363-2378.

Lesnewich, A. (1958), Control of melting rate and metal transfer in gas-shielded metal-arc welding – Part 1 – Control of electrode melting rate*, Welding Journal*, **37**(8), p. 343s-353s.

Levy, G. N., Schindel, R. and Kruth, J. P. (2003), Rapid manufacturing and rapid tooling with layer manufacturing (LM) technologies, state of the art and future perspectives*, CIRP Annals - Manufacturing Technology*, **52**(2), p. 589-609.

Lewis, G. K. and Schlienger, E. (2000), Practical considerations and capabilities for laser assisted direct metal deposition*, Materials and Design*, **21**(4), p. 417-423.

Li, X., Wang, C., Zhang, W. and Li, Y. (2009), Fabrication and characterization of porous Ti6Al4V parts for biomedical applications using electron beam melting process*, Materials Letters*, **63**(3-4), p. 403-405.

Li, Y., Yang, H., Lin, X., Huang, W. *et al.* (2003), The influences of processing parameters on forming characterizations during laser rapid forming*, Materials Science and Engineering A*, **360**(1-2), p. 18-25.

Lim, Y. C., Farson, D. F., Cho, M. H. and Cho, J. H. (2009), Stationary GMAW-P weld metal deposit spreading*, Science and Technology of Welding and Joining*, **14**(7), p. 626-635.

Lim, Y. C., Yu, X., Cho, J. H., Sosa, J. *et al.* (2010), Effect of magnetic stirring on grain structure refinement: Part 2 - Nickel alloy weld overlays*, Science and Technology of Welding and Joining*, **15**(5), p. 400-406.

Lin, J. and Steen, W. M. (1998), Design characteristics and development of a nozzle for coaxial laser cladding*, Journal of Laser Applications*, **10**(2), p. 55-63.

Llewellyn, D. T. and Hudd, R. C. (1998), *Steels: metallurgy and applications*. 3rd ed., Butterworth-Heinemann, Oxford.

Lohwasser, D. and Chen, Z. (2010), *Friction stir welding : from basics to applications*, Woodhead Publishing Limited, Cambridge.

Lorant, E. (2010), Effect of microstructure on mechanical properties of Ti-6Al-4V structures made by Additive Layer Manufacturing (unpublished MSc thesis), School of Applied Sciences (SAS), Welding Engineering and Laser Processing Centre (WELPC), Cranfield University, Cranfield, UK.

Lorenzin, G. and Rutili, G. (2009), The innovative use of low heat input in welding: Experiences on 'cladding' and brazing using the CMT process*, Welding International*, **23**(8), p. 622-632.

Lucas, B., Verhaeghe, G. and Leggatt, R., Job knowledge for welders 33: Distortion - types and causes (TWI) (1999), available from: http://www.twi.co.uk/content/jk33.html (accessed 4th February 2011).

Lütjering, G. and Williams, J. C. (2007), *Titanium*. 2nd ed., Springer, Berlin; New York.

Makoto, C. (2004), Development of titanium and titanium alloy welding wire "G-Coat" for GMAW, *Daido Steel Co. Ltd*, Aichi, Japan.

Manonmani, K., Murugan, N. and Buvanasekaran, G. (2007), Effects of process parameters on the bead geometry of laser beam butt welded stainless steel sheets*, International Journal of Advanced Manufacturing Technology*, **32**(11-12), p. 1125-1133.

Martina, F. (2010), Study of the benefits of plasma deposition of Ti-6Al-4V structures made by Additive Layer Manufacture (unpublished MSc thesis), School of Applied Sciences (SAS), Welding Engineering and Laser Processing Centre (WELPC), Cranfield University, Cranfield, UK.

Martina, F., Mehnen, J., Williams, S. W., Colegrove, P. *et al.* (2012), Investigation of the benefits of plasma deposition for the additive layer manufacture of Ti–6Al–4V*, Journal of Materials Processing Technology*, **212**(6), p. 1377-1386.

Matsuda, F., Nakata, K. and Sano, N. (1983), Effect of electromagnetic stirring on weld solidification structure of austenitic stainless steels*, Transactions of the Joining and Welding Research Institute of Osaka University*, **15**(2), p. 155-166.

Matsuda, F., Ushio, M., Nakagawa, H. and Nakata, K. (1979), Effects of electromagnetic stirring on the weld solidification structure of aluminium alloys, in: *Arc physics and weld pool behaviour: an international conference*, The Welding Institute, 8-10th May, London, UK, paper 10, p. 337-347.

Mazumder, J., Choi, J., Nagarathnam, K., Koch, J. *et al.* (1997), The direct metal deposition of H13 tool steel for 3-D components*, Journal of the Minerals, Metals and Materials Society*, **49**(5), p. 55-60.

McAninch, M. D. and Conrardy, C. C. (1991), Shape melting - a unique near-net shape manufacturing process*, Welding Review International*, **10**(1), p. 33-40.

McCusker, L. B., Von Dreele, R. B., Cox, D. E., Louër, D. *et al.* (1999), Rietveld refinement guidelines*, Journal of Applied Crystallography*, **32**(1), p. 36-50.

McGlone, J. C. (1980), The submerged arc butt welding of mild steel – A decade of procedure optimisation, *The Welding Institute*, Research Report 133/1980, December, 1980.

McGlone, J. C. (1982), Weld bead geometry prediction - A review*, Metal Construction*, **14**(7), p. 378-384.

McGlone, J. C. and Chadwick, D. B. (1978), The submerged-arc butt welding of mild steel, Part 2: The prediction of weld bead geometry from the procedure parameters, *The Welding Institute*, Research Report 80/1978/PE, December.

Mehnen, J., Ding, J., Lockett, H. and Kazanas, P. (2010), Design for wire and arc additive layer manufacture, in: *20th CIRP Design Conference (CIRP DESIGN 2010)*, 19-21 April, Nantes, France., p. 721-727.

Mehrabi, M. G., Ulsoy, A. G. and Koren, Y. (2000), Reconfigurable manufacturing systems: key to future manufacturing*, Journal of Intelligent Manufacturing*, **11**(4), p. 403-419.

Menzel, M. (2003), The influence of individual components of an industrial gas mixture on the welding process and the properties of welded joints*, Welding International*, **17**(4), p. 262-264.

Million, K., Datta, R. and Zimmermann, H. (2005), Effects of heat input on the microstructure and toughness of the 8 MnMoNi 5 5 shape-welded nuclear steel*, Journal of Nuclear Materials*, **340**(1), p. 25-32.

Million, K., Datta, R. and Zimmermann, H., Maschf Augsburg Nuernberg AG (DE) (1985), *Method for the production of a structural part by shaping building-up welding, and structural part produced according to this method.*, Patent No.EP0163828.

Million, K. and Zimmerman, H., Maschinenfabrik, Augsburg-nurnberg M. A. N. (DE) (1987), *Method of preparing structural components having a symmetrically curved wall by buildup welding*, United States Patent No.4,671,448.

Million, K. and Zimmermann, H., M.A.N. Maschinenfabrik Augsburg-Nürnberg Aktiengesellschaft (DE) (1985), *Method and apparatus for manufacturing a tube bend metal*, United States Patent No.4,517,434.

Mills, K. C. (2002), *Recommended values of thermophysical properties for selected commercial alloys*, Woodhead, Cambridge.

Miranda, R. M., Lopes, G., Quintino, L., Rodrigues, J. P. *et al.* (2008), Rapid prototyping with high power fiber lasers*, Materials and Design*, **29**(10), p. 2072-2075.

Mitchell, D. R. and Feige, N. G. (1967), Welding of alpha-beta titanium alloys in one inch plate, *Welding Journal*, **46**(5), p. 193s-202s.

Mizutani, Y., Kawata, J., Miwa, K., Yasue, K. *et al.* (2004), Effect of the frequency of electromagnetic vibrations on microstructural refinement of AZ91D magnesium alloy, *Journal of Materials Research*, **19**(10), p. 2997-3003.

Moat, R. J., Pinkerton, A. J., Li, L., Withers, P. J. *et al.* (2011), Residual stresses in laser direct metal deposited Waspaloy, *Materials Science and Engineering A*, **528**(6), p. 2288-2298.

Mok, S. H., Bi, G., Folkes, J. and Pashby, I. (2008a), Deposition of Ti-6Al-4V using a high power diode laser and wire, Part I: Investigation on the process characteristics, *Surface and Coatings Technology*, **202**(16), p. 3933-3939.

Mok, S. H., Bi, G., Folkes, J., Pashby, I. *et al.* (2008b), Deposition of Ti-6Al-4V using a high power diode laser and wire, Part II: Investigation on the mechanical properties, *Surface and Coatings Technology*, **202**(19), p. 4613-4619.

Montgomery, D. C. (2009), *Design and analysis of experiments*. 7th ed., Wiley, Hoboken, N.J.

Montgomery, D. C., Peck, E. A. and Vining, G. G. (2006), *Introduction to linear regression analysis*. 4th ed., Wiley-Interscience, New York; Chichester.

Morgan, R., Sutcliffe, C. J. and O'Neill, W. (2004), Density analysis of direct metal laser re-melted 316L stainless steel cubic primitives, *Journal of Materials Science*, **39**(4), p. 1195-1205.

Mughal, M. P., Fawad, H. and Mufti, R. A. (2006), Three-dimensional finite-element modelling of deformation in weld-based rapid prototyping, *Proceedings of the Institution of Mechanical Engineers, Part C: Journal of Mechanical Engineering Science*, **220**(6), p. 875-885.

Mughal, M. P., Fawad, H., Mufti, R. A. and Siddique, M. (2005), Deformation modelling in layered manufacturing of metallic parts using gas metal arc welding: Effect of process parameters, *Modelling and Simulation in Materials Science and Engineering*, **13**(7), p. 1187-1204.

Mughal, M. P., Mufti, R. A. and Fawad, H. (2007), The mechanical effects of deposition patterns in welding-based layered manufacturing, *Proceedings of the Institution of Mechanical Engineers, Part B: Journal of Engineering Manufacture*, **221**(10), p. 1499-1509.

Murphy, A. B. (1997), Transport coefficients of helium and argon-helium plasmas, *IEEE Transactions on Plasma Science*, **25**(5), p. 809-814.

Murugan, N. and Parmar, R. S. (1994), Effects of MIG process parameters on the geometry of the bead in the automatic surfacing of stainless steel, *Journal of Materials Processing Tech.*, **41**(4), p. 381-398.

Murugan, N., Parmar, R. S. and Sud, S. K. (1993), Effect of submerged arc process variables on dilution and bead geometry in single wire surfacing, *Journal of Materials Processing Tech.*, **37**(1-4), p. 767-780.

Muscato, G., Spampinato, G. and Cantelli, L. (2008), A closed loop welding controller for a rapid manufacturing process, in: *13th IEEE International Conference on Emerging Technologies and Factory Automation, ETFA 2008*, 15-18th September, Hamburg, Germany, p. 1080-1083.

Myers, J. R., Bomberger, H. B. and Froes, F. H. (1984), Corrosion behavior and use of titanium and its alloys, *Journal of Metals*, **36**(10), p. 50-59.

Nagarajan, K. V., Vasudevan, R., Thomas, G., Ramachandra, V. *et al.* (1992), Effect of preweld and postweld heat treatment on the properties of GTA welds in Ti-6Al-4V sheet, *Welding Journal*, **71**(1), p. 15s-25s.

Nagesh, D. S. and Datta, G. L. (2002), Prediction of weld bead geometry and penetration in shielded metal-arc welding using artificial neural networks, *Journal of Materials Processing Technology*, **123**(2), p. 303-312.

Nickel, A. H., Barnett, D. M. and Prinz, F. B. (2001), Thermal stresses and deposition patterns in layered manufacturing, *Materials Science and Engineering A*, **317**(1-2), p. 59-64.

Noble, P. O., General Electric Co. (1933), *Method and apparatus for electric arc welding*, United States Patent No.1,898,060.

Norman, R. D. and Dickens, P. M. (1995), 3D welding fabrication: Strategies for sloped surfaces, in: *Proceedings of the 1st National Conference on Rapid Prototyping and Tooling Research*, Mechanical Engineering Publications Limited,London and Bury St Edmunds, UK, Department of Engineering Technology, Buckinghamshire College, UK, p. 51-65.

Onuki, J., Anazawa, Y., Nihei, M., Katou, M. *et al.* (2002), Development of a new high-frequency, high-peak current power source for high constricted arc formation, *Japanese Journal of Applied Physics, Part 1: Regular Papers and Short Notes and Review Papers*, **41**(9), p. 5821-5826.

Pal, K. and Pal, S. K. (2011), Effect of pulse parameters on weld quality in pulsed gas metal arc welding: A review, *Journal of Materials Engineering and Performance*, **20**(6), p. 918-931.

Palani, P. K. and Murugan, N. (2006), Selection of parameters of pulsed current gas metal arc welding, *Journal of Materials Processing Technology*, **172**(1), p. 1-10.

Paul, B. K. and Baskaran, S. (1996), Issues in fabricating manufacturing tooling using powder-based additive freeform fabrication, *Journal of Materials Processing Technology*, **61**(1-2), p. 168-172.

Pawley, G. S. (1981), Unit-cell refinement from powder diffraction scans, *Journal of Applied Crystallography*, **14**, p. 357-361.

Pearce, S. V., Linton, V. M. and Oliver, E. C. (2008), Residual stress in a thick section high strength T-butt weld, *Materials Science and Engineering A*, **480**(1-2), p. 411-418.

Peel, M., Steuwer, A., Preuss, M. and Withers, P. J. (2003), Microstructure, mechanical properties and residual stresses as a function of welding speed in aluminium AA5083 friction stir welds, *Acta Materialia*, **51**(16), p. 4791-4801.

Pépe, N. V. C. (2010), Advances in gas metal arc welding and application to corrosion resistant alloy pipes (unpublished PhD thesis), School of Applied Sciences (SAS), Welding Engineering and Laser Processing Centre (WELPC), Cranfield University, Cranfield, UK.

Pham, D. T. and Dimov, S. S. (2003), Rapid prototyping and rapid tooling - The key enablers for rapid manufacturing, *Proceedings of the Institution of Mechanical Engineers, Part C: Journal of Mechanical Engineering Science*, **217**(1), p. 1-24.

Pham, D. T. and Gault, R. S. (1998), A comparison of rapid prototyping technologies, *International Journal of Machine Tools and Manufacture*, **38**(10-11), p. 1257-1287.

Pickin, C. G. and Young, K. (2006), Evaluation of cold metal transfer (CMT) process for welding aluminium alloy, *Science and Technology of Welding and Joining*, **11**(5), p. 583-585.

Piehl, K.-H. (1989), Shape welding of heavy components, "Formgebendes Schweißen von Schwerkomponenten", *Technische Berichte - Thyssen*, **21**(1), p. 53-71.

Pinkerton, A. J. and Lin, L. (2004), Modelling powder concentration distribution from a coaxial deposition nozzle for laser-based rapid tooling, *Journal of Manufacturing Science and Engineering, Transactions of the ASME*, **126**(1), p. 33-41.

Pinkerton, A. J., Syed, W. U. H. and Li, L. (2007), Theoretical analysis of the coincident wire-powder laser deposition process, *Journal of Manufacturing Science and Engineering, Transactions of the ASME*, **129**(6), p. 1019-1027.

Pires, I., Quintino, L. and Miranda, R. M. (2007), Analysis of the influence of shielding gas mixtures on the gas metal arc welding metal transfer modes and fume formation rate, *Materials and Design*, **28**(5), p. 1623-1631.

Prask, H. J. and Choi, C. S. (1984), NDE of residual stress in uranium by means of neutron diffraction, *Journal of Nuclear Materials*, **126**(2), p. 124-131.

Praveen, P., Yarlagadda, P. K. D. V. and Kang, M. J. (2005), Advancements in pulse gas metal arc welding, *Journal of Materials Processing Technology*, **164-165**, p. 1113-1119.

Price, J. W. H., Ziara-Paradowska, A., Joshi, S., Finlayson, T. *et al.* (2008), Comparison of experimental and theoretical residual stresses in welds: The issue of gauge volume, *International Journal of Mechanical Sciences*, **50**(3), p. 513-521.

Pulnikov, A., Permiakov, V., Petrov, R., Gyselinck, J. *et al.* (2004), Investigation of residual stresses by means of local magnetic measurement, *Journal of Magnetism and Magnetic Materials*, **272-276**(III), p. 2303-2304.

Quintino, L. and Allum, C. J. (1984), Pulsed GMAW: interactions between process parameters - Part 2, *Welding and Metal Fabrication*, **52**(3), p. 126-129.

Raja, V., Zhang, S., Garside, J., Ryall, C. *et al.* (2006), Rapid and cost-effective manufacturing of high-integrity aerospace components, *International Journal of Advanced Manufacturing Technology*, **27**(7-8), p. 759-773.

Rajasekaran, S. (1999), Weld bead characteristics in pulsed GMA welding of Al-Mg alloys, *Welding Journal (Miami, Fla)*, **78**(12), p. 397s-407s.

Rangaswamy, P., Griffith, M. L., Prime, M. B., Holden, T. M. *et al.* (2005), Residual stresses in LENS® components using neutron diffraction and contour method*, Materials Science and Engineering A*, **399**(1-2), p. 72-83.

Rao, K. P., Angamuthu, K. and Srinivasan, P. B. (2008), Fracture toughness of electron beam welded Ti6Al4V*, Journal of Materials Processing Technology*, **199**(1), p. 185-192.

Raveendra, J. and Parmar, R. S. (1987), Mathematical models to predict weld bead geometry for flux cored arc welding*, Metal Construction*, **19**(1), p. 31r-35r.

Ribeiro, A. F. (1995), Automated off-line programming for rapid prototyping using gas metal arc welding (unpublished PhD thesis), School of Industrial and Manufacturing Science (SIMS), Welding Engineering Research Centre (WERC), Cranfield University, Cranfield, UK.

Ribeiro, A. F. and Norrish, J. (1996a), Metal based rapid prototyping for more complex shapes, in: *Proceedings of the 6th International Conference in Computer Technology in Welding*, Abington Publishing UK. , Vol.Paper 60, 9-12 June 1996, Lanaken, Belgium.

Ribeiro, A. F. and Norrish, J. (1996b), Rapid prototyping process using metal directly, in: *Proccedings of the 7th Annual International Solid Freeform Fabrication Symposium*, August 12-14, The University of Texas at Austin, Austin, Texas, USA, p. 249-256.

Ribeiro, A. F., Norrish, J. and McMaster, R. S. (1994), Practical case of rapid prototyping using gas metal arc welding, in: *Fifth International Conference on "Computer Technology in Welding"*, The Welding Institute, printed by Cramptons Printers, 15-16th June, Paris, France, paper 55, p. 1-6.

Ribeiro, A. F., Ogunbiyi, B. and Norrish, J. (1997), Mathematical model of welding parameters for rapid prototyping using robot welding*, Science and Technology of Welding and Joining*, **2**(5), p. 185-190.

Ribeiro, F. (1998), 3D printing with metals*, Computing and Control Engineering Journal*, **9**(1), p. 31-38.

Rogante, M. (2000), Stress-free reference sample: The problem of the determination of the interplanar distance d0*, Physica B: Condensed Matter*, **276-278**, p. 202-203.

Rutter, J. W. and Chalmers, B. (1953), A prismatic substructure formed during solidification of metals*, Canadian Journal of Physics*, **31**(1), p. 15-39.

Salminen, A. S., Kujanpää, V. P. and Moisio, T. J. I. (1996), Interactions between laser beam and filler metals*, Welding Journal (Miami, Fla)*, **75**(1), p. 9s-13s.

Salter, G. R. and Doherty, J. (1981), Procedure selection for arc welding*, Metal Construction*, **13**(9), p. 544-550.

Salter, G. R. and Scott, M. H. (1967), The pulsed inert gas metal-arc welding 1 in. thick titanium 721 alloy*, Welding Journal (Miami, Fla)*, **46**(4), p. 154s-167s.

Santisteban, J. R., Daymond, M. R., James, J. A. and Edwards, L. (2006), ENGIN-X: A third-generation neutron strain scanner*, Journal of Applied Crystallography*, **39**(6), p. 812-825.

Santos, E. C., Shiomi, M., Osakada, K. and Laoui, T. (2006), Rapid manufacturing of metal components by laser forming, *International Journal of Machine Tools and Manufacture*, **46**(12-13), p. 1459-1468.

Schajer, G. S. (1988), Measurement of non-uniform residual stresses using the hole-drilling method. Part I. Stress calculation procedures, *Journal of Engineering Materials and Technology, Transactions of the ASME*, **110**(4), p. 338-343.

Schmidt, J., Dorner, H. and Tenckhoff, E. (1990), Manufacture of complex parts by shape welding, *Journal of Nuclear Materials*, **171**(1), p. 120-127.

Schoch, F.-W. (1984), Properties of large shape-welded items, material tests carried out on a 72 t test piece made from 10MnMoNi55 all-weld metal (Dissertation, Staatl.), Materialprüfungsanstalt Universität Stuttgart, Stuttgart (Vaihingen), Deutschland.

Semwogerere, D. and Weeks, E. R. (2005), Confocal Microscopy, in: Wnek, G. E. and Bowlin, G. L., (editors), *Encyclopedia of Biomaterials and Biomedical Engineering*, Taylor & Francis: Emory University, p. 1-10.

Senkov, O. N. and Froes, F. H. (1999), Thermohydrogen processing of titanium alloys, *International Journal of Hydrogen Energy*, **24**(6), p. 565-576.

Sequeira Almeida, P. M. and Williams, S. (2010a), Innovative process model of Ti–6Al–4V additive layer manufacturing using cold metal transfer (CMT), in: *Proccedings of the 21st Annual International Solid Freeform Fabrication Symposium*, August 9-11, The University of Texas at Austin, Austin, Texas, USA, p. 25-36.

Sequeira Almeida, P. M. and Williams, S. (2010b), Stable Gas Metal Arc Welding (GMAW) of titanium: the effect of Cold Metal Transfer (CMT) dip transfer mode mechanism on grain refinement, *Internal report*, Cranfield University, School of Applied Sciences (SAS), Welding Engineering Research Centre (WERC), Cranfield (unpublished report).

Serrano, G. L. (1999), Direct shape forming of aluminium alloys (unpublished MSc thesis), School of Industrial and Manufacturing Science (SIMS), Welding Engineering Research Centre (WERC), Cranfield University, Cranfield, UK.

Shinn, B. W., Farson, D. F. and Denney, P. E. (2005), Laser stabilisation of arc cathode spots in titanium welding, *Science and Technology of Welding and Joining*, **10**(4), p. 475-481.

Shinoda, T. and Doherty, J. (1978), The relationship between arc welding parameters and weld bead geometry - A literature survey, *The Welding Institute*, Research Report 74/1978/PE, October.

Shockey, H. K., (1932), *Machine for reclaiming worn brake drums*, United States Patent No.1,886,503.

Smati, Z. (1986), Automatic pulsed MIG welding, *Metal Construction*, **18**(1), p. 38R-44R.

Smith, A. A. (1978), Classification of shielding gases used in the gas shielded arc welding of ferrous metals - on the basis of their oxidation potential, *Welding in the World*, **16**(1/2), p. 25.

Song, Y. A., Park, S., Choi, D. and Jee, H. (2005), 3D welding and milling: Part I-a direct approach for freeform fabrication of metallic prototypes, *International Journal of Machine Tools and Manufacture*, **45**(9), p. 1057-1062.

Spencer, J. D. and Dickens, P. M. (1995), Production of metal parts featuring heavy sections using 3D welding, in: *Proceedings of the 1st National Conference on Rapid Prototyping and Tooling Research*, Mechanical Engineering Publications Limited,London and Bury St Edmunds, UK, 6-7th November, Department of Engineering Technology, Buckinghamshire College, UK, p. 127-137.

Spencer, J. D., Dickens, P. M. and Wykes, C. M. (1998), Rapid prototyping of metal parts by three-dimensional welding, *Proceedings of the Institution of Mechanical Engineers, Part B: Journal of Engineering Manufacture*, **212**(3), p. 175-182.

Sreenathbabu, A., Karunakaran, K. P. and Amarnath, C. (2005), Statistical process design for hybrid adaptive layer manufacturing, *Rapid Prototyping Journal*, **11**(4), p. 235-248.

Stark, L. E. (1966), Weldability of Ti-7Al-2Cb-1Ta plate, *Welding Journal*, **45**(2), p. 70s-81s.

Stark, L. E., Bartlo, L. J. and Porter, H. G. (1962), Welding of one-inch thick Ti-6Al-4V plate, *Welding Journal*, **41**(9), p. 805-814.

Starling, C. M. D., Marques, P. V. and Modenesi, P. J. (1995), Statistical modelling of narrow-gap GTA welding with magnetic arc oscillation, *Journal of Materials Processing Technology*, **51**(1-4), p. 37-49.

Stenbacka, N. and Persson, K.-A. (1989), Shielding gases for gas metal arc welding, *Welding Journal*, **68**(11), p. 41-47.

Steuwer, A., Withers, P. J., Santisteban, J. R., Edwards, L. *et al.* (2001), Bragg edge determination for accurate lattice parameter and elastic strain measurement, *Physica Status Solidi (A) Applied Research*, **185**(2), p. 221-230.

Stone, K. H. and Pearce, N. P., Rolls-Royce PLC (2000), *Method and apparatus for building up a workpiece by deposit welding*, European Patent No.1,005,941A2.

Stott, I. A. (1999), Metallurgical characteristics of Ti-6Al-4V and alloy 718 components produced using the direct shape forming process (unpublished MSc thesis), School of Industrial and Manufacturing Science (SIMS), Welding Engineering Research Centre (WERC), Cranfield University, Cranfield, UK.

Suárez, A., Amado, J. M., Tobar, M. J., Yáñez, A. *et al.* (2010), Study of residual stresses generated inside laser cladded plates using FEM and diffraction of synchrotron radiation, *Surface and Coatings Technology*, **204**(12-13), p. 1983-1988.

Subramaniam, S., White, D. R., Jones, J. E. and Lyons, D. W. (1999), Experimental approach to selection of pulsing parameters in pulsed GMAW, *Welding Journal (Miami, Fla)*, **78**(5), p. 166s-172s.

Sundaresan, S., Janaki Ram, G. D. and Madhusudhan Reddy, G. (1999), Microstructural refinement of weld fusion zones in α-β titanium alloys using pulsed current welding, *Materials Science and Engineering A*, **262**(1-2), p. 88-100.

Syan, C. S. and Menon, U. (1994), *Concurrent engineering: concepts, implementation and practice*, Chapman & Hall London.

Syed, W. U. H. and Li, L. (2005), Effects of wire feeding direction and location in multiple layer diode laser direct metal deposition, *Applied Surface Science*, **248**(1-4), p. 518-524.

Syed, W. U. H., Pinkerton, A. J. and Li, L. (2006), Combining wire and coaxial powder feeding in laser direct metal deposition for rapid prototyping, *Applied Surface Science*, **252**(13), p. 4803-4808.

Syed, W. U. H., Pinkerton, A. J. and Li, L. (2005), A comparative study of wire feeding and powder feeding in direct diode laser deposition for rapid prototyping, *Applied Surface Science*, **247**(1-4), p. 268-276.

Taminger, K. M. and Hafley, R. A. (2003), Electron beam freeform fabrication: A rapid metal deposition in: *Proceedings of the 3rd Annual Automotive Composites Conference (Society of Plastic Engineers SPE)*, September 9-10th, Troy, MI, USA, p. 1-6.

Taminger, K. M., Hafley, R. A. and Domack, M. S. (2006), Electron beam freeform fabrication for cost effective near-net shape manufacturing, in: *NATO/RTO AVT-139 Specialists' Meeting on Cost-Effective Manufacture via Net Shape Processing (NATO unclassified)*, 15th May Amsterdam, Netherlands., p. 10.

Tamirisakandala, S., Bhat, R. B., Tiley, J. S. and Miracle, D. B. (2005), Grain refinement of cast titanium alloys via trace boron addition, *Scripta Materialia*, **53**(12), p. 1421-1426.

Thorn, K., Feenstra, M., Young, J. C., Lawson, W. H. S. *et al.* (1982), The interaction of process variables - Their influence on weld dimensions in GMA welds on steel plate, *Metal Construction*, **14**(3), p. 128-133.

Tiller, W. A., Jackson, K. A., Rutter, J. W. and Chalmers, B. (1953), The redistribution of solute atoms during the solidification of metals, *Acta Metallurgica*, **1**, p. 428-437.

Tsao, K. C. and Wu, C. S. (1988), Fluid flow and heat transfer in GMA weld pools, *Welding Journal (Miami, Fla)*, **67**(3), p. 70s-75s.

Tsui, Y. C. and Clyne, T. W. (1997), An analytical model for predicting residual stresses in progressively deposited coatings: Part 1: Planar geometry, *Thin Solid Films*, **306**(1), p. 23-33.

Ujiie, A., Mitsubishi Jukogyo Kabushik Kaisha (Chiyoda-Ku, Tokyo, Japan) (1971), *Method of and apparatus for constructing substantially circular cross section vessel by welding*, United States Patent No.3,558,846.

Ujiie, A., Mitsubishi Jukogyo Kabushiki Kaisha (Tokyo, Japan) (1972), *Method of constructing substantially circular cross-section vessel by welding*, United States Patent No.3,665,143.

Vander Voort, G. F. (1991), *Atlas of time-temperature diagrams for irons and steels*, ASM International, Materials Park, Ohio.

Vasinonta, A., Beuth, J. L. and Griffith, M. L. (2001), A process map for consistent build conditions in the solid freeform fabrication of thin-walled structures, *Journal of Manufacturing Science and Engineering, Transactions of the ASME*, **123**(4), p. 615-622.

Vernyi, B. (2007), Welding equipment manufacturers provide free software upgrades, *Welding Design and Fabrication*, **80**(3), p. 32.

Vilar, R. (1999), Laser cladding, *Journal of Laser Applications*, **11**(2), p. 64-79.

Vivès, C. (1996a), Effects of forced electromagnetic vibrations during the solidification of aluminum alloys: Part I. Solidification in the presence of crossed alternating electric fields and stationary magnetic fields, *Metallurgical and Materials Transactions B: Process Metallurgy and Materials Processing Science*, **27**(3), p. 445-455.

Vivès, C. (1996b), Effects of forced electromagnetic vibrations during the solidification of aluminum alloys: Part II. Solidification in the presence of colinear variable and stationary magnetic fields, *Metallurgical and Materials Transactions B: Process Metallurgy and Materials Processing Science*, **27**(3), p. 457-464.

Wang, F., Mei, J., Jiang, H. and Wu, X. (2007), Laser fabrication of Ti6Al4V/TiC composites using simultaneous powder and wire feed, *Materials Science and Engineering A*, **445-446**, p. 461-466.

Wang, F., Williams, S. and Rush, M. (2011), Morphology investigation on direct current pulsed gas tungsten arc welded additive layer manufactured Ti6Al4V alloy, *International Journal of Advanced Manufacturing Technology*, **57**(5-8), p. 597-603.

Wang, H. and Kovacevic, R. (2001), Rapid prototyping based on variable polarity gas tungsten arc welding for a 5356 aluminium alloy, *Proceedings of the Institution of Mechanical Engineers, Part B: Journal of Engineering Manufacture*, **215**(11), p. 1519-1527.

Wang, L., Felicelli, S. D. and Pratt, P. (2008), Residual stresses in LENS-deposited AISI 410 stainless steel plates, *Materials Science and Engineering A*, **496**(1-2), p. 234-241.

Wang, Y. and Tsai, H. L. (2001), Impingement of filler droplets and weld pool dynamics during gas metal arc welding process, *International Journal of Heat and Mass Transfer*, **44**(11), p. 2067-2080.

Weber, C. M. and Dingman, B. M. (1988), Robotic manufacture of near net shape components by the shape melting process, in: *9th International Conference on Vacuum Matallurgy; Special Melting and Processing Technologies* American Vacuum Society, April 1988, San Diego, California, US, p. 801-821.

Webster, G. A. and Ezeilo, A. N. (2001), Residual stress distributions and their influence on fatigue lifetimes, *International Journal of Fatigue*, **23**(SUPPL. 1), p. S375-S383.

Weisberg, S. (2005), *Applied linear regression*. 3rd ed., Wiley, Hoboken, New Jersey.

Wells, A. A. (1952), Heat flow in welding, *Welding Journal*, **32**(5), p. 263s-267s.

Welsch, G., Boyer, R. R. and Collings, E. W. (1994), *Materials Properties Handbook:Titanium alloys*, ASM International, Materials Park, Ohio.

Whitcomb, P. J. and Anderson, M. J., Problems Analyzing Historical Data), available from: http://www.statease.com/webinars/analyzing_historical_data_webinar.pdf (accessed 02 October 2009).

White, W. D., (1964), *Pressure roller and method of manufacture*, United States Patent No.3,156,968

Williams, J. C. and Starke Jr, E. A. (2003), Progress in structural materials for aerospace systems, *Acta Materialia*, **51**(19), p. 5775-5799.

Winder, J. and Bibb, R. (2005), Medical rapid prototyping technologies: State of the art and current limitations for application in oral and maxillofacial surgery, *Journal of Oral and Maxillofacial Surgery*, **63**(7), p. 1006-1015.

Withers, P. J. (2007), Mapping residual and internal stress in materials by neutron diffraction, *Comptes Rendus Physique*, **8**(7-8), p. 806-820.

Withers, P. J. and Bhadeshia, H. K. D. H. (2001), Residual stress part 1 - Measurement techniques, *Materials Science and Technology*, **17**(4), p. 355-365.

Withers, P. J., Preuss, M., Steuwer, A. and Pang, J. W. L. (2007), Methods for obtaining the strain-free lattice parameter when using diffraction to determine residual stress, *Journal of Applied Crystallography*, **40**(5), p. 891-904.

Wolfe, R. J., Nagler, H., Crisci, J. R. and Frank, A. L. (1965), Out-of-chamber welding of Ti-7Al-2Cb-1Ta alloy titanium plate, *Welding Journal*, **44**(10), p. 443s-456s.

Wood, D., Additive layer manufacturing at AIRBUS - Reality check or view into the future? (2009), *Time compression technologies (TCT)*, UK, March.

Wu, X., Liang, J., Mei, J., Mitchell, C. *et al.* (2004), Microstructures of laser-deposited Ti-6Al-4V, *Materials and Design*, **25**(2), p. 137-144.

Xiong, X., Zhang, H. and Wang, G. (2009), Metal direct prototyping by using hybrid plasma deposition and milling, *Journal of Materials Processing Technology*, **209**(1), p. 124-130.

Yan, X. and Gu, P. (1996), A review of rapid prototyping technologies and systems, *CAD Computer Aided Design*, **28**(4), p. 307-318.

Yang, L. J., Bibby, M. J. and Chandel, R. S. (1993a), Linear regression equations for modelling the submerged-arc welding process, *Journal of Materials Processing Tech.*, **39**(1-2), p. 33-42.

Yang, L. J., Chandel, R. S. and Bibby, M. J. (1993b), The effects of process variables on the weld deposit area of submerged arc welds, *Welding Journal*, **72**(1), p. 11s-18s.

Yang, S., Leong, K. F., Du, Z. and Chua, C. K. (2002), The design of scaffolds for use in tissue engineering. Part II. Rapid prototyping techniques, *Tissue Engineering*, **8**(1), p. 1-11.

Yeong, W. Y., Chua, C. K., Leong, K. F. and Chandrasekaran, M. (2004), Rapid prototyping in tissue engineering: Challenges and potential, *Trends in Biotechnology*, **22**(12), p. 643-652.

Zhang, K., Liu, W. and Shang, X. (2007), Research on the processing experiments of laser metal deposition shaping, *Optics and Laser Technology*, **39**(3), p. 549-557.

Zhang, Y., Chen, Y., Li, P. and Male, A. T. (2003), Weld deposition-based rapid prototyping: A preliminary study*, Journal of Materials Processing Technology*, **135**(2-3 SPEC.), p. 347-357.

Zhang, Y. M. and Li, P. J. (2001), Modified active control of metal transfer and pulsed GMAW of titanium*, Welding Journal (Miami, Fla)*, **80**(2), p. 54S-61S.

Zhao, H., Zhang, G., Yin, Z. and Wu, L. (2011), A 3D dynamic analysis of thermal behavior during single-pass multi-layer weld-based rapid prototyping*, Journal of Materials Processing Technology*, **211**(3), p. 488-495.

Zhao, H., Zhang, G., Yin, Z. and Wu, L. (2012), Three-dimensional finite element analysis of thermal stress in single-pass multi-layer weld-based rapid prototyping*, Journal of Materials Processing Technology*, **212**(1), p. 276-285.

Zhou, W. and Chew, K. G. (2003), Effect of welding on impact toughness of butt-joints in a titanium alloy*, Materials Science and Engineering A*, **347**(1-2), p. 180-185.

Appendices

Appendix A – Calibration curves

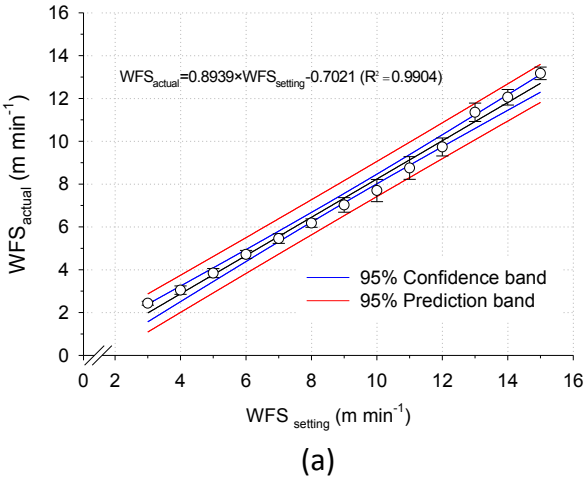

(a)

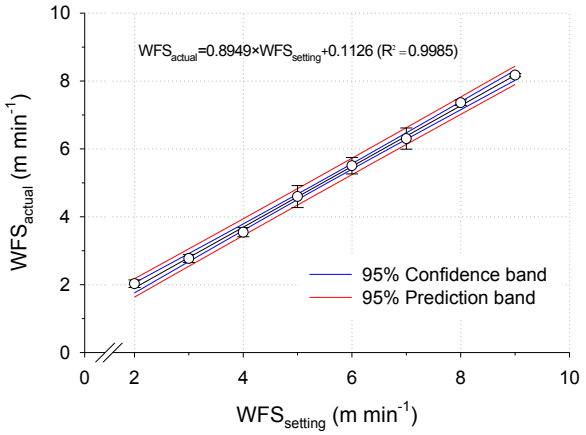

(b)

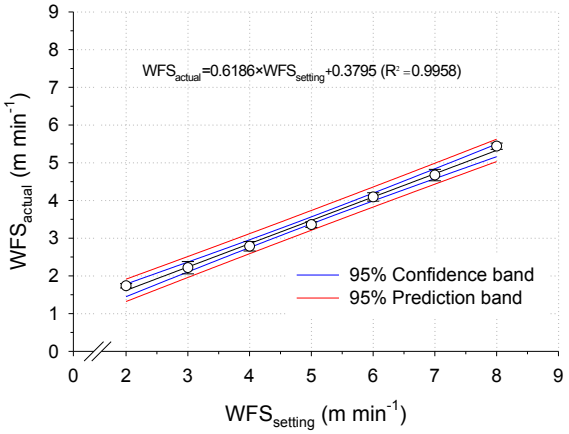

(c)

Figure A 1. CMT calibration curves showing the dependence of the WFS_{actual} on the $WFS_{setting}$ for distinct mild steel wire diameters: (a) 0.8 mm, (b) 1.0 mm and (c) 1.2 mm (95% CI).

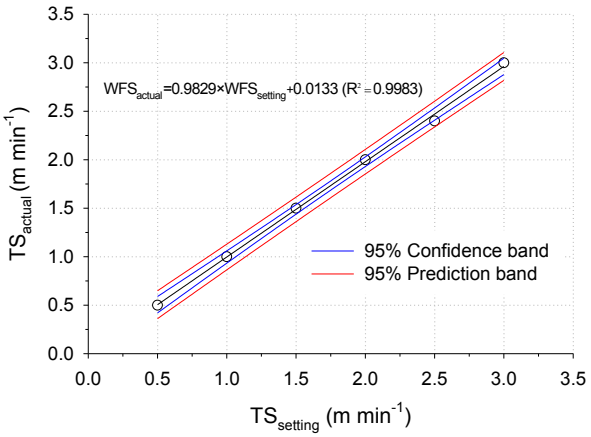

Figure A 2. Calibration curve for the 5 axis *Trio Motion* system.

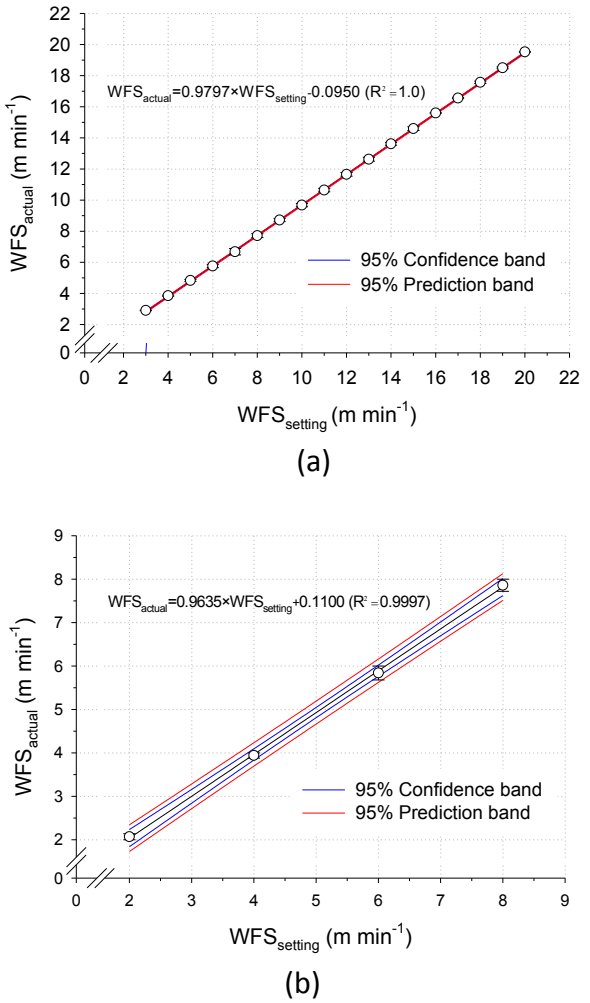

Figure A 3. GMAW-P (Lincoln Power Wave® 455/STT) calibration curves showing the relationship between the WFS_{actual} on the $WFS_{setting}$ for distinct mild steel wire diameters: (a) 0.8 mm, and (b) 1.2 mm (for a 95% CI).

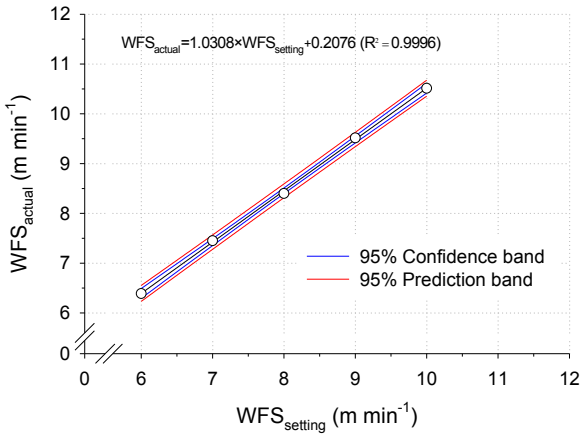

Figure A 4. GMAW-P (Lincoln Power Wave® F355i) calibration curve showing the relationship between the WFS_{actual} on the $WFS_{setting}$ for a 0.8 mm steel wire diameter.

Appendix B – Current research on MAM technologies

Table B 1. Comprehensive list of the current research activities on AM technologies for the fabrication of metallic parts using powder as material feedstock.

Technique	Variant	Affiliation	Ref.	Year	Obs.
Laser	Laser Melting Deposition (LMD)	Beihang University (China)	[1]	2010	The microstructure of LMD samples of Rene'41 was characterized by optical and scanning electron microscopy and X-ray diffraction.
	Laser Net Shape Manufacturing (LNSM)	General Electric Global Research Center (US)	[2]	2010	A geometry-based adaptive toolpath laser powder deposition method was developed for the manufacture and repair of turbine engine compressor or blisk airfoils. The toolpath was designed with predetermined bead width, stable layer height, and bead overlap ratios.
	Direct Metal Deposition (DMD)	University of Michigan	[3-9]	2000,2009,2000, 2007	A closed loop control system is described. Part dimension, cooling rate, microstructure and properties are assessed. The structure and properties of the multilayer deposits were investigated using optical and scanning electron microscopy, X-ray diffraction and microhardness test. Environmental impact of DMD is discussed.
	Laser Powder Deposition (LPD)	Instituto Superior Técnico	[10] [11]	2005,2010	Process optimisation by FEA is presented and the microstructure and properties of the final part analysed. A model coupling finite element heat transfer calculations, phase transformation kinetics and microstructure-property relations in Ti64 is presented and processing maps relating the deposition parameters to the microstructure and therefore properties of the parts.
	Laser Engineered Net Shaping (LENS®)	Sandia National Laboratories	[12] [13]	2007, 2005	Thermomechanical models are presented. This are able to predict residual stresses and melt pool size in order to optimize the manufacturing strategy; Two residual stresses methods have been employed are compared.
	Laser Powder Micro Deposition (LPmD)	General Research Institute for Non-ferrous Metals	[14]	2010	Composition gradient thin walls manufactured from Ti to Ti-60 at. % Cr were prepared utilizing this process.
	Laser Rapid Manufacturing (LRM)	Raja Ramanna Centre for Advanced Technology (India)	[15-17]	2006,2007,2010	A new RM technique is described (LRM) for the manufacture of exotic Inconel alloys (*e.g.* Inconel 625).
	Selective Laser Melting (SLM)	Loughborough University, Department of Metallurgy and Materials Engineering, Leuven, Belgium	[18-20]	2008,2010	Waspaloy® specimens were manufactured utilising SLM. A high power pulsed Nd:YAG laser was used and laser parameters such as pulse energy (J), pulse width (ms), repetition rate (Hz) and scan speed (mm/min) were varied; The microstructure of the Ti-6Al-4V alloy processed by SLM and the influence of the scanning parameters and scanning strategy on this microstructure are studied by light optical microscopy.

Electron beam+ powder	Electron Beam Melting (EBM)	Arcam AB, Mölndal, Sweden	[21]	2009	The paper demonstrates the EBM capabilities (complex parts, fine network structures, internal cavities and channels) for the manufacture of materials with a high affinity to oxygen, e. g. titanium. Mechanical and chemical properties of EBM built Ti6A14V have shown that the material properties are comparable to wrought Ti6A14V.
	Electron Beam Sintering (EBS)	University of Virginia, Charlottesville	[22]	2010	EBS of ultra-high-temperature ceramic material of zirconium diboride (ZrB2) has been reported in this paper.
Hybrid	Hybrid Plasma Deposition and Milling (HPDM)	Wuhan University of Science and Technology (China)	[23-25]	2009,2008	The process description and initial results (demonstration parts) are reported in this paper. The microstructure is examined as well and the applicability of the HPDM process demonstrated.

Table B 2. Comprehensive list of the current research activities on AM technologies for fabrication of metallic parts using wire material only, and wire + powder material as feedstock.

Technique	Variant	Affiliation	Ref.	Year	Obs.
Arc Welding	3D Welding	The University of Nottingham, University of Kentucky, Academy of Armored Force Engineering, Southern Methodist University	[26] [27]	2003, 2010	Deposition accuracy is investigated by means of a metal transfer control system (size and frequency of the droplets in GMAW).
	Shaped Metal Deposition (SMD)	Rolls-Royce plc, Nottingham University University of Catania (Italy); Katholieke Universiteit Leuven (Belgium); Universidad Politécnica de Cataluña	[28-34]	2005,2008, 2008, 2004,2008, 2010	States important benefits of the SMD technique and relevant economic data; Closed loop SMD controller (GTAW)-RAPOLAC; multi-pass linear weld deposition beads were performed on super alloy 718 and characterized; Al deposition with VP-GTAW; SMD numerical simulation.
	3D Micro-Welding	Osaka University	[35-38]	2009,2008	The welding process parameters such as the waveform characteristics and electrode materials were investigated on superalloys, Ti alloy and Ti-cp.
Electron beam+ wire	Electron Beam Free Form Fabrication (EBF^3)	State University, Blacksburg; NASA Langley Research Center	[39-41]	2010,2009, 2006	The present work deals with optimized placement of stiffened panels with straight and curvilinear stiffeners for desired structural and acoustic response (EBF3); The advantages of wire-fed EBF3 are discussed for large-scale titanium parts manufacture. The vaporization issues of high vapour pressure elements *e.g.* Al are reported as well.
	Electron Beam Direct Manufacturing (EBDM)	Lockheed Martin Aeronautics Company (US)	[42]	2010	The paper demonstrates that EBDM processing substantially increases the solubility of Sc in α(Al) and the hardening effect is about twice that attained from solid solution and ageing (Scandium is a light but highly potent hardening element for Al).
Laser wire+ powder	Direct Laser Deposition (DLD)	Laser Processing Research Centre, University of Manchester	[43-48]	2005,2006	Process characteristics, advantages and disadvantages are assessed. Surface finish, microstructure and deposition efficiency.

	Direct Laser Fabrication (DLF)	The University of Birmingham	[49]	2007	The volume fraction of TiC has been varied throughout the build-up process and the resultant microstructure analysed by SEM and TEM.
Laser wire	Direct Metal Deposition (DLD)	Laser Processing Research Centre, University of Manchester, University of Nottingham	[50] [51]	2005,2008	The effect of wire feeding direction, angle and laser location is investigated in single and multi-layered parts; A study of multilayer deposition of Waspaloy is presented using a high power diode laser.
	Robotized Laser Metal-wire Deposition (RLMwD)	University West (Sweden), University of Nottingham	[52] [53]	2010,2009	A monitoring system, comprising two cameras and a projected laser line, is developed for on-line control of the deposition process. The controller combines of a PI-controller (bead width) and a feed-forward compensator (bead height).
	Laser Additive Manufacture (LAM)	Welding Engineering Research Centre, Cranfield University	[54]	2008	The feasibility of the process was demonstrated. The relative position between the wire and the substrate and the laser beam to wire width ratio was investigated.
	Laser Additive Layer Manufacturing (LALM)	EADS	[55-57]	2009,2008	The advantages of the wire feedstock (low impurity levels, compositional tolerances, and high deposition rate) are highlight. Microstructure, mechanical properties and chemical analysis results are shown as well.
Hybrid	Arc Hybrid Layered Manufacturing (ArcHLM)	Indian Institute of Technology Bombay	[58] [59]	2010,2006	A low cost CNC + arc welding unit retrofitment is described; A slicing routine is described for dies manufacture (GMAW).
	3D Welding + milling	Korea Institute of Science and Technology	[60] [61]	2005	Net shape components (geometrical accuracy and surface finish tackled); Optimisation described using a statistical approach (GMAW).
	Hybrid welding/ milling based rapid prototyping	University of Engineering and Technology (Pakistan)	[62]	2009	Material properties comparison is made between weld based prototype parts, produced both with and without intermediate machining after each deposited layer (GMAW).

1. Li, J. and H.M. Wang, *Microstructure and mechanical properties of rapid directionally solidified Ni-base superalloy Rene'41 by laser melting deposition manufacturing.* Materials Science and Engineering A, 2010. **527**(18-19): p. 4823-4829.
2. Qi, H., M. Azer, and P. Singh, *Adaptive toolpath deposition method for laser net shape manufacturing and repair of turbine compressor airfoils.* International Journal of Advanced Manufacturing Technology, 2010. **48**(1-4): p. 121-131.
3. Mazumder, J., et al., *Closed loop direct metal deposition: Art to Part.* Optics and Lasers in Engineering, 2000. **34**(4-6): p. 397-414.
4. Dinda, G.P., A.K. Dasgupta, and J. Mazumder, *Laser aided direct metal deposition of Inconel 625 superalloy: Microstructural evolution and thermal stability.* Materials Science and Engineering A, 2009. **509**(1-2): p. 98-104.
5. He, X., G. Yu, and J. Mazumder, *Temperature and composition profile during double-track laser cladding of H13 tool steel.* Journal of Physics D: Applied Physics, 2010. **43**(1).
6. Morrow, W.R., et al., *Environmental aspects of laser-based and conventional tool and die manufacturing.* Journal of Cleaner Production, 2007. **15**(10): p. 932-943.
7. He, X. and J. Mazumder, *Transport phenomena during direct metal deposition.* Journal of Applied Physics, 2007. **101**(5).

8. Mazumder, J., A. Schifferer, and J. Choi, *Direct materials deposition: Designed macro and microstructure.* Materials Research Innovations, 1999. **3**(3): p. 118-131.

9. Mazumder, J., et al., *The direct metal deposition of H13 tool steel for 3-D components.* JOM, 1997. **49**(5): p. 55-60.

10. Costa, L., et al., *Rapid tooling by laser powder deposition: Process simulation using finite element analysis.* Acta Materialia, 2005. **53**(14): p. 3987-3999.

11. Crespo, A. and R. Vilar, *Finite element analysis of the rapid manufacturing of Ti-6Al-4V parts by laser powder deposition.* Scripta Materialia, 2010. **63**(1): p. 140-143.

12. Vasinonta, A., J.L. Beuth, and M. Griffith, *Process maps for predicting residual stress and melt pool size in the laser-based fabrication of thin-walled structures.* Journal of Manufacturing Science and Engineering, Transactions of the ASME, 2007. **129**(1): p. 101-109.

13. Rangaswamy, P., et al., *Residual stresses in LENSÂ® components using neutron diffraction and contour method.* Materials Science and Engineering A, 2005. **399**(1-2): p. 72-83.

14. Zhang, Y.Z., C. Meacock, and R. Vilar, *Laser powder micro-deposition of compositional gradient Ti-Cr alloy.* Materials and Design, 2010. **31**(8): p. 3891-3895.

15. Paul, C.P., et al., *Laser rapid manufacturing of Colmonoy-6 components.* Optics and Lasers in Engineering, 2006. **44**(10): p. 1096-1109.

16. Paul, C.P., et al., *Investigating laser rapid manufacturing for Inconel-625 components.* Optics and Laser Technology, 2007. **39**(4): p. 800-805.

17. Ganesh, P., et al., *Fatigue and fracture toughness characteristics of laser rapid manufactured Inconel 625 structures.* Materials Science and Engineering A, 2010.

18. Mumtaz, K.A., P. Erasenthiran, and N. Hopkinson, *High density selective laser melting of Waspaloy^{Â®}*. Journal of Materials Processing Technology, 2008. **195**(1-3): p. 77-87.

19. Khan, M. and P. Dickens, *Selective Laser Melting (SLM) of pure gold.* Gold Bulletin, 2010. **43**(2): p. 114-121.

20. Thijs, L., et al., *A study of the microstructural evolution during selective laser melting of Ti-6Al-4V.* Acta Materialia, 2010. **58**(9): p. 3303-3312.

21. Svensson, M. and U. Ackelid. *Titanium alloys manufactured with electron beam melting mechanical and chemical properties*. in *Medical Device Materials V - Proceedings of the Materials and Processes for Medical Devices Conference*. 2009. Minneapolis, MN.

22. Sun, C.N., M.C. Gupta, and K.M.B. Taminger, *Electron beam sintering of zirconium diboride.* Journal of the American Ceramic Society, 2010. **93**(9): p. 2484-2486.

23. Xiong, X., H. Zhang, and G. Wang, *Metal direct prototyping by using hybrid plasma deposition and milling.* Journal of Materials Processing Technology, 2009. **209**(1): p. 124-130.

24. Xiong, X., *A new method of direct metal prototyping: Hybrid plasma deposition and milling.* Rapid Prototyping Journal, 2008. **14**(1): p. 53-56.

25. Qian, Y.P., J.H. Huang, and H.O. Zhang, *Study on the factors influencing the layer precision in hybrid plasma-laser deposition manufacturing*, in *Advanced Materials Research*. 2010: Zhuhai. p. 3828-3831.

26. Zhang, Y., et al., *Weld deposition-based rapid prototyping: A preliminary study.* Journal of Materials Processing Technology, 2003. **135**(2-3 SPEC.): p. 347-357.

27. Jandric, Z., M. Labudovic, and R. Kovacevic, *Effect of heat sink on microstructure of three-dimensional parts built by welding-based deposition.* International Journal of Machine Tools and Manufacture, 2004. **44**(7-8): p. 785-796.

28. Brian, R., *Assembly in aerospace features at IEE seminar.* Assembly Automation, 2005. **25**(2): p. 108-111.

29. Muscato, G., G. Spampinato, and L. Cantelli. *A closed loop welding controller for a rapid manufacturing process*. in *IEEE Symposium on Emerging Technologies and Factory Automation, ETFA*. 2008. Hamburg.

30. Clark, D., M.R. Bache, and M.T. Whittaker, *Shaped metal deposition of a nickel alloy for aero engine applications.* Journal of Materials Processing Technology, 2008. **203**(1-3): p. 439-448.

31. Baufeld, B., O.V.D. Biest, and R. Gault, *Additive manufacturing of Ti-6Al-4V components by shaped metal deposition: Microstructure and mechanical properties.* Materials and Design, 2010. **31**(SUPPL. 1).

32. Wang, H., et al., *Rapid prototyping of 4043 Al-alloy parts by VP-GTAW.* Journal of Materials Processing Technology, 2004. **148**(1): p. 93-102.

33. Fachinotti, V. and A. Cardona, *Computational simulation of shaped metal deposition*, in *XVII Congreso sobre Metodos Numericos y sus Aplicaciones ENIEF 2008*, M.C. Asociación Argentina de Mecánica Computacional, Editor. 2008: San Luis, Argentina, 10-13 Noviembre. p. 1531-1543.

34. Chiumenti, M., et al., *Finite element modeling of multi-pass welding and shaped metal deposition processes.* Computer Methods in Applied Mechanics and Engineering. **199**(37-40): p. 2343-2359.

35. Horii, T., S. Kirihara, and Y. Miyamoto, *Freeform fabrication of superalloy objects by 3D micro welding.* Materials and Design, 2009. **30**(4): p. 1093-1097.

36. Horii, T., S. Kirihara, and Y. Miyamoto, *Freeform fabrication of Ti-Al alloys by 3D micro-welding.* Intermetallics, 2008. **16**(11-12): p. 1245-1249.

37. Katou, M., et al., *Freeform fabrication of titanium metal and intermetallic alloys by three-dimensional micro welding.* Materials and Design, 2007. **28**(7): p. 2093-2098.

38. Terakubo, M., et al., *Freeform fabrication of titanium metal by 3D micro welding.* Materials Science and Engineering A, 2005. **402**(1-2): p. 84-91.

39. Joshi, P., et al., *Design optimization for minimum sound radiation from point-excited curvilinearly stiffened panel.* Journal of Aircraft, 2010. **47**(4): p. 1100-1110.

40. Brice, C.A., et al., *Chemistry control in electron beam deposited titanium alloys*, in *Materials Science Forum*. 2009: Gold Coast, QLD. p. 155-158.

41. Domack, M.S., K.M.B. Taminger, and M. Begley, *Metallurgical mechanisms controlling mechanical properties of aluminum alloy 2219 produced by electron beam freeform fabrication*, in *Materials Science Forum*. 2006: Vancouver. p. 1291-1296.

42. Tomus, D., et al., *Electron beam processing of Al-2Sc alloy for enhanced precipitation hardening.* Scripta Materialia, 2010. **63**(2): p. 151-154.

43. Syed, W.U.H., A.J. Pinkerton, and L. Li, *A comparative study of wire feeding and powder feeding in direct diode laser deposition for rapid prototyping.* Applied Surface Science, 2005. **247**(1-4): p. 268-276.

44. Syed, W.U.H., A.J. Pinkerton, and L. Li, *Combining wire and coaxial powder feeding in laser direct metal deposition for rapid prototyping.* Applied Surface Science, 2006. **252**(13 SPEC. ISS.): p. 4803-4808.

45. Syed, W.U.H., A.J. Pinkerton, and N. Li, *Simultaneous wire- and powder-feed direct metal deposition: An investigation of the process characteristics and comparison with single-feed methods.* Journal of Laser Applications, 2006. **18**(1): p. 65-72.

46. Pinkerton, A.J., W.U.H. Syed, and L. Li, *Theoretical analysis of the coincident wire-powder laser deposition process.* Journal of Manufacturing Science and Engineering, Transactions of the ASME, 2007. **129**(6): p. 1019-1027.

47. Syed, W.U.H., et al., *Single-step laser deposition of functionally graded coating by dual 'wire-powder' or 'powder-powder' feeding-A comparative study.* Applied Surface Science, 2007. **253**(19): p. 7926-7931.

48. Syed, W.U.H., et al., *Coincident wire and powder deposition by laser to form compositionally graded material.* Surface and Coatings Technology, 2007. **201**(16-17): p. 7083-7091.

49. Wang, F., et al., *Laser fabrication of Ti6Al4V/TiC composites using simultaneous powder and wire feed.* Materials Science and Engineering A, 2007. **445-446**: p. 461-466.

50. Syed, W.U.H. and L. Li, *Effects of wire feeding direction and location in multiple layer diode laser direct metal deposition.* Applied Surface Science, 2005. **248**(1-4): p. 518-524.

51. Hussein, N.I.S., et al., *Microstructure formation in Waspaloy multilayer builds following direct metal deposition with laser and wire.* Materials Science and Engineering A, 2008. **497**(1-2): p. 260-269.

52. Heralić, A., et al., *Increased stability in laser metal wire deposition through feedback from optical measurements.* Optics and Lasers in Engineering, 2010. **48**(4): p. 478-485.

53. Medrano, A., et al. *Fibre laser metal deposition with wire: Parameters study and temperature monitoring system*. in *Proceedings of SPIE - The International Society for Optical Engineering*. 2009. Lisboa.

54. Miranda, R.M., et al., *Rapid prototyping with high power fiber lasers.* Materials and Design, 2008. **29**(10): p. 2072-2075.

55. Brandl, E., et al., *Deposition of Ti-6Al-4V using Nd:YAG laser & wire: Microstructure and mechanical properties*, in *NATO AVT-163 Specialists Meeting on Additive Technology For Repair of Military Hardware*. 2009: Bonn.

56. Brandl, E., C. Leyens, and F. Palm, *Mechanical properties of additive manufactured Ti-6Al-4V using wire and powder based processes*, in *Trends in Aerospace Manufacturing, Sheffield (UK), IOP Conference Series: Materials Science and Engineering*. 2009.

57. Brandl, E., et al. *Wire instead of powder? Properties of additive manufactured Ti-6Al-4V for aerospace applications*. in *proceedings of Euro-uRapid*. 2008. R. Meyer, Berlin, Germany, Fraunhofer Allianz.

58. Karunakaran, K.P., et al., *Low cost integration of additive and subtractive processes for hybrid layered manufacturing.* Robotics and Computer-Integrated Manufacturing, 2010.

59. Akula, S. and K.P. Karunakaran, *Hybrid adaptive layer manufacturing: An Intelligent art of direct metal rapid tooling process.* Robotics and Computer-Integrated Manufacturing, 2006. **22**(2): p. 113-123.

60. Song, Y.A., et al., *3D welding and milling: Part I-a direct approach for freeform fabrication of metallic prototypes.* International Journal of Machine Tools and Manufacture, 2005. **45**(9): p. 1057-1062.

61. Song, Y.A., S. Park, and S.W. Chae, *3D welding and milling: Part II - Optimization of the 3D welding process using an experimental design approach.* International Journal of Machine Tools and Manufacture, 2005. **45**(9): p. 1063-1069.

62. Mughal, M.P., R.A. Mufti, and H. Fawad, *The effects of machining on material properties in hybrid welding/ milling based rapid prototyping.* International Journal of Computational Materials Science and Surface Engineering, 2009. **2**(1-2): p. 3-17.

Appendix C – Experimental design for single layer deposits

Table C 1. Statistical design of experiments matrix for single layer deposits using CMT.

Exp. No.	Run	Factors			Responses								
		WD (mm)	WFS_{actual} (m min^{-1})	WFS/TS	W (mm)	H (mm)	RR (%)	P (mm)	D (%)	DR (kg h^{-1})	CA (º)	A_2 (mm^2)	A_1 (mm^2)
1	11	0.8	2.36	7.87	2.52	~~2.00~~	0.06	0.37	5.84	0.6	91.5	~~4.19~~	0.26
2	5	0.8	2.90	7.26	3.1	1.77	0.10	0.35	8.97	0.7	72.6	4.16	0.41
3	78	0.8	4.01	8.01	3.74	1.81	0.15	0.55	12.71	0.9	65.0	4.6	0.67
4	48	0.8	4.80	8.00	4.18	1.69	0.14	0.5	12.36	1.1	56.1	4.61	0.65
5	79	0.8	5.66	8.08	3.99	1.67	0.15	0.49	13.20	1.3	58.5	4.47	0.68
6	47	0.8	6.22	7.77	4.05	1.61	0.18	0.53	15.04	1.5	57.9	4.35	0.77
7	53	0.8	7.35	8.17	4.47	1.62	0.23	0.66	18.57	1.7	52.8	4.78	1.09
8	70	0.8	8.23	8.23	4.39	1.64	0.26	0.72	20.76	1.9	52.3	4.58	1.20
9	55	0.8	9.01	8.19	4.60	~~1.73~~	0.22	0.64	18.04	2.1	52.2	4.77	1.05
10	14	0.8	10.00	8.34	4.83	1.63	0.31	0.77	23.45	2.4	48.8	4.70	1.44
11	38	0.8	11.54	8.88	5.00	1.67	0.35	0.95	25.95	2.7	~~46.2~~	5.08	1.78
12	25	0.8	12.26	8.76	4.95	1.69	0.38	0.84	27.36	2.9	~~49.7~~	4.78	1.80
13	31	0.8	13.29	8.86	4.51	1.73	0.35	0.78	26.13	3.1	~~47.8~~	4.89	1.73
14	27	0.8	2.52	12.60	2.93	2.51	0.05	0.33	5.17	0.6	98.2	~~6.24~~	0.34
15	81	0.8	3.24	12.14	3.47	2.30	0.07	0.4	6.68	0.8	91.7	6.71	0.48
16	6	0.8	3.89	11.67	4.03	2.16	0.10	0.43	8.94	0.9	73.2	6.52	0.64
17	49	0.8	4.52	11.30	4.19	1.98	0.16	0.61	14.10	1.1	66.4	5.97	0.98
18	58	0.8	5.44	11.67	4.57	1.92	0.16	0.62	14.08	1.3	58.7	6.04	0.99
19	29	0.8	6.33	11.87	4.92	1.96	0.18	0.63	15.16	1.5	55.2	6.38	1.14
20	63	0.8	6.97	11.61	4.99	1.89	0.22	0.67	18.00	1.6	56.0	6.24	1.37
21	67	0.8	7.48	11.21	5.02	1.90	0.26	0.77	20.62	1.8	53.1	6.16	1.60
22	7	0.8	9.04	12.32	5.33	1.96	0.29	0.86	22.48	2.1	53.0	6.62	1.92
23	28	0.8	9.89	12.36	5.38	1.94	0.35	0.96	25.79	2.3	51.2	6.59	2.29
24	52	0.8	11.60	13.39	5.73	2.01	0.39	1.13	27.87	2.7	49.8	7.17	2.77
25	59	0.8	12.22	13.09	5.68	1.94	0.38	1.06	27.39	2.9	52.3	6.76	2.55
26	82	0.8	13.35	13.35	5.51	2.06	0.39	1.11	28.13	3.1	50.6	7.05	2.76
27	44	0.8	2.42	16.12	3.48	2.96	0.03	0.27	3.24	0.6	113.2	8.67	0.29
28	18	0.8	2.99	14.97	3.60	2.61	0.06	0.35	5.23	0.7	95.9	~~8.69~~	0.48
29	26	0.8	3.64	14.55	4.39	2.40	0.08	0.46	7.59	0.9	86.0	~~8.89~~	0.73
30	13	0.8	4.82	16.07	4.61	2.38	0.12	0.58	10.33	1.1	72.4	8.68	1.00
31	46	0.8	5.26	15.04	4.84	2.42	0.10	0.48	8.89	1.2	66.0	8.30	0.81
32	40	0.8	5.99	14.97	5.18	2.31	0.16	0.58	13.52	1.4	58.2	8.19	1.28
33	61	0.8	6.76	15.01	5.64	2.22	0.21	0.81	17.16	1.6	56.0	8.45	1.75
34	10	0.8	7.39	14.79	5.72	2.08	0.25	0.93	20.20	1.7	52.0	8.10	2.05
35	72	0.8	8.21	14.93	6.05	2.09	0.26	0.93	20.95	1.9	48.6	8.34	2.21
36	16	0.8	9.31	15.52	6.20	2.14	0.33	1.08	24.82	2.2	48.7	8.48	2.80
37	80	0.8	10.92	16.79	6.43	2.09	0.43	1.42	30.20	2.6	46.3	8.92	3.86
38	2	0.8	11.68	16.69	6.28	2.24	0.37	1.26	27.02	2.7	47.2	9.05	3.35
39	54	0.8	12.88	17.17	6.21	2.36	~~37.09~~	~~1.19~~	~~27.06~~	3.0	44.6	8.95	3.32
40	68	1.0	2.13	10.65	3.95	2.73	0.05	0.35	~~4.73~~	0.8	111.3	8.86	~~0.44~~
41	3	1.0	2.89	9.64	4.55	2.33	0.13	0.64	11.44	1.1	72.8	8.59	1.11
42	62	1.0	3.66	9.15	5.39	2.10	0.21	0.91	17.19	1.3	59.5	8.19	1.70
43	83	1.0	4.79	9.58	5.69	1.99	0.27	1.11	21.23	1.8	56.5	8.09	2.18
44	20	1.0	5.75	9.58	5.83	2.16	0.27	1.13	21.52	2.1	60.6	8.97	2.46
45	60	1.0	6.57	9.39	5.90	1.96	0.35	1.24	26.07	2.4	54.8	8.11	2.86
46	74	1.0	7.41	9.26	5.85	2.01	0.40	1.25	28.40	2.7	54.8	8.12	3.22

47	37	1.0	8.13	9.04	5.64	2.00	0.48	1.40	32.26	3.0	55.4	7.96	3.79
48	41	1.0	2.01	15.11	4.42	3.35	0.04	~~0.30~~	3.83	0.7	113.0	12.29	~~0.49~~
49	45	1.0	2.73	13.65	4.77	2.90	0.10	0.71	8.85	1.0	98.6	11.85	1.15
50	8	1.0	3.55	13.33	5.74	2.52	0.20	1.06	16.44	1.3	76.0	11.54	2.27
51	36	1.0	4.73	14.19	6.74	2.58	0.26	1.39	20.59	1.7	57.2	12.07	3.13
52	69	1.0	5.34	13.34	6.29	2.51	0.28	1.40	21.83	2.0	68.2	11.96	3.34
53	34	1.0	6.32	13.54	7.02	2.36	0.33	1.48	24.72	2.3	56.5	12.15	3.99
54	75	1.0	7.28	13.65	7.14	2.44	0.39	1.59	27.93	2.7	46.0	11.61	4.50
55	32	1.0	8.22	13.70	7.22	2.40	0.48	1.75	32.58	3.0	47.9	11.63	5.62
56	43	1.0	1.93	19.34	5.09	3.62	0.02	~~0.25~~	2.40	0.7	120.3	15.05	~~0.37~~
57	17	1.0	2.69	17.94	5.32	3.40	0.08	0.63	7.34	1.0	97.3	16.03	1.27
58	4	1.0	3.42	17.10	6.16	3.02	0.16	1.08	13.91	1.3	73.0	15.16	2.45
59	12	1.0	4.27	17.06	7.05	3.00	0.22	1.40	18.17	1.6	57.4	15.31	3.40
60	19	1.0	5.43	18.10	6.95	3.10	0.25	1.50	19.91	2.0	59.6	15.89	3.95
61	24	1.0	6.02	17.20	7.28	3.06	0.27	1.57	21.28	2.2	57.1	15.46	4.18
62	51	1.0	7.40	18.50	8.65	2.85	0.35	1.97	25.86	2.7	45.0	16.63	5.80
63	33	1.0	8.17	18.15	8.83	~~2.55~~	0.48	2.13	32.62	3.0	42.8	15.10	7.31
64	84	1.2	1.77	8.85	4.86	2.52	0.11	0.62	10.03	0.9	96.1	10.23	1.14
65	22	1.2	2.37	7.89	5.21	2.56	0.16	0.81	13.73	1.3	72.0	9.80	1.56
66	76	1.2	2.86	7.14	5.95	2.25	0.26	1.07	20.73	1.5	~~51.0~~	8.95	2.34
67	39	1.2	3.31	6.62	5.69	2.18	0.29	1.06	22.43	1.8	54.2	8.30	2.40
68	42	1.2	4.00	6.66	5.42	2.29	0.32	1.22	24.47	2.1	60.8	8.58	2.78
69	23	1.2	4.66	6.66	6.25	2.24	0.32	1.14	24.23	2.5	57.6	8.85	2.83
70	66	1.2	5.50	6.88	6.34	2.15	0.48	1.46	32.51	2.9	52.6	8.76	4.22
71	50	1.2	1.76	13.23	5.42	3.22	0.05	~~0.41~~	5.11	0.9	100.4	15.41	~~0.83~~
72	77	1.2	2.20	11.00	6.02	2.75	0.19	1.05	15.64	1.2	76.6	13.27	2.46
73	30	1.2	2.85	10.67	6.83	2.83	0.22	1.24	17.86	1.5	66.1	14.17	3.08
74	57	1.2	3.34	10.01	6.40	2.75	0.31	1.58	23.40	1.8	66.8	13.42	~~4.10~~
75	9	1.2	4.09	10.22	6.46	2.83	0.28	1.54	22.15	2.2	74.2	13.88	3.95
76	71	1.2	4.54	9.74	6.94	2.65	0.29	1.56	22.62	2.4	60.3	12.9	3.77
77	15	1.2	5.46	10.24	7.71	2.59	0.35	1.81	26.10	2.9	55.8	14.47	5.11
78	64	1.2	1.68	16.78	6.28	3.53	0.03	~~0.37~~	2.96	0.9	132.4	18.00	~~0.55~~
79	73	1.2	2.08	13.88	6.33	3.19	0.12	0.89	10.68	1.1	91.7	17.23	2.06
80	1	1.2	2.66	13.29	7.07	3.04	0.17	1.28	14.71	1.4	81.1	16.99	2.93
81	56	1.2	3.44	13.74	7.14	3.34	0.23	1.58	18.77	1.8	79.0	18.35	4.24
82	21	1.2	4.20	13.98	7.17	3.39	0.26	1.62	20.33	2.2	74.4	17.91	4.57
83	35	1.2	4.81	13.75	7.75	3.02	0.29	1.7	22.34	2.5	62.6	16.76	4.82
84	65	1.2	5.36	13.39	7.85	3.01	0.36	2.08	26.65	2.8	60.8	16.79	6.10

Exp. No., experiment number; *WD,* wire diameter; WFS_{actual}, wire feed speed actual; *WFS*/*TS,* wire feed speed/travel speed ratio; *W*, bead width; *H*, bead height; *RR*, remelting ratio; *P*, penetration; *D*, dilution; *DR*, deposition rate considering the mild steel density of ρ(kg m^{-3})=7800; *CA,* contact angle; A_2, reinforcement area; A_1, penetration area.

Table C 2. Statistical design of experiments matrix for single layer deposition using CMT**.**

Exp. No.	Run	Factors			Responses		
		WD (mm)	WFS_{actual} (m min^{-1})	WFS/TS	AR	HI (J mm^{-1})	HSL (mm)
1	11	0.8	2.36	7.87	0.826	118.10	4.90
2	5	0.8	2.90	7.26	0.571	115.80	5.50
3	78	0.8	4.01	8.01	0.484	127.80	7.20
4	48	0.8	4.80	8.00	0.404	123.70	7.90
5	79	0.8	5.66	8.08	0.419	121.60	9.00
6	47	0.8	6.22	7.77	0.398	120.60	9.30
7	53	0.8	7.35	8.17	0.362	128.00	10.80
8	70	0.8	8.23	8.23	0.374	128.10	11.10
9	55	0.8	9.01	8.19	0.376	126.70	12.50
10	14	0.8	10.00	8.34	0.337	130.10	11.40
11	38	0.8	11.54	8.88	0.334	133.20	14.60
12	25	0.8	12.26	8.76	0.341	129.20	12.30
13	31	0.8	13.29	8.86	0.350	127.70	15.20
14	27	0.8	2.52	12.60	0.988	183.62	4.90
15	81	0.8	3.24	12.14	0.663	178.39	5.50
16	6	0.8	3.89	11.67	0.536	182.24	6.40
17	49	0.8	4.52	11.30	0.473	172.51	7.50
18	58	0.8	5.44	11.67	0.420	175.88	8.10
19	29	0.8	6.33	11.87	0.398	180.43	9.30
20	63	0.8	6.97	11.61	0.379	181.29	10.00
21	67	0.8	7.48	11.21	0.378	179.66	11.90
22	7	0.8	9.04	12.32	0.368	191.22	12.60
23	28	0.8	9.89	12.36	0.361	193.80	13.30
24	52	0.8	11.60	13.39	0.351	202.02	14.80
25	59	0.8	12.22	13.09	0.342	194.38	15.60
26	82	0.8	13.35	13.35	0.374	191.58	16.40
27	44	0.8	2.42	16.12	1.147	239.33	4.90
28	18	0.8	2.99	14.97	0.725	236.04	6.00
29	26	0.8	3.64	14.55	0.547	240.36	6.70
30	13	0.8	4.82	16.07	0.516	245.92	7.30
31	46	0.8	5.26	15.04	0.500	235.66	8.50
32	40	0.8	5.99	14.97	0.446	240.07	10.30
33	61	0.8	6.76	15.01	0.394	253.74	12.10
34	10	0.8	7.39	14.79	0.364	251.81	13.30
35	72	0.8	8.21	14.93	0.345	251.34	14.80
36	16	0.8	9.31	15.52	0.345	~~186.01~~	15.50
37	80	0.8	10.92	16.79	0.325	265.41	16.20
38	2	0.8	11.68	16.69	0.357	257.84	17.20
39	54	0.8	12.88	17.17	0.386	256.13	18.00
40	68	1.0	2.13	10.65	0.815	-	6.00
41	3	1.0	2.89	9.64	0.512	-	7.50
42	62	1.0	3.66	9.15	0.390	-	9.50
43	83	1.0	4.79	9.58	0.350	-	13.30
44	20	1.0	5.75	9.58	0.370	-	15.90
45	60	1.0	6.57	9.39	0.332	-	15.20

46	74	1.0	7.41	9.26	0.344	-	17.30
47	37	1.0	8.13	9.04	0.355	-	19.50
48	41	1.0	2.01	15.11	0.882	353.17	6.00
49	45	1.0	2.73	13.65	0.608	357.53	8.50
50	8	1.0	3.55	13.33	0.439	360.97	10.90
51	36	1.0	4.73	14.19	0.383	378.30	13.00
52	69	1.0	5.34	13.34	0.399	343.87	14.10
53	34	1.0	6.32	13.54	0.336	340.55	14.80
54	75	1.0	7.28	13.65	0.342	364.47	15.40
55	32	1.0	8.22	13.70	0.332	362.95	18.20
56	43	1.0	1.93	19.34	0.931	454.27	5.80
57	17	1.0	2.69	17.94	0.639	471.18	8.60
58	4	1.0	3.42	17.10	0.490	469.26	9.60
59	12	1.0	4.27	17.06	0.426	476.28	13.20
60	19	1.0	5.43	18.10	0.446	459.60	16.60
61	24	1.0	6.02	17.20	0.420	442.58	17.30
62	51	1.0	7.40	18.50	0.329	495.16	18.40
63	33	1.0	8.17	18.15	0.289	479.09	21.70
64	84	1.2	1.77	8.85	0.519	341.71	8.10
65	22	1.2	2.37	7.89	0.491	304.93	10.40
66	76	1.2	2.86	7.14	0.378	289.18	12.30
67	39	1.2	3.31	6.62	0.383	262.73	14.20
68	42	1.2	4.00	6.66	0.423	235.29	14.40
69	23	1.2	4.66	6.66	0.358	239.96	15.80
70	66	1.2	5.50	6.88	0.339	256.20	18.50
71	50	1.2	1.76	13.23	0.594	506.36	8.10
72	77	1.2	2.20	11.00	0.457	454.55	9.90
73	30	1.2	2.85	10.67	0.414	437.72	14.40
74	57	1.2	3.34	10.01	0.430	399.38	15.40
75	9	1.2	4.09	10.22	0.438	364.58	16.00
76	71	1.2	4.54	9.74	0.382	355.60	16.80
77	15	1.2	5.46	10.24	0.336	371.89	18.50
78	64	1.2	1.68	16.78	0.666	635.35	7.80
79	73	1.2	2.08	13.88	0.504	578.12	9.70
80	1	1.2	2.66	13.29	0.430	562.55	13.20
81	56	1.2	3.44	13.74	0.468	531.57	15.30
82	21	1.2	4.20	13.98	0.473	483.23	16.30
83	35	1.2	4.81	13.75	0.390	481.83	17.00
84	65	1.2	5.36	13.39	0.383	480.96	21.60

AR, aspect ratio*; HI,* heat input considering an efficiency of 0.9 for the CMT; *HSL*, heat source length. The contact tip to work distance was held constant during all experiments, CTWD (mm) = 13.

Appendix D – Experimental design for CMT vs. GMAW-P study

Table D 1. Welding conditions and respective bead profiles measurements.

Sample No.	WD (mm)	$WFS_{C/S}$ (m min^{-1})	V (V)	I (A)	Power (W)	HI^a (J $mm)^{-1}$	W (mm)	H (mm)	P (mm)	A_{pm} (mm^2)	A_{reinf} (mm^2)	CA_{avg} (º)	DR_R (kg h^{-1})
CMT 1	0.8	2.5/3.0	9.89	58.9	582	183.6	2.54	2.51	0.33	0.34	6.24	98.2	0.59
CMT 2	0.8	3.9/5.0	11.04	77.3	853	182.2	4.03	2.16	0.43	0.64	6.52	73.2	0.92
CMT 3	0.8	5.5/7.0	11.54	90.7	1046	175.9	4.57	1.92	0.62	0.99	6.04	58.7	1.29
GMAW-P1	0.8	2.9/3.0	20.68	37.0	928	222.7	3.68	2.41	0.53	0.68	7.32	100.2	0.68
GMAW-P2	0.8	4.9/5.0	20.50	56.8	1372	197.5	4.86	2.11	1.02	1.85	7.39	64.6	1.15
GMAW-P3	0.8	6.7/7.0	21.65	76.9	1852	190.5	5.52	1.92	1.20	2.64	7.32	54.6	1.58
CMT 4	1.2	1.77/2.0	11.10	91.2	1012	341.7	4.86	2.52	0.62	1.14	10.23	96.1	0.95
CMT 5	1.2	1.75/2.0	10.93	89.5	977	506.4	5.42	3.22	0.41	0.83	15.41	100.4	0.95
CMT 6	1.2	1.68/2.0	10.47	84.2	882	635.4	5.30	3.53	0.37	0.55	18.00	132.4	0.95
GMAW-P4	1.2	10.7	24.55	324.4	8400	550.1	8.45	3.19	4.99	17.74	17.91	53.3	5.66
GMAW-P5	1.2	12.6	26.83	372.4	10300	570.2	6.93	3.72	6.07	22.31	17.86	63.5	6.67
GMAW-P6	1.2	14.6	27.07	407.3	11274	541.2	5.87	3.65	6.21	22.60	16.40	80.0	7.73
GMAW-P7	1.2	12.5	26.4	375.5	10217	377.2	5.45	3.20	4.31	15.67	12.20	64.3	6.35
GMAW-P8	1.2	12.5	26.83	372.4	10300	570.2	6.93	3.72	6.07	22.31	17.86	63.5	6.35
GMAW-P9	1.2	12.5	27.00	367.8	10244	756.5	9.41	3.74	7.75	29.75	22.86	56.3	6.35

WD, wire diameter; $WFS_{C/S}$, wire feed speed calibrated / wire feed speed setting; *Volt*, voltage; *I*, current; HI^a, heat input considering an efficiency of 0.9 for CMT and 0.8 for GMAW-P; *W*, bead width; *H*, bead height; *P*, penetration; A_{pm}, parent metal cross section area; $A_{reinf,}$ reinforcement cross section area; CA_{avg}, average contact angle; $DR_{R/S}$, obtained deposition rate considering the WFS_{actual}.

Appendix E – Experimental design for multi-layer deposits

Table E 1. Experimental design used for modelling multi-layer welds in steel (4 layers high).

Trial No.	WFS_{set} (m min^{-1})	WFS_{cal} (m min^{-1})	WFS/TS	T (°C)	H_1 (mm)	H_1 CI (95%)	H_2 (mm)	H_2 CI (95%)	H_3 (mm)	H_3 CI (95%)	H_4 (mm)	H_4 CI (95%)
1	4.00	3.46	10	40	2.27	0.02	3.94	0.03	5.42	0.03	6.94	0.08
2	6.00	5.41	10	40	2.14	0.04	3.68	0.07	4.97	0.02	6.45	0.10
3	8.00	7.04	10	40	2.04	0.03	3.47	0.03	4.73	0.02	6.23	0.21
4	6.00	5.12	15	40	2.51	0.02	4.34	0.04	5.83	0.04	7.61	0.01
5	8.00	6.73	15	40	2.25	0.01	3.94	0.06	5.60	0.06	7.22	0.13
6	10.00	8.72	15	40	2.17	0.03	3.74	0.08	5.37	0.11	7.10	0.09
7	4.00	3.13	20	40	3.13	0.02	5.09	0.09	7.11	0.10	9.23	0.12
8	6.00	4.92	20	40	2.75	0.01	4.78	0.03	6.67	0.05	8.64	0.02
9	8.00	6.65	20	40	2.63	0.02	4.57	0.10	6.45	0.10	8.16	0.08
10	4.00	3.35	10	200	2.08	0.03	3.69	0.06	5.07	0.03	6.50	0.03
11	6.00	5.13	10	200	1.96	0.02	3.48	0.01	4.73	0.03	5.95	0.03
12	8.00	6.86	10	200	1.78	0.02	3.36	0.04	4.61	0.01	5.90	0.12
13	6.00	5.07	15	200	2.38	0.03	4.04	0.05	5.51	0.01	7.14	0.03
14	8.00	6.85	15	200	2.30	0.01	4.20	0.09	5.48	0.05	7.19	0.06
15	10.00	8.76	15	200	2.28	0.04	4.11	0.09	5.43	0.03	7.02	0.06
16	4.00	3.17	20	200	2.90	0.03	4.89	0.02	6.82	0.05	8.82	0.02
17	6.00	4.87	20	200	2.76	0.01	4.47	0.07	6.20	0.04	8.18	0.03
18	8.00	6.77	20	200	2.63	0.01	4.42	0.02	6.09	0.09	7.85	0.03
19	4.00	3.36	10	350	1.98	0.02	3.59	0.08	4.85	0.03	6.19	0.03
20	6.00	5.16	10	350	1.91	0.01	3.23	0.05	4.55	0.08	5.77	0.02
21	8.00	7.12	10	350	1.91	0.02	3.21	0.04	4.49	0.10	5.96	0.06
22	6.00	5.17	15	350	2.29	0.02	3.93	0.01	5.36	0.01	6.80	0.02
23	8.00	7.05	15	350	2.25	0.02	3.96	0.06	5.30	0.06	6.82	0.06
24	10.00	8.99	15	350	2.21	0.05	3.79	0.03	5.23	0.04	6.66	0.05
25	4.00	3.34	20	350	2.78	0.06	4.77	0.02	6.73	0.02	8.67	0.03
26	6.00	5.07	20	350	2.61	0.01	4.47	0.09	6.19	0.03	8.02	0.06
27	8.00	7.04	20	350	2.55	0.01	4.25	0.03	5.95	0.04	7.81	0.06

T, temperature; $H_1, H_2, \ldots, H_4$, absolute bead height at the nominal layer one, layer two and so forth; *CI(95%)*, 95% confidence interval.

Table E 2. Experimental design matrix used for modelling SW_{wav}, W_{eff}, and MDE of multi-layer welds in steel utilising a 0.8 mm wire (10 layers high).

Exp. No.	Run	WFS_{set} (m min^{-1})	WFS_{actual} (m min^{-1})	WFS/TS	ΔSW_{av} (µm)	ΔSW_{av} CI (95%)	W_{eff} (mm)	W_{eff} CI (95%)	MDE (%)
1a	39	3.00	1.98	30.00	657.31	45.45	4.26	0.03	84.14
1b	15	3.00	1.98	15.00	214.59	7.33	3.63	0.01	91.69
1c	6	3.00	1.98	10.00	205.40	40.59	2.99	0.02	94.03
1d	42	3.00	1.98	7.50	141.78	10.10	2.63	0.03	94.53
1e	17	3.00	1.98	6.00	101.73	4.76	2.32	0.02	92.89
1f	44	3.00	1.98	5.00	129.49	15.37	2.13	0.03	93.72
1g	-	3.00	1.98	4.29	-	-	-	-	-
1h	-	3.00	1.98	3.75	-	-	-	-	-
1i	-	3.00	1.98	3.33	-	-	-	-	-
1j	-	3.00	1.98	3.00	-	-	-	-	-
2a	20	5.00	3.77	50.00	833.50	41.34	6.55	0.08	90.59
2b	33	5.00	3.77	25.00	287.45	17.82	5.12	0.06	93.68
2c	35	5.00	3.77	16.67	270.67	48.11	4.49	0.05	93.21
2d	10	5.00	3.77	12.50	268.65	33.11	3.80	0.05	91.49
2e	7	5.00	3.77	10.00	250.62	21.88	3.34	0.03	93.01
2f	12	5.00	3.77	8.33	196.50	16.98	3.16	0.04	94.67
2g	22	5.00	3.77	7.14	341.17	22.15	2.58	0.01	88.50
2h	-	5.00	3.77	6.25	-	-	-	-	-
2i	-	5.00	3.77	5.56	-	-	-	-	-
2j	-	5.00	3.77	5.00	-	-	-	-	-
3a	41	7.50	6.00	75.00	797.17	50.48	8.11	0.07	86.49
3b	19	7.50	6.00	37.50	289.11	25.65	6.11	0.12	93.39
3c	2	7.50	6.00	25.00	325.98	60.27	5.22	0.07	90.08
3d	1	7.50	6.00	18.75	267.64	19.53	4.63	0.02	94.20
3e	14	7.50	6.00	15.00	283.46	27.48	4.34	0.09	93.24
3f	38	7.50	6.00	12.50	225.78	13.91	3.66	0.01	93.70
3g	25	7.50	6.00	10.71	255.67	22.42	3.23	0.09	92.67
3h	23	7.50	6.00	9.38	232.35	33.95	2.93	0.03	95.83
3i	-	7.50	6.00	8.33	-	-	-	-	-
3j	-	7.50	6.00	7.50	-	-	-	-	-
4a	30	10.00	8.24	100.00	1602.09	61.16	9.56	0.09	72.51
4b	16	10.00	8.24	50.00	413.94	52.47	7.45	0.08	91.90
4c	5	10.00	8.24	33.33	309.70	24.00	6.21	0.03	91.90
4d	11	10.00	8.24	25.00	315.67	17.88	5.63	0.03	93.49
4e	3	10.00	8.24	20.00	180.66	37.79	5.24	0.06	94.99
4f	46	10.00	8.24	16.67	195.47	16.61	4.52	0.01	93.39
4g	26	10.00	8.24	14.29	178.31	4.88	4.13	0.03	93.25
4h	28	10.00	8.24	12.50	229.09	21.79	3.35	0.01	83.40
4i	-	10.00	8.24	11.11	-	-	-	-	-
4j	-	10.00	8.24	10.00	-	-	-	-	-
5a	43	12.50	10.47	125.00	2300.00	45.98	12.27	0.01	69.38
5b	18	12.50	10.47	62.50	646.29	14.49	9.47	0.01	90.43
5c	32	12.50	10.47	41.67	511.00	10.08	7.36	0.02	90.06
5d	13	12.50	10.47	31.25	431.07	20.59	6.73	0.05	92.63
5e	24	12.50	10.47	25.00	361.36	16.45	5.88	0.04	93.12
5f	8	12.50	10.47	20.83	232.34	5.63	5.22	0.01	87.44

5g	21	12.50	10.47	17.86	206.92	12.02	5.13	0.02	91.61
5h	40	12.50	10.47	15.63	245.65	29.26	4.73	0.04	86.57
5i	-	12.50	10.47	13.89	-	-	-	-	-
5j	-	12.50	10.47	12.50	-	-	-	-	-
6a	9	15.00	12.71	150.00	4300.00	58.56	13.35	0.05	-
6b	37	15.00	12.71	75.00	968.30	24.97	10.07	0.04	86.08
6c	27	15.00	12.71	50.00	740.26	33.51	8.79	0.01	90.56
6d	36	15.00	12.71	37.50	400.42	6.96	7.66	0.03	92.78
6e	31	15.00	12.71	30.00	272.41	17.73	6.65	0.03	92.90
6f	4	15.00	12.71	25.00	564.94	15.10	6.00	0.02	89.31
6g	34	15.00	12.71	21.43	456.65	24.16	5.43	0.07	92.82
6h	45	15.00	12.71	18.75	435.23	29.49	4.72	0.04	86.60
6i	29	15.00	12.71	16.67	517.90	54.11	4.42	0.02	82.59
6j	-	15.00	12.71	15.00	-	-	-	-	-

WFS, wire feed speed; SW_{av}, surface waviness; W_{eff}, effective wall width; *MDE*, metal deposition efficiency.

Appendix F – Trailing shielding device

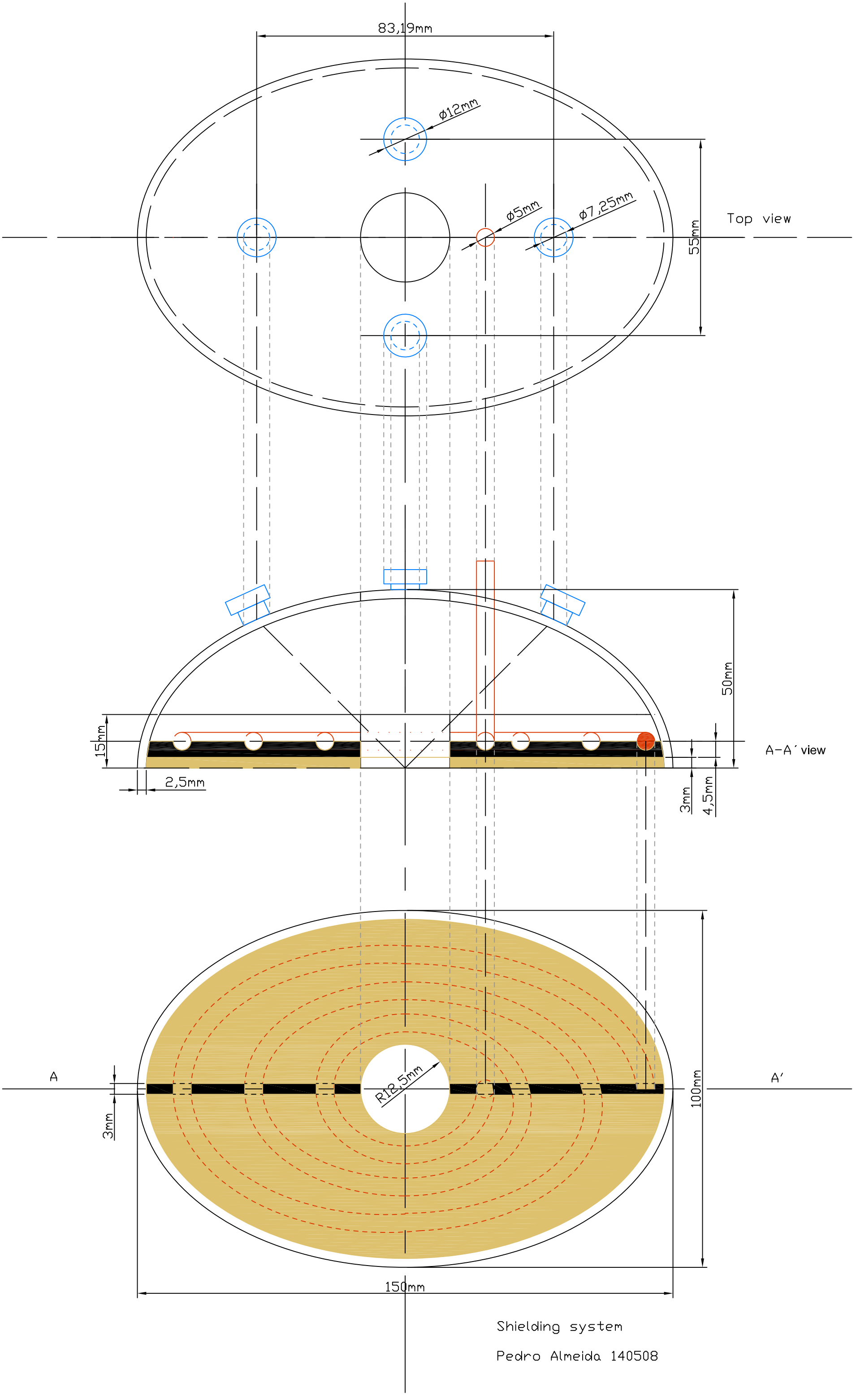
83,19mm
ϕ12mm
ϕ5mm
ϕ7,25mm
55mm
Top view
50mm
15mm
2,5mm
3mm
4,5mm
A-A´ view
A
A´
3mm
R12,5mm
100mm
150mm
Shielding system
Pedro Almeida 140508

Appendix G – Optimised modelling equations

Final predictive models for single and multi-layer deposition, as determined by Design Expert®7.15 software, in terms of *actual factors* were as follows:

Bead width:

$$W \text{ (mm)} = (-0.73543 + 2.36891\times WD - 0.074616\times WFS/TS + 0.33048\times WFS_{actual} + 0.12406\times WD\times WFS/TS + 7.44404E^{-3}\times WFS/TS\times WFS_{actual} - 0.020592\times WFS_{actual}^{2})^{(1/0.75)}$$

Bead height:

$$H \text{ (mm)} = (0.86842 - 0.36539\times WD - 0.065844\times WFS/TS + 0.081251\times WFS_{actual} + 0.023863\times WD\times WFS/TS - 0.049914\times WD\times WFS_{actual} + 9.98404E^{-4}\times WFS/TS^{2} - 2.09468E^{-3}\times WFS_{actual}^{2})^{(-1/1.62)}$$

Remelting ratio:

$$RR \text{ (\%)} = (-0.57042 + 1.14830\times WD - 6.54392E^{-5}\times WFS/TS - 0.023473\times WFS_{actual} - 0.013978\times WD\times WFS/TS + 0.083825\times WD\times WFS_{actual} + 1.70963E^{-3}\times WFS/TS\times WFS_{actual} - 0.42285\times WD^{2} - 1.72126E^{-3}\times WFS_{actual}^{2})^{(1/0.78)}$$

Penetration:

$$P \text{ (mm)} = (0.60331 - 0.29181\times WD - 0.12349\times WFS/TS - 0.15108\times WFS_{actual} + 0.12132\times WD\times WFS/TS + 0.25931\times WD\times WFS_{actual} + 6.97472E^{-3}\times WFS/TS\times WFS_{actual} - 5.00983E^{-3}\times WFS_{actual}^{2})^{(1/0.81)}$$

Dilution:

$$D \text{ (\%)} = (-59.73894 + 116.06462\times WD - 0.041035\times WFS/TS - 1.36652\times WFS_{actual} - 1.10988\times WD\times WFS/TS + 5.96588\times WD\times WFS_{actual} + 0.13769\times WFS/TS\times WFS_{actual} - 44.93685\times WD^{2} - 0.13639\times WFS_{actual}^{2})^{(1/1.07)}$$

Deposition rate:

$$DR \text{ (kg h}^{-1}\text{)} = (1.68585 - 3.62263\times WD + 6.99989E^{-3}\times WFS/TS - 0.38407\times WFS_{actual} - 5.26222E^{-3}\times WD\times WFS/TS + 0.77723\times WD\times WFS_{actual} - 3.37836E^{-4}\times WFS/TS\times WFS_{actual} + 1.83051\times WD^{2} + 1.00075E^{-3}\times WFS_{actual}^{2})^{(1/1.04)}$$

Contact angle:

$$CA \text{ (º)} = (-3.48965E^{-3} + 0.026195\times WD - 1.22768E^{-3}\times WFS/TS + 2.35519E^{-3}\times WFS_{actual} - 7.32269E^{-4}\times WD\times WFS_{actual} + 7.35982E^{-5}\times WFS/TS\times WFS_{actual} - 0.010254\times WD^{2} + 3.06546E^{-5}\times WFS/TS^{2} - 1.32686E^{-4}\times WFS_{actual}^{2})^{(-1/1.09)}$$

Penetration area:

$$A_1 \text{ (mm}^2\text{)} = (-0.051465 + 0.34667\times WD - 0.10959\times WFS/TS - 0.13445\times WFS_{actual} + 0.12026\times WD\times WFS/TS + 0.32060\times WD\times WFS_{actual} + 7.95452E^{-3}\times WFS/TS\times WFS_{actual} - 7.86287E^{-3}\times WFS_{actual}^{2})^{(1/0.51)}$$

Reinforcement area:

A_2 (mm^2) = $(1.38473 - 1.32497\times WD - 0.048655\times WFS/TS - 3.03921E^{-3}\times WFS_{actual} + 0.016736\times WD\times WFS/TS + 0.40819\times WD^2 + 8.12645E^{-4}\times WFS/TS^2 + 2.03999E^{-4}\times WFS_{actual}{}^2)^{(-1/0.7)}$

Aspect ratio:

AR (mm^2) = $(- 13.00069 + 22.96931\times WD - 0.13471\times WFS/TS + 1.67289\times WFSactual - 0.60751\times WD\times WFS_{actual} + 0.011024\times WFS/TS\times WFS_{actual} - 8.43407\times WD^2 - 0.062777\times WFS_{actual}{}^2)^{(-1/1.56)}$

Heat input:

HI ($J\ mm^{-1}$) = $(0.14040 - 0.14273\times WD - 4.94485E^{-3}\times WFS/TS - 1.74710E^{-3}\times WFS_{actual} + 1.94848E^{-3}\times WD\times WFS/TS + 1.36089E^{-3}\times WD\times WFS_{actual} + 0.043161\times WD^2 + 7.72641E^{-5}\times WFS/TS^2 + 4.42630E^{-5}\times WFS_{actual}{}^2)^{(-1/0.73)}$

Heat source length:

HSL (mm) = $(-0.75535 + 2.77710\times WD - 0.018265\times WFS/TS + 0.10780\times WFS_{actual} + 0.36786\times WD\times WFS_{actual} + 8.33117\ E^{-3}\times WFS/TS\times WFS_{actual} - 0.018831\times WFS_{actual}{}^2)^{(1/0.56)}$

Surface waviness:

SW_{av} (μm) = $(0.32717 - 0.037825\times WFS_{actual} + 0.68504\times TS + 6.17615E^{-3}\times WFS_{actual}\times TS + 4.75528E^{-3}\times WFS_{actual}{}^2 - 1.07442\times TS^2 - 2.18211E^{-4}\times WFS_{actual}{}^3 + 0.49261\times TS^3)^{(-1/0.18)}$

Effective wall width:

W_{eff} (mm) = $(0.93329 - 8.08170E^{-3}\times WFS_{actual} + 0.095960\times TS + 2.56366E^{-4}\times WFS_{actual}{}^2 - 0.037904\times TS^2)^{(-1/0.05)}$

Metal deposition efficiency:

MDE (%) = $(80.86750 + 0.80267\times WFS_{actual} + 66.25218\times TS + 4.64051\times WFS_{actual}\times TS - 0.21774\times WFS_{actual}{}^2 - 153.39274\times TS^2 + 0.40820\times WFS_{actual}{}^2\times TS - 11.56339\times WFS_{actual}\times TS^2 + 135.89951\times TS^3)$

Appendix H – Optimised ANOVA outputs

Analysis of variance (ANOVA) and Fisher´s hypothesis testing for single layer deposition:

Table H 1. Computed ANOVA for the bead W regression model (quadratic).

Source	Sum of Squares (SS)	d.f.	VIF	Contrib. (%)	Mean Square	*F* value	*p*-value Prob>F
Model	31.38	6		95.76	5.23	289.19	<0.0001
WD	19.66	1	1.81	59.99	19.66	1087.2	<0.0001
WFS/TS	5.91	1	1.80	18.03	5.91	327.06	<0.0001
WFS_{act}	7.38	1	1.50	22.52	7.38	408.21	<0.0001
WD × WFS/TS	0.25	1	1.78	0.76	0.25	13.56	0.0004
WFS/TS × WFS_{act}	0.37	1	1.93	1.13	0.37	20.35	<0.0001
WFS_{act}^2	3.67	1	1.11	11.20	3.67	203.23	<0.0001
Residual	1.39	77		4.24	0.018		
Corrected total	32.77	83					
Std. Dev.	0.13				R^2		0.9575
Mean	3.60				Adj. R^2		0.9542
C.V. (%)	3.73				Pred. R^2		0.9495
PRESS	1.66				Adeq. Precision		72.202

Tabulated values of Fisher's F-test: $F_{0.05}$ (6,77)=2.10.

Table H 2. Computed ANOVA for the bead H regression model (quadratic).

Source	Sum of Squares (SS)	d.f.	VIF	Contrib. (%)	Mean Square	F value	p-value Prob>F
Model	0.64	7		96.97	0.092	512.91	<0.0001
WD	0.057	1	7.16	8.64	0.057	316.62	<0.0001
WFS/TS	0.18	1	1.24	27.27	0.18	1026.97	<0.0001
WFS_{act}	2.160×10-6	1	6.32	0.00	2.160×10-6	0.012	0.9130
WD × WFS/TS	0.011	1	1.30	1.67	0.011	63.95	<0.0001
WD × WFS_{act}	0.011	1	6.70	1.67	0.011	58.61	<0.0001
WFS/TS^2	9.379×10-3	1	1.18	1.42	9.379×10-3	52.24	<0.0001
WFS_{act}^2	0.018	1	2.26	2.73	0.018	99.30	<0.0001
Residual	0.013	73		1.97	1.795×10-4		
Corrected total	0.66	80					
Std. Dev.	0.013				R^2		0.9801
Mean	0.27				Adj. R^2		0.9782
C.V. (%)	5.02				Pred. R^2		0.9761
PRESS	0.016				Adeq. Precision		81.422

Tabulated values of Fisher's F-test: $F_{0.05}$ (7,73)=2.01.

Table H 3. Computed ANOVA for the RR regression model (quadratic).

Source	Sum of Squares (SS)	d.f.	VIF	Contrib. (%)	Mean Square	F value	p-value Prob>F
Model	1.40	8		95.89	0.17	190.04	<0.0001
WD	0.14	1	8.72	9.59	0.14	156.36	<0.0001
WFS/TS	6.494×10-4	1	2.07	0.04	6.494×10-4	0.71	0.4032
WFS_{act}	0.35	1	6.79	23.97	0.35	383.99	<0.0001
WD × WFS/TS	3.036×10-3	1	1.78	0.21	3.036×10-3	3.31	0.0731
WD × WFS_{act}	0.027	1	7.62	1.85	0.027	29.15	<0.0001
WFS/TS × WFS_{act}	0.017	1	2.14	1.16	0.017	18.45	<0.0001
WD^2	3.098×10-3	1	1.58	0.21	3.098×10-3	3.37	0.0703
WFS_{act}^2	0.012	1	2.26	0.82	0.012	13.37	0.0005
Residual	0.068	74		4.66	9.185×10-4		
Corrected total	1.46	82					
Std. Dev.	0.030				R^2		0.9536
Mean	0.31				Adj. R^2		0.9486
C.V. (%)	9.65				Pred. R^2		0.9414
PRESS	0.086				Adeq. Precision		47.821

Tabulated values of Fisher's F-test: $F_{0.05}$ (7,74)=2.01.

Table H 4. Computed ANOVA for the HI regression model (quadratic).

Source	Sum of Squares (SS)	d.f.	VIF	Contrib. (%)	Mean Square	F value	p-value Prob>F
Model	3.116×10-3	8		99.58	3.895×10-4	1978.4	<0.0001
WD	1.011×10-4	1	9.52	3.23	1.011×10-4	513.56	<0.0001
WFS/TS	4.351×10-4	1	2.00	13.91	4.351×10-4	2209.8	<0.0001
WFS_{act}	8.170×10-6	1	7.12	0.26	8.170×10-6	41.49	<0.0001
WD × WFS/TS	7.209×10-5	1	1.48	2.30	7.209×10-5	366.16	<0.0001
WD × WFS_{act}	6.612×10-6	1	8.27	0.21	6.612×10-6	33.58	<0.0001
WD^2	1.855×10-5	1	2.02	0.59	1.855×10-5	94.23	<0.0001
WFS/TS^2	5.464×10-5	1	1.26	1.75	5.464×10-5	277.52	<0.0001
WFS_{act}^2	8.164×10-6	1	2.07	0.26	8.164×10-6	41.46	<0.0001
Residual	1.299×10-5	66		0.42	1.969×10-7		
Corrected total	3.129×10-3	74					
Std. Dev.	4.437×10-4				R^2		0.9958
Mean	0.018				Adj. R^2		0.9953
C.V. (%)	2.45				Pred. R^2		0.9946
PRESS	1.688×10-5				Adeq. Precision		146.770

Tabulated values of Fisher's F-test: F0.05 (8,66)=1.94.

Table H 5. Computed ANOVA for the DR regression model (quadratic).

Source	Sum of Squares (SS)	d.f.	VIF	Contrib. (%)	Mean Square	F value	p-value Prob>F
Model	53.83	8		99.98	6.73	43516.81	<0.0001
WD	8.61	1	8.80	15.99	8.61	55703.40	<0.0001
WFS/TS	3.164×10-4	1	1.94	0.00	3.164×10-4	2.05	0.1567
WFS_{act}	18.76	1	6.93	34.84	18.76	1.213×105	<0.0001
WD × WFS/TS	4.303×10-4	1	1.82	0.00	4.303×10-4	2.78	0.0994
WD × WFS_{act}	2.31	1	7.81	4.29	2.31	14935.44	<0.0001
WFS/TS × WFS_{act}	7.534×10-4	1	1.94	0.00	7.533×10-4	4.87	0.0304
WD^2	0.058	1	1.58	0.11	0.058	375.54	<0.0001
WFS_{act}^2	4.419×10-3	1	2.18	0.01	4.419×10-3	28.58	<0.0001
Residual	0.012	75		0.02	1.546×10-4		
Corrected total	53.84	83					
Std. Dev.	0.012				R^2		0.9998
Mean	1.84				Adj. R^2		0.9998
C.V. (%)	0.68				Pred. R^2		0.9997
PRESS	0.015				Adeq. Precision		674.443

Tabulated values of Fisher's F-test: F0.05 (8,75)=1.94.

Table H 6. Computed ANOVA for the CA regression model (quadratic).

Source	Sum of Squares (SS)	d.f.	VIF	Contrib. (%)	Mean Square	F value	p-value Prob>F
Model	5.998×10-4	8		92.95	7.498×10-5	117.08	<0.0001
WD	9.241×10-9	1	7.97	0.00	9.241×10-9	0.014	0.9047
WFS/TS	6.266×10-6	1	2.09	0.97	6.266×10-6	9.79	0.0026
WFS_{act}	3.280×10-5	1	6.78	5.08	3.280×10-5	51.22	<0.0001
WD × WFS_{act}	1.959×10-6	1	7.46	0.30	1.959×10-6	3.06	0.0846
WFS/TS × WFS_{act}	2.968×10-5	1	1.95	4.60	2.968×10-5	46.34	<0.0001
WD^2	1.842×10-6	1	1.53	0.29	1.842×10-6	2.88	0.0943
WFS/TS^2	9.083×10-6	1	1.14	1.41	9.083×10-6	14.18	0.0003
WFS_{act}^2	6.044×10-5	1	2.62	9.37	6.044×10-5	94.38	<0.0001
Residual	4.547×10-5	71		7.05	6.404×10-7		
Corrected total	6.453×10-4	79					
Std. Dev.	8.002×10-4				R^2		0.9295
Mean	0.011				Adj. R^2		0.9216
C.V. (%)	7.25				Pred. R^2		0.9113
PRESS	5.721×10-5				Adeq. Precision		39.271

Tabulated values of Fisher's F-test: $F_{0.05}$ (7,71)=1.94.

Table H 7. Computed ANOVA for the A_2 regression model (quadratic).

Source	Sum of Squares (SS)	d.f.	VIF	Contrib. (%)	Mean Square	F value	p-value Prob>F
Model	0.35	7		100.00	0.048	2055.19	<0.0001
WD	0.087	1	2.10	24.86	0.087	3601.67	<0.0001
WFS/TS	0.077	1	1.40	22.00	0.077	3218.12	<0.0001
WFS_{act}	3.081×10-7	1	1.63	0.00	3.081×10-7	0.013	0.9102
WD × WFS/TS	5.382×10-3	1	1.40	1.54	5.382×10-3	223.77	<0.0001
WD^2	3.488×10-3	1	1.28	1.00	3.488×10-3	145.03	<0.0001
WFS/TS^2	6.359×10-3	1	1.16	1.82	6.359×10-3	264.40	<0.0001
WFS_{act}^2	3.269×10-4	1	1.17	0.09	3.269×10-4	13.59	0.0004
Residual	1.732×10-3	72		0.49	2.405×10-5		
Corrected total	0.35	79					
Std. Dev.	4.904×10-3				R^2		0.9950
Mean	0.22				Adj. R^2		0.9945
C.V. (%)	2.21				Pred. R^2		0.9940
PRESS	2.102×10-3				Adeq. Precision		153.614

Tabulated values of Fisher's F-test: F0.05 (7,72)=2.01.

Table H 8. Computed ANOVA for the A_1 regression model (quadratic).

Source	Sum of Squares (SS)	d.f.	VIF	Contrib. (%)	Mean Square	F value	p-value Prob>F
Model	20.20	7		97.49	2.89	384.61	<0.0001
WD	6.16	1	6.21	29.73	6.16	821.25	<0.0001
WFS/TS	2.52	1	1.71	12.16	2.52	335.90	<0.0001
WFS_{act}	3.51	1	5.95	16.94	3.51	468.30	<0.0001
WD × WFS/TS	0.21	1	1.87	1.01	0.21	28.24	<0.0001
WD × WFS_{act}	0.44	1	6.36	2.12	0.44	58.98	<0.0001
WFS/TS × WFS_{act}	0.37	1	1.76	1.79	0.37	49.79	<0.0001
$WFScal^2$	0.26	1	1.82	1.25	0.26	34.83	<0.0001
Residual	0.53	70		2.56	7.502×10-3		
Corrected total	20.72	77					
Std. Dev.	0.087				R^2		0.9747
Mean	1.48				Adj. R^2		0.9721
C.V. (%)	5.86				Pred. R^2		0.9674
PRESS	0.68				Adeq. Precision		77.571

Tabulated values of Fisher's F-test: F0.05 (7,70)=2.01.

Table H 9. Computed ANOVA for the P regression model (quadratic).

Source	Sum of Squares (SS)	d.f.	VIF	Contrib. (%)	Mean Square	F value	p-value Prob>F
Model	10.13	7		95.21	1.45	201.52	<0.0001
WD	3.44	1	6.35	32.33	3.44	479.78	<0.0001
WFS/TS	1.17	1	1.82	11.00	1.17	163.32	<0.0001
WFS_{act}	1.74	1	6.00	16.35	1.74	242.48	<0.0001
WD × WFS/TS	0.22	1	1.84	2.07	0.22	30.11	<0.0001
WD × WFS_{act}	0.29	1	6.26	2.73	0.29	40.44	<0.0001
WFS/TS × WFS_{act}	0.25	1	1.96	2.35	0.25	35.12	<0.0001
WFS_{act}^2	0.10	1	1.89	0.94	0.10	14.30	0.0003
Residual	0.51	71		4.79	7.179×10-3		
Corrected total	10.64	78					
Std. Dev.	0.085				R^2		0.9521
Mean	0.99				Adj. R^2		0.9474
C.V. (%)	8.53				Pred. R^2		0.9415
PRESS	0.62				Adeq. Precision		56.877

Tabulated values of Fisher's F-test: F0.05 (7,71)=2.01.

Table H 10. Computed ANOVA for the D regression model (quadratic).

Source	Sum of Squares (SS)	d.f.	VIF	Contrib. (%)	Mean Square	F value	p-value Prob>F
Model	8342.10	8		95.69	1042.76	202.67	<0.0001
WD	806.79	1	8.81	9.25	806.79	156.81	<0.0001
WFS/TS	6.10	1	2.07	0.07	6.10	1.19	0.2798
WFS_{act}	2051.99	1	6.72	23.54	2051.99	398.82	<0.0001
WD × WFS/TS	19.14	1	1.78	0.22	19.14	3.72	0.0576
WD × WFS_{act}	135.03	1	7.65	1.55	135.03	26.24	<0.0001
WFS/TS × WFS_{act}	108.54	1	2.14	1.25	108.54	21.10	<0.0001
WD^2	32.80	1	1.63	0.38	32.80	6.38	0.0137
WFS_{act}^2	76.12	1	2.22	0.87	76.12	14.79	0.0003
Residual	375.59	73		4.31	5.15		
Corrected total	8717.69	81					
Std. Dev.	2.27				R^2		0.9569
Mean	22.69				Adj. R^2		0.9522
C.V. (%)	10.00				Pred. R^2		0.9458
PRESS	472.67				Adeq. Precision		49.942

Tabulated values of Fisher's F-test: F0.05 (8,73)=1.94.

Table H 11. Computed ANOVA for the AR regression model (quadratic).

Source	Sum of Squares (SS)	d.f.	VIF	Contrib. (%)	Mean Square	F value	p-value Prob>F
Model	125.13	8		91.00	17.88	108.35	<0.0001
WD	0.63	1	8.37	0.46	0.63	3.84	0.0538
WFS/TS	1.66	1	1.50	1.21	1.66	10.04	0.0022
WFS_{act}	7.90	1	7.04	5.75	7.90	47.91	<0.0001
WD × WFS_{act}	1.38	1	7.97	1.00	1.38	8.36	0.0050
WFS/TS × WFS_{act}	1.03	1	1.52	0.75	1.03	6.22	0.0148
WD^2	1.26	1	1.50	0.92	1.26	7.65	0.0072
WFS_{act}^2	17.37	1	2.15	12.63	17.37	105.31	<0.0001
Residual	12.37	75		9.00	0.16		
Corrected total	137.50	82					
Std. Dev.	0.41				R^2		0.9100
Mean	3.90				Adj. R^2		0.9016
C.V. (%)	10.42				Pred. R^2		0.8889
PRESS	15.27				Adeq. Precision		38.871

Tabulated values of Fisher's F-test: F0.05 (8,75)=1.94.

Table H 12. Computed ANOVA for the HSL regression model (quadratic).

Source	Sum of Squares (SS)	d.f.	VIF	Contrib. (%)	Mean Square	F value	p-value Prob>F
Model	53.89	6		95.70	8.98	285.05	<0.0001
WD	10.90	1	6.32	19.36	10.90	346.01	<0.0001
WFS/TS	1.33	1	1.41	2.36	1.33	42.26	<0.0001
WFS_{act}	11.93	1	6.04	21.19	11.93	378.75	<0.0001
WD × WFS_{act}	0.64	1	6.27	1.14	0.64	20.44	<0.0001
WFS/TS × WFS_{act}	0.62	1	1.44	1.10	0.62	19.59	<0.0001
WFS_{act}^2	1.60	1	2.14	2.84	1.60	50.65	<0.0001
Residual	2.43	77		4.32	0.032		
Corrected total	56.31	83					
Std. Dev.	0.18				R^2		0.9569
Mean	4.00				Adj. R^2		0.9536
C.V. (%)	4.44				Pred. R^2		0.9484
PRESS	2.90				Adeq. Precision		63.088

Tabulated values of Fisher's F-test: F0.05 (6,77)=2.10.

Analysis of variance (ANOVA) and Fisher´s hypothesis testing for multi-layer deposition:

Table H 13. Computed ANOVA for the SW_{av} regression model (cubic).

Source	Sum of Squares (SS)	d.f.	VIF	Contrib. (%)	Mean Square	F value	p-value Prob>F
Model	0.071	7		87.65	0.010	39.63	<0.0001
WFS_{act}	4.219×10-6	1	8.18	0.01	4.219×10-6	0.016	0.8987
TS	3.028×10-4	1	5.55	0.37	3.028×10-4	1.18	0.2844
WFS_{act}× TS	9.448×10-4	1	1.50	1.17	9.448×10-4	3.68	0.0626
WFS_{act}^2	1.456×10-4	1	1.09	0.18	1.456×10-4	0.57	0.4561
TS^2	8.315×10-3	1	1.82	10.27	8.315×10-3	32.38	<0.0001
WFS_{act}^3	2.527×10-3	1	8.24	3.12	2.527×10-3	9.84	0.0033
TS^3	1.171×10-3	1	6.94	1.45	1.171×10-3	4.56	0.0393
Residual	9.759×10-3	38		12.05	2.568×10-4		
Corrected total	0.081	45					
Std. Dev.	0.014				R^2		0.8856
Mean	0.59				Adj. R^2		0.8645
C.V. (%)	2.32				Pred. R^2		0.8247
PRESS	0.011				Adeq. Precision		28.431

Tabulated values of Fisher's F-test: F0.05 (7,38)=2.01.

Table H 14. Computed ANOVA for the W_{eff} regression model (quadratic).

Source	Sum of Squares (SS)	d.f.	VIF	Contrib. (%)	Mean Square	F value	p-value Prob>F
Model	0.018	4		100.00	4.379×10-3	658.18	<0.0001
WFS_{act}	0.011	1	1.08	61.11	0.011	1620.3	<0.0001
TS	6.466×10-3	1	1.26	35.92	6.466×10-3	971.92	<0.0001
WFS_{act}^2	4.297×10-4	1	1.01	2.39	4.297×10-4	64.59	<0.0001
TS^2	1.577×10-4	1	1.22	0.88	1.577×10-4	3.70	<0.0001
Residual	2.728×10-4	41		1.52	6.653×10-6		
Corrected total	0.018	45					
Std. Dev.	2.579×10-3				R^2		0.9847
Mean	0.92				Adj. R^2		0.9832
C.V. (%)	0.28				Pred. R^2		0.9807
PRESS	3.429×10-4				Adeq. Precision		95.621

Tabulated values of Fisher's F-test: F0.05 (4,41)=2.37.

Table H 15. Computed ANOVA for MDE regression model (cubic)

Source	Sum of Squares (SS)	d.f.	VIF	Contrib. (%)	Mean Square	F value	p-value Prob>F
Model	900.86	8		72.48	112.61	11.85	<0.0001
WFS_{act}	13.93	1	9.14	1.12	13.93	1.47	0.2339
TS	57.60	1	5.58	4.63	57.60	6.06	0.0187
WFS_{act} × TS	9.573×10-3	1	2.13	0.00	9.573×10-3	1.008×10-3	0.9749
WFS_{act}^2	3.60	1	1.17	0.29	3.60	0.38	0.5421
TS^2	111.39	1	2.40	8.96	111.39	11.72	0.0016
WFS_{act}× TS^2	107.17		3.68	8.62	107.17	11.28	0.0019
WFS_{act}^3	23.67	1	7.96	1.90	23.67	2.49	0.1232
TS^3	99.37	1	8.73	8.00	99.37	10.46	0.0026
Residual	342.04	36		27.52	9.50		
Corrected total	1242.90	44					
Std. Dev.	3.08				R^2		0.7248
Mean	90.34				Adj. R^2		0.6636
C.V. (%)	3.41				Pred. R^2		0.5132
PRESS	605.02				Adeq. Precision		15.355

Tabulated values of Fisher's F-test: F0.05 (8,36)=1.94.

Appendix I – Experimental designs

Table I 1. Welding conditions applied in the *TRIM* study, alongside the measured weld bead characteristics (GMAW-P and P19).

TRIM	W (mm)	H (mm)	RR (%)	P (mm)	D (%)	DR_{macro} (kg h^{-1})	CA_{avg} (º)	CI (95%)	A_1 (mm^2)	A_2 (mm^2)
0.70	8.32	3.00	28.38	1.57	22.10	1.52	47.74	5.11	4.60	16.21
0.80	9.04	2.88	29.43	1.57	22.74	1.50	39.94	1.72	4.73	16.07
0.90	9.68	2.96	21.95	1.46	18.00	1.83	45.83	4.74	4.29	19.54
1.00	8.65	2.80	26.34	1.60	20.85	1.65	57.33	2.94	4.63	17.58
1.15	9.29	2.62	39.32	1.72	28.22	1.57	39.14	1.73	6.61	16.81
1.25	10.15	2.59	45.01	1.97	31.04	1.68	37.48	0.99	8.07	17.93
1.35	10.32	2.43	51.27	2.22	33.90	1.69	36.23	4.95	9.25	18.04

W, bead width; *H*, bead height; *RR*, remelting ratio; *P*, penetration; *D*, dilution; DR_{macro}, deposition rate calculated from the transverse macro section, CA_{avg}, average contact angle, *CI*, confidence interval of 95%, A_1, penetration cross section area; A_2, reinforcement cross section area.

Table I 2. Welding conditions applied in the CTWD study, alongside the measured weld bead characteristics (GMAW-P and P19).

CTWD (mm)	W (mm)	H (mm)	RR (%)	P (mm)	D (%)	DR_{macro} (kg h^{-1})	CA_{avg} (º)	CI (95%)	A_1 (mm^2)	A_2 (mm^2)
7	11.69	2.20	74.67	2.50	42.75	1.70	33.28	2.01	13.53	18.12
8	11.36	2.21	71.30	2.58	41.62	1.66	31.47	1.31	12.62	17.70
9	11.16	2.25	65.45	2.36	39.56	1.60	32.62	0.81	11.16	17.05
10	11.09	2.26	63.46	2.22	38.82	1.57	34.89	1.56	10.63	16.75
11	10.52	2.37	59.08	2.36	37.14	1.60	34.82	1.11	10.12	17.13
12	9.61	2.43	47.35	2.09	32.13	1.57	40.15	0.41	7.95	16.79
13	9.31	2.70	43.92	1.94	30.52	1.65	42.85	1.63	7.73	17.60
14	9.57	2.63	45.51	2.05	32.45	1.68	41.31	2.07	8.15	17.91
15	9.82	2.51	49.92	2.26	33.30	1.67	39.15	2.43	8.91	17.85
16	10.09	2.43	53.37	2.03	34.80	1.60	39.19	2.54	9.11	17.07
17	10.23	2.44	54.91	2.25	35.45	1.64	37.21	4.16	9.62	17.52
18	10.11	2.55	51.33	2.21	33.92	1.69	35.94	5.35	9.26	18.04
19	9.88	2.59	52.40	2.31	34.38	1.68	33.60	2.35	9.40	17.94
20	9.97	2.57	53.85	2.28	35.00	1.64	34.57	4.12	9.44	17.53

Table I 3. Welding conditions used in the study of the effect of the WFS and TS on the weld bead characteristics, alongside measured response data. (P19 was used and WFS/TS=10).

WFS_{set} (m min^{-1})	TS (m min^{-1})	WFS/TS	W (mm)	H (mm)	RR (%)	P (mm)	D (%)	DR_{macro} (kg h^{-1})	CA_{avg} (º)	CI (95%)	A_1 (mm^2)	A_2 (mm^2)
1.5	0.150	10	7.66	3.46	1.63	0.26	1.60	1.293	62.04	0.5978	0.30	18.42
2.0	0.200	10	6.48	2.85	11.66	0.70	10.44	1.116	65.83	0.5194	1.39	11.92
3.0	0.300	10	7.51	2.38	37.96	1.45	27.51	1.609	40.93	2.4108	4.35	11.46
4.0	0.400	10	7.30	2.40	62.00	1.83	38.27	1.981	41.96	0.3332	6.56	10.58
5.0	0.500	10	7.28	2.40	71.16	2.34	41.58	2.742	42.18	1.5582	8.34	11.72
6.0	0.600	10	7.17	2.48	80.62	2.58	44.64	3.246	49.69	0.8722	9.32	11.56
7.0	0.700	10	6.20	2.57	88.57	2.66	46.97	3.440	55.29	1.9502	9.30	10.50
8.0	0.800	10	5.95	2.84	85.35	2.79	46.05	4.395	61.90	3.0085	10.02	11.74
9.0	0.900	10	5.64	2.90	91.44	3.10	47.76	4.823	65.07	3.3515	10.47	11.45
10.0	1.000	10	6.46	2.70	91.93	3.22	47.90	5.396	56.08	2.6558	10.60	11.53
11.0	1.100	10	6.30	2.87	116.85	3.81	53.89	6.080	56.75	2.4892	13.80	11.81
12.0	1.200	10	5.96	3.06	126.34	4.01	55.82	6.823	62.62	1.2740	15.35	12.15
13.0	1.300	10	5.55	3.20	126.75	4.31	55.90	7.483	65.76	0.1666	15.59	12.30
14.0	1.400	10	4.87	3.18	140.59	4.45	58.44	7.279	71.10	1.9796	15.62	11.11
15.0	1.500	10	4.32	2.96	154.57	4.51	60.72	7.217	79.40	2.4598	15.89	10.28

Table I 4. Welding conditions used in the study of the effect of the WFS and TS on the weld bead characteristics, alongside measured response data. (P19 was used and WFS/TS=15).

WFS_{set} (m min^{-1})	TS (m min^{-1})	WFS/TS	W (mm)	H (mm)	RR (%)	P (mm)	D (%)	DR_{macro} (kg h^{-1})	CA_{avg} (º)	CI (95%)	A_1 (mm^2)	A_2 (mm^2)
1.5	0.100	15	8.03	4.16	1.31	0.24	1.29	1.215	78.68	1.7346	0.34	25.97
2.0	0.133	15	7.60	3.04	8.40	0.81	7.75	1.114	66.96	2.4304	1.50	17.86
3.0	0.200	15	9.09	2.81	29.33	1.72	22.68	1.612	48.30	4.3707	5.05	17.22
4.0	0.267	15	9.26	2.69	51.75	2.16	34.10	2.028	41.11	0.5488	8.41	16.25
5.0	0.333	15	9.19	2.59	72.46	2.71	42.02	2.379	40.36	2.0972	11.05	15.25
6.0	0.400	15	9.72	2.66	69.92	2.84	41.15	3.224	37.48	1.5778	12.04	17.22
7.0	0.467	15	9.61	2.84	71.07	3.00	41.55	3.964	44.35	3.4789	12.90	18.15
8.0	0.533	15	8.65	2.97	79.22	3.15	44.20	4.121	45.90	2.4696	13.08	16.51
9.0	0.600	15	8.67	2.87	89.35	3.52	47.19	4.720	51.71	0.9016	15.02	16.81
10.0	0.667	15	8.75	2.85	109.73	4.33	52.32	4.939	45.29	2.4010	17.37	15.83
11.0	0.733	15	8.55	3.22	98.77	5.00	49.69	6.147	51.98	3.9493	17.69	17.91
12.0	0.800	15	7.66	3.42	124.82	5.85	55.52	6.608	60.27	0.0196	22.03	17.65
13.0	0.867	15	6.91	3.71	125.33	6.10	55.62	7.285	64.45	2.6754	22.51	17.96
14.0	0.933	15	6.51	3.81	127.40	6.34	56.03	7.906	69.60	2.2344	23.06	18.10
15.0	1.000	15	5.95	3.70	140.22	6.45	58.37	7.797	75.31	2.9693	23.36	16.66

Table I 5. Welding conditions used in the study of the effect of the WFS and TS on the weld bead characteristics, alongside measured response data. (P19 was used and WFS/TS=20).

WFS_{set} (m min^{-1})	TS (m min^{-1})	WFS/TS	W (mm)	H (mm)	RR (%)	P (mm)	D (%)	DR_{macro} (kg h^{-1})	CA_{avg} (º)	CI (95%)	A_1 (mm^2)	A_2 (mm^2)
1.5	0.075	20	8.69	4.85	0.06	0.06	0.06	1.233	92.70	0.5978	0.02	35.12
2.0	0.100	20	9.45	3.63	7.73	1.07	7.17	1.181	77.26	0.9408	1.95	25.23
3.0	0.150	20	10.84	3.16	28.79	2.09	22.36	1.731	50.28	4.4001	7.10	24.66
4.0	0.200	20	10.67	3.06	49.96	2.73	33.31	2.097	44.45	1.9600	11.19	22.40
5.0	0.250	20	10.39	3.13	63.48	2.81	38.83	2.556	45.63	4.9097	13.87	21.85
6.0	0.300	20	10.91	3.04	75.15	3.39	42.91	3.096	45.49	1.2446	16.57	22.05
7.0	0.350	20	11.47	3.04	72.79	3.39	42.13	3.835	36.53	1.9796	17.04	23.41
8.0	0.400	20	10.75	3.04	79.77	3.72	44.37	4.109	43.40	1.6758	17.51	21.95
9.0	0.450	20	10.11	3.18	81.47	4.13	44.90	4.604	49.29	1.3818	17.81	21.86
10.0	0.500	20	10.86	3.44	89.83	4.88	47.32	5.616	43.79	0.6468	21.56	24.00
11.0	0.550	20	11.07	3.46	100.78	6.20	50.19	6.270	43.60	0.2254	24.55	24.36
12.0	0.600	20	10.67	3.64	113.96	7.19	53.26	6.919	45.37	1.3916	28.08	24.64
13.0	0.650	20	9.41	3.74	130.14	7.75	56.55	6.954	56.37	3.7435	29.75	22.86
14.0	0.700	20	8.57	4.04	122.16	8.17	54.99	8.013	68.70	0.6272	29.88	24.46
15.0	0.750	20	7.89	4.53	120.21	9.27	54.59	9.172	74.20	1.4994	31.41	26.13

Table I 6. Welding conditions used in the study of the effect of the WFS, TS, and WD on the weld bead characteristics, alongside measured response data. (P14 was used and WFS/TS=15).

WFS_{set} (m min^{-1})	TS (m min^{-1})	WFS/TS	W (mm)	H (mm)	RR (%)	P (mm)	D (%)	DR_{macro} (kg h^{-1})	CA_{avg} (º)	CI (95%)	A_1 (mm^2)	A_2 (mm^2)
1.5	0.100	15	3.86	3.29	0.64	0.10	0.64	0.509	98.50	14.2587	0.07	10.87
2.0	0.133	15	4.50	3.00	1.56	0.15	1.53	0.681	76.65	4.4001	0.17	10.92
3.0	0.200	15	5.43	2.61	9.57	0.58	8.73	0.969	61.85	1.7150	0.99	10.35
4.0	0.267	15	5.73	2.58	18.18	0.95	15.38	1.345	54.02	0.3724	1.96	10.78
5.0	0.333	15	6.78	2.48	27.32	1.35	21.46	1.816	54.20	0.7350	3.18	11.64
6.0	0.400	15	6.98	2.43	38.37	1.46	27.73	2.093	49.90	3.1359	4.29	11.18
7.0	0.467	15	7.00	2.38	44.81	1.63	30.94	2.354	45.73	2.8811	4.83	10.78
8.0	0.533	15	7.12	2.42	47.30	1.76	32.11	2.823	48.24	3.3025	5.35	11.31
9.0	0.600	15	7.49	2.46	45.30	1.82	31.18	3.409	49.46	2.5088	5.50	12.14
10.0	0.667	15	7.27	2.39	50.83	1.74	33.70	3.554	49.09	2.3030	5.79	11.39
11.0	0.733	15	7.57	2.38	51.56	1.87	34.02	3.961	46.29	1.1956	5.95	11.54
12.0	0.800	15	7.34	2.55	54.27	1.94	35.18	4.333	51.21	0.5390	6.28	11.57
13.0	0.867	15	6.70	2.62	47.08	1.85	32.01	4.652	57.20	2.2638	5.40	11.47
14.0	0.933	15	6.54	2.73	47.89	1.95	32.38	4.980	53.37	1.9502	5.46	11.40
15.0	1.000	15	6.32	2.86	44.35	1.76	30.72	5.593	55.09	1.1074	5.30	11.95

Table I 7. Welding conditions applied in the study of the effect of the CTWD and welding operation mode on the electrical transient (P12), alongside measured electrical responses.

CTWD (mm)	V_{AVG} (V)	I_{AVG} (A)	AIP (kW)	I_p (A)	I_b (A)	T_p (ms)	T_b (ms)	I_p/I_b	T_p/T_b	*f* (Hz)	LDC (%)	DR_{wire} (kg h^{-1})
10	20.57	94.47	2.30	312.66	33.61	4.31	5.31	9.30	0.81	103.97	44.84	1.378
11	20.80	92.67	2.27	311.54	33.85	4.39	5.19	9.20	0.85	104.38	45.82	1.356
12	20.54	94.87	2.31	310.92	33.44	4.27	5.11	9.30	0.84	106.59	45.56	1.389
13	20.56	92.18	2.26	310.25	34.03	4.31	5.31	9.12	0.81	103.97	44.84	1.387
14	20.77	85.82	2.15	310.00	34.05	4.24	6.45	9.10	0.66	93.57	39.64	1.384
15	20.74	84.31	2.12	314.17	34.24	4.47	6.37	9.18	0.70	92.25	41.20	1.383
16	20.75	82.18	2.08	312.69	33.71	4.50	7.10	9.28	0.63	86.18	38.82	1.383
17	20.71	79.61	2.03	313.56	33.84	4.50	7.82	9.26	0.58	81.12	36.53	1.376
18	20.72	77.90	2.00	313.58	34.03	4.58	7.94	9.21	0.58	79.88	36.59	1.380
19	21.36	77.44	2.05	308.33	33.86	4.20	8.57	9.10	0.49	78.30	32.88	1.380
20	22.24	77.43	2.13	311.42	34.04	4.31	8.47	9.15	0.51	78.21	33.73	1.371
21	23.07	77.42	2.20	304.40	33.67	4.16	8.63	9.04	0.48	78.21	32.54	1.373
22	23.88	77.42	2.27	313.13	33.89	4.20	8.59	9.24	0.49	78.21	32.84	1.380

CTWD, contact tip to work distance; V_{AVG} , I_{AVG} , AIP , average voltage, current, and power, respectively; I_p , pulse current; I_b , background current; T_p , duration of pulse current; T_b , duration of background current; *f,* frequency; *LDC*, load duty cycle; DR_{wire} , deposition rate calculated from the actual WFS and wire transverse cross section.

Table I 8. Welding conditions applied in the study of the effect of the CTWD and welding operation mode on the electrical transient (P12), alongside measured weld bead responses.

CTWD (mm)	TS (m min^{-1})	WFS/TS	W (mm)	H (mm)	RR (%)	P (mm)	D (%)	DR_{macro} (kg h^{-1})	CA_{avg} (º)	CI (95%)	A_1 (mm^2)	A_2 (mm^2)
10	0.40	15	5.81	1.84	38.84	1.41	27.98	1.393	51.19	2.0090	2.89	7.44
11	0.40	15	5.84	1.88	37.24	1.42	27.13	1.438	51.46	1.4602	2.86	7.68
12	0.40	15	5.89	1.81	38.43	1.41	27.76	1.408	49.60	3.9787	2.89	7.52
13	0.40	15	5.56	1.85	36.31	1.38	26.64	1.382	52.06	0.7252	2.68	7.38
14	0.40	15	5.46	2.02	32.77	1.28	24.68	1.428	53.84	1.8816	2.50	7.63
15	0.40	15	5.34	2.09	30.98	1.16	23.65	1.432	55.60	0.6174	2.37	7.65
16	0.40	15	5.36	2.06	29.40	1.14	22.72	1.445	55.37	3.1653	2.27	7.72
17	0.40	15	5.18	2.11	29.13	1.12	22.56	1.440	60.12	2.1070	2.24	7.69
18	0.40	15	5.06	2.12	28.51	1.06	22.19	1.411	61.22	3.4593	2.15	7.54
19	0.40	15	5.16	2.18	27.43	1.05	21.52	1.447	60.78	1.4308	2.12	7.73
20	0.40	15	5.18	2.11	28.00	1.04	21.88	1.404	59.72	0.5096	2.10	7.50
21	0.40	15	5.16	2.09	26.92	0.95	21.21	1.391	57.75	0.4802	2.00	7.43
22	0.40	15	5.10	2.13	22.22	0.86	18.18	1.398	58.11	5.4389	1.66	7.47

CTWD, contact tip to work distance; *TS*, travel speed, *WFS/TS*, wire feed speed to travel speed ratio; *W*, bead width; *H*, bead height; *RR*, remelting ratio; *P*, penetration; *D*, dilution; DR_{macro}, deposition rate calculated from the transverse macro section, CA_{avg}, average contact angle, *CI*, confidence interval of 95%, A_1, penetration cross section area; A_2, reinforcement cross section area.

Table I 9. Welding conditions applied in the study of the effect of the CTWD and welding operation mode on the electrical transient (P13), alongside measured electrical responses.

CTWD (mm)	V_{AVG} (V)	I_{AVG} (A)	AIP (kW)	I_p (A)	I_b (A)	T_p (ms)	T_b (ms)	I_p/I_b	T_p/T_b	*f* (Hz)	LDC (%)	DR_{wire} (kg h^{-1})
10	18.97	93.05	2.06	365.67	30.88	3.55	5.34	11.84	0.66	112.45	39.91	1.381
11	19.71	87.49	2.04	363.88	30.42	3.55	5.23	11.96	0.68	113.91	40.43	1.378
12	20.30	85.74	2.10	365.27	29.96	3.51	5.15	12.19	0.68	115.42	40.53	1.376
13	20.94	85.84	2.18	363.25	30.17	3.55	5.11	12.04	0.69	115.42	40.97	1.376
14	21.85	85.76	2.27	364.42	30.13	3.51	5.19	12.10	0.68	114.91	40.35	1.378
15	22.46	85.58	2.33	362.77	30.36	3.51	5.19	11.95	0.68	114.91	40.35	1.376
16	23.12	85.65	2.40	364.77	30.26	3.55	5.19	12.05	0.68	114.41	40.59	1.369
17	23.84	85.54	2.47	367.04	30.43	3.58	5.16	12.06	0.69	114.41	40.93	1.369
18	24.57	85.59	2.54	362.46	30.22	3.55	5.19	11.99	0.68	114.41	40.61	1.370
19	25.51	85.59	2.62	363.81	30.33	3.47	5.23	11.99	0.66	114.91	39.91	1.363
20	25.89	85.53	2.65	364.42	30.19	3.57	5.13	12.07	0.69	114.91	41.00	1.361

Table I 10. Welding conditions applied in the study of the effect of the CTWD and welding operation mode on the electrical transient (P13), alongside measured weld bead responses.

CTWD (mm)	TS (m min^{-1})	WFS/TS	W (mm)	H (mm)	RR (%)	P (mm)	D (%)	DR_{macro} (kg h^{-1})	CA_{avg} (º)	CI (95%)	A_1 (mm^2)	A_2 (mm^2)
10	0.40	15	6.18	1.99	27.47	1.10	21.55	1.499	44.62	0.6958	2.2	8.01
11	0.40	15	5.49	2.04	28.26	1.14	22.03	1.464	55.06	2.3618	2.21	7.82
12	0.40	15	5.16	2.05	29.37	1.17	22.70	1.434	56.42	1.4700	2.25	7.66
13	0.40	15	5.28	2.09	28.65	1.19	22.27	1.451	56.52	1.0094	2.22	7.75
14	0.40	15	5.28	2.10	28.19	1.15	21.99	1.455	56.81	1.9502	2.19	7.77
15	0.40	15	5.14	2.10	28.22	1.18	22.01	1.440	58.67	1.5190	2.17	7.69
16	0.40	15	5.02	2.15	28.09	1.16	21.93	1.440	60.89	2.2442	2.16	7.69
17	0.40	15	4.90	2.23	25.06	1.12	20.04	1.449	61.57	2.1168	1.94	7.74
18	0.40	15	4.60	2.24	24.56	1.06	19.72	1.387	63.15	0.2254	1.82	7.41
19	0.40	15	4.58	2.28	23.87	1.05	19.27	1.411	62.25	4.9587	1.8	7.54
20	0.40	15	4.73	2.20	22.24	1.02	18.19	1.389	62.78	1.0094	1.65	7.42

Table I 11. Welding conditions applied in the study of the effect of the CTWD and welding operation mode on the electrical transient (P14), alongside measured electrical responses.

CTWD (mm)	V_{AVG} (V)	I_{AVG} (A)	AIP (kW)	I_p (A)	I_b (A)	T_p (ms)	T_b (ms)	I_p/I_b	T_p/T_b	*f* (Hz)	LDC (%)	DR_{wire} (kg h^{-1})
10	20.36	96.68	2.34	370.44	42.98	4.43	7.18	8.62	0.62	86.18	38.16	1.372
11	20.49	94.23	2.30	367.71	42.51	4.43	7.48	8.65	0.59	83.98	37.18	1.366
12	20.58	92.08	2.26	366.08	41.52	4.47	7.67	8.82	0.58	82.39	36.79	1.363
13	20.71	89.87	2.22	363.71	41.69	4.35	8.17	8.72	0.53	79.88	34.76	1.363
14	20.91	87.00	2.18	363.27	41.07	4.35	8.47	8.84	0.51	77.98	33.93	1.355
15	20.95	84.87	2.14	361.85	39.96	4.39	9.01	9.06	0.49	74.64	32.76	1.356
16	20.97	83.01	2.10	359.58	39.80	4.31	9.35	9.03	0.46	73.19	31.56	1.356
17	20.78	80.53	2.04	358.00	39.85	4.24	9.58	8.98	0.44	72.37	30.66	1.344
18	20.85	79.08	2.01	358.98	38.56	4.16	9.85	9.31	0.42	71.39	29.70	1.345
19	21.95	78.46	2.10	357.40	39.30	4.16	10.11	9.09	0.41	70.05	29.14	1.357
20	22.36	78.52	2.14	354.08	39.13	4.12	10.11	9.05	0.41	70.24	28.95	1.382
21	23.28	78.47	2.22	353.81	38.90	4.11	10.09	9.10	0.41	70.43	28.97	1.380
22	23.90	78.40	2.27	359.08	38.78	4.12	10.04	9.26	0.41	70.62	29.11	1.371

Table I 12. Welding conditions applied in the study of the effect of the CTWD and welding operation mode on the electrical transient (P14), alongside measured weld bead responses.

CTWD (mm)	TS (m min^{-1})	WFS/TS	W (mm)	H (mm)	RR (%)	P (mm)	D (%)	DR_{macro} (kg h^{-1})	CA_{avg} (º)	CI (95%)	A_1 (mm^2)	A_2 (mm^2)
10	0.40	15	6.35	1.76	44.03	1.37	30.57	1.411	43.55	4.6941	3.32	7.54
11	0.40	15	6.25	1.87	41.98	1.27	29.57	1.400	44.38	0.0882	3.14	7.48
12	0.40	15	6.00	1.94	37.68	1.24	27.37	1.436	49.12	0.4214	2.89	7.67
13	0.40	15	5.94	1.96	36.06	1.26	26.50	1.443	50.31	0.5880	2.78	7.71
14	0.40	15	5.66	2.05	33.59	1.22	25.14	1.460	55.17	1.2054	2.62	7.80
15	0.40	15	5.65	2.03	32.69	1.19	24.64	1.455	53.72	0.8330	2.54	7.77
16	0.40	15	5.57	2.06	32.31	1.17	24.42	1.460	58.38	2.7146	2.52	7.80
17	0.40	15	5.00	2.25	28.52	1.11	22.19	1.477	62.63	2.8125	2.25	7.89
18	0.40	15	4.90	2.19	26.47	1.06	20.93	1.436	65.07	0.0784	2.03	7.67
19	0.40	15	4.87	2.23	25.00	1.02	20.00	1.430	65.78	1.2152	1.91	7.64
20	0.40	15	5.22	2.31	23.81	1.05	19.23	1.494	59.32	0.7056	1.90	7.98
21	0.40	15	4.66	2.23	23.17	0.90	18.81	1.382	63.66	0.6272	1.71	7.38
22	0.40	15	4.85	2.20	21.94	0.86	17.99	1.408	63.96	3.5769	1.65	7.52

Table I 13. Welding conditions applied in the study of the effect of the CTWD and welding operation mode on the electrical transient (P95), alongside measured electrical responses.

CTWD (mm)	V_{AVG} (V)	I_{AVG} (A)	AIP (kW)	I_p (A)	I_b (A)	T_p (ms)	T_b (ms)	I_p/I_b	T_p/T_b	*f* (Hz)	LDC (%)	DR_{wire} (kg h^{-1})
10	19.75	96.00	2.18	330.60	35.54	4.27	3.97	9.30	1.08	121.30	51.85	1.359
11	20.20	92.65	2.17	321.33	35.13	4.05	4.50	9.15	0.90	116.96	47.32	1.358
12	20.45	89.62	2.14	319.46	35.36	4.05	4.73	9.03	0.85	113.91	46.09	1.355
13	20.59	86.60	2.09	315.44	35.17	4.05	5.15	8.97	0.79	108.71	43.98	1.360
14	20.64	84.80	2.06	309.85	35.27	4.05	5.42	8.78	0.75	105.65	42.74	1.353
15	20.80	82.64	2.04	302.29	34.53	4.05	5.57	8.75	0.73	103.97	42.06	1.343
16	20.92	80.59	2.00	295.63	33.60	4.08	5.73	8.80	0.71	101.95	41.63	1.343
17	20.99	78.74	1.97	291.92	33.03	4.05	6.15	8.84	0.66	98.13	39.70	1.343
18	20.96	77.05	1.94	287.36	33.02	4.05	6.37	8.70	0.63	95.97	38.83	1.347
19	20.95	75.44	1.90	285.36	32.39	4.08	6.45	8.81	0.63	94.93	38.77	1.343
20	21.01	73.87	1.88	280.60	32.72	4.05	6.76	8.58	0.60	92.58	37.45	1.341
21	21.08	72.43	1.85	275.48	31.70	4.05	6.99	8.69	0.58	90.65	36.68	1.345
22	21.16	70.61	1.82	271.94	31.78	4.05	7.21	8.56	0.56	88.81	35.93	1.337

Table I 14. Welding conditions applied in the study of the effect of the CTWD and welding operation mode on the electrical transient (P95), alongside measured weld bead responses.

CTWD (mm)	TS (m min^{-1})	WFS/TS	W (mm)	H (mm)	RR (%)	P (mm)	D (%)	DR_{macro} (kg h^{-1})	CA_{avg} (º)	CI (95%)	A_1 (mm^2)	A_2 (mm^2)
10	0.40	15	5.95	1.87	32.28	1.05	24.40	1.415	45.59	2.5970	2.44	7.56
11	0.40	15	5.88	1.85	32.12	1.08	24.31	1.387	48.35	4.3021	2.38	7.41
12	0.40	15	6.00	1.91	30.81	1.16	23.55	1.434	46.55	0.7154	2.36	7.66
13	0.40	15	5.28	2.00	30.91	1.17	23.61	1.417	55.77	0.4410	2.34	7.57
14	0.40	15	5.43	2.00	30.38	1.13	23.30	1.436	52.85	1.6170	2.33	7.67
15	0.40	15	5.44	2.04	29.59	1.14	22.83	1.468	55.81	1.5582	2.32	7.84
16	0.40	15	5.37	2.06	28.76	1.10	22.33	1.445	56.52	0.4018	2.22	7.72
17	0.40	15	5.34	2.14	27.81	1.08	21.76	1.447	58.59	0.5684	2.15	7.73
18	0.40	15	5.22	2.12	27.64	1.04	21.65	1.436	61.02	1.9306	2.12	7.67
19	0.40	15	5.15	2.17	26.65	1.00	21.04	1.475	59.32	2.8125	2.10	7.88
20	0.40	15	5.08	2.18	25.80	0.98	20.51	1.458	60.28	3.4103	2.01	7.79
21	0.40	15	4.84	2.13	25.68	0.96	20.43	1.385	63.20	3.6063	1.90	7.40
22	0.40	15	4.94	2.20	24.04	0.88	19.38	1.417	62.48	2.9889	1.82	7.57

Table I 15. Welding conditions applied in the study of the effect of the WFS on the electrical transient (P12), alongside measured weld bead responses.

WFS_{set} (m min^{-1})	WFS_{actual} (m min^{-1})	V_{AVG} (V)	I_{AVG} (A)	AIP (kW)	I_p (A)	I_b (A)	T_p (ms)	T_b (ms)	I_p/I_b	T_p/T_b	*f* (Hz)	LDC (%)	DR_{wire} (kg h^{-1})
2.0	1.977	21.55	36.11	0.91	251.69	20.69	5.51	36.94	12.17	0.15	23.56	12.97	0.465
4.0	3.832	21.01	54.28	1.47	286.56	22.26	4.31	15.00	12.87	0.29	51.78	22.33	0.902
6.0	5.784	23.01	76.59	2.17	307.71	33.10	4.20	8.55	9.30	0.49	78.44	32.93	1.361
8.0	7.789	25.36	100.31	3.00	348.83	50.55	3.97	7.07	6.90	0.56	90.65	35.95	1.832
10.0	9.793	26.56	116.67	3.69	399.50	59.55	3.78	6.22	6.71	0.61	100.00	37.79	2.304

WFS_{set} , WFS_{actual} , wire feed speed setting and actual; V_{AVG} , I_{AVG} , AIP , instantaneous voltage, current and power, respectively; I_p , pulse current; I_b , background current; T_p , duration of pulse current; T_b , duration of background current; *f,* frequency; *LDC*, load duty cycle; DR_{wire} , deposition rate calculated from the actual WFS and wire transverse cross section.

Table I 16. Welding conditions employed in study (S_1) of the effect of the waveform on the bead surface quality and process stability (*non-adaptive control* mode).

Study (S_x)	Trial No.	I_p (A)	T_p (ms)	I_p/T_p	I_b (A)	T_b (ms)	LDC (%)	$I_p \times T_p$ (A ms)	$I_b \times T_b$ (A ms)	I_{AVG} (A)	*f* (Hz)
	1	200	1.75	114.29	42	4.50	28.00				
	2	240	1.46	164.57	39	4.79	23.33				
S_1	3	280	1.25	224.00	38	5.00	20.00	350.00	188.12	86.10	110.50
	4	320	1.09	292.57	36	5.16	17.50				
	5	360	0.97	370.29	36	5.28	15.56				

Note: Some of the values can be limited to one decimal place by the Wave Designer Pro ™ interface software.

Table I 17. Welding conditions employed in study (S_2) of the effect of the waveform on the bead surface quality and process stability (*non-adaptive control* mode).

Study (S_x)	Trial No.	I_p (A)	T_p (ms)	I_b (A)	T_b (ms)	T_p/T_b	LDC (%)	$I_p \times T_p$ (A ms)	$I_b \times T_b$ (A ms)	I_{AVG} (A)	*f* (Hz)
	1		1.75	11	4.50	0.39	28.00	490.00	48.13		
	2		1.46	27	4.79	0.30	23.33	408.33	129.79		
S_2	3	280	1.25	38	5.00	0.25	20.00	350.00	188.12	86.10	110.50
	4		1.09	45	5.16	0.21	17.50	306.25	231.87		
	5		0.97	50	5.28	0.18	15.52	271.60	266.53		

Table I 18. Welding conditions employed in study (S_3) of the effect of the waveform on the bead surface quality and process stability (*non-adaptive control* mode).

Study (S_x)	Trial No.	I_p (A)	T_p (ms)	I_b (A)	T_b (ms)	I_p/I_b	LDC (%)	$I_p \times T_p$ (A ms)	$I_b \times T_b$ (A ms)	I_{AVG} (A)	*f* (Hz)
	1	200		58		3.47		250.00	288.12		
	2	240		48		5.04		300.00	238.12		
S_3	3	280	1.25	38	5.00	7.44	20.00	350.00	188.12	86.10	110.50
	4	320		28		11.58		400.00	138.13		
	5	360		18		20.43		450.00	88.13		

Table I 19. Welding conditions employed in study (S_4) of the effect of the waveform on the bead surface quality and process stability (*non-adaptive control* mode).

Study (S_x)	Trial No.	I_p (A)	T_p (ms)	I_b (A)	T_b (ms)	$f./T_b$	LDC (%)	$I_p \times T_p$ (A ms)	$I_b \times T_b$ (A ms)	I_{AVG} (A)	f (Hz)
	1			45	5.89	17.07	17.50		265.00		100.57
	2			41	5.42	19.50	18.75		224.00		105.63
S_4	3	280	1.25	38	5.00	22.10	20.00	350.00	188.12	86.10	110.50
	4			34	4.63	24.86	21.25		156.47		115.18
	5			30	4.31	27.80	22.50		128.33		119.68

Table I 20. Welding conditions employed in study (S_5) of the effect of the waveform on the bead surface quality and process stability (*non-adaptive control* mode).

Study (S_x)	Trial No.	I_p (A)	T_p (ms)	I_b (A)	T_b (ms)	$f./T_p$	LDC (%)	$I_p \times T_p$ (A ms)	$I_b \times T_b$ (A ms)	I_{AVG} (A)	f (Hz)
	1		1.42		5.67	71.36		396.88	213.32		101.14
	2		1.35		5.42	77.16		379.16	203.81		104.48
S_5	3	280	1.25	38	5.00	88.40	20.00	350.00	188.12	86.10	110.50
	4		1.16		4.63	100.52		324.27	174.29		116.41
	5		1.08		4.31	113.55		301.39	162.00		122.22

Table I 21. Welding conditions used in the study of the effect of ALC on the electrical transients and bead profiles (study ALC using CMT).

Study (ALC)	V_{AVG} (V)	I_{AVG} (A)	P_{AVG} (kW)	HI (J mm^{-1})	W (mm)	H (mm)	RR (%)	P (mm)	D (%)	CA (º)	CI (95%)	A_1 (mm^2)	A_2 (mm^2)	DR (kg h^{-1})
-30	9.78	136.75	1.34	180.63	4.91	2.31	13.57	0.60	11.95	69.53	2.60	1.11	8.18	1.46
-20	10.48	141.31	1.48	199.98	5.03	2.41	18.10	0.79	15.33	66.27	1.18	1.60	8.84	1.53
-10	11.20	145.36	1.63	219.78	5.61	2.35	24.72	1.03	19.82	59.58	3.55	2.19	8.86	1.58
0	12.00	148.64	1.78	240.78	6.03	2.15	23.42	1.02	18.98	57.81	4.32	2.23	9.52	1.63
10	12.37	152.86	1.89	255.20	6.25	2.14	29.43	1.18	22.74	57.69	4.64	2.84	9.65	1.65
20	13.51	155.78	2.11	284.20	6.47	2.35	29.54	1.21	22.80	59.84	4.16	3.09	10.46	1.70
30	14.99	150.99	2.26	305.54	6.69	2.18	32.07	1.38	24.28	53.36	1.88	3.30	10.29	1.75

V_{AVG}, averaged voltage; I_{AVG}, averaged current; P_{AVG}, averaged power; *HI*, heat input (η=0.9); *W*, bead width; *H*, bead height; *RR*, remelting ratio; *P*, penetration; *D*, dilution; CA_{avg}, averaged contact angle, *CI*, confidence interval of 95%, A_1, penetration cross section area; A_2, reinforcement cross section area; *DR*, wire deposition rate taken from WFS_{actual}.

Table I 22. Welding conditions used in study of the effect of DC_{corr} on the electrical transient and bead profiles (study DC_{corr} using CMT).

Study (DC_{corr})	V_{AVG} (V)	I_{AVG} (A)	P_{AVG} (kW)	HI (J mm^{-1})	W (mm)	H (mm)	RR (%)	P (mm)	D (%)	CA (º)	CI (95%)	A_1 (mm^2)	A_2 (mm^2)	DR (kg h^{-1})
-5	12.16	155.60	1.89	255.40	6.28	2.19	24.80	1.11	19.87	62.37	1.24	2.52	10.16	1.70
-3	12.10	153.05	1.85	250.09	6.11	2.27	22.72	1.06	18.51	62.91	5.27	2.29	10.08	1.68
-2	12.06	150.96	1.82	245.78	6.12	2.23	24.52	1.10	19.69	61.63	1.84	2.44	9.95	1.66
0	12.00	148.64	1.78	240.78	6.03	2.15	23.42	1.02	18.98	57.81	4.32	2.23	9.52	1.63
2	11.90	144.69	1.72	232.52	6.03	2.20	24.50	1.08	19.68	57.40	0.13	2.31	9.43	1.60
3	11.80	144.08	1.70	229.51	5.99	2.10	24.24	1.09	19.51	57.64	1.89	2.23	9.20	1.59
5	11.85	140.08	1.66	224.07	6.01	2.21	24.86	1.06	19.91	56.44	0.80	2.28	9.17	1.57

Table I 23. Welding conditions used in study of the effect of CTWD on the electrical transient and bead profiles (study CTWD using CMT).

Study (CTWD)	V_{AVG} (V)	I_{AVG} (A)	P_{AVG} (kW)	HI (J mm^{-1})	W (mm)	H (mm)	RR (%)	P (mm)	D (%)	CA (º)	CI (95%)	A_1 (mm^2)	A_2 (mm^2)	DR (kg h^{-1})
10	11.62	146.34	1.70	229.51	5.87	2.05	24.27	0.97	19.53	60.32	2.50	2.00	8.24	1.56
11	11.84	146.08	1.73	233.41	5.97	2.13	26.39	0.99	20.88	51.16	0.11	2.18	8.26	1.57
12	12.05	145.05	1.75	235.87	6.08	2.13	22.89	0.96	18.63	54.38	2.14	2.09	9.13	1.63
13	12.10	146.64	1.77	239.50	6.06	2.27	18.86	0.92	15.87	63.31	8.20	1.92	10.18	1.70
14	12.33	145.70	1.80	242.57	6.21	2.35	18.83	0.97	15.85	63.72	7.93	2.03	10.78	1.74
15	12.40	146.49	1.82	245.27	6.19	2.44	20.09	0.98	16.73	66.08	7.53	2.22	11.05	1.77
16	12.53	148.39	1.86	251.10	6.00	2.40	22.29	1.08	18.23	68.21	4.33	2.39	10.72	1.81
17	12.63	148.05	1.87	252.37	6.29	2.33	23.79	1.15	19.22	61.39	8.17	2.55	10.72	1.83
18	12.75	147.92	1.89	254.58	6.19	2.42	23.15	1.07	18.80	63.11	6.98	2.53	10.93	1.87

Table I 24. Welding conditions employed in study of the effect of the shielding gas on electrical transients (CMT).

Study	Shielding gas	Trial No.	WFS_{set} (m min^{-1})	WFS_{actual} (m min^{-1})	V_{AVG} (V)	I_{AVG} (A)	AIP (kW)	DR (kg h^{-1})	HI (J mm^{-1})
G_1	Ar/ CO_2(8%)	1	4	3.06	9.49	68.37	0.80	0.72	107.71
		2	6	4.77	10.55	86.00	1.24	1.12	166.90
		3	8	6.05	11.22	100.02	1.61	1.42	217.33
		4	10	7.60	12.66	120.74	2.10	1.79	283.41
		5	12	8.93	13.91	141.53	2.57	2.10	347.04
G_2	Ar/ CO_2(20%)	1	4	2.95	10.45	66.35	0.87	0.70	117.23
		2	6	4.77	11.72	87.19	1.39	1.12	187.70
		3	8	6.22	12.51	100.21	1.81	1.46	243.93
		4	10	7.70	14.00	122.45	2.35	1.81	317.29
		5	12	9.21	15.24	137.18	2.77	2.17	374.47
G_3	Ar/CO_2(20%)/ O_2(2%)	1	4	3.11	9.21	67.07	0.77	0.73	103.39
		2	6	4.50	10.06	82.72	1.15	1.06	154.90
		3	8	6.14	10.85	99.74	1.55	1.44	209.24
		4	10	7.72	12.49	120.50	2.06	1.82	278.14
		5	12	8.97	13.76	140.71	2.53	2.11	341.04

Appendix J – Power Wave® 455/STT database of programs

Power Wave 455M/STT

Weld Set Reference: Z051971i

Stainless

Procedure	Gas Type	Mode
.030 Wire Size		
CV	Argon Mix	61
CV	He Ar CO_2	63
Pulse	He Ar CO_2	64
Pulse	Argon CO_2	66
Pulse	Argon O_2	62
.035 Wire Size		
CV	Argon Mix	31
CV	He Ar CO_2	33
Pulse	He Ar CO_2	34
Pulse	Argon CO_2	36
Pulse	Argon O_2	32
STT	Argon CO_2	131
STT	He Ar CO_2	127
STT Open Root	He Ar CO_2	135
.045 Wire Size		
CV	Argon Mix	41
CV	He Ar CO_2	43
Pulse	He Ar CO_2	44
Pulse	Argon CO_2	46
Pulse	Argon O_2	42
STT	Argon CO_2	133
STT	He Ar CO_2	129
STT Open Root	He Ar CO_2	137

Steel

Procedure	Gas Type	Mode
.030 Wire Size		
CV	CO_2	93
CV	Argon Mix	94
Pulse	Argon Mix	95
.035 Wire Size		
CV	CO_2	10
CV	Argon Mix	11
Pulse Crisp	Argon Mix	12
Pulse Soft	Argon Mix	14
Pulse RapidArc	Argon CO_2	13
STT	Argon CO_2	112
STT	CO_2	111
STT Open Root	CO_2	113
.045 Wire Size		
CV	CO_2	20
CV	Argon Mix	21
Pulse Crisp	Argon Mix	22
Pulse Soft	Argon Mix	19
Pulse RapidArc	Argon CO2	18
STT	Argon CO_2	118
STT	CO_2	117
STT Open Root	CO_2	119

Steel

Procedure	Gas Type	Mode
.052 Wire Size		
CV	CO_2	24
CV	Argon Mix	25
Pulse Crisp	Argon Mix	26
Pulse Soft	Argon Mix	28
Pulse RapidArc	Argon CO_2	27
STT	Argon CO_2	121
STT	CO_2	120
STT Open Root	CO_2	122
1/16 Wire Size		
CV	Argon Mix	107
Pulse	Argon Mix	108

General

Stick/Tig/Gouge		
Stick Soft		1
Stick Crisp		2
Touch Start TIG	Argon	3
Gouging		9
Wire Welding (Non Synergic)		
CV MIG		5
FCAW-SS	Self Shielded	6
Power mode		40

Non Synergic STT II	≤.035	≥.045
STT II (No Tailout)	109	125
STT II (w/ Tailout)	110	126
STT II (w/ Hot Start)	123	124

Aluminum 4043

Procedure	Gas Type	Mode
.035 Wire Size		
CV	Argon	148
Pulse	Argon	149
Pulse on Pulse	Argon	98
3/64 Wire Size		
CV	Argon	71
Pulse	Argon	72
Pulse on Pulse	Argon	99
1/16 Wire Size		
CV	Argon	73
Pulse	Argon	74
Pulse on Pulse	Argon	100

Flux Core

Procedure	Gas Type	Mode
.045 Wire Size		
CV	CO_2	90
CV	Argon CO_2	91

Metal Core

Procedure	Gas Type	Mode
.045 Wire Size		
CV	Argon CO_2	81
Pulse	Argon CO_2	82
Pulse RapidArc	Argon CO_2	87
.052 Wire Size		
CV	Argon CO_2	83
Pulse	Argon CO_2	84
Pulse RapidArc	Argon CO_2	88
1/16 Wire Size		
CV	Argon CO_2	85
Pulse	Argon CO_2	86
Pulse RapidArc	Argon CO_2	89

Aluminum 5356

Procedure	Gas Type	Mode
.035 Wire Size		
CV	Argon	151
Pulse	Argon	152
Pulse on Pulse	Argon	101
3/64 Wire Size		
CV	Argon	75
Pulse	Argon	76
Pulse on Pulse	Argon	102
1/16 Wire Size		
CV	Argon	77
Pulse	Argon	78
Pulse on Pulse	Argon	103

Silicon Bronze

Procedure	Gas Type	Mode
.035 Wire Size		
Pulse	Argon	192

Nickel Alloy

Procedure	Gas Type	Mode
.035 Wire Size		
Pulse	Ar He	170
.045 Wire Size		
Pulse	Ar He	175

LINCOLN® ELECTRIC
THE WELDING EXPERTS

CONTENTS OF WELDING SOFTWARE Z051971i

Mode	Process	Procedure	Wire Size	Wire Type	Gas Type	ArcControl	
1	SMAW	Stick Soft				Arc Force	N.A.
2	SMAW	Stick Crisp				Arc Force	N.A.
3	GTAW	Touch Start TIG			Argon	n/a	N.A.
5	GMAW	CV MIG (Non Syn)				Pinch	N.A.
6	FCAW-S	FCAW-SS (Non Syn)			Self Shielded	Pinch	N.A.
9	GOUGING	Gouging				Arc Force	N.A.
10	GMAW	CV	0.035	Steel	CO2	Pinch	
11	GMAW	CV	0.035	Steel	Argon Blends	Pinch	
12	GMAW-P	Pulse - Crisp	0.035	Steel	Argon Blends	Wave Control	
13	GMAW-P	Pulse - RapidArc	0.035	Steel	Argon CO2	Wave Control	
14	GMAW-P	Pulse - Soft	0.035	Steel	Argon Blends	Wave Control	
18	GMAW-P	Pulse - RapidArc	0.045	Steel	Argon CO2	Wave Control	
19	GMAW-P	Pulse - Soft	0.045	Steel	Argon Blends	Wave Control	
20	GMAW	CV	0.045	Steel	CO2	Pinch	
21	GMAW	CV	0.045	Steel	Argon Blends	Pinch	
22	GMAW-P	Pulse - Crisp	0.045	Steel	Argon Blends	Wave Control	
24	GMAW	CV	0.052	Steel	CO2	Pinch	
25	GMAW	CV	0.052	Steel	Argon Blends	Pinch	
26	GMAW-P	Pulse - Crisp	0.052	Steel	Argon Blends	Wave Control	
27	GMAW-P	Pulse - RapidArc	0.052	Steel	Argon CO2	Wave Control	
28	GMAW-P	Pulse - Soft	0.052	Steel	Argon Blends	Wave Control	
31	GMAW	CV	0.035	Stainless	Argon Blends	Pinch	
32	GMAW-P	Pulse	0.035	Stainless	Argon Oxy	Wave Control	
33	GMAW	CV	0.035	Stainless	He Ar CO2	Pinch	
34	GMAW-P	Pulse	0.035	Stainless	He Ar CO2	Wave Control	
36	GMAW-P	Pulse	0.035	Stainless	Argon CO2	Wave Control	
40	GMAW	Power Mode (Non Syn)				Pinch	N.A.
41	GMAW	CV	0.045	Stainless	Argon Blends	Pinch	
42	GMAW-P	Pulse	0.045	Stainless	Argon Oxy	Wave Control	
43	GMAW	CV	0.045	Stainless	He Ar CO2	Pinch	
44	GMAW-P	Pulse	0.045	Stainless	He Ar CO2	Wave Control	
46	GMAW-P	Pulse	0.045	Stainless	Argon CO2	Wave Control	
61	GMAW	CV	0.030	Stainless	Argon Blends	Pinch	
62	GMAW-P	Pulse	0.030	Stainless	Argon Oxy	Wave Control	
63	GMAW	CV	0.030	Stainless	He Ar CO2	Pinch	
64	GMAW-P	Pulse	0.030	Stainless	He Ar CO2	Wave Control	
66	GMAW-P	Pulse	0.030	Stainless	Argon CO2	Wave Control	
71	GMAW	CV	3/64	Aluminum 4043	Argon	Pinch	
72	GMAW-P	Pulse	3/64	Aluminum 4043	Argon	Wave Control	
73	GMAW	CV	1/16	Aluminum 4043	Argon	Pinch	
74	GMAW-P	Pulse	1/16	Aluminum 4043	Argon	Wave Control	
75	GMAW	CV	3/64	Aluminum 5356	Argon	Pinch	
76	GMAW-P	Pulse	3/64	Aluminum 5356	Argon	Wave Control	
77	GMAW	CV	1/16	Aluminum 5356	Argon	Pinch	
78	GMAW-P	Pulse	1/16	Aluminum 5356	Argon	Wave Control	
81	GMAW	CV	0.045	Metal Core	Argon CO2	Pinch	
82	GMAW-P	Pulse	0.045	Metal Core	Argon CO2	Wave Control	
83	GMAW	CV	0.052	Metal Core	Argon CO2	Pinch	
84	GMAW-P	Pulse	0.052	Metal Core	Argon CO2	Wave Control	
85	GMAW	CV	1/16	Metal Core	Argon CO2	Pinch	
86	GMAW-P	Pulse	1/16	Metal Core	Argon CO2	Wave Control	
87	GMAW-P	Pulse - RapidArc	0.045	Metal Core	Argon CO2	Wave Control	
88	GMAW-P	Pulse - RapidArc	0.052	Metal Core	Argon CO2	Wave Control	
89	GMAW-P	Pulse - RapidArc	1/16	Metal Core	Argon CO2	Wave Control	
90	FCAW-GS	CV	0.045	Outershield	CO2	Pinch	
91	FCAW-GS	CV	0.045	Outershield	Argon CO2	Pinch	
93	GMAW	CV	0.03	Steel	CO2	Pinch	
94	GMAW	CV	0.030	Steel	Argon Blends	Pinch	
95	GMAW-P	Pulse	0.030	Steel	Argon Blends	Wave Control	

Mode	Process	Procedure	Wire Size	Wire Type	Gas Type	ArcControl	
98	GMAW-P	Pulse on Pulse	0.035	Aluminum 4043	Argon	Modulation Freq	
99	GMAW-P	Pulse on Pulse	3/64	Aluminum 4043	Argon	Modulation Freq	
100	GMAW-P	Pulse on Pulse	1/16	Aluminum 4043	Argon	Modulation Freq	
101	GMAW-P	Pulse on Pulse	0.035	Aluminum 5356	Argon	Modulation Freq	
102	GMAW-P	Pulse on Pulse	3/64	Aluminum 5356	Argon	Modulation Freq	
103	GMAW-P	Pulse on Pulse	1/16	Aluminum 5356	Argon	Modulation Freq	
107	GMAW	CV	1/16	Steel	Argon Blends	Pinch	
108	GMAW-P	Pulse - Crisp	1/16	Steel	Argon Blends	Wave Control	
109	GMAW	STT II (No Tailout)	<=.035	Steel/Stainless	CO_2, $ArCO_2$, $HeArCO_2$	STT II Controls	N.A., N.B.
110	GMAW	STT II (w/ Tailout)	<=.035	Steel/Stainless	CO_2, $ArCO_2$, $HeArCO_2$	STT II Controls	N.A., N.B.
111	GMAW	STT	0.035	Steel	CO2	Peak	N.C.
112	GMAW	STT	0.035	Steel	Argon CO2	Peak	N.C.
113	GMAW	STT- Open Root	0.035	Steel	CO2	Peak	N.C.
117	GMAW	STT	0.045	Steel	CO2	Peak	N.C.
118	GMAW	STT	0.045	Steel	Argon CO2	Peak	N.C.
119	GMAW	STT- Open Root	0.045	Steel	CO2	Peak	N.C.
120	GMAW	STT	0.052	Steel	CO2	Peak	N.C.
121	GMAW	STT	0.052	Steel	Argon CO2	Peak	N.C.
122	GMAW	STT- Open Root	0.052	Steel	CO2	Peak	N.C.
123	GMAW	STT II (w/ Hot Start)	<=.035	Steel/Stainless	CO_2, $ArCO_2$, $HeArCO_2$	STT II Controls	N.A., N.B., N.D.
124	GMAW	STT II (w/ Hot Start)	>=.045	Steel/Stainless	CO_2, $ArCO_2$, $HeArCO_2$	STT II Controls	N.A., N.B., N.D.
125	GMAW	STT II (No Tailout)	>=.045	Steel/Stainless	CO_2, $ArCO_2$, $HeArCO_2$	STT II Controls	N.A., N.B.
126	GMAW	STT II (w/ Tailout)	>=.045	Steel/Stainless	CO_2, $ArCO_2$, $HeArCO_2$	STT II Controls	N.A., N.B.
127	GMAW	STT	0.035	Stainless	He Ar CO2	Peak	N.C.
129	GMAW	STT	0.045	Stainless	He Ar CO2	Peak	N.C.
131	GMAW	STT	0.035	Stainless	Argon CO2	Peak	N.C.
133	GMAW	STT	0.045	Stainless	Argon CO2	Peak	N.C.
135	GMAW	STT- Open Root	0.035	Stainless	He Ar CO2	Peak	N.C.
137	GMAW	STT- Open Root	0.045	Stainless	He Ar CO2	Peak	N.C.
148	GMAW	CV	0.035	Aluminum 4043	Argon	Pinch	
149	GMAW-P	Pulse	0.035	Aluminum 4043	Argon	Wave Control	
151	GMAW	CV	0.035	Aluminum 5356	Argon	Pinch	
152	GMAW-P	Pulse	0.035	Aluminum 5356	Argon	Wave Control	
170	GMAW-P	Pulse - Non Adaptive	0.035	Ni Alloy	Argon Helium	Wave Control	
175	GMAW-P	Pulse - Non Adaptive	0.045	Ni Alloy	Argon Helium	Wave Control	
192	GMAW-P	Pulse	0.035	Si Bronze	Argon	Wave Control	

Notes: All GMAW-P procedures accept Trim input of 1.00 ± 0.50 (2 decimal places)
This may require resetting the weld mode with Fanuc robots or rescaling Trim input from PLC programs when updating from earlier weld sets.

N.A. May not be available on machines equipped with analog interface.
Not fully supported by Fanuc/DeviceNet implementation.

N.B. Peak, Background, Tailout and Hot Start set via Wave Controls 1-4 in STT II procedures.
Not supported by semi-automatic feeders with MSP3 panel or PF15M.

N.C. Trim adjusts background current and Wave Control 1 adjusts peak current in synergic STT procedures.

N.D. Not supported by Fanuc/ArcLink implementation prior to Fanuc ArcTool Version 6.4.

THE LINCOLN ELECTRIC COMPANY
World's Leader in Welding and Cutting Products
Sales and Service through Subsidiaries and Distributors Worldwide
Cleveland, Ohio 44117-1199 U.S.A.

Appendix K – HV microstructural inspection of macrosections

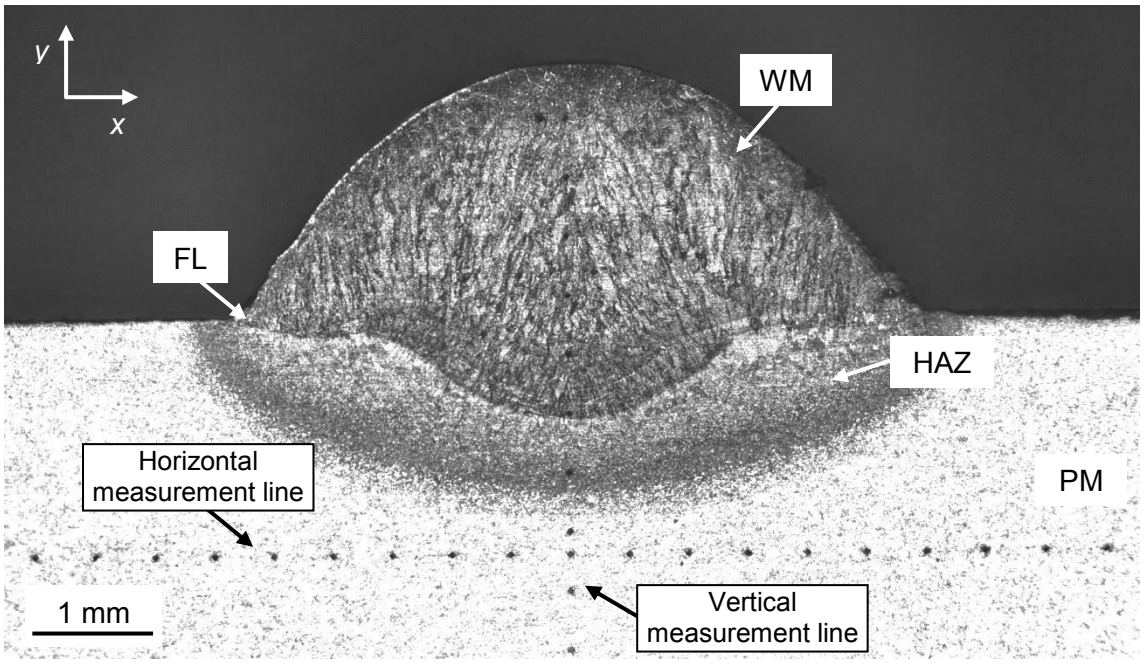

Figure K 1. Transverse macro-photograph of *specimen 1 layer* showing horizontal and vertical HV indentation measurement lines.

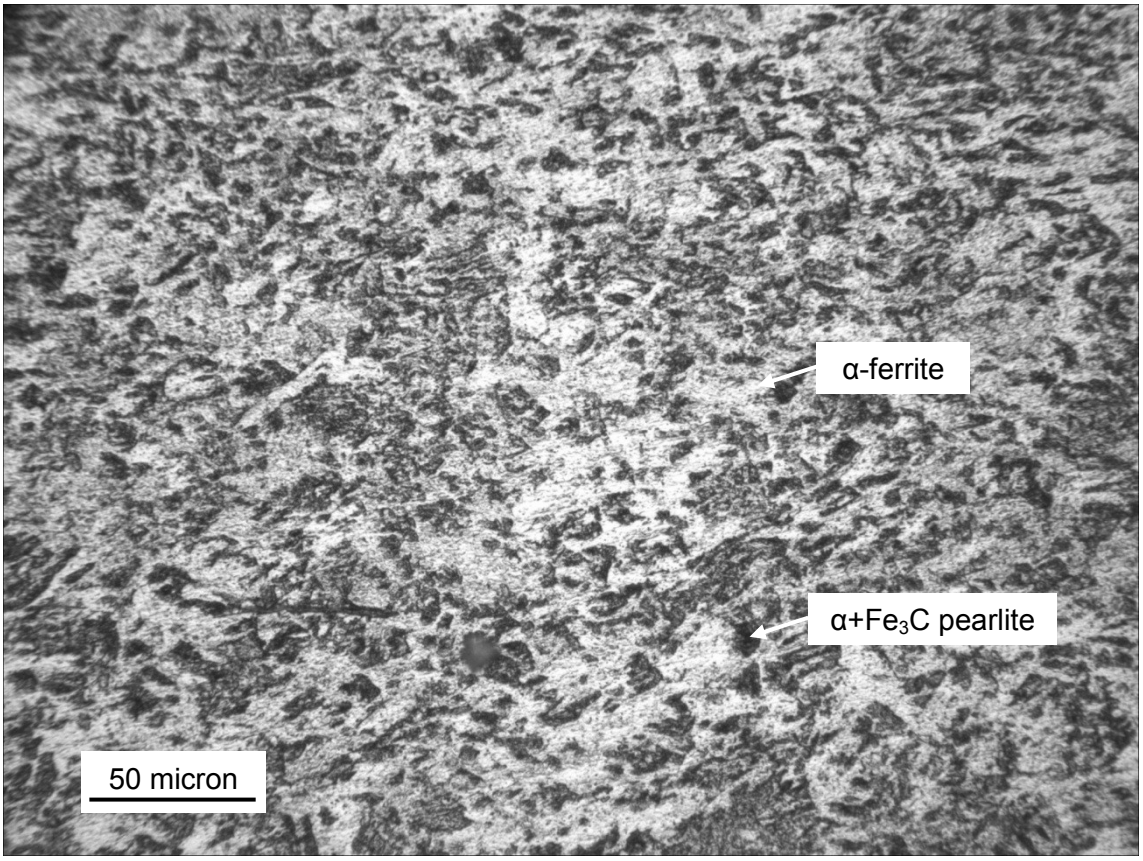

Figure K 2. Macro-photograph of the PM region, in *specimen 1 layer*.

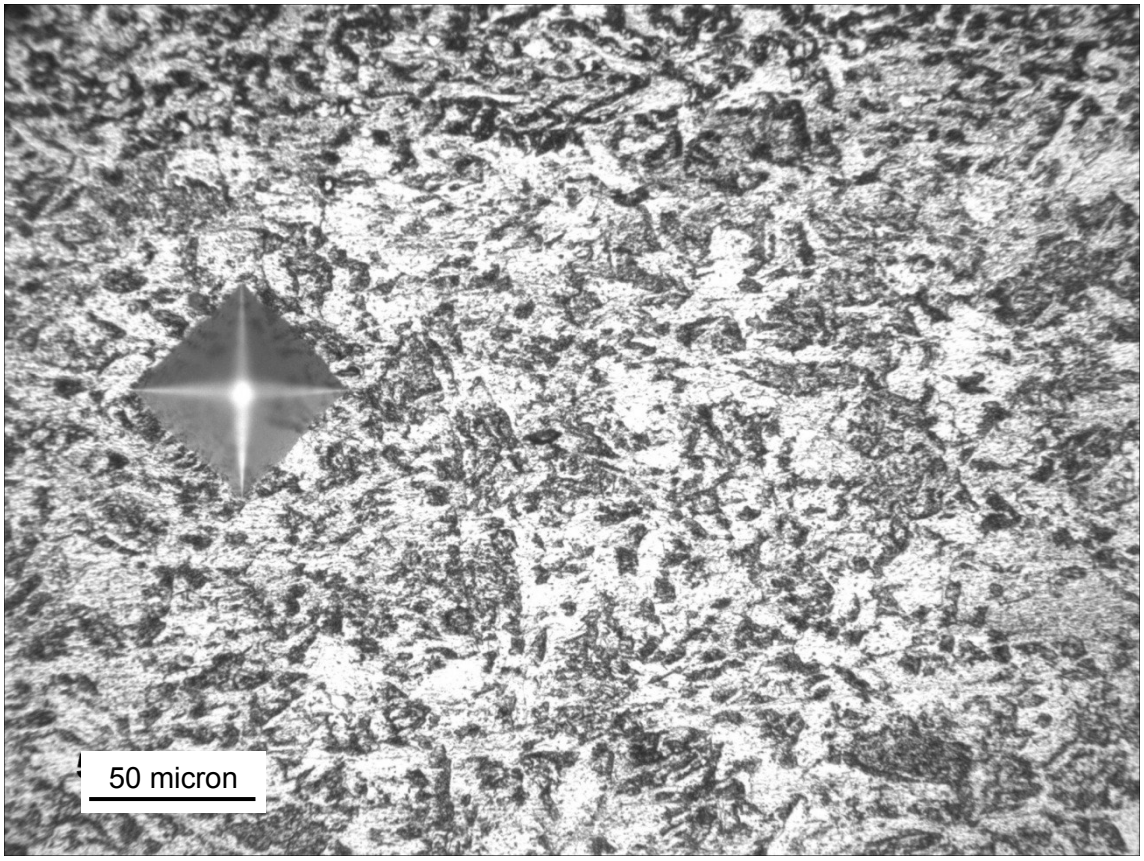

Figure K 3. Macro-photograph of the HAZ region (not visible to naked eye) showing an indentation at x=0 mm and y=0.25 mm, in *specimen 1 layer*.

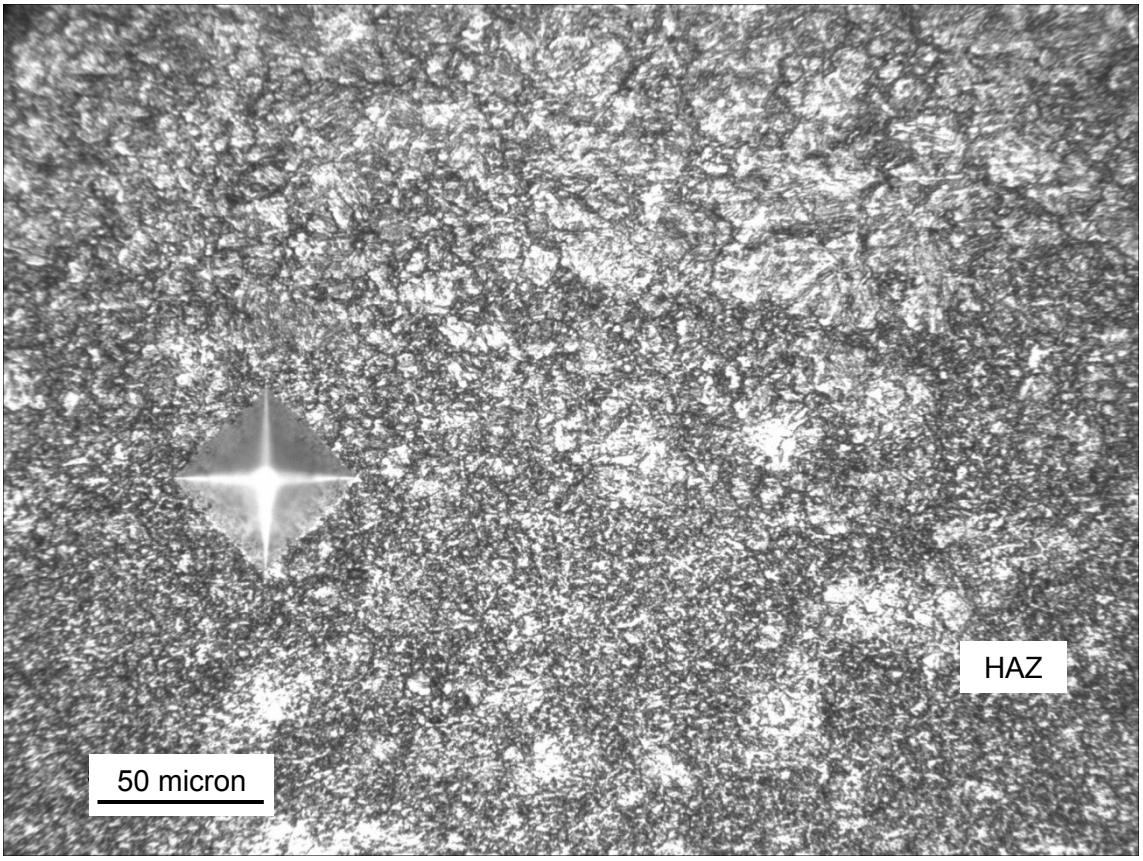

Figure K 4. Macro-photograph of the HAZ region showing an indentation at x=0 mm and y=0.75 mm, in *specimen 1 layer*.

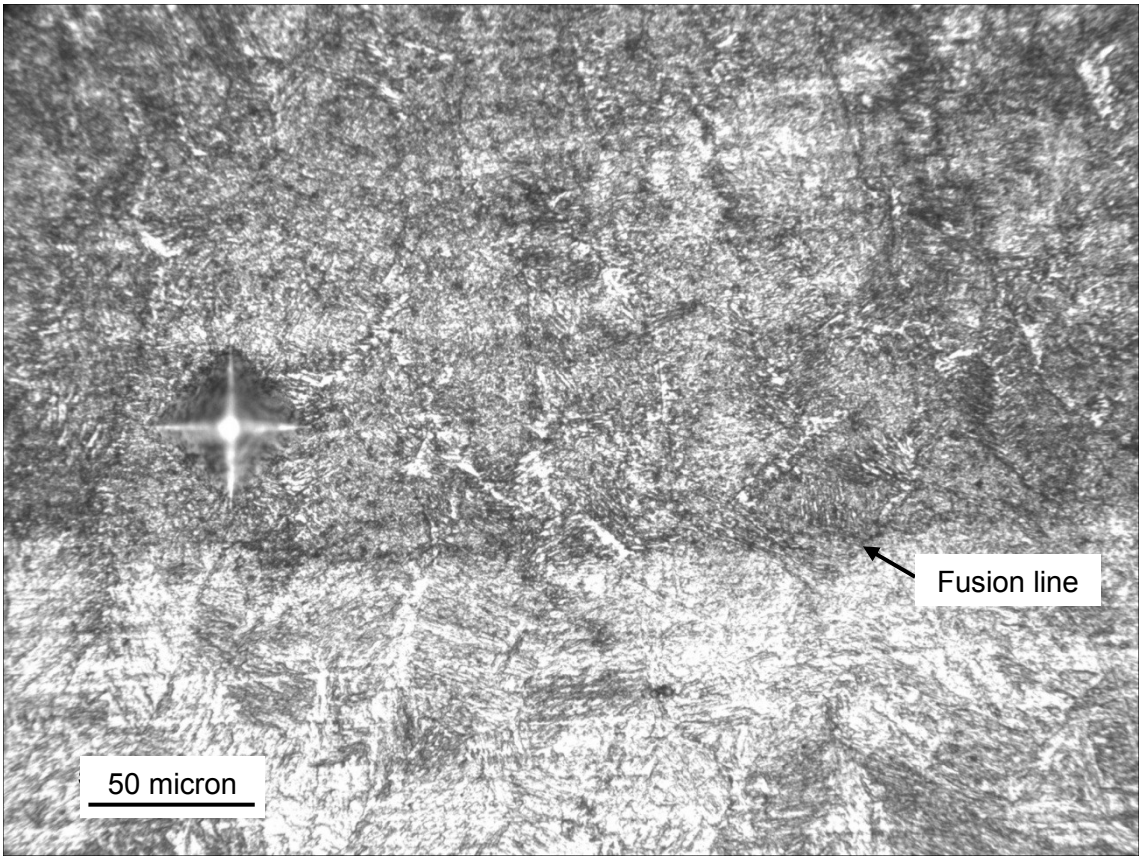

Figure K 5. Macro-photograph of the FL region showing an indentation at x=0 mm and y=1.25 mm, in *specimen 1 layer*.

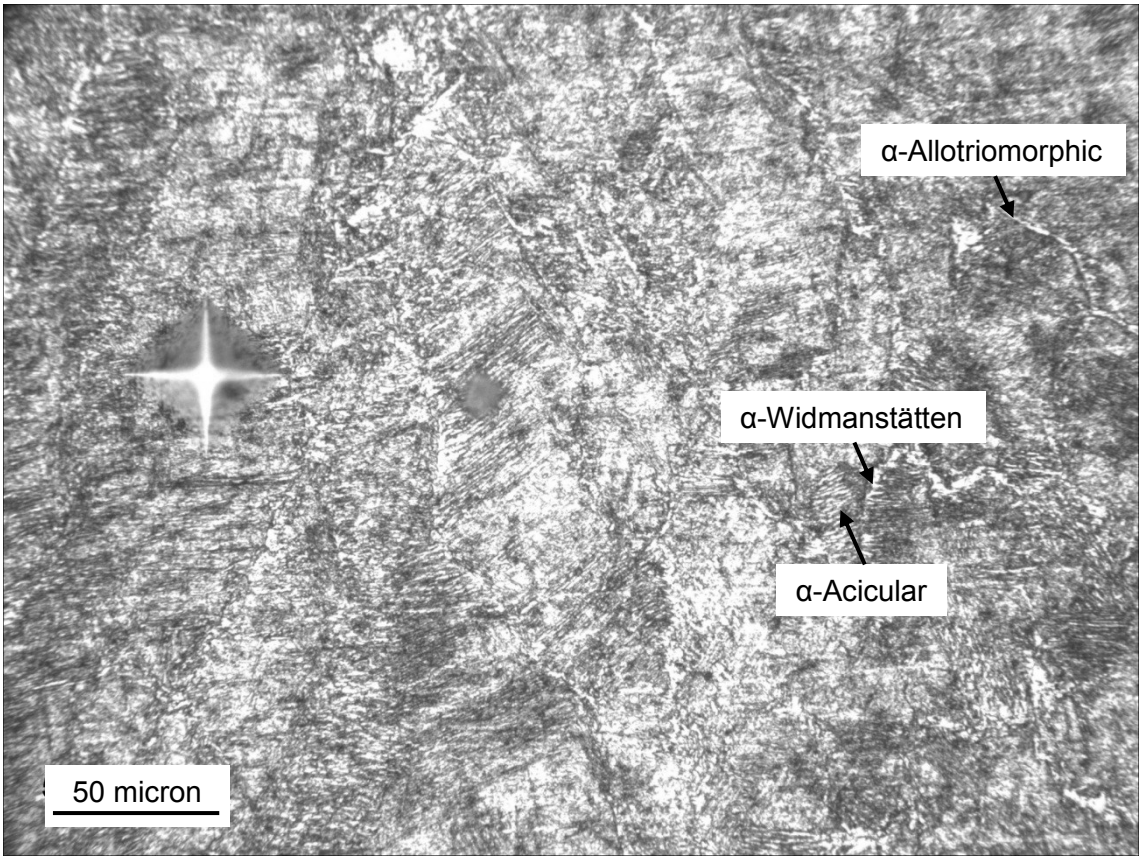

Figure K 6. Macro-photograph of the WM region showing an indentation at x=0 mm and y=2.25 mm, in *specimen 1 layer*.

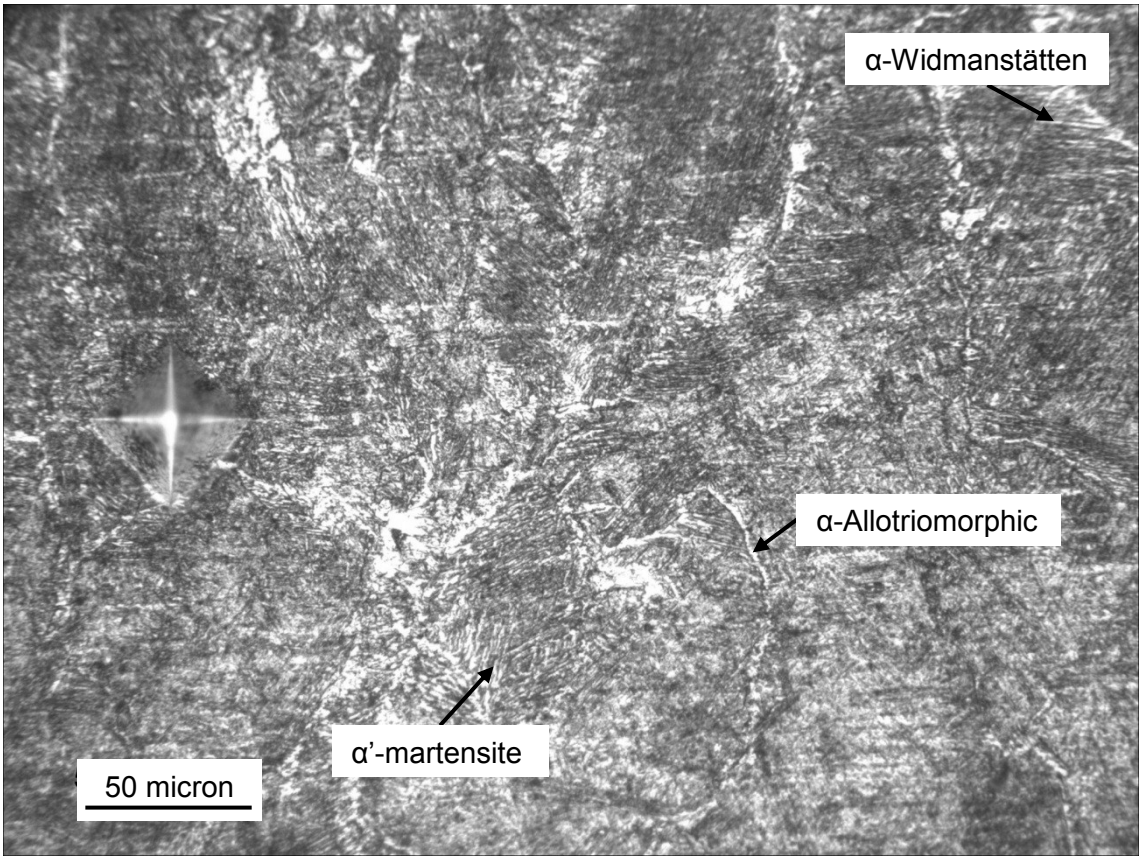

Figure K 7. Macro-photograph of the WM region showing an indentation at x=0 mm and y=3.75 mm, in *specimen 1 layer*.

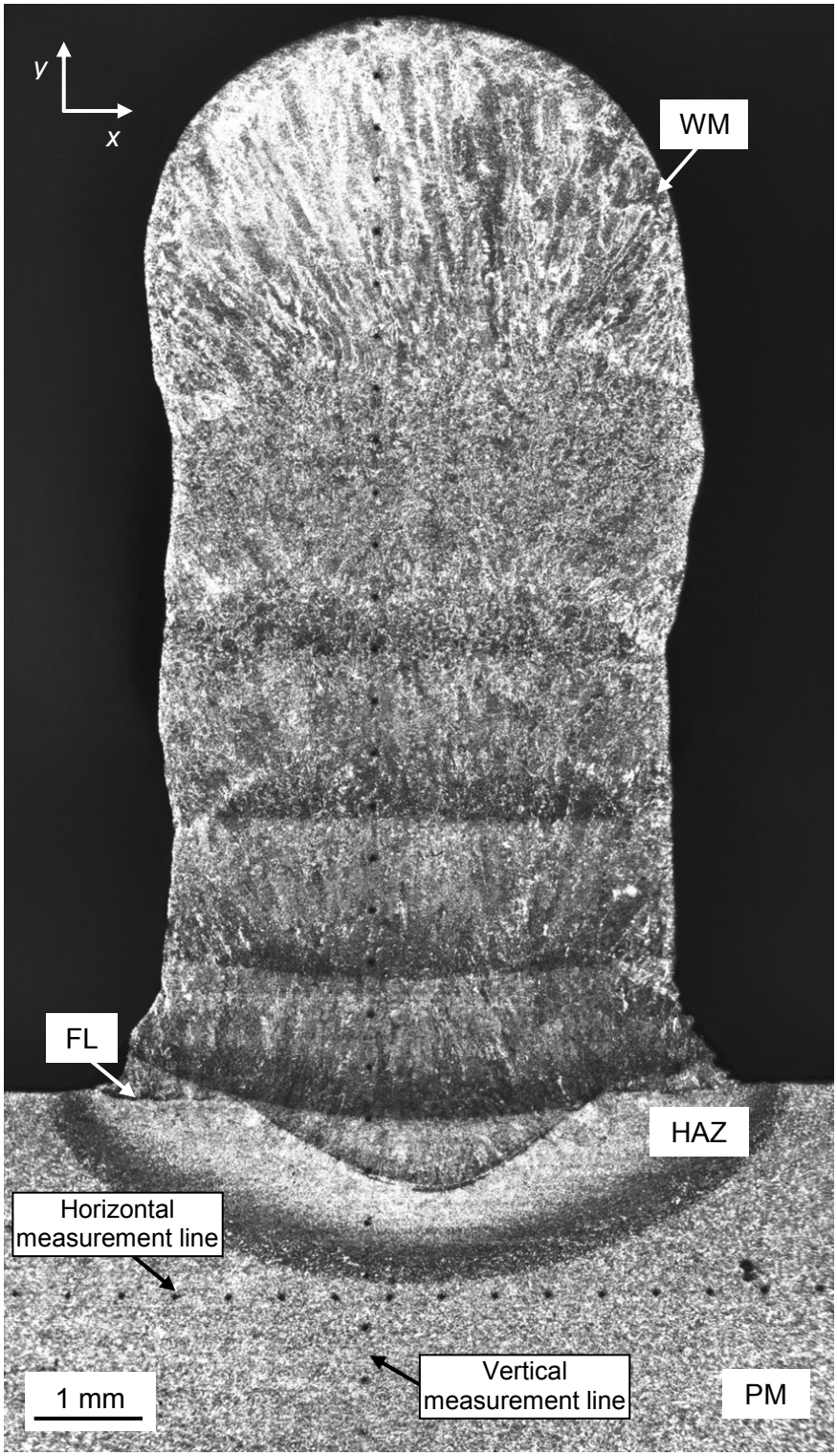

Figure K 8. Transverse macro-photograph of *specimen 5 layers* showing horizontal and vertical indentation measurement lines.

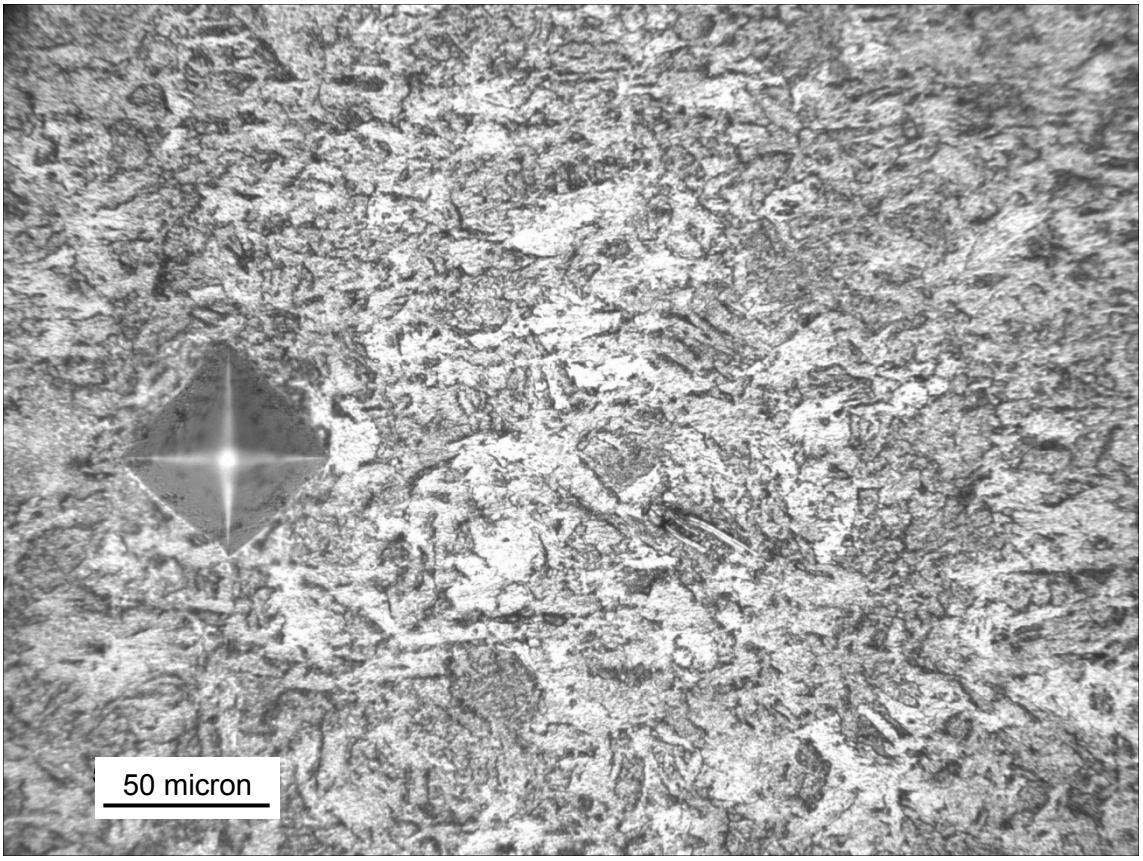

Figure K 9. Macro-photograph of the HAZ region (not visible to naked eye) showing an indentation at x=0.75 mm and y=0.0 mm, in *specimen 5 layers*.

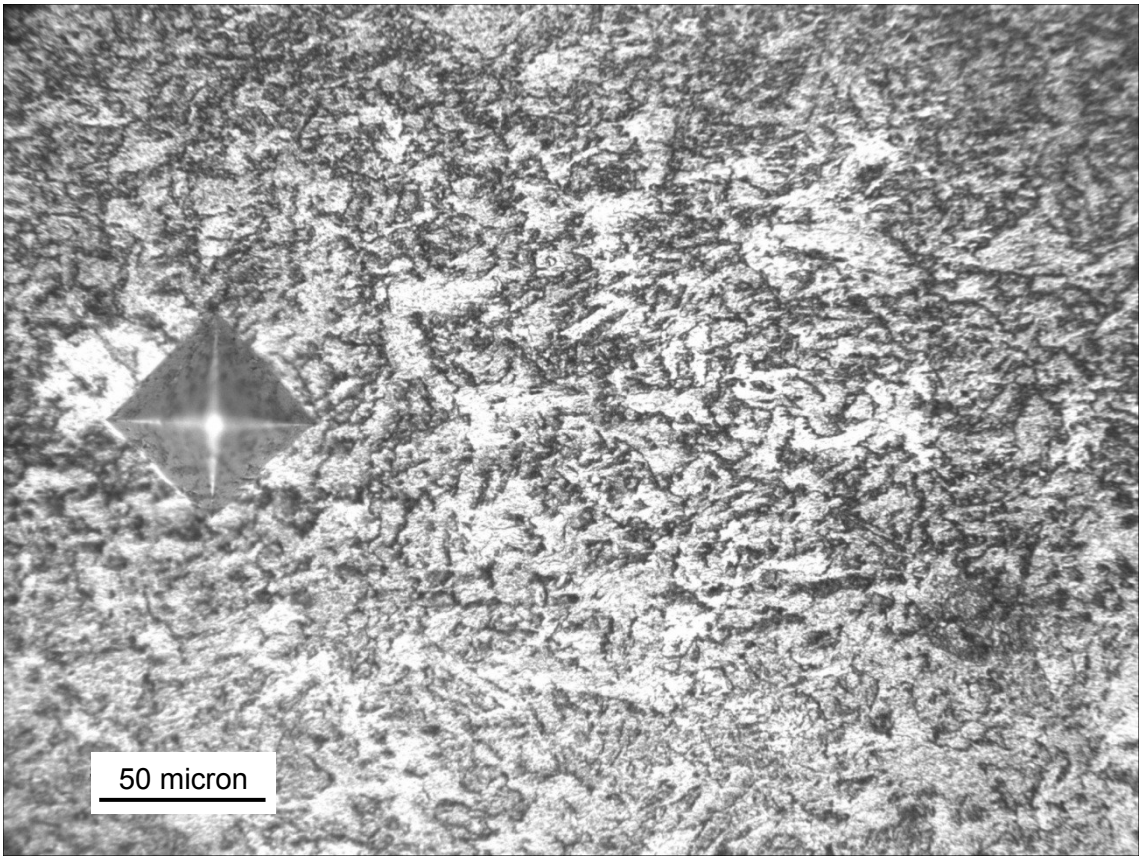

Figure K 10. Macro-photograph of the far HAZ region showing an indentation at x=0 mm and y=0.25 mm, in *specimen 5 layers*.

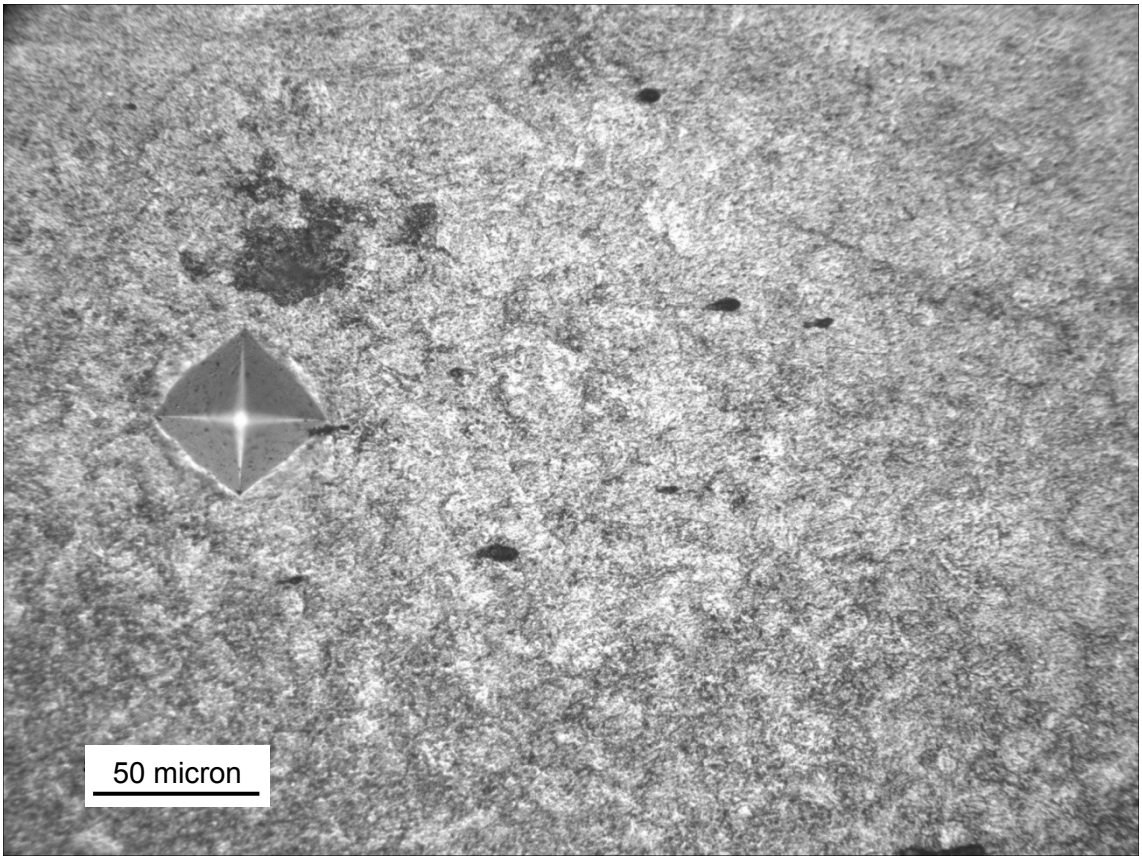

Figure K 11. Macro-photograph of the HAZ region showing an indentation at x=0 mm and y=0.75 mm, in *specimen 5 layers*.

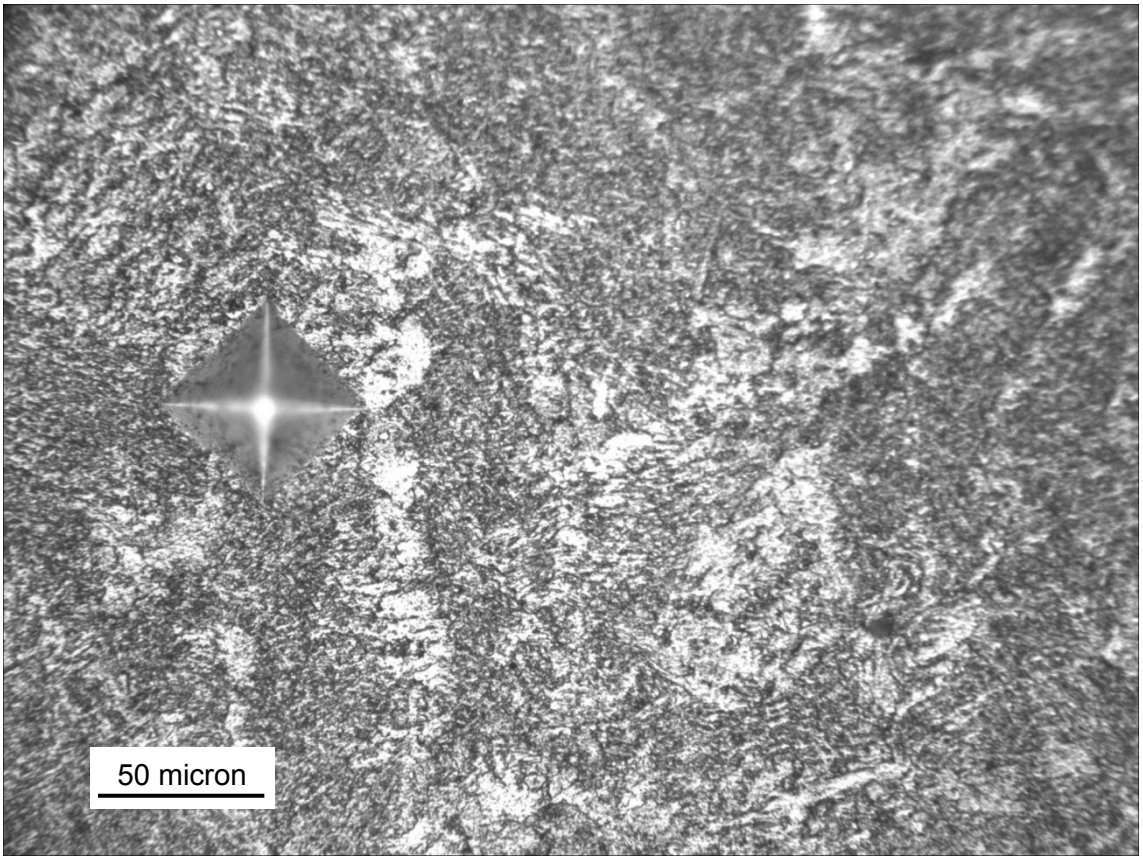

Figure K 12. Macro-photograph of the middle WM region showing an indentation at x=0 mm and y=4.25 mm, in *specimen 5 layers*.

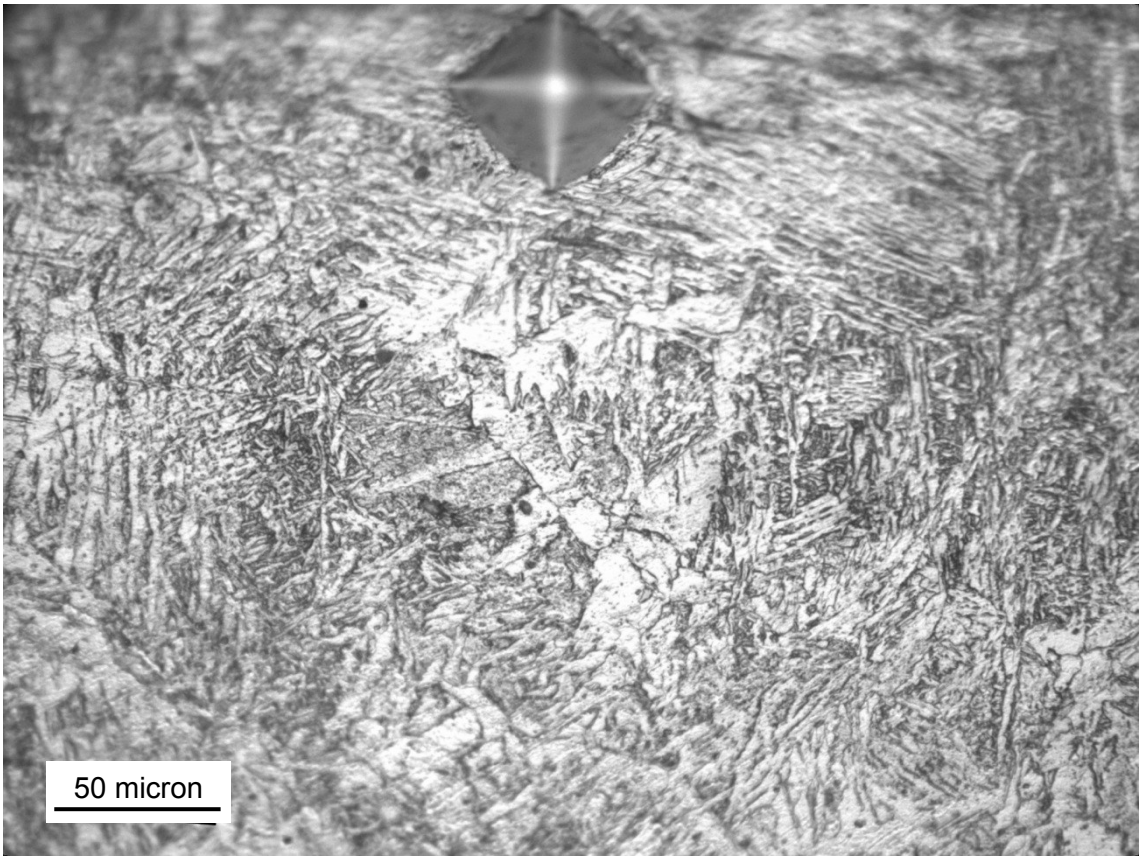

Figure K 13. Macro-photograph of the top WM region showing an indentation at x=0 mm and y=12.25 mm, in *specimen 5 layers*.4.25

Appendix L – Complementary results

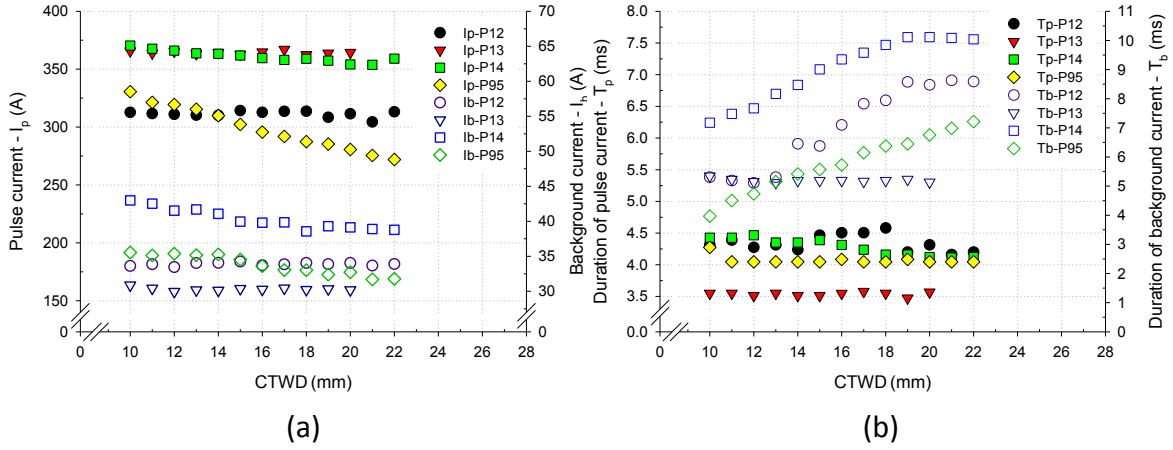

Figure L 1. Effect of CTWD on (a) pulse (I_p) and background current (I_b), and (b) duration of pulse (T_p) and background current (T_b) for different GMAW-P operation modes.

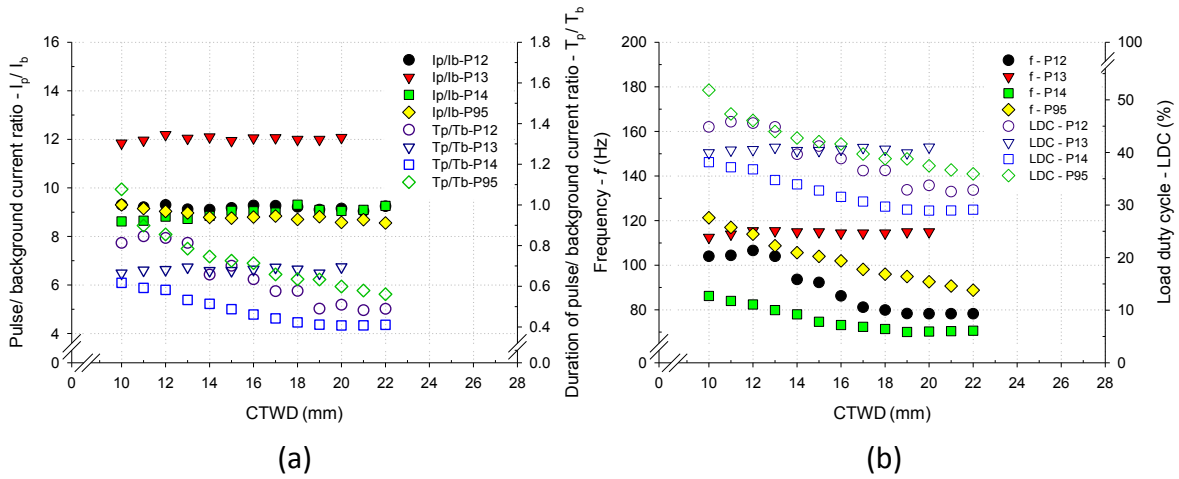

Figure L 2. Effect of CTWD on (a) pulse to background current ratio (I_p/I_b) and duration of pulse to background current ratio (T_p/T_b), and (b) frequency (*f*) and load duty cycle (LDC).

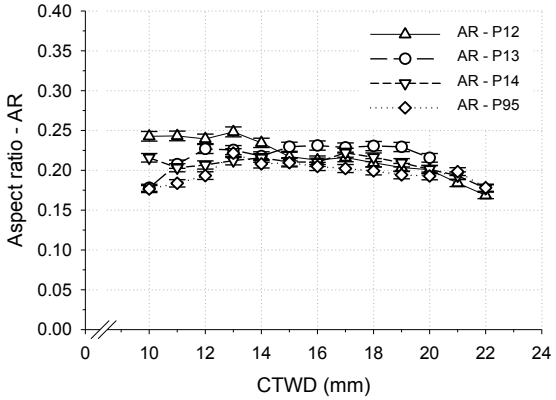

Figure L 3. Effect of CTWD on the weld bead aspect ratio (AR).

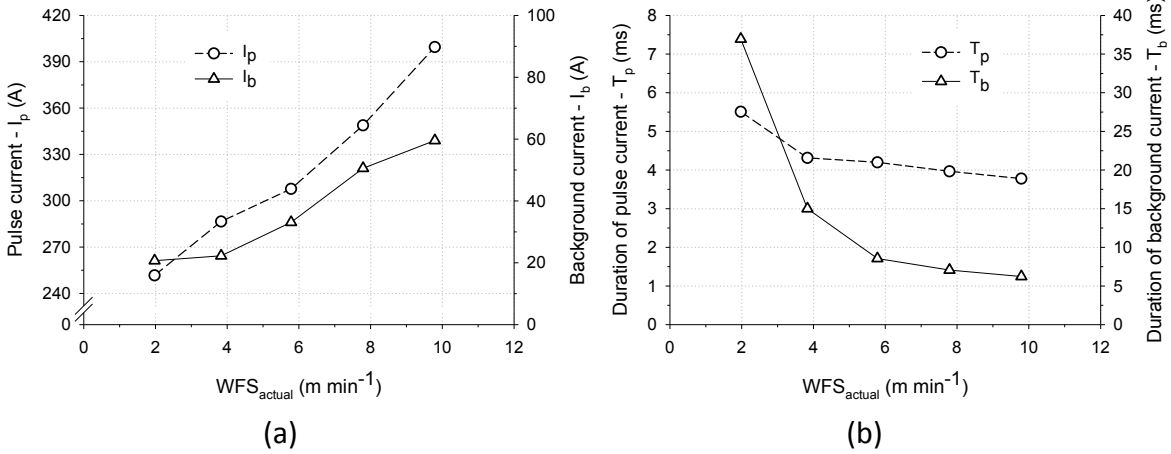

Figure L 4. Effect of WFS_{actual} on (a) pulse (I_p) and background current (I_b), and (b) duration of pulse (T_p) and background current (T_b).

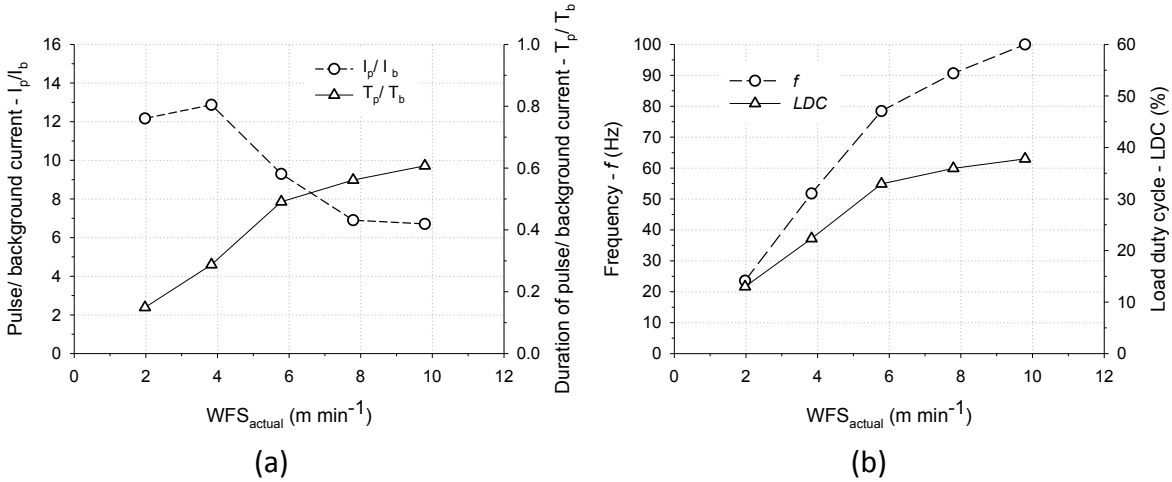

Figure L 5. Effect of WFS_{actual} on (a) pulse to background current ratio (I_p/I_b) and duration of pulse to background current ratio (T_p/T_b), and (b) frequency (f) and load duty cycle (LDC).

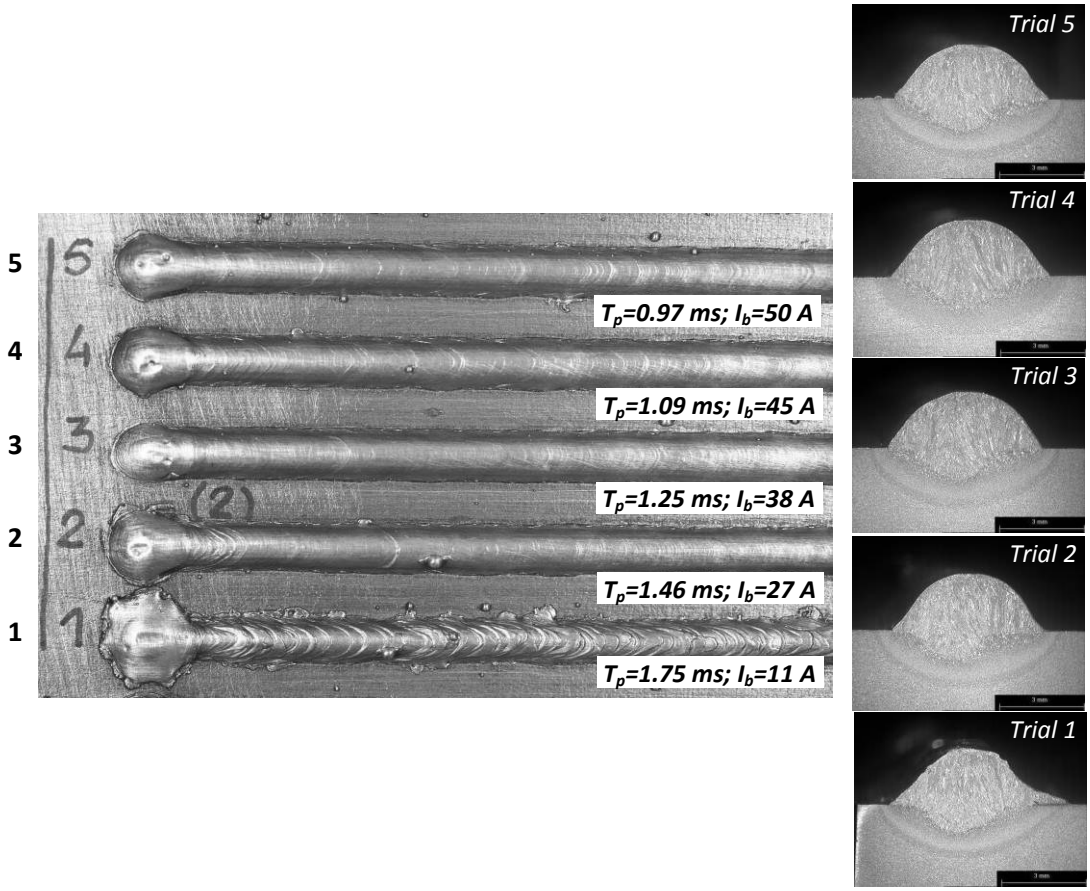

Figure L 6. Illustration showing bead top surfaces, transverse cross sections, and control parameters applied in study S_2.

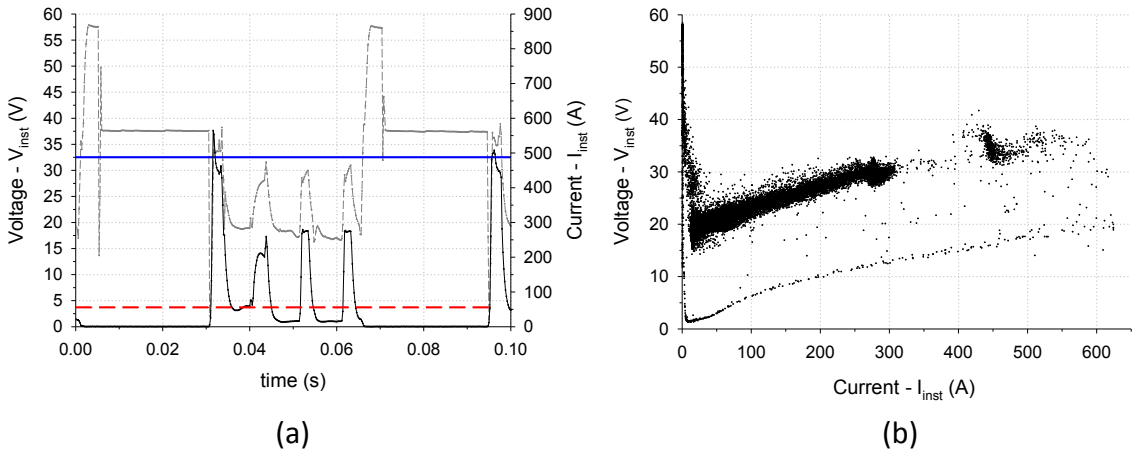

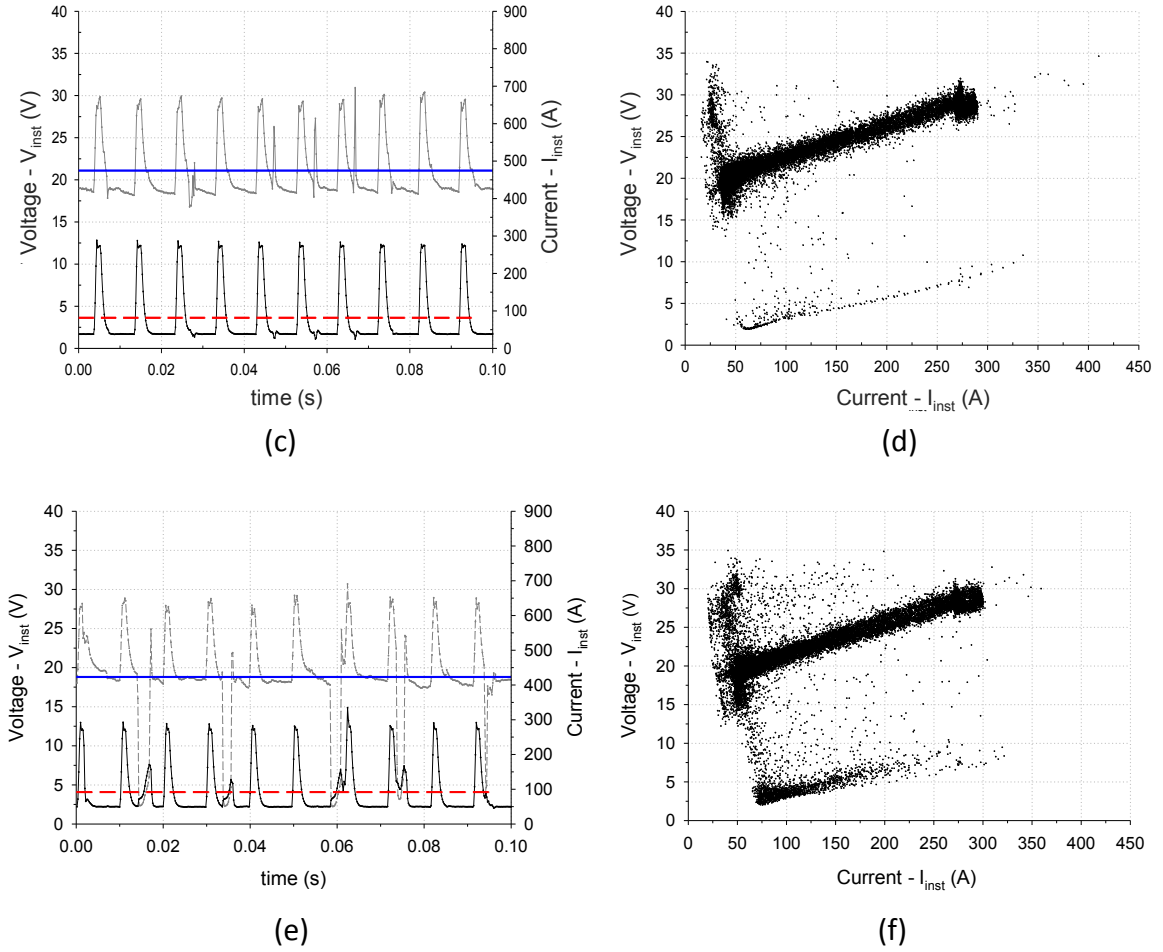

Figure L 7. Electrical transients in study S_2 showing V_{inst} (dashed grey) and I_{inst} (continuous black) lines on the left, and scatter plots on the right. Trial 1 is represented in (a) and (b), trial 3 in (c) and (d), and trial 5 in graphs (e) and (f). Represented are also averaged V_{inst} (solid blue) and I_{inst} (dashed red) lines.

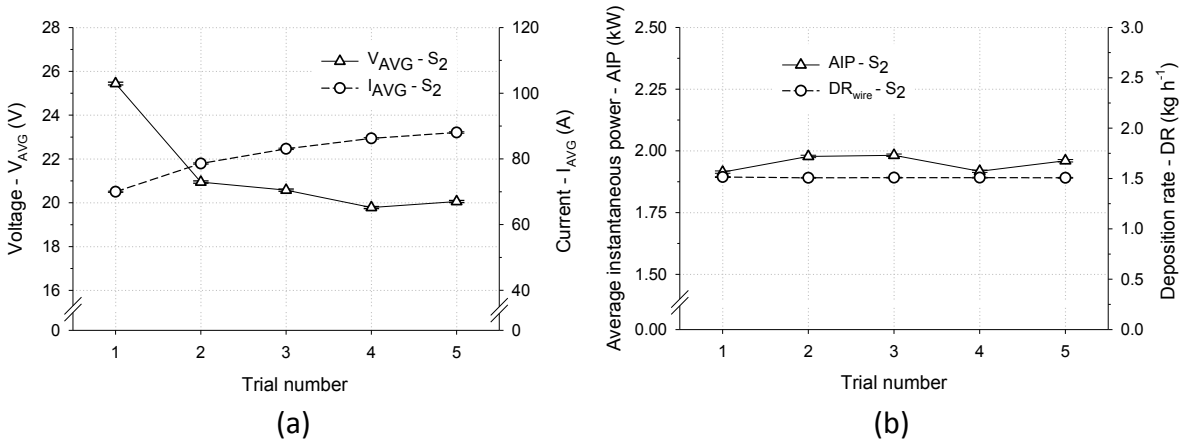

Figure L 8. Dependence of (a) V_{inst} and I_{inst}, and on (b) AIP and DR on the trial number (S_2).

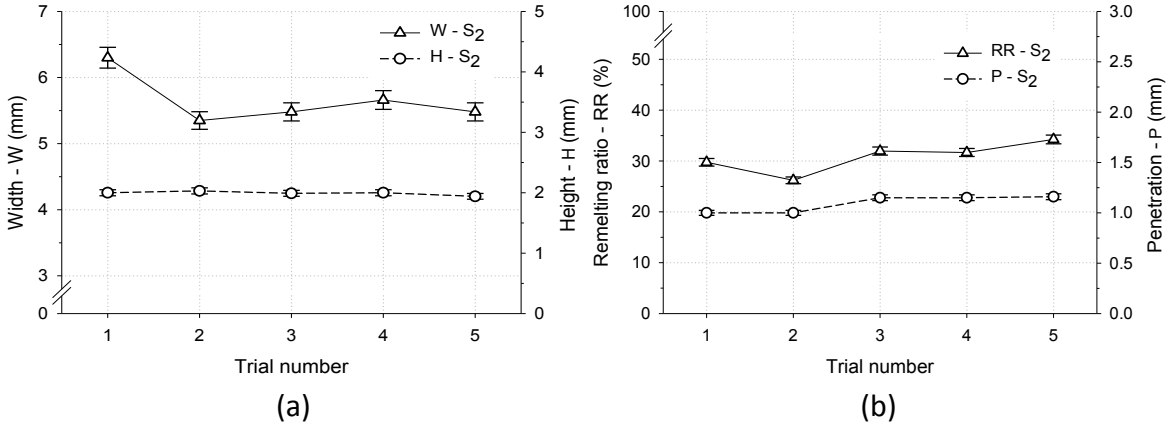

Figure L 9. Effect of T_p/I_b ratio on bead (a) W and H, as well as on (b) RR and P (S_2).

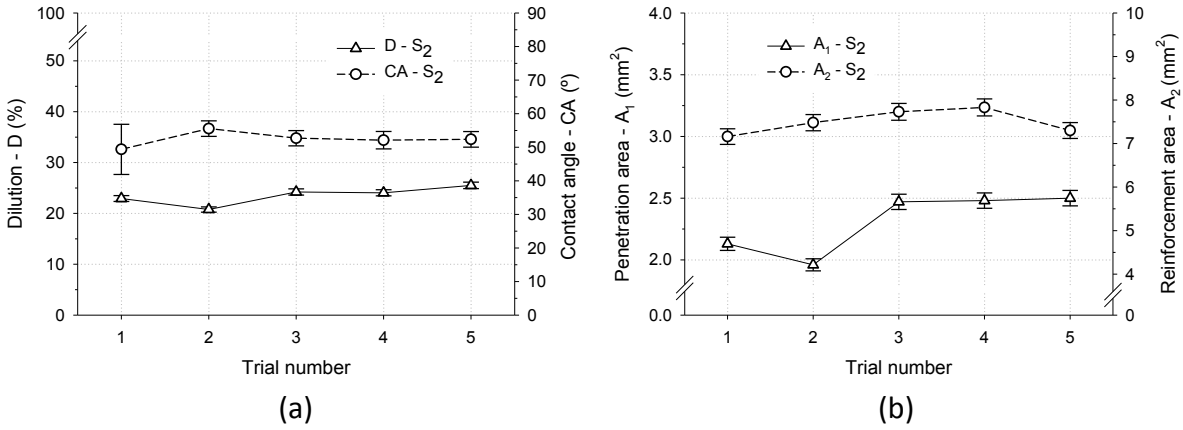

Figure L 10. Effect of T_p/I_b on (a) D and CA (95% confidence interval), as well as on (b) A_1 and A_2 (S_2).

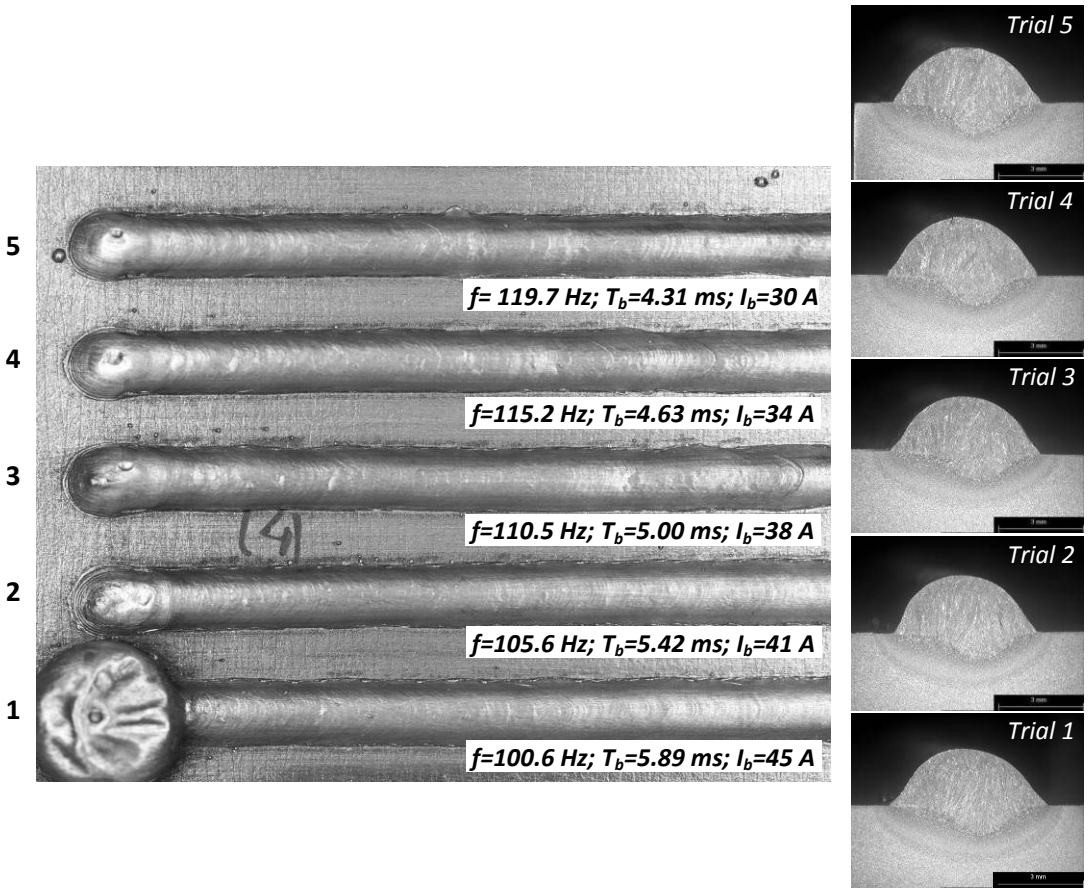

Figure L 11. Illustration showing bead top surfaces, transverse cross sections, and control parameters applied in study S_4.

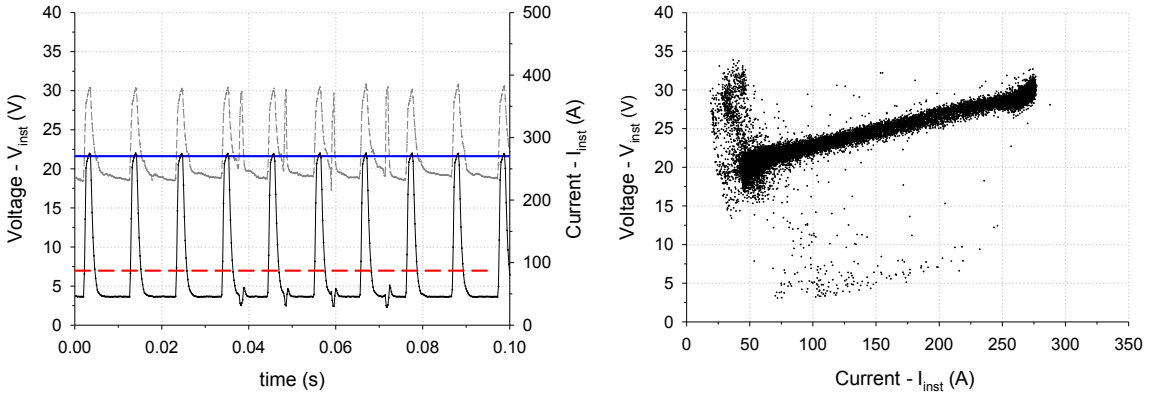

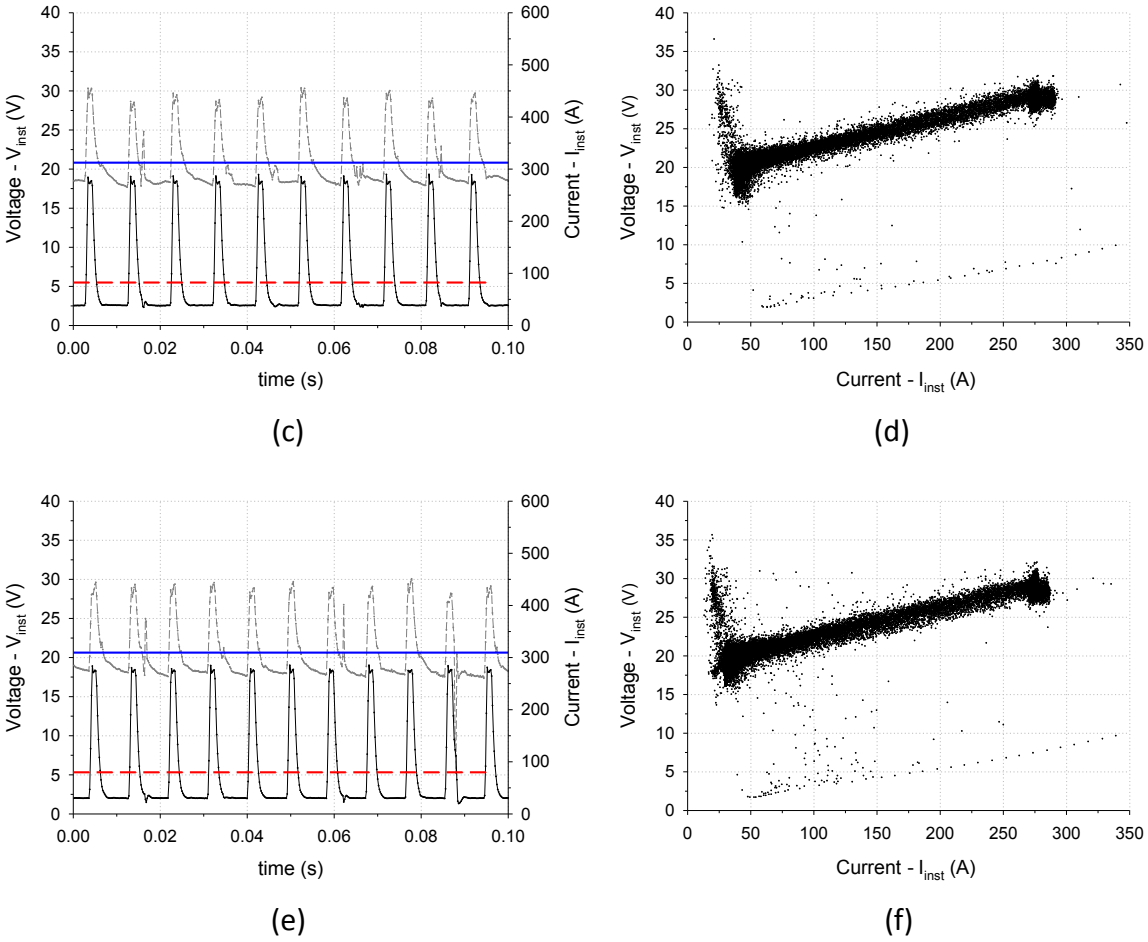

Figure L 12. Electrical transients in study *S*$_4$ showing V_{inst} (dashed silver) and I_{inst} (continuous black) lines on the left, and scatter plots on the right. Trial 1 is represented in (a) and (b), trial 3 in (c) and (d) and trial 5 in graphs (e) and (f).

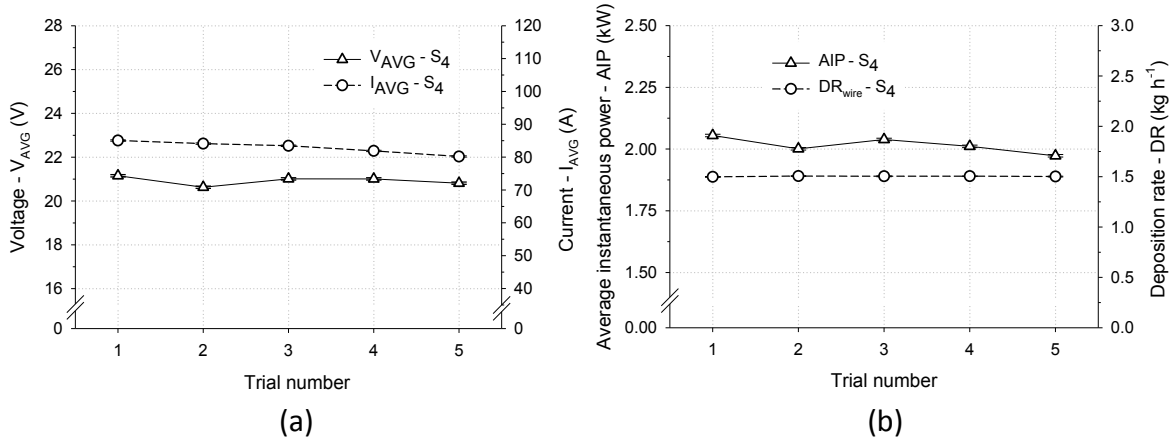

Figure L 13. Dependence of (a) V_{inst} and I_{inst}, and on (b) AIP and DR on the trial number (*S*$_4$).

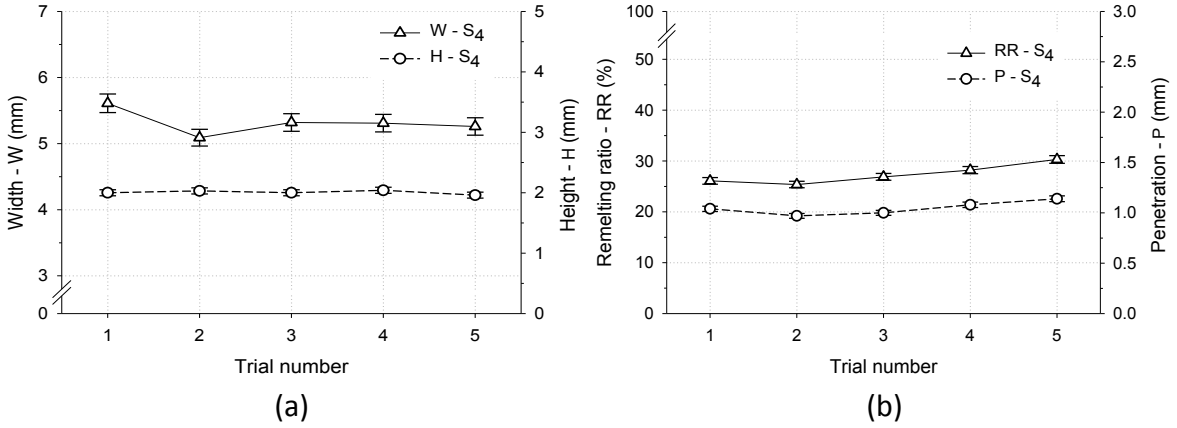

Figure L 14. Effect of I_p/I_b ratio on bead (a) W and H, as well as on (b) RR and P (S_4).

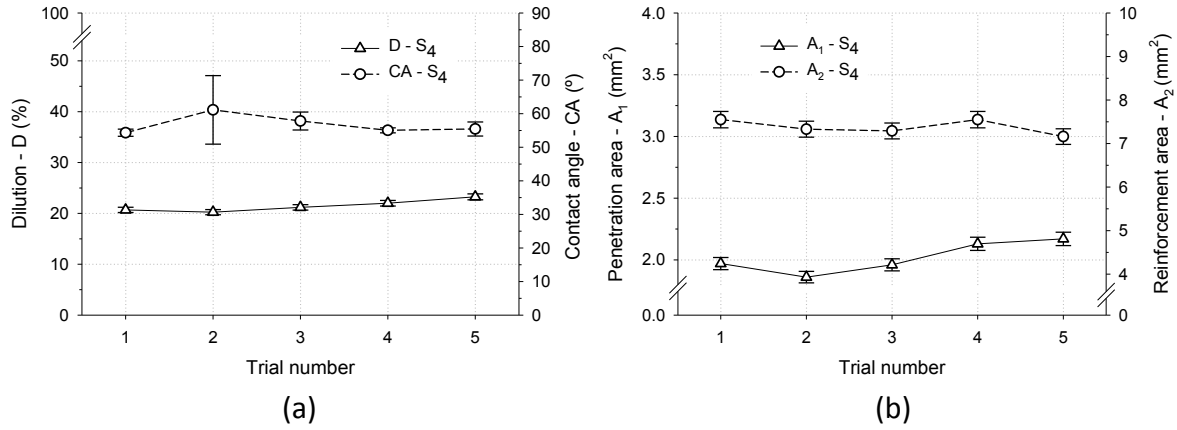

Figure L 15. Effect of I_p/I_b on (a) D and CA (95% confidence interval), and on (b) A_1 and A_2 (S_4).

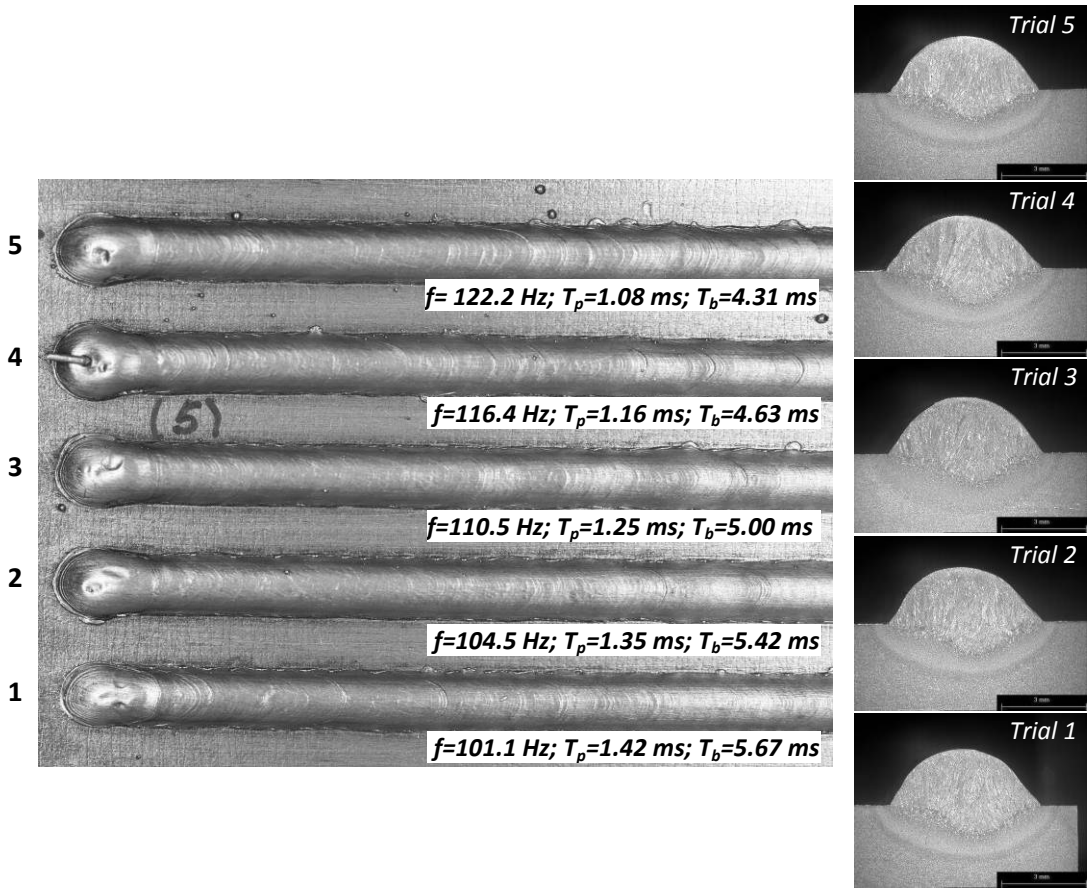

Figure L 16. Illustration showing bead top surfaces, transverse cross sections, and control parameters applied in study S_5.

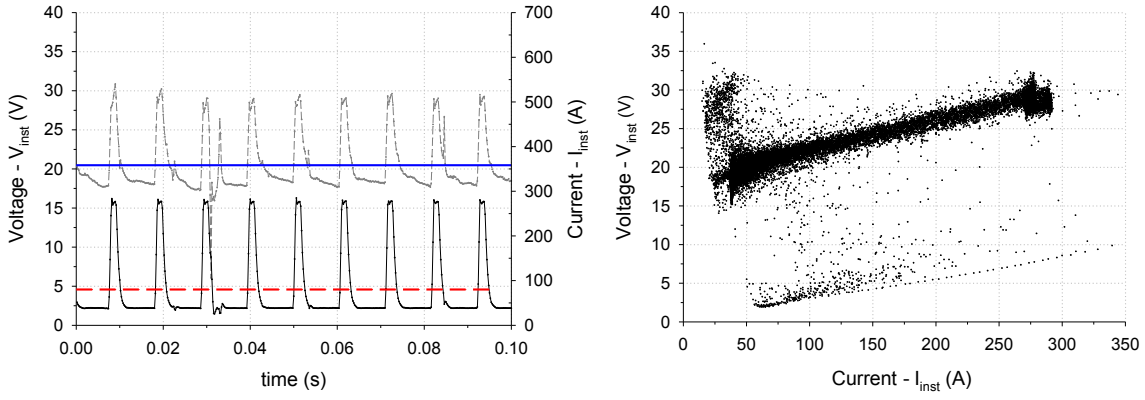

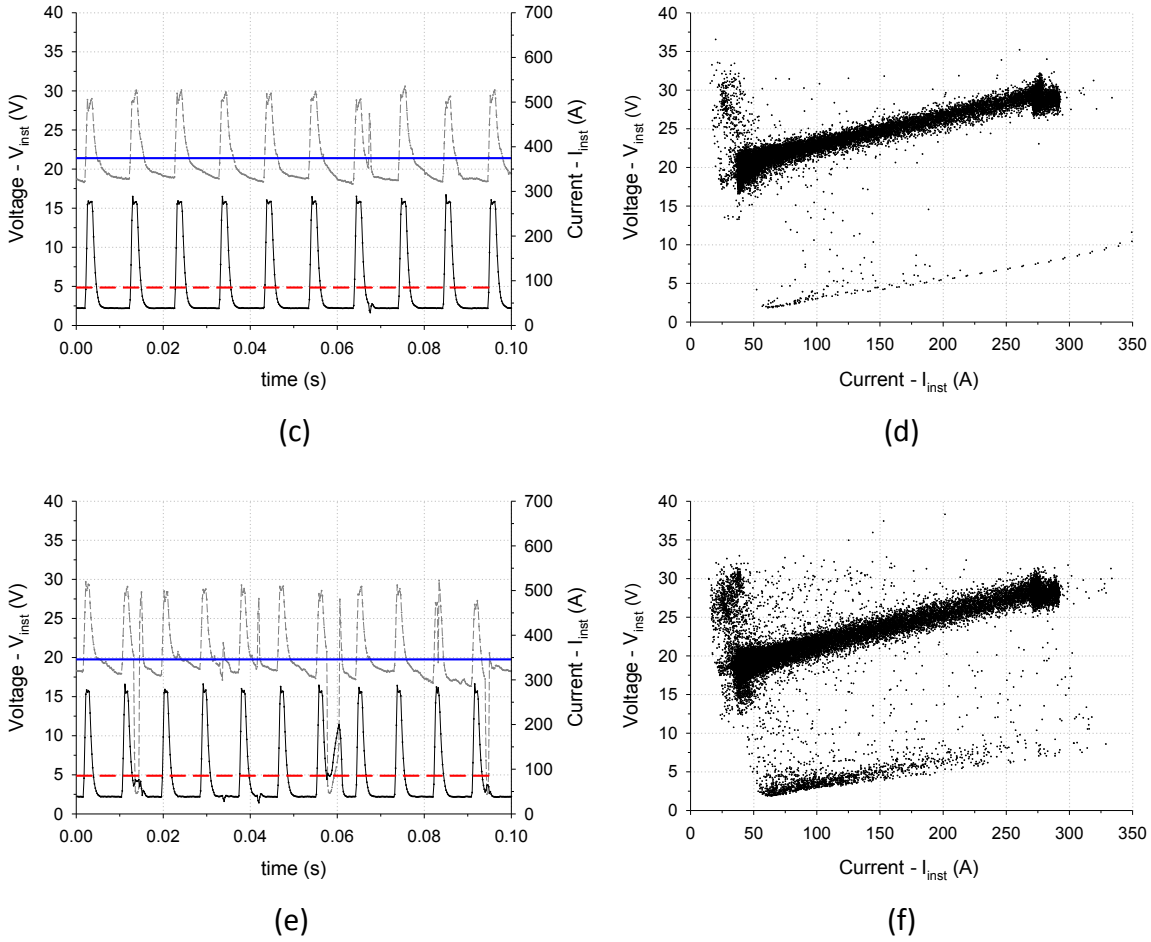

Figure L 17. Electrical transients in study S_5 showing V_{inst} (dashed silver) and I_{inst} (continuous black) lines on the left, and scatter plots on the right. Trial 1 is represented in (a) and (b), trial 2 in (c) and (d) and trial 5 in graphs (e) and (f).

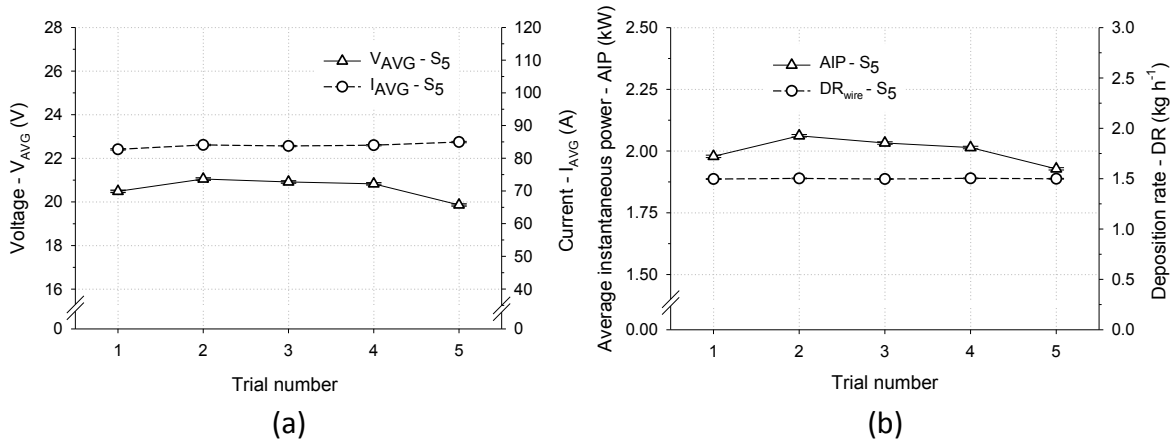

Figure L 18. Dependence of (a) V_{inst} and I_{inst}, and of (b) AIP and DR on the trial number (S_5).

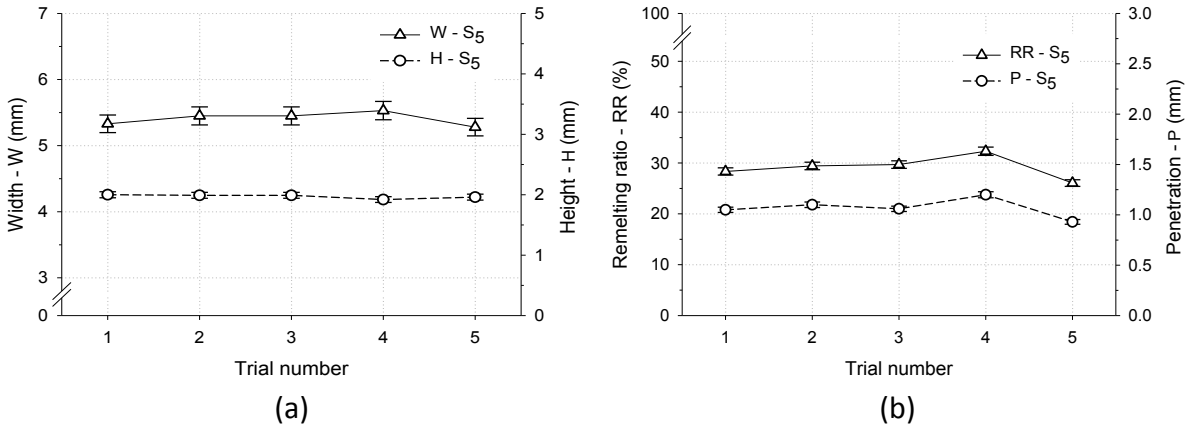

Figure L 19. Effect of *f* on (a) W and H, and on (b) RR and P (S_5).

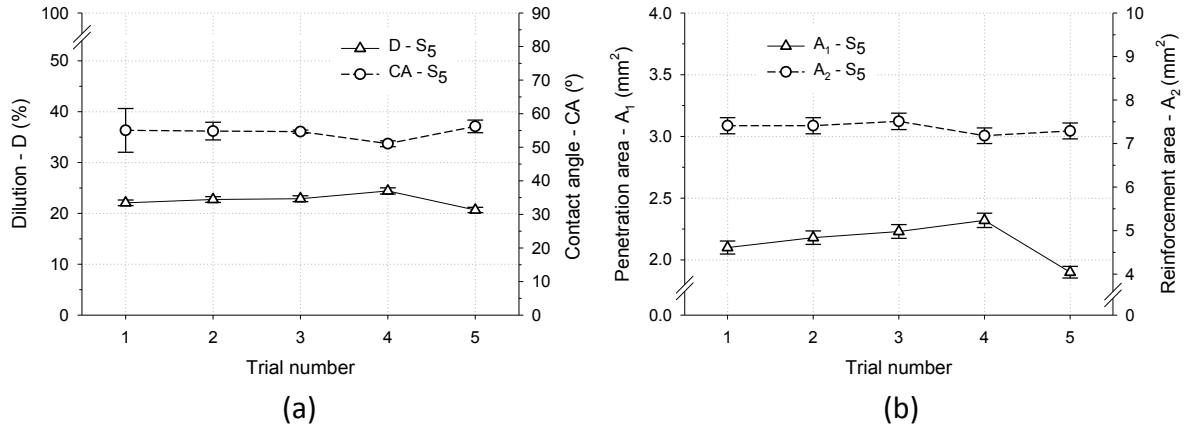

Figure L 20. Effect of *f* on (a) D and CA (95% confidence interval), as well as on (b) A_1 and A_2 (S_5).

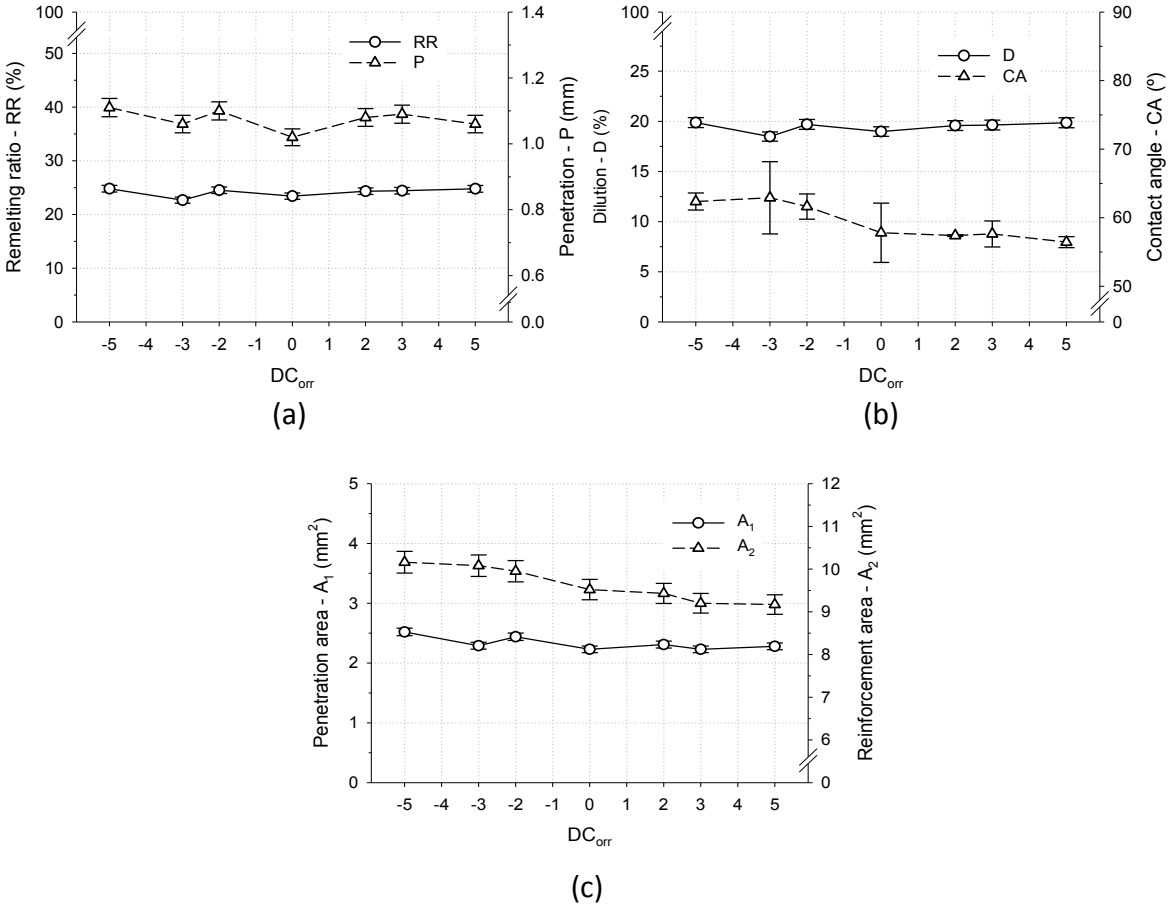

Figure L 21. Effect of DC_{orr} on (a) RR and P, (b) D and CA (95% confidence interval), as well as on (c) A_1 and A_2.

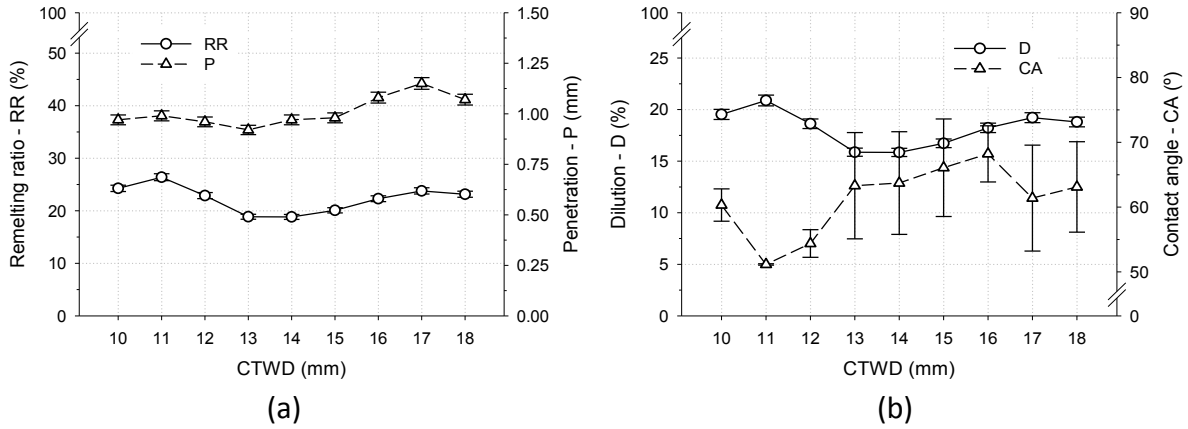

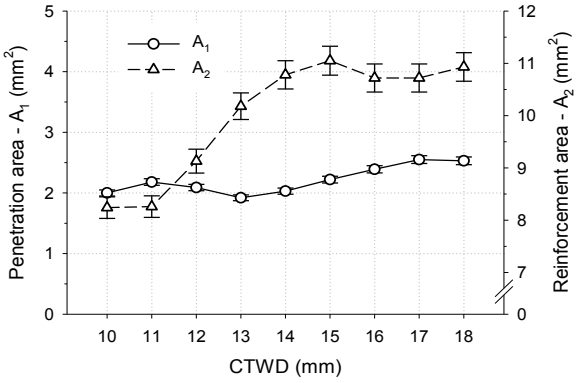

(c)

Figure L 22. Effect of CTWD on (a) RR and P, (b) D and CA (for a confidence level of 95%), and (c) A_1 and A_2.

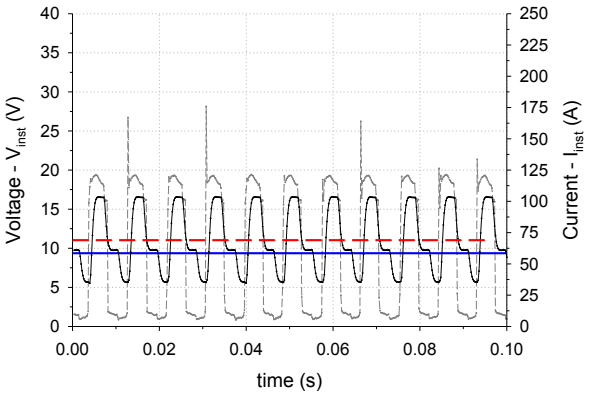

(a)

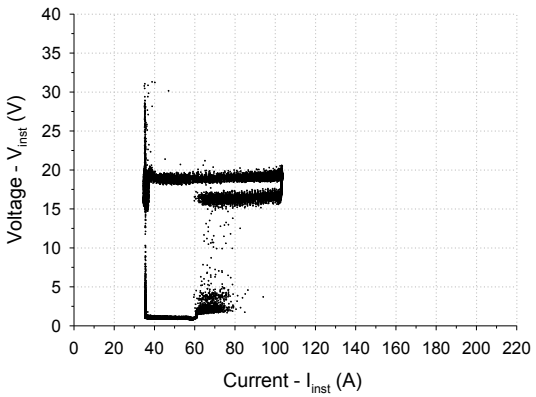

(b)

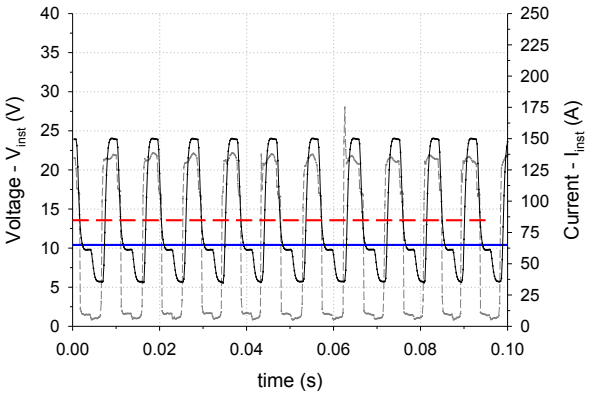

(c)

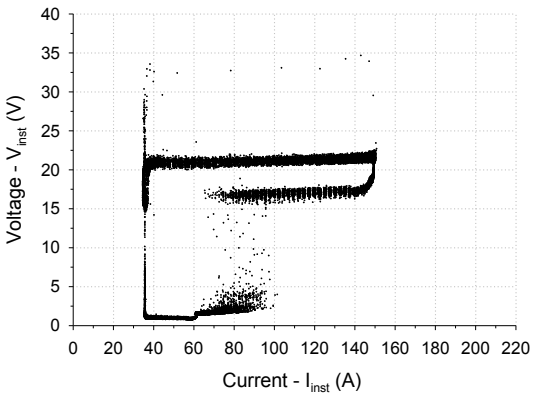

(d)

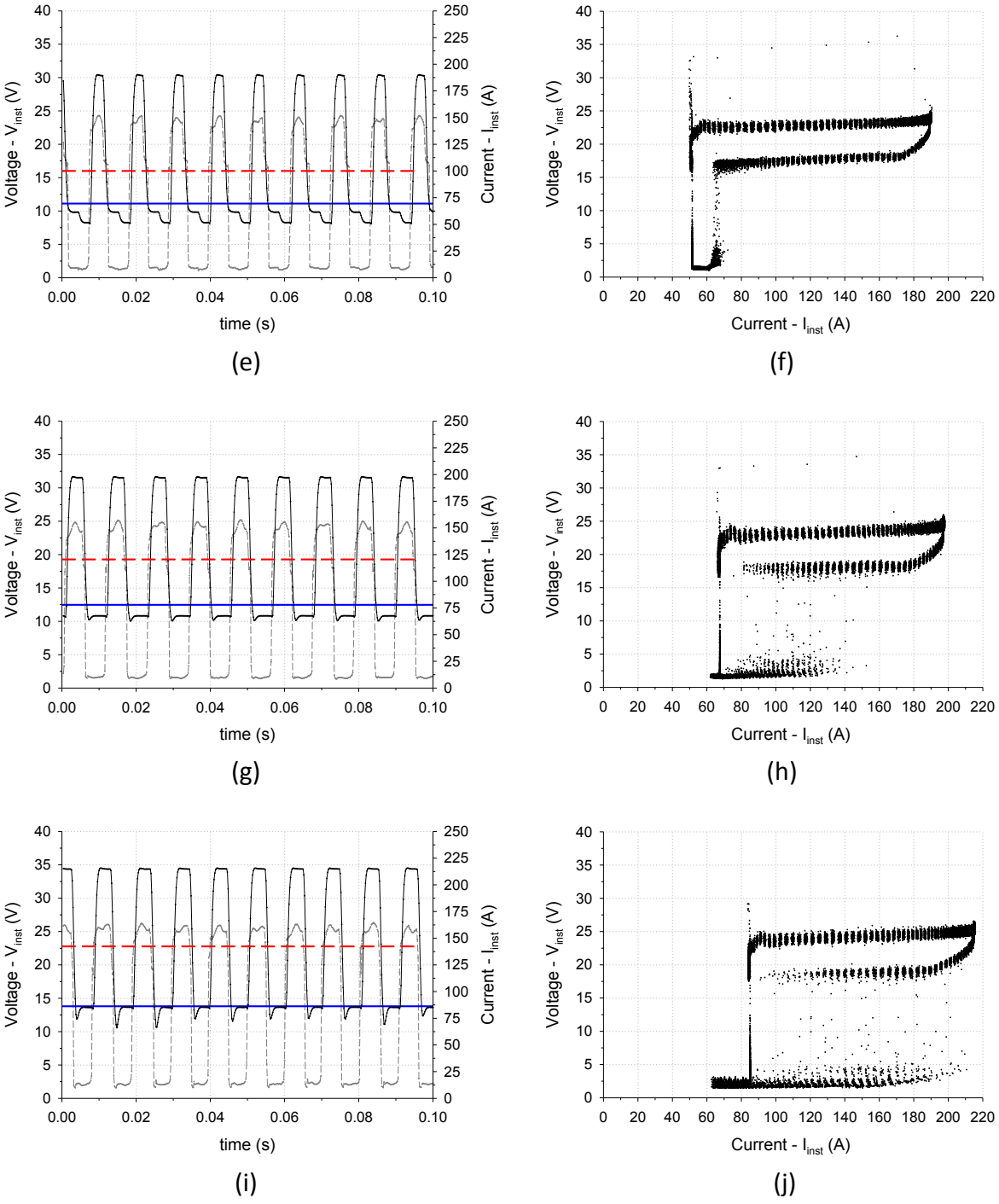

Figure L 23. Electrical transients in study G_1 showing V_{inst} (dashed grey) and I_{inst} (continuous black) lines on the left, and scatter plots on the right. Trial 1 is represented in (a) and (b), trial 2 in (c) and (d), trial 3 in (e) and (f), trial 4 in (g) and (h), and trial 5 in graphs (i) and (j). Represented are also averaged V_{inst} (solid blue) and I_{inst} (dashed red) lines.

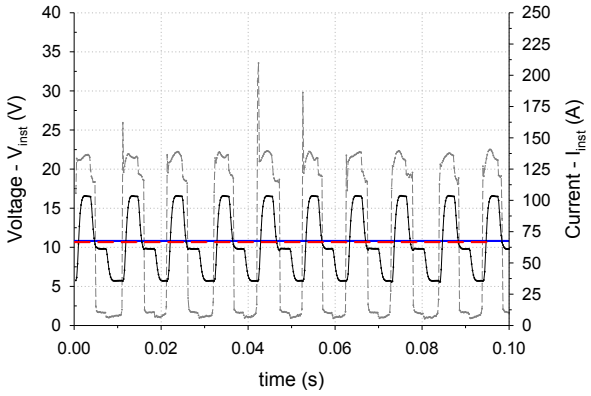
Voltage - V_{inst} (V)
Current - I_{inst} (A)
time (s)

(a)

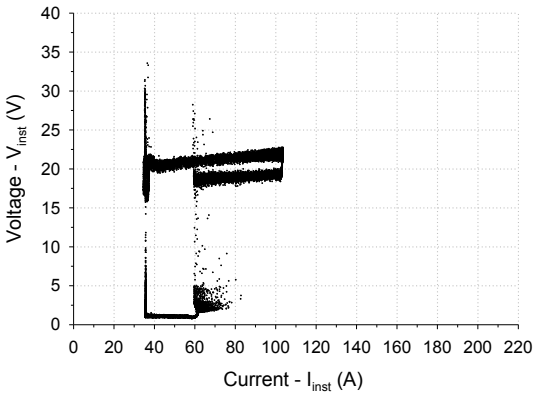
Voltage - V_{inst} (V)
Current - I_{inst} (A)

(b)

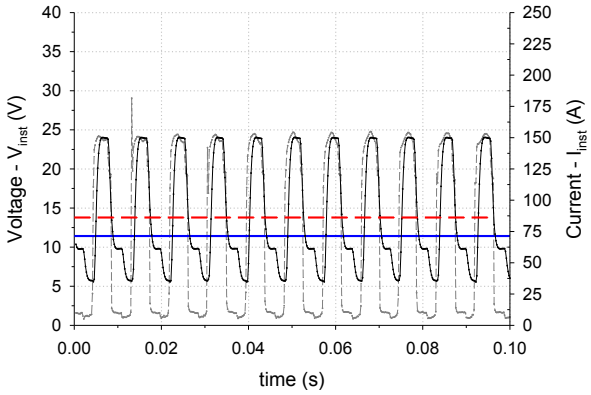
Voltage - V_{inst} (V)
Current - I_{inst} (A)
time (s)

(c)

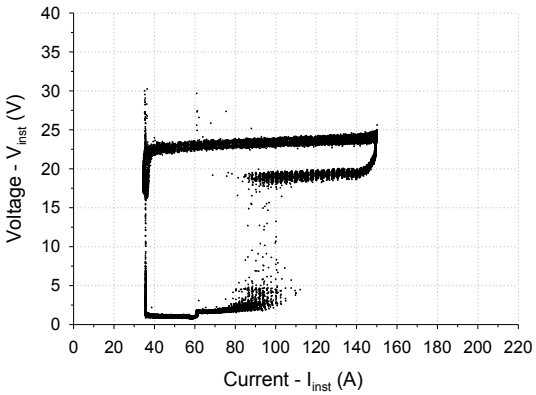
Voltage - V_{inst} (V)
Current - I_{inst} (A)

(d)

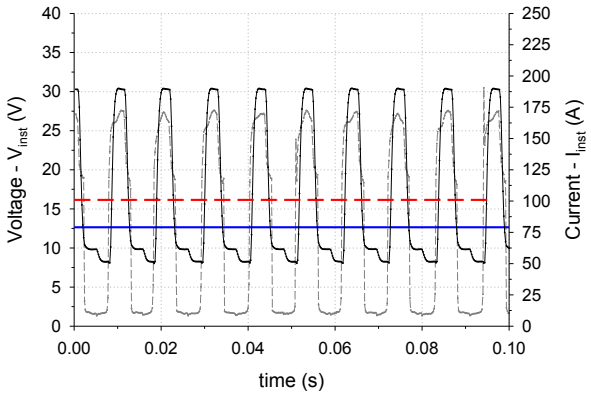
Voltage - V_{inst} (V)
Current - I_{inst} (A)
time (s)

(e)

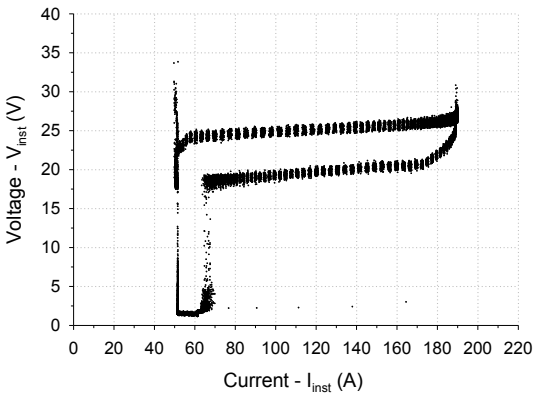
Voltage - V_{inst} (V)
Current - I_{inst} (A)

(f)

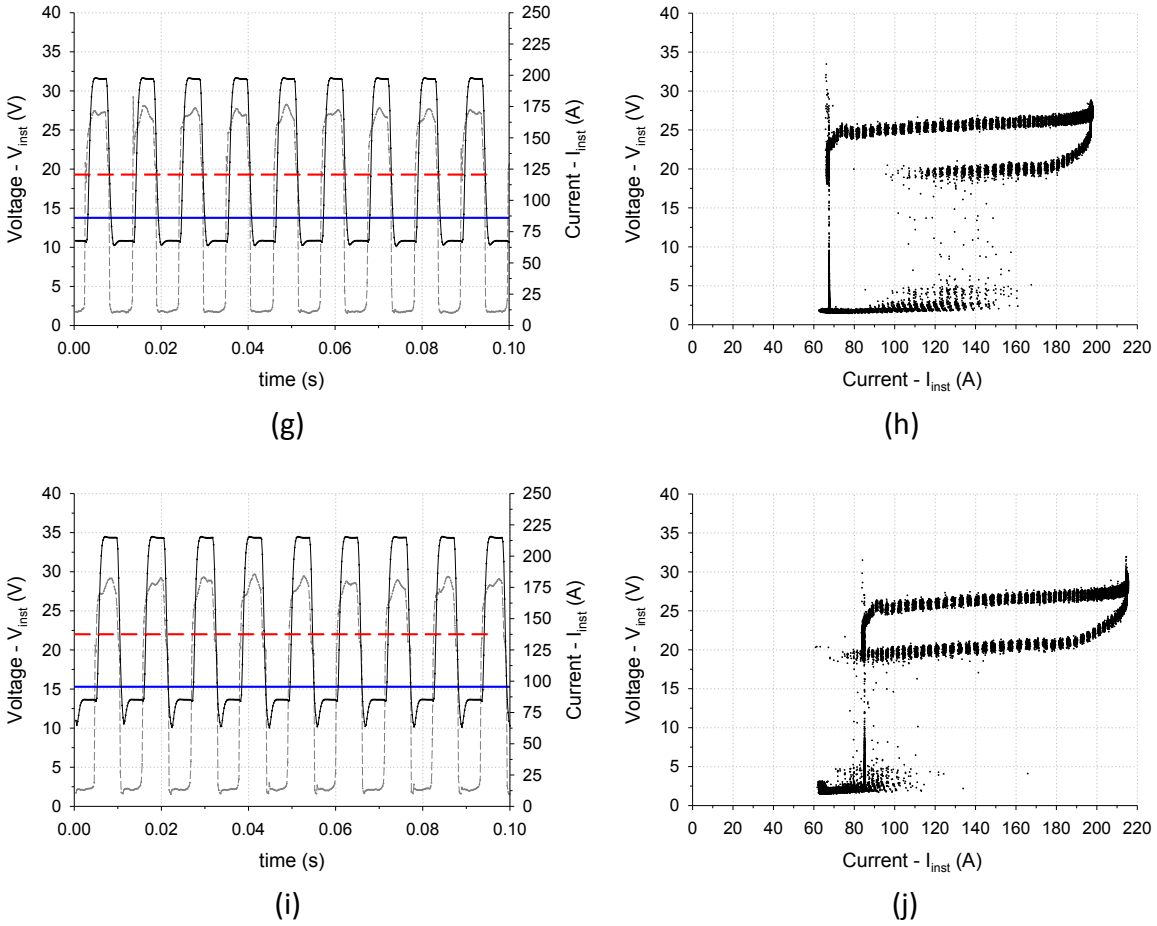

Figure L 24. Electrical transients in study G_2 showing V_{inst} (silver) and I_{inst} (black) on the left, and scatter plots on the right. Trial 1 is represented in (a) and (b), trial 2 in (c) and (d), trial 3 in (e) and (f), trial 4 in (g) and (h), and trial 5 in graphs (i) and (j).

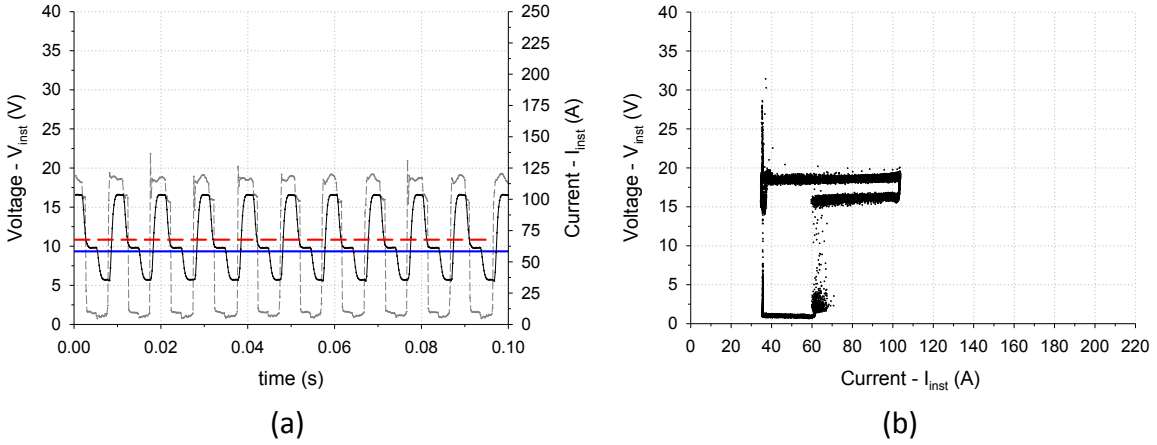

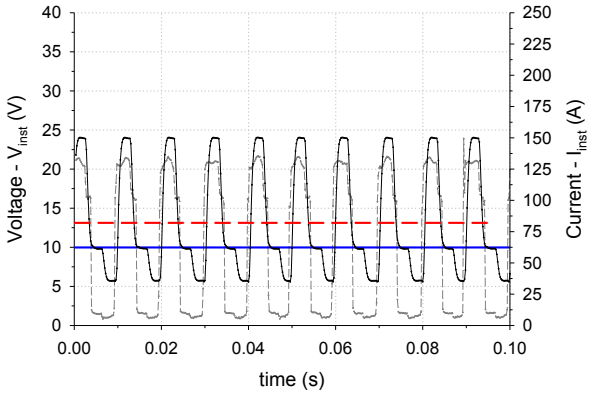
Voltage - V_{inst} (V)
Current - I_{inst} (A)
time (s)

(c)

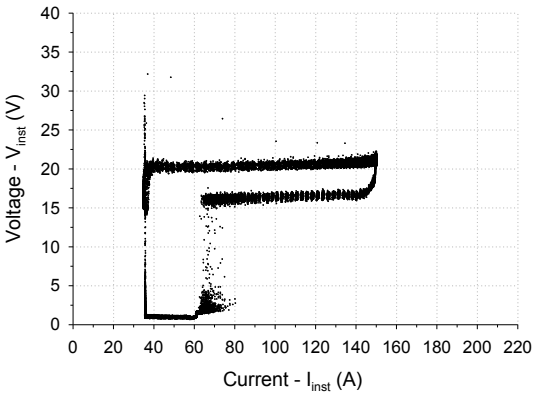
Voltage - V_{inst} (V)
Current - I_{inst} (A)

(d)

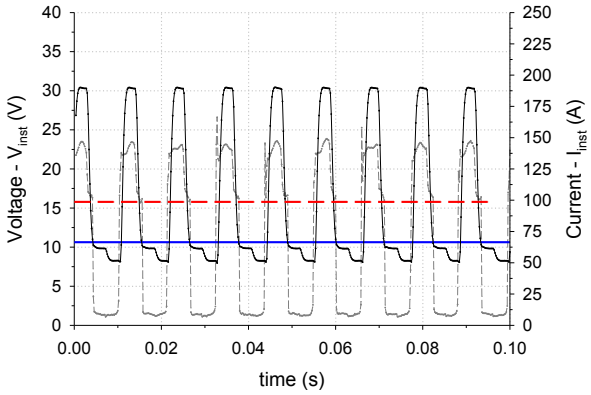
Voltage - V_{inst} (V)
Current - I_{inst} (A)
time (s)

(e)

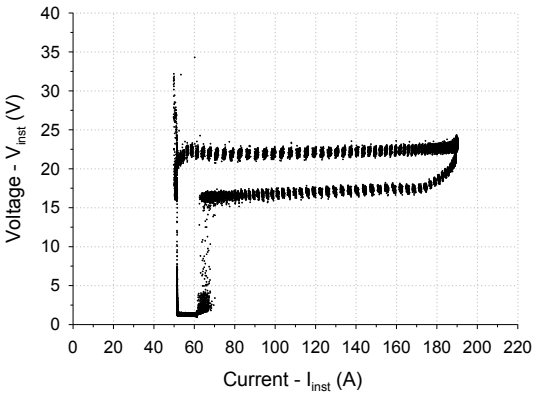
Voltage - V_{inst} (V)
Current - I_{inst} (A)

(f)

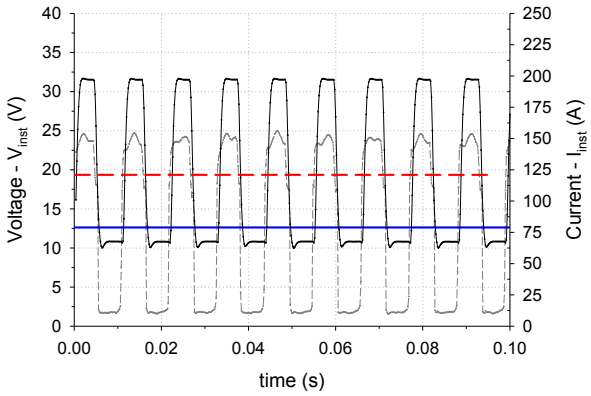
Voltage - V_{inst} (V)
Current - I_{inst} (A)
time (s)

(g)

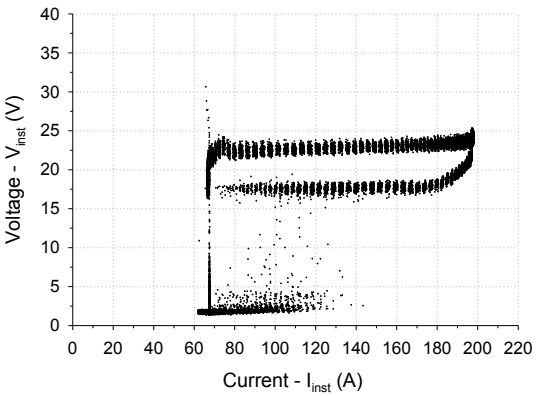
Voltage - V_{inst} (V)
Current - I_{inst} (A)

(h)

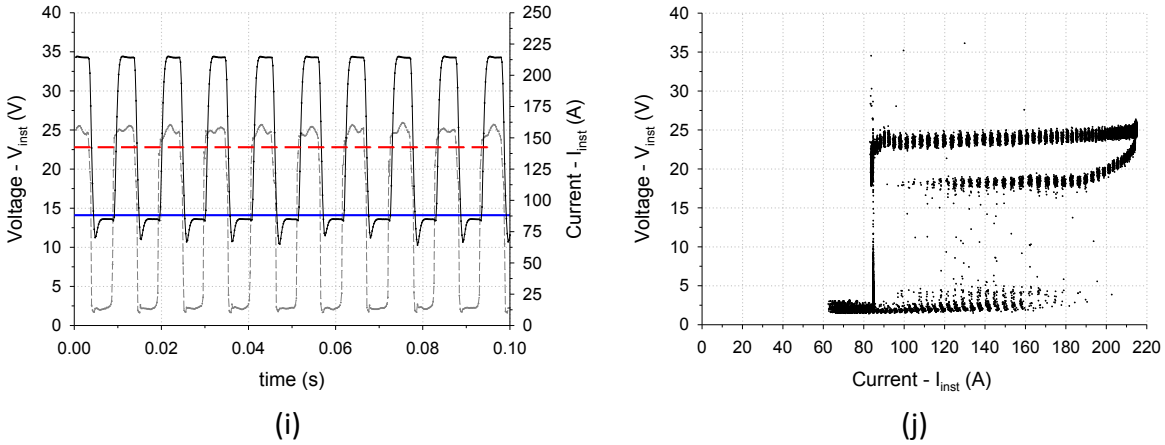

Figure L 25. Electrical transients in study *G3* showing V_{inst} (dashed grey) and I_{inst} (continuous black) lines on the left, and scatter plots on the right. Trial 1 is represented in (a) and (b), trial 2 in (c) and (d), trial 3 in (e) and (f), trial 4 in (g) and (h), and trial 5 in graphs (i) and (j).

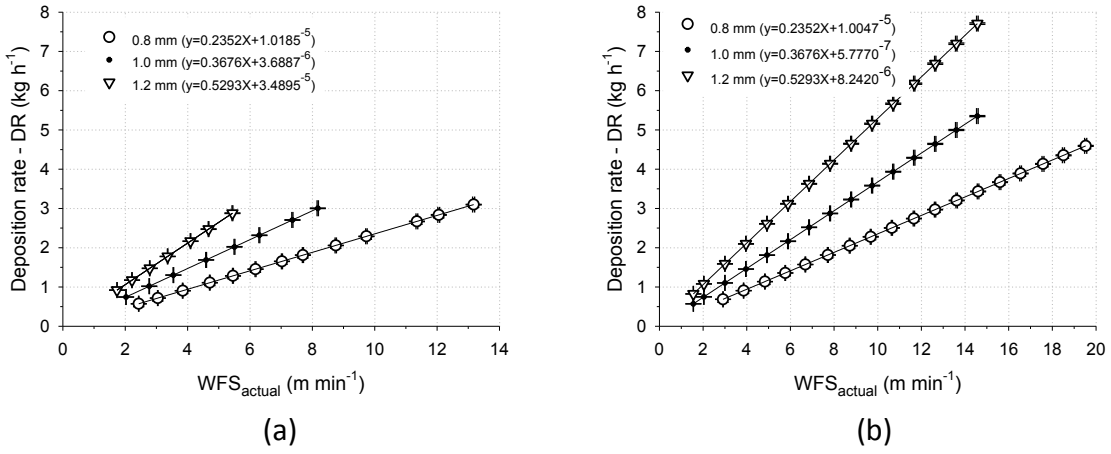

Figure L 26. Effect of WFS_{actual} on DR in (a) CMT and (b) GMAW-P.

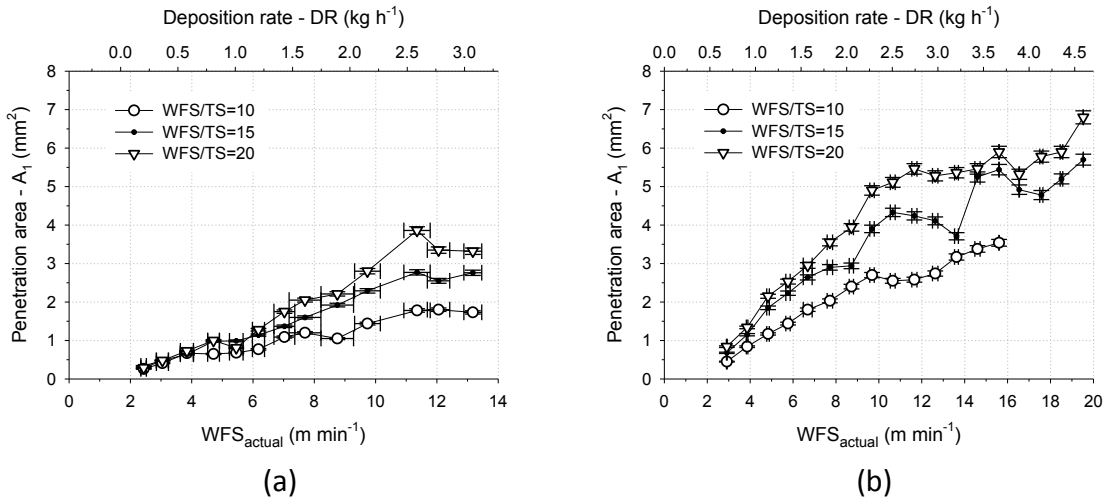

Figure L 27. Effect of WFS_{actual} on A_1 in (a) CMT and (b) GMAW-P.

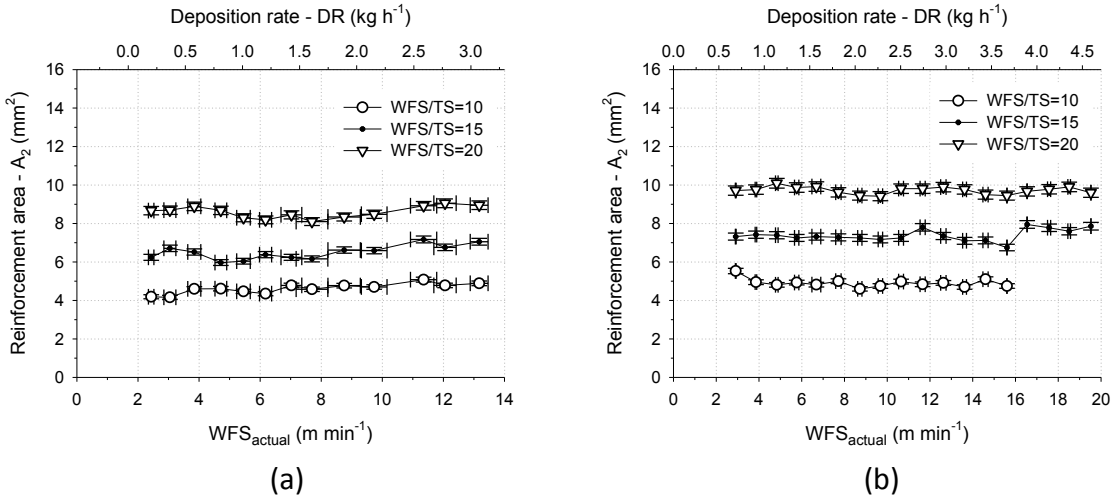

Figure L 28. Effect of WFS_{actual} on A_2 in (a) CMT and (b) GMAW-P.

Appendix M – Machined test pieces of rectangular cross-section (according to ASTM E8/E8M-8)

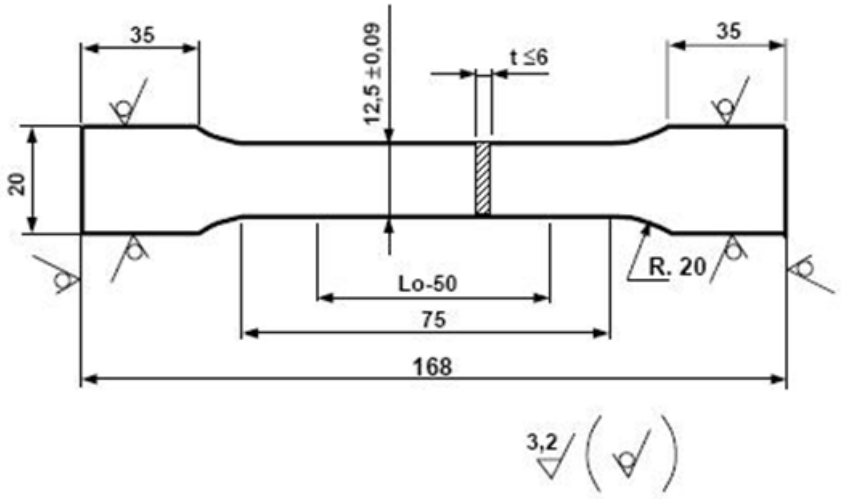

Appendix N – Stress-strain diagrams

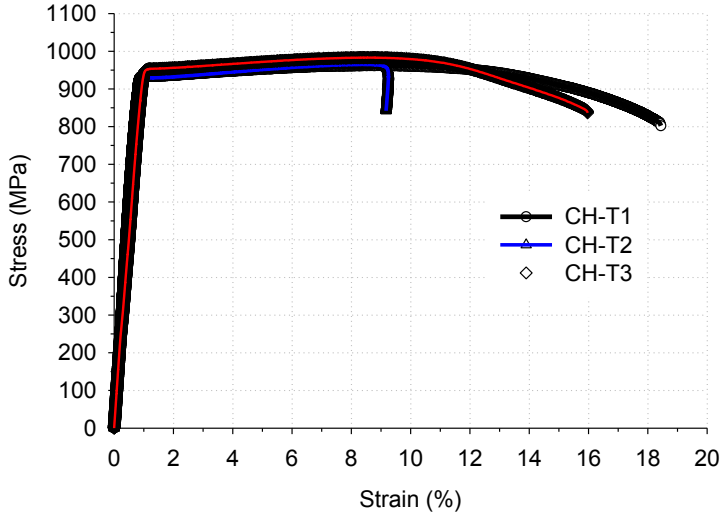

Young Modulus data fitted to equations:

a) *CL-T1: stress = 129095 × strain - 11.014 (R2=0.9994);*
b) *CL-T2: stress = 110414 × strain + 14.761 (R2=0.9999);*
c) *CL-T3: stress = 98646 × strain + 13.393 (R2=0.9996).*

Figure N 1. Stress-strain curves and *E* data obtained for specimens CL-TN.

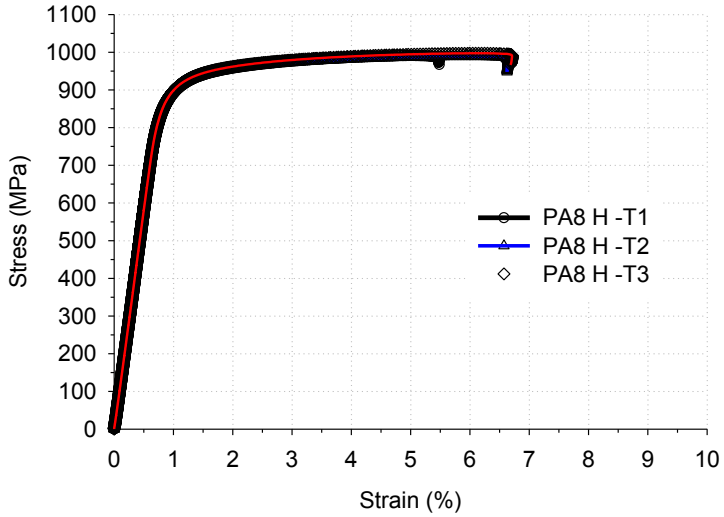

Young Modulus data fitted to equations:

a) *PA8-T1: stress = 123527 × strain - 18.832 (R2=0.9997);*
b) *PA8-T2: stress = 118188 × strain - 8.6934 (R2=0.9999);*
c) *PA8-T3:stress = 117383 × strain - 7.1128 (R2=1.0000);*

Figure N 2. Stress-strain curves and *E* data obtained for specimens PA8 H-TN.

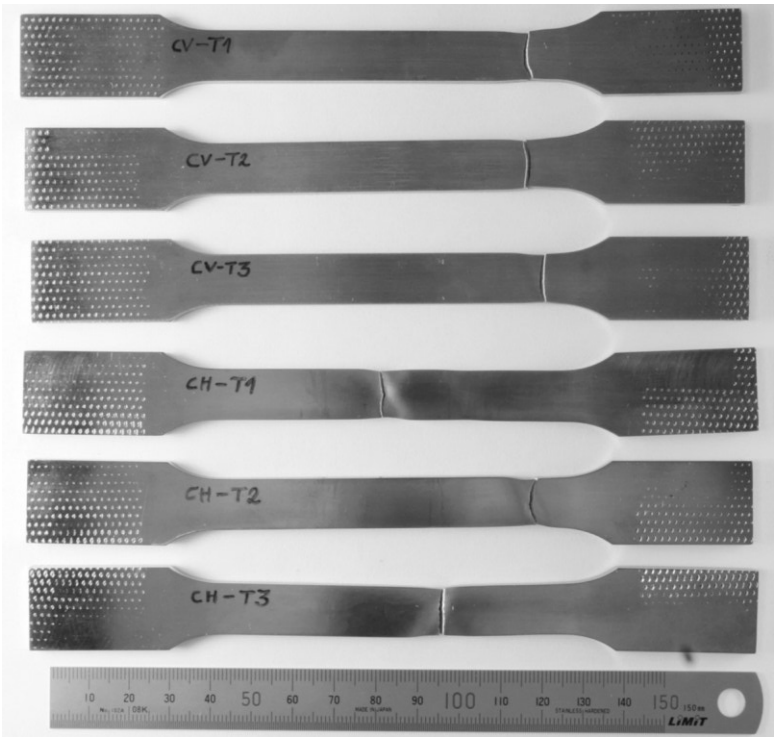

Figure N 3. Location of fracture in tensile specimens machined from Ti-6Al-4V base plate in the parallel (labelled CH) and perpendicular (labelled CV) directions to rolling.

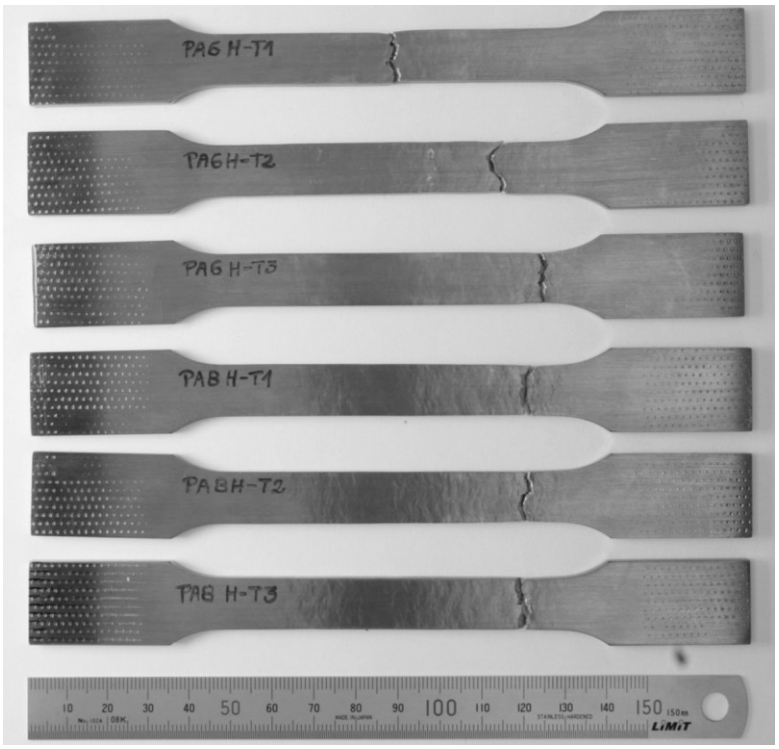

Figure N 4. Location of fracture in tensile specimens machined from WAAM Ti-6Al-4V walls (labelled PA6 and PA8) with their longitudinal axis parallel to the welding direction.

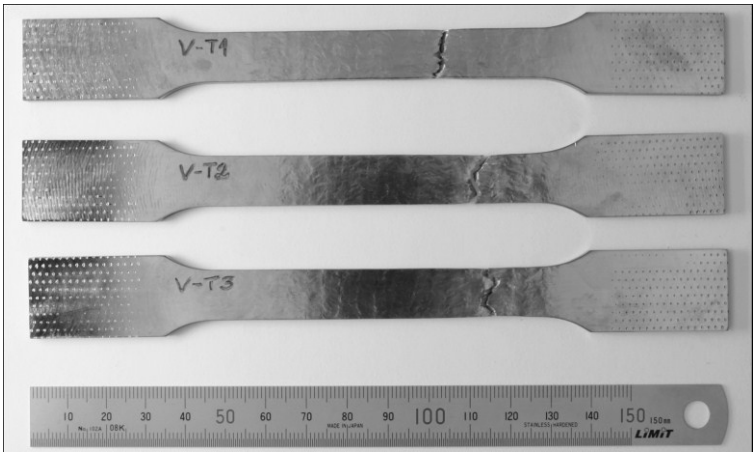

Figure N 5. Location of fracture in tensile specimens machined from WAAM Ti-6Al-4V walls (labelled V) with their longitudinal axis perpendicular to the welding direction.